PH S

Volume

THE PHYSICAL REVIEW

A journal of experimental and theoretical physics established by E. L. Nichols in 1893

Published by the American Institute of Physics for the

AMERICAN PHYSICAL SOCIETY

Officers

President

C. C. LAURITSEN
California Institute of Technology
Pasadena, California

Vice-President

J. H. VAN VLECK
Harvard University
Cambridge, Massachusetts

Secretary

K. K. DARROW
Bell Telephone Laboratories
Office:
Columbia University
New York 27, New York

Treasurer

G. B. PEGRAM
Columbia University
New York 27, New York

Local Secretary for the Pacific Coast

J. KAPLAN
University of California at Los Angeles
Los Angeles, California

Managing Editor

S. A. GOUDSMIT
Brookhaven National Laboratory
Upton, Long Island
New York

BOARD OF EDITORS

Editor

S. A. Goudsmit

Assistant Editor

S. Flügge

Associate Editors

J. Barnes
T. Bonner
R. G. Herb
W. E. Lamb, Jr.
A. J. F. Siegert
W. E. Stephens

Harvey Brooks
R. F. Christy
C. L. Critchfield
M. Deutsch
T. H. Johnson
Bruno Rossi

M. Goldhaber
R. Hofstadter
A. W. Lawson
A. Pais
R. Serber
C. H. Townes

Manuscripts for publication should be submitted to S. A. Goudsmit, Brookhaven National Laboratory, Upton, Long Island, New York. Authors' institutions are requested to pay a publication charge of $10 per page which, if honored, entitles them to 100 free reprints. Instructions will be sent with galley proofs.

Proof and all correspondence concerning papers in the process of publication should be addressed to the Publication Manager, American Institute of Physics, 57 East 55 Street, New York 22, New York.

Subscription Price

United States and Canada $25.00
Elsewhere $27.00

Back Numbers[1]

Yearly back number rate when complete year is available:
Prior to 1949: $20.00
Thereafter: $27.00

Single copies: $2.00 each, prior to July, 1929;
$1.50 each, July, 1929–December, 1941;
$2.00 each, January, 1942–December, 1946;
$1.00 each, January, 1947–December, 1948;
$1.25 each, thereafter.

General Index, 1893–1920: $4.00.

Subscriptions, renewals, and orders for back numbers should be addressed to the American Institute of Physics, 57 East 55 Street, New York 22, New York.

Changes of address in the case of members of the American Physical Society should be addressed to the Treasurer; in the case of other subscribers to the American Institute of Physics.

[1] Per Taylor V Inquiries of Physics Department, Cornell University, Ithaca, New York.

This publication is published semi-monthly at Prince and Lemon Streets, Lancaster, Pennsylvania.

Entered as second-class matter August 6, 1947, at the Post Office at Lancaster, Pennsylvania, under the Act of March 3, 1879.

Acceptance for mailing at special rate of postage provided for in paragraph (d-2), section 34.40, P. L. & R. of 1948, authorized January

THE
PHYSICAL REVIEW

A journal of experimental and theoretical physics established by E. L. Nichols in 1893

SECOND SERIES, VOL. 82, NO. 6 JUNE 15, 1951

The Scattering of 10.4-Mev Deuterons by Hydrogen*

LOUIS ROSEN AND J. C. ALLRED
University of California, Los Alamos Scientific Laboratory, Los Alamos, New Mexico
(Received February 19, 1951)

The $d-p$ elastic scattering cross section has been measured in the angular region 30°–160° CM (center-of-mass system) by means of a nuclear multiple photographic plate camera. Thin hydrogen gas targets were bombarded by the deuterons from the Los Alamos cyclotron, the incident deuteron energy at the center of the reaction volume being 10.4 Mev. Values of the scattering differential cross section are given within an absolute standard error of ±3 percent in the range 40°–140° CM and to ±5 percent in the remainder of the angular range observed. Results of this measurement are in good agreement with previously reported data. The estimated total nuclear cross section, 1.5×10^{-24} cm², is essentially that observed for the $n-d$ collision at the same center of mass energy. A least squares curve fit indicates S-, P- and D-wave interactions to be present at this energy.

I. INTRODUCTION

THE general theoretical interest in the scattering of nuclei involving a small number of nucleons has led us to extend the measurements on the $d-p$ interaction[1] to the region of 10.4-Mev deuteron bombarding energy. A further stimulus for such measurements is to be found in the possibility of comparison between $p-d$ and $n-d$ scatterings as a means of comparing $p-p$ and $n-n$ forces in this energy region. The fact that considerable theoretical work has already been carried out on the $p-d$ and $n-d$ interactions offers encouragement in this direction.[2] Of the experimental data, the most complete are those of Sherr, *et al.* These data were analyzed by Critchfield, who concluded that in the range of energy investigated, the scattering was due principally to S- and P-wave interactions. At higher center-of-mass energies it might be expected that partial waves of higher order would make themselves evident, and it was hoped that the present investigation would provide such information at this higher energy. Preliminary results of the measurements to be discussed in this paper have already been reported,[3] and these are in good agreement with our final results. More recently Mather, *et al.*,[4] and Rodgers, *et al.*,[5] published results for the aforementioned reaction at 10.0- and 9.94-Mev deuteron energies, respectively. These results agree very well with our own results, when a slight correction is made for the small difference in deuteron bombarding energies. It is indeed very gratifying that all three sets of data, obtained by widely different techniques, show substantial agreement to well within quoted accuracies.

II. EXPERIMENTAL

The experiment essentially consists of bombarding thin hydrogen gas targets with 10.4-Mev deuterons and recording on photographic plates the numbers and ranges of the particles emitted into known solid angles. Data are taken at 2.5° intervals between 10° and 65° in the laboratory system with respect to the incident deuteron beam. In order to take data simultaneously at all angles we utilized the nuclear plate camera previously described.[6] This camera is mounted inside a vacuum chamber, at the center of which the cyclotron deuteron beam is brought to a focus by an auxiliary focusing magnet.[7] The focused beam passes through the

* Work done under the auspices of the AEC.
[1] Tuve, Heydenburg, and Hafstad, Phys. Rev. **50**, 806 (1936); R. F. Taschek, Phys. Rev. **61**, 13 (1942); Sherr, Blair, Kratz, Bailey, and Taschek, Phys. Rev. **72**, 662 (1947); Heitler, May, and Powell, Proc. Roy. Soc. (London) **190**, 180 (1947).
[2] H. Primakoff, Phys. Rev. **52**, 1000 (1937); K. Ochiai, Phys. Rev. **52**, 1221 (1937); C. L. Critchfield, Phys. Rev. **73**, 1 (1948); H. S. Massey and R. A. Buckingham, Phys. Rev. **73**, 260 (1948).
[3] J. C. Allred and L. Rosen, Phys. Rev. **79**, 227 (1950).
[4] Mather, Karr, and Bondelid, Phys. Rev. **78**, 292 (1950).
[5] Rodgers, Leiter, and Kruger, Phys. Rev. **78**, 656 (1950).
[6] Allred, Rosen, Tallmadge, and Williams, Rev. Sci. Instr., to be published.
[7] Curtis, Fowler, and Rosen, Rev. Sci. Instr. **20**, 388 (1949).

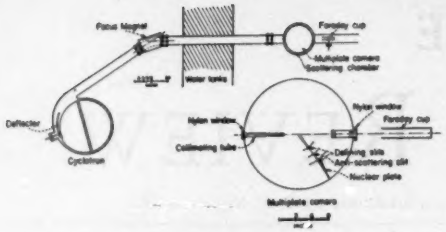

FIG. 1. Experimental arrangement, showing detail of camera geometry.

camera, which contains the hydrogen gas as well as the detectors, and into a well-insulated faraday cup. The front and back windows of the camera are of Nylon, one mil thick.

Figure 1 shows a plan view of the cyclotron and scattering chamber. At the point of entrance into the camera the deuteron beam has a maximum angular divergence of 1.2° in the horizontal plane and 0.85° in the vertical plane by virtue of the slit system geometry in the focus magnet and scattering chamber. The effective angular divergence is probably somewhat less due to the large distance (15 ft) between the cyclotron and the scattering chamber. After passing through the entrance window, the beam passes through four additional circular slits, two of which are $\frac{3}{16}$ inch in diameter and 6 inches apart, the remaining two being antiscattering slits of somewhat larger diameter. Deuterons unduly scattered by the entrance window are thus eliminated before they enter the reaction volume. The scattered particles go directly from the scattering volume to the detectors without further window traversals. Absorbers are, however, sometimes utilized in front of the detectors at the forward angles for the purpose of reducing the background due to low energy multiply-scattered deuterons from the primary beam, or to absorb the scattered deuterons so as to facilitate counting the scattered protons.

The scattering chamber is evacuated by means of an auxiliary pumping stand on which is mounted a liquid air trap and an oil diffusion pump having a pumping speed of 275 liters per second, the diffusion pump being backed by a mechanical fore pump. Without plates in the chamber a pressure of 10^{-5} mm Hg can be easily attained. When the camera is loaded for a run, it is found that four hours of pumping is adequate to give a negligible number of tracks due to scattering from the water vapor and gas liberated by the emulsion during a run. The duration of a run in the present experiment was 5 to 10 minutes, during which time an integrated current of from 12 to 30 microcoulombs of deuterons was passed through the camera. The liquid air trap is isolated from the system during the insertion of gas into the camera as well as during the actual exposure.

The pressure of gas in the camera is measured by means of a mercury manometer and cathetometer. The temperature of the gas is taken to be room temperature, which is the temperature of the camera both before and after a run.

Measurements on the ranges of the scattered deuterons and protons are made on each side of the deuteron direction, i.e., at positive and negative angles with respect to the deuteron beam. From these measurements it is possible to determine precisely the energy and direction of the beam for each run by the method outlined in a previous publication.[8]

The measurement of integrated current is made by connecting the faraday cup to an electronic current integrator. The faraday cup is maintained at a negative potential of 120 volts in order to prevent the collection of stray electrons. Two permanent magnets are mounted longitudinally along the outside of the faraday cup such that their magnetic field will provide a barrier to the outward passage of secondary electrons formed inside the cup. This cylindrical cup is 9 inches long by $1\frac{3}{4}$ inch i.d. The current integrator is calibrated before and after each run, the calibration current being measured by determining with a type K potentiometer the potential drop across a standard resistor which is connected in series with appropriate current limiting resistors between the faraday cup and ground for purposes of the calibration. The counting rate during a given experiment is monitored by a recording galvanometer. The above method of measuring current has been checked by a thermal heating experiment[9] and found to be reliable to two percent or better. Data taken on $p-p$ and $p-He^4$ scattering with the University of Minnesota van de graaff at 3-Mev bombarding energy[6] shows that, at least at this energy, the above method of measuring current is accurate to 1.5 percent.

The general features of the technique for analyzing the plates are given in references 6 and 8. For the present experiment Ilford 100-micron C2 plates were used. These plates are processed for 20 minutes in one part D-19 to three parts water. After 15 minutes in a 2 percent acetic acid stop bath, the plates are fixed for 2 hours in fresh neutral hypo, followed by 30 minutes in acid hypo. The plates are then given a $1\frac{1}{2}$-hour wash in running water, a 5-minute bath in 1 percent glycerine to prevent peeling, and then permitted to dry slowly. The developing and fixing is accompanied by good agitation. All temperatures are kept at 68 F. For most of the analysis work, Leitz Ortholux microscopes are used with 90× oil immersion apochromatic objectives and 6× compensating eyepieces. Eyepiece reticules 7.2 mm×7.2 mm divided into 100 squares are used for making range determination as well as for defining the swath width being counted. The eyepiece reticules are calibrated with stage micrometers.

[8] Rosen, Tallmadge, and Williams, Phys. Rev. **76**, 1283 (1949).
[9] Erickson, Fowler and Stovall, Phys. Rev. **76**, 1141 (1949).

III. DEUTERON-PROTON SCATTERING

For the deuteron-proton collision, the velocity of the center of mass is such that at angles greater than 30° with respect to the incident deuteron beam direction in the laboratory system, only recoil protons are observed. At angles smaller than 30°, two groups of scattered deuterons are detected, one group having quite low energy. However, all three groups were found to be well resolved, and it was therefore possible at a number of angles to obtain a value of cross section for each of three different center-of-mass angles from data at a single laboratory angle. A range distribution showing the three different groups is shown in Fig. 2. It should be mentioned that at the larger angles, the background is considerably less than that shown in Fig. 2. (At angles below 29° it is energetically possible to observe protons from the reaction $D+P\rightarrow P+P+n-2.2$ Mev.) Figure 3 is a typical number *vs* range curve for one of the larger angles. The width of the number *vs* range distribution is mainly due to the finite angular resolution ($\pm 0.9°$) of the slit system geometry between the detectors and the reaction volume.

If Ω is the angle of scattering of the deuteron in the center-of-mass system and θ and ϕ are the corresponding angles in the laboratory system of the scattered deuteron and recoil proton, respectively, we have the following relationships:

$$\cot\theta=(2+\cos\Omega)/\sin\Omega \tag{1}$$

and

$$\Omega=180°-2\phi. \tag{2}$$

If one defines the scattering angle in the center-of-mass system as the angle through which the particles are deflected, Eq. (2) also gives the angle of scattering of the proton, and there is no ambiguity concerning which particle is the incident particle in the laboratory system. The laboratory angular cross sections are given by the following:

$$\sigma(\theta)=(YK\sin\theta)/n_0N \tag{3}$$

where $\sigma(\theta)$ is the laboratory cross section per unit solid angle at the angle θ, Y is the number of tracks counted, n_0 is the number of scattering nuclei per cubic centimeter, N is the number of incident particles, and $K\sin\theta$ is the geometrical term defining target volume and solid angle subtended by detector.

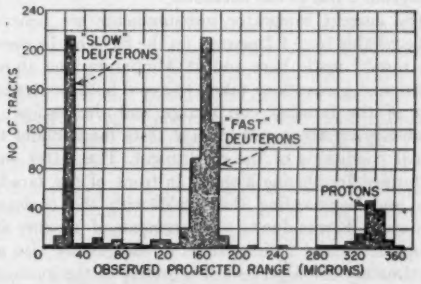

FIG. 2. Number *vs* range histogram for laboratory angle of 25°, showing three particle groups.

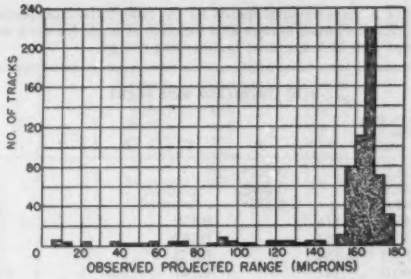

FIG. 3. Number *vs* range histogram for laboratory angle of 42.5°, showing single proton group.

The target volume seen by a given detector is a function only of the slit system geometry and the angle that the slit axis associated with that particular detector makes with the incident beam direction. The defining slits have a width of 0.0450 ± 0.0002 inch and are 2.972 inches apart.

The solid angle subtended by the detector is determined by the slit system geometry and the total swath width on the plate over which tracks are counted. Each swath is normally about 100 microns in width, the beam current and gas pressure being adjusted such that approximately 100 tracks are recorded on each such swath. In order to obtain the statistical accuracy desired, one simply reads an appropriate number of swaths. Each plate contains about 100 usable swaths on the basis of 100 microns per swath. The equation giving an expression for the geometrical factor K in terms of the geometric parameters mentioned above was developed by Critchfield and is given in reference 6, as is also a more detailed discussion of the analysis of the photographic plates.

To convert the laboratory angular cross section, obtained from Eq. (3), to angular cross sections in the center-of-mass system, we have

$$\sigma(\Omega)\sin\Omega d\Omega=\sigma(\theta)\sin\theta d\theta.$$

Since $\sigma(\theta)$ is given by Eq. (3), using Eq. (1), we have

$$\begin{aligned}\sigma(\Omega)&=\sigma(\theta)(1+2\cos\Omega)/\sin\Omega\csc^2\theta\sin^2\Omega\\&=YK(1+2\cos\Omega)/n_0N\csc^4\theta\sin^3\Omega\end{aligned} \tag{4}$$

for the case in which Y refers to the deuterons. Similarly, when Y refers to the protons,

$$\sigma(\Omega)=YK\sin\phi/4\cos\phi n_0N.$$

IV. EXPERIMENTAL RESULTS

Table I gives the results of our measurements. The values given under run P were obtained in a slightly modified version of the experimental set up at the time

TABLE I. Experimental results for the differential cross sections in the center-of-mass system as a function of angle for $d-p$ scattering at 10.4-Mev deuteron bombarding energy.

Center-of-mass angle \ Run	O	Σ	Γ	N	L	P
	$\sigma(\Omega)$ (barns/unit solid angle)					
28.0		0.211[a]				
35.4		0.206[a]				
44.0		0.177[a]				
45.0	0.174		0.170			
50.0	0.163		0.162			
55.0	0.154		0.153			
60.0	0.141		0.147	0.143		0.140
61.5		0.134[a]				
65.0	0.126		0.128			
70.0	0.112		0.119	0.115		0.115
75.0	0.100	0.107[a]	0.108			0.102
80.0	0.0902		0.0961			0.092
80.8		0.0915				
81.0		0.0903[a]				
84.2		0.0821				
85.0	0.0818					
90.0	0.0707					0.073
90.8		0.0727				
95.0	0.0660		0.0694			
100.0	0.0604		0.0587			
105.0	0.0536		0.0558		0.0573	
110.0	0.0543				0.0537	
115.0	0.0526					
120.0	0.0574					
125.0	0.0612					
130.0	0.0742					
130.8		0.0800				
135.0	0.0847					
140.0	0.1077					
148.4		0.164[b]				
150.8		0.177				
151.8		0.178[b]				
155.8		0.207				
157.5		0.248[b]				
161.2		0.238				

[a] Fast deuterons.
[b] Slow deuterons.

of writing of this paper, one year after the original results were obtained.

V. EVALUATION OF ERRORS; CORRECTIONS

The internal consistency of the data for any given run indicates a relative standard deviation which is essentially that of the counting statistics. This should indeed be the case, since for any given run each of the cross sections obtained at the various angles suffers from precisely the same systematic errors. However, as will be seen from Table I, there is also good agreement from one run to the other. This is rather more encouraging, since it gives one confidence in the absolute accuracy of the results.

At each angle investigated at least 4000 tracks were counted. This implies a standard error of ± 1.5 percent due to statistics. The errors incurred because of slit penetration, slit scattering, and other background (see Fig. 2) are approximately ± 1.0 percent. Discrimination against background tracks is here achieved by counting only tracks which have the proper length and direction to have originated in the reaction volume and proceeded through the slit system to the appropriate detectors. Background runs were taken without gas in the camera and with gas in the camera, but with the reaction particles from the center of the camera being prevented from entering the detector collimating slits by an absorber of 30-mil brass placed in front of the slits nearest the reaction volume. These runs showed that errors introduced by the recording of tracks due to protons scattered by $n-p$ collisions in the gas of the chamber and neutron produced proton recoils originating near enough to the surface of the emulsion to make them indistinguishable from tracks of charged particles entering the emulsion surface were completely negligible. Some background tracks due to slit edge scattering and penetration, deuteron disintegration, and multiple scattering were observed; but most of these could be eliminated through range discrimination. Those background tracks which had sufficient length to be included in the range of particles counted were corrected for on the basis of the shape of the number *vs* range curve. This correction, however, never amounted to more than 3 percent and was usually less than 1 percent (see Fig. 3). (Deuteron disintegration could not occur at angles greater than 30°. Multiple scattering of the primary beam was negligible at angles greater than 17.5°.)

Calculations based on Critchfield's analysis of second-order geometry corrections[10] show that such corrections are entirely negligible for angles greater than 15° and amount to approximately 1 percent at 10°. No second-order geometry corrections were made, therefore. In the runs where absorbers were used at the forward angles (10°–25°) empirical corrections were applied for the scattering of the particles which were being observed. These corrections amounted to 8 percent at 10° but were less than 2 percent at 20°. These corrections account for the assignment of larger errors at the smaller angles. The largest angles also were assigned additional errors, since here the tracks were quite short and the plates were difficult to read because of considerable neutron and gamma induced background originating at the collimation slits. Also, for these angles, range straggling made the discrimination against background tracks less accurate.

The current integrator measurements are believed to be reliable to ± 1.7 percent on the basis of the previous tests[6,9] made here and at Minnesota, the above-mentioned precautions taken to avoid both neutralization of the faraday cup charge and the escape of secondary electrons and leakage tests made under the actual conditions of the experiment. The latter were performed by placing a shield in front of the faraday cup and bombarding the shield with the cyclotron deuterons. Errors due to measurements of pressure and temperature and to impurities in the gas are also approximately ± 0.5 percent. The purity of the hydrogen

[10] C. L. Critchfield and D. C. Dodder, Phys. Rev. 75, 419 (1948).

TABLE II. H^1 pressures used and statistical counting errors for various experimental runs.

Run	O	Σ	Γ	N	L	P
Pressure (cm Hg)	10.00	1.030	3.99	22.73	3.14	9.92
Statistical standard error (percent)	±1.5	±3	±3	±3	±3	±2

was accurately determined from the range analyses of the scattered particles. In Fig. 3, for example, O_2 impurities would have given a peak at 325 microns due to elastically scattered deuterons, and He^4 contamination would have given a peak at 230 microns. Errors introduced by geometrical factors are believed to be less than ±1.0 percent. Errors due to microscope calibration and personal factors are also estimated to be ±1.0 percent. All these give an rms absolute standard error of ±2.9 percent in the interval 40°–140° CM. The data in the intervals 30°–40° and 140°–160° are believed to have an absolute standard error of ±5.0 percent for the reasons stated above.

It is felt that negligible error is introduced by multiple small angle scatterings in the hydrogen, since data taken with 1-cm Hg pressure and 20-cm Hg pressure gave the same cross-section values. The pressures used for the various runs are given in Table II. Most of the data were taken at a pressure of 10 cm Hg. Calculations on multiple small-angle scattering using the results of Williams[11] show that in the worst cases only one percent of the protons are deviated by more than 0.005 degree.

The direction and energy of the beam for each of the runs were determined by the method previously described.[8] The direction was thus known to an accuracy of ±0.15° and the energy to an accuracy of ±1.2 percent. The range-energy curves of Lattes, Fowler, and Cuer,[12] corrected in accordance with more recent determinations of the Q values for some of the reactions which they utilized, were used for the energy determination. A check calibration was made at 14.2 Mev, using neutrons from the $D-T$ reaction. The value for the mean proton range thus obtained was in excellent agreement with the range-energy curves of Lattes, *et al.*

It should be pointed out that the very recent work of Rotblat[13] is in good agreement with the corrected results of Lattes, *et al.*, in the region in which they overlap. The fact that the accuracy in energy of the range-energy curve given by Rotblat would appear to be considerably less than ±1 percent in the 5-Mev region lends further credence to the conclusion that the error in energy for a given range in the 10-Mev energy region as deduced from the data of Lattes, Fowler and Cuer is not more than ±1 percent. Indeed, the

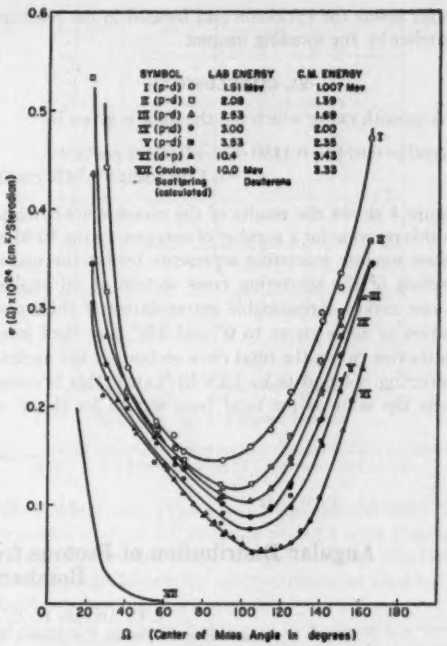

FIG. 4. Differential cross section as function of center-of-mass angle for various bombarding energies, showing present data and those of Sherr, *et al.* Curves I through IV are those of Sherr, *et al.* The present data are represented by curve VI.

recent data of Bradner, *et al.*,[14] bear this out. The error assigned by these authors to the range for a given energy is ±2 percent, which implies an error less than ±1 percent in energy for a given range in the 10-Mev region. Again the data of Bradner, *et al.*, is in excellent agreement with that of Lattes, *et al.*, where the two sets of data overlap. Our own range determination at 14.2 Mev in turn agrees with the value of Bradner, *et al.*, at this energy to better than 1.5 percent. It is therefore felt that the assignment of an error of ±1.2 percent to the energy in the present experiment is rather conservative.

An estimate of the homogeneity of the beam can be obtained from Fig. 3. The width at half-maximum of the peak is about 4.2 percent in energy. Consideration of the width introduced by the finite angular resolution of the slit system and the collimation system, and widening introduced by range straggling, leads to the conclusion that the energy width at half-maximum of the primary deuteron beam is not more than 0.2 Mev. This is indeed what one would expect on the assumption that deuterons from only one orbit are pulled out by the de-

[11] E. J. Williams, Phys. Rev. **58**, 292 (1939).
[12] Lattes, Fowler, and Cuer, Proc. Phys. Soc. (London) **59**, 883 (1947).
[13] J. Rotblat, Nature **165**, 387 (1950).
[14] Bradner, Smith, Barkas, and Bishop, Phys. Rev. **77**, 462 (1950).

flector inside the cyclotron and focused in the reaction chamber by the focusing magnet.

VI. CONCLUSIONS

A smooth curve which fits the data is given by

$$\sigma(\cos\Omega)=0.0740+0.1150\cos\Omega+0.00492\cos^2\Omega -0.1214\cos^3\Omega+0.1424\cos^4\Omega.$$

Figure 4 shows the results of the measurements made on this reaction for a number of energies. In the 10-Mev region nuclear scattering represents by far the major fraction of the scattering cross section at all angles. If one makes a reasonable extrapolation of the cross-section *vs* angle curve to 0° and 180° and then integrates this curve, the total cross section for the nuclear scattering is found to be 1.5×10^{-24} cm². This is essentially the same as the total cross section for the $n-d$ collision at the same center-of-mass energy.[15] It should be pointed out that little error is introduced in the extrapolation of the cross-section curve from 29° to 0° and from 161° to 180°, since the integrand is $\sigma(\Omega)\sin\Omega d\Omega$. The continued shift in the minimum to larger angles at our energy indicates the increased effectiveness of waves of higher order than S-waves. The Legendre expansion indicates that D-waves are in evidence.

We take pleasure in acknowledging the helpful cooperation of Dr. J. L. Fowler, Mr. Alvin M. Hudson, and the entire Los Alamos cyclotron group. For the analysis of most of the plates we are indebted to Mrs. M. Bergstresser, Mrs. R. Booth, Mrs. M. Downs, Mrs. M. Gibson, Mrs. F. Forbes, Mrs. C. Hart, Mrs. C. Lacey, Mrs. O. Milligan, Mrs. M. Osborn, Mrs. F. Peet, Mrs. V. Stovall, and Mrs. L. Tallmadge.

[15] Nuckolls, Bailey, Bennett, Bergstralh, Richards, and Williams, Phys. Rev. 70, 805 (1946).

PHYSICAL REVIEW VOLUME 82, NUMBER 6 JUNE 15, 1951

Angular Distribution of Protons from the D(d, p)T Reaction at 10.3-Mev Bombarding Energy

J. C. ALLRED, D. D. PHILLIPS, AND LOUIS ROSEN
University of California, Los Alamos Scientific Laboratory, Los Alamos, New Mexico

(Received February 19, 1951)

The differential cross section of the D(d, p)T reaction for 10.3-Mev bombarding deuterons has been measured by a nuclear emulsion technique, using a multiple nuclear-plate camera. Values of the cross section are given over essentially the entire range of the center-of-mass angle. The results are fitted within experimental error by the expression:

$$\sigma(\cos\Omega)=6.24P_0+8.28P_2+13.16P_4+8.24P_6+2.31P_8,$$

where Ω is the center-of-mass angle, σ is expressed in millibarns per unit solid angle, and the P_i's are Legendre polynomials. For angles between 20° and 160° the average rms absolute standard error is ±3.8 percent. For angles greater than 160° and less than 20° this error approaches ±5 percent.

I. INTRODUCTION

THE investigation of the D(d, p)T reaction is of special interest because the small number of nucleons involved in the reaction makes possible detailed theoretical treatments such as have been carried out by Konopinski and Teller,[1] Nakano,[2] and Beiduk, Pruett, and Konopinski.[3] Such theoretical analyses are likely to be most fruitful if they are based on accurate experimental data measured over as large an angular interval as possible. In the present experiment, data are taken from 10° to 172.5° in the laboratory system. This makes it possible to obtain the differential cross section as a function of angle over the entire angular range in the center-of-mass system except between 0° and 4°, where geometric conditions prevented the taking of data.

Both the D(d, p)T and D(d, n)He³ reactions have been investigated rather extensively below 3.7 Mev. The latter reaction has been investigated recently at this laboratory[4] using 10.3-Mev deuterons. It is of interest to determine whether the differential cross sections for the two reactions continue to vary with energy as they do from 1 Mev to 3.5 Mev. Furthermore, if, as one might infer from the low energy data, the two reactions are reasonably similar at 10.3 Mev, the differential cross-section curve for the reaction yielding protons might be normalized to the curve for the reaction yielding neutrons in order to make possible a prediction of the latter differential cross section between 4° and 40° in the center-of-mass system, which interval could not be investigated in the D(d, n)He³ experi-

* Work done under the auspices of the AEC.
[1] E. J. Konopinski and E. Teller, Phys. Rev. 73, 822 (1948).
[2] Y. Nakano, Phys. Rev. 76, 981 (1949).
[3] Beiduk, Pruett, and Konopinski, Phys. Rev. 77, 622, 628 (1950).
[4] Erickson, Fowler, and Stovall, Phys. Rev. 76, 1141 (1949).

ment.[4] The reaction yielding protons has been studied recently with 9.94-Mev deuterons at the University of Illinois.[5] The angular region covered in this work was 20°–90° in the center-of-mass system.

II. EXPERIMENTAL

The apparatus and techniques employed in the present experiment are the same as those described by Rosen and Allred[6] for their $d-p$ scattering investigation. The present experiment consists essentially of bombarding a thin deuterium gas target with 10.3-Mev deuterons from the Los Alamos 42-inch cyclotron and recording on photographic plates the intensity and range of the reaction particles which come off at various angles with respect to the incident deuteron beam. The purity of the deuterium gas was determined spectroscopically to be 99.5 percent. The cyclotron instrumentation is the same as that described by Curtis, Fowler, and Rosen.[7] Experimentally, one measures the integrated beam current, the pressure and temperature of the deuterium gas in the camera, the detector and slit system geometry, and the number of tracks of proper range in a rectangular swath of known width along the photographic plate. From these data, the differential cross sections at the various angles of observation can be calculated.[8]

Most of the data for the differential cross-section curves are in the laboratory interval from 65° to 172.5° and in this region elastically scattered deuterons cannot be confused with the reaction protons when range discrimination is used. Figure 1 shows a range distribution of the charged particles arriving at the 132.5° detector. At the more forward angles it is necessary to absorb the elastically scattered deuterons with aluminum foils of appropriate thickness, since here the number of deuterons is sufficient to interfere with the reading of proton tracks. These absorbers are located in front of the plates just behind the outer slit ring (see reference 6). The net effect of such absorbers is to scatter more protons out of the detectors than are scattered into them. Consequently, it is necessary to apply a correction to the number of protons observed at these forward angles where absorbers are used. This correction, which is due principally to multiple scattering, has been evaluated theoretically by Dickinson and Dodder[9] as well as empirically in a previous experiment. It varies from 9 percent at 10° to 1 percent at 40° in the laboratory system for the absorbers and proton energies used here. It was found that the cross sections measured at the forward angles, when corrected as indicated above for absorber scattering, were in statistical agreement with the corresponding cross sections measured at backward angles where no absorbers were used. (The angular distribution must be symmetrical about 90° center-of-mass.) Figure 2 shows a range distribution of the charged particles observed at 12.8° in the laboratory system, where an aluminum absorber 0.018 inch thick was used.

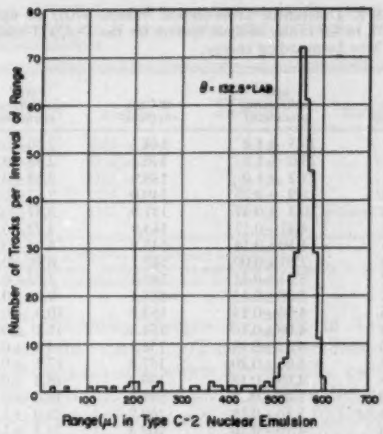

FIG. 1. Range vs number histogram for charged particles observed at 132.5° lab from the D(d, p)T reaction. 1018 tracks.

Deuterium gas pressures from 2 to 20 cm of Hg were used. Integrated deuteron currents from 20 to 120 microcoulombs were found to be necessary to give an adequate number of tracks per unit area of plate.

III. RESULTS AND EVALUATION OF ERRORS

The differential cross section for the reaction D+D→T+P+Q as a function of center-of-mass angle is tabulated in Table I. In the coordinate transformation

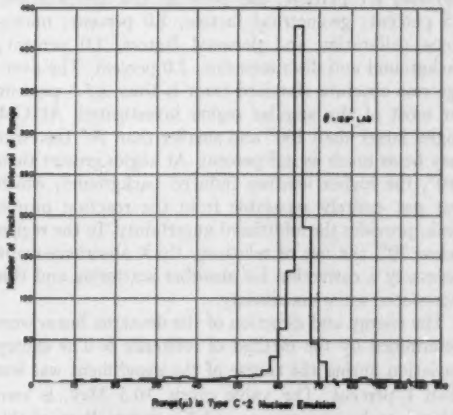

FIG. 2. Range vs number histogram for charged particles observed at 12.8° lab from the D(d, p)T reaction. 18-mil aluminum absorber used. 321 tracks.

[4] Leiter, Rodgers, and Kruger, Phys. Rev. 78, 663 (1950).
[5] Louis Rosen and J. C. Allred, Phys. Rev. 82, 777 (1951).
[7] Curtis, Fowler, and Rosen, Rev. Sci. Instr. 20, 388 (1949).
[8] Allred, Rosen, Tallmadge, and Williams, Rev. Sci. Instr., to be published.
[9] W. C. Dickinson and D. C. Dodder, private communication.

TABLE I. Differential cross-section values, $\sigma(\Omega)$, at various angles, Ω, in the center-of-mass system for the D(d, p)T reaction at 10.3-Mev bombarding energy.

Ω(CM) (degrees)	σ(Ω) (millibarns/ steradian)	Ω(CM) (degrees)	σ(Ω) (millibarns/ steradian)
14.3	28.5 ±1.4	134.1	2.30±0.09
17.4	23.0 ±1.1	136.1	2.38±0.09
18.3	21.2 ±1.0	138.1	2.58±0.10
21.0	18.9 ±0.75	140.0	2.82±0.11
28.5	10.3 ±0.41	141.9	3.37±0.13
35.5	4.47±0.17	143.9	4.22±0.17
35.5	4.50±0.18	145.8	4.63±0.18
49.4	2.61±0.09	147.7	6.16±0.24
56.2	3.31±0.11	149.4	7.42±0.26
56.2	3.38±0.13	151.1	9.24±0.37
62.6	4.04±0.14	152.8	10.6 ±0.42
62.8	4.08±0.16	154.4	11.7 ±0.46
72.6	4.82±0.19	156.1	14.1 ±0.49
75.8	4.95±0.20	157.8	17.1 ±0.60
75.8	4.69±0.18	159.2	18.2 ±0.72
82.0	5.00±0.20	159.4	18.6 ±0.65
85.1	5.16±0.18	160.9	21.0 ±1.1
88.0	4.70±0.16	162.3	21.5 ±1.1
88.0	5.24±0.20	162.5	22.3 ±1.0
95.2	4.53±0.18	164.0	23.6 ±1.1
99.7	4.68±0.18	165.4	28.1 ±1.4
99.7	5.03±0.20	165.5	27.4 ±1.2
105.3	4.64±0.16	167.0	28.3 ±1.3
108.1	4.62±0.16	168.3	30.3 ±1.5
110.6	4.69±0.18	168.5	28.8 ±1.3
115.6	3.87±0.15	170.0	31.5 ±1.4
115.7	4.02±0.16	171.3	33.8 ±1.5
118.1	3.92±0.16	171.4	34.2 ±1.5
120.5	3.96±0.16	172.9	35.3 ±1.6
122.8	3.59±0.14	174.1	37.9 ±1.9
125.1	3.18±0.12	174.3	37.5 ±1.7
129.8	2.69±0.10	175.9	36.4 ±1.8

from laboratory to center-of-mass system, the value of Q is taken as 4.01 Mev.

The average errors involved in the evaluation of cross sections from the data of this experiment are estimated to be as follows: statistical standard error for each angle investigated, 2.3 percent; current integrator, 1.7 percent; gas pressure and temperature, 0.5 percent; geometrical factors, 1.0 percent; microscope calibration and personal factors, 1.0 percent; background and discrimination, 2.0 percent. The average rms absolute standard error is thus ±3.8 percent for most of the angular region investigated. At CM angles larger than 160° and smaller than 20° the error may be as much as ±5 percent. At angles greater than 160°, the higher neutron induced background, which was not entirely separable from the reaction proton peak, provides the additional uncertainty. In the region below 20°, the use of relatively thick absorbers made necessary a correction for absorber scattering and this introduced some uncertainty.

The energy and direction of the deuteron beam were determined by the method of reference 6. The energy variation during the course of the experiment was less than 1 percent. The value given, 10.3 Mev, is considered to be accurate to ±1.5 percent. Part of this error is due to the uncertainty in the value of Q for the D(d, p)T reaction. The absolute values of the angles are considered accurate to ±0.2 degree. Since, however, data were taken simultaneously on both sides of the incident beam direction, the errors in angle on one side of the camera will be compensated, to a large extent, by corresponding errors on the other side.

Background runs were made both with the camera evacuated and with the camera filled with deuterium gas. In the latter case, a thick absorber was placed inside the camera between the target region and the inner slit rings so as to remove charged particles produced by the action of the direct beam. The latter technique was used to investigate the possibility that recoil deuterons resulting from $n-d$ scatterings in the camera might produce tracks which would be confused with those due to the protons from the D(d, p)T reaction. In both cases it was found that the background was negligible at laboratory angles of observation less than 150°. That is, the production of tracks satisfying the applied criteria of direction, range, and origin at the surface of the emulsion comprised less than 0.5 percent of the number of tracks attributed to the protons being observed. For the very large angles of observation, the proton tracks were extremely short and were more easily confused with deuteron tracks resulting from $n-d$ collisions.

When the range criterion can be applied rigorously, however, the possibility of confusing the proton tracks with those of recoil deuterons from $n-d$ collisions is severely limited. This follows from the considerations that (1) the Q for D(d, n)He^3 is less than that for D(d, p)T, and hence a neutron originating in the camera will have a lesser energy than that of a proton emitted in the same direction; (2) the recoil deuteron which such a neutron may produce can receive, at most, only eight-ninths of the energy of the colliding neutron; and (3) the range of a deuteron of given energy is less than that of a proton of the same energy by an appreciable factor.

IV. DISCUSSION

The results of the present work are in good agreement with those of Leiter, Rodgers, and Kruger[5] except at 20° CM at which angle the differential cross section obtained by them is approximately 13 percent lower than our value. Also, our data give no indication of a dip in the cross-section curve at 90° CM as is perhaps suggested by the curve given by Leiter, *et al.*[5]

An expression in terms of Legendre polynomials giving our values of the differential cross section in millibarns per unit solid angle within experimental accuracy is, for $\mu=\cos\Omega$,

$$\sigma(\mu)=6.24P_0+8.28P_2+13.16P_4+8.24P_6+2.31P_8.$$

An additive term, $0.69P_{10}$, gives a better fit for the extrapolated cross section at zero degrees; but this term is essentially unimportant for the curve fit at other angles. If this expression is transformed to one in powers of $\cos\Omega$, it appears that the coefficients of terms

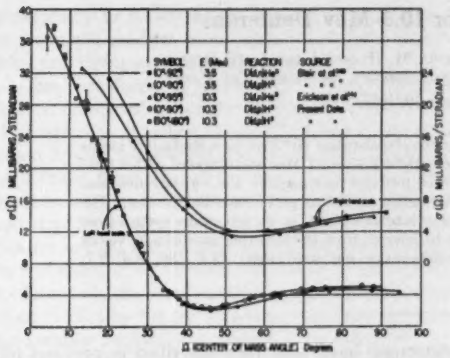

FIG. 3. Differential cross section vs center-of-mass angle for the D(d, p)H³ and D(d, n)He³ reactions for bombarding energies of 3.5 Mev and 10.3 Mev.

containing powers of cosΩ equal to or greater than two are extremely sensitive to the number of terms used in the Legendre expansion. This is due to the very large coefficients of $\cos^n\Omega$ which appear in the higher order Legendre polynomials. For this reason, the power expansion in cosΩ is not given.

In Fig. 3, the results of Blair, *et al.*[10] for a deuteron bombarding energy of 3.5 Mev are shown. It is seen that the cross section for the reaction yielding protons follows very closely the cross section for the reaction yielding neutrons for the same bombarding energy. This is also true for a bombarding energy of 10.3 Mev as can be seen by comparing our results for the D(d, p)T reaction with those of Erickson, *et al.*,[4] for the D(d, n)He³ reaction.

Values of the differential cross section in the center-of-mass coordinate system at zero degrees for different bombarding energies are given in Table II. Assuming that the D(d, p)T reaction does indeed yield a cross-section curve which is essentially parallel to the corresponding curve for the D(d, n)He³ reaction when the incident deuteron energy is 10.3 Mev, our zero-degree value seems to be in agreement with the results of Hunter and Richards[11] obtained for the D(d, n)He³ reaction at deuteron bombarding energies below 3.7 Mev. It is not in agreement with the value obtained at zero degrees for the D(d, n)He³ reaction by Erickson, *et al.*[4] However, this latter value is considered quite approximate by the authors, since it was obtained by measuring the Cu^{62} activity induced in Cu^{63} by the $n-2n$ reaction, and the method for calibrating the counters may have introduced a rather large inaccuracy.

TABLE II. Differential cross sections in the center-of-mass coordinate system at zero degrees using bombarding deuterons of various energies.

E (Mev)	Reaction	σ(Ω=0°) (millibarns/steradian)	Reference
2.54	D(d, n)He³	26	11
3.40	D(d, n)He³	27	11
3.69	D(d, n)He³	36	11
10.3	D(d, n)He³	25[a]	4
10.3	D(d, p)T	39[b]	present report

[a] This value is listed as approximate in reference 4.
[b] This value was obtained by extrapolating our results to zero degrees (Fig. 1) and is considered accurate to ±7 percent.

Thanks are due Dr. J. L. Fowler and the Los Alamos cyclotron group for their cooperation during the experimental runs. For the analysis of most of the plates, we wish to thank P. Agee, M. Bergstresser, R. Booth, N. Brown, M. Downs, J. Frazer, M. Gibson, C. Hart, C. Lacey, O. Milligan, M. Osborn, F. Peet, L. Shackelford, V. Stovall, and L. Tallmadge.

[10] Blair, Freier, Lampi, Sleator, and Williams, Phys. Rev. 74, 1599 (1948).

[11] G. T. Hunter and H. T. Richards, Phys. Rev. 76, 1445 (1949)

The D−He⁴ Interaction for 10.3-Mev Deuterons*

JOHN C. ALLRED, DAROL K. FROMAN, ALVIN M. HUDSON,† AND LOUIS ROSEN
University of California, Los Alamos Scientific Laboratory, Los Alamos, New Mexico
(Received February 19, 1951)

Elastic scattering and disintegration of 10.3-Mev deuterons bombarding He^4 have been studied by means of a multiple nuclear plate camera. The reaction $D+He^4 \rightarrow He^4+p+n-2.2$ Mev was observed with a total cross section of 0.3 ± 0.1 barn. The protons show a marked tendency to emerge in the forward direction, and there is some, not very strong, evidence for the formation of He^5 as an intermediate product. The differential elastic scattering cross section was measured at intervals of 2.5° in the laboratory system from 12.5° to 140°. The shape of this cross-section curve can be inferred from the following approximate values (angles in CM system and differential cross sections in millibarns per unit solid angle): 29.4°, 186; 58.4°, 9.7; 97.7°, 69; 129.3°, 37; 157.4°, 82.4.

I. INTRODUCTION

As part of our program for studying light particle interactions, we have recently investigated the angular distribution of the charged products arising from the D−He^4 interaction when 10.3-Mev deuterons are the bombarding particles.

Although the number of nucleons involved in this reaction is larger than desirable for direct theoretical interpretation of the results, the experiment was felt to be worthwhile for the following reasons:

A. Low energy data are already available for this reaction.[1] The use of electronic computers and the low energy data may make interpretation of the results from the present experiment entirely feasible.

B. The bombarding energy available is sufficiently high to afford an opportunity to learn something about the unstable nucleus He^5 and/or the disintegration of the deuteron in its more conventional sense.

The Los Alamos cyclotron served as the accelerator and photographic emulsions as the detectors in the present experiment. Both the experimental arrangement for utilizing the cyclotron beam and the nuclear plate camera (which contains the scattering gas as well as the detectors) have been fully described in previous publications.[2–5]

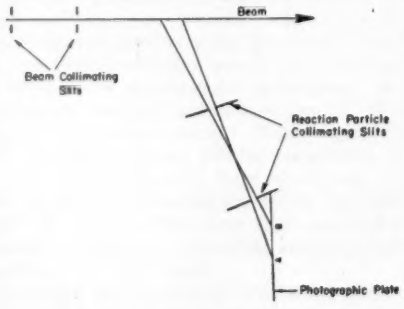

FIG. 1. Slit system-detector geometry.

II. EXPERIMENTAL PROCEDURE

The procedure for making a run is identical to that previously described,[3,4] as is also the method for determining the energy and direction of the projectile deuterons. The range and intensity distribution of the charged products from the subject reaction were recorded every 2.5° in the laboratory interval between 12.5° and 140° with respect to the beam direction.

The angular resolution of the incident beam was ±1.2° in horizontal direction and ±0.8° in vertical direction. The angular resolution of detection was ±0.9°.

Helium pressures of 5 to 20 cm Hg were utilized in order to obtain proper track intensities on the plates as well as to check the effects of multiple scattering in the gas. Beam currents of approximately 0.1 microampere were utilized for times varying from 3 to 10 minutes, depending upon the gas pressure in the camera and the angular region in which good statistics were desired in the particular run. Although spectroscopically pure He^4 was used, the usual range analyses were investigated to determine the extent of impurities present in the scattering gas during the run.

Because of the large inelastic cross sections which the data from this reaction seemed to indicate, the techniques for analyzing the data are somewhat more specialized for this experiment than those previously described. This is caused by the necessity for verifying that the tracks of ranges other than those predicted from conservation of energy and momentum on the basis of elastic scattering are actually representative of reaction products originating in the reaction volume seen by a particular slit system and not due to some kind of background. In order to discuss in detail the method of analyzing the present plates so as to preclude confusion from spurious or background tracks, it will

* This document is based on work performed under the auspices of the AEC.
† Now at Stanford University, Stanford, California.
[1] Blair, Freier, Lampi, and Sleator, Phys. Rev. **75**, 1678 (1949).
[2] Curtis, Fowler, and Rosen, Rev. Sci. Instr. **20**, 388 (1949).
[3] Rosen, Tallmadge, and Williams, Phys. Rev. **76**, 1283 (1949).
[4] L. Rosen and J. C. Allred, Phys. Rev. **82**, 777 (1951).
[5] Allred, Rosen, Tallmadge, and Williams, Rev. Sci. Instr. **22**, 191 (1951).

be necessary to review briefly some of the features of the technique used for taking data in this type of scattering and disintegration experiment.

As has been described previously,[3,4] the photographic plates are mounted around the periphery of the 18-inch i.d. scattering chamber, each plate being mounted behind its own slit system, the axis of which intersects the incident beam axis at the center of the scattering chamber. Figure 1 illustrates the slit system-detector geometry. Each plate can be mounted so that the plane of each emulsion and the long edge of the plate make an angle of either 6° or 12° with the axis of its slit system. In either case, the plate extends lengthwise beyond the region defined by the slit system as seen from the reaction volume. To analyze a plate it is necessary to

1. Make a range analysis of all tracks starting on the surface and proceeding into the emulsion with initial orientation corresponding with origin of the particles in the reaction volume defined by the slits.

2. Count the number of tracks in any desired range interval within an accurately measured width of swath extending lengthwise over the entire region of the plate exhibiting tracks. Examples of range distributions at various angles for the D − He⁴ interaction are shown in Fig. 2. Tracks in the groups *b* and *c* correspond to elastically scattered alpha-particles and deuterons respectively. The differential cross section for elastic scattering at an angle corresponding with a given plate can be determined from the number of such tracks, corrected for background where necessary, observed in a swath of known width, say 1000 microns, together with the slit system-detector geometry, the pressure and temperature of the gas in the camera, and the integrated beam current. The number of swaths counted is determined by the statistical accuracy desired.

Usually, observing the range and direction criteria mentioned above is sufficient precaution to take against counting spurious tracks. However, it can be seen from Fig. 2 that there exists a considerable number of tracks of range other than that attributable to elastically scattered deuterons and alpha-particles, and it is not possible to apply energy and momentum considerations to these tracks in order to have assurance that they are not spurious. It is, therefore, desirable to use another criterion based on the density distribution of the tracks on the plate. As can be seen from Fig. 1, all of the particles which arise in the reaction volume and proceed in such a direction as to pass through a particular slit system must impinge upon the plate in the region *AB* and produce tracks whose lengths bear a fixed relation to the energy of the particles. Tracks which arise by other mechanisms, such as slit scatterings, reactions in the slit system, and neutron induced reactions in the plates or in the gas surrounding the plates, will have a density distribution which, in general, will not be confined to the region *AB* on the plate. Furthermore, the density distribution of such tracks along the plate will not correspond to that predicted by the slit system-detector geometry. Thus, in cases exhibiting broad range distributions, as in the present experiment, it is desirable to plot the density distribution of each range of tracks of interest at each angle

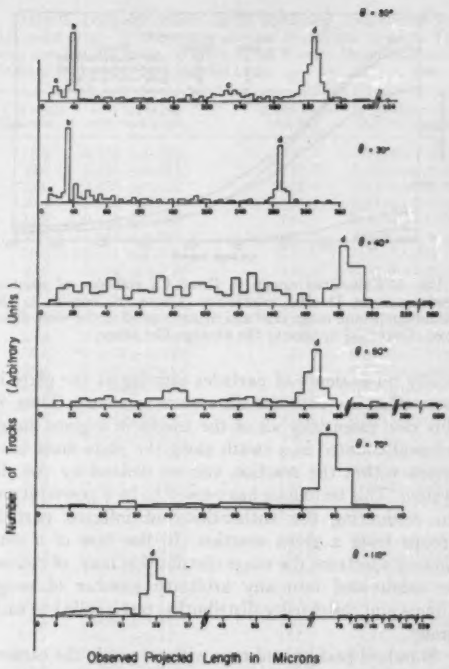

FIG. 2. Histograms of measured track lengths. Groups (b) and (d) represent the elastically projected alpha-particles and scattered deuterons, respectively. Group (a) consists of alpha-particles from either reaction B or reaction C. Other tracks (c) are protons from deuteron disintegration.

investigated. Such density distributions for $\theta = 20°$ are shown in Fig. 3 for the scattered deuterons, *d*, the recoil alphas, *b*, the almost continuous spectrum of protons from D^2 disintegration, *c*, and reaction alphas, *a*. The track density distributions plotted in Fig. 3 show prac-

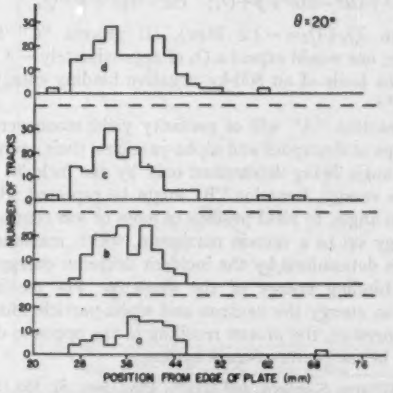

FIG. 3. Density distribution of track groupings designated (a), (b), (c), and (d) in Fig. 2.

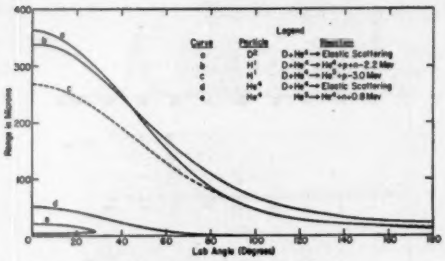

FIG. 4. Calculated ranges in Ilford C2 emulsion of reaction products from D−He⁴ interaction. Curve (b) applies to the maximum proton range (He⁴ and neutron go off in the same direction). Curve (e) applies to the average He⁴ range.

tically no evidence of particles arriving at the plate in nonconformity with the slit system geometry. Thus, in this case essentially all of the tracks in a given range interval counted in a swath along the plate must have arisen within the reaction volume defined by the slit system. This technique has proved to be a powerful one for evaluating the authenticity of inferred particle groups from a given reaction. In the case of a continuous spectrum the range distribution may, of course, be subdivided into any arbitrary number of range groups and the density distribution test applied to each group.

Standard background runs without gas in the camera were made to determine corrections necessary because of primary beam interactions with slits, diaphragms, or water vapor and other gases from plates and camera.

III. THE D−He⁴ INTERACTION

A high energy deuteron can, in principle, interact with an alpha-particle in the following ways:

A. $D+He^4 \rightarrow D+He^4$ (elastic scattering),

B. $D+He^4 \rightarrow He^4+p+n-2.2$ Mev (deuteron disintegration),

C. $D+He^4 \rightarrow He^5+p+Q_1$; $He^5 \rightarrow He^4+n+Q_2$,

where $(Q_1+Q_2=-2.2$ Mev). (If process "C" takes place, one would expect a Q_1 of approximately -3 Mev on the basis of an 800-kv negative binding energy for He^5.[6,7]

Reaction "A" will of necessity yield monoenergetic groups of deuterons and alpha-particles, their energy at any angle being determined only by the incident deuteron energy. Reaction "B" might be expected, at any given angle, to yield protons of more or less continuous energy up to a certain maximum, which maximum is again determined by the incident deuteron energy and the binding energy of the deuteron. For maximum proton energy the neutron and alpha-particle must go off together, the proton recoiling in the opposite direction in the center-of-mass system.

[6] Williams, Shepherd, and Haxby, Phys. Rev. 51, 888 (1937).
[7] Guggenheimer, Heitler, and Powell, Proc. Roy. Soc. (London) 190, 196 (1946).

Reaction "C" might be expected to yield monoenergetic groups of protons. On the other hand, the He^5 nuclei will decay into alpha-particles and neutrons long before they reach the detectors.[8] Since the neutrons will come off in all directions and with energies of approximately 0.64 Mev, the corresponding He^4 nuclei will have a considerable spread in energy at any given angle in the laboratory system.

Let us now consider the collision mechanics of the D−He⁴ interaction for the various possibilities mentioned. Suppose that an incident nucleus of mass m_1 and energy E_0 reacts with a target nucleus of mass m_2 initially at rest, giving rise to two nuclei of masses M_3 and M_4 and energies E_3 and E_4 where the subscript (3) refers to the lighter nucleus. Let θ and ϕ denote the angles which M_3 and M_4, respectively, make with the incident beam direction in the laboratory system of coordinates, and let Ω denote the angle of emission of M_3 in the center-of-mass coordinate system. It can be shown quite generally, on the basis of conservation of energy and momentum, that[8]

$$E_3=E_TA_1\{\cos\theta\pm[(B_1/A_1)-\sin^2\theta]^{\frac{1}{2}}\}^2, \quad (1)$$

$$E_4=E_TA_2\{\cos\phi\pm[(B_2/A_2)-\sin^2\phi]^{\frac{1}{2}}\}^2, \quad (2)$$

$$\sin\theta=\{M_4(E_4/E_T)/M_3[1-(E_4/E_T)]\}^{\frac{1}{2}}\sin\phi, \quad (3)$$

$$\sin\theta=(B_1E_T/E_4)^{\frac{1}{2}}\sin\Omega, \quad (4)$$

$$\cos\Omega=[E_3/(E_TB_1)]^{\frac{1}{2}}\cos\theta-(A_1/B_1)^{\frac{1}{2}} =-[E_4/(E_TB_2)]^{\frac{1}{2}}\cos\phi+(A_2/B_2)^{\frac{1}{2}}, \quad (5)$$

where

$$A_1=m_1M_3(1-Q/E_T)/(M_3+M_4)^2,$$
$$A_2=m_1M_4(1-Q/E_T)/(M_3+M_4)^2,$$
$$B_1=m_2M_4(1+m_1Q/m_2E_T)/(M_3+M_4)^2,$$
$$B_2=m_2M_3(1+m_1Q/m_2E_T)/(M_3+M_4)^2,$$
$$E_T=E_0+Q.$$

Further, it can be shown from geometrical considerations that the intensities per unit solid angle for particle emission in the center-of-mass system and in the laboratory system are related by the following:

$$I(\Omega)/I(\theta)=\sin\theta d\theta/\sin\Omega d\Omega =(A_1B_1)^{\frac{1}{2}}(B_1/A_1-\sin^2\theta)^{\frac{1}{2}}E_T/E_3, \quad (6)$$

$$I(\Omega)/I(\phi)=\sin\phi d\phi/\sin\Omega d\Omega =(A_1B_1)^{\frac{1}{2}}(B_2/A_2-\sin^2\phi)^{\frac{1}{2}}E_T/E_4. \quad (7)$$

Now for the case of elastic scattering (Case A), we have $Q=0$, $m_1=M_3=2$, $m_2=M_4=4$. For the case of simple deuteron disintegration (Case B) we have $Q=-2.2$ Mev. Since this is a three-body problem, we can evaluate the case only if the neutron and alpha-particle go off in the same direction. For this case $m_1=2$, $m_2=4$, $M_3=1$, $M_4=5$, and the proton energy will be a maximum. For Case C, where we assume the formation of a short-lived He^5 nucleus, we have, for

[8] Carlson, Goldstein, Rosen, and Sweeney, Los Alamos Report 723 (unpublished).

ground-state formation, $Q=-3.0$ Mev with the remaining notation identical to that for Case B.

Figure 4 shows the calculated variations of the range with angle in C2 emulsion for the various particles in all three cases. The values obtained differ somewhat from the measured values, since no account is taken of the absorption of energy by the gas in the camera or by absorbers placed in front of plates. Also, the observed values represented projected ranges rather than absolute ranges. It can be seen, however, that the various particle groups to be expected are, for the most part, sufficiently separated in range as to be resolvable. The range-energy relations of Lattes, Fowler, and Cuer[9] were used for these calculations.

IV. RESULTS

The results obtained for the differential elastic scattering cross section as a function of angle are given in Table I. Wherever possible, projected He⁴ particles as well as scattered deuterons were counted; and, in this way, two points on the cross-section curve were obtained from a single plate. Wherever such checks were made, reasonably good agreement was obtained.

The absolute accuracy of the elastic scattering cross sections is not as good as one might wish, owing to some confusion about counting protons in the deuteron peak. Although corrections were applied for this effect on the basis of the shapes of number *versus* range curves, it is felt that significant errors still remain. These errors depend upon the extent of this so-called background which varies with angle.

No second-order geometry corrections were made. It was, however, necessary to make corrections at 12.5° and 15° for scattering from oxygen in water vapor from the plates. This effect is exaggerated at the small angles because of the low gas pressure used and the relatively high coulomb scattering cross section at forward angles. Coulomb scattering was assumed for the deuterons on oxygen; and, from observations at angles of 20° and 22.5°, where deuterons scattered from oxygen are clearly distinguishable from those scattered by helium, corrections for the effect of oxygen contamination were calculated at smaller angles. These corrections were 8 percent at 12.5° and 4 percent at 15°. At the forward angles it was necessary to apply a further correction for absorbers which were used in some of the exposures to remove alpha-particles and/or background resulting from multiple scattering of the primary beam. This correction was a maximum of 10 percent at 12.5° but less than 1 percent for angles larger than 20°. At angles above 20°, runs were made with and without absorbers and these agreed quite well. The corrections for absorbers were determined empirically and are believed to be accurate to ±15 percent. Calculations by D. C. Dodder and W. C. Dickinson on the basis of multiple small angle scattering agreed well with the empirical corrections.

[9] Lattes, Fowler, and Cuer, Proc. Phys. Soc. (London) **59**, 883 (1947).

TABLE I. Deuteron-helium elastic scattering cross section per unit solid angle in the center-of-mass coordinate system. The cross sections are given in units of 10^{-24} cm². These data were obtained from three experimental runs.

Ω CM angle (degrees)	$\sigma(\Omega)$ barns per unit solid angle	Ω CM angle (degrees)	$\sigma(\Omega)$ barns per unit solid angle
18.4	0.452 ±0.036	109.2	0.0616±0.0028
22.0	0.356 ±0.021	110.6	0.0587±0.0026
23.0	0.326 ±0.020	112.4	0.0576±0.0026
29.4	0.186 ±0.011	114.6	0.0519±0.0023
34.0	0.143 ±0.009	119.8	0.0434±0.0020
36.6	0.112 ±0.007	119.8	0.0445±0.0020
36.6	0.111 ±0.007	119.8	0.0455±0.0027
40.8	0.0761±0.0046	120.6	0.0418±0.0019
43.8	0.0571±0.0034	124.6	0.0378±0.0017
48.2	0.0369±0.0022	127.2	0.0362±0.0016
51.0	0.0223±0.0013	129.3	0.0370±0.0017
55.4	0.0105±0.0006	133.6	0.0374±0.0017
58.4	0.0098±0.0006	133.6	0.0329±0.0020
58.4	0.0097±0.0006	133.6	0.0343±0.0017
62.5	0.0118±0.0007	133.6	0.0371±0.0017
65.4	0.0171±0.0010	134.4	0.0371±0.0017
69.4	0.0217±0.0013	137.8	0.0400±0.0018
72.2	0.0250±0.0011	140.6	0.0436±0.0035
72.2	0.0257±0.0012	141.7	0.0440±0.0035
76.1	0.0343±0.0015	141.7	0.0506±0.0040
78.8	0.0396±0.0024	145.3	0.0454±0.0036
78.8	0.0427±0.0026	145.3	0.0477±0.0038
82.6	0.0467±0.0023	147.4	0.0522±0.0042
82.6	0.0495±0.0030	147.4	0.0551±0.0044
85.2	0.0548±0.0025	149.0	0.0596±0.0048
85.4	0.0570±0.0026	149.0	0.0573±0.0046
85.4	0.0587±0.0026	152.3	0.0683±0.0055
91.6	0.0629±0.0028	152.3	0.0729±0.0058
95.2	0.0694±0.0031	154.1	0.0700±0.0056
97.7	0.0691±0.0031	154.1	0.0755±0.0060
100.6	0.0679±0.0031	155.4	0.0729±0.0058
101.2	0.0709±0.0032	155.4	0.0756±0.0060
103.6	0.0646±0.0029	157.4	0.0824±0.0066
103.6	0.0690±0.0031	158.6	0.0861±0.0069

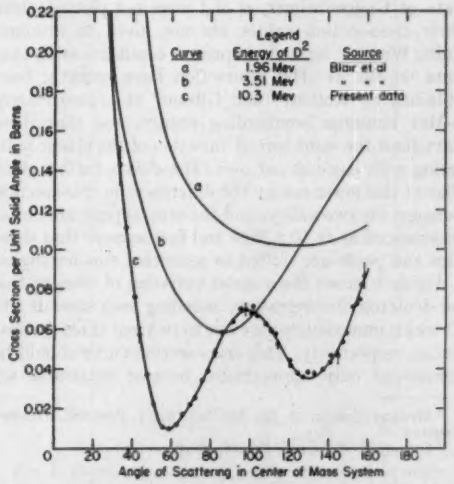

FIG. 5. D−He⁴ differential elastic scattering cross section in the center-of-mass coordinate system for various deuteron energies in the laboratory system of coordinates.

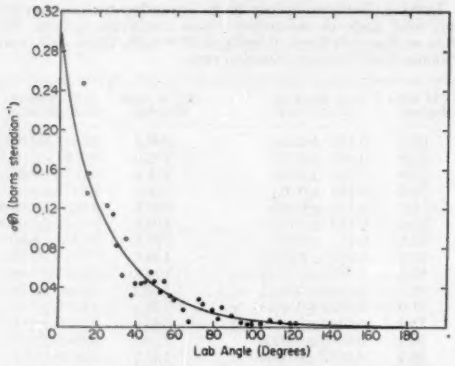

FIG. 6. Differential cross section in the laboratory coordinate system for deuteron disintegration when 10.3-Mev deuterons are incident upon helium. No distinction is made here between reactions B and C.

The root-mean-square standard error estimated from the measurements of temperature, integrated current, geometry, and counting statistics is in most cases less than 4 percent. Since, however, disintegration protons introduced rather large errors, it is estimated that the over-all accuracy of the cross sections at the angles investigated is 18°–22.5°, ±8 percent; 22.5°–70°, ±6 percent; 70°–140°, ±4.5 percent; 140°–160°, ±8 percent. The data of Table I are based on three runs. The deuteron bombarding energy averaged over all three runs is 10.3±0.5 Mev. The maximum variation in energy between runs was 0.1 Mev.

Figure 5 shows the results of the present experiment together with the low energy data of Blair, *et al.*[6] The data of Guggenheimer, *et al.*,[7] were not plotted, since their cross-section values are not given in absolute units. We have learned via private communication that data on the D−He^4 interaction have recently been obtained by Rotblat[10] and Gibson[11] at approximately 8-Mev deuteron bombarding energy, and that these data show the same sort of variation of the elastic scattering with angle as our own. These data further show that at this lower energy the differences in cross section between the two valleys and the central peak are not as pronounced as at 10.3 Mev and furthermore that these dips and peaks are shifted to somewhat smaller angles.

Figure 6 shows the angular variation of cross section for deuteron disintegration, including both cases B and C, which immediately give rise to two and three residual nuclei, respectively. This cross-section curve should be considered only approximate because statistical accuracies were sometimes no better than ±15 percent. Moreover, it was quite impossible to subtract accurately the neutron background and that due to slit edge scattering and penetration. The total cross section for deuteron disintegration over the angular region investigated is $0.3\pm0.1\times10^{-24}$ cm^2. This is to be compared with a total cross section of $1.01\pm0.06\times10^{-24}$ cm^2 for elastic scattering over the same angular region.

[10] Medical College of St. Bartholomew's Hospital, London, England.
[11] University of Bristol, Bristol, England.

V. DISCUSSION

An interesting feature of the number *versus* range curves at small angles is the presence of a group of particles of charge two, lower in energy than the elastically projected He^4 particles. The second group of particles of charge two may result from either reaction *B* or reaction *C*. If these are alpha-particles from reaction *B*, it follows that they are being produced by virtue of some preferential mode of disintegration of the compound Li^6 nucleus. On the other hand, energy grouping would be expected for helium particles arising from reaction C. For example, at 20° in the laboratory system, the He^4 particles would have an average energy of 3.8 Mev and a width at half-maximum of approximately 1.6 Mev. This is not incompatible with the energy and width of the low energy group of alpha-particles observed at this angle (Fig. 2, Group a). It should, however, be pointed out that even a line spectrum of alpha-particles at this low energy would be recorded as a group of approximately this same width.

Before the inelastic part of the D−He^4 interaction can be interpreted with certainty, it will be necessary to perform a coincidence experiment in which the energies of the He^4 particles and protons are observed simultaneously.

No serious attempt has been made to interpret, theoretically, the observed variation with angle of the differential elastic scattering cross section for deuterons on helium; the experimental curve has not even been fitted by a power series in the cosine of the scattering angle. However, it is obvious that the experimental results shown in Fig. 5, taken together with those of Rotblat and Gibson mentioned earlier, form a self-consistent picture in which the angular moments involved in the scattering process progressively increase to higher order as the energy increases.

The authors are indebted to the following personnel of the nuclear plate laboratory for analyzing the many plates from which the present data were taken: E. Agee, M. Bergstresser, R. Booth, F. Forbes, M. Gibson, C. Hart, C. Lacey, O. Milligan, M. Osborn, F. Peet, V. Stovall, and L. Tallmadge. The authors wish also to acknowledge the help of Miss Leona Shackelford in the calculation and compilation of the data as well as in the preparation of the manuscript.

The Application of Proportional Scintillation γ-Ray Counters to the Determination of the Decay Scheme of Au^{198}

PATRICK E. CAVANAGH
Atomic Energy Research Establishment, Harwell, England
(Received November 14, 1950)

Besides the main γ-ray at 0.411 Mev, Au^{198} also emits two higher energy γ-rays of energy 0.67 and 1.09 Mev, present to the extent of only 1.4 and 0.4 percent, respectively. Using large clear blocks of naphthalene +1 percent anthracene as crude γ-ray separators, it has been established, by coincidence absorption measurements, that the high energy γ-rays are in coincidence with β-rays of maximum energy 295 kev. Moreover, it has been established that γ–γ-coincidences also occur, and that the 0.67-Mev γ-ray is in cascade with the 0.411-Mev γ-ray. The 1.09-Mev γ-ray is not in coincidence with either of the others. By comparing the γ–γ-coincidence rate and the β–γ-coincidence rate taken under appropriate conditions, it was possible to determine branching ratios for the 0.67- and 1.09-Mev γ-rays. These are (1.43±0.10) percent, (0.33 ±0.07) percent, respectively, these results being in excellent agreement with those derived from spectrometer measurements. The β–γ- and γ–γ coincidence measurements establish that Hg^{198} has energy levels at 0.411 and 1.09 Mev.

INTRODUCTION

MANY workers have examined Au^{198} with rather conflicting results, especially in regard to the γ-rays emitted. A detailed study of the secondary electron spectrum has been made in this laboratory[1] using sources as large as 0.3 curie; and in addition to the main γ-ray of 0.411 Mev, evidence was found in the Compton and photoelectric spectra for γ-rays of energy 0.67 Mev and 1.09 Mev present to the extent of 1.4 and 0.4 percent, respectively, of the main branch. No evidence of any γ-rays of energy less than 0.411 Mev was found, in agreement with Siegbahn.[2] There is a possibility of the occurrence of a second mode of decay by *K*-capture to Pt^{198}, though this branch could not be greater than about 5 percent of the main branch by β-decay. There is consequently no *a priori* reason for assigning the higher energy γ-rays to the β-decay branch, though the approximate equality of 0.41+0.67 and 1.09 Mev makes it rather tempting. The object of the present work was to establish if there were β-rays in cascade with the higher energy γ-rays and if so, of what maximum energy. It having been established that these results were consistent with a level scheme with energy levels at 0.41 and 1.09 Mev, it remained to show that the 0.67- and 0.41-Mev γ-rays are in cascade and to obtain some estimate of the branching ratio for the 0.67- and 1.09-Mev γ-rays.

γ-RAY COUNTERS

Since the three γ-rays are well spaced in energy, it was possible to use a proportional scintillation γ-ray counter to separate the higher energy γ-rays from the much more intense low energy γ-rays, in the same way as was done previously for the γ-rays of I^{131}.[3] A similar use of a scintillation counter as a crude γ-ray spectrometer had previously been reported by Bell,[4] but where he used pure anthracene, in this case large clear blocks of naphthalene plus 1 percent anthracene were used. These were grown from the melt by Mr. R. F. Jackson, Jr., of this laboratory, who has developed the technique to such a point that it is possible to obtain blocks of optical clarity and uniformity, completely free from any cracks or faults, several inches in diameter and up to two inches thick. These were cut to cylinders of one and three quarter inches in diameter and sealed directly onto an E.M.I. 5032 multiplier. This was followed by a head amplifier of small gain with an input time constant usually of 1 μsec, and a

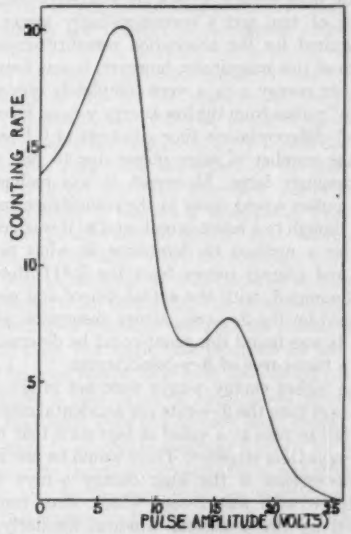

FIG. 1. Distribution of pulses from a well-collimated source of Na^{24} γ-rays showing the resolution of the 1.4- and 2.8-Mev γ-rays.

[1] Cavanagh, Turner, Booker, and Dunster, Proc. Phys. Soc. (London) A64, 13 (1951).
[2] K. Siegbahn and A. Hedgran, Phys. Rev. 75, 523 (1949).
[3] P. E. Cavanagh, Nature 165, 889 (1950).
[4] W. H. Jordan and P. R. Bell, Nucleonics 5, No. 4, 30 (1949).

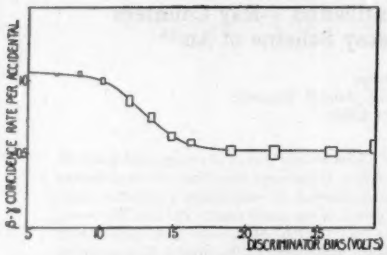

FIG. 2. Bias curve of the ratio of genuine β–γ-coincidences to accidental coincidences for Au^{198} with ~8 mg/cm² Al β-counter window thickness.

1049A 2 Mc/sec pulse amplifier. The crystals were covered with a matte white reflector of magnesium oxide. The energy resolution obtained is illustrated in Fig. 1 with a pulse analyzer curve for the γ-rays of Na^{24}. The general form of the pulse distribution and the resolution is similar to that obtained by Bell.

β–γ-COINCIDENCE MEASUREMENTS

It was necessary to bias out completely the pulses from the 0.411-Mev γ-rays, and then to measure coincidences between the higher energy γ-rays and β-rays recorded by a short dead-time counter. Previously, in the case of I^{131}, it was possible to ascertain the point at which the lower energy γ-rays were biased out by means of absorption measurements in good geometry, as a function of the bias. In this case, however, the high energy γ-rays are relatively weaker by a factor of ten, and a correspondingly larger source was required for the absorption measurements. With a source of this magnitude, however, it was found that the higher energy γ-rays were completely obscured by "pile-up" pulses from the low energy γ-rays. Even when an input differentiation time constant of 0.1 μsec was used, the number of large pulses due to pile up was embarrassingly large. Moreover, it was realized that pile-up pulses would occur in the coincidence measurements, though to a lesser extent, and so it was necessary to devise a method to determine at what point all pulses and pile-up pulses from the 0.411-Mev γ-ray were eliminated, with the actual source and geometry to be used for the β–γ-coincidence absorption measurements. It was found this point could be determined by taking a bias curve of β–γ-coincidences.

If the higher energy γ-rays were not in coincidence with β-rays then the β–γ-rate per accidental coincidence would fall to zero at a value of bias such that no 0.41-Mev γ-rays were recorded. There would be precisely the same occurrence if the high energy γ-rays were in coincidence with soft β-rays which were completely absorbed by the β-counter window. Similarly, if the window were sufficiently thick to absorb the low energy β-group differentially with respect to the high energy β-group, say by a factor of two, then the β–γ-coincidence rate per accidental coincidence would fall to half-value as the bias was increased, and level out at that value of bias, such that the effect of the 0.411-Mev γ-rays was eliminated. Such a characteristic of the bias curve of β–γ-coincidences was in fact found.

The β-rays were recorded by means of a Geiger counter operated about 50 volts below the threshold and working into a 1049A pulse amplifier which has very good overload characteristics. The counter window, together with the air gap, was sufficient to reduce the intensity of 300-kev β-rays to about half-value, whereas it reduced that of the 960-kev β-rays by only a few percent. Both amplifiers were fed via discriminators to a coincidence unit of conventional design. Delays between the two channels were matched out using a variable delay unit, and the coincidence unit was used at such a value of resolving time that not only were all genuine coincidences recorded (to within 1 percent) but some margin was left for the small delays introduced by the variable setting of the two discriminators. This value was 0.3 μsec, and it was measured at intervals throughout the experiment and found to remain constant within the statistical accuracy of 1 percent.

For these measurements the source was in the form of an 0.2 mg/cm² layer evaporated onto 1 mg/cm² distrene sheet. The gold had previously been analyzed and found to contain not more than a few p.p.m. of any impurity. The source was activated in the larger Harwell pile, and a small amount of activity was found to be induced in the distrene. This was allowed to decay before coincidence measurements were started. The two counters were used in a close geometry with respect to the source, and counting rates in excess of 50,000/sec and 5000/sec for the β- and γ-counter, respectively, were recorded, together with the coincidence rate, with type 200 scalers.

The bias curve for β–γ-coincidences is shown in Fig. 2 in the form genuine rate/accidental rate, a small genuine rate arising from Compton scattering γ–γ and cosmic coincidences being subtracted. The experimental points are shown as boxes in which the height is the mean error and the width an estimate of the uncertainty of the overall gain of the γ-ray counting system. This gain usually fluctuated by 2 or 3 percent and sometimes drifted by more than this. The gain variations were followed by a recording ratemeter set at a low value of bias, and fed in parallel from the amplifier. It will be seen from the figure that the curve has substantially flattened out at a pulse height corresponding to 20 volts, and it was at about this value of bias that the β–γ-coincidence absorption measurements were made.

It was found possible to follow the absorption of coincidences to 30 mg/cm² aluminum and still retain reasonable accuracy. Beyond this point not only were the counts becoming excessively long, but, also, the genuine rate was rather small compared with the accidental rate and of the same order as the cosmic coincidence rate. It can be proved easily that to a high

degree of approximation, the value of $G/N_\beta N_\gamma$ at zero absorber is the same as that at zero bias, and is, in fact, equal to the reciprocal of the source strength. G/N_γ is obtained by multiplying by the β-ray counting rate, corrected for paralysis loss, and extrapolated to zero absorber. This gives a zero point for the coincidence absorption curve, which is shown in Fig. 3. An absorption curve for the β-rays of Co^{60} of maximum energy 0.310 Mev was measured in the same geometry and under the same conditions of backscattering. The energies of the two β-rays were obviously very close, and the application of the Feather method of comparison gives the maximum energy of the β-rays in coincidence with the high energy γ-rays of Au^{198} as 0.295 Mev. This, together with the γ-ray energies of 0.41, 0.67, and 1.09 Mev, and the main β-ray of maximum energy 0.96 Mev, is compatible with a level scheme for Hg^{198} with energy levels at 0.41 and 1.09 Mev. γ-ray transitions occur between these levels and the ground state and also between the two levels. On this basis, one would expect coincidences between the 0.67- and 0.41-Mev γ-rays.

THE INVESTIGATION OF $\gamma-\gamma$-COINCIDENCES

Since the 0.67-Mev γ-ray is present only in a 1.4 percent branch, it was anticipated that it would only be possible to demonstrate in a qualitative manner that coincidences occur between this and the 0.41-Mev γ-ray. Two proportional scintillation counters were used in this work. One, which was normally used at high gain, so that the great majority of pulses arising from γ-rays were recorded, had an input time constant of 1 μsec; the other, with which a variable bias level was used, had an input time constant of 0.1 μsec to minimize "pile-up." In view of the expected small genuine coincidence rate, it was necessary to ensure that no spurious coincidences occurred owing to scattering processes. The two crystals were mounted facing each other with a lead absorber placed in between and a Na^{24} source to one side such that each counter had an unrestricted view of the source but was entirely obscured from the other by lead. The ratio of the genuine coincidence rate to the product of the two single channel rates was then measured as a function of the thickness of the lead. It fell by about 10 percent in the first 10 g/cm² and thereafter remained constant for increasing thickness of absorber. This geometry with a lead separator of 10 g/cm² was used for the measurements with Au^{198}. Again for these measurements a coincidence resolving time of 0.3 μsec was used.

Briefly, the method of the experiment was to hold one counter at high gain and low bias so as to record most of the γ-rays, while coincidences were measured as a function of bias on the second counter. At low bias on the latter, most of the low energy γ-rays were recorded, and there were a large number of accidental coincidences arising from 0.411-Mev γ-rays being recorded in both counters. The number of genuine

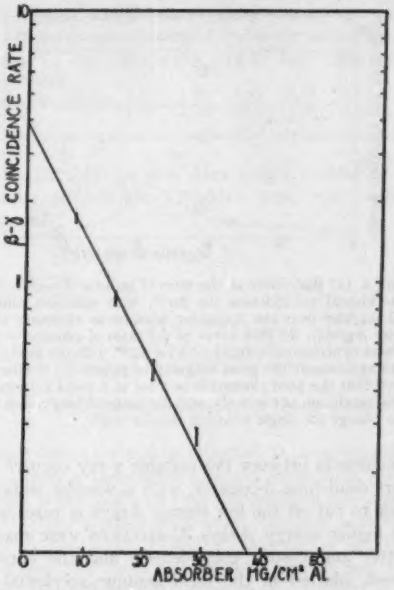

FIG. 3. Coincidence absorption curve of the low energy β-group in Au^{198}.

coincidences between 0.411 and 0.67-Mev γ-rays recorded was relatively low. As the bias on the second counter was increased the number of 0.411-Mev γ-rays recorded fell off relative to that of the 0.67-Mev γ-ray; consequently, the number of accidental coincidences fell off relative to the genuine, or, to put it the other way, the genuine/accidental coincidence rate rises with increasing bias. But for the presence of the noncoincident 1.09-Mev γ-ray, this rise would continue until the 0.411-Mev γ-ray was completely biased out. As it is, the curve rises until the effect of the differential biasing out of the 0.67- and 1.09-Mev γ-rays becomes important, when it reaches a maximum, then it decreases and ideally falls to zero at that value of bias such that the 0.67-Mev γ-ray is completely eliminated. In the first experiment, it was possible to follow the curve barely to the maximum, the genuine coincidence rate becoming of the same order as the cosmic rate. At the same time, the single rate recorded by the second counter became comparable with the background rate. Fortunately, a bias curve of background coincidences showed that most were due to very large pulses, and it was possible to eliminate some 80 percent by a crude pulse analyzer technique. Using this it was possible to work at bias values well over the maximum of the curve. This is given in Fig. 4(a) and shows qualitatively very well the characteristics we have described.

A bias curve for the lower energy γ-ray alone, under the same conditions, was obtained by taking $\beta-\gamma$-

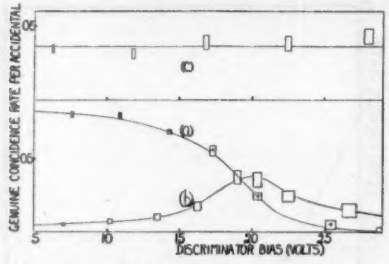

FIG. 4. (*a*) Bias curve of the ratio of genuine β–γ-coincidences to accidental coincidences for Au^{198}, with sufficient aluminum $\sim$80 mg/cm^2 over the β-counter window to eliminate the low energy β-group. (*b*) Bias curve of the ratio of genuine γ–γ-coincidences to accidental coincidences for Au^{198}, with the fixed channel set so as to count the great majority of pulses. (*c*) Similar to (*b*) except that the fixed channel is now set at a point corresponding to the maximum of curve (*b*), and the range of bias values is such as to change the single counting rate by $\sim$10.

coincidences between the variable γ-ray counter and a short dead-time β-counter, with a window sufficiently thick to cut off the low energy β-rays in cascade with the higher energy β-rays. Corrections were made for scatter and cosmic coincidences, and the curve obtained, plotted in the form genuine/accidental coincidence rate, is shown in the same figure. As expected, the curve falls off slowly at first, when the counting rate due to the 0.411-Mev γ-ray is much larger than that due to the higher energy γ-rays. As the bias increases, the genuine/accidental rate falls off more quickly, and thereafter approaches zero at that value of the bias such that the 0.411-Mev γ-ray is eliminated. The very gradual approach of the curve to the horizontal axis is almost certainly due to pile-up pulses. Qualitatively, therefore, these results are in agreement with a decay scheme in which the two lower energy γ-rays are in cascade, but not the high energy γ-ray. As further evidence of the coincidences having arisen from the 0.67-Mev and the 0.41-Mev γ-rays, the bias which had hitherto been varied was held constant at about the maximum of the γ–γ-coincidence curve. The bias on the other scintillation counter was then varied. This variation was such that, although the counting rate decreased by a factor of about 10 over all, the counting rate owing to the low energy γ-ray was always very much larger than that owing to the high energy γ-rays. Under these circumstances, if the coincidences are caused by 0.411-Mev γ-rays, the genuine/accidental rate should be approximately independent of bias value. That this is so is seen in Fig. 4(c).

Subsequently, it was found that more quantitative deductions could be made from these experiments.

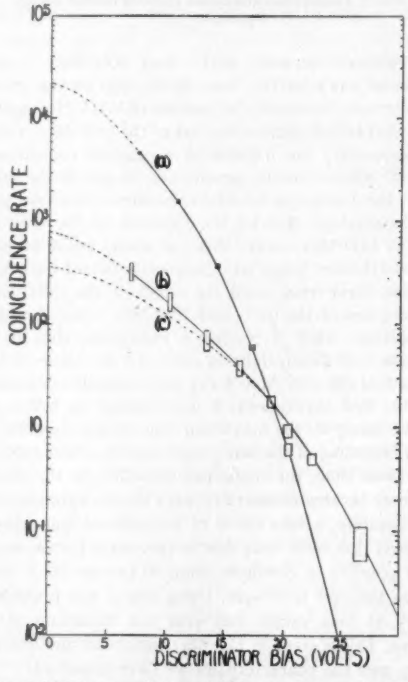

FIG. 5. (*a*) Bias curve of β–γ-coincidences corresponding to 4(*a*). (*b*) Bias curve of γ–γ-coincidences corresponding to 4(*b*). (*c*) Bias curve of 0.67-Mev γ-ray derived from (*b*).

DETERMINATION OF THE BRANCHING RATIOS OF THE 0.67- AND 1.09-MEV γ-RAYS

Let p be the branching ratio of the low energy β-ray, and let a fraction q of these β-rays be in cascade with the 1.09-Mev γ-rays, so that the 0.41- and 0.67-Mev γ-rays are in cascade to the extent of $p(1-q)$ per disintegration. Let the efficiencies of the 0.41-, 0.67-, and 1.09-Mev γ-rays in the fixed bias counter be E_1, E_2, and E_3, and for the variable bias counter, be ϵ_1, ϵ_2, ϵ_3, respectively. Then the counting rate in the fixed bias counter is

$$N_1=N\{E_1(1-pq)+E_2p(1-q)+E_3pq\},$$

and in the variable bias counter

$$N_2=N\{\epsilon_1(1-pq)+\epsilon_2p(1-q)+\epsilon_3pq\}.$$

The γ–γ-coincidence rate is

$$G_{\gamma\gamma}=Np(1-q)\{E_1\epsilon_2+E_2\epsilon_1\}.$$

Now $N_1\doteq NE_1$, since the gain on this counter is high and p is small.

$$\therefore\ G_{\gamma\gamma}/N_1\doteq p(1-q)\{\epsilon_2+(E_2/E_1)\epsilon_1\}$$
$$=0.98p(1-q)\{\epsilon_2+(E_2/E_1)\epsilon_1\},$$

where the factor 0.98 arises on putting in approximate values for p, q, E_2/E_1, and E_3/E_1 in the expression for N_1.

In the β–γ-coincidence measurements, sufficient absorber was placed over the β-counter to exclude the

low energy β-group.

$$\therefore \quad N_\beta = N(1-p)\epsilon_\beta,$$

and

$$G_{\beta\gamma} = N(1-p)\epsilon_\beta\epsilon_1, \quad G_{\beta\gamma}/N_\beta = \epsilon_1.$$

The curve for ϵ_1 [Fig. 5(a)] was extrapolated to low bias values by comparison with a bias curve of the single rate taken at high gain. A bias curve was measured for the counter normally held at fixed bias during the γ–γ-measurement and was extrapolated to zero bias. From this, on the basis that bias curves for γ-rays of different energies fall off in the same ratio at values of bias in the ratio of the energies, it could be determined that E_2/E_1 at the operating point was 1.20 times the value at zero bias.

$$\left(\frac{G_{\gamma\gamma}}{N_1}\right)\Big/\left(\frac{G_{\beta\gamma}}{N_\beta}\right) = 0.98p(1-q)\left(\frac{\epsilon_2}{\epsilon_1}\right)_0\left\{\frac{r_2}{r_1}+1.20\right\},$$

where $(\epsilon_2/\epsilon_1)_0$ is the ratio of the efficiencies for the two γ-rays, and r_2 and r_1 are the fraction of the values at zero bias to which the counting rates due to the two γ-rays are reduced at equal values of bias. The ratio $(\epsilon_2/\epsilon_1)_0$ is given by the ratio of the Compton cross sections, corrected for the finite absorption within the crystal and crystal holder. By experiments with several γ-ray energies ranging from 0.41 to 1.30 Mev, and using uncollimated sources, we have found, as an empirical fact, that within a few percent, the bias curves for γ-rays of different energies fall off in the same ratio at values of bias in the ratio of the energies, provided that there are no effects owing to "pile-up." On this basis, the bias curve for the 0.67-Mev γ-ray can be constructed from that due to the 0.41-Mev γ-ray, which is known experimentally, and in this way (r_2/r_1) may be determined. With this assumption it is possible to calculate a value for the branching ratio $p(1-q)$ for each of the experimental points. These are given in Table I. Over a range of values of bias corresponding to three decades in the bias curve of the 0.41-Mev γ-ray, the value of $p(1-q)$ derived in this way remains remarkably constant. Beyond this point the value falls off, and this may be ascribed to the effects of "pile-up" of the 0.41-Mev γ-rays. The constancy of the value of the branching ratio confirms that the assumption regarding the similarity of bias curves is substantially correct over a wide range of values of counting rate; moreover, it shows that it is the 0.67-Mev γ-ray which is in coincidence with the 0.41-Mev γ-ray. Taking an average over the first five values of bias, the value of the branching ratio for the 0.67-Mev γ-ray is 1.43±0.10 percent.

By considering the ratio of genuine γ–γ-coincidences to accidental coincidences and making the same assumption concerning the similarity of the bias curves for the 0.67- and 1.09-Mev γ-rays as was previously made for the 0.41- and 0.67-Mev γ-rays, a value for the branching ratio of the 1.09-Mev γ-ray may also be determined.

TABLE I. Values of the branching ratio $p(1-q)$.

Bias value	7.0	10.3	13.5	16.3	19.0	20.4	22.5
Limits of values of $p(1-q)$, percent	1.76	1.86	1.66	1.62	1.55	1.15	1.08
	1.21	1.19	1.04	1.19	1.21	0.88	0.85

$$\frac{G_{\gamma\gamma}}{N_1N_2 2\tau} = \frac{1}{2\tau N} \cdot \frac{1.40\times10^{-2}(1+1.20r_1/r_2)}{[(0.83r_1/r_2)+1.40\times10^{-2}+pq(\epsilon_2/\epsilon_1)_0 r_2/r_1]},$$

and $1/(2\tau N)$ can be determined from the β–γ-measurements.

In this case, as would be expected, it is only possible to get values of reasonable accuracy from those points at values of the bias such that the counting rate due to the 0.411-Mev γ-ray is fairly small compared with that of the 0.67-Mev γ-ray. This limits us to values, obtained at 22.5 and 26.7 volts bias, of 0.34 percent and 0.20 percent, respectively, with an over-all statistical accuracy of about 15 percent and 40 percent. The value for the branching ratio of the 1.09-Mev γ-ray is therefore 0.33±0.07 percent. These values for the branching ratios agree very well with those determined by the spectrometer, 1.4 and 0.4 percent, respectively, for the 0.67- and 1.09-Mev γ-rays.

CONCLUSIONS

It has been possible, using proportional scintillation counters, to establish a decay scheme where branching ratios of only about one percent are involved. Moreover it has been possible to measure these branching ratios with good accuracy, entirely by coincidence methods, and obtain results in good agreement with spectrometer measurements. It can now be taken as established that there are energy levels of the Hg^{198} nucleus at 0.411 and 1.09 Mev. Transitions occur between these states and the ground state, and also between the two states. The energy of the main β-branch to the 0.411-Mev level is 0.96 Mev, and that to the 1.09 Mev-level is 0.295 Mev. The branching ratio for the 0.295-Mev β-ray is (1.76 ±0.12) percent. The branching ratios for the 0.67- and 1.09-Mev γ-rays separately are (1.43±0.10) percent and (0.33±0.07) percent, respectively. The accuracies quoted are statistical only. For the 0.67-Mev γ-ray this is believed to represent a fair estimate of the actual accuracy, but the value obtained for the 1.09-Mev γ-ray is probably less reliable.

This work was carried out at the Atomic Energy Research Establishment, Britain, and acknowledgment is made to the Director for permission to publish.

The $3p^3\Sigma \rightarrow 2s^3\Sigma$-Bands of TH and T_2

G. H. DIEKE
*Johns Hopkins University, Baltimore, Maryland**

AND

F. S. TOMKINS
Argonne National Laboratory, Chicago, Illinois

(Received July 14, 1950)

The molecular spectra of TH and T_2 were photographed under high dispersion. The classification of the $3p^3\Sigma \rightarrow 2s^3\Sigma$-system is given for these two molecules as well as the molecular constants for the $3p^3\Sigma$-state. Irregularities in the structure including typical perturbations are accounted for by interaction with the $3p^3\Pi$-state. This system, with 58 known bands and more than 1150 classified lines, is now known considerably better for T_2 than for any other species of hydrogen molecule, including H_2.

I. INTRODUCTION

IN a previous paper[1] the production of the spectra of molecular hydrogen containing tritium was described and details given for the Fulcher band system $3p^3\Pi \rightarrow 2s^3\Sigma$. The present paper gives data on another extensive band system for TH and T_2, preceded by an account of progress in the experimental work.

II. EXPERIMENTAL PROCEDURE

The discharge tube with nickel electrodes described in the previous paper was sealed off with a filling of 77 percent T and 23 percent H at about 2-mm pressure. This tube was used to obtain a series of exposures with the 21-ft Paschen mounting at Johns Hopkins University. The spectrum was photographed from 3000A to 5000A in the second order with a dispersion of 0.6A per mm, and from 5000A to beyond 9000A in the first order (dispersion 1.2A/mm). Except at the extreme long wavelength end the spectrum could be obtained everywhere saturated, that is, with a density such that no additional lines would appear with increased exposures. The exposure times ranged from a few minutes to several hours, depending on the region of the spectrum and the discharge current. At discharge currents of the order of magnitude of one ampere the limit of resolution for the spectrum was determined by the widths of the lines themselves and not by the resolving power of the spectrograph. Lower currents would increase the sharpness of the lines, and therefore the resolution. Usually a compromise had to be reached between very sharp lines at low intensity and somewhat broader lines with high intensity.

The spectrum beyond 9000A to about 12,000A was obtained in the first order of a 21-ft Wadsworth spectrograph with a dispersion of 5 A/mm with exposure times of up to 48 hours.

A second tube was used with a tritium concentration of about 87 percent in the same way. A small tritium reservoir was sealed to the tube so that tritium could be admitted to the discharge tube when through clean-up the pressure in the tube had become so low that the discharge could no longer be maintained. The character of the discharge permitted a rough estimate of the pressure. A comparison of the spectra obtained with the two tubes made it possible to decide which lines belonged to TH and which to T_2. Unfortunately for this purpose, the relative intensities in the molecular spectrum depend strongly on discharge conditions, such as pressure and current. It was not easy to reproduce these conditions exactly, since it was impossible to measure accurately the pressure in the sealed-off tube. Various degrees of clean-up would cause quite considerable pressure changes. For this reason the difference between the concentrations of 70 and 87 percent was not large enough to determine the molecular species to which each line belonged in all cases unequivocally. This was particularly difficult for TH and T_2 blends or H_2 and T_2 blends, which are not infrequent in a spectrum as crowded as the molecular spectrum of hydrogen.

The availability of a tube with a tritium concentration of 99 percent makes the identification of TH and T_2 lines much easier. This tube was used for obtaining the T_2 spectrum with great completeness, as the spectrum is virtually free from contamination by TH and H_2 lines.

We owe this 99 percent tritium sample to the efforts of Dr. B. Weinstock, who enriched an original sample with a tritium concentration of about 90 percent by passing it slowly through palladium. This, as was stated in our previous paper, gives a residue enriched in tritium. The results obtained with the 99 percent tube were, however, not yet used to any extent for the preparation of the present paper.

The variability of the relative intensities with discharge conditions can be used as a help in the classification of difficult parts of the spectrum. Extensive use was made of this by obtaining the spectrum under as divergent discharge conditions as possible. Details of this will be given in a subsequent paper. These aids

* The spectroscopic work at Johns Hopkins University was done under contract between the AEC and Johns Hopkins University.

[1] G. H. Dieke and F. S. Tomkins, Phys. Rev. **76**, 283 (1949).

were not very important for the bands dealt with here as they have a simple and fairly regular structure and usually consist of very strong lines.

The total spectrum is photographed under the conditions just described on 18 plates each 16 inches long. At the present time a considerable part of the spectrum has been measured on at least two plates.

The measurements are carried out in the conventional way under the comparator against iron reference lines. Measurements of good lines on different plates agree usually to within a few thousands of an angstrom unit. The greatest single error is due to uncertainties in the iron comparison spectrum. This situation probably could be remedied somewhat by extreme care. It is doubtful, however, that the considerable additional expenditure of time and effort would be commensurate with the slight improvement which could thus be obtained.

In the very long exposures a systematic shift between tritium and iron lines sometimes cannot be entirely avoided. This shift is due to changes in temperature or barometric pressure during the exposure. Such a shift, which never has been large, is accounted for by applying a constant correction to all wavelengths from such an exposure.

The decrease in dispersion from 0.5A/mm below 5000A to 1.2A/mm between 5000 and 9000A and 5A/mm beyond 9000A brings with it, of course, a correspondingly decreased accuracy in the wavelength measurements. The accuracy in the wave numbers, however, which is the most important feature for the analysis, is the same at about 3500, 5000, and 10,000A.

III. THE $3p^3\Sigma \rightarrow 2s^3\Sigma$ SYSTEM

This is a very extensive band system which extends from about 6000A to 12,000A and almost certainly beyond, and accounts for most of the strongest lines in the photographic infrared. The structure of the analogous bands was given by Richardson and Das[2] and Sandeman[3] for H_2 and by Dieke[4] for DH and D_2.

Table I lists the data for T_2.† The intensities are eye estimates only, obtained from typical plates. They give only a very rough idea of the relative intensities of the lines in one band and no indication at all of bands lying in different regions of the spectrum. This is due to the strong variation of plate sensitivity with wavelength in this region (plate types F, U, N, M, Z chiefly were used). Some of the individual bands extend over more than one thousand angstrom units. Quantitative intensity measurements which will bring out the true intensity relations are now being undertaken.

Greater effort has been made to obtain complete data for T_2 than for TH. This is desirable because T_2 is the heaviest of the six isotopic molecules and is therefore of greater importance than the intermediate ones. It is also a matter of expediency, as the TH spectrum cannot be obtained without the presence of the H_2 and T_2 spectra and therefore blends are more frequent in TH and the weakest lines are more difficult to obtain.

The T_2 system as given in Table I is reasonably complete, but further work will probably extend the system somewhat. The plates from which the data were obtained were not the most suitable ones for the lines with high rotational quantum numbers, so that when it becomes possible to measure further plates the number of lines in most of the bands will be extended.

As is usual in the molecular spectrum of hydrogen the lines of one band system are interlaced with those of many other band systems. In order to analyze the $3p^3\Sigma \rightarrow 2s^3\Sigma$ system, the region between 5700A and 12,000A had to be measured. Our present catalog of lines contains about 10,700 lines in this region, most of which were measured on at least two plates. This does not count thousands of readings on the iron comparison lines.

We believe that this system is now better known for T_2 than for any of the other hydrogen molecules including H_2. Table I contains 58 bands with more than 1150 lines. For the analogous H_2 system 20 bands are known with 135 lines, for DH 14 bands with 173 lines, and for D_2 24 bands with 350 lines.[5]

In a spectrum as complicated as the molecular spectrum of hydrogen it is essential to use all possible criteria by which the correctness of the classification can be judged. Such criteria are the fulfillment of the combination relations, the intensities of the individual lines, and the intensity changes with changes in discharge conditions. The weaker and the more irregular the bands are, the more important is a careful scrutiny of the data with the help of these criteria.

Most of the bands of the $3p^3\Sigma \rightarrow 2s^3\Sigma$ system have a regular structure and are so strong and prominent that there is no doubt whatsoever about the correctness of the classification. The combination relations are satisfied to within a few hundreds of a wave number unless obvious blends are involved. The tables proving this have been omitted here in order to save space. There is usually no need to apply the intensity criteria except for a general qualitative check.

Some of the lines in Table I coming from the highest rotational levels may be uncertain, and so are some lines in the bands with the highest initial vibrational

[2] O. W. Richardson and K. Das, Proc. Roy. Soc. (London) A122, 688; A125, 309 (1929). See also O. W. Richardson, *Molecular Hydrogen and Its Spectrum* (Yale University Press, New Haven, 1934).

[3] I. Sandeman, Proc. Roy. Soc. Edinburgh 49, 245 (1929).

[4] G. H. Dieke, Phys. Rev. 48, 606 (1935).

† The TH data have been omitted to save space.

[5] These figures apply to the published data. These are somewhat defective in the infrared. Before the war new infrared data were obtained at Johns Hopkins University for H_2, DH, and D_2, which resulted in a considerable extension of the $3p^3\Sigma \rightarrow 2s^3\Sigma$ bands for all three molecules. The completeness of these unpublished data is more nearly comparable to that of the T_2 bands given here without, however, quite reaching it.

TABLE I. The $3p^3\Sigma \rightarrow 2s^3\Sigma$ bands of T_2.

K	P-branch ν	P-branch I	R-branch ν	R-branch I
	The 0→0 band at 8532A			
0	...	...	11 689.18	7
1	11 648.51	9	702.86	10
2	621.62	8	712.05	7 z, A
3	590.48	10	716.75	10
4	555.12	9	716.94	9
5	515.69	10	712.65	10
6	472.25	10 z, D	703.89	9
7	424.99	10	690.73	9
8	374.01	9	673.19	5
9	319.37	10	651.36	8
10	261.33	8	625.31	3
11	199.97	9	595.14	7
12	135.49	6	560.91	4
13	067.96	9	522.76	6
14	10 997.62	5	480.79	3
15	924.58	8	435.11	7
16	848.99	5	385.82	3
17	771.07	8	333.10	6
18	690.85	6	277.03	3 x
19	608.57	8	217.80	5
20	524.32	5		
21	438.29	5	090.13	5
22	350.63	3		
23	261.28	3		
	The 0→1 band at 9773A			
0	...	...	10 195.49	1
1	10 155.40	7	209.79	9
2	130.00	9 y	220.26	7
3	100.58	9	226.86	9
4	067.79	7	229.62	7
5	031.53	8	228.48	9
6	9 991.89	5	223.55	6
7	949.03	8	214.78	8
8	902.98	3	202.23	4
9	854.07	6	186.09	7
10	802.20	1	166.18	2
11	747.54	2	142.70	4
12	689.	2	115.85	1
13	639.75	1	085.55	4
14			051.86	0
	The 1→0 band at 7727A			
0	...	...	12 915.25	7
1	12 875.17	9	927.80	10
2	847.73	9	935.26	8
3	815.36	10	937.68	10
4	778.32	9	934.98	9
5	736.61	8	927.30	10
6	690.33	9	914.55	8
7	639.62	10	896.86	10
8	584.64	9	874.25	7
9	525.51	10	846.82	8
10	462.38	7	814.64	5
11	395.44	9	777.79	8
12	324.80	3	736.89	8 z
13	250.48	10 z, D	691.78	8
14	173.13	1		

K	P-branch ν	P-branch I	R-branch ν	R-branch I
	The 1→1 band at 8733A			
0	...	...	11 421.54	7
1	11 382.12	9	434.71	10
2	355.92	9	443.47	7
3	325.51	9 z	447.75	10 z
4	290.99	10	447.75	10 z
5	252.44	10	443.14	10
6	209.95	9	434.19	7
7	163.66	10	420.89	8
8	113.68	8	403.30	2
9	060.15	10	381.47	7
10	003.21	7	355.48	2
11	10 943.03	9	325.51	9 z
12	879.71	5	291.51	6 y
13	813.34	7	253.35	4
14	744.25	4		
15	672.44	6		
16	598.00	5 y, D		
17	521.34	4		
18	442.37	1		
19	361.32	3		
20	278.21	1 ?		
21	193.38	1 ?		
	The 1→2 band at 9991A			
0	...	...	9 974.30	5
1	9 935.48	8	988.19	9 x
2	910.55	7	997.79	8 z
3	882.06	10	10 004.28	10
4	850.03	7	006.68	8
5	814.58	10	005.24	10
6	775.80	3	000.01	8
7	733.84	8	9 991.13	9
8	688.80	3	978.36	4
9	640.70	8	962.00	6
10	589.81	4	941.99	6 y
11	536.26	7	918.59	7
12	480.09	2	891.66	1
13	421.50	3	861.50	2
14	360.53	1		
	The 2→0 band at 7083A			
0	...	...	14 096.32	1
1	14 056.78	6	107.69	8
2	028.71	6	113.52	9 z
3	13 995.27	9	113.52	9 z
4	956.49	8	108.04	4
5	912.47	9	096.91	9
6	863.36	7 z, D	080.22	7 z, D
7	809.23	9	057.99	8 z, D
8	750.28	6	030.29	3
9	686.64	7	13 997.25	7
10	618.43	1	958.78	7 z
11	545.88	5	915.31	5 x
12	469.05	1	866.74	0
13	388.06	3 x	813.13	2
	The 2→1 band at 7919A			
0	...	...	12 602.39	10 x
1	12 563.66	10	614.56	10
2	536.94	9 z	621.58	10
3	505.34	10	623.61	10
4	469.09	10	620.65	9
5	428.22	10	612.69	10

TABLE I.—(*Continued*).

K	P-branch ν	I	R-branch ν	I
	The 2→1 band at 7919A			
6	12 382.95	10	12 599.78	9
7	333.24	10	581.96	10
8	279.31	9	559.30	8
9	221.26	10	531.87	9
10	159.25	8	499.73	6
11	093.46	9	462.98	7
12	023.94	6	421.73	5
13	11 951.00	8	376.09	6
14	874.69	4	326.15	5
15	795.19	6	272.07	6
16	712.65	10 *z*	213.95	0
17	627.27	5	151.84	3
	The 2→2 band at 8842A			
0	...	...	11 155.18	8 *y*
1	11 117.03	7	167.91	8
2	091.48	6	176.20	6
3	061.85	9	180.12	9
4	028.12	7	179.59	6
5	10 990.40	9	174.78	7
6	948.79	7	165.59	3
7	903.38	9	152.05	7
8	854.34	6	134.31	1
9	801.79	8	112.50	4
10	745.84	4	086.35	3 *y*
11	686.68	6		
12	624.38	5		
13	559.11	3		
14	491.02	0		
15	420.29	2		
	The 2→3 band at 10 218A			
0	...	...	9 753.62	1
1	9 716.01	6	766.87	7
2	691.73	5 *x*, *z*	776.40	3
3	663.87	9 *x*	782.24	8 *z*, *x*
4	632.59	7	784.12	3
5	597.90	9	782.24	8 *x*, *z*
6	559.92	7	776.78	3
7	518.79	9 *x*	767.55	7
8	474.55	7	754.66	1
9	427.44	9 *z*	738.05	5
10	377.47	3	717.94	1
11	324.80	10 *z*, *D*	694.32	2
12	269.49	1		
13	211.81	3		
14	151.99	1 *x*		
15	089.67	2		
	The 3→0 band at 6557A			
0	...	...	H_α	
1	15 193.21	9	15 242.41	10
2	164.56	8	246.40	8
3	129.97	10	244.23	10
4	089.47	9	235.86	9
5	043.09	10 *z*	221.30	10
6	14 991.20	10 *z*	200.61	7
7	933.59	10 *z*	173.85	9
8	870.68	8	141.06	6
9	802.53	9	102.43	8
10	729.23	10 *z*	057.79	6 *x*
11	651.04	8	007.72	6
12				
13	480.56	3		

K	P-branch ν	I	R-branch ν	I
	The 3→1 band at 7268A			
0	...	...	13 738.43	8
1	13 700.11	9	749.29	10
2	672.78	8	754.61	9
3	640.09	10	754.33	10
4	602.11	9	748.50	9
5	558.98	10	737.12	10 *z*
6	510.78	9	720.21	7
7	457.65	8	697.87	10
8	399.72	9	670.10	5
9	337.13	10	637.04	9
10	270.05	6	598.82	7
11	198.60	9	555.31	6
12	122.84	10 *y*	506.37	0
13	043.28	4		
	The 3→2 band at 8120A			
0	...	...	12 291.14	8
1	12 253.47	9	302.63	10
2	227.40	9	309.20	9
3	196.57	10	310.82	10
4	161.10	9	307.47	9
5	121.06	10	299.19	10
6	076.60	9	286.02	8
7	027.75	10	268.00	10
8	11 974.75	8	245.16	6
9	917.66	10	217.58	9
10	856.63	7	185.34	2
11	791.81	8	148.50	6
12	723.35	5	107.22	1
13	651.36	10 *z*	061.55	3
	The 3→4 band at 10 456A			
0	...	...	9 532.54	4
1	9 496.08	8	545.25	8
2	472.36	7	554.24	6
3	445.31	9	559.49	9
4	414.65	8	561.02	7
5	380.72	10	558.81	9
6	343.45	5	552.87	6
7	303.05	9	543.28	7
8	259.59	6	529.99	4
9	213.22	8	513.08	7
10	164.01	2	492.75	2
11	112.17	7 *x*, *A*	468.79	6
12	057.63	1	441.83	1
13	000.68	3		
	The 4→0 band at 6120A			
0	...	...	16 322.60	10 *z*
1	283.95	4 *x*	331.57	6
2			334.14	8 *y*
3	(219.16)	9 *z*	329.36	7
4	(176.92)	8 *z*	318.08	3
5			300.12	7
6			275.47	10 *z*, *D*
	The 4→1 band at 6736A			
0	...	...	14 828.74	9
1	14 791.03	10	838.53	10
2	763.12	10	842.02	10
3	729.23	10 *z*	839.40	10
4	689.59	9	830.73	9
5	644.10	10	815.85	10

TABLE I.—(*Continued*).

K	P-branch ν	P-branch I	R-branch ν	R-branch I
	The 4→1 band at 6736A			
6	14 593.01	8	14 794.97	9
7	536.41	10	768.01	10
8	474.46	7	735.11	8
9	407.29	8	690.32	9
10	335.05	2	651.80	6
11	257.94	4	601.60	8 *x, z*
12			545.49	6
	The 4→2 band at 7462A			
0	...	...	13 381.50	7
1	13 344.39	9	391.82	10
2	317.75	8	396.65	9
3	285.74	10	395.92	10
4	248.55	9	389.71	9
5	206.20	10	377.97	10
6	158.84	9	360.77	9
7	106.55	10	338.17	10
8	049.49	8	310.23	10 *z, D*
9	987.83	8	277.10	9
10	921.61	7	238.56	9
11	851.13	8		
12	776.39	4 *z*		
13	697.67	6		
14	615.03	1		
15	528.69	3		
	The 4→3 band at 8332A			
0	...	...	11 979.78	6
1	11 943.31	9	990.72	10
2	917.87	8	996.77	8
3	887.74	10	997.91	10
4	852.98	8	994.12	8
5	813.68	10	985.44	10
6	769.97	8	971.90	7
7	721.93	10	953.54	9
8	669.71	8 *z*	930.36	5
9	613.41	8 *z*	902.48	7
10	553.19	5	869.95	2
11	489.20	7	832.85	4
12	421.87	0	791.31	0
13			745.34	3
	The 4→4 band at 9392A			
0	...	...	10 622.86	4
1	10 587.01	7	634.40	9
2	562.79	5	641.69	7
3	534.42	8	644.63	9
4	502.06	5	643.23	7
5	465.78	8	637.55	9
6	425.66	8 *y*		
7	381.81	7	613.38	8
8	334.34	2	595.03	5
9	283.39	4	572.43	4
10	229.04	1		
	The 4→5 band at 10 708A			
0	...	...	9 310.04	
1	9 274.75	7	322.17	7
2	251.69	3	330.64	8
3	225.19	8	335.34	8
4	195.19	3	336.35	6
5	161.90	9	333.63	8
6	10 125.30	6	10 327.19	2
7	085.53	9	317.10	7
8	042.74	2	303.43	1
9	9 997.00	8	286.04	3
10	948.42	1	265.03	1
11	897.09	3 *z*		
	The 5→1 band at 6294A			
0	...	...	15 872.93	8
1	15 835.79	9	881.30	10 *z*
2	807.28	8	883.24	8
3	772.22	10	878.30	10
4	730.76	8	866.66	8
5	682.96	10	848.28	10
6	628.93	7	823.19	8 *z*
7	568.79	10	791.66	9
8	502.75	6	753.52	7
9	430.94	8	708.95	8
10	353.43	3	657.91	9 *z, D*
11	270.49	5		
	The 5→2 band at 6924A			
0	...	...	14 425.62	9 *z*
1	14 389.12	10 *z*	434.76	10 *z*
2	361.80	10 *z*	437.82	9
3	328.70	10 *z*	434.76	10 *z*
4	289.74	8	425.62	10 *z*
5	245.06	10	410.42	10 *z*
6	194.73	8	389.12	10 *z*
7	138.96	10	361.80	10 *z*
8	077.84	7	328.70	10 *z*
9	011.45	9	289.48	8
10	13 940.04	4		
11	863.74	8		
	The 5→3 band at 7668A			
0	...	...	13 023.97	8
1	12 988.04	9	033.68	10
2	962.02	9	037.98	9
3	930.72	10	036.75	10
4	894.15	9 *z*	030.05	9
5	852.52	10 *z*	017.85	10
6	805.88	9	000.20	8
7	754.32	10	12 977.15	10
8	697.98	8	948.68	8
9	637.03	10	915.05	8
10	571.57	7	876.16	3
11	501.76	8	832.12	6
	The 5→4 band at 8557A			
0	...	...	11 667.04	6 *z*
1	11 631.71	5	677.36	7
2	606.98	6	682.86	5
3	577.39	9	683.45	7
4	543.27	6	679.14	4
5	504.64	9	669.88	7 *z, D*
6	461.56	7	655.89	3
7	414.17	8	637.01	4
8	362.61	6	613.41	7 *y, z*
9	306.95	7	584.98	1
10	247.30	3		
11	183.99	5		

TABLE I.—(*Continued*).

K	P-branch ν	I	R-branch ν	I
	The 5→5 band at 9637A			
0	...	...	10 354.15	7
1	10 319.48	8	365.08	9
2	295.84	6	371.79	8
3	268.10	9	374.18	10
4	236.36	7	372.24	8
5	200.69	9	365.97	9
6	161.16	5	355.48	6
7	117.89	7	340.73	8
8	071.03	3	321.72	4
9	020.44	3 z	298.58	4
10			271.34	3
11	909.74	2	240.06	2
	The 5→6 band at 10 975A			
0	...	...	9 084.79	3
1	9 050.71	3	096.37	4
2	028.26	1	104.35	7 z, *A*
3	002.31	7	108.76	7 z
4	8 972.88	3	108.76	7 z
5	940.14	7	105.45	6
6	904.13	2	098.40	1
7	864.90	7	087.79	2 z
8	822.63	1	073.37	1
9	777.38	3	055.25	9 z, *D*
10			033.79	0
	The 6→2 band at 6478A			
0	...	...	15 422.40	7
1	15 386.50	9	430.36	10
2	358.64	8	431.62	9
3	324.27	10	426.14	10
4	283.51	9	414.00	9
5	236.47	10	395.15	10
6	183.12	9	369.72	9
7	123.75	10	337.69	10
8	058.45	7	299.19	7
9	14 987.34	9	254.15	9 z
10	910.62	8	202.07	3
11	828.34	6 z	143.15	6
12			077.89	2
	The 6→3 band at 7125A			
0	...	...	14 020.67	7
1	13 985.39	8	029.27	10 z
2	958.78	9 z	031.74	9
3	926.28	10	028.15	10
4	887.96	9	018.42	9
5	843.92	10	002.64	10 z
6	794.26	9	13 980.82	8
7	739.14	10	953.06	10 z
8	678.62	8	919.40	6
9	612.86	9 z	880.03	8
10	542.30	8	835.44	3
11	466.71	7	785.31	5
	The 6→4 band at 7866A			
0	...	...	12 663.73	8
1	12 629.05	9	672.84	10
2	603.65	8	676.60	9
6	572.93	10	674.79	10
4	536.94	10 z	667.49	9
5	495.95	10	654.73	10

K	P-branch ν	I	R-branch ν	I
	The 6→4 band at 7866A			
6	12 449.90	9	12 636.51	8
7	398.97	10	612.90	9 z
8	343.24	7	583.97	6
9	282.83	10	549.89	7
10	217.98	6	510.77	3
11	148.88	7	466.91	10 z, *D*
	The 6→5 band at 8796A			
0	...	...	11 350.75	4 z
1	11 316.62	4	360.63	3 z
2	292.55	5	365.48	5 z
3	263.66	5	365.48	5 z
4			360.63	3 z
5	192.01	6	350.75	4 z
6				
7	102.68	1		
	The 6→6 band at 9899A			
0	...	...	10 081.53	3
1	10 048.02	6	091.87	7
2	024.83	4	097.94	5
3	9 997.79	7 z	099.68	9
4	966.61	5	097.09	5
5	931.44	7	090.20	8
6	892.38	3	079.02	3
7	849.65	6	063.58	5
8	803.15	1	043.96	1
9	753.25	0	020.44	5 z, z
	The 7→2 band at 6105A			
0	...	...	16 369.67	2
1	16 334.69	8 z	376.25	7
2	305.91	2	375.54	2
3			367.61	7
4			352.19	1
5			329.68	3
	The 7→3 band at 6676A			
0	...	...	14 967.95	5
1	14 933.59	10 z	975.14	10
2	905.99	10	975.68	9
3	872.07	10	969.54	10
4	831.88	9	956.68	9
5	785.26	10	937.14	10
6	732.49	8	910.91	9
7	673.59	10	878.07	10
8	608.63	10 z	838.53	10 z, z
9	537.97	9	792.73	9
10			740.70	5
11			682.53	1
	The 7→4 band at 7340A			
0	...	...	13 610.96	5 z
1	13 577.31	8	618.82	10
2	550.91	7	620.57	8
3	518.84	10	616.22	10
4	480.98	8	605.83	8
5	437.41	10	589.25	10
6	388.21	8	566.63	8 z
7	333.47	10	537.96	9
8	273.32	7	503.27	5
9	207.87	9	462.65	8 z
10	137.13	10 y	416.20	7 y
11	061.55	9	363.85	4

TABLE I.—(*Continued*).

K	P-branch ν	P-branch I	R-branch ν	R-branch I
	The 7→5 band at 8122A			
0	...	...	12 298.08	7
1	12 265.03	8	306.52	10
2	239.84	6	309.48	8
3	209.55	10	306.94	10
4	174.06	8	298.85	7
5	133.45	10	285.27	10
6	087.78	8	266.18	6
7	037.14	9	241.62	7
8	11 981.51	9 *z, D*	211.62	2
9	921.46	8	176.25	4
10	856.93	5	135.54	0
11	788.37	0		
	The 8→2 band at 5788A*			
0	... ...	.	17 265.80	8 *y*
1	17 231.02	10 *y*	271.26	7
2	202.29	8 *x*	268.61	9 *x, y*
3			257.88	10
4	120.39	8	239.18	9
5	068.22	6	212.66	6
6			178.09	9
7	16 941.20	7		
	The 8→3 band at 6299A			
0	...	...	15 864.13	7
1	15 830.22	10 *z*	870.08	10
2	802.21	8	868.74	8 *x*
3	767.08	10 *z, A*	859.86	10 *z, A*
4	724.86	8	843.69	9
5	675.62	10	820.10	10
6	619.48	8	789.19	8
7	556.55	9	751.00	10
8	487.00	6	705.53	7
9	410.89	8	652.93	8
10	328.35	6	593.17	4
11	T_α		526.34	7
12			452.44	7 *y*
	The 8→4 band at 6888A			
0	...	...	14 507.16	8
1	14 473.80	9	513.73	10
2	447.08	8	513.55	8
3	413.77	10	506.54	10
4	373.95	8	492.73	9 *z, D*
5	327.72	10	472.19	10
6	275.16	7	444.74	10 *z, D*
7	216.43	10	410.86	9
8	151.59	5	370.15	6
9	080.81	8	322.83	6
10	004.15	4	269.03	0
11	13 921.83	6	208.53	2
12	833.82	1 ?		
13	740.45	2 ?		
	The 8→5 band at 7572A			
0	...	...	13 194.25	7
1	13 161.51	9	201.47	10
2	136.07	8 *x*	202.50	10
3	104.53	10 *x*	197.15	10 *x*
4	067.09	10 *y*	185.82	8
5	023.74	10	168.22	10
6	12 974.73	8	144.45	7
7	920.10	10	114.52	9
8	859.98	8 *x*	078.50	4
9	794.35	9 *z*	036.41	9
10	723.28	8	988.49	4
11			934.61	4
	The 8→6 band at 8377A			
0	...	...	11 924.89	2
1	11 892.68	5	932.64	7
2	868.35	3	934.80	4
3	838.58	8	931.35	7
4	803.50	7	922.29	5
5	763.15	8	907.65	7
6	717.64	5	887.34	2
7	667.04	8 *z*	861.48	5
8	611.54	4		
	The 9→3 band at 5983A			
0	...	...		
1	16(617.02)	10 *z*	16 708.97	7
2			705.52	4
3	605.93	7	693.78	10
4	561.51	3		
5	509.54	8	646.24	7
	The 9→4 band at 6512A			
0	...	...	15 347.43	7
1	15 314.74	9	352.59	10
2	287.33	7	350.29	8
3	252.64	10	340.44	10
4	210.60	10 *z, D*	323.15	9
5	161.50	10 *z*	298.34	10 *z*
6	105.57	9	266.07	9
7	042.57	10	226.35	10
8	14 972.74	8	179.24	7
9	896.25	9	124.80	9
10	813.22	6	063.30	5
11	723.73	7	994.62	4
	The 9→5 band at 7120A			
0	...	...	14 034.55	5
1	14 002.64	10 *z*	040.33	9
2	976.16	7 *x, z*	039.23	8
3	943.30	10	031.17	10
4	903.77	8	016.22	7
5	857.70	10	13 994.36	9
6	805.15	8	965.61	6
7	746.25	9	930.02	8
8	681.13	4	887.64	3
9	609.83	9	838.51	8 *z, D*
10	532.61	5	782.71	8 *z, D*
11	449.51	8		
	The 9→6 band at 7828A			
0	...	...	12 765.29	10 *z*
1	12 733.74	9 *z*	771.52	9 *z*
2	708.55	7 *z*	771.52	9 *z*
3	677.43	10	765.29	10 *z*
4	640.23	8	752.68	7
5	597.06	10	733.74	9 *z*

* Note: This band falls in a very dense region with many strong lines, most of them as yet unclassified. Most of the lines listed, although close to the expected position, are probably blends with lines of different origin.

TABLE I.—(*Continued*).

K	P-branch ν	I	R-branch ν	I
	The 9→6 band at 7828A			
6	12 548.00	7	12 708.55	7 *z*
7	493.17	9	676.94	8
8	432.67	6	(639.11)	10 *z*, *D*
9	366.59	8	595.13	6
10	295.05	3	545.32	0
11	218.19	5		
12	136.19	2 ?		
	9→7 band too weak for observation			
	The 10→5 band at 6747A			
0	...	...	14 813.71	7
1	14 782.30	10	818.10	10
2	755.39	7	815.04	10 *z*
3	721.09	9	806.71	10
4	679.76	8	781.13	0
5	633.20	9	755.78	9
6	570.07	7		
7	507.64	8		
	The 10→6 band at 7378A			
0	...	...	13 544.28	10 *z*
1	13 513.51	6	549.30	8
2	487.76	4	547.51	9 *y*
3	455.24	10	540.94	2
4	416.20	8 *z*	517.65	6
5	372.72	9	495.20	9
6	313.04	9 *x*, *z*, *D*		
7	254.69	9		
	The 10→7 band at 8012A			
0	...	...	12 317.98	6 *x*, *z*
1	12 287.63	7 *x*	323.46	7
2	263.11	5	322.92	6
3	232.32	8	317.98	6 *x*, *z*
4	195.67	4	297.20	7
5	155.03	5	277.50	6
6	098.75	4		
7	044.40	7		
	The 11→4 band at 5937A			
0	...	...	16 835.92	7
1	16 805.00	8	837.61	10
2	775.77	4	830.29	7
3	737.66	9 *x*, *z*	813.52	8
4		*z*	787.52	4
5	634.72	6	752.22	10 *z*, *D*
6	569.92	10 *z*, *D*	707.46	9 *x*
7	496.44	10 *y*	653.71	8
	The 11→5 band at 6439A			
0	...	...	15 523.08	6
1	15 492.71	8	525.41	10
2	464.77	6	519.15	7
3	428.43	9	504.21	10
4	383.70	7	480.59	8
5	330.71	10	448.27	10
6	269.51	8	407.19	8
7	200.16	9	357.33	9
8	122.68	7	298.87	5
9	037.18	7	231.80	9 *xx*
10	14 943.64	3	56.08	6 ?
11	842.02	10 *z*		

K	P-branch ν	I	R-branch ν	I
	The 11→6 band at 7012A			
0	...	...	14 253.71	2
1	14 223.91	5	256.65	8
2	197.15	3	251.51	5
3	162.56	8	238.34	8
4	120.21	5	217.08	4
5	070.14	9 *z*, *D*	187.66	8
6	012.41	6	149.94	7 *x*
7	13 947.10	8	104.32	6
8	874.25	5	050.25	3
9	793.95	7	987.81	4
	The 11→7 band at 7672A			
0	...	...	13 027.29	1
1	12 998.10	9	030.79	10
2	972.44	6	026.29	7
3	939.64	9	015.45	8
4	899.60	5	12 996.49	8
5	852.52	10 *z*	969.97	8
6	798.17	5	935.86	4
7	736.89	8 *z*	894.15	10 *z*
8	687.59	2 ?	844.60	0
9			787.18	8
	The 11→8 band at 8438A			
0	...	...		
1			847.67	2
2				
3	759.36	4	835.16	1
4				
5			97.89	2
	The 12→5 band at 6190A			
0	...	...	16	
1	16 120.15	7	149.73	6
2			140.17	6
3	052.75	8	120.40	7
4				
5	15 946.99	9		
6	880.54	6		
7	801.68	5		
	The 12→6 band at 6718A			
0	...	...	14 880.15	5
1	14 851.48	8	880.91	10
2	823.64	5	872.51	8
3	786.85	10	854.56	9
4	741.18	7	828.06	8
5	686.34		792.17	10
6	623.39	7	746.59	5
7			691.85	8
8	470.64	1		
9	381.38	3 *x*		
	The 12→7 band at 7321A			
0	...	...	13 653.85	1
1	13 625.61	8	655.12	4
2	598.82	8 *z*	647.75	3 *xx*
3	563.97	6	631.70	8
4	520.65	1	607.54	6
5	468.66	7	575.41	3
6	409.06	10 *z*		
7	338.17	9 *z*		

TABLE I.—(*Continued*).

K	P-branch ν	I	R-branch ν	I
	The 12→8 band at 8016A			
0	...	...	12	
1	12 442.49	2	471.91	5
2	416.96	1		
3	383.55	8	451.34	5
4				
5	293.22	1		
	The 13→6 band at 6492A			
0	...	...	15 399.90	4 *y, D*
1	15 372.93	7 *x, z, D*	397.43	7
2	343.54	3 *x*	384.22	6
3	303.34	8 *A*	360.13	8
4	253.11	8 *y*		
5	191.92	8		

K	P-branch ν	I	R-branch ν	I
	The 13→7 band at 7053A			
0	...	...	14	
1	14 146.92	2	171.63	4
2	118.68	1	159.64	1
3	080.50	6	137.24	5
4	032.35	2		
5	974.23	7		
	The 13→8 band at 7697A			
0	...	...		
1	12 963.74	1	12 988.49	4
2				
3	900.18	5	956.96	6
4	854.39	5 *y*		
5	798.70	5		

quantum numbers. Where there was a considerable degree of uncertainty, the lines have been omitted.

IV. THE $3p^2\Sigma$ STATE

The final state ($2s^2\Sigma$) is the same as the final state of the Fulcher bands and its properties were given in our previous paper.[1,6]

The constants for the $3p^2\Sigma$ state are given in Tables II and III with the conventional meaning for the symbols used. The rotational constants B_V and D_V were found by a least-square method from the first six rotational differences of every vibrational state for T_2 and from the first four differences for TH. The reason for the different treatment is as follows: The best values for the constants are obtained when the systematic errors caused by the omission of higher terms in the expression for the rotational energy,

$$E_r(K) = B_V K(K+1) - D_V K^2(K+1)^2, \qquad (1)$$

are of the same order of magnitude as the errors of observation. If more differences are used, the systematic errors are pronounced; if fewer are used, the influence of the random errors of measurement is unnecessarily large. For TH the omitted term in $K^3(K+1)^3$ would be 8 times larger for a given K than for T_2 and therefore fewer rotational differences can be used. The stated numbers 6 for T_2 and 4 for TH seem to be close to the optimum numbers.

The vibrational constants were obtained from the first four vibrational differences. To use more differences would have been futile as the formula

$$E_V = Y_{10}(V+\tfrac{1}{2}) + Y_{20}(V+\tfrac{1}{2})^2 + Y_{30}(V+\tfrac{1}{2})^3 + Y_{40}(V+\tfrac{1}{2})^4 \cdots \qquad (2)$$

does not converge sufficiently well for higher values of V.

TABLE II. Constants of the $2p^2\Sigma$-state of TH.

V	B_V	D_V	ω_V
0	17.898	0.00716	1705.84
1	17.080	0.00690	1615.76
2	16.256	0.00661	1524.82
3	15.389	0.00582	1431.57
4	14.560	0.00605	1333.86
5	13.701	0.00617	1228.10
6	perturbed		1110.55
7	11.580	0.00599	

Y_{10}	1796.42	Y_{01}	18.3167
Y_{10}^0	1798.09	Y_{01}^0	18.4455
Y_{20}	−45.69	Y_{11}	−0.819
Y_{30}	0.34	Y_{21}	−0.0039
Y_{40}	−0.060	Y_{02}	0.00744
		Y_{12}	−0.00041
ν_e	11 821.86	ν_e^0	11 785.23

TABLE III. Constants of the $2p^2\Sigma$-state of T_2.

V	B_V	D_V	ω_V
0	9.0676	0.00185	1226.67
1	8.7787	0.00179	1181.55
2	8.4956	0.00181	1136.47
3	8.2061	0.00176	1090.94
4	7.9137	0.00171	1044.75
5	7.6175	0.00167	977.35
6	7.3177	0.00164	948.25
7	(6.9875)	(0.00142)	896.47
8	6.6689	0.00164	840.94
9	6.3170	0.00168	779.66
10	perturbed		710.41
11	5.4658	0.00198	

Y_{10}	1272.28	Y_{01}	9.2056
Y_{10}^0	1272.86	Y_{01}^0	9.2385
Y_{20}	−23.03	Y_{11}	−0.2803
Y_{30}	0.170	Y_{21}	−0.00156
Y_{40}	−0.0204	Y_{02}	0.001887
		Y_{12}	−0.000045
ν_e	11 805.16	ν_e^0	11 786.75

[6] The results there presented were based on the older plates, which have a dispersion of one-half or a quarter of the dispersion of our present plates. The Fulcher bands have been reanalyzed on the new plates with essentially the same results except somewhat more accurate values for the constants. Moreover, the analysis is now much more complete. There are usually more lines known in a band than previously, and the number of bands in the system has been greatly extended.

TABLE IV. Band origins of the $3p^3\Sigma \rightarrow 2s^3\Sigma$-system of TH.

V' \ V''	0	1	2	3	4	5
0	11,631.98	9549.17				
1	13,337.83	11,254.97	9263.76			
2	14,953.59	12,870.73	10,879.48	8977.57		
3	16,478.44	14,395.55	12,404.26	10,502.27	8687.82	
4		15,827.10	13,835.86	11,933.83		
			15,169.72	13,267.69	11,453.17	
6			16,397.78*	14,495.86*	12,681.24*	
7				15,606.39	13,791.82	12,063.21

* These values are obtained from the $P(1)$ line only as the other lines are perturbed.

Finally, the band origins ν_0 were calculated with the help of the constants in Tables II and III and collected in Tables IV and V. Usually 14 band lines were used to do this for T_2 and 10 for TH. The values for the band origins obtained from the individual lines of one band generally agree within the limits of experimental errors, showing that formula (1) is an adequate representation of the rotational energy levels. For those bands which have the initial state perturbed, the origin was determined from the $P(1)$ line only, as it can never be perturbed (Sec. V). Such values are marked by an asterisk in the tables. The origin of the system, ν_e, can be obtained with the help of the vibrational constants.

If the physical significance of the constants is to be evaluated it must be remembered that the constants $Y_{n,m}$ calculated in the usual way do not have the simple meaning of the elementary theory of band spectra. The discrepancy is largest for the $3p^3\Sigma$ state. The energy has an extra term $2B_V$ which originates from the interaction between electronic motion and rotation.[7] Furthermore,

$$B_V = B_V^0(1 - B_V^0/2\delta),$$

where B_V are the values obtained directy from the empirical data and B_V^0 the value which this constant would have if the interaction with the $3p^3\Pi$ state were zero. δ is the difference between the two interacting states (both having the same values of K and V). With B_V and δ known the B_V^0 values can be found and in particular $Y_{01}^0 = h/8\pi^2\mu r_e^2$, which is entered in Tables II and III.

That the correction term $2B$ is essential is shown by the following facts: In Table VI the second column gives the uncorrected origin ν_e of the $2p^3\Sigma \rightarrow 2s^3\Sigma$ system in the five hydrogen molecules now known. It is obvious that this cannot represent the electronic frequency of the molecule at rest, since this frequency must be independent of the masses. The ν_e values show a systematic trend which is quite outside the limits of any errors of measurement or extrapolation. The ν_e^0 values in the third column which are obtained from those of the second column by subtracting $2Y_{01}$ are much more constant. The small differences can be explained easily by small omitted additional interaction terms, which the theory predicts but which are much more difficult to evaluate quantitatively. Also, small systematic errors in the vibrational constants due to imperfect convergence of the expression (2) may be partly responsible for the remaining discrepancies.

Another way of checking the correctness of the interaction terms is possible by comparison of the ratio of molecular constants of T_2 and TH with the theoretical value for such ratios. Only the constants Y_{10} and Y_{01} have the required accuracy for this.

In Table VII the Y_{10} and Y_{01} ratios are listed before and after the corrections for the interaction are applied. In both cases the corrected values are much closer to the theoretical ones. That the agreement is not perfect is again due to the reasons given above to account for the remaining discrepancies in Table VI.

A more thorough and complete comparison of the molecular constants in all isotope hydrogen molecules will be feasible when the TD data are also available.

TABLE V. Band origins of the $3p^3\Sigma \rightarrow 2s^3\Sigma$-system of T_2.

V' \ V''	0	1	2	3	4	5	6	7	8
0	11,671.06	10,177.36							
1	12,897.73	11,404.03	9956.74						
2	14,079.30	12,585.54	11,138.23	9736.61					
3	15,215.75	13,722.02	12,274.71		9516.11				
4	16,306.71	14,812.96	13,365.66	11,963.97	10,607.04	9294.16			
5		15,857.72	14,410.40	13,008.72	11,651.78	10,338.88	9069.57		
6			15,407.77	14,006.08	12,649.10	11,336.10	10,066.88		
7			16,355.96*	14,954.29*	13,597.36*	12,284.47*			
8			17,252.52	15,850.79	14,493.83	13,180.91	11,911.54		
9				16,691.78	15,334.79	14,022.08	12,752.50		
10						14,801.74*	13,532.37*	12,305.91*	
11					16,825.00	15,512.09	14,242.74	13,016.35	11,832.69
12						16,139.59*	14,870.34*	13,643.89*	12,460.20*
13							15,391.79*	14,165.20*	12,981.45*

These values are obtained from the $P(1)$ line only as the other lines are perturbed.

[7] See, e.g., G. H. Dieke, Phys. Rev. 47, 661 (1935).

TABLE VI. Origin of the $2p^3\Sigma \rightarrow 2s^3\Sigma$ system.

	ν_0	ν_0^0
H_2	11 838.91	11 783.49
DH	825.68	784.14
TH	821.86	785.23
D_2	813.40	785.69
T_2	805.16	786.75

TABLE VII. Ratios of constants.

Y_{10}	0.708 23	Y_{01}	0.502 58
Y_{10}^0	0.707 90	Y_{01}^0	0.500 85
Theor.	0.707 75	Theor.	0.500 91

V. PERTURBATIONS

The lower vibrational levels of the $3p^3\Sigma$-state have the regular rotational structure expected for a Σ-state. There are irregularities in some of the higher vibrational states which give rise to typical perturbations. These are due to the interaction with other electronic states of appropriate symmetry. It is important to identify the states causing the perturbations, for mere irregularities in the rotational structure might be spurious, because of a wrong classification. The $3p^3\Sigma$-state is an odd state and only other odd Σ- and Π-states can interact with it. The states $3p^3\Pi$, $4p^3\Sigma$, $4p^3\Pi$ are the only known states satisfying these conditions. The situation for T_2 is illustrated in Fig. 1, which gives the vibrational levels as far as they are known for these states. It is reasonably certain that there can be no other low-lying states capable of interacting with $3p^3\Sigma$ but there may be additional ones in the upper part of the figure, notably $4f\Sigma$ and $4f\Pi$, which are, however, not empirically known for any of the hydrogen molecules. A perturbation arises when two levels with the same value of K nearly coincide and the matrix element of the interaction is not zero.

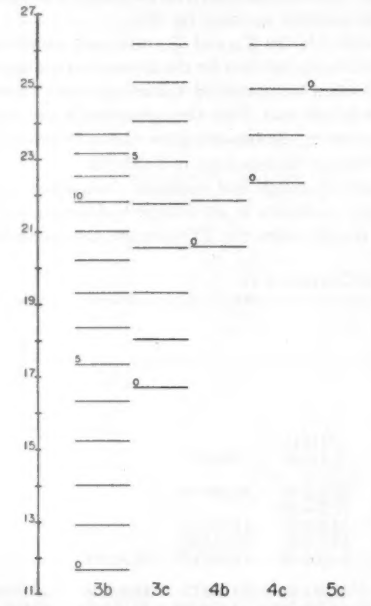

FIG. 1. Vibrational levels of the odd electronic states known empirically in T_2:

$3b = 3p^3\Sigma$, $3c = 3p^3\Pi$, etc.

The scale represents the position of the levels (in 1000 cm^{-1}) above the lowest triplet level ($2s^3\Sigma(V=0)$).

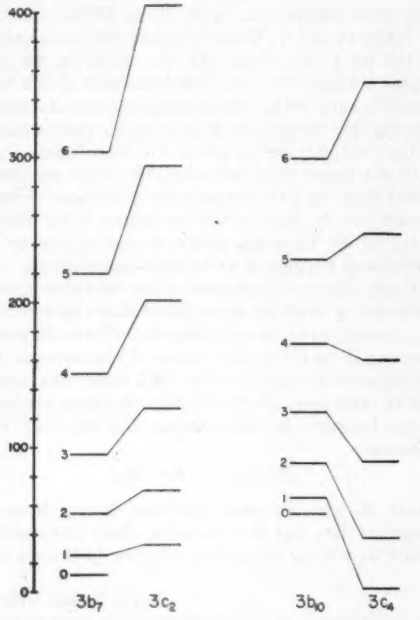

FIG. 2. Rotational structure of two pairs of interacting states.

Left: $3p^3\Sigma(V=7)$ and $3p^3\Pi(V=2)$.
Right: $3p^3\Sigma(V=10)$ and $3p^3\Pi(V=4)$.

The scale represents wave numbers (zero arbitrary).

All the observed perturbations can be accounted for by interaction with the $3p^3\Pi^+$ state. Figure 1 shows that there is near coincidence for the $V=7$ state of $3p^3\Sigma$ with the $V=2$ state of $3p^3\Pi$ and for $V=10$ of $3p^3\Sigma$ with $V=4$ of $3p^3\Pi$.

Perturbations are observed in both these cases and no others.[8] The complementary perturbations in the appropriate levels of $3p^3\Pi$ are observed too.

[8] Possible exceptions are the states with $V \geqq 12$. All of the potential perturbing states are not known for these high energies; and, moreover, the identification of these lines is in general less certain than for the lower vibrational quantum numbers. Further work will have to straighten this out.

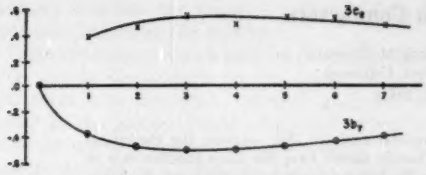

FIG. 3. Magnitude of perturbation in $3p^3\Sigma_7(V=7)(0)$ and $3p^3\Pi_8=(x)$.

Figure 2 shows the situation on a larger scale so that the individual rotational levels can be shown. We see that the situation is different in the two cases. The $K=1$ state of $\Sigma(V=7)$ lies just below the corresponding level of $\Pi(V=2)$. As the rotational spacing of $3p^3\Sigma$ is smaller than that of $3p^3\Pi$ successive rotational levels separate more and more. There is a small shift downward for $K=1$ and successively smaller shifts for the higher rotational states. This is accompanied by a corresponding shift upward in the $3p^3\Pi^+(V=2)$ states which results in an abnormally large Λ-doubling.

Figure 3 shows the perturbation for all the observed tational levels. The unperturbed levels were calculated by interpolating between the unperturbed vibrational states with $V=5$, 6, 8, 9, and 11. The differences between the observed and interpolated levels represent the magnitude of the perturbation. All levels are depressed for $3p^3\Sigma(V=7)$ as they should be except the $K=0$ level. If the perturbations of the $3p^3\Pi(V=2)$ level are plotted in the same way, we obtain the values marked with an x in Fig. 3. These lie on a curve, which within the limits of experimental errors is the mirror image of the curve for $3p^3\Sigma(V=7)$.

The situation is different for the other perturbing pair $3p^3\Sigma(V=10)$ and $3p^3\Pi(V=4)$. For low rotational quantum numbers the Σ-states lie above the Π-states and are, therefore, pushed up, whereas the Π-states are depressed. This is exactly as observed (Fig. 4). Between $K=4$ and $K=5$ the levels cross, and for $K\geqslant 5$ the Σ-levels are depressed. The break in the continuity between $K=4$ and $K=5$ is characteristic for a typical perturbation.

Again the curve for the Π-levels is the mirror image of the curve for the Σ-levels, at least below the break. For $K=5$ and 6 the perturbation in the Π-level (3*c*)

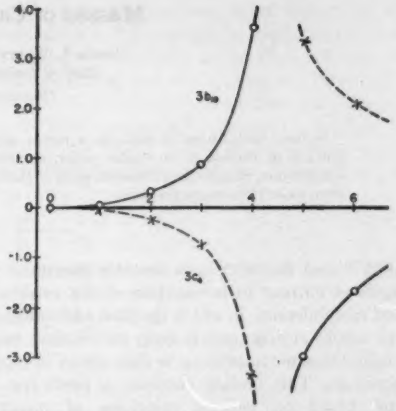

FIG. 4. Magnitude of perturbation in $3p^3\Sigma_{10}(0)$ and $3p^3\Pi_4(x)$.

is about 0.3 wave numbers higher than that in the Σ-level (3*b*). This may be due to the fact that the interpolation necessary to obtain the unperturbed level is somewhat uncertain as the neighboring vibrational levels may not be entirely free from perturbations. Another reason for this may be the presence of a third interfering state [possibly $4p^3\Sigma(V=1)$].

In all cases of an interaction between a Σ- and Π-state the lowest rotational Σ-level cannot be perturbed, as there is no $K=0$ level for the Π-state. The $P(1)$ line in the perturbed bands which originates from the $K=0$ level is, therefore, not affected by the perturbation and may be used to find the origin of these bands unaffected by the interaction.

A similar case of interaction resulting in typical perturbations is found between $3p^3\Sigma(V=6)$ and $3p^3\Pi(V=3)$ of TH.

A quantitative study of the perturbations is most interesting when all the isotopic species can be compared. This will be deferred until the results for TD are available also.

We are indebted to Mr. F. T. Byrne who photographed the spectrum, to Mrs. Dorothy McVay who made the wavelength measurements, and to Dr. B. Weinstock who carried out the purification of the tritium sample.

Masses of Carriers in Conductors

DAVID L. WEBSTER AND CAROL M. NEWTON
Stanford University, Stanford, California
(Received March 1, 1951)

Barnett and Brown present, in a recent paper, experimental evidence that supports the theoretical findings of Darwin in an earlier paper; namely, that all metals should have the same effective m/e in acceleration, despite the differences in their Hall coefficients. The present paper derives the same conclusion from more elementary premises.

BROWN and Barnett[1] have recently measured the ratio of current to momentum of the carriers in zinc and molybdenum, in which the Hall effect suggests positive values of e/m; and in both metals they found practically the same negative e/m that occurs in copper or aluminum. This finding confirms a prediction by Darwin[2] based on general principles of quantum mechanics; so perhaps the question may be considered as finally answered. Nevertheless, there may be some interest in another approach, from more elementary principles.

Effective masses more like those of atoms than electrons were postulated by Tolman, Osgerby, and Stewart[3] for successful calculations of emf's owing to accelerations in their experiments on solutions of iodides. So the principle especially needed here is the one which most clearly distinguishes metals from electrolytes; namely, that at a junction between different metals, a steady current does not cause any accumulation or disappearance of matter of any kind. We assume now, and shall refer to this as "the basic assumption," that this principle can take the following form: If a current crosses a junction between two metals, but no charge is accumulating at or near the junction, there is no accumulation of mass in any amount appreciable in comparison with the mass of the electrons which could carry this current.

Postponing consideration of why this basic assumption is stated as an approximation, we may note here that it is also a restriction on the class of materials to be compared. We may assume very safely that it classifies zinc and molybdenum with the metals having more normal Hall effects; but we are not prepared to say how far from such metals this class extends, and we should note the existence of other classes of materials which satisfy this assumption. Another such class, for example, must include all the types of glass which conduct, when fairly hot but not hot enough to be soft, by migration of sodium ions through fixed silicate networks. This class and the class including metals are made mutually exclusive by the basic assumption; but some of our reasoning applies equally well to any such class and suggests interesting possibilities for tests on electrolytes.

Metals have been tested, both for emf due to acceleration and for the converse effect, ponderomotive force due to time-change of current. Data on either effect may be used with the same principles to calculate a ratio of momentum per unit volume to current density; and both effects have given the same value for this ratio, within limits of error, for each metal tested in both ways. Since it is the ratio of mass current to electric current, it is conventionally called the effective m/e of the carriers.

In comparing theoretical m/e values for different metals, therefore, we need not be concerned with time changes, but only with the ratios of mass current to electric current in steady flow.

On this principle we shall now apply the basic assumption stated above to a circular ring of uniform cross section, made of semicircles of different materials, A and B, belonging to the same class, like a ring once used experimentally by Malinowski.[4] The contacts between their ends are assumed to be good; their insulation from everything else is assumed to be perfect. We shall assume that a steady current is maintained for a time long enough to damp out any free oscillations on the ring. Then no charge is accumulating at either junction, so any mass carried to either junction in any way must be compensated by an equal mass carried away (or perhaps by mass of the opposite sign if negative mass can exist). That is, when the electric currents in the two metals are equal, their mass currents and their effective values for m/e must also be equal, at least approximately. For reasons to appear later, this equality is probably not quite so exact as one might expect at this point.

It is clear that the above argument applies to all pairs of conducting materials classified together by the basic assumption, whether they are metals or nonmetals. Only for metals, however, can we extend it so as to equate the effective m/e approximately to the m/e of slow electrons in vacuum.

In the ring discussed above, the two metals did not necessarily have to cover equal arcs. So now we may make one of them very short; remove it, leaving a

[1] Sheldon Brown and S. J. Barnett, Phys. Rev. **81**, 657 (1951).
[2] C. G. Darwin, Proc. Roy. Soc. (London) **A154**, 61 (1936).
[3] Tolman, Osgerby, and Stewart, J. Am. Chem. Soc. **36**, 466 (1914).
[4] A. E. Malinowski, Z. Physik **42**, 319 (1927).

vacuum; then heat the remaining metal so that electrons can flow across the vacuum.

These electrons in the vacuum must be slow. If they were moving fast enough for the Lorentz factor in their mass to be significant, the additional mass thus carried in the vacuum would accumulate, where they strike the metal, as relativistic mass of heat. The basic assumption does not, therefore, classify metals with electrons in vacuum unless the latter are slow.

Even if they are very slow, there is a little accumulation of heat where they strike the metal. The ratio of its mass to that of the electrons, however, is only the ratio of the work function of the metal to the half-million-volt energy equivalent of the electronic rest mass. So the basic assumption, though not strictly exact, is a very good approximation; and the effective m/e for the metal seems practically sure to equal the m/e for slow electrons in vacuum to within a few parts in 10^5.

Paradoxically, this accumulation of heat indicates that the little difference in these m/e values is as if the carriers in the metal were slightly lighter than slow electrons in vacuum, whereas we should expect them to be slightly heavier because of their kinetic energy. Therefore, it should be noted here that both this kinetic energy and the heat come from potential energy released where the electrons enter the metal. If this release is by a fall through an electrostatic potential barrier, and if this barrier exists all over the surface of the incomplete ring of metal, then in considering such small masses as these differences from the vacuum rest mass we must not neglect the mass transported in this surface barrier by the Poynting vector made up out of its electric field and the magnetic field of the current in the ring. The direction of this Poynting vector is opposite to that of the flow of electrons. In short, its relation to the main mass current is that of a backwater. It is very weak; but if the pd in the barrier is uniform over the whole surface, it is just strong enough to resolve the paradox.

This view of it, however, may be far too simple, especially if the metal is not all at the same temperature. The discrepancy is so small that no detailed analysis of it will be attempted here, but we should note that it is likely to have different values for different metals.

In short, the main conclusion here is that, while the effective values of m/e for carriers in metals are probably not perfectly equal, they must all equal the m/e of slow electrons in vacuum to within a few parts in a hundred thousand.

PHYSICAL REVIEW VOLUME 82, NUMBER 6 JUNE 15, 1951

The Transmutation of N^{14} by Protons*

D. B. Duncan† and J. E. Perry‡
Kellogg Radiation Laboratory, California Institute of Technology, Pasadena, California
(Received March 9, 1951)

The reaction $N^{14}(p,\gamma)O^{15}$ has been studied experimentally in the energy range 0.25 to 2.6 Mev, using protons accelerated by an electrostatic generator and observing the induced O^{15} positron activity. Excitation curves have been obtained from Be_3N_2 targets, nitrogen gas targets, and a thin target formed by proton bombardment of a copper foil in a nitrogen atmosphere. The experimental cross section can be described by nine resonances, whose parameters are given. The bearing of these results on the yield of this reaction at stellar temperatures is discussed.

I. INTRODUCTION

BY observing the cross section for the $N^{14}(p,\gamma)O^{15}$ reaction, the only transmutation energetically possible when protons of energy less than 3.2 Mev are incident on N^{14}, it is possible to study the properties of certain of the excited states of O^{15}. This particular reaction is also of interest as the slowest of the reactions occurring in the production of stellar energy through the carbon-nitrogen cycle. Previous studies[1–4] had been either of a qualitative nature or confined to proton energies of less than 1 Mev. The completion of an electrostatic generator capable of attaining voltages somewhat above 2.5 Mev permitted the investigation of a large, unexplored energy range.

II. EXPERIMENTAL TECHNIQUE

The protons were accelerated by the 8′×22′ electrostatic generator of this laboratory and were analyzed by a 90° double focusing magnetic analyzer.[5] The

* This work was assisted by the joint program of the AEC and ONR.

† AEC Predoctoral Research Fellow. Now at Aerophysics Laboratory, North American Aviation, Downey, California.

‡ Now at Los Alamos Scientific Laboratory, Los Alamos, New Mexico.

[1] DuBridge, Barnes, Buck, and Strain, Phys. Rev. **53**, 447 (1938).

[2] Curran and Strothers, Nature **145**, 224 (1940).

[3] R. Tangen, Kgl. Norske Videnskab. Selskabs. Skrafter No. 1 (1946).

[4] Woodbury, Hall, and Fowler, Phys. Rev. **75**, 1462A (1949).

[5] D. B. Duncan, Phys. Rev. **76**, 587A (1949).

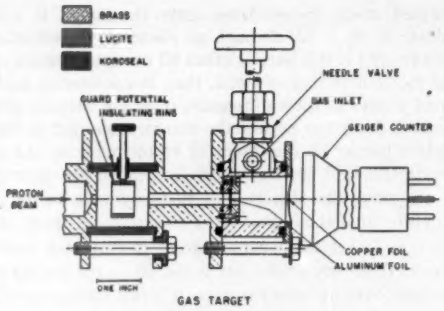

FIG. 1. Nitrogen gas target assembly.

strength of the field in the analyzer was determined by means of a null-reading fluxmeter.[6]

No attempt was made to determine absolute energy, the Al(p,γ) and F$(p,\alpha\gamma)$ resonances at 0.9933 and 0.8735 Mev being used as calibration standards.[7] Thick target aluminum excitation curves were obtained immediately before and after any nitrogen bombardments, where accurate energy values were needed. A procedure of checking the zero of the fluxmeter at short time intervals was adopted, limiting drifts in energy measurements to less than 0.1 percent. The linearity of the fluxmeter was checked by studying the excitation curves for F$(p,\alpha\gamma)$ in some detail and by determining the resonance energy in Al(p,γ), using protons and singly charged hydrogen molecules. No detectable dependence of the fluxmeter constant on energy was observed.

The reaction was detected by observing, with a Geiger-Müller counter, the positrons emitted when O^{15} decays to N^{15}, a technique having numerous advantages over that of observing the immediate γ-radiation. It was realized that the choice of target material would be particularly critical. To eliminate errors caused by possible escape of O^{15} from the target before decay and by chemical decomposition of the target, a gas target was used. The gas chamber was separated from the evacuated accelerating system by a thin foil. Absolute yield determinations were based on results obtained with these gas targets. However, because of the straggling in proton energy produced by passage through the entrance foil, solid targets were necessary to investigate the details of sharp resonance structure. Beryllium nitride and a thin nitrogen layer absorbed on a copper foil were used. It is to be noted that no loss of activity through escape of the O^{15} was detected in extensive use of these targets. Many other compounds of nitrogen are definitely not satisfactory in this regard nor in their ability to withstand decomposition under bombardment.

The procedure followed was to bombard the target for a time t_1 (usually 2 minutes), to count the activity for a time t_2 (usually 3 minutes) with high voltage off to reduce background, and to begin bombardment again after a definite time. Under these conditions, the yield in transmutations per proton is a function of the number of counts observed corrected for previous activity and background, the integrated proton current, the half-life of O^{15}, the times t_1 and t_2, and the counting efficiency.[8]

The proton current was measured by charging the condenser in an integrator of standard design. The time was controlled automatically from a synchronous motor. The half-life of O^{15} has been measured previously by many observers. A determination was also made in the course of this work giving a value of 127 ± 2 sec. A value of 126 sec was used in calculations.[9]

The counting efficiency is the most difficult quantity to measure, and a determination was made only for the gas target. The target chamber is pictured in Fig. 1. The proton beam was defined by the aperture stop $\frac{3}{16}''$ in diameter; the aluminum foil at the entrance was placed over a hole $\frac{1}{4}''$ in diameter. With foils 0.00015″ thick, seals which would stand a pressure differential of half an atmosphere were made. The foil was "sandwiched" between two brass disks, as indicated on the drawing, the seals being made with O-rings.

Copper foil 0.001″ thick was used between the counter and the target. Standard needle valves were modified and used as the chamber valves, the valve seat being made flush with the inside bore. The counter was mounted on a lead block and held a fixed distance from the target. The entire assembly was surrounded by lead.

Neglecting absorption of the positrons in the copper foil, the counting efficiency can be expressed as an integral over the volume of the target chamber and the surface of the counter, involving the dimensions of the apparatus and the variation of counter efficiency over

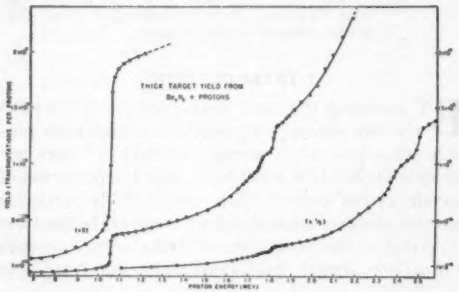

FIG. 2. Thick target yield of positrons from $N^{14}(p,\gamma)O^{15}$. The target material was Be_3N_2. However, the yield calibration shown is that of a pure nitrogen target.

[6] C. C. Lauritsen and T. Lauritsen, Rev. Sci. Instr. **19**, 916 (1948).
[7] Herb, Snowdon, and Sala, Phys. Rev. **75**, 346 (1949).
[8] R. N. Hall and W. A. Fowler, Phys. Rev. **77**, 197 (1950).
[9] G. T. Seaborg and I. Perlman, Revs. Modern Phys. **20**, 585 (1948).

the surface of the counter. The latter was determined empirically using collimated natural beta-particles. The integration was then carried out numerically. The correction for positron absorption was studied experimentally by determining the yield as a function of absorber thickness for otherwise identical conditions of bombardment. The linear relationship obtained was extrapolated to zero-absorber thickness. The over-all determination of counting efficiency made in this way is believed to be accurate to 10 percent.

If the variation in the cross section for a nuclear reaction is small over the energy range corresponding to target thickness and dispersion in proton energy, a condition often satisfied in this experiment, the yield is given by $y=\sigma nl$.[10] Thus with a gas target, where it is possible to measure the thickness (l) and the density (n) by measuring pressure and temperature, the cross section can be directly determined.

After bombarding for several days, two-minute activity was observed to come from the spot on the copper foil which had been hit by the proton beam in a nitrogen atmosphere. Hence to obtain cross-section values it was necessary to obtain plots of yield against target pressure. Linear relationships were obtained at several energies and the correction for the foil activity determined. This thin layer of nitrogen necessitated a correction to the gas target data, but it furnished a remarkably stable thin target for investigation the details of resonant structure.[10a] The method of obtaining it would seem to form a useful technique for making thin targets whenever the target element is a gas. For thick target data, pressed Be_3N_2 was used. This compound was chosen because of its chemical stability, because beryllium does not give a radioactive product upon proton bombardment, and because a large proportion of the total stopping power is attributable to the nitrogen.

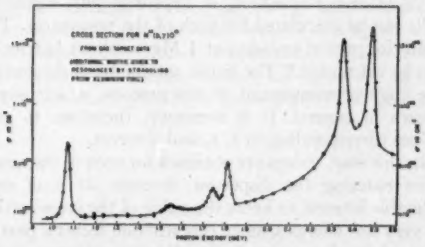

FIG. 3. Thin gas target yield of positrons from $N^{14}(p,\gamma)O^{15}$. The target length along the beam was approximately $1\frac{1}{2}''$, pressure approximately 1.6 cm Hg, thickness 16 kev at 1 Mev. The energy scale has been corrected to the mean energy of the protons after penetrating the target entrance foil.

[10] Fowler, Lauritsen, and Lauritsen, Revs. Modern Phys. **20**, 236 (1948).

[10a] This absorbed target was formed by bombarding the copper foil with 1.5×10^{4}-Mev coulomb of protons in the energy range 0.7 Mev to 2.6 Mev through a nitrogen atmosphere whose pressure was 1.6 cm of Hg. No deterioration of the target was observed during its subsequent use.

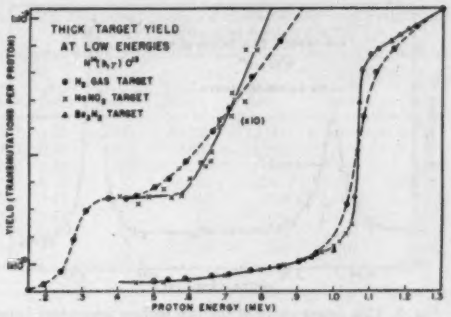

FIG. 4. Thick target yield at low energy.

III. EXPERIMENTAL RESULTS

The thick target curve from bombarding Be_3N_2 is given in Fig. 2. The ordinate has been normalized to give yield in transmutations per proton from gas target data as described below. The data from thin gas targets is given in Fig. 3. The yield has been plotted against mean proton energy after passing through the foil. This was determined by plotting the measured energy at the resonances against resonance energy as determined from the Be_3N_2 curve and extrapolating between these points using the known energy dependence of proton range in aluminum.[11]

As indicated above, the ordinate can be normalized to give the cross section directly. This will not be valid near the resonances where the simple form $y=\sigma nl$ does not hold. The half-life of the activity at each of the resonances was checked to have the correct value. Particular care was used near the peak at 1.55 Mev to show that it was not due to carbon on the front of the entrance foil.

A thick target excitation curve obtained at low energies, using a one-atmosphere nitrogen gas target, is given in Fig. 4. The yield, calibrated by comparison with the Be_3N_2 target, is plotted against mean proton energy. Professor W. A. Fowler also kindly made available data obtained from a thick $NaNO_2$ target bombarded at energies between 300 and 1300 kev by the $8'\times13'$ electrostatic generator of this laboratory. These data are included in Fig. 4. The thin layer of nitrogen absorbed on the copper foil was also used as a target. Excitation curves for various resonances were obtained. The two highest energy resonances are given in Fig. 5.

DISCUSSION AND CONCLUSION

The experimental data indicate five resonances whose energy can be determined from the midpoints of the steps in the thick target Be_3N_2 curve. Such a determination can be made quite accurately, to within 0.1 percent to 0.4 percent, depending on the width and on the ratio of resonant to nonresonant yield. Data

[11] H. A. Bethe, Brookhaven Publication BNL T-7 (1950) (unpublished).

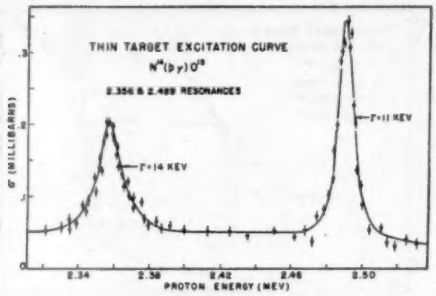

FIG. 5. Thin target curve of the two highest resonances found. The target consisted of nitrogen driven into the copper window of the gas target during the period when the data of Fig. 3 were taken. For the above curves, the entrance foil of the gas chamber was removed and the chamber evacuated.

from the solid thin target curve was used to give the most accurate values of the widths of the resonances. The uncertainties arise primarily from statistical deviations of the data.

Relative values of the thick target step in yield $Y_{max}(\infty)$ were obtained from the Be_3N_2 target curve. An absolute value for the 1-Mev resonance can be accurately obtained from the thin gas target, using the relationship $\xi Y_{max}(\infty)=A(\xi)$, where ξ is the target thickness and $A(\xi)$ is the area under the yield curve.[10] The value of $Y_{max}(\infty)$ obtained in this way serves to normalize the ordinates of thick target curves.

Two additional resonances are immediately indicated which cannot be handled this way. The 277-kev resonance of Fig. 4 could not be studied with solid targets because the generator would not operate successfully at this energy. The yield was measured, but values of resonance energy and width were not obtained. The resonance at 1.5 Mev on Fig. 3 was too broad and weak to be observed with other targets. It was necessary to estimate the parameters from this curve alone with a corresponding decrease in accuracy.

Finally, it is possible to subtract out the yield of these resonances in both thick and thin target curves to look for an adequate description of the remaining

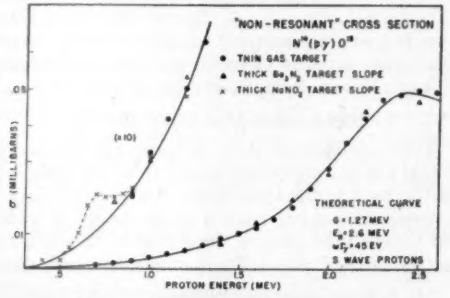

FIG. 6. Thin target curve with sharp resonances omitted.

yield. The experimental values for this cross section are given in Fig. 6. The gas target data represents merely a replotting of previous data with the points near resonances omitted. The points from the thick targets are obtained from the relationship[10] $\sigma=\epsilon(dY/dE)$. Such an evaluation is less accurate than direct measurement. At higher energies, the points are given merely to indicate the degree of consistency between the thick and thin targets. However, the values at low energies could only be obtained in this way.

An attempt was made to fit these data to a resonance of the form[10]

$$\sigma=\pi\lambda^2\frac{\Gamma_p\Gamma_\gamma}{(E-E_R)^2+\frac{1}{4}(\Gamma_p+\Gamma_\gamma)^2},$$

where $\Gamma_p=E^{\frac{1}{2}}P(E)G$. The function $E^{\frac{1}{2}}P$ has been tabulated by Christy and Latter.[12] For s-wave protons, it was possible to construct a curve which quite adequately described the data. For other than s-wave protons, even an approximate fit was found to be impossible. The continuous background can thus be explained in terms of a very broad s-wave excited resonance.

A second feature of the cross section as presented in Fig. 6 is the anomaly at 700 kev. This can most reasonably be explained by assuming a small resonance in this region. The energy and width of this resonance were estimated from the dashed curve of Fig. 6.

A complete description of the experimental cross section from 0.25 to 2.6 Mev is given by tabulating values of E_R, Γ, and $Y_{max}(\infty)$ for the nine resonances that were found. These values and the cross section at resonance, as determined from the relationship[10] $\sigma_R=2\epsilon Y_{max}(\infty)/(\pi\Gamma)$, are tabulated in Table I.

Various other quantities which are of interest can now be calculated. The quantity $\omega\gamma$ defined[10] as $\omega\Gamma_\gamma\Gamma_p(\Gamma_\gamma+\Gamma_p)^{-1}$, which is approximately equal to $\omega\Gamma_\gamma$, can be calculated for each of the resonances. The width for proton emission at 1 Mev without barrier G, can be calculated.[12] The value obtained will depend on the angular momentum of the protons, which is not known in general. It is necessary, therefore, to give values corresponding to s, p, and d-waves.

In this way, values are obtained for each of the quantities entering the dispersion formula. It is of considerable interest to know the value of the cross section at very low energies, since this reaction forms a part of the carbon-nitrogen cycle. For this reason extrapolated values at 128 kev and 28 kev, for each of the resonances, were calculated. The value at 128 kev is given because the yield has been measured independently at this energy;[4] the value at 28 kev because this is the approximate energy of interest in stellar calculations. In each case, the resonance has been assumed to be caused by s-wave protons which give the largest extrapolated

[12] R. F. Christy and R. Latter, Revs. Modern Phys. **20**, 185 (1948).

TABLE I. Resonance characteristics for $N^{14}(p,\gamma)O^{15}$.

E_R (Mev)	Γ (kev)	$Y_{max}(\infty)$ (β^+/proton)	$\omega\gamma_R$ (millibarns)
0.277[a]	<2[a]	$0.35\pm0.03\times10^{-10}$	>0.15
0.70 ±0.03	100 ±30	0.2 ±0.07	0.001
1.064±0.002	4.8±1	5.5 ±0.1	0.37
1.55 ±0.02	50 ±20	1.2 ±0.2	0.006
1.748±0.005	11 ±3	1.5 ±0.3	0.03
1.815±0.004	7 ±1.5	3.7 ±0.3	0.11
2.356±0.008	14 ±4	15 ±2	0.21
2.489±0.007	11 ±3	21 ±1	0.35
2.60 ±0.05	1270 ±50	300 ±50	0.05

[a] See reference 3.

TABLE II. Computed resonance characteristics and extrapolated low energy cross sections for $N^{14}(p,\gamma)O^{15}$.

E_R (Mev)	$\omega\Gamma_\gamma$ (ev)	$G(s)$ (kev)	$G(p)$ (kev)	$G(d)$ (kev)	σ (128 kev) (10^{-11} barn)	σ (28 kev) (10^{-12} barn)
0.277	0.02	<3000	<20,000	<70,000	<2.5	<1.5
0.70	0.02	1700	8000	15,000	1.1	1.5
1.064	0.63	24	80	960	0.02	0.03
1.55	0.16	110	250	2000	0.01	0.02
1.748	0.21	20	44	280	0.0015	0.003
1.815	0.52	12	27	170	0.002	0.004
2.356	2.4	17	28	140	0.007	0.015
2.489	3.3	12	20	85	0.007	0.015
2.60	46	1250	——	——	8.7	15.0

yield values. The resonances that make appreciable contributions do seem to be s-wave. A tabulation of these values is given in Table II.

The arithmetic sum of the contributions of the cross sections at 128 kev is 1.24×10^{-10} barn. The value computed from the thick target yield measured at this energy is 7×10^{-10} barn.[4] The discrepancy in these values can be explained in terms of constructive interference effects between the contributions of the numerous resonances, by the existence of additional low energy resonances, or in part at least by experimental errors. The best extrapolation to stellar energies is made, using the experimental data at 128 kev and assuming no low lying resonances, and gives $\sigma=0.025E^{-1}\exp(-6.95E^{-\frac{1}{2}})$ barns for the proton energy in Mev. At 28 kev this yields σ (28 kev)$=0.9\times10^{-12}$ barn. It must be emphasized that this extrapolation will be meaningless if low energy resonances actually exist. These can be investigated at the present time only by the study of the excited states of O^{15} occurring in other reactions, such as $N^{14}(dn')O^{15*}$. Studies of this nature are underway in this laboratory at the present time.

The widths for γ-ray emission for each of the levels having been measured, the associated oscillator strengths could be calculated if the γ-ray energy were known. A determination of these energies was not attempted. The problems which present experimental difficulties are the low yield of the reaction studied, the high yield of the $N^{15}(p,\gamma)$ reaction even from a non-enriched target, and the high yield from aluminum and beryllium reactions from any of the solid targets found satisfactory. Values have been calculated assuming the transitions are to the ground state. Even if this is correct, the usefulness in determining the multipole order of γ-rays present is quite limited. About all that can be said is that the strong, broad resonance at 2.6 Mev appears to be electric dipole although magnetic dipole cannot be excluded. The other transitions seem to be quite weak for electric dipole.

The values of G permit some few conclusions concerning the angular momentum of the protons. The 2.6-Mev resonance is definitely s-wave, the 0.277- and 0.700-Mev resonances are probably s-wave, and the others give unusually small values if they are ascribed to s-wave.

The yield data presented here are sufficient to describe the observed cross section in the energy range 270 kev to 2.6 Mev and to determine certain of the properties of the excited levels of O^{15}. It does not seem to be possible to obtain a complete description of these levels, including their angular momentum and parity, from these yield measurements alone.

The authors wish to thank the staff of the Kellogg Radiation Laboratory and in particular Professor C. C. Lauritsen, Professor W. A. Fowler, and Professor R. F. Christy for their guidance during the progress of this research.

Energy Distribution of External Photoelectrons from *F*-Centers in RbI

L. APKER AND E. TAFT
General Electric Research Laboratory, Schenectady, New York
(Received February 19, 1951)

Energy distributions of the external photoelectrons from *F*-centers in RbI were determined by retarding-potential techniques. Precautions were taken to secure electrically uniform surfaces. The photoelectrons then emerged in two separable groups. The first, termed the *f*-group, was composed of relatively fast electrons that were attributed to direct photon ionization of *F*-centers. Photoelectron energies were distributed in a band, roughly gaussian in form, that was treated according to a theory given by Herring. The Franck-Condon principle was taken into account; scattering of excited electrons was neglected. The second group of photoelectrons, termed the *s*-group, was comparatively slow. The energy distribution had an unusual form and peaked at the surprisingly low value of 0.3 or 0.4 ev, independent of $h\nu$. Exciton-enhanced emission was almost entirely of this type. Three factors that may influence the *s*-type distribution are mentioned: Hebb's calculations indicate that lattice scattering of exciton-induced emission may be important because of the relatively large depth of origin of these photoelectrons. As suggested by Seitz, degradation of exciton energy prior to *F*-center stimulation may be involved. Finally, some of the photoelectrons in the *s*-group may arise in other types of centers.

I. INTRODUCTION

PREVIOUS reports have treated the frequency variation of the exciton-enhanced photoelectric emission from *F*-centers in alkali iodides.[1] Energy distribution data, giving additional information on the processes involved, are reported here for RbI. The results show that the photoelectrons emerge in two distinct energy groups. The first group consists of relatively fast electrons. Apparently, they arise by direct photon ionization of *F*-centers. Their energy distribution is treated here by a method due to Herring. The Franck-Condon principle is taken into account, but the scattering of excited electrons is neglected since it does not appear to change the main features of the distribution.

The second group consists mainly of slow photoelectrons. They have an unusual energy distribution, approximately exponential in character. Exciton-enhanced emission consists almost entirely of this type. The energy distribution is not as easily interpreted as that for the first group, and this paper discusses it only in qualitative fashion. Three factors mentioned are lattice scattering of exciton-induced emission as calculated by Hebb, degradation of exciton energy as suggested by Seitz, and ejection of photoelectrons from initial states in other types of centers.

II. TREATMENT OF THE EMITTERS

The general technique and the phototubes used in this work have been described in (I).[1] Five evaporated RbI films (in two tubes) were studied in detail; they ranged from 10^{-5} to 10^{-3} cm in thickness. The *F*-centers were produced by three methods given in (II): (1) irradiation with monochromatic ultraviolet of known intensity; (2) flooding with a broad band of ultraviolet overlying the first fundamental absorption band of RbI; (3) electron bombardment for several seconds at current densities varying from 2 μa/cm^2 at 25 v to 1 ma/cm^2 at 500 v. Results were reproducible under these different conditions except that the equilibrium concentration of *F*-centers (as indicated by photoelectric yields) varied by a factor of 2 or 3.

Retarding-potential measurements impose more stringent requirements on surface uniformity than do the yield determinations reported in (I) and (II). Although RbI seemed much more tractable in this respect than KI, non-uniform surfaces, nevertheless, occurred in most cases. Current-voltage characteristics then failed to show clear-cut saturation points, indicating that relatively large scale patch structures were present. (For the samples discussed in (I) and (II), this condition was always evident, but it was of no serious importance.) These patches often appeared after several activations with ultraviolet irradiation, but electron bombardment sometimes eliminated them. In spite of time-consuming difficulties from this source, uniform surfaces were finally produced by all three of the methods mentioned above. Only such surfaces are discussed in this report. Twenty separate successful activations were carried out on the samples considered here.

The chemical constitution of the samples is a particularly important variable in this type of work. It is not very easy to determine or to control. Evaporation of a salt like RbI in a sealed-off, gettered vacuum obviously does not constitute a definite chemical situation. Experiments in auxiliary tubes showed, for example, that the following process may occur: When the source material is heated, it may lose a very small amount of I. It thereby acquires a corresponding amount of excess Rb in the form of permanent *F*-centers or more complicated aggregates. The concentration of these may be high enough to color the salt. A transient pressure of free I thus may build up during the deposition of the sample. This has its greatest effect, naturally, on the part of the RbI that deposits last. If it persists appreciably after the evaporation ceases, it may continue to react with the outer layers of the material already deposited.

[1] L. Apker and E. Taft, Phys. Rev. **79**, 964 (1950); **81**, 698 (1951)—hereafter denoted in the text by (I) and (II), respectively. M. Hebb, Phys. Rev. **81**, 702 (1951).

We do not understand this process in any complete detail. It is clear, however, that the spatial distribution of I ion vacancies and their number may be greatly affected. The pronounced "self-reversal" effect exhibited by the exciton-induced photoelectric yield from RbI in (II) was doubtless influenced by this phenomenon. A sparsity of F-centers near the sample surfaces could easily have arisen, particularly since the tubes used in this earlier work were of relatively small volume. Thus, "dead layers" 140A thick were found by Hebb[1] in his quantitative treatment of these previous data. They probably originated largely in an F-center sparsity.

One way to minimize this difficulty (or at least to obtain *different* difficulties) is to evaporate the RbI in a very low pressure of Rb vapor. This we have done in the present work. A glass pellet of Rb metal was incorporated in a side arm on the evaporation chamber of the second phototube. This pellet was broken before the tube was sealed off. The vapor pressure of Rb at 300°K is roughly 10^{-7} mm Hg. Samples were deposited and investigated in the presence of this vapor, which could be frozen out with liquid nitrogen if desired.

The photoelectric yields, at the exciton-induced peak near $h\nu = 5.56$ ev, amounted to as much as 0.04 electron/quantum under these conditions. Auxiliary tubes like those in (II) showed that the "self-reversal" effect at 85°K was either very small or even absent. In agreement with this, the "dead layer" thickness estimated by Hebb's method had an upper limit much smaller than the 140A above. It is even conceivable, of course, that the F-center concentration was non-uniform and relatively high near the surfaces of these samples. At any rate, the situation represents an opposite extreme from that in (II).

For purposes of comparison, the Rb pellet was omitted from the first phototube used in the present work. The photoelectric yields at the exciton-induced peaks were roughly 8×10^{-3} electron/quantum. Hebb's[1] calculations indicate that the "dead layer" thickness for these samples was 80A or less. Energy distribution data were not significantly different in form from those determined with the second tube, and they are therefore used in this paper.

Other details are mentioned where pertinent in succeeding sections.

III. EMITTER "WORK FUNCTIONS"

Figure 1 shows typical current-voltage characteristics for an RbI emitter containing F-centers made by irradiation near $h\nu = 5.56$ ev. In all cases, the concentration of centers was close to the limiting value attainable with 4×10^{11} quanta sec^{-1} cm^{-2} incident on the surface at 300°K. (The activation curve was practically the same as that for KI in reference 1. It will not be repeated here.) Values of the parameter V_0, "the stopping potential for an ideal metal at 0°K," are marked for the various values of $h\nu$ in question.[2] The

[2] See (I), reference 5, for details of the experimental technique.

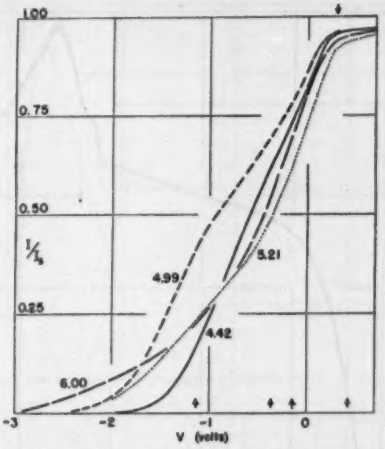

FIG. 1. Typical current-voltage characteristics for RbI. Arrow at the top marks V_s. From left to right at the bottom, arrows mark values of V_0 for decreasing values of $h\nu$ as indicated by numbers next to the corresponding curves. Curves are normalized with $I/I_s = 1.0$ at $V = 10$ v.

collector work function is $\varphi_c = h\nu + eV_0 = 4.8$ ev. The saturation point V_s, which determines the condition of zero field between emitter and collector, is indicated at +0.3 v.

We note that the RbI is not in an equilibrium state during these photoelectric measurements. The F-centers and V-centers[3] are metastable. The electric current in the sample may be carried by both electrons and ions. The potential just outside the surface therefore may not be fixed by an ordinary Fermi level for the electrons in the occupied states from which the photoelectrons are ejected. In extreme cases, involving film thicknesses greater than those used here, there may not be enough conductivity of any kind to replace the charge carried away by the photoelectrons. A significant voltage may then appear across the RbI layer, and the surface may not reach a steady potential for several minutes. It is thus clear that V_s may not have the same connotation as it does when thermal and electrical equilibrium exists.

Under these conditions, precautions are obviously necessary in coming to meaningful conclusions. The following points were noted here: Current-voltage characteristics were independent of incident radiation intensity over at least a factor of ten.[4] As shown in Fig. 1, V_s did not depend on $h\nu$ and thus was normal in behavior. At collecting fields near 1000 v cm^{-1}, currents were about 4 percent larger than at 10 v cm^{-1}. This rate of increase is comparable with that for the common metals in the auxiliary emitters used to determine V_0.

[3] F. Seitz, Phys. Rev. **79**, 529 (1950); see also (I), reference 4; E. Burstein and J. J. Oberly, Phys. Rev. **79**, 903 (1950).

[4] It was possible to distort the characteristics by using radiation intensities an order of magnitude or more in excess of those discussed here.

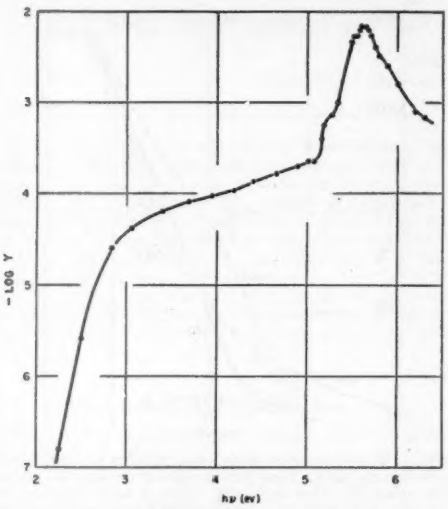

FIG. 2. Spectral distribution of photoelectric yield Y in electrons/quantum for the sample of Fig. 1.

We believe, therefore, that patch structures were not serious enough to affect the conclusions in this paper. As mentioned in (I) and (II), photocurrents were proportional to radiation intensity. A steady state was always observed, and it must have been reached within two seconds after the incidence of the radiation. We conclude that there was no important voltage drop in the emitters and proceed to treat the currents in the manner customary for ordinary photoelectric emission.

Returning to Fig. 1, we take $V_s=0.3$ v. Thus, the electric field outside the RbI is the same as would be found outside a good electronic conductor with a work function $\varphi=\varphi_c-eV_s=4.5$ ev. For an equilibrium case, the Fermi level for the electrons in the occupied energy states would thus lie 4.5 ev below the vacuum potential just outside the surface barrier. This Fermi level would coincide with that in the metal substrate on which the RbI film was deposited.[5] Electrons from energy levels more than 0.2 ev above it would not be detected in practice, the population probability for such states being less than 5×10^{-4} at 300°K. Hence, no current would be observed at room temperature for applied potentials 0.2 v more negative than V_0.

Clearly, this type of argument cannot apply to the data for RbI in Fig. 1. Currents are observed for applied potentials more negative than V_0 by over 1 v. The current-voltage characteristics do not approach zero in the exponential way typical of a Fermi distribution of electrons in fixed, one-electron energy levels.

We take the following viewpoint in discussing this situation: Although there is apparently no genuine electronic equilibrium between the RbI and its surroundings, the definite saturation point V_s shows that the salt behaves as though it had a definite work function. We shall call this quantity φ'', using the primes to distinguish it from the work function of an emitter in true equilibrium. We associate with φ'' a fictitious "Fermi level" μ'' that may be found unambiguously from the data in Fig. 1.

Samples of KI investigated in parallel fashion have shown values of φ'' which decreased from about 4 ev to 2.5 ev in the course of an extended series of measurements. The current-voltage characteristics retained their form, however, merely shifting bodily toward more positive values of V. This is quite like the behavior observed when a true Fermi level rises in the forbidden energy band of an ordinary semiconductor in true equilibrium. We prefer to leave further consideration of this point entirely open here, since the topic appears to need more experimental study than it was accorded in this work.

IV. ENERGY DISTRIBUTIONS

Differentiating characteristics like those in Fig. 1 and using the spectral distribution of Fig. 2, we obtain the energy distributions in Figs. 3 and 4. In Fig. 3, one notices that the photoelectrons emerge in two groups. The first we shall call the f-group, since it is faster than

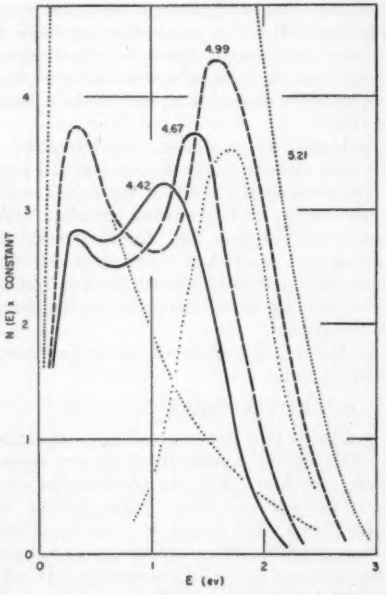

FIG. 3. Energy distributions for values of $h\nu$ on the low energy side of the fundamental absorption band of RbI. Ordinates should be multiplied by 2.8×10^{-4} to obtain N in electrons quantum^{-1} ev^{-1}. The curve for 4.99 ev is separated into f- and s-groups as shown by dotted lines (see text).

[5] We avoid discussing possible complications due to barrier layers comparable in thickness to the sample.

the second. It produces clear-cut high energy peaks in Fig. 3. (That near $E=1.6$ ev on the curve for $h\nu=4.99$ ev is an example.)

Now, the precision of this type of measurement on such intractable materials is obviously limited. Errors of the order of 10 percent may easily appear in these distributions. Thus, the locations of these f-peaks may be uncertain within, say, 0.1 or 0.2 ev. (An idea of these errors may be gained by observing that the high energy tail for $h\nu=4.67$ ev seems to lie too close to that for 4.42 ev.) We consider it significant, however, that the f-group peak progresses linearly toward higher energy with increasing $h\nu$. Thus, these photoelectrons behave as though ejected in normal fashion from a rather narrow band of ordinary electron energy levels, the excitation probability varying only slowly with $h\nu$. In contrast, this type of description does not appear useful for the other group of photoelectrons; it would lead to a density of initial states that decreases exponentially with increasing energy and to an excitation probability that changes violently with $h\nu$.

We have proceeded, tentatively, by attributing the f-group to direct ionization of F-centers and shall discuss the mechanism in more detail later.[6] We have assumed that the f-type energy distribution is symmetrical (similar to a gaussian distribution, for example). In this way, it is possible to isolate it crudely from the other group of electrons, which does not affect it greatly in the region of high energies (Fig. 3).

The slow, second group we shall term the s-group. As seen in Fig. 3, it produces the peaks near $E=0.3$ ev. In the separation process mentioned above, this s-group maximum is practically undisturbed, since the f-group makes only a small contribution to the composite distribution in this region of low energy. Toward higher energies, the derived s-type distribution falls off roughly along an exponential at a rate near one decade per 1.8 ev.

This s-group energy distribution is unusual in form and is peaked at a surprisingly low energy. The phenomenon appears to be characteristic of exciton-induced emission. Thus, the f-group predominates for $h\nu<5$ ev, where exciton production is small. When exciton stimulation and direct ionization become comparable, as at $h\nu=5$ ev, the photoelectrons emerge in the two clearly separable f- and s-groups of comparable magnitude. Above 5 ev, exciton stimulation increases greatly; the additional current appears almost entirely in the s-group. In the same region, the f-group is practically unchanged (even below 5 ev, the f-peak increases in height no more rapidly than the first power of $(h\nu-3.3$ ev)). Thus, it is practically undetectable at $h\nu=5.56$ ev in the presence of an s-group 50 times larger (Fig. 4).

This suggests that the f- and s-groups of photoelectrons arise by direct ionization and by exciton stimulation, respectively, in these experiments. We shall take this point of view in this paper. We should point out, however, that work now in progress on RbBr indicates that distributions similar to those of the s-group may arise well outside of the fundamental absorption band if more permanent centers (perhaps associated with impurities or with aggregates of F-centers) are present. Phenomena other than simple exciton stimulation of F-centers, therefore, appear capable of producing energy distributions of this same general character.

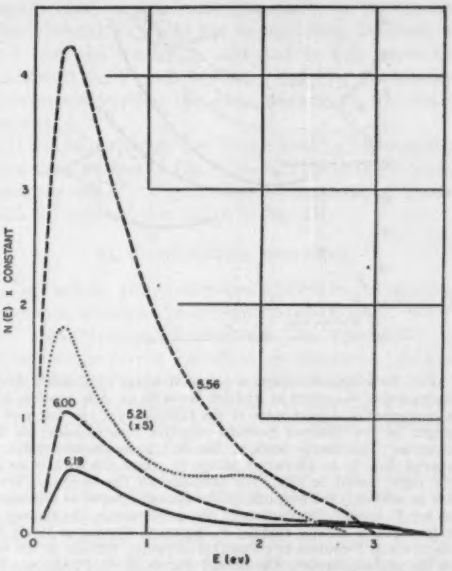

FIG. 4. Energy distributions for values of $h\nu$ in the fundamental absorption band. Ordinates should be multiplied by 2.8×10^{-4} for $h\nu=5.21$ ev and by 1.4×10^{-2} for the other three values. Thus, the curves are actually 10 and 50 times higher, respectively, than those in Fig. 3.

As discussed below in Sec. V, a theory worked out by Herring[6] affords an attractive simple explanation of the f-group. In contrast, the exciton-induced s-group appears to be more complex, and a definite interpretation will not be attempted here. For the sake of completeness, however, we shall mention factors that may be involved and that depend on further theoretical work for satisfactory comparison with experiment.

Several independent mechanisms may tend to produce slow electrons like those in the s-group. One is lattice scattering of excited electrons during their migration to the surface. This phenomenon has been treated quantitatively by Hebb,[1] who has arrived at a distribution quite similar to that given here for $h\nu=5.56$ ev. The "dead layer" thickness characteristic of this sample was estimated to be 80A or less.

[6] C. Herring, Phys. Rev. 73, 1238T (1948), has given a theory of this type of emission (in the absence of scattering) in another connection; the treatment in Sec. V is based on his work.

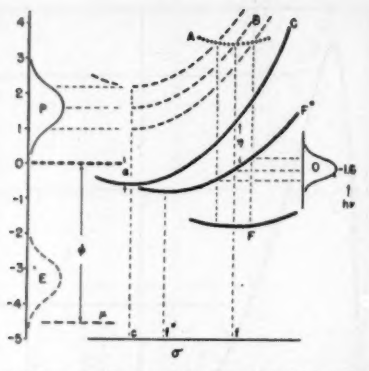

FIG. 5. Schematic diagram (after Herring) illustrating direct ionization of F-centers in RbI for $h\nu = 4.99$ ev. The abscissa σ is a configurational parameter of the familiar type; in this case it might be the distance between negative ions adjacent to the F-center. The energy scale at the left is in electron volts; it applies directly to all curves except O, where the scale of $h\nu$ on the right should be used. The abscissas for the auxiliary curves are as follows: O, absorption in the optical F-band as a function of $h\nu$; P, energy distribution of photoelectrons in the f-group as a function of kinetic energy; E, apparent density of levels for electrons in F-centers as a function of energy relative to the top of the surface barrier. The energy curves B, C, F, etc. are for illustrative purposes and have only semiquantitative significance (see reference 10, p. 136).

In order to avoid a similar effect on the f-group, we must assume that these electrons arise closer to the surface. This would happen if excitons were destroyed at surfaces, as suggested by Fano.[7] From this point of view, the separability of the f- and s-groups constitutes evidence for Fano's hypothesis, and the 80A "dead layer" derived by Hebb for this sample must be attributed primarily to this phenomenon.

Another effect which would produce relatively slow electrons has been suggested by Seitz,[8] namely, degradation of exciton energy before F-center stimulation. This would be particularly probable if the excitons were not mobile but instead interacted with F-centers in a process like that considered by Foerster.[9] Energy would then be dissipated by lattice polarization after exciton formation. Another possibility involves selection rules that limit the optical transition to a state at the top, rather than at the bottom, of the exciton energy band. Then excitons could be degraded by inelastic scattering during migration to F-centers. If only processes like these are important, it is not necessary to invoke surface destruction of excitons, of course, in explaining the differences between f- and s-groups.

A third factor that may be partially responsible for the s-group is the ejection of photoelectrons from more complicated initial states such as may arise from impurities or aggregates of F-centers. These aggregates may form when F-centers are bleached with light in their absorption band or when they decay because of thermal agitation. They are more permanent than F-centers and have higher photoelectric threshold energies. It is difficult to avoid small concentrations of such centers. They may well account for the slight rise in the photoelectric yield between 4 and 5 ev in Fig. 2.

One notes that a complete explanation of the effects reported here must account for energy losses of the order of magnitude 1 ev for that part of the s-group arising in F-centers. In particular, quanta of energy 5.6 ev are required to form excitons at the peak of the fundamental absorption band. However, the energies of the photoelectrons produced are, in the main, no greater than those ejected by direct ionization due to quanta of energy between 4 and 5 ev. These large losses and the unusual energy distribution associated with the s-group are in obvious contrast with the apparently simple behavior of the f-group.

V. ORIGIN OF THE f-GROUP

Figure 5 is a schematic diagram patterned after one used by Herring[6] to describe photoelectric emission from an impurity level in an ionic semiconductor. The abscissa is a configurational parameter σ describing qualitatively the position of ions in the distorted lattice near an F-center. The ordinate is the total energy of the F-center system. In the customary way, this total energy is considered to be distributed between the F-center electron and the ions in the lattice around it. Initially, the electron is in the state F in Fig. 4. At 300°K, σ vibrates about an equilibrium value f, and the various configurations assumed by the center have a Boltzmann distribution in energy. If we approximate F by a parabola, they have a gaussian distribution in σ.

Quanta, of 5-ev energy in Fig. 5, excite electrons from the state F to a group of levels lying along the dotted curve A in the conduction band of the crystal. According to a strict interpretation of the Franck-Condon principle, the curve A lies directly above F and is parallel to it. It represents total energy distributed among a free electron in the conduction band and ions in the distorted lattice around the vacancy which was formerly an F-center. When the lattice relaxes to the configuration c, the equilibrium position for a vacancy, the released energy (of the order of 1 ev) is carried away by the lattice vibrations. The kinetic energies of the electrons are measured by their positions above the bottom C of the conduction band. (The other curves, B for example, are parallel to C.) It is evident that the distribution of kinetic energies is similar to a gaussian distribution in character. The half-width of the band should be of the order of 1 ev, and it should vary with the square root of the tempera-

[7] U. Fano, Phys. Rev. **58**, 544 (1940).
[8] Frederick Seitz, private communication; *The Modern Theory of Solids* (McGraw-Hill Book Company, Inc., New York, 1940), Secs. 96, 108, 148; *Pittsburgh Symposium on Plastic Deformation of Crystalline Solids* (Naval Research Laboratory).
[9] T. Foerster, Ann. Physik **2**, 55 (1948).

ture.[10] For purposes of comparison, the analogous behavior of the absorption in the optical F-band is indicated in the familiar way.[10]

Some of the excited electrons escape over the barrier at the crystal surface and emerge with a band of kinetic energies, P in Fig. 5, which is similar to the corresponding band inside the surface. The average kinetic energy is lower, of course, and the distribution is distorted by the decrease of the escape probability with decreasing energy.[2] In experiments like those described here, it is doubtful that the distortions can be detected. When viewed against a background like that due to the s-group, this distribution would thus appear as a partially resolved peak similar to a gaussian distribution. Thus, we correlate it directly with the f-group of photoelectrons found in these experiments. For $h\nu = 4.99$ ev, the center of the band lies about 1.7 ev above the zero level. Thus, the photoelectrons appear to have come from a similar band E centered roughly 3.3 ev below the surface barrier.

Let us say for the moment that the F^* level, the excited state of an F-center, lies below C by an amount η, for the configuration $\sigma = f$. Then the electron affinity (α in Fig. 5) of RbI becomes $\alpha = 4.99 - 1.6 - 1.7 - \eta = 1.7 - \eta$ ev, since the center of the band P is at 1.7 ev for $h\nu = 4.99$ ev, and the center of the optical absorption band 0 is at $h\nu = 1.6$ ev. In Fig. 5, η is taken for purposes of illustration to be near 1 ev; thus, α is 0.7 ev, consistent with the upper limit of 1.9 ev obtained in (II).

The spectral distribution[6] in Fig. 2 is also in qualitative agreement with that expected on the basis of Herring's work. It indicates that the center of the band E in Fig. 5 lies below the vacuum level by about 3 ev, a value slightly smaller than was obtained above. The discrepancy may not be significant in view of our experimental uncertainties (especially in the energy distributions). It would not be surprising, however, to find that the scattering neglected in this treatment could shift the F peaks in Figs. 3 and 4 by this amount without obliterating the main features of the distributions.

It will be noted that the "Fermi level" μ'', determined from the V_0 values in Fig. 1, lies well below the F-center energy levels E in Fig. 5. This is consistent, of course, with the point of view taken in Sec. III.

[10] See, for example, N. F. Mott and R. W. Gurney, *Electronic Processes in Ionic Crystals* (Clarendon Press, Oxford, England, 1940), chapter IV. Zero point vibrations are neglected here.

VI. CONCLUDING REMARKS

The salient point discussed above is the striking difference between the energy distributions of the f- and s-groups of photoelectrons. The separability of these groups was a fortunate circumstance. Such a separation cannot always be effected. As mentioned before, the pronounced tendency of the alkali iodides to exhibit non-uniform surfaces is a serious hindrance. A more fundamental consideration involves the electronic energy structure of the emitter; if a separation is to be convincing, the energy at the f-group peak must reach values of 1 or 2 ev before exciton-induced emission becomes important. (From this point of view, the iodides present a less favorable case than bromides, for example.)

In parallel work on KI, results were less clear-cut than those given here. Using the behavior of RbI as a guide, however, we have convinced ourselves that the same phenomena appear.

It is a pleasure to record our thanks to Malcolm Hebb for many stimulating conversations. To Harvey Brooks, we are grateful for helpful discussions, especially regarding the energy distributions; and to Frederick Seitz we are indebted for many suggestions regarding exciton behavior. Jean Dickey has given us her generous help in the phototube design.

Relative Photoneutron Yields from the 330-Mev Bremsstrahlung*

K. M. TERWILLIGER, L. W. JONES, AND W. N. JARMIE
Radiation Laboratory, Department of Physics, University of California, Berkeley, California
(Received February 8, 1951)

Relative photoneutron yields were determined for 50 elements bombarded by the 330-Mev x-ray bremsstrahlung of the Berkeley synchrotron. The determinations were made at 90° to the beam axis with a paraffin moderated BF_3 proportional counter. Relative yields for elements above atomic number 30 were proportional to $Z^{1.7}$. Yields for low Z elements show a correlation with the binding energy of the last neutron. Angular distributions of photoneutrons were briefly investigated, and a Pb transition curve for photoneutrons was run.

PREVIOUS to July, 1950, workers at the General Electric laboratories had determined yields from some (γ,n), $(\gamma,2n)$, and (γ,np) reactions by studying the induced activities.[1] Kerst and Price[2] had studied relative neutron yields for over 50 elements from x-rays of the 22-Mev Illinois betatron by neutron counting. Strauch[3] had studied a few reactions by induced activities, and with transition curves had determined the reaction energies for these reactions, finding effective energies as high as 80 Mev.

In view of Strauch's findings, a comprehensive study was made of photoneutron yields from the 330-Mev x-ray bremsstrahlung by a direct neutron counting experiment. The experiment here described consisted of bombarding various elements with the x-ray beam of the synchrotron and counting the ejected photoneutrons in a direction 90° to the beam axis with a BF_3 proportional counter.

The counter was imbedded in a paraffin cylinder in order to moderate and count high energy neutrons. This long counter geometry is given in Rossi and Staub[4] as having a uniform response to neutrons of all energies to 5 Mev, and Kerst[5] mentions that his laboratory has estimated that a similar counter is 60 percent as efficient for 15-Mev neutrons as for low energies. An overhead view of the experimental arrangement is shown in Fig. 1. The beam was monitored by an ionization chamber, which was energy calibrated by Blocker and Kenney.[6] This calibration, in conjunction with a standard 500-mg radium beryllium neutron source, enabled reduction of the data to neutrons/(erg×moles/cm²). The targets consisted of plates and powders, the latter sometimes in compound form. The thickness of the targets was kept less than ¼ shower unit to keep the loss of counts due to beam degradation less than 4 percent. The targets were tipped to prevent the neutrons from having to traverse the entire target width before reaching the counter. Checks showed that when the plane of the target was on the axis of the counter, the yield was considerably reduced.

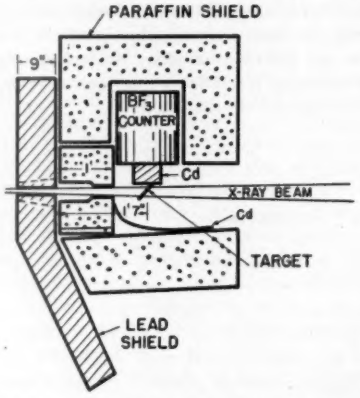

FIG. 1. Overhead view of the experimental arrangement. The x-ray beam originates in the synchrotron to the left of the lead shield.

Counting errors, including background, varied from 2 percent to 10 percent. Counts from background, which included the counts from the other elements of the targets in compound form, varied from 250 percent of the counts for vanadium (taken from $V_2O_2Cl_4$) to 4 percent of the counts for the metallic uranium target. The mean background was 20 percent of target counts. The total relative probable error varied from 4 percent to 12 percent with a mean of 6 percent.

The relative photoneutron yields of the elements *vs* Z (plotted in Fig. 2) show that the yield goes as $Z^{1.7}$ for Z greater than 30. U and Th lie high, owing to photofission neutron yields adding to the normal photoneutron yields. The points are in substantial agreement with those of Kerst obtained with the 320-Mev Illinois betatron.[7] The Illinois and Berkeley high energy data are both plotted in Fig. 3, with the Illinois data normalized to the Berkeley data at Pb. The normalization factor is 1.27. This 27 percent discrepancy is assumed to

* This work was performed under the auspices of the AEC.
[1] M. L. Perlman and G. Friedlander, Phys. Rev. **74**, 442 (1948). G. C. Baldwin and G. S. Klaiber, Phys. Rev. **73**, 1156 (1948). J. L. Lawson and M. L. Perlman, Phys. Rev. **74**, 1190 (1948).
[2] G. A. Price and D. W. Kerst, Phys. Rev. **77**, 806 (1950).
[3] Karl Strauch, Phys. Rev. **81**, 973 (1951).
[4] B. Rossi and H. Staub, *Ionization Chambers and Counters* (McGraw-Hill Book Company, Inc., New York, 1949), pp. 196–197.
[5] D. W. Kerst, private communication.
[6] Blocker, Kenney, and Panofsky, Phys. Rev. **79**, 419 (1950).
[7] D. W. Kerst and G. A. Price, Phys. Rev. **79**, 725 (1950).

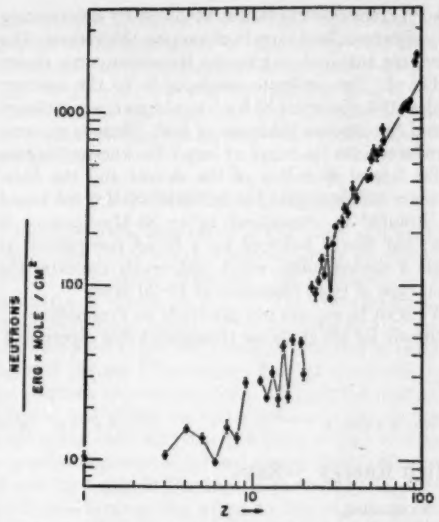

FIG. 2. Photoneutron yield in neutrons/(erg×moles/cm²) from 330-Mev bremmstrahlung plottted *vs* Z of the elements on a log log scale, showing relative errors. For $Z>30$ the yield goes as $Z^{1.7}$.

be due to beam energy and neutron source calibrations. Price and Kerst[7] and Baldwin and Elder[8] have reported a Z^2 yield at lower energies. For the low Z elements there is an even-odd alternation in yields. The low Z patterns for both the 22-Mev Illinois data and the 330-Mev Berkeley data are plotted in Fig. 3 and appear quite similar. This alternation is roughly related to the binding energy of the last neutron, as may be seen from the correlation plot of yield/A *vs* the binding energy of the last neutron in Fig. 4.

The yield in neutrons/(erg×moles/cm²) corresponds

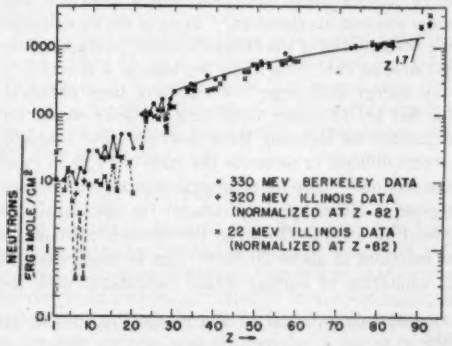

FIG. 3. Photoneutron yield in neutrons/(erg×moles/cm²) from 330-Mev bremmstrahlung plotted *vs* Z on a semilog graph, including data of Kerst and Price at 22 Mev and 320 Mev normalized to lead.

[8] G. C. Baldwin and F. R. Elder, Phys. Rev. **78**, 76 (1950).

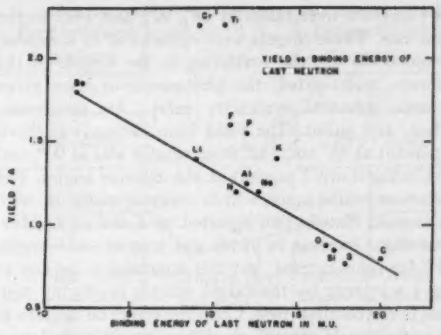

FIG. 4. Photoneutron yield/A *vs* the binding energy of the last neutron. Correlation with the binding energy of the last neutron is evident.

to $\int_0^{330} f(W)\sigma(W)dW$, where W is the photon energy, $\sigma(W)$ the photoneutron cross section at that energy, and $f(W)$ the number of photons of energy W in the beam. For a bremsstrahlung, $f(W)\sim 1/W$. The theory of Levinger and Bethe[9] would give a lower Z dependence of yield than the $Z^{1.7}$ dependence found experimentally.

A brief investigation was made into the angular distribution of the photoneutrons from D, C, S, Fe, Ni,

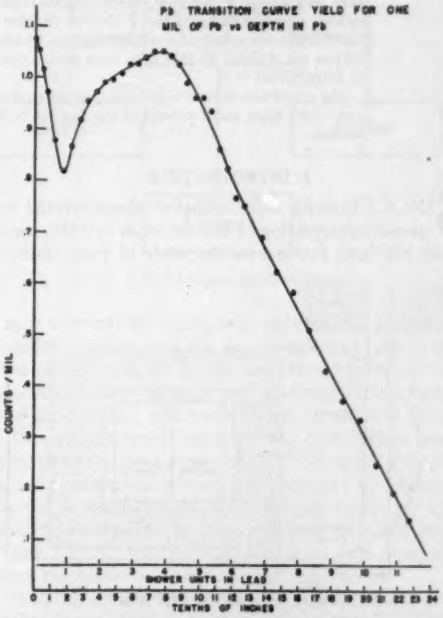

FIG. 5. Transition curve of photoneutrons from lead. The ordinate is the photoneutron yield from a unit thickness of lead placed behind the abscissa thickness of lead. The units of the ordinate are arbitrary.

[9] J. S. Levinger and H. A. Bethe, Phys. Rev. **78**, 115 (1950).

and Cu. Data were taken at 38°, 90°, and 142° to the beam axis. These targets were cylindrical to minimize asymmetrical neutron scattering in the target. Of the elements investigated, the photoneutrons were given off with spherical symmetry except for deuterium, carbon, and sulfur. The yield from carbon was down 10 percent at 38° and 142° from what it was at 90°, and from sulfur down 5 percent at the extreme angles. The deuterium results agree, within counting statistics, with the angular distribution reported by Kerst at 22 Mev. Some slight increase in yields was seen at small angles (38°) for some targets, but this appeared to be due to x-rays scattered by the target sample producing neutrons in the counter itself. Counting errors on deuterium ran as high as 25 percent, the others considerably lower.

A Pb transition curve was obtained by determining the yields from lead targets of varying thicknesses. The data were analyzed to give the transition curve shown in Fig. 5. The ordinate corresponds to the neutron yield a unit thickness of lead would give when placed behind the abscissa thickness of lead. There is an error introduced into the curve at larger thicknesses because of the lateral spreading of the shower and the finite diameter of the target. The initial sharp descent found by Strauch[8] to correspond to an 80-Mev process is seen; but this is followed by a broad rise peaked at about 4 shower units, which apparently indicates the usual type of (γ,n) resonance at 15–20 Mev.

We wish to express our gratitude to Professor A. C. Helmholz for his guidance throughout this experiment.

PHYSICAL REVIEW VOLUME 82, NUMBER 6 JUNE 15, 1951

Production of Protons by High Energy γ-Rays*

C. LEVINTHAL† AND A. SILVERMAN‡
Radiation Laboratory, University of California, Berkeley, California
(Received January 22, 1951)

The protons ejected from various nuclei by the gamma-ray beam of the 320-Mev Berkeley synchrotron have been studied with a proportional counter telescope system. The energy distribution of the protons from carbon, copper, and lead from 7 Mev to 70 Mev at 90° was roughly proportional to $1/E^3$. The angular distribution was spherically symmetrical for 10-Mev protons and showed a pronounced forward maximum for protons of about 40 Mev. The cross section per nucleus for the ejection of 40-Mev protons was found to be proportional to Z.

The experimental results indicate that protons above 30 Mev arise primarily from the interaction of the γ-ray with some small subunit of the nucleus rather than through the formation of an excited compound nucleus.

I. INTRODUCTION

SINCE Chadwick and Goldhaber[1] demonstrated the photodisintegration of the deuteron in 1935, much work has been devoted to the study of γ-ray induced nuclear reactions. Studies have been made using various target nuclei bombarded with γ-rays from several radioactive sources[2] and from the $Li^7(p,\gamma)Be^8$ reaction.[3,4] Recently, the work has been extended to the high energy regions using the γ-ray beams from the high energy electron accelerators.[5,6] Most of the experiments have been studies of the radioactive end products of the reactions, so that total cross sections as a function of γ-ray energy and target nucleus have been obtained. This has led to rather conflicting evidence about the mechanism for inducing these reactions. For example, it seems difficult to reconcile the ratio of (γ,p) to (γ,n) cross sections[5,6] with an evaporation process unless one supposes a rather special character for the transitions allowed by γ-rays.[7] However, the resonances found for the reactions at about 20 Mev[5,6] can be understood as the excitation of nuclear dipole oscillations with the

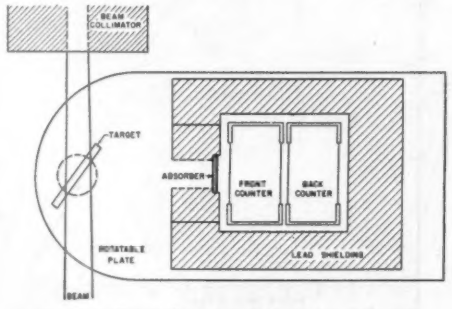

FIG. 1. Geometry of apparatus.

* This work was performed under the auspices of the AEC.
† Now at University of Michigan, Ann Arbor, Michigan.
‡ Now at Laboratory of Nuclear Studies, Cornell University, Ithaca, New York.
[1] J. Chadwick and M. Goldhaber, Proc. Roy. Soc. (London) **151**, 479 (1935).
[2] Russell, Sachs, Wattenberg, and Fields, Phys. Rev. **73**, 545 (1948).
[3] W. Bothe and W. Gentner, Z. Physik **106**, 236 (1937).
[4] Huber, Lienhard, Scherrer, and Wäffler, Helv. Phys. Acta **11**, 139 (1944).
[5] M. L. Perlman and G. Friedlander, Phys. Rev. **74**, 442 (1948).
[6] K. Strauch, thesis, University of California, February (1950)
[7] L. I. Schiff, Phys. Rev. **73**, 1311 (1948).

subsequent evaporation of a neutron.[8] The present work consists of measurements of the energy and angular distribution of protons ejected from various nuclei by high energy γ-rays. It was felt that this kind of investigation could yield more detailed information about the mechanism than the method of detecting radioactive end products.

II. EXPERIMENTAL ARRANGEMENT

Measurements were made of the range and angular distribution of the emitted protons with a proportional counter coincidence telescope. The geometry of the apparatus is shown in Fig. 1. The counters had an active cylindrical region 2½" in diameter and 2" deep, and were filled to one-half atmosphere with a 95 percent argon, 5 percent CO_2 mixture. Two-mil Dural was used for entrance and exit windows. To limit the proton to a region well within the active volume of the counters, a collimator consisting of a lead brick with an inch-and-a-quarter diameter hole was placed directly in front of the telescope. At the back of the collimator, a one-quarter-inch recess was milled so that absorbers could be placed adjacent to the counters.

The front of the telescope was six inches from the target, which was large enough to intercept the entire beam. The target thickness was kept small compared with the total range being measured. The telescope and target could be rotated independently about the target center, which was aligned photographically with the beam.

A block diagram of the electronic components is shown in Fig. 2. Since the rise-time of the pulses out of the proportional counters was about 0.3 μsec, one could clip the pulses at 0.4 μsec without destroying the proportionality. The short duration was desirable to minimize the problem of pile-up of electrons. The gate generated by the variable gate circuit, which determined the resolving time of the apparatus, was of 0.5-μsec duration.

For all the measurements the synchrotron beam was spread out to about 2 millisecond duration per pulse. With a repetition rate of 6/sec this gave a duty cycle of about 1/80. With the expanded beam the energy of the electrons striking the internal target varies from 290 Mev to 320 Mev.

III. BACKGROUND

The electron background near the synchrotron beam was eliminated by demanding large pulses out of both counters. The amplifier gains were set so that neither counter could detect any radiation from a one-millicurie radium source. Then the g^- in on the amplifier connected to the rear counter was reduced by a factor of two. Therefore, for electrons to produce a coincidence, two of them must stop in the rear counter and one in the front counter, all within about 0.5 μsec. Furthermore,

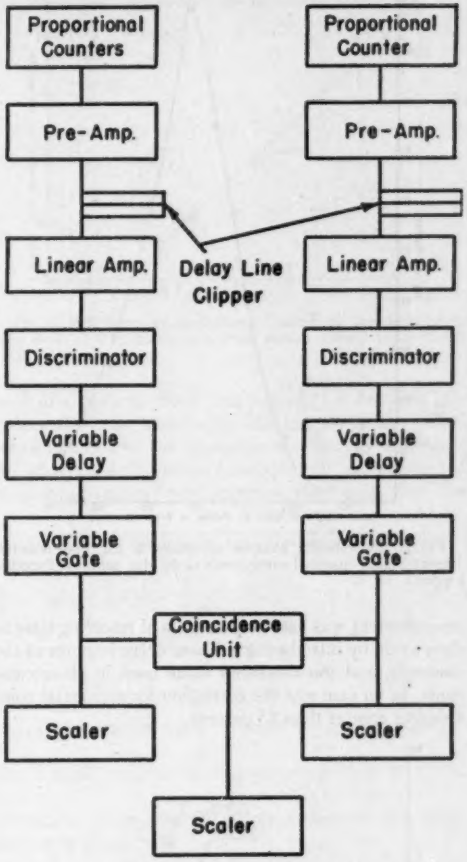

FIG. 2. Block diagram of electronics.

if such an event did occur, as in the case of a shower, it would be equally likely for two electrons to stop in the front counter and one in the rear. However, when the gains on the two channels were reversed, it was found that the counting rate was reduced by about a factor of two, as one would expect if the coincidences were being produced by a single particle.[8a] Further evidence that the coincidences were not produced by electron showers is furnished by the following facts: (a) the relative cross sections are proportional to Z rather than Z^2 (see Fig. 5); (b) the cross section in lead decreases below the proton coulomb barrier (see Fig. 4).

The accidental coincidences were calculated and corrections made for them in all the data. An experimental

[8] M. Goldhaber and E. Teller, Phys. Rev. 74, 1046 (1948).

[8a] The expected reduction of a factor of two arises from the fact that the absorber between the counters was about 30 mg/cm² of Al and the residual range on leaving the second counter could be as great at 60 mg/cm². (See section on calculation of absolute cross section.)

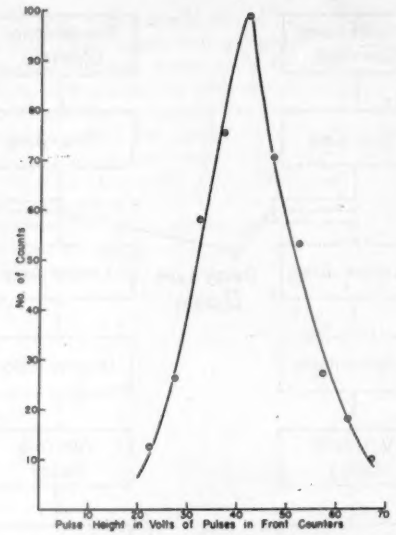

FIG. 3. Pulse-height analysis of counts in the first counter. Energy region observed corresponds to 40-Mev protons. Target is copper.

measurement was made of the ratio of resolving time to duty cycle by introducing a 4-μsec delay into one of the channels, and the measured value used in all calculations. In no case was the correction for accidental coincidences greater than 15 percent.

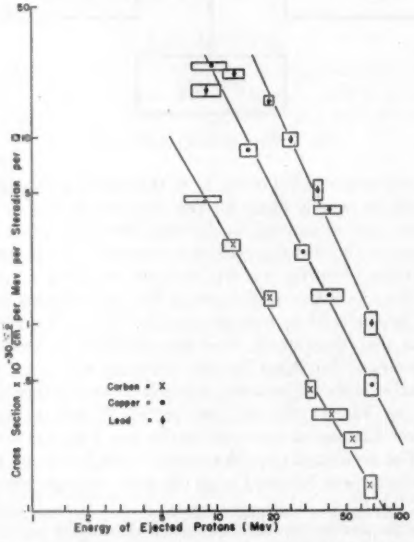

FIG. 4. Energy dependence of the cross section in carbon, copper, and lead at 90° with respect to the beam direction.

The tests described above were sufficient to insure that the coincidence counting rate was due primarily to a single heavy particle. They yield no information about the nature of the particle, that is, whether the particle is a proton, meson, alpha-particle, etc. To obtain such information, a pulse-height analysis was made of the pulses in the first counter which were in coincidence with those of the second counter. For this purpose a ten-channel pulse height analyzer was used. Pulse-height analysis was done using several different targets and absorbers. A typical example is shown in Fig. 3. These results showed that the coincidences were due primarily to a single particle. To check that these were protons, the apparatus was used to detect 30-Mev protons from the Berkeley linear accelerator elastically scattered by carbon. The results of the measurements were sufficient to rule out any background but deuterons.[8b] The resolving power of the apparatus was not sufficient to distinguish protons from deuterons.

IV. CALCULATIONS AND CORRECTIONS

The measurements made gave the number of protons with a range between R and $R+\Delta R$, where R = thickness of the total absorber up to the rear counter and ΔR = maximum residual range on entering the rear counter of a proton which would produce a sufficiently large pulse to register in that counter. ΔR was measured in two independent ways: (a) from the width of the pulse-height curve (Fig. 3); (b) from the fact that a proton had to lose twice the maximum energy possible for an electron in the rear counter in order to register. Method (a) gave $\Delta R = 60$ mg/cm^2 of Al; method (b) gave $\Delta R = 90$ mg/cm^2 of Al. The former result was considered more reliable and was used in all calculations of the absolute cross section. It is the uncertainty in ΔR which produces the maximum error in the absolute cross section, which is estimated to be accurate to within a factor of two. The cross sections are calculated per "Q," where "Q" = total energy of the beam divided by the maximum energy of the γ-rays = 320 Mev. The conversion from range to energy was made from the range energy relation of Aron, Hoffman, and Williams.[9]

For the low energy region of the energy distribution where very thin targets must be used, the no-target background becomes significant. By means of added shielding, the no-target background was reduced to about 15 percent at the lowest energy point.

There are two other sources of error which must be considered. These are nuclear absorption in the absorber and multiple scattering in the absorber. The correction for nuclear absorption was made assuming an absorption cross section of the geometrical area of the absorbing nucleus. For the highest energy point, this correction was six percent. The correction for multiple

[8b] Only in the cases of a carbon target with no absorber was any substantial alpha-particle component observed. In this case, the alpha-particles contributed about 20 percent of the total number of coincidences.

[9] Aron, Hoffman, and Williams, UCRL-12 (unpublished).

scattering in the absorber was estimated to be five percent at the highest energy.

V. RESULTS

Figure 4 shows the energy distribution on carbon, copper, and lead taken at 90° with respect to the beam direction. The height of the blocks show the standard error due to statistics of counting. The width of the blocks show the energy interval represented by the thickness of the target. The results indicate a differential cross section proportional to E^{-S}, where E=proton energy and $S=1.7\pm0.1$ for carbon, 1.9 ± 0.1 for copper, and 2.2 ± 0.2 for lead. The decrease in cross section in the lead distribution at low energy is presumed to be due to the effects of the coulomb barrier.

The relative cross sections at 40 Mev were taken for Be, C, Al, Zn, Cu, Ag, Pb, and W. This was done at 90° using targets of equal stopping power. The measurements were taken on the same day with all conditions remaining fixed. The results are shown in Fig. 5. As may be seen in the curve the cross sections are proportional to Z, to the accuracy obtained in the experiment.

The angular distributions shown in Figs. 6 and 7 were taken for Be, C, and Cu at 10 and 40 Mev. The 90°, 112°, and 135° points were taken with the target normal to the 112° point. The 90° point was repeated for the forward angles, where the target was rotated so that it was normal to the 67° point.

VI. DISCUSSION OF RESULTS

In trying to understand the mechanism for the ejection of protons from nuclei by γ-rays, two possibilities suggest themselves. One is that the γ-ray is absorbed by the nucleus, exciting it to the energy of the γ-ray with the subsequent loss of excitation by emission of a proton. The other is that the γ-ray interacts directly with some subunit of the nucleus, e.g., proton, deuteron, alpha-particle, etc., of which the proton is a constituent. The experimental indication is that the latter process is predominant for protons of energies above about 30 Mev and that the former process gives rise, primarily, to protons below that energy. The evidence for this conclusion is the following. The cross section is a much more slowly varying function of energy than one would predict from an evaporation process regardless of how the absorption cross section for γ-rays varies with energy.[9a] Further evidence against an evaporation process is the fact that the angular distribution at 40 Mev has a forward peak (Fig. 7). It seems difficult to understand any pronounced deviation from spherical symmetry at these energies if one assumes an evaporation process. The simplest assumption one can make about the process is that the γ-ray interacts directly

[9a] Even under the assumption that the absorption cross section is a step function, zero everywhere except at and above the maximum beam energy (this assumption leads to the most high energy protons) one can still not account for the observed high enery protons by an evaporation process.

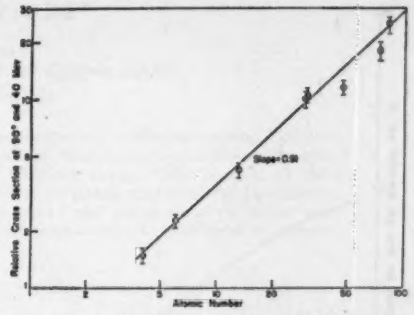

FIG. 5. Relative cross section as a function of atomic number. The slope of 0.91 indicates a cross section closely proportional to Z.

with the protons. With this assumption one can calculate the cross section for the process if the initial wave function of the proton in the nucleus is known; or, what amounts to the same thing, if one knows the momentum space wave function. Assuming that the

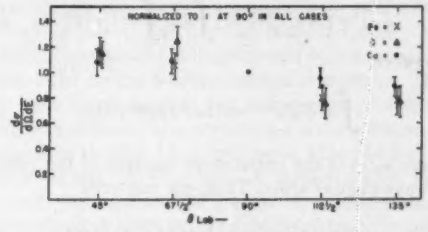

FIG. 6. Angular distribution of 10-Mev protons from Be, C, Cu.

transition is an electric dipole transition the cross section is given by[10]

$$\sigma=8\pi^3e^2\nu c^{-1}|Z_{0a}|^2, \tag{1}$$

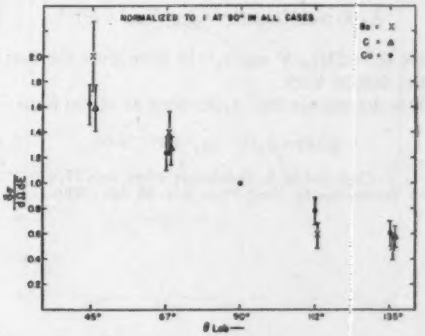

FIG. 7. Angular distribution of 40-Mev protons from Be, C, Cu.

[10] H. A. Bethe and R. Peierls, Proc. Roy. Soc. (London) A148, 146 (1935).

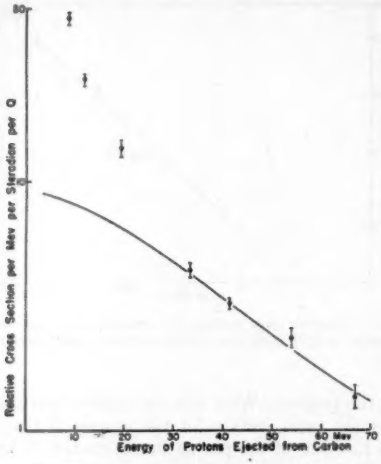

FIG. 8. Energy dependence of cross section. Solid curve is calculated as described in text. Points are experimental.

$$|Z_{0e}|^2=[Mk/(2\pi)^3\hbar^2]\int d\Omega\left|\int d\tau U_0 Ze^{i\mathbf{k}\cdot\mathbf{r}}\right|^2. \quad (2)$$

However,

$$\int d\tau U_0 Ze^{i\mathbf{k}\cdot\mathbf{r}}=i(2\pi)^{\frac{1}{2}}\partial\phi_0(k)/\partial k_Z, \quad (3)$$

where $\phi_0(k)$ is the initial wave function of the proton in wave number space. Thus, one can write

$$\sigma=(8\pi^3e^2\nu Mk/ch^2)\int d\Omega|\partial\phi_0(k)/\partial k_Z|^2. \quad (4)$$

To find $\phi_0(k)$ we proceed as follows: Chew and Goldberger,[11] using the data of York[12] on the production of fast deuterons by neutrons, deduce a momentum distribution for protons in carbon given by

$$N_0(k)=\phi_0^*(k)\phi_0(k)=\alpha_p\pi^{-2}(\alpha_p^2+k^2)^{-2}, \quad (5)$$

where $\alpha_p^2=2M\epsilon_p/\hbar^2$ and $\epsilon_p=18$ Mev gives the best fit to the data of York.

This determines that $\phi_0(k)$ must be of the form

$$\phi_0(k)=\alpha_p^{\frac{1}{2}}\pi^{-1}(\alpha_p^2+k^2)^{-1}e^{if(k)}. \quad (6)$$

[11] G. F. Chew and M. L. Goldberger, Phys. Rev. **77**, 470 (1950).
[12] J. Hadley and H. York, Phys. Rev. **80**, 345 (1950).

Unfortunately, the phase factor is undetermined. Since the cross section involves the derivative of $\phi_0(k)$, the phase enters in an essential way unless, $f(k)=$constant. Hence, we make the assumption that $f(k)=$constant.[12a] The cross section is then given by

$$\sigma=16\pi e^2(h\nu/\epsilon_p)\gamma^{\frac{1}{2}}/3\hbar c\alpha_p{}^2[1+\gamma]^4, \quad (7)$$

where $\gamma=E_p/\epsilon_p$, and $E_p=$proton energy.

We take $\epsilon_p=18$ Mev and $h\nu=E_p+25$ Mev, as given by Chew and Goldberger.[11] The solid curve shown on Fig. 8 is a plot of this cross section multiplied by the bremsstrahlung spectrum as given by Heitler.[13] The experimentally observed cross section is shown on the same curve for comparison. The two are made to coincide at 41.5 Mev. It is seen that in the region from 30 Mev to 70 Mev the calculated and observed cross sections agree very well. Below this energy, the experimental cross section is higher than the calculated one. This can be understood by assuming that most of the low energy protons are due to an evaporation process. This is consistent with the fact that the angular distribution is spherically symmetric at energies about 10 Mev.

The absolute values of the observed and calculated cross sections at 41.5 Mev are

$$\sigma_{\text{calc}}=8.3\times10^{-28}\text{ cm}^2,$$
$$\sigma_{\text{obs}}=3.1\times10^{-28}\text{ cm}^2.^{13a}$$

The value of σ_{calc} per nucleus is determined by multiplying the value obtained from Eq. (7) by $Z=6$.

Probably both the energy distribution and the absolute cross sections agree more closely than one might reasonably expect from the crude choice of initial proton wave functions.

It is a pleasure to thank Professors W. K. H. Panofsky and A. C. Helmholtz for their frequent advice and guidance. Thanks are also due Professor E. M. McMillan for his continued interest in this work and the synchrotron crew under W. A. Gibbons for their complete cooperation at all times.

[12a] This choice of $f(k)$ leads to a configuration space wave function of the form $U^0=e^{-\alpha r}/r$. This is equivalent to the assumption that the proton is in an S-state in a well of zero range.
[13] W. Heitler, *The Quantum Theory of Radiation* (Oxford University Press, London, 1944), p. 170.
[13a] The observed cross section now has no ambiguity, since we assume a proton of energy E produced by a γ-ray of energy $E+25$ Mev.

The Dual Decay of Re^{186}

ROLF M. STEFFEN
Department of Physics, Purdue University, Lafayette, Indiana*
(Received March 5, 1951)

The decay of Re^{186} (91 hr) has been investigated using spectrometer and coincidence methods. Two beta-groups with maximum energies of 1.070±0.005 Mev and 0.942±0.008 Mev have been observed. The lower energy beta-spectrum leads to an excited state in Os^{186} of 0.136-Mev energy. Nine percent of all disintegrations are by *K*-capture; two-thirds of which lead directly to the ground state of W^{186} and one-third to an excited state of 0.122-Mev energy. Evidence is given for a spin 1 and odd parity of the ground state of Re^{186}. These assignments agree with the predictions of the one-particle spin-orbit coupling model extended to odd-odd nuclei.

I. INTRODUCTION

THE nuclear radiations of Re^{186} were studied by Beach, Peacock, and Wilkinson.[1] The beta-ray spectrum was found to be simple, and each beta-ray to be followed by a 0.212-Mev and a 0.138-Mev gamma-ray in cascade. Grant and Richmond,[2] however, observed a complex beta-spectrum and three gamma-lines of 0.132 Mev, 0.275 Mev, and 0.7 Mev. In order to obtain more information on the excited levels of Os^{186}, it was attempted to measure the angular correlation of the gamma-rays supposedly emitted in cascade. No gamma-gamma-coincidences could be observed in contradiction to the results reported by Beach *et al.* A reinvestigation of the disintegration of Re^{186} was therefore undertaken. During the progress of our work, measurements on the decay of Re^{186}, independent from ours, have been reported by Metzger and Hill.[3] Their results are in very good agreement with the disintegration scheme reported here.

The neutron-activated Re-powder was obtained from the Isotopes Division of the U. S. Atomic Energy Commission, Oak Ridge. In order to prepare sources free from other radioactive material, a chemical separation was performed. The metallic rhenium was dissolved in hot nitric acid and was separated from elements other than molybdenum by addition of $SnCl_2$ and KCNS and extraction of the rhenium complex with successive portions of ether. The rhenium recovered from this extraction was purified of molybdenum by precipitation of the latter as the 8-hydroxyquinoline complex. The very thin source used in the spectrometer measurements was prepared by evaporating a water solution of perrhenic acid on a 12 $\mu g/cm^2$ zapon film and had a surface density of 40 $\mu g/cm^2$. A thicker source (50 mg/cm^2) was used for the gamma-ray measurements and consisted of black Re_2S_7 precipitated from hot acid solution and collected on a small filter paper.

In order to reduce the 18-hr Re^{183} to a negligible amount, the measurements were commenced 10 days after the end of the neutron irradiation in the pile.

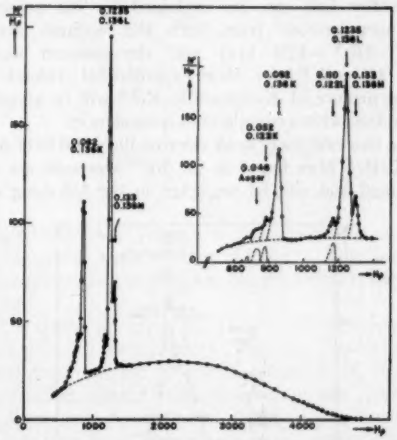

FIG. 1. The electron spectrum of Re^{186}. Arrows mark internal conversion lines. The energy values of the conversion lines and of the associated gamma-rays are given in Mev.

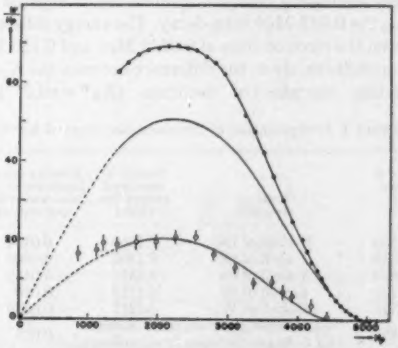

FIG. 2. Beta-spectra of Re^{186}. The two partial spectra are determined from the Fermi plot analysis. The shape of the lower energy spectrum has also been determined directly by measurements of beta-gamma-coincidences in the spectrometer (open circles).

* This work was supported in part by the AEC.

[1] Beach, Peacock, and Wilkinson, Phys. Rev. **76**, 1585 (1949).
[2] P. J. Grant and R. Richmond, Proc. Phys. Soc. (London) **62**, 573 (1949).
[3] F. R. Metzger and P. D. Hill, Phys. Rev. **81**, 300 (1951).

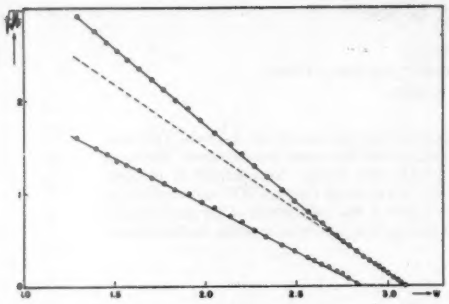

FIG. 3. Fermi plot of the Re^{186} spectra. It is assumed that the two spectra are of the allowed form.

II. THE ELECTRON SPECTRUM OF Re^{186}

The momentum distribution of the electrons from Re^{186}, obtained with a double-lens spectrometer,[4] using a zapon counter window of 0.2 mg/cm² thickness, is shown in Fig. 1. The continuous beta-spectrum (Fig. 2) can be resolved into two groups on the basis of a Fermi analysis of the data. Figure 3 shows the Fermi plot and the result of the subtraction of the higher energy beta-ray group, assuming that the spectra are of the allowed form. This analysis yields two beta-ray groups of 1.070±0.005-Mev and 0.942±0.008-Mev maximum energy, with intensities 73±5 and 27±5 percent, respectively. The resulting momentum distributions are shown in Fig. 2. Direct measurements of the shape of the lower energy beta-ray group using coincidence techniques (see Sec. IV) are in good agreement with the results obtained by the Fermi analysis.

The energies of the three strongest conversion lines correspond to a gamma-ray of 0.136-Mev energy converted in the K, L, and M shell of osmium. The energy of this gamma-ray is, within the experimental error, equal to the energy difference of the partial beta-spectra, indicating that this gamma-ray is emitted following the 0.942-Mev beta-decay. The energy difference between the electron lines of 0.0525 Mev and 0.110 Mev corresponds exactly to the difference between the K- and L-binding energies of wolfram ($E_K^W = 69.2$ kev; $E_L^W = 11.8$ kev). One is therefore tempted to interpret these two lines as the K- and L-components associated with a single gamma-ray of 0.122 Mev emitted from an excited state of W^{186}. This implies that the Re^{186} nuclide decays not only by electron emission to Os^{186}, but also by electron capture to W^{186}. The occurrence of K-capture is further indicated by the presence of a rather broad electron line of medium energy, 0.046 Mev, which probably must be considered as due to Auger-electrons resulting from K-capture and K-conversion. The latter alone could not account for the relatively large number of observed Auger-electrons. The broadening of the 0.046-Mev line can be explained by the presence of Auger-electrons from both the wolfram atoms ($E_K^W - 2E_L^W = 45.0$ kev) and the osmium atoms ($E_K - 2E_L = 47.8$ kev). More experimental evidence for the occurrence of K-capture in Re^{186} will be given in connection with x-ray-electron coincidences.

The two extremely weak electron lines of 0.0315 Mev and 0.0375 Mev found in the Re^{186} spectrum are not explained and will be neglected in the following dis-

TABLE I. Interpretation of the conversion lines of Re^{186}.

Energy of electron line Mev	Origin of electrons	Energy of associated gamma-line (Mev)	Relative intensity. (Intensity of whole continuous beta-spectrum = 1.0)
0.1330	M-shell of Os	0.1360	0.0154
0.1235	L-shell of Os	0.1362	0.0800
0.0620	K-shell of Os	0.1357	0.0485
0.1103	L-shell of W	0.1223	0.010
0.0525	K-shell of W	0.1217	0.0059
0.046	{KLL-Auger-electrons from osmium / KLL-Auger-electrons from wolfram}		0.005
0.0373	?	?	0.0001
0.0315	?	?	0.00002

[4] Bleuler, Blue, and Johnson, to be published.

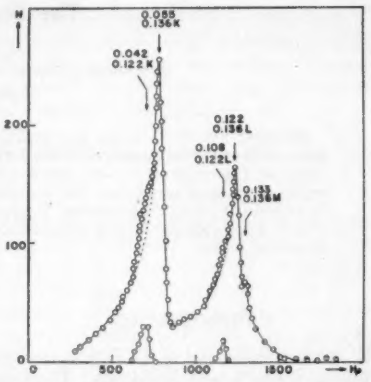

FIG. 4. Photoelectrons ejected from a 5 mg/cm² gold radiator by the gamma-rays following the decay of Re^{186}.

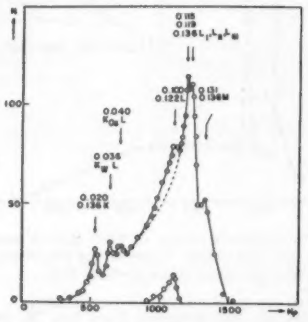

FIG. 5. Photoelectrons ejected from a 0.3 mg/cm² uranium radiator by the gamma- and x-rays emitted during the decay of Re^{186}.

cussion. The interpretation of the conversion lines given in Table I is confirmed by the following measurements of gamma- and x-rays emitted during the decay of Re^{186}.

III. THE GAMMA-RAY SPECTRUM OF Re^{186}

The gamma- and x-ray spectrum of Re^{186} has been measured by observing the photoelectrons ejected from Pb, Au, and U radiators of 19 mg/cm², 5 mg/cm², and 0.3 mg/cm² thickness, respectively. The results are shown in Figs. 4 and 5. The source was contained in a copper capsule thick enough to stop all beta-rays. Only two gamma-lines of 0.136±0.001-Mev and 0.122±0.002-Mev energy could be associated with the observed photo peaks from the three different radiators. The relative intensities of the two gamma-rays have been calculated from the heights of the photoelectron lines, taking into account the effect of finite radiator thickness and the variation of the photoelectric cross section with energy.

TABLE II. The gamma- and x-rays emitted by Re^{186}.

Radiator	Energy of photo-electron peak (corrected for finite thickness of radiator) Mev	Shell	Corresponding gamma-energy or x-ray-energy Mev	Relative intensities of the associated gamma-rays
Pb (19 mg/cm²)	0.048	K	0.136	1.0
	0.120	L	0.136	
	0.132	M	0.136	
	0.035	K	0.123	0.10±0.02
	0.106	L	0.122	
Au (5 mg/cm²)	0.055	K	0.135	1.0
	0.122	L	0.136	
	0.133	M	0.136	
	0.042	K	0.1225	0.10±0.02
	0.108	L	0.122	
U (0.3 mg/cm²)	0.020	K	0.136	
	0.115	$L_I L_{II}$	0.136	1.0
	0.119	L_{III}	0.136	
	0.100	L	0.122	0.11±0.03
	0.036	L	0.057 (W K-radiation)	
	0.040	L	0.061 (Os K-radiation)	

The results are given in Table II. The photoelectron peak at 0.036 Mev, observed with the U-radiator and interpreted as due to the L-photoline of wolfram K-radiation, gives further evidence of the occurrence of K-capture. A search for gamma-rays of energies greater than 0.136 Mev gave negative results, in contradiction to the measurements reported by Beach, Peacock, and Wilkinson.[1]

IV. COINCIDENCE MEASUREMENTS WITH SPECTROMETER

From the results of the above measurements, it must be concluded that the 0.136-Mev gamma-ray is emitted from an excited state of Os^{186} which is reached by the 27 percent partial electron spectrum of 0.942-Mev maximum energy and that the 0.122-Mev gamma-ray is emitted following K-capture into W^{186}.

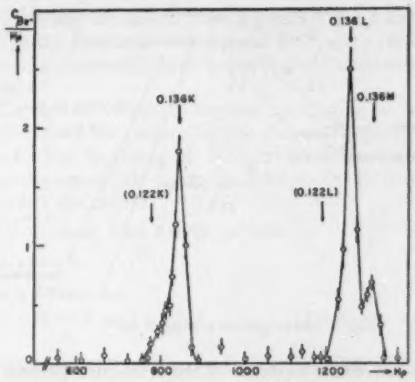

FIG. 6. Momentum distribution of the conversion electrons coincident with the beta-spectrum. The two peaks due to the K- and L-conversion of the 0.122-Mev gamma-ray measured in the single-count spectrum (Fig. 1) have disappeared by detecting β^-–e^- coincidences.

To verify this mode of decay, coincidence measurements have been performed between conversion electrons focused in the spectrometer and beta-rays detected by an end-window counter placed near the source in the spectrometer. A 24 mg/cm² Al absorber between the counter and source was thick enough to stop all conversion electrons from reaching the end-window counter. The momentum distribution of the electrons coincident with the beta-rays emitted by Re^{186} is shown in Fig. 6. Only β^-–e^- coincidences involving

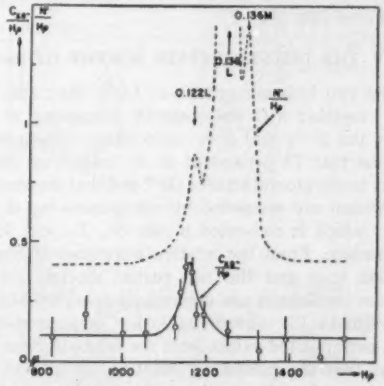

FIG. 7. Momentum distribution of the L-conversion electrons coincident with K-x-rays. For comparison, the single count spectrum (see also Fig. 1) of the same energy region has been included. The two peaks due to the L- and M-conversion of the 0.136-Mev gamma-ray have disappeared in the x–e^- coincidence measurements.

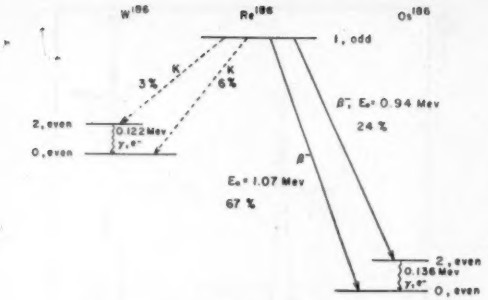

FIG. 8. Disintegration scheme of Re^{186}.

the conversion electrons of the 0.136-Mev gamma-ray have been observed, demonstrating that the 0.122-Mev gamma-ray is not emitted following the beta-decay into osmium. In order to give positive evidence that the 0.122-Mev gamma-ray is emitted following K-capture, coincidences have been measured between the wolfram K-x-rays detected by a krypton filled x-ray counter and the L-conversion electrons of the 0.122-Mev gamma-line (Fig. 7). The electrons were prevented from entering the x-ray counter by a 0.2 g/cm² paraffin absorber and a 0.3 g/cm² aluminum foil. The latter also absorbed all L-x-ray quanta from osmium or wolfram. The measurements show conclusively that the 0.122-Mev gamma-transition is preceded by K-capture.

The shape of the low energy beta-ray spectrum has been determined directly by observing beta-gamma-coincidences in the spectrometer. A 0.9 g/cm² Sn-absorber placed between source and gamma-counter prevented recording of any electron x-ray coincidences. The result of these measurements is consistent with the momentum distribution as derived from the analysis of the Fermi plot (Fig. 2).

V. THE DISINTEGRATION SCHEME OF Re^{186}

The two beta-ray groups of 1.070 Mev and 0.942 Mev, together with the observed gamma-ray of 0.136 Mev, the β^--γ and β^--e^- coincidence measurements, suggest that 73 percent of all β^- transitions lead directly to the ground state of Os^{186} and that the remaining 27 percent are succeeded by one gamma-ray of 0.136 Mev, which is converted in the K-, L-, and M-shell of osmium. From the relative intensities of the conversion lines and the two partial spectra, the conversion coefficients are determined as $\alpha_K=0.37\pm0.08$, $\alpha_L=0.61\pm0.13$, $\alpha_M=0.12\pm0.03$. Comparison of α_K with extrapolated values from the tables of Rose *et al.*[5] shows that the gamma-ray must be interpreted as an electric quadrupole transition. Since, at the present, no reliable theory of the L- or M-conversion for the energy and the atomic number involved here is available, no attempt is made to compare these conversion data with theoretical calculations.

The discussion of the K-capture of Re^{186} in connection with our data is somewhat more complex. From the relative number of observed Auger-electrons, it is possible to determine the relative number of K-capture processes,[6] taking into account that Auger-electrons are also emitted following K-conversion. The Auger-electrons due to the latter process can easily be calculated by using the relative intensities of the K-conversion lines (Table I). The result is that, in 9±2.5 percent of all disintegrations, the Re^{186} decays by K-capture into W^{186}; in 6±2 percent, the K-capture leads directly to the ground state, it is followed by a gamma-ray of 0.122-Mev energy in the remaining 3.0±0.5 percent. The latter can be determined from the relative number of 0.136-Mev and 0.122-Mev gamma-quanta and from a comparison of the number of the conversion electrons associated with these two transitions. This comparison also leads to the following conversion coefficients of the 0.122-Mev gamma-transition: $\alpha_K=0.45\pm0.1$ and $\alpha_L=0.73\pm0.15$. The 0.122-Mev gamma-transition in W^{186} must thus also be considered as an electric quadrupole transition.

Figure 8 summarizes the results and suggests our decay scheme. A further verification of this disintegration scheme was made in performing x-gamma and x-x-coincidences using two scintillation counters and also using thin-walled Bi-counters of known efficiency.[7] Our failure to detect any gamma-gamma-coincidences with the sensitive scintillation counters indicates that there are less than 10^{-5} percent positrons emitted in all disintegrations. The number of coincidences observed showed good agreement between the coincidence rates calculated, assuming the decay scheme of Fig. 8. The absorption curve of the electromagnetic radiation in Sn showed an intensity ratio of

$$(I_{0.136}+I_{0.122})/I_K=1.0\pm0.2.$$

The ratio expected from the mode of decay, as represented by Fig. 8, is 0.9±0.1.

VI. DISCUSSION

The ft-values for the two beta-ray groups of 1.07-Mev and 0.94-Mev maximum energy are $\log(ft)_{1.07}=7.68$ and $\log(ft)_{0.94}=7.93$, respectively. This suggests, for both spectra, a first-forbidden transition with $\Delta I=\pm1$.[8] This result is consistent with the allowed shape of the spectra, since first-forbidden spectra of heavy elements are nearly identical with allowed spectra for $\Delta I=0, \pm1$.[9]

Since the product nucleus Os^{186} is *even-even* and hence presumably has even parity and spin 0, odd parity and a spin 1 may be assigned to the ground state of Re^{186}. The same result also follows from a consideration of the

[5] Rose, Goertzel, Spinrad, Harr, and Strong, *Tables of K-Shell Internal Conversion Coefficients* (privately distributed).

[6] Steffen, Huber, and Humbel, Helv. Phys. Acta **22**, 167 (1949).

[7] Hart, Russel, and Steffen, Phys. Rev. **81**, 460 (1951).

[8] L. W. Nordheim, Phys. Rev. **78**, 294 (1950); L. W. Nordheim, Tables for beta-decay systematics (tables privately circulated).

[9] E. Konopinsky, Revs. Modern Phys. **15**, 209 (1943).

angular momentum and the parity of the 0.136-Mev excited level of Os^{186}. The comparative half-lives for the two beta-transitions to the ground and excited states of Os^{186} are of the same order of magnitude and hence must be of the same order of forbiddeness, involving probably the same spin change. This again suggests that the ground state of Re^{186} must have a spin 1. The same applies to the *K*-capture decay to the excited and ground states of W^{186}, which is also an *even-even* nucleus.

The extension of the one-particle spin-orbit coupling model to odd-odd nuclei,[10] also suggests a spin 1 and an odd parity for the ground state of Re^{186}, since the odd proton is presumably in a $d_{\frac{3}{2}}$ and the odd neutron in a $f_{\frac{1}{2}}$ state.[8]

The author wishes to express his thanks to Miss Phyllis Allen for performing the chemical separations and to Mr. Raymond R. McLeod for preparing the krypton-counter. He is also indebted to Dr. E. Bleuler for many discussions.

[10] M. G. Mayer, Phys. Rev. 78, 16 (1950).

PHYSICAL REVIEW VOLUME 82, NUMBER 6 JUNE 15, 1951

Neutron Energy Distributions in Proton Bombardment of Be and C at 100 Mev*

DAVID BODANSKY† AND NORMAN F. RAMSEY
Nuclear Laboratory, Harvard University, Cambridge, Massachusetts
(Received March 1, 1951)

The energy distributions of neutrons emitted in the forward direction when beryllium and carbon targets are bombarded by 100-Mev protons were investigated. The neutron energy distribution was found from the range distribution of recoil protons from a polyethylene target, measured with a scintillation counter telescope. The distribution for beryllium was found to be peaked at about 93 Mev, while the distribution for carbon fell off rapidly above 70 Mev. The influence on the observed distribution of energy resolution effects, particularly those involving energy spread of the cyclotron proton beam, is discussed.

I. INTRODUCTION

AN investigation has been made of the energy distributions of the neutrons emitted in the forward direction when beryllium and carbon targets were bombarded by 100-Mev protons from the internal proton beam of the Harvard cyclotron. A collimated beam of the neutrons was allowed to fall upon two polyethylene scatterers. The recoil protons from one of these scatterers served as a monitor of the beam intensity while the range distribution of the recoil protons from the other scatterer was studied. From these results the energy distribution of the neutron beam was inferred.

II. DESCRIPTION OF EXPERIMENT

A diagram of the experimental arrangement is given in Fig. 1. The target was placed within the cyclotron tank at a location such that neutrons emitted in the forward direction with respect to the incident protons passed through a $\frac{1}{2}$-inch thick Lucite window in the cyclotron vacuum tank and through a collimating hole in the 6-foot shielding surrounding the cyclotron.

The targets were rectangular bars $1\frac{3}{4}$ inches high, and, as held in the cyclotron, with a radial dimension of $\frac{1}{4}$ inch. The target was held by two light phosphor bronze clips which gripped the target at its top and bottom with small caps and which extended radially back from the target to a supporting probe. With this arrangement the entire direct beam struck the target, and the contribution of scattered protons striking the holder was small. The beryllium target was 0.125 inch thick for all runs. Different carbon targets were used for runs A and B, 0.125 and 0.196 inch thick, respectively.

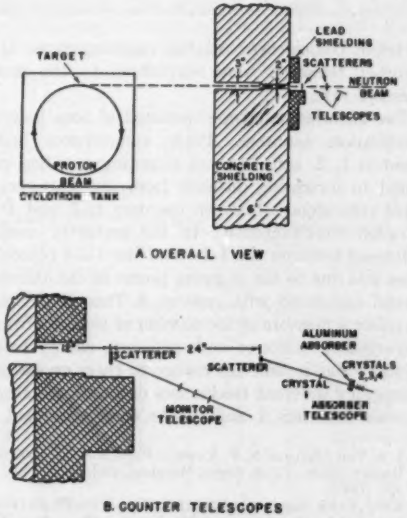

FIG. 1. Experimental arrangement.

* This work was partially supported by the joint program of the ONR and AEC.
† AEC Predoctoral Fellow. Now at Columbia University, New York, New York.

The collimated neutron beam fell upon two polyethylene scatterers. Scintillation counter telescopes, with 1P21 phototubes and anthracene crystals, were used to detect the resulting recoil protons. A monitor telescope viewed the first scatterer, and an absorber telescope viewed the second scatterer. The latter telescope was similar in principle to that first used with recoil protons by Van Allen and Ramsey[1] and subsequently used in similar experiments by many other observers. Arrangements quite similar to that in the present experiment were the ones used for neutron-proton scattering by Hadley[2] and Kelly *et al.*[3] and for total cross sections of nuclei by Fox *et al.*[4]

The collinearity of the target, the axis of the collimating hole, and the centers of the scatterers were verified with the aid of a cathetometer and of plugs, with small centered holes, placed in the collimating hole. The center lines of the monitor and absorber telescopes made angles of 21 degrees and 15 degrees, respectively, with the axis of the collimating hole.

The monitor telescope used three scintillation counters

TABLE I. Dimensions of anthracene crystals.

Crystal	Distance from scatterer (cm)	Dimensions (cm)	Thickness (g/cm²)
Monitor tel.			
1	27.3	2.64×2.60×0.44	0.54
2	33.6	3.42×1.98×0.43	0.54
3	40.0	3.74×2.12×0.41	0.52
Absorber tel.			
1	28.8	3.24×1.74×0.41	0.51
2	45.8	3.18×1.78×0.41	0.52
3	47.6	4.06×2.34×0.43	0.55
4	48.9	4.08×2.46×0.46	0.59

in triple coincidence. All the counting rates of the absorber telescope were normalized to the monitor telescope rate.

The absorber telescope consisted of four individual scintillation counters. Triple coincidences between counters 1, 2, and 3 (where increasing numbers correspond to increasing distance from the scatterer) and triple coincidences between counters 1, 2, and 4 were recorded simultaneously. In the geometry used the difference between the 1-2-3 and the 1-2-4 coincidence rates was due to the stopping power of the anthracene crystal associated with counter 3. This difference was therefore a measure of the number of particles from the polyethylene scatterer with sufficient energy to enter crystal 3 but insufficient energy to enter crystal 4. By interposing different thicknesses of aluminum absorber between counters 1 and 2, the energy interval thus defined was increased from a lower limit imposed by the thickness of the first three crystals.

The measurement was repeated with a carbon scatterer and the polyethylene-carbon subtraction performed to obtain data for a differential range distribution of the recoil protons. From this the energy distribution of the incident neutrons was calculated.

Both polyethylene scatterers were $\frac{1}{4}$ inch thick. The monitor telescope scatterer was circular with a $2\frac{3}{4}$-inch diameter. This was larger than the area of the incident neutron beam. The absorber telescope scatterer was rectangular with vertical and horizontal dimensions of $2\frac{1}{2}$ and $\frac{3}{4}$ inches, respectively. The carbon scatterer, used only with the absorber telescope, was of the same area and the same thickness, in carbon nuclei per cm², as the polyethylene scatterer.

Details of the telescope geometry are indicated in Table I. The anthracene crystals were obtained from the Harshaw Chemical Company. In the absorber telescope, where the thickness of wrapping and correct geometry were important, the crystals were wrapped in aluminum foil and centered using Lucite spacers between the crystals and phototubes.

The absorbers were placed between counters 1 and 2, as closely as possible to counter 2 to minimize scattering effects. They were 3 inches high, $1\frac{1}{2}$ inches wide, and of various thicknesses. 2s aluminum absorbers were used except for certain comparison tests in which lead absorbers were used.

In the absorber telescope, pulses from each counter were fed into Jordan-Bell amplifiers,[5] which were modified to reduce overloading[6] and dead-time effects. The amplifier discriminator outputs were fed into diode cut-off coincidence circuits and the coincidences counted with scalers. For the monitor telescope the amplifiers were replaced by two electron tubes for amplification and pulse shaping, which was ample in view of the large pulses obtained from scintillation counters.

Under typical conditions, with no absorbers, the observed counting rates were of the order of 600 monitor coincidences per minute, 200 absorber telescope coincidences per minute, and 5000 absorber telescope single-channel counts per minute.

III. TESTS OF EQUIPMENT

As recoil protons of different initial energies undergo different ionization losses in a given crystal, and therefore produce different size output pulses from the phototube, it was necessary to insure that the efficiency of the counting system was independent of the size of the phototube pulses over a reasonable range of sizes. This, and other features of proper telescope performance, were verified for both telescopes by obtaining triple coincidence plateaus with respect to phototube voltage, amplifier gain of each absorber telescope channel, and coincidence resolving time.

[1] J. A. Van Allen and N. F. Ramsey, Phys. Rev. **57**, 1069 (1940).
[2] Hadley, Kelly, Leith, Segrè, Wiegand, and York, Phys. Rev. **75**, 351 (1949).
[3] Kelly, Leith, Segrè, and Wiegand, Phys. Rev. **79**, 96 (1950).
[4] Fox, Leith, Wouters, and MacKenzie, Phys. Rev. **80**, 23 (1950).
[5] W. H. Jordan and P. R. Bell, Rev. Sci. Instr. **18**, 703 (1947).
[6] W. G. Cross, Phys. Rev. **78**, 185 (1950).

Counter 3 had the least transparent crystal and exhibited the poorest plateau with respect to amplifier gain. Its efficiency, for particles passing through it, was checked by simultaneous measurement of the 1-2-4 triple and 1-2-3-4 quadruple coincidence rates. At the gain which was used in the final runs, the 1-2-3-4 rate was 99 percent of the 1-2-4 rate. This discrepancy is attributed to possible failure to detect small pulses from counter 3, dead time losses, and an excess of accidental triple coincidences over accidental quadruple coincidences.

The over-all performance of the experimental arrangement was checked by a group of tests in which successively the cyclotron proton beam current was varied over a wide range, the target was removed, the collimating hole was plugged, the scatterer was moved off the axis of the hole, the scatterer thickness was varied, the anthracene crystal was removed from one phototube, the last counter of the telescope was moved out of line, and a thick absorber was placed in the telescope. No significant spurious effects were noted in any of these tests.

A difference between the 1-2-3 and 1-2-4 rates other than that due to the stopping power of crystal 3 would be uncovered by integral energy distribution curves. For a given absorber thickness the minimum energy which a proton must have for a 1-2-3 or 1-2-4 coincidence count is known. Figure 2 shows the 1-2-3 and 1-2-4 rates, after a polyethylene-carbon subtraction, as a function of minimum proton energy. The two sets of points appear randomly distributed about a mean curve, implying that there were no discrepancies between the two arising from faulty geometry.

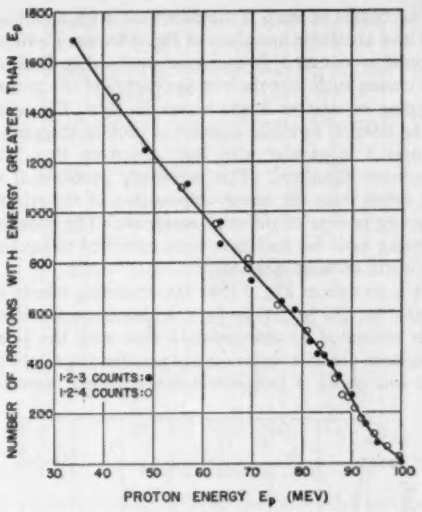

FIG. 2. Consistency test. Comparison of 1-2-3 and 1-2-4 coincidence counting rates.

IV. FACTORS DISTORTING ENERGY DISTRIBUTION

In addition to energy resolution effects, which will be discussed in the section on results, the observed energy distribution was distorted by attenuation of the neutron beam and scattering of the recoil protons. An order-of-magnitude calculation has been made which shows that these effects were not large enough to significantly alter the shape of the observed distributions, especially as the effects partially canceled each other.

The attenuation of the neutron beam in the target, the Lucite window of the cyclotron, and the polyethylene scatterers may be calculated from the total nuclear cross sections for neutrons at 42 Mev[7] and 95 Mev.[8] It is found, with the beryllium target, that the attenuation is 17 percent at 42 Mev and 8 percent at 95 Mev, causing a depression of the low energy end of the distribution with respect to the high energy end of about 10 percent.

The recoil protons from the polyethylene underwent coulomb and nuclear scattering in the absorbers, the greatest scattering, and therefore the greatest depression of the distribution, occurring at the high energy end of the distribution where thick absorbers were used. This scattering has been investigated by an experimental method in which the location of the absorbers was changed. In the absorber telescope the crystals of counters 1 and 2 were 17 cm apart. Normally, the absorber was placed as closely as possible to counter 2 to minimize the effects of scattering. On moving the absorber back from counter 2 towards counter 1, the solid angle subtended by counter 2, as seen by the absorber, decreases. The resulting decrease in counting rate can be used to estimate part of the scattering loss which occurred when the absorber was in its normal position.

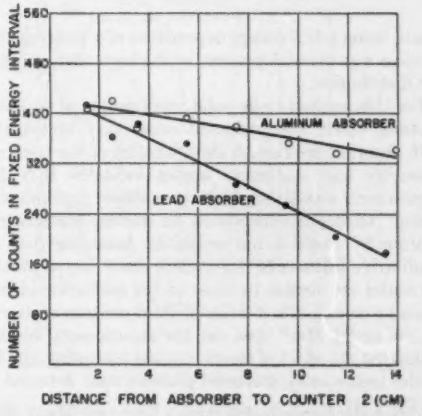

FIG. 3. Effect of scattering of recoil protons in the absorbers.

[7] R. H. Hildebrand and C. E. Leith, Phys. Rev. **80**, 842 (1950).
[8] J. DeJuren and N. Knable, Phys. Rev. **77**, 606 (1950).

The results of such a measurement with aluminum and lead absorbers are given in Fig. 3 for recoil protons stopped in counter 3. In each case an absorber thickness was chosen such that the average energy of the protons stopping in counter 3 was about 70 Mev. The width of the interval in initial energies of protons stopping in counter 3 is greater with lead absorbers than with aluminum absorbers. (This seemingly paradoxical result arises from the energy dependence of the relative stopping powers of different materials.) The observed counting rates for lead have been corrected to equalize the width of these intervals.

It is seen from Fig. 3 that the scattering effects are greater for the lead than for the aluminum absorbers. It is estimated by extrapolation that with the ½-inch aluminum absorber in its normal position the scattering loss was about 3 percent. It is calculated from this result, using a $1/E$ energy dependence of scattering, that the loss was about 5 percent at the high energy end of the distribution.

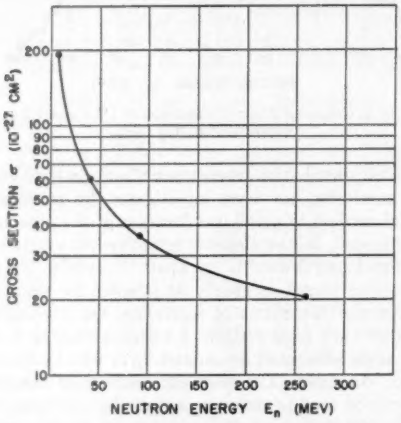

FIG. 4. Assumed neutron-proton scattering cross section σ for the scattering of recoil protons into an angle of 15 degrees in the laboratory system (per unit solid angle).

For this method to be valid, the fraction of scattered protons which were detected must vary appreciably with absorber position. A consideration of the telescope geometry and scattering angles indicates that this requirement was satisfied for the multiple coulomb scattering. Adequate information on nuclear scattering of protons by nuclei is not available. Assuming that the qualitative features of the nuclear scattering of protons by nuclei are similar to those of the scattering of neutrons by nuclei, it is concluded from neutron scattering results at 84 Mev[9] that (a) the experimental method estimated the effect of elastic nuclear scattering, (b) few of the inelastically scattered protons were detected by the telescope in any absorber position and therefore the experimental method did not measure the inelastic scattering loss, and (c) the loss at the high energy end of the distribution due to inelastic nuclear scattering was about 10 percent, as calculated from the inelastic cross section for neutrons.

On this basis, which can only indicate orders of magnitude, the total loss due to scattering in the thickest absorbers was about 15 percent. This loss was partly compensated for, in the energy distribution results, by the attenuation of the neutron beam. Considerably larger distortions than this would be required to change the main features of the observed energy distributions.

V. CALCULATIONS

To find the energy distribution of the neutron beam, different thicknesses of absorber were placed in the absorber telescope. For each thickness the normalized 1-2-3 and 1-2-4 rates were obtained with a polyethylene scatterer and with a carbon scatterer. As the carbon scatterer was chosen to have the same number of carbon nuclei per cm² as the polyethylene, a direct subtraction gives the number of recoil protons from the hydrogen atoms in the polyethylene. (The error introduced due to the different stopping power of the two scatterers is small.) Background counts are subtracted out in the carbon subtraction. The difference between the 1-2-3 and 1-2-4 rates gives the number of protons within a particular range interval.

The proton energy, E_p, associated with a proton range was calculated using the Bethe-Bloch ionization loss formula. Previously calculated tables[10] and graphs[11] were employed both directly where applicable and by use of the relative stopping powers of the substances involved in the other cases. The mean ionization potentials were taken as: air, 80.5 ev; aluminum, 150 ev; carbon, 69 ev; hydrogen, 17.5 ev; lead, 943 ev.

The corresponding neutron energy, E_n, was calculated from the approximate two-body collision equation,

$$E_n = E_p \sec^2\theta(1+E_p \tan^2\theta/2Mc^2),$$

where θ is the angle of the recoil proton in the laboratory system and Mc^2 is the rest energy of a nucleon.

In calculating the number of neutrons per unit energy interval corrections were made for the energy dependence of the neutron-proton scattering cross section and for the energy dependence of the width of the energy intervals defined by the crystal of counter 3.

The energy dependence of the scattering is not known in detail, but data is available which allows a reasonable interpolation. The scattering cross section per unit solid angle, σ, for recoil protons at an angle of 15 degrees in the laboratory system is tabulated in measurements at 40 Mev,[2] 90 Mev[2] and 260 Mev.[3] It can be calculated from a measurement at 14 Mev[12] assuming

[9] Bratenahl, Fernbach, Hildebrand, Leith, and Moyer, Phys. Rev. 77, 597 (1950).

[10] J. H. Smith, Phys. Rev. 71, 32 (1947).

[11] Prepared by E. P. Gross, Princeton University (1947).

[12] H. H. Barshall and R. F. Taschek, Phys. Rev. 75, 1819 (1949).

spherical symmetry in the center-of-mass system. These values are plotted in Fig. 4 and a smooth curve used to interpolate for values of σ at intermediate energies. The errors introduced by this method are limited by the fact that the values at 40 and 90 Mev correspond closely to the extent of the region of interest of this experiment.

The energy interval defined by the crystal of counter 3 decreases in width, from about 9 Mev to 4 Mev, as thicker absorbers are used and higher energy protons counted. To obtain the number of protons per unit energy interval, one divides the observed counting rate by the width of the interval, or, equivalently for narrow intervals, by the rate of ionization energy loss, dE/dx (in Mev per g/cm^2), evaluated at the initial energy of the recoil proton. Except for a small relativistic term the width of the neutron energy interval is proportional to the width of the proton energy interval.

The relative neutron energy distribution was obtained by multiplying the observed range distribution by $1.69\times10^{-25}/[\sigma(E_n)(dE/dx)_{E_p}]$, where an arbitrary multiplicative factor has been included. No corrections have been made for the distortion effects discussed in Sec. IV.

VI. RESULTS

The results of three runs with a beryllium target, and two runs with a carbon target are shown in Figs. 5 and 6. Between the time that runs A were taken and runs B were taken, the absorber telescope was dismantled and changes were made in the cyclotron oscillator and target probe systems. It was not expected that these changes would alter the observed distributions. However, there is a clear discrepancy between the A runs and the B runs.

The qualitative features of the results are not affected by these discrepancies. It is to be noted that there is a peak in the neutron energy distribution from beryllium at about 93 Mev, while the carbon distribution falls off rapidly above 70 Mev.

The relative normalization for the beryllium and carbon targets is significant only as to orders of magnitude. The relative normalization is based on run B, in which the beryllium and carbon targets were held on a single probe, and alternated, by rotation of the probe, to provide measurements with the same cyclotron beam current. Targets of the same thickness in nuclei per cm^2 were used in run B; but owing to the greater rms angle of multiple scattering in the carbon, it is believed that there were fewer multiple traversals and therefore a smaller effective beam current for the carbon target.[13]

The stable orbit energy of the cyclotron protons, as calculated from the target radius and magnetic field, was approximately 116 Mev. The actual energy distribution of the protons incident upon the beryllium target has been measured by Bloembergen and Van Heerden using a method in which protons scattered from the target are focused by the cyclotron magnetic field and detected by photographic plates.[14] They found the incident proton distribution of Fig. 7 which is similar in shape and width to the neutron energy distribution for beryllium of Fig. 5. The wide distribution of incident proton energies is believed due to oscillations of the circulating proton beam and to multiple traversals of the target. The proton distribution with

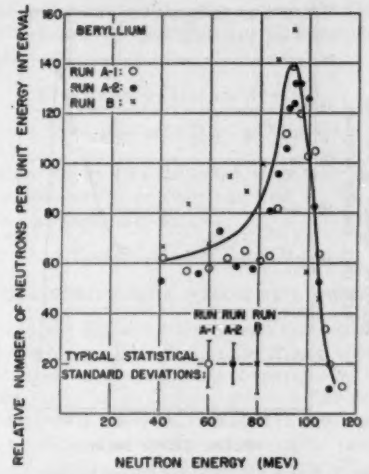

FIG. 5. Energy distribution of neutrons from beryllium target bombarded by 100-Mev protons.

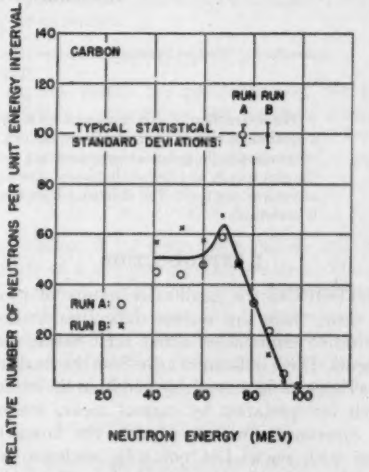

FIG. 6. Energy distribution of neutrons from carbon target bombarded by 100-Mev protons.

[13] See W. J. Knox, Phys. Rev. 81, 693 (1951), for a study of the relation between target thickness and effective beam current.

[14] N. Bloembergen and P. J. Van Heerden, Phys. Rev. (to be published) and further work to be published.

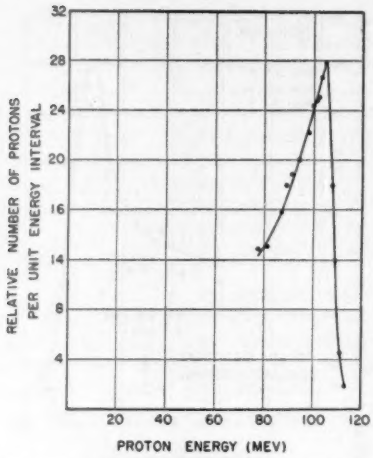

FIG. 7. Energy distribution of protons incident upon beryllium target.

the two carbon targets is believed, from considerations of the target thicknesses, to have not been significantly different from that of Fig. 7.

The wide proton beam energy distribution overshadows other energy resolution effects such as energy loss and coulomb scattering of the recoil protons in the polyethylene scatterer, limited angular resolution in the counting telescopes, and straggling in the absorbers. These effects would introduce a half-width of about 7 Mev and a lowering of the position of the peak by about 3 Mev were the neutron beam from the beryllium target monoenergetic. In the present case they increase the width of the observed peak by only about 1 Mev but still lower the energies by about 3 Mev.

Comparison of Figs. 5 and 7 indicates that the peak of the neutron energy distribution from beryllium is about 10 Mev below the peak of the energy distribution of the incident protons and that a considerable portion of the width of the neutron energy distribution curve is due to the spread in energy of the incident protons. A further comparison with Fig. 7 indicates a much lower mean energy for the neutrons from carbon than for those from beryllium.

We are indebted to J. A. Hofmann for his assistance in much of this work. We wish to express our gratitude to the staff of the Harvard Nuclear Laboratory for their help and particularly to A. C. Grant and the cyclotron operating crew for the many hours contributed to the experiment. Thanks are due R. W. Birge, W. G. Cross, N. M. Hintz, and L. S. Lavatelli for their suggestions and aid, and to N. Bloembergen for the measurement of the proton beam energy.

PHYSICAL REVIEW VOLUME 82, NUMBER 6 JUNE 15, 1951

Interaction of Mesons with Nuclei

SATIO HAYAKAWA*
Laboratory of Nuclear Science and Engineering, Massachusetts Institute of Technology, Cambridge, Massachusetts
(Received October 9, 1950)

The interaction of slow π-mesons with nuclei is treated phenomenologically. A nucleus is assumed to be a continuum with potential with respect to a meson. The potential consists of real and imaginary parts, corresponding to the polarization caused by a meson and the absorption of a meson, respectively. The scattering, the absorption, and the production of mesons are qualitatively discussed by analogy with the current theory of nuclear reactions. The difference from the theory based on the weak interaction of mesons with nucleons is presented.

I. INTRODUCTION

ALTHOUGH the qualitative nature of mesons is clear, there are serious difficulties in deducing quantitative information about their nature from experiments. These difficulties arise from the small amount of experimental data available and from the inadequacy of their interpretation by current meson theories. In most experiments we can observe the interaction of mesons with nuclei but not with nucleons, whereas meson theory is related most simply to the interaction of mesons with individual nucleons. There have been several works in which the effect of nuclear binding is taken into account.[1-3] These works, however, start from the interaction between a meson and a nucleon, and the effect of nuclear binding is considered afterwards in such a way that the nucleons obey some momentum distribution law and the Pauli principle. Furthermore, it is assumed that a meson does not interact with any nucleon after it is produced or before it is

* On leave from Osaka City University, Osaka, Japan.

[1] Fujimoto, Nishijima, Okabayashi, Takayanagi, and Yamaguchi, Prog. Theor. Phys. 5, 870 (1950).
[2] Fujimoto, Takayanagi, and Yamaguchi, Prog. Theor. Phys. 5, 498 (1950).
[3] M. Lax and H. Feshback, Phys. Rev. 81, 189 (1951). This gives good agreement with experiments for the production of charged mesons, but for the production of neutral mesons a certain modification is required.

absorbed. Therefore, these theories have essentially to do with the interaction between two elementary particles.

The above line of approach has a defect in that we must start from the interaction between a meson and a nucleon, which contains much ambiguity coming from meson theory. We think it better to retreat a step from meson theory and first consider the interaction of a meson with a nucleus phenomenologically. It may provide an alternative way to study the nature of mesons and may, in addition, clarify some properties so far overlooked. The proposed method exploits the experimentally observed strong interaction between mesons and nucleons.

If the collision mean free path of mesons with nucleons is smaller than the nuclear diameter, and when the wavelength of the mesons is not short compared with the internucleon distance, a nucleus may be considered as a continuum of nuclear matter. This nuclear matter could be characterized by a di-mesonic constant (not necessarily constant) and mesonic conductivity, which correspond to the polarization caused by meson wave and the absorption of a meson.[4] On this assumption we can construct a theory analogous to current nuclear reaction theory. This would allow us to anticipate the results of future experiments with a suitable choice of our parameters.

We shall confine ourselves in the present paper only to a qualitative discussion of the above idea, because at the present stage of our knowledge a more quantitative investigation is of little use and only of mathematical interest. The main purpose is to show how we can consider the nuclear reaction of mesons phenomenologically.

II. TRANSMISSION OF A MESON IN NUCLEAR MATTER

First, we confine ourselves to the one-dimensional case, in which a meson travelling in the positive x direction strikes some nuclear matter extending from zero to plus infinity. Assuming that the meson has a constant potential W in nuclear matter and neglecting the coulomb potential for simplicity, the wave equation of the meson is expressed by

$$\{-d^2/dx^2+w(x)-\epsilon\}\psi(x)=0, \tag{2.1}$$

where

$$w(x)=\begin{cases} w=2\mu W/\hbar^2 & \text{for } x\geq 0, \\ 0 & \text{for } x<0, \end{cases} \tag{2.2}$$

and $\epsilon=2\mu E/\hbar^2=k^2$. The quantities μ, E, and k are the mass, the energy, and the wave number of the meson outside of nuclear matter.

The potential can be constituted of two parts, real and imaginary, $w=w'+iw''$, which correspond to the polarization and the absorption, respectively, so that the wave number K inside of nuclear matter is also constituted of real and imaginary parts; $K=K'+iK''$. These two sets of quantities are combined by the formulas

$$\begin{aligned} K'^2&=\tfrac{1}{2}(\epsilon-w')+\tfrac{1}{2}\{(\epsilon-w')^2+w''^2\}^{\frac{1}{2}}, \\ K''^2&=-\tfrac{1}{2}(\epsilon-w')+\tfrac{1}{2}\{(\epsilon-w')^2+w''^2\}^{\frac{1}{2}}. \end{aligned} \tag{2.3}$$

The probability that the meson wave can penetrate into nuclear matter or come out from it, the transmission coefficient, is given by

$$T=4kK'/\{(k+K')^2+K''^2\}. \tag{2.4}$$

III. SCATTERING OF A MESON BY A NUCLEUS

We consider the three-dimensional case, where nuclear matter is a sphere with radius R, and apply the current theory of the scattering of neutrons by nuclei.

If the energy of an incident meson is low enough, i.e., <3 Mev for heavy nuclei and <12 Mev for light nuclei which are contained in photographic emulsion, only the S-wave need be taken into account. The scattering cross section is given by

$$\sigma_{sc}=\frac{4\pi}{k^2}\left\{\frac{k^2}{(k+K')^2+K''^2}-\frac{2k(k+K')\sin^2kR+2kK''\sin kR\cos kR}{(k+K')^2+K''^2}+\sin^2kR\right\}. \tag{3.1}$$

For small energy of the incident meson, we may take only the first term. This is to be compared with the capture cross section

$$\sigma_c=(4\pi/k^2)T, \tag{3.2}$$

where capture means the penetration of the meson into the nucleus, whereupon the meson is either absorbed in the nucleus or goes out again.

The ratio of both cross sections in the low energy limit is

$$\sigma_{sc}/\sigma_c\approx k/K'. \tag{3.3}$$

We shall discuss it for some cases, mainly relating to the capture of a stopped negative π-meson. The wave of the bound meson is not exactly a plane wave, as discussed above, but the meson can be captured from a high quantum state with considerable probability, which may allow us to consider the general behavior of the capture process in the plane wave approximation.

Attractive Potential, $w'<0$

$K'>k$ in any case, and capture exceeds scattering even at higher energy, although σ_{sc} increases when the range of k is such that the terms containing $\sin(kR)$ are not negligible. Here, K'' is at most $w''^{\frac{1}{2}}$ and is usually considered to be small. Therefore, the meson

[4] Y. Nambu, Soryusiron Kenkyu 2, No. 2, 170 (1950).

has little difficulty penetrating into nuclear matter and being absorbed equally in any part of the nucleus.

Repulsive Potential, $w'>0$

For larger meson energy, $\epsilon>w'$, $k>K'$, unless w'' is larger than $2k^2$. In this case we expect more scattering than capture. Decreasing the energy of the meson, K' can be larger than K depending upon the magnitude of w'', and capture can exceed scattering. For a bound meson, which is of particular interest, the main terms of K'^2 and K''^2 are $w''^2/4w'$ and w' or $w''/2$ and $w''/2$, according to whether $w'>w''$ or $w'<w''$. If either of w' and w'' were large, giving large K'', the meson wave could not penetrate deep into the nucleus and would be absorbed near the surface. This would bring about a smaller excitation energy, because about half of the rest energy of the meson should be taken away by a recoil nucleon, which escapes the nucleus without colliding with other nucleons. On the other hand, we get a reasonable excitation energy assuming that the absorption takes place equally in any part of the nucleus.[5,6] This seems to rule out a large magnitude for K'', i.e., large w' and w''; but this conclusion may not be definite if one takes into account the inaccuracy of the theory.

For still higher energy of the incident meson, the higher angular momentum states must be taken into account. If the wavelength of the meson is much smaller than the radius of nucleus, both scattering and capture cross sections are close to the geometrical one, and the scattering is almost the shadow one. In the shadow scattering, the scattered particles are confined within an angle of about $1/kR$. For 50 Mev this angle corresponds to $\sim 30°$ or $\sim 15°$, according to whether the nucleus is light or heavy. Within these angles it is very difficult to differentiate the scattering from coulomb scattering. Therefore, if one obtains the nuclear scattering, which is defined as larger than 30° in most experiments, this should be mainly capture scattering and would not include the shadow scattering.[7]

IV. CAPTURE OF A MESON BY A NUCLEUS

When the higher angular momentum is effective, the capture cross section is roughly approximated by

$$\sigma_c=\pi(R+1/k)^2T. \tag{4.1}$$

The cross section approaches the geometrical one with increasing energy, but at low energy the situation is different, according to whether the potential is attractive or repulsive.

Attractive Potential, $w'<0$

For a strong attractive potential, i.e., $1/R\ll k\ll K'$ or K'', σ_c decreases with decreasing energy as $\sim k/K'$ or k/K''. For smaller energy, $k<1/R$, σ_c goes up as $\sim 1/k$. When the attractive potential is not so strong and the nucleus is small, the cross section increases monotonically with decreasing incident energy. If there is appreciable absorption, large w'', the cross section is effectively reduced.

Repulsive Potential, $w'>0$

Near $\epsilon\sim w'$, K' is so small that the transmission coefficient is very small. Above this energy, σ_c goes up to the geometrical value. Below w', the behavior of σ_c is somewhat complicated, depending upon the magnitudes of w' and w''. Decreasing the energy, σ_c increases as $\sim 1/k$. In the case of a repulsive potential, we could observe more reduction of the cross section in some energy region than in the case of an attractive potential.

Now we consider the behavior of a meson once it has penetrated into a nucleus. Let the meson be reflected at the surface of the nucleus with a probability $1-T$, and be absorbed with a probability $1-P$ upon passing through the nucleus. Then the probability of escaping the nucleus is given by

$$PT\sum_{n=0}^{\infty}\{P(1-T)\}^n=PT/\{1-(1-T)P\}. \tag{4.2}$$

The probability of survival P, is

$$P=\exp(-2K''\langle x\rangle_{Av}), \tag{4.3}$$

where $\langle x\rangle_{Av}$ means the average path length in the nucleus. For the meson coming from outside of the nucleus, $\langle x\rangle_{Av}=4R/3$.

The probability that the meson cannot escape the nucleus but is absorbed is given by

$$(1-P)/\{1-(1-T)P\}. \tag{4.4}$$

The ratio of escape probability to absorption probability is

$$PT/(1-P). \tag{4.5}$$

This may give the observed ratio of scattering to star production, since escape is observed as a scattering.

Also, when a meson is produced in a nucleus we can apply the same considerations, only changing P in the first term in Eq. (4.2) into P_0, because the average path length for the first step is different from before, being now $\langle x\rangle_{Av}=3R/4$. This makes the escape probability increase and the absorption one decrease. If the latter were still larger than the former, most mesons produced in the inner part of the nucleus would be reabsorbed and could not appear. Then we would observe the production cross section to be proportional[8] to $A^{\frac{1}{3}}$. One must notice, however, that this behavior is largely

[5] Fujimoto, Hayakawa, and Yamaguchi, Prog. Theor. Phys. 4, 576 (1949).

[6] Menon, Muirhead, and Rochat, Phil. Mag. 41, 583 (1950).

[7] The shadow scattering was observed and reported by the following experimenters: G. Bernaldini, Phys. Rev. 82, 313 (1951); Bernardini, Booth, Lederman, and Tinlot, Phys. Rev. 82, 105 (1951); Camac, Corson, Littauer, Shapiro, Silverman, Wilson, and Woodward, Phys. Rev. 82, 335 (1951).

[8] R. F. Mozley, Phys. Rev. 80, 493 (1950).

dependent upon the energy of the mesons under consideration, since P and T vary with the energy ϵ. We could see the magnitudes of w' and w'', if we could observe the nuclear reactions caused by mesons or the production of mesons at different energies.

So far we have considered only the case where the meson wave strikes the nuclear surface normally. This is a good approximation when its wavelength is larger than the nuclear radius. For higher energy, however, we can define the path of the meson in the nucleus, and we would have to take into account oblique incidence. The transmission coefficient for this case is considerably smaller than for the case of normal incidence, because of the energy barrier due to the centrifugal force at high momenta. Furthermore, there can be total reflection when a meson wants to go out from lower to higher potential regions. The reduction of T is more serious in the transit from inside to outside of the nucleus, since the incident angle is conserved in each reflection and the meson with a bad incident angle finds it difficult to come out.

V. MEANING OF THE POTENTIAL W

In the above treatment we consider w' and w'' as parameters independent of the energy of the meson and the state of the nucleus. Here we see how these quantities are related to current notions.

In the system which consists of a meson and a nucleus, the Schrödinger equation is given by

$$\{H_m+H_n+H'+(\hbar/i)(\partial/\partial t)\}\Psi=0, \qquad (5.1)$$

where H_m, H_n, and H' are the hamiltonians of a meson, a nucleus, and their mutual interaction, respectively. The wave function describing the whole system, Ψ, may be expressed by the product, $\Psi=\Psi_m\Psi_n$, as a first approximation, where Ψ_m expresses the mesonic state, and Ψ_n the state of the nucleus. If Ψ_n can be expanded in terms of the eigenfunctions of the nucleus without interaction, Eq. (5.1) is reduced to the equation only for the mesonic state.

$$\{H_m+(\Psi_n, H'\Psi_n)+(\hbar/i)(\partial/\partial t)\}\Psi_m=0. \qquad (5.2)$$

The second term in the face bracket corresponds to W and certainly depends upon the state of the nucleus. In a similar way we can write down the equation for Ψ_n, representing the variation of the state of the nucleus due to its interaction with the meson. The period of the variation of Ψ_n is presumably of the order of the reciprocal reaction width in the usual nuclear reaction and may be longer than that of Ψ_m, which is presumably several times the meson time, $\hbar/\mu c^2$. We may, therefore, consider the interaction energy approximately as a potential.

In the limit of individual interaction, the interaction energy can be expressed, as shown by the closure approximation of Lax and Feshbach,[8] by single-particle terms each of which corresponds to the emission or the absorption of a meson by a nucleon. If the interaction between a meson and a nucleus is so strong that the higher order terms, corresponding to scattering, splitting, and so on, are not negligible, the reduction to the single-particle terms will no longer be guaranteed, but they will be considered to be the correspondence to the potential W in the continuum theory.

As an example manifesting the characteristic feature of the meson-nucleus system, we consider the emission of a meson from a nucleus in which the meson is trapped. The behavior of the meson is described by Eq. (5.2) under the approximation mentioned above. The emission of the meson is considered to be caused by the transition between the excited and the ground *mesonic* states, in each of which there are various states of the nucleus. The transition may rather take place between the ground and the excited states of the *nucleus* than between its ground states because of the Franck-Condon principle, as suggested by Tomonaga.[9] Therefore, it seems likely that a slow meson is emitted, leaving the nucleus in an excited state. This may explain the recent experiment of the Columbia group, in which the nuclear scattering of mesons results in slow secondary mesons in most cases.[10] In the capture of a meson, the Franck-Condon principle predicts little change in the state of the nucleus.

As seen above, the potential W is not exactly constant as assumed before, but is dependent on the energy of a meson through H' and on the state of a nucleus through Ψ_n. Such dependence may, however, be negligible in the first approximation, since the variation of H' is presumably small as far as artificial mesons are concerned, and the variation of Ψ_n is considered to be slow, as in the case of the nuclear motion in molecular spectra.

I would like to express my sincerest thanks to the Foreign Student Summer Project of M.I.T. and to Professor Rossi for making possible my stay at M.I.T. Many thanks are also offered to Professors Feshbach and Nambu for showing me their manuscripts before publication and for their kind interest; and to Drs. Goldberger and Kraushaar for their discussions.

[9] S. Tomonaga, Prog. Theor. Phys. 2, 63 (1947).

[10] G. Bernaldini, reference 7. The author thanks Professor Bernaldini and his collaborators for informing him of their experimental results before publication.

On the Scattering of a Particle by a Static Potential

R. JOST AND A. PAIS
Institute for Advanced Study, Princeton, New Jersey
(Received February 7, 1951)

The behavior of the solutions of scattering integral equations is studied as a function of the potential strength λ. From an analysis of the second Born approximation for a Yukawa potential it seems indicated that the Born expansion for a nuclear potential has no useful domain of applicability. The convergence of the Born expansion is discussed. It is shown that the Fredholm theory of integral equations enables one to express the solutions as a quotient of infinite power series in λ which still converge when the Born expansion breaks down. Only in exceptional cases can this method be used for obtaining rapid numerical estimates.

I. INTRODUCTION

THE energy range over which experimental data on nucleon-nucleon scattering are available has in recent years been considerably extended. It seems worthwhile, therefore, to inquire how suitable the various theoretical methods for analyzing these data are, especially in the domain of higher energies. We shall here consider the scattering theory in terms of a conventional potential picture, an assumption which may well turn out to be inadequate.

The general situation in the low energy region (up to ~10 Mev, say) is quite satisfactory. A phase shift analysis is not too involved owing to the fact that the problem is essentially one of S-states only. Moreover, variational methods have proved to be quite powerful for the codification of the low energy experimental material.[1]

For higher energies the variational approach has, to our knowledge, not been applied. The phase shift method still seems the most reliable one so far devised, but it is well known to become an increasingly cumbersome tool.

For rapid estimates in this region one often takes recourse to the first Born approximation. But apart from general statements that this will be more trustworthy the higher the energy, or the weaker the potential strength, little is known about the convergence of the Born expansion (for its definition see Sec. IIa). It is, of course, illuminating to have information on the higher approximations in this expansion. Few attempts in this direction are known to us. We may mention here the work of Wu[2] on the Born approximation for the scattering by a gaussian potential and that of Källén[3] who calculated in second Born approximation the S, P, D-phase shifts for a central Yukawa potential. In Sec. IIb of this paper we will present a case where the second Born approximation is actually very amenable to evaluation, *viz.*, that of the Yukawa potential. It is particularly convenient for the discussion that the results for this case are presentable in closed form. It will be shown that the Born expansion for a central Yukawa potential fitted to describe the low energy interactions is quite unreliable, even at energies of ~100 Mev and more. Indeed, bearing in mind that at not very much higher energies the potential picture is bound to break down anyway, it would seem justified to state that there is no really useful domain of applicability, whatsoever, for the Born expansion for a nuclear potential.

Apart from the investigation of some of the lower order Born approximations it would seem not without interest to study the general behavior of the solutions of scattering integral equations as a function of the potential strength λ. To this subject[3a] Secs. III and IV of the present paper are devoted. In Sec. III we treat the scattering in S-states only. It is easy to find the radius λ_0 of convergence of the Born expansion for the example of the Hulthén potential. More generally, it is then shown that also for values of λ lying outside the convergence domain the solutions of the problem satisfying the required boundary conditions can be obtained by invoking convergent power series in λ. Indeed, it suffices that $\int_0^\infty r|V(r)|\,dr$ is finite to express these solutions (and thus also the scattering matrix) as a quotient of two such series, each of which converges for arbitrarily large λ. This method, which essentially is based on Fredholm's theory of integral equations, constitutes a departure from the usual Born expansion. But for $\lambda<\lambda_0$ this new representation can, of course, be reduced to the Born series. However, the calculation of a number of terms sufficient for a good numerical estimate is possible only in exceptional cases. The exponential potential is one such instance, and in Sec. III the rapidity of convergence and a comparison with the Born expansion is illustrated with the help of this example.

In Sec. IV the general problem is discussed where one does not confine oneself to S-states, in fact, where no use of a development in spherical harmonics is made. Here too one can show the convergence of a quotient representation of the solutions under similar conditions

[1] J. Schwinger, hectographed notes on nuclear physics, Harvard (1947); J. M. Blatt and J. D. Jackson, Phys. Rev. **76**, 18 (1949); Revs. Modern Phys. **22**, 77 (1950).
[2] T. Y. Wu, Phys. Rev. **73**, 934 (1948).
[3] G. Källén, Ark. Fysik **2**, 33 (1950).
[3a] See also T. Kato, Prog. Theor. Phys. **4**, 514 (1949); J. Phys. Soc. Japan **4**, 334 (1949); Prog. Theor. Phys. **5**, 207 (1950). This author investigates the dependence of eigenvalues and eigenvectors on λ.

as for S-states. These requirements are actually fulfilled for the case of the Yukawa potential already mentioned. However, the convergence is too slow for the energies of interest to make rapid estimates by means of this method. It would seem that the best one can hope for is still a good variational guess (see also Sec. IV).

II. THE SCATTERING INTEGRAL EQUATION; THE BORN EXPANSION

(a) General Formalism

In this section we will first collect some preliminary formulas for the scattering of a particle in a central field of force and will then discuss the results of the first and second Born approximation for the case of the Yukawa potential. The details of this calculation will be found in Appendix I.

The Schroedinger equation for the neutron-proton system referring to the center of mass is[4]

$$[\Delta+k^2-\lambda V(r)]\psi=0, \tag{1}$$

where the customary dimensionless units have been introduced: length is measured in units r_0, the characteristic length of the potential, and

$$k=(ME_0r_0^2/2\hbar^2)^{\frac{1}{2}},$$

where E_0 is the energy of the incident particle in the laboratory system. λ is the potential strength, defined by the usual conditions of normalization of $V(r)$ at small distances. Whatever spin and exchange dependence the interaction may have is implicitly contained in λ.

We look for the solution of Eq. (1) which is regular and which at large distances behaves like a plane wave plus an outgoing spherical wave; i.e., we want to solve the integral equation

$$\psi(\mathbf{x})=\psi_0(\mathbf{x})+\lambda\int K(\mathbf{x},\mathbf{y})\psi(\mathbf{y})d\mathbf{y}, \tag{2}$$

$$\psi_0(\mathbf{x})=\exp(i\mathbf{kx}),$$

$$K(\mathbf{x},\mathbf{y})=-\exp(ik|\mathbf{x}-\mathbf{y}|)V(y)/4\pi|\mathbf{x}-\mathbf{y}|$$
$$=-G(\mathbf{x},\mathbf{y})V(y). \tag{3}$$

The Green's function G which we have picked guarantees that the required boundary conditions are fulfilled.

Asymptotically $\psi(\mathbf{x})$ as given by Eq. (2) is of the following general form

$$\psi(\mathbf{x})\sim\psi_0(\mathbf{x})+|\mathbf{x}|^{-1}\exp(ik|\mathbf{x}|)\cdot f(\theta), \tag{4}$$

where $f(\theta)$ is the amplitude for the scattering over an angle θ. The differential cross section is given by

$$d\sigma/d\Omega=r_0^2|f(\theta)|^2, \tag{5}$$

where, in the presence of spin-dependent forces, the appropriate averages over spin states have to be performed.

The Born expansion is defined as the representation of $\psi(\mathbf{x})$ in Eq. (2), and thus of $f(\theta)$ (or more generally of the scattering matrix), and of $d\sigma/d\Omega$ as a power series in λ. This amounts to iterating Eq. (2), which gives

$$\psi(\mathbf{x})=\psi_0(\mathbf{x})+\sum_{n=1}^{\infty}\lambda^n\int K_n(\mathbf{x},\mathbf{y})\psi_0(\mathbf{y})d\mathbf{y}, \tag{6}$$

in which

$$K_1=K,\quad K_n(\mathbf{x},\mathbf{y})=\int K(\mathbf{x},\mathbf{z})K_{n-1}(\mathbf{z},\mathbf{y})d\mathbf{z},\quad n>1. \tag{7}$$

It has to be verified, however, under what conditions this procedure is consistent, i.e., whether the necessary convergence requirements for the series occurring on the right-hand side of Eq. (7) are fulfilled. This question will be discussed in the following sections.

The expansion of $f(\theta)$ corresponding to that of ψ given by Eq. (6) is

$$f(\theta)=-\frac{1}{4\pi}\sum_{n=1}^{\infty}\lambda^n\int\exp(-i\mathbf{k}'\mathbf{x}_1)V(x_1)K_{n-1}(\mathbf{x}_1,\mathbf{x}_2)\times\exp(i\mathbf{k}\mathbf{x}_2)d\mathbf{x}_1d\mathbf{x}_2,$$
$$K_0(\mathbf{x}_1,\mathbf{x}_2)=\delta(\mathbf{x}_1-\mathbf{x}_2). \tag{8}$$

Here θ is the angle between $\mathbf{k}$ and $\mathbf{k}'$. The vector $\mathbf{k}'$ has the same direction as $\mathbf{x}$, and $|\mathbf{k}'|=|\mathbf{k}|$.

It is often convenient to express the right-hand side of Eq. (8) as an integral over momentum space. To achieve this put

$$(\mathbf{p}|V|\mathbf{q})=\int d\mathbf{x}V(x)\exp(-i(\mathbf{p}-\mathbf{q})\mathbf{x}), \tag{9}$$

$$K_n(\mathbf{p},\mathbf{q})=(1/8\pi^3)\int d\mathbf{x}d\mathbf{y}K_n(\mathbf{x},\mathbf{y})\exp(-i\mathbf{p}\mathbf{x}+i\mathbf{q}\mathbf{y}). \tag{10}$$

Then

$$f(\theta)=-\frac{1}{4\pi}\sum_{n=1}^{\infty}\lambda^n\int d\mathbf{p}(\mathbf{k}'|V|\mathbf{p})K_{n-1}(\mathbf{p},\mathbf{k}). \tag{11}$$

We note the following useful formulas:

$$K_{n+1}(\mathbf{p},\mathbf{q})=\int K_n(\mathbf{p},\mathbf{t})K(\mathbf{t},\mathbf{q})d\mathbf{t}, \tag{12}$$

$$\int K_n(\mathbf{x},\mathbf{x})d\mathbf{x}=\int K_n(\mathbf{p},\mathbf{p})d\mathbf{p}, \tag{13}$$

$$K(\mathbf{p},\mathbf{q})=-(\mathbf{p}|V|\mathbf{q})/8\pi^3(p^2-k^2-i\epsilon),\quad \epsilon>0, \tag{14}$$

where in Eq. (14) k^2 has been given a small positive imaginary part $i\epsilon$ which serves to make integrations over $\mathbf{p}$ well defined and in accordance with the condition that our kernel corresponds to outgoing waves only. In all final results one should let ϵ tend to zero.

[4] It is, of course, irrelevant for the subsequent discussion of some general properties of the solutions of Eq. (1) that we consider here the particular physical system of two interacting nucleons.

For the purpose of the discussion given in the next section we subject Eq. (2) to an expansion in spherical harmonics. Thus, G is written as follows[5]

$$G(\mathbf{x},\mathbf{x}')=\tfrac{1}{4}\sum_{l=0}^{\infty}(l+\tfrac{1}{2})^{\frac{1}{2}}G_l(r,r')P_l(\vartheta),$$

where ϑ denotes the angle between $\mathbf{x}$ and $\mathbf{x}'$ and $r=|\mathbf{x}|$, $r'=|\mathbf{x}'|$. $P_l(\vartheta)$ are the normalized Legendre polynomials, while

$$G_l(r,r')=(rr')^{-\frac{1}{2}}J_{l+\frac{1}{2}}(kr)[(-)^lJ_{-l-\frac{1}{2}}(kr') +iJ_{l+\frac{1}{2}}(kr')],\quad r'>r. \tag{15}$$

For $r'<r$, $G_l(r,r')$ is defined by the right-hand side of Eq. (15), where now r and r' are interchanged. Put

$$\psi(\mathbf{x})=\textstyle\sum_l P_l(\theta)\varphi_l(r),\quad \exp(i\mathbf{kx})=\sum_l f_l(r)P_l(\theta).$$

Using the well-known expansion of a plane wave with respect to Legendre polynomials and applying the addition theorem for spherical harmonics, one gets

$$\varphi_l(r)=\{\pi(2l+1)/kr\}^{\frac{1}{2}}i^lJ_{l+\frac{1}{2}}(kr) -\tfrac{1}{2}\lambda\pi\int_0^{\infty}G_l(r,r')V(r')\varphi_l(r')r'^2dr'.$$

For S-states ($l=0$) one therefore has, with $-ikr\varphi_0(r)2^{\frac{1}{2}}=\varphi(r)$:

$$\varphi(r)=e^{-ikr}-e^{ikr}+\lambda\int_0^{\infty}g(r,r')V(r')\varphi(r')dr', \tag{16a}$$

$$g(r,r')=-(1/2ik)\{\exp[ik(r+r')]-\exp(ik|r-r'|)\}.$$

The asymptotic form of $\varphi(r)$ is

$$\varphi(r)\sim e^{-ikr}-S_0(\lambda,k)e^{ikr}. \tag{16b}$$

$S_0(\lambda,k)$, the eigenvalue of the scattering matrix corresponding to angular momentum zero and wave number k is given by

$$S_0(\lambda,k)=1+(\lambda/k)\int_0^{\infty}\sin krV(r)\varphi(r)dr. \tag{16c}$$

In accordance with the definition introduced above, the Born expansion of $\varphi(r)$ and of $S_0(\lambda,k)$ is obtained by developing these quantities in a power series in λ.

(b) Example: The Yukawa Potential

Disregarding for the moment the question whether Eq. (7) has any meaning at all, we will next investigate an example in which the terms $\sim\lambda$ and λ^2 of Eq. (6) are calculated explicitly; or, more precisely, we shall compute the contributions $\sim\lambda^2$ and λ^3 to Eq. (5).

The case to be considered is that of the n-p-scattering by a spin and exchange dependent central Yukawa potential with constants fitted so as to account for the deuteron binding energy and the epithermal scattering. We are well aware of the academic character of a purely central force for the n-p system, but then our present investigation is one of method. We thus have

$$\begin{aligned}V(x)&=e^{-x}/x,\\ \lambda_{\mathrm{tr}}&=(a_{\mathrm{tr}}P_x+b_{\mathrm{tr}})B_{\mathrm{tr}},\\ \lambda_{\mathrm{s}}&=(a_{\mathrm{s}}P_x+b_{\mathrm{s}})B_{\mathrm{s}}.\end{aligned} \tag{17}$$

"tr" and "s" refer to triplet and singlet states, respectively. P_x is the space exchange operator. The constants a, b determine the exchange type of the forces and are normalized so that

$$a_{\mathrm{s}}+b_{\mathrm{s}}=1,\quad a_{\mathrm{tr}}+b_{\mathrm{tr}}=-3.$$

We will consider two cases of exchange type for which numerical results by means of phase shift analysis are available in the literature, for energies which are of interest for the present purposes. These are first the "even" theory, proposed by Serber, for which

$$a_{\mathrm{s}}=b_{\mathrm{s}}=\tfrac{1}{2};\quad a_{\mathrm{tr}}=b_{\mathrm{tr}}=-\tfrac{3}{2}\quad\text{(even theory)}; \tag{18}$$

secondly, the "symmetrical" theory, for which

$$a_{\mathrm{s}}=2,\quad b_{\mathrm{s}}=-1;\quad a_{\mathrm{tr}}=-2,\quad b_{\mathrm{tr}}=-1 \quad\text{(symmetrical theory)}. \tag{19}$$

The constants B depend on what range is chosen for the Yukawa potential. We shall use the following set of values:

$$r_0=1.18\times10^{-13}\text{ cm},\quad B_{\mathrm{s}}=-1.58,\quad B_{\mathrm{tr}}=+0.76. \tag{20}$$

For the time being we shall drop the subscripts "tr" and "s" and turn to the evaluation of the differential cross section up to the order indicated above. In the result so obtained we then must perform the spin averaging. Thus we have in our approximation, using Eqs. (5), (11), and (14):

$$\frac{d\sigma}{d\Omega}=\left(\frac{r_0}{4\pi}\right)^2\left|(\mathbf{k}'|\lambda V|\mathbf{k}) -\frac{1}{8\pi^3}\int d\mathbf{p}(\mathbf{k}'|\lambda V|\mathbf{p})\frac{1}{p^2-k^2-i\epsilon}(\mathbf{p}|\lambda V|\mathbf{k})\right|^2.$$

According to Eq. (17)

$$\begin{aligned}(\mathbf{k}'|V|\mathbf{k})&=4\pi/(|\mathbf{k}-\mathbf{k}'|^2+1),\\ (\mathbf{k}'|P_xV|\mathbf{k})&=4\pi/(|\mathbf{k}+\mathbf{k}'|^2+1).\end{aligned}$$

Inserting this, one readily obtains

$$\frac{d\sigma}{d\Omega}=B^2r_0^2\left|\frac{a}{2\eta(1+\xi)+1}+\frac{b}{2\eta(1-\xi)+1} -\frac{B(a^2+b^2)}{2\pi^2}\Phi(\xi)-\frac{Bab}{\pi^2}\Phi(-\xi)\right|^2, \tag{21}$$

$$\eta=k^2,\quad \xi=\cos\theta.$$

[5] See G. N. Watson, *Theory of Bessel Functions* (Cambridge University Press, London, 1944), second edition, p. 366, Eqs. (9) and (10).

Here

$$\Phi(\xi)=\int d\mathbf{p}\frac{1}{|\mathbf{p}-\mathbf{k}'|^2+1}\cdot\frac{1}{p^2-\eta-i\epsilon}\cdot\frac{1}{|\mathbf{p}-\mathbf{k}|^2+1}. \quad (22)$$

To be consistent we may retain only the terms $\sim B^2$ and B^3 in Eq. (21). Evidently, we then need only the real part $\mathrm{Re}\Phi(\xi)$ of $\Phi(\xi)$. Hence,

$$d\sigma/d\Omega=d\sigma_2/d\Omega+d\sigma_3/d\Omega,$$

where

$$\frac{d\sigma_2}{d\Omega}=B^2r_0^2\left[\frac{a}{2\eta(1+\xi)+1}+\frac{b}{2\eta(1-\xi)+1}\right]^2, \quad (23)$$

$$\frac{d\sigma_3}{d\Omega}=-\frac{B^3r_0^2}{\pi^2}\left[\frac{a}{2\eta(1+\xi)+1}+\frac{b}{2\eta(1-\xi)+1}\right]\times[(a^2+b^2)\mathrm{Re}\Phi(\xi)+2ab\mathrm{Re}\Phi(-\xi)]. \quad (24)$$

It will be shown in Appendix I that

$$\mathrm{Re}\Phi(\xi)=\frac{\sqrt{2}\pi^2}{\{\eta(1-\xi)(2\eta^2+4\eta+1-2\eta^2\xi)\}^{\frac{1}{2}}}\times\tan^{-1}\left\{\frac{\eta(1-\xi)}{2(2\eta^2+4\eta+1-2\eta^2\xi)}\right\}^{\frac{1}{2}}. \quad (25)$$

Thus Eqs. (23)–(25) give us the differential cross section. By carefully performing the limiting transition $r_0\to 0$ which leads to the coulomb case, one will verify that the right-hand side of Eq. (24) vanishes. This is in accordance with the well-known circumstance that the approximation $\sim\lambda^2$ happens to give the rigorous answer for the coulomb potential.

The total cross section σ is obtained by integration over ξ. Putting again $\sigma=\sigma_2+\sigma_3$, we get

$$\sigma_2=4\pi B^2r_0^2\left[\frac{a^2+b^2}{1+4\eta}+\frac{ab}{2\eta(1+2\eta)}\ln(1+4\eta)\right].$$

For the purpose of integrating over angles, the expression (25) can be considerably simplified, provided we restrict ourselves to sufficiently high energies. It is then not hard to see that the $\tan^{-1}$ can be replaced by its argument. We have verified that in this way one obtains an error which is only $\sim 2\%$ at 90 Mev and which gets progressively smaller for still higher energies. Proceeding in this way, one obtains

$$\sigma_3=-\frac{\pi B^3r_0^2}{2\eta^3}\cdot\frac{1}{\beta^2-\gamma^2}\left[\{\beta(a+b)^2-\gamma(a-b)^2\}\ln\frac{\gamma+1}{\gamma-1}-\{\gamma(a+b)^2-\beta(a-b)^2\}\ln\frac{\beta+1}{\beta-1}\right], \quad (26a)$$

where the following abbreviations have been used:

$$\beta=(2\eta^2+4\eta+1)/2\eta^2,\quad \gamma=(2\eta+1)/2\eta. \quad (26b)$$

We now apply these results to the two cases mentioned above.

1. Even Theory

Using Eq. (18), approximating the expression (25) in the way mentioned above, and performing the spin averaging, one obtains

$$\frac{d\sigma_2}{d\Omega}=\frac{r_0^2}{16}(B_s^2+27B_{tr}^2)\left[\frac{1}{2\eta(1+\xi)+1}+\frac{1}{2\eta(1-\xi)+1}\right]^2,$$

$$\frac{d\sigma_3}{d\Omega}=\frac{r_0^2}{16\eta^3}(|B_s|^2+81B_{tr}^2)\cdot\frac{\beta\gamma}{(\beta^2-\xi^2)(\gamma^2-\xi^2)},$$

$$\sigma_2=\frac{\pi r_0^2}{8}(B_s^2+27B_{tr}^2)\left[\frac{4}{1+4\eta}+\frac{1}{\eta(1+2\eta)}\ln(1+4\eta)\right],$$

$$\sigma_3=\frac{\pi r_0^2(|B_s|^2+81B_{tr}^2)}{4\eta(3\eta+1)(4\eta^2+5\eta+1)}\times[(4\eta^2+5\eta+1)-2\eta(2\eta+1)\ln(2\eta+1)].$$

Using Eq. (20) we compute the various quantities for $E_0=90$ Mev, corresponding to $\eta=1.5$. This energy is chosen so as to enable a comparison with the values given by Christian and Hart,[6] which were obtained by numerical evaluation of phase shifts. According to these authors

$$\sigma=90\text{ mb},\quad R=d\sigma(180°)/d\sigma(90°)=3.25,$$

whereas

$$\sigma_2=88\text{ mb},\ R_2=d\sigma_2(180°)/d\sigma_2(90°)=20.5/3.9=5.2,$$

$$\sigma_3=52\text{ mb},\ R_3=\frac{d\sigma_2(180°)+d\sigma_3(180°)}{d\sigma_2(90°)+d\sigma_3(90°)}=\frac{20.5+8.1}{3.9+3.0}=4.1.$$

Thus, the first Born approximation seems to give a good approximation to σ; but evidently this is misleading, as follows from the comparison of R_2 and R. Going to the next approximation gives a better picture of the angular distribution, but now one is far off again with respect to the total cross section. Clearly, the Born expansion is still quite useless at this energy, and the situation does not get much better for larger E_0, as is shown by Table I. Thus, even at 270 Mev (where for that matter the potential picture is getting to be quite far fetched) σ_3 still gives a correction of more than 20 percent to σ_2. One must therefore conclude that the Born expansion is nowhere quantitatively reliable.

2. Symmetrical Theory

In view of the experimental evidence this seems a quite academic case. We are mentioning it only in order

[6] R. S. Christian and E. W. Hart, Phys. Rev. 77, 441 (1949), see especially Table III. We are indebted to Dr. Christian for supplying us with further unpublished numerical results.

TABLE I. Born approximation for Yukawa potential.

E_0(Mev)	σ_2(mb)	σ_3(mb)	R_2	R_3
120	66	31	7.7	6.1
150	51	18	10.7	8.5
180	42	14	14	11.5
210	36	11	18	15.0
240	31	8	22	18.5
270	27	6	29	24.6

to have another means of comparison, *viz.*, with the results of Chew and Goldberger.[7] Also working with a Yukawa potential and with the constants (20), they found

$$\sigma = 140 \text{ mb}, \quad R = 6.81 \text{ for } E_0 = 80 \text{ Mev}.$$

Using Eq. (19) we obtain

$$\sigma_2 = 133 \text{ mb}, \quad R_2 = 56.9/4.7 = 12.1;$$
$$\sigma_3 = 46 \text{ mb}, \quad R_3 = (56.9-3.7)/(4.7+3.9) = 6.2.$$

Note that $d\sigma_3(180°)$ is negative, which is not unexpected for an interaction of which a big part is exchange force. Qualitatively the same situation obtains as for the even theory.

Rather than pursue the investigation to higher terms in the expansion—the calculation of which is very much more complicated—it would seem preferable at this stage to inquire into the general validity of power series expansions in λ for scattering problems. To this subject the next two sections are devoted.

III. λ-DEPENDENCE OF THE SOLUTIONS; S-STATES

In this section we will discuss the general structure of the solution $\varphi(\lambda; k, r)$ of the integral equation (16a) for S-states. This will lead us to conclusions about the validity of the Born expansion. For reasons of simplicity we will assume that the potential $\lambda V(r)$ contains no exchange operators unless otherwise stated. Our results, however, will be general. Further, we will assume that $\int_0^\infty r|V(r)|dr$ is finite, which condition could be replaced by more general ones.

$\varphi(\lambda; k, r)$ is a solution of the differential equation

$$\varphi'' + k^2\varphi - \lambda V\varphi = 0 \tag{27}$$

and is completely characterized by the boundary conditions (16b), and $\varphi(\lambda; k, 0) = 0$.

Since, in the first place, we are interested in the series expansion of $\varphi(\lambda; k, r)$ and $S_0(\lambda; k)$ in powers of λ, we have to investigate the analytical character of these quantities as functions of λ. It is then convenient to build up the solution φ from such other solutions of Eq. (27) for which a power series expansion in λ is always possible. It is easy to find functions of this kind. We have, in fact, only to look for solutions of Eq. (27), which are defined by *initial values which are independent of* λ. Since we can solve Eq. (27) under the given initial conditions for any complex value of λ, it is intuitively clear that for given k and r such solutions are entire functions of λ. This is the assertion of a theorem by H. Poincaré.[8] A convenient choice (although not the only one) for such a solution is defined by

$$\lim_{r\to\infty} e^{ikr} f(\lambda; k, r) = 1; \tag{28}$$

and $f(\lambda; k, r)$ is seen to satisfy the integral equation:

$$f(\lambda; k, r) = e^{-ikr} + (\lambda/k)\int_r^\infty \sin k(r'-r) V(r') f(\lambda; k\ r') dr'. \tag{29}$$

The power series in λ, which one gets by successive iteration of Eq. (29), converges[9] for any λ. Of course, $f(\lambda; k, r)$ will not be zero for $r = 0$. However, the solution $\varphi(\lambda; k, r)$ which does vanish at the origin, can easily be expressed in terms of f:

$$\varphi(\lambda; kr) = [1/f(\lambda; -k)][f(\lambda; -k)f(\lambda; k, r) - f(\lambda; k)f(\lambda; -k, r)], \tag{30}$$

where

$$f(\lambda; k) \equiv f(\lambda; k, 0) \tag{31}$$

and [see Eq. (16b)]

$$S_0(\lambda; k) = f(\lambda; k)/f(\lambda; -k). \tag{32}$$

Thus, $\varphi(\lambda; k, r)$ and $S_0(\lambda; k)$ are meromorphic functions in λ with poles at the zero's of $f(\lambda; -k)$, which we denote by $\lambda_1, \lambda_2 \cdots \lambda_n \cdots$. If λ_1 is the zero with the smallest absolute value, then the Born expansion will certainly diverge for $|\lambda| > |\lambda_1|$ and converge for $|\lambda| < |\lambda_1|$. We will not try here to give estimates for λ_1 or $|\lambda_1|$. However, it is easy to see that: (1) for the Born expansion to converge it suffices that

$$|\lambda| \int_0^\infty r|V(r)|dr < 1.$$

This is an immediate consequence of (16a) and

$$|e^{ik(r+r')} - e^{ik|r-r'|}| \leq 2|k|r'.$$

(2) For real, nonvanishing k the λ_n cannot be real, for the Wronskian of $f(\lambda; k, r)$ and $f(\lambda; -k, r)$ is independent of r, and from (28) it follows that

$$f(\lambda; k, r)[\partial f(\lambda; -k, r)/\partial r] - [\partial f(\lambda; k, r)/\partial r] f(\lambda; -k, r) = 2ik. \tag{33}$$

[7] G. F. Chew and M. L. Goldberger, Phys. Rev. **73**, 1409 (1948). For a correction see F. Rohrlich and J. Eisenstein, Phys. Rev. **75**, 705 (1949), footnote on p. 711.

[8] H. Poincaré, Acta Math. 4, 215 (1884); see, e.g., *Enzyklopädie der Mathematischen Wissenschaft*, Vol. 2, part 2, p. 501. Compare for this and the following discussion, R. Jost, Helv. Phys. Acta **22**, 256 (1947); V. Bargmann, Phys. Rev. **75**, 301 (1949); Revs. Modern Phys. **21**, 488 (1949). A solution with this property was used by M. Born, Z. Physik **38**, 803 (1926) [p. 810] for the discussion of the one-dimensional scattering. The statement made in Born's paper, p. 816, concerning the convergence of the three-dimensional Born expansion seems to us erroneous, however, (see Sec. IV of this paper). Instead of using the solution (28), one may for the present purpose equally well use a solution $U(\lambda; k, r)$ specified by $U(\lambda; k, 0) = 0$, $U'(\lambda; k, 0) = 1$. This solution was used by C. E. Fröberg, Ark. Mat. Astron. Fysik **34 A**, No. 28 (1948). However, Eq. (4) for the determination of the phase shift is incorrect.

[9] V. Bargmann, Revs. Modern Phys. **21**, 488 (1949), Appendix.

Furthermore, $f(\lambda; -k, r)=f^*(\lambda^*; k, r)$. If, therefore, λ_n would be real; Eq. (33) would yield a contradiction for $r=0$, since the left-hand side would vanish.

The following example of a $V(r)$, for which the λ_n are simple functions of n and k, may serve to illustrate the general situation:[10]

$$V(r)=e^{-r}/(1-e^{-r}). \tag{34}$$

Here

$$f(\lambda; k, r)=e^{-ikr}F(i[k+(k^2+\lambda^2)^{\frac{1}{2}}], \; i[k-(k^2+\lambda^2)^{\frac{1}{2}}]; \; 1+2ik; \; e^{-r}), \tag{35}$$

where $F(\alpha, \beta; \gamma; z)$ is the hypergeometric function, and

$$f(\lambda; k)=\prod_{n=1}^{\infty}\left(1+\frac{\lambda}{n(n+2ik)}\right). \tag{36}$$

The zero's λ_n of $f(\lambda; -k)$ lie at the points

$$\lambda_n=-n^2+2ikn, \tag{37}$$

and the Born expansion converges for

$$|\lambda|<(1+4k^2)^{\frac{1}{2}}. \tag{38}$$

It is desirable to relate the form (30) for the solution $\varphi(\lambda; k, r)$ directly to the original integral equation (16a). This is indeed necessary for the extension of the present discussion to the more general Eq. (2). The way to do this is the application of Fredholm's[11] theory to the integral equation (16a).

Putting

$$g(r, r')V(r')=K(r, r'), \tag{39}$$

we get

$$\varphi(\lambda; k, r)=(e^{-ikr}-e^{ikr})+[\lambda/\Delta(\lambda; k)]\int_0^{\infty}\Delta(\lambda; k; r, r')(e^{-ikr'}-e^{+ikr'})dr', \tag{40}$$

with

$$\Delta(\lambda; k)=1+\sum_{n=1}^{\infty}\frac{(-\lambda)^n}{n!}\int_0^{\infty}dr_1\cdots\int_0^{\infty}dr_n\begin{vmatrix} K(r_1, r_1) & K(r_1, r_2) & \cdots & K(r_1, r_n) \\ \vdots & & & \\ K(r_n, r_1) & K(r_n, r_2) & \cdots & K(r_n, r_n)\end{vmatrix} \tag{41}$$

and

$$\Delta(\lambda; k; r, r')=K(r, r')+\sum_{n=1}^{\infty}\frac{(-\lambda)^n}{n!}\int_0^{\infty}dr_1\cdots\int_0^{\infty}dr_n\begin{vmatrix} K(r, r') & K(r, r_1) & \cdots & K(r, r_n) \\ K(r_1, r') & K(r_1, r_1) & \cdots & K(r_1, r_n) \\ \vdots & & & \\ K(r_n, r') & K(r_n, r_1) & \cdots & K(r_n, r_n)\end{vmatrix}. \tag{42}$$

The series implied in Eq. (40) converge absolutely for any λ. Again $\varphi(\lambda; k, r)$ appears as the quotient of two entire functions, and we will prove in Appendix II that Eqs. (40) and (30) are actually identical in the sense that

$$\Delta(\lambda; k)\equiv f(\lambda; -k). \tag{43}$$

The zero's of $\Delta(\lambda; k)$, i.e., λ_n, now appear as eigenvalues of the kernel $K(r, r')$; i.e., for $\lambda=\lambda_n$ there exists a solution of Eq. (27) for which

$$\psi(\lambda_n; k, 0)=0 \quad \text{and} \quad \psi(\lambda_n; k, r)\sim e^{ikr}. \tag{44}$$

The fact that the imaginary part of λ_n does not vanish means that a stationary solution of the Schroedinger equation with the property (44) exists only if the potential $\lambda_n V(r)$ acts as a source (see Sec. IV).

We conclude this section with an example which shows how rapid a convergence one can expect for $f(\lambda, k)$, or rather the phase shift η, as a power series in λ for nuclear potentials. We take

$$V=e^{-r}.$$

Then

$$f(\lambda; k, r)=\exp\{-ir\ln(-\lambda)\}\Gamma(2ik+1)\times J_{2ik}[2(-\lambda)^{\frac{1}{2}}\exp(-r/2)],$$

$$f(\lambda; k)=\sum_0^{\infty}\lambda^n\alpha_n(k),$$

$$\alpha_0=1,$$

$$\alpha_n(k)=[n!(2ik+1)(2ik+2)\cdots(2ik+n)]^{-1}.$$

We further use $r_0=0.75\times10^{-13}$ cm, $\lambda=2.13$. For these values Eq. (27) can be considered as the radial equation for ^3S-states, with the binding energy of the deuteron appropriately fitted. We have calculated η for $E_0=40$ Mev ($k=0.514$). The results are collected in Table II. The first column indicates the highest power of λ which has been included. η_F is the phase shift computed by the Fredholm method from $f(\lambda; k)$. For comparison we also give η_B, the phase shift calculated

[10] L. Hulthén, Ark. Mat. Astron. Fysik **28A**, No. 5 (1942); **29B**, No. 1 (1942).

[11] See, e. g., A. B. Whittaker and C. D. Watson, *Modern Analysis* (Cambridge University Press, London, 1940), fourth edition, Chap. XI.

TABLE II. Phase shifts for exponential potential $E_0=40$ Mev.

Approx.	η^P	η^B
1	1.602	2.613
2	1.156	0.392
3	1.259	3.157
4	1.258	0.559

in the corresponding four Born approximations. The results are self-explanatory.

IV. THE λ-DEPENDENCE OF THE SOLUTIONS; GENERAL CASE

We now go back to the discussion of Eqs. (2) and (3). Following the Fredholm procedure, already outlined in the previous section, we will show that for all finite λ the solution $\psi(\lambda;\mathbf{k},\mathbf{x})$ can again be represented as the quotient of two convergent power series in λ.

However, we cannot without further ado apply the general formulas of the Fredholm theory [see Eqs. (40)–(42)]. The reason for this is that $K(\mathbf{x},\mathbf{x})$ becomes infinite, owing to the singularity of the Green's function, so that the Fredholm determinants do not exist. It is, however, easy to circumvent this obstacle. Obviously, the formulas of Fredholm still give solutions (proper convergence assumed), if we replace all those elements along the diagonal of the determinants which are of the form $K(\mathbf{x},\mathbf{x})$ by zero.[12] We will see in Appendix III that the following conditions, imposed[13] on $V(|\mathbf{x}|)$, are sufficient to insure the convergence of this procedure:

$$|V(|\mathbf{x}|)|\leq|\mathbf{x}|^{-1}F(|\mathbf{x}|), \tag{45}$$

where the function $F(r)$ satisfies the inequalities

$$\int F(r)dr\leq M, \tag{46}$$

$$F(r)\leq M'r^{-1}. \tag{47}$$

Equation (47) is a condition of smoothness on the potential prohibiting, e.g., the occurrence of high "peaks." (Since the conditions (46) and (47) look very reasonable from a physical standpoint, we have not tried to replace them by weaker ones.)

Thus,

$$\psi(\lambda;\mathbf{k},\mathbf{x})=\exp(i\mathbf{k}\mathbf{x})+\lambda\int[\Delta(\lambda;\mathbf{x},\mathbf{x}')/\Delta(\lambda)]\exp(i\mathbf{k}\mathbf{x}')d\mathbf{x}', \tag{48}$$

$$\Delta(\lambda;\mathbf{x},\mathbf{x}')=K(\mathbf{x},\mathbf{x}')+\sum_{n=1}^{\infty}\frac{(-\lambda)^n}{n!}\int d\mathbf{x}_1\cdots\int d\mathbf{x}_n\begin{vmatrix} K(\mathbf{x},\mathbf{x}') & K(\mathbf{x},\mathbf{x}_1) & K(\mathbf{x},\mathbf{x}_2) & \cdots & K(\mathbf{x},\mathbf{x}_n)\\ K(\mathbf{x}_1,\mathbf{x}') & 0 & K(\mathbf{x}_1,\mathbf{x}_2) & \cdots & K(\mathbf{x}_1,\mathbf{x}_n)\\ K(\mathbf{x}_2,\mathbf{x}') & K(\mathbf{x}_2,\mathbf{x}_1) & 0 & \cdots & K(\mathbf{x}_2,\mathbf{x}_n)\\ \vdots & & & & \\ K(\mathbf{x}_n,\mathbf{x}') & K(\mathbf{x}_n,\mathbf{x}_1) & K(\mathbf{x}_n,\mathbf{x}_2) & \cdots & 0 \end{vmatrix}, \tag{49}$$

$$\Delta(\lambda)=1+\sum_{n=1}^{\infty}\frac{(-\lambda)^n}{n!}\int d\mathbf{x}_1\cdots\int d\mathbf{x}_n\begin{vmatrix} 0 & K(\mathbf{x}_1,\mathbf{x}_2) & \cdots & K(\mathbf{x}_1,\mathbf{x}_n)\\ K(\mathbf{x}_2,\mathbf{x}_1) & 0 & \cdots & K(\mathbf{x}_2,\mathbf{x}_n)\\ & & & \\ K(\mathbf{x}_n,\mathbf{x}_1) & K(\mathbf{x}_n,\mathbf{x}_2) & \cdots & 0 \end{vmatrix}. \tag{50}$$

So we conclude that $\psi(\lambda;\mathbf{k},\mathbf{x})$ is again a meromorphic function of λ with poles at the zeros λ_n of $\Delta(\lambda)$, and the same is true for the function $f(\theta)$ defined in Eq. (4). The zero λ_1 with the smallest absolute value gives the radius of convergence for the Born expansion (6). Since it is easy to prove[14] that the Born expansion converges for $\lambda M<1$, it follows that $|\lambda_1|\geqq M^{-1}$, for any value of k.

The λ_n are eigenvalues of the kernel $K(\mathbf{x},\mathbf{y})$, and this means that the homogeneous equation

$$\psi_n(\mathbf{k},\mathbf{x})=\lambda_n\int K(\mathbf{x},\mathbf{x}')\psi_n(\mathbf{k},\mathbf{x}')d\mathbf{x}' \tag{51}$$

has at least one nontrivial solution with the asymptotic behavior

$$\psi_n(\mathbf{k},\mathbf{x})\sim|\mathbf{x}|^{-1}f_n(\theta)\exp(ik|\mathbf{x}|). \tag{52}$$

From (51) and (52) we can conclude that the imaginary part of λ_n for $\mathbf{k}\neq0$ cannot vanish. In fact:

$$i\frac{\partial}{\partial x_\nu}\left(\psi_n^*\frac{\partial\psi_n}{\partial x_\nu}-\psi_n\frac{\partial\psi_n^*}{\partial x_\nu}\right)=i(\lambda_n-\lambda_n^*)\psi^*V\psi \tag{53}$$

integrating (53) over a large sphere and using (52) yields[15]

$$k\cdot\int|f(\theta)|^2d\Omega=-i(\lambda_n^*-\lambda_n)\int\psi_n^*V\psi_n dx, \tag{54}$$

[12] This device is due to D. Hilbert, *Grundzüge einer allgemeinen Theorie der Integralgleichungen* (Leipzig, 1912), p. 30. H. Poincaré, *Oeuvres* (Paris, 1934), Vol. III, p. 560; Acta Math. 33, 57 (1901). It consists in multiplying formally numerator and denominator of the resolvent by $\exp[\lambda\int K(\mathbf{x},\mathbf{x})d\mathbf{x}]$.

[13] The generalization to noncentral potentials presents no difficulties.

[14] This follows from

$$\left|\int K_{n+1}(\mathbf{x},\mathbf{y})\exp(i\mathbf{k}\mathbf{y})d\mathbf{y}\right|\leq M\left|\int K_n(\mathbf{x},\mathbf{y})\exp(i\mathbf{k}\mathbf{y})d\mathbf{y}\right|.$$

[15] For positive imaginary k the eigenvalues of $K(\mathbf{x},\mathbf{y})$ are real and give the potential strengths necessary for a bound state with an energy given by k.

which proves the point. Equation (53) shows that $i(\lambda_n-\lambda_n^*)\psi^*V\psi$ acts as a source distribution allowing a stationary outgoing current distribution asymptotically described by Eq. (52).

Breaking off the summation in Eqs. (49) and (50) at a certain $n=n_0$, we are allowed to rearrange the terms and thus see that the solution $\psi(\lambda;\mathbf{k},\mathbf{x})$ can always be represented to an arbitrary high accuracy by a polynomial in the iterated kernels K_n of the form

$$\psi_{n_0}(\lambda;\mathbf{k},\mathbf{x})=\exp(i\mathbf{kx})+\sum_{n=1}^{n_0}a_n\int K_n(\mathbf{x},\mathbf{x}')\exp(i\mathbf{kx}')d\mathbf{x}', \quad (55)$$

with the a_n composed of the integrals $\int K_m(\mathbf{x},\mathbf{x})d\mathbf{x}$. In the same sense, $f(\theta)$ can be approached by a linear combination of Born approximations $f_n^{(B)}(\theta)$:

$$f_{n_0}(\theta)=\frac{1}{4\pi}\sum_1^{n_0}a_nf_n^{(B)}(\theta), \quad (56)$$

[compare Eq. (8)] in which, according to Eqs. (48)–(50), the a_n are rational functions of λ, but, of course, not simply λ^n.

From the foregoing considerations it follows that the right-hand side of Eq. (55) with unknown parameters a_n is in principle well suited as Ansatz for a variational procedure. But this clearly does not save labor as compared with the evaluation of an adequate number of terms in the Fredholm expansion itself. However, it certainly is unwarranted to employ a partial Born expansion, i.e., Eq. (55) with $a_n=\lambda^n$, for such purposes whenever the potential strength gets too large.

Despite the formal appeal of the Fredholm procedure, it is not suited for numerical work, because of its slow convergence. We will briefly exemplify this by considering again the Yukawa potential and going up to the second power in numerator and denominator of Eq. (48). Up to this approximation the numerator is identical in the second Born approximation for $f(\theta)$. In the foregoing, we have tacitly assumed that λV did not involve exchange operators, but the extension to their being present is straightforward.

Using Eqs. (17) and (13) we find in our approximation for the denominator $\Delta(\lambda)$ in Eq. (48) (for both singlet and triplet states)

$$\Delta(\lambda)=1-\tfrac{1}{2}\lambda^2[(a^2+b^2)D_1+2abD_2], \quad (57)$$

$$D_1=(1/4\pi^4)\int d\mathbf{p}dt[(p^2-\eta-i\epsilon)\times(t^2-\eta-i\epsilon)(|\mathbf{p}-\mathbf{t}|^2+1)^2]^{-1}, \quad (58)$$

$$D_2=(1/4\pi^4)\int d\mathbf{p}dt[(p^2-\eta-i\epsilon)(t^2-\eta-i\epsilon)\times(|\mathbf{p}-\mathbf{t}|^2+1)(|\mathbf{p}+\mathbf{t}|^2+1)]^{-1}. \quad (59)$$

D_1 and D_2 are evaluated in Appendix III. Their respective real parts are

$$\mathrm{Re}D_1=[2(4\eta+1)]^{-1} \quad (60)$$

$$\mathrm{Re}D_2=-(1/2\eta+1)\cdot\ln[2(\eta+1)/(4\eta+1)]. \quad (61)$$

The right-hand side of both Eq. (60) and Eq. (61) are positive for $\eta=1.5$ corresponding to the energy $E_0=90$ Mev used in Sec. II. Therefore, the cross section increases over that obtained in the second Born approximation, which itself was already too large.

In conclusion, we remark that the analysis of the legitimacy of power series expansions put forward in this paper is to a large extent specific for the simple problem of scattering by a static potential. The situation is much more intricate for the Born expansions of relativistic field theories. In fact, the kernels encountered there are of a much more singular nature, so that one certainly cannot hope to apply the simple Fredholm theory to this case. This is, of course, merely a reflection on the deep-lying differences in mathematical structure between the fairly simple differential equations of the nonrelativistic Schroedinger theory and the basic field-theoretical equations. In fact, in those cases where the development of the scattering matrix in powers of the coupling parameter fails, we are confronted with a situation where one does not even know what to mean by a solution. It seems to us that a clarification of this point is needed before one can attempt actual evaluations in problems where the coupling constants involved are large.

One of us (R.J.) would like to express his gratitude to the Institute for Advanced Study for a grant-in-aid.

APPENDIX

(I) Born Approximation for the Yukawa Potential

We shall here compute $\Phi(\xi)$ defined by Eq. (22). Introducing auxiliary variables x_1, x_2, x_3 whose ranges are confined to $x_i\geq 0$, we may write[16]

$$\Phi(\xi)=2\int d\mathbf{p}\int dx_1dx_2dx_3\frac{\delta(x_1+x_2+x_3-1)}{[\{(\mathbf{p}-\mathbf{k}')^2+1\}x_1+(p^2-\eta-i\epsilon)x_2+\{(\mathbf{p}-\mathbf{k})^2+1\}x_3]^3}$$

Transforming from $\mathbf{p}$ to the new variable

$$\mathbf{P}=\mathbf{p}-\mathbf{k}'x_1-\mathbf{k}x_3,$$

[16] See R. P. Feynman, Phys. Rev. 76, 769 (1949).

one gets upon performing the $\mathbf{P}_3$-integration

$$\Phi(\xi)=\tfrac{1}{2}\pi^2\int\frac{\delta(x_1+x_2+x_3-1)dx_1dx_2dx_3}{[\eta\{x_1(1-x_1)+x_2(1-x_2)-x_3-2\xi x_1x_2\}+x_1+x_2-i\epsilon x_3]^{\frac{1}{2}}}$$

Integrate over x_3 and put $x_1+x_2=u$, $x_1-x_2=v$:

$$\Phi(\xi)=\tfrac{1}{2}\pi^2\int_0^1 du\int_{-u}^{u}dv[u-\eta\{1-2u+\tfrac{1}{2}(u^2+v^2)+\tfrac{1}{2}(u^2-v^2)\xi\}-i\epsilon(1-u)]^{-\frac{1}{2}}.$$

Owing to the imaginary term in the square bracket, this expression is never zero for $-u\leq v\leq u$. Hence, the v-integration is well-defined and yields

$$\Phi(\xi)=\tfrac{1}{2}\pi^2\int_0^1 udub^{-1}(u)\{b(u)-au^2\}^{-\frac{1}{2}},\quad a=\tfrac{1}{2}\eta(1-\xi),\quad b=u-\eta\{1-2u+\tfrac{1}{2}u^2(1+\xi)\}-i\epsilon(1-u). \tag{I.1}$$

The integrand has branch points at u_+^0 and u_-^0, where

$$u_\pm^0=(1/2\eta)[2\eta+1\pm(4\eta+1)^{\frac{1}{2}}+i\epsilon\{1\pm(4\eta+1)^{\frac{1}{2}}\}],$$

and poles at $u_\pm$:

$$u_\pm=[1/\eta(1+\xi)][2\eta+1\pm\chi(\eta)+i\epsilon\{1\pm(\eta(1-\xi)+1)\chi^{-1}(\eta)\}],\quad \chi(\eta)=\{(2\eta+1)^2-2\eta^2(1+\xi)\}^{\frac{1}{2}}.$$

The position of these points in the complex u plane is sketched in Fig. 1.

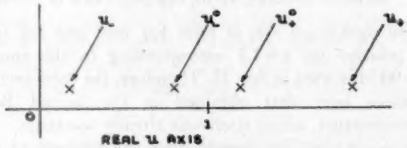

FIG. 1. Position of poles and branch points of the integrand in Eq. (I.1).

It is easy to find the indefinite integral over u. In substituting the limits one has to take care in the choice of branch. At $u=1$ the limit value is real. Since

$$\mathrm{Im}\{b(u)-au^2\}\leq 0,\quad 0\leq u\leq 1,$$

it follows from the position of u_-^0 that

$$\{b(u)-au^2\}^{\frac{1}{2}}_{u=0}=\{-\eta(1+i\epsilon)\}^{\frac{1}{2}}=(-\eta)^{\frac{1}{2}}(1+\tfrac{1}{2}i\epsilon\eta^{-1})=-i\eta^{\frac{1}{2}}(1+\tfrac{1}{2}i\epsilon\eta^{-1}).$$

One may now let $\epsilon\to 0$, and one finds after some calculation

$$\Phi(\xi)=\frac{i\pi^2}{\eta(1+\xi)(u_+-u_-)}\ln\frac{u_+(1-u_-)I_-N_+}{u_-(1-u_+)I_+N_-},$$

$$I_\pm=(2\eta+1)u_\pm-2\eta-u_\pm\eta\{2(1-\xi)\}^{\frac{1}{2}},$$

$$N_\pm=1+u_\pm-iu_\pm\{2(1-\xi)\}^{\frac{1}{2}}.$$

The real and imaginary part of Φ are now readily found. We will only consider $\mathrm{Re}\Phi(\xi)$. As (see Fig. 1)

$$u_+(1-u_-)I_-/u_-(1-u_+)I_+>0,$$

we can for this purpose replace the ln in Φ by $\ln N_+/N_-$.

Upon taking the imaginary part of the latter quantity we get

$$\mathrm{Re}\Phi(\xi)=\frac{\pi^2}{\{2\eta(1-\xi)(2\eta^2+4\eta+1-2\eta^2\xi)\}^{\frac{1}{2}}}\cdot\tan^{-1}\left[\frac{2\{2\eta(1-\xi)(2\eta^2+4\eta+1-2\eta^2\xi)\}^{\frac{1}{2}}}{4\eta^2(1-\xi)+\eta(7+\xi)+2}\right].$$

(II) Proof that $\Delta(\lambda;\mathbf{k})=\mathbf{f}(\lambda;-\mathbf{k})$

Using $2\tan^{-1}a=\tan^{-1}[2a/(1-a^2)]$ we are led to the expression quoted in Eq. (25). It is convenient to discuss for this proof the function $g(\lambda;k,r)=\exp(ikr)f(\lambda;k,r)$ rather than $f(\lambda;k,r)$ of Eq. (28). One verifies that g satisfies

$$g(\lambda;-k,r)=1+(\lambda/2ik)\int_r^\infty[\exp(2ik\{r'-r\})-1]V(r')g(\lambda;-k,r')dr'.$$

Now we get for $f(\lambda;-k)$ the expansion:

$$f(\lambda;-k)=g(\lambda;-k,0)=1+\sum_{n=1}^{\infty}\left(\frac{\lambda}{2ik}\right)^n\int_0^\infty dr_1\int_{r_1}^\infty dr_2\cdots\int_{r_{n-1}}^\infty dr_n(\exp 2ikr_1-1)$$
$$\times(\exp 2ik\{r_2-r_1\}-1)\cdots(\exp 2ik\{r_n-r_{n-1}\}-1)V(r_1)V(r_2)\cdots V(r_n).$$

On the other hand,

$$\Delta(\lambda;k)=1+\sum_{n=1}^{\infty}(n!)^{-1}\left(\frac{\lambda}{2ik}\right)^n\int_0^\infty dr_1\cdots\int_0^\infty dr_n\,\mathrm{Det}_{\mu\nu}\|\exp(ik\{r_\mu+r_\nu\})-\exp(ik|r_\mu-r_\nu|)\|V(r_1)V(r_2)\cdots V(r_n).$$

The integrand of the last integral is symmetric in all the variables; therefore,

$$\Delta(\lambda;k)=1+\sum_{n=1}^{\infty}\left(\frac{\lambda}{2ik}\right)^n\int_0^\infty dr_1\int_{r_1}^\infty dr_2\cdots\int_{r_{n-1}}^\infty dr_n\,\mathrm{Det}_{\mu\nu}\|\exp(ik\{r_\mu+r_\nu\})-\exp(ik|r_\mu-r_\nu|)\|V(r_1)V(r_2)\cdots V(r_n).$$

Writing $\xi_n=\exp(ikr_n)$, the determinant reads (remembering $r_1\leq r_2\leq r_3\cdots\leq r_n$)

$$D_n=\begin{vmatrix}(\xi_1^2-1) & \xi_2(\xi_1-1/\xi_1) & \xi_3(\xi_1-1/\xi_1) & \cdots & \xi_{n-1}(\xi_1-1/\xi_1) & \xi_n(\xi_1-1/\xi_1)\\ \xi_2(\xi_1-1/\xi_1) & (\xi_2^2-1) & \xi_3(\xi_2-1/\xi_2) & \cdots & \xi_{n-1}(\xi_2-1/\xi_2) & \xi_n(\xi_2-1/\xi_2)\\ \cdot & & & & & \\ \cdot & & & & & \\ \cdot & & & & & \\ \xi_{n-1}(\xi_1-1/\xi_1) & \xi_{n-1}(\xi_2-1/\xi_2) & \xi_{n-1}(\xi_3-1/\xi_3) & \cdots & (\xi_{n-1}^2-1) & \xi_n(\xi_{n-1}-1/\xi_{n-1})\\ \xi_n(\xi_1-1/\xi_1) & \xi_n(\xi_2-1/\xi_2) & \xi_n(\xi_3-1/\xi_3) & \cdots & \xi_n(\xi_{n-1}-1/\xi_{n-1}) & (\xi_n^2-1)\end{vmatrix}.$$

This determinant is obviously a linear function of ξ_n^2 and it vanishes for $\xi_n=\xi_{n-1}$, so

$$D_n=[(\xi_n^2/\xi_{n-1}^2)-1]F(\xi_1\cdots\xi_{n-1}).$$

By putting $\xi_n=0$, one sees that $F(\xi_1\cdots\xi_{n-1})=D_{n-1}$. Therefore,

$$D_n=[(\xi_n^2/\xi_{n-1}^2)-1]D_{n-1},\quad n=2,3\cdots;$$

but $D_1=\xi_1^2-1$, and thus, inserting the definition of ξ_n, one gets

$$D_n=(\exp 2ik|r_1-r_1|-1)(\exp 2ik|r_2-r_1|-1)\cdots(\exp 2ik|r_n-r_{n-1}|-1)$$

which completes the proof.

(III) The Convergence Proof for the Expansions (48)

As a preliminary step we will prove that the Fredholm formulas apply for the kernel of the iterated integral equation (2):

$$\psi(\lambda;\mathbf{k},\mathbf{x})=\exp(i\mathbf{kx})+\lambda\int K(\mathbf{x},\mathbf{x}')\exp(i\mathbf{kx}')d\mathbf{x}'+\lambda^2\int K_2(\mathbf{x},\mathbf{x}')\psi(\lambda;\mathbf{k},\mathbf{x}')d\mathbf{x}', \tag{III.1}$$

i.e., that

$$\psi(\lambda;\mathbf{k},\mathbf{x})=F_0(\mathbf{k},\mathbf{x})+\lambda^2\int H_2(\lambda^2;\mathbf{x},\mathbf{x}')F_0(\mathbf{k},\mathbf{x}')d\mathbf{x}', \tag{III.2}$$

where

$$F_0(\mathbf{k},\mathbf{x})=\exp(i\mathbf{kx})+\lambda\int K(\mathbf{x},\mathbf{x}')\exp(i\mathbf{kx}')d\mathbf{x}' \tag{III.3}$$

and

$$H_2(\lambda^2;\mathbf{x},\mathbf{x}')=\Delta_2(\lambda^2;\mathbf{x},\mathbf{x}')/\Delta_2(\lambda^2), \tag{III.4}$$

with

$$\Delta_2(\lambda^2;\mathbf{x},\mathbf{x}')=K_2(\mathbf{x},\mathbf{x}')+\sum_1^\infty\frac{(-\lambda^2)^n}{n!}\int d\mathbf{x}_1\cdots\int d\mathbf{x}_n\begin{vmatrix}K_2(\mathbf{x},\mathbf{x}') & K_2(\mathbf{x},\mathbf{x}_1) & \cdots & K_2(\mathbf{x},\mathbf{x}_n)\\ K_2(\mathbf{x}_1,\mathbf{x}') & K_2(\mathbf{x}_1,\mathbf{x}_1) & \cdots & K_2(\mathbf{x}_1,\mathbf{x}_n)\\ \cdot & \cdot & & \cdot\\ \cdot & \cdot & & \cdot\\ K_2(\mathbf{x}_n,\mathbf{x}') & K_2(\mathbf{x}_n,\mathbf{x}_1) & \cdots & K_2(\mathbf{x}_n,\mathbf{x}_n)\end{vmatrix} \tag{III.5}$$

and

$$\Delta_2(\lambda^2)=1+\sum_1^\infty\frac{(-\lambda^2)^n}{n!}\int d\mathbf{x}_1\cdots\int d\mathbf{x}_n\begin{vmatrix}K_2(\mathbf{x}_1,\mathbf{x}_1) & \cdots & K_2(\mathbf{x}_1,\mathbf{x}_n)\\ K_2(\mathbf{x}_n,\mathbf{x}_1) & \cdots & K_2(\mathbf{x}_n,\mathbf{x}_n)\end{vmatrix}. \tag{III.6}$$

As assumptions for the potential $V(x)$, we need Eqs. (46), (47). We first prove the convergence of the series for $\Delta(\lambda^2)$. For this we note

$$\begin{aligned}K_2(\mathbf{x},\mathbf{x}')&=\frac{1}{16\pi^2}\int d\mathbf{x}_1\frac{\exp(ik|\mathbf{x}-\mathbf{x}_1|)}{|\mathbf{x}-\mathbf{x}_1|}V(|\mathbf{x}_1|)\frac{\exp(ik|\mathbf{x}_1-\mathbf{x}'|)}{|\mathbf{x}_1-\mathbf{x}'|}V(|\mathbf{x}'|)\\&=A(\mathbf{x},\mathbf{x}')(4\pi|\mathbf{x}'|)^{-1}V(|\mathbf{x}'|),\end{aligned} \tag{III.7}$$

and we are going to show that, using (46) and (47),

$$|A(\mathbf{x},\mathbf{x}')|\leq N<\infty. \tag{III.8}$$

Introducing the definition of $F(|\mathbf{x}|)$ from Eq. (45), we have

$$|A(\mathbf{x},\mathbf{x}')|\leq(1/4\pi)|\mathbf{x}'|\int d\mathbf{x}_1F(|\mathbf{x}_1|)/(|\mathbf{x}_1|\cdot|\mathbf{x}-\mathbf{x}_1|\cdot|\mathbf{x}_1-\mathbf{x}'|)=B(\mathbf{x},\mathbf{x}'). \tag{III.9}$$

The integral on the right-hand side is obviously only a function of $|\mathbf{x}|=R$, $|\mathbf{x}'|=Q$, and $\sphericalangle(\mathbf{x},\mathbf{x}')=\Phi$, and we claim that for given R and Q it takes its maximum value for $\Phi=0$. This is intuitively clear from symmetry reasons, and it can be proved as follows:

$$B(x,x')=\frac{1}{4\pi}Q\int_0^\infty rdrF(r)\int_0^\pi\sin\vartheta d\vartheta\int_0^{2\pi}d\varphi\frac{1}{[R^2+r^2-2R\sin\vartheta\cos(\varphi-\frac{1}{2}\Phi)]^{\frac{1}{2}}[Q^2+r^2-2Qr\sin\vartheta\cos(\varphi+\frac{1}{2}\Phi)]^{\frac{1}{2}}}. \tag{III.10}$$

By use of the standard methods for evaluating elliptic integrals[17] one gets for the integral over φ:

$$[2/(a-b\cos\Phi)]K\{[(a'-b\cos\Phi)/(a-b\cos\Phi)]^{\frac{1}{2}}\}, \tag{III.11}$$

where $a\geq a'\geq b\geq 0$ are still functions of R, Q, r, ϑ.

Differentiating Eq. (III.11) with respect to $\cos\Phi$ yields[18]

$$[b/2^{\frac{1}{2}}(a-b\cos\Phi)^{\frac{1}{2}}]^{\frac{1}{2}}D\{[(a'-b\cos\Phi)/(a-b\cos\Phi)]^{\frac{1}{2}}\}\geq 0.$$

Therefore, we can restrict ourselves to the case $\Phi=0$, for which the integral $B(\mathbf{x},\mathbf{x}')$ can be evaluated simply by using polar coordinates with a polar axis along the common direction of the vectors $\mathbf{x}$ and $\mathbf{x}'$. The result is

$$B(\mathbf{x},\mathbf{x}')\leq\frac{1}{2}\left(\frac{Q}{R}\right)^{\frac{1}{2}}\left[\int_0^R drF(r)\log\left|\frac{r+(QR)^{\frac{1}{2}}}{r-(QR)^{\frac{1}{2}}}\right|+\int_Q^\infty drF(r)\log\left|\frac{r+(QR)^{\frac{1}{2}}}{r-(QR)^{\frac{1}{2}}}\right|+\log\frac{Q^{\frac{1}{2}}+R^{\frac{1}{2}}}{Q^{\frac{1}{2}}-R^{\frac{1}{2}}}\cdot\int_R^Q drF(r)\right], \tag{III.12}$$

where we assumed $Q\geq R$ which, for the estimate of B, is the less favorable case. Noting that the three logarithms are equal for $r=Q$, or $r=R$, we get the first estimate:

$$B(\mathbf{x},\mathbf{x}')\leq\tfrac{1}{2}(Q/R)^{\frac{1}{2}}\cdot M\cdot\log\{[(Q/R)^{\frac{1}{2}}+1]/[(Q/R)^{\frac{1}{2}}-1]\} \tag{III.13}$$

(where $M=\int_0^\infty drF(r)$) and, remembering the assumption $F(r)\leq M'/r$, a second estimate

$$B(\mathbf{x},\mathbf{x}')\leq\frac{1}{2}\left(\frac{Q}{R}\right)^{\frac{1}{2}}M'\int_0^\infty\frac{dr}{r}\log\left|\frac{r+(QR)^{\frac{1}{2}}}{r-(QR)^{\frac{1}{2}}}\right|=\frac{1}{2}\left(\frac{Q}{R}\right)^{\frac{1}{2}}M'\int_0^\infty\frac{dr}{r}\log\left|\frac{r+1}{r-1}\right|=\frac{\pi^2}{4}\left(\frac{Q}{R}\right)^{\frac{1}{2}}M'. \tag{III.14}$$

[17] A. B. Frank and C. D. Mises, *Differential und Integralgleichungender Physik* (1930), second edition, Vol. 1, p. 172. For the definitions of the complete elliptic integrals $K(k)$ and $D(k)$ see Jahnke-Emde, *Tables of Functions* (Dover Publications, New York, 1943), p. 73.

[18] Jahnke-Emde, reference 17, p. 76 and p. 73.

Therefore,

$$B(\mathbf{x},\mathbf{x}')\leq\frac{1}{2}\left(\frac{Q}{R}\right)^{\frac{1}{2}}\operatorname{Min}\left(M\log\frac{(Q/R)^{\frac{1}{2}}+1}{(Q/R)^{\frac{1}{2}}-1};\frac{\pi^2}{2}M'\right)\leq\frac{\pi^2}{4}M'\coth\frac{\pi^2}{4}\frac{M'}{M}=N. \tag{III.15}$$

and *a fortiori* Eq. (III.8).

The completion of the convergence proof now goes along standard lines. First we estimate the determinant of Eq. (III.6):

$$\left|\det_{1\leq i,k\leq n}\|K_2(\mathbf{x}_i,\mathbf{x}_k)\|\right|=\left|\det\|A(\mathbf{x}_i,\mathbf{x}_k)\|\cdot\frac{V(\mathbf{x}_1)}{4\pi|\mathbf{x}_1|}\frac{V(\mathbf{x}_2)}{4\pi|\mathbf{x}_2|}\cdots\frac{V(\mathbf{x}_n)}{4\pi|\mathbf{x}_n|}\right|.$$

By Hadamard's lemma[19] and Eq. (45) this is

$$\left|\det_{1\leq i,k\leq n}\|K_2(\mathbf{x}_i,\mathbf{x}_k)\|\right|\leqq N^n n^{n/2}\frac{F(|\mathbf{x}_1|)}{4\pi|\mathbf{x}_1|^2}\frac{F(|\mathbf{x}_2|)}{4\pi|\mathbf{x}_2|^2}\cdots\frac{F(|\mathbf{x}_n|)}{4\pi|\mathbf{x}_n|^2},$$

and because of Eq. (46)

$$\left|\int d\mathbf{x}_1\cdots\int d\mathbf{x}_n\,\det\|K_2(\mathbf{x}_i,\mathbf{x}_k)\|\right|\leq M^n N^n n^{n/2}, \tag{III.16}$$

which assures the convergence of Eq. (III.6) for any finite λ. To prove the convergence of

$$\int\Delta_2(\lambda^2,\mathbf{x},\mathbf{x}')F_0(\mathbf{k},\mathbf{x}')d\mathbf{x}', \tag{III.17}$$

we first note that

$$|F_0(\mathbf{k},\mathbf{x})|\leq 1+\frac{|\lambda|}{4\pi}\int d\mathbf{x}'\left|\frac{V(\mathbf{x}')}{\mathbf{x}-\mathbf{x}'}\right|\leq 1+\frac{|\lambda|}{4\pi}\int d\mathbf{x}'\frac{F(|\mathbf{x}'|)}{|\mathbf{x}'||\mathbf{x}-\mathbf{x}'|}\leqq 1+|\lambda|M$$

and therefore the determinant in Eq. (III.5) is less than

$$M^{n+1}N^{n+1}n^{\frac{1}{2}(n+1)}(1+|\lambda|M),$$

which makes Eq. (III.17) convergent for any finite λ.

The representation (III.2–6) of the solution for the scattering integral equation (2) has the disadvantage that the denominator $\Delta_2(\lambda^2)$ of the resolvent $H_2(\lambda^2;\mathbf{x},\mathbf{x}')$ vanishes for $\pm\lambda_i$, where λ_i are the eigenvalues of the original integral equation. It is therefore possible to factor an entire function in the numerator and denominator of Eq. (III.4). This fact was proved in general by H. Poincaré.[20]

Since we know the convergence of our series, we can immediately use his results, which lead to the prescriptions of Sec. IV, Eqs. (49), (50), where numerator and denominator have no zero's in common.

(IV) The Fredholm Method for the Yukawa Potential

In this section we calculate the integrals D_1 and D_2 given by Eqs. (58), (59). D_1 is easily found by using the configuration space representation in which

$$D_1=(1/16\pi^2)\int d\mathbf{x}d\mathbf{y}\,\exp(2ik|\mathbf{x}-\mathbf{y}|)\,\exp(-x-y)/(|\mathbf{x}-\mathbf{y}|^2xy).$$

This integral is elementary, and its outcome is given in Eq. (60). D_2 is treated by introducing again auxiliary integrations over variables $x_i\geq 0$, $i=1,\cdots,4$:

$$D_2=\frac{3!}{4\pi^4}\int d\mathbf{p}d\mathbf{q}\int dx_i\frac{\delta(x_1+x_2+x_3+x_4-1)}{[x_1(p^2-\eta)+x_2(q^2-\eta)+x_3\{(\mathbf{p}-\mathbf{q})^2+1\}+x_4\{(\mathbf{p}+\mathbf{q})^2+1\}-i\epsilon(x_1+x_2)]^4}.$$

The expression in square brackets can be written as the sum of a symmetrical quadratic expression $\Sigma a_{ik}y_iy_k$, where $(y_1,y_2,y_3)=\mathbf{p}$ and $(y_4,y_5,y_6)=\mathbf{q}$, and a constant term. We transform the six dimensional quadratic expression on principal axes:

$$\Sigma a_{ik}y_iy_k=\Sigma\lambda_iP_i^2.$$

One easily sees that

$$\Pi_i\lambda_i=d^2=[(x_1+x_3+x_4)(x_2+x_3+x_4)-(x_3-x_4)^2]^2.$$

Introducing $\lambda_i^{\frac{1}{2}}P_i$ as new variables and putting $\Sigma P_i^2=P^2$ we get

$$D_2=(3!O_6/4\pi^4)\int dx_i\frac{\delta(\Sigma x_i-1)}{d^{\frac{1}{2}}}\int\frac{P^5dP}{(P^2+A)^4},$$

where $O_6=\pi^3$ is the surface of a 6-dimensional unit sphere and

$$A=x_3+x_4-\eta(x_1+x_2)-i\epsilon(x_1+x_2).$$

Hence,

$$D_2=(1/4\pi)\int dx_i\delta(\Sigma x_i-1)d^{-\frac{1}{2}}A^{-1}.$$

We introduce

$$\begin{aligned}x_1+x_2&=x,\quad x_3+x_4=v_1,\quad -x\leq y\leq x,\\ x_1-x_2&=y,\quad x_3-x_4=v_2,\quad -v_1\leq v_2\leq v_1.\end{aligned}$$

One can then integrate over v_2 and thereupon over v_1, noting that the argument of the δ-function now reads $x+v_1-1$. The result is

$$\begin{aligned}D_2&=\frac{1}{\pi}\int_0^1\frac{dx(1-x)}{(2-x)\{1-(\eta+1)x-i\epsilon x\}}\int_{-x}^{x}\frac{dy}{(2-x+y)(4x-3x^2-y^2)^{\frac{1}{2}}}\\&=\frac{1}{\pi}\int_0^1\frac{dx}{(2-x)\{1-(\eta+1)x-i\epsilon x\}}\tan^{-1}\left[\frac{(x-x^2)^{\frac{1}{2}}}{2-x}\right]\\&=-\frac{i(\eta+1)}{2\eta+1}\tan^{-1}\frac{\eta^{\frac{1}{2}}}{2\eta+1}+\frac{1}{\pi}\mathrm{P}\int_0^1\frac{dx}{\{1-(\eta+1)x\}(2-x)}\tan^{-1}\left[\frac{(x-x^2)^{\frac{1}{2}}}{2-x}\right],\end{aligned}$$

[19] See reference 11, p. 212.
[20] H. Poincaré, reference 12.

where P indicates that the principal value has to be taken with respect to the point $x=(\eta+1)^{-1}$. It is readily seen that the principal value integral can be written as

$$-(i/4\pi)\oint \frac{dx}{\{1-(\eta+1)x\}\{2-x\}} \ln\frac{2-x+i(x-x^2)^{\frac{1}{2}}}{2-x-i(x-x^2)^{\frac{1}{2}}} \quad \text{(IV.1)}$$

taken along the contour I of Fig. 2 which encircles the branch points $x=0, 1$ of $(x-x^2)$ in the negative sense (the plane is cut along the segment $0\leq x\leq 1$). The contributions of the two infinitesimal semi-circles near $x=(\eta+1)^{-1}$ cancel each other; indeed, the value of the logarithm in any given point of the path above the cut is equal and opposite in sign in the corresponding point below it.

We next deform I to the contour II, coming from $x=\infty$, encircling the pole of the integrand at $x=2$ and the branch point of the logarithm at $x=4/3$ in the negative sense, and then returning to ∞. The plane is cut along that part of the real axis for which $x\geq 4/3$. Care has to be exercised in continuing $(x-x^2)^{\frac{1}{2}}$ to points on path II as well as in choosing the branch of the logarithm on the upper and lower half of this contour. The contributions near the pole $x=2$ cancel again and the final result is

$$D_3=-(1/2\eta+1)\{\tfrac{1}{2}\ln[2(\eta+1)/(4\eta+1)]+i\tan^{-1}(\eta^{\frac{1}{2}}/(2\eta+1))\},$$

which was used in Eq. (61).

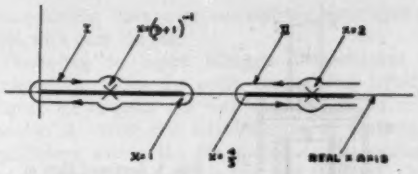

FIG. 2. Deformation of the integration path of the integral (IV.1).

PHYSICAL REVIEW VOLUME 82, NUMBER 6 JUNE 15, 1951

Transport Rates of the Helium II Film Over Various Surfaces*

JAY GREGORY DASH†‡ AND HENRY A. BOORSE§
Columbia University, New York, New York

(Received March 2, 1951)

Liquid helium II film transport over various surfaces has been studied by a new method in which a cylindrical capacitor using liquid helium as the dielectric is employed as a depth gauge. Changes in liquid level resulting from film transport produce changes in capacitance which in turn cause frequency changes in a high frequency circuit. The details of this method are described. The film transport rates, measured to 1.25°K, were found to depend on the substrate; at 1.25°K, the highest rate observed was 51×10^{-8} cm³/cm sec for etched copper and the lowest, 7.5×10^{-8} cm³/cm sec for glass. The rates were also measured over iron in the magnetized and unmagnetized state and over a superconductor in the superconducting and in the normal state. No differences were noted. In the latter case the thermal conductivity of the container is abruptly changed and the absence of an effect supports the view that heat transfer plays no significant role in determining the transport rate.

INTRODUCTION

SINCE the discovery[1] of the film transport phenomenon of liquid helium II, various investigations have been made to determine the characteristics of the transport. Among the phenomena studied was the effect of the underlying surface material.[2] These studies indicated that the transport rate is independent of surface material. However, a recent examination of this property by Mendelssohn and White[3,4] and the present authors[5,6] has shown that this is not the case.

Theories of the HeII film have been advanced by Frenkel,[7] Schiff,[8] Temperley,[9] and Bijl, de Boer, and Michels.[10] The first two authors have considered helium atoms to be under the influence of gravity and of the van der waals attractive forces of the walls. This treatment indicates that film thicknesses on conducting surfaces are greater, by about a factor of two, than films on dielectrics. Film flow, according to Frenkel, should be limited by viscosity. For the case of HeII, the theoretical result becomes ambiguous owing to the presence of a zero viscosity, or superfluid component. Temperley has treated the film as an adsorbed phase in which He atoms occupy bound sites on the surface of the solid walls. The adsorbed layers farthest from the wall are assumed to occupy only a fraction of the available sites, and film flow is considered to arise from a transition of atoms from their existing sites to empty neighbors. The influence of the wall is considerably

* Assisted in part by the ONR.
† Submitted in partial fulfillment of the requirements for the degree of Doctor of Philosophy at Columbia University.
‡ Research completed under an AEC Predoctoral Fellowship. Present address: Los Alamos Scientific Laboratory, Los Alamos, New Mexico.
§ Barnard College, Columbia University, New York, New York.
[1] B. V. Rollin and F. Simon, Physica **6**, 219 (1939).
[2] J. G. Daunt and K. Mendelssohn, Proc. Roy. Soc. (London) **A170**, 423, 439 (1939).
[3] K. Mendelssohn and G. K. White, Nature **166**, 27 (1950).
[4] K. Mendelssohn and G. K. White, Proc. Phys. Soc. (London) **A63**, 1328 (1950).
[5] H. A. Boorse and J. G. Dash, Phys. Rev. **79**, 734 (1950).
[6] H. A. Boorse and J. G. Dash, Phys. Rev. **79**, 1008 (1950).
[7] J. Frenkel, J. Phys. U. S. S. R. **II**, No. 5, 365 (1940).
[8] L. I. Schiff, Phys. Rev. **59**, 839 (1941).
[9] H. N. V. Temperley, Proc. Roy. Soc. (London) **A198**, 438 (1948).
[10] Bijl, de Boer, and Michels, Physica **8**, 655 (1941).

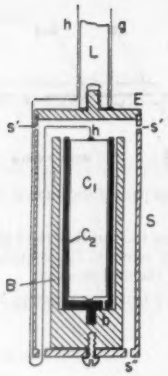

FIG. 1. Sectional view of container, depth gauge, and radiation shield assembly.

smaller for these layers than the influence of the underlying He layers, and film flow rates should be essentially the same for all wall materials. Bijl, de Boer, and Michels limit the film thickness by means of the de Broglie wavelength of the superfluid particles, thus implying that film thickness and transport rate are independent of surface material. Finally, it may be mentioned that no attempt has been made to account for the fact that the film flow is directed toward a region of lower gravitational potential.

The unsatisfactory predictions of, and the general disagreements between the proposed explanations of the HeII film, together with the paucity of observations of rates on surfaces other than glass, have led the authors to undertake a new study of the transport phenomenon.

EXPERIMENTAL METHOD

Measurement of the film transport through direct visual observation of the rise or fall of the liquid helium surface in the transport vessel was considered to hold two disadvantages for this research. First, while the optical method is straightforward for transparent containers, it is not as convenient for measuring rates over opaque materials. Second, possible disturbing effects of thermal radiation incident upon the film could not be entirely eliminated in this method. For these reasons, it was decided to abandon the direct viewing procedure and to develop a more favorable technique.

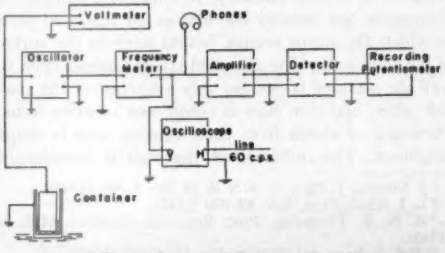

FIG. 2. Block diagram of the measuring circuits.

The use of liquid HeII as the dielectric in a suitably constructed capacitor appeared to offer a simple and convenient method for measuring film transport. Experiment showed that as the liquid flowed from the capacitor, the resulting change in capacitance could easily be determined with the aid of a high frequency circuit. The fact that the electric polarization of HeII is almost independent of the temperature[11,12] and that its dielectric loss is very small[12] gave added assurance of the suitability of this method.

The capacitor design is given in Fig. 1. The container B, which provides the surface for film creep to or from the surrounding bath, was constructed of the material over whose surface the transport rate was desired. The varying level of liquid HeII within B was indicated by the varying capacitance of the cylindrical capacitor C_1-C_2, the hole b permitting equilibrium between the two levels. C_1 was centered within C_2 by four longitudinal strips of Teflon sheet. The mean annular separation between the walls of the capacitor was 0.0050 ± 0.0001 inch, the capacitor being centered within the container by means of the threaded post. C_1-C_2 therefore served as a depth gauge for the liquid in B and operated for transport rate measurements over conducting and nonconducting surfaces. Typical dimensions for the container B were $\frac{3}{8}$ in. inner diameter, and 1.7 in. over-all length.

The container and depth gauge assembly were mounted within a copper radiation shield S. The copper cap E soldered to S provided additional radiation shielding and was connected to a raising and lowering device by means of the Lucite rod L. During transport rate measurements, the lower part of the shield was immersed in the bath, hence any possible temperature gradients between the container and the bath were minimized. As a further precaution in this direction, holes s' and s'' were pierced in the shield to allow He liquid and vapor to pass between the surrounding bath and the container assembly.

The inner cylinder C_1 of the capacitor was electrically connected to the external measuring apparatus by the fine copper wire h. C_2 was grounded outside the cryostat by means of the direct contact between C_2 and S, and the copper wire g.

The circuit for the measurement of the capacitance changes is given by the block diagram in Fig. 2. The cylindrical capacitor is connected in parallel with the tuned circuit of a radiofrequency oscillator of high stability.[13] A voltmeter provides a continuous reading of the tuned circuit excitation which is set by a bias control. Bias may be set in excess of cut-off value to stop oscillation by opening the cathode-to-ground connection. An amplifying and buffering stage feeds the oscillator signal to a General Radio Company hetero-

[11] M. Wolfke and W. H. Keesom, Physica **3**, 823 (1936).
[12] C. J. Grebenkemper and J. P. Hagen, Phys. Rev. **80**, 89 (1950).
[13] J. K. Clapp, Proc. Inst. Radio Engrs. **36**, 356 (1948).

dyne frequency meter, where the note is beat against one of nearly the same frequency. The beat note is observed on an oscilloscope and fed to an audio amplifier. This amplified signal is connected to a simple frequency discriminator consisting of a large resistance in series with an air core inductance. The voltage across the inductance, proportional to frequency, is rectified, filtered, and supplied to a Brown recording potentiometer. It is thus possible to obtain an instantaneous and continuous record of the liquid level in the capacitor. The frequency dependence of the potentiometer circuits is obtained by calibrating the recording potentiometer response by means of the harmonics of line frequency as seen on the oscilloscope. Alternatively, depth measurements can be made by reading the vernier scale of the frequency meter, with the beat frequency set to zero on the oscilloscope.

The fractional frequency change of the oscillator from the completely full to the completely empty condition of the capacitor was approximately 1 percent of the mean frequency. The frequency instability of the oscillator and heterodyne frequency meter was approximately 60 cps per hour at 100 kilocycles. Under the various experimental conditions, emptying times ranged between extremes of about two and thirty minutes. The over-all reproducibility of the observations is estimated at about 5 percent.

CRYOSTAT DESIGN

The mechanical mounting of the depth gauge and container assembly within the cryostat is shown in Fig. 3. The inner He Dewar is of Pyrex glass completely silvered except for a half-inch clear vertical stripe. Copper-glass seals J_1 and J_2 provide vacuum tight joints between the Dewar and its top cap, and a pump line, respectively.

Liquid He was introduced through the filling tube F, and was subsequently cooled by pumping through the tube P. He bath temperatures were determined by a vapor pressure thermometer, consisting of mercury manometers attached to the low conductivity tube V, which ended below the surface of the liquid.

A vacuum tight winch W was used to raise and lower the container assembly. Wires h and g were brought out of the cryostat through the seals K. Several Pyrex glass containers M, attached to the supporting rod L, were used to check transport rates over glass by the visual method.

EXPERIMENTAL DETAILS

Bowers and Mendelssohn[14] have demonstrated that films of solid air deposited on container surfaces lead to He transport rates considerably higher than those obtained with clean surfaces. Accordingly, precautions were taken to avoid this contamination. Before filling the inner Dewar with liquid helium, the liquid space and pumping lines were successively evacuated and filled with pure He gas.

Precooling to liquid nitrogen temperatures was achieved by filling the outer Dewar with liquid nitrogen; He transfer gas was then introduced to the annulus A. After the establishment of temperature equilibrium within the He space, A was evacuated and a thermal isolation vacuum was obtained. Liquid He was then transferred into the cryostat.

Vapor pressures of the liquid He were determined by a 12-mm bore mercury manometer and a calibrated Dubrovin scale-of-nine vacuum gauge. Vapor pressures were maintained constant to 0.1 mm by a manostat-controlled[15] solenoid valve located in the pumping line. Heat influx to the He bath, measured by the rate of descent of the liquid level, was approximately 50 cal/hr, and a single filling of liquid sufficed for seven hours' experimentation.

Calibration of the depth gauge with changes in depth of the liquid He in the container was carried out in the following manner. The container was lowered into the bath until fully immersed, and the bath maintained at a constant temperature below the lambda-point. Oscillator frequency readings and cathetometer observations of the bath level were taken simultaneously, as normal evaporation caused the height of liquid in the He Dewar to fall. The rate of decline of the bath level at the calibrating temperatures was considerably smaller than the rate of fall of liquid level in the container arising from film transport. This condition assured that the levels of the liquid in the bath and in the container dropped at the same rate. The calibration procedure therefore gave an over-all measure of depth gauge "sensitivity" in frequency meter scale divisions per centimeter change in liquid level. The most frequently used depth gauge had a sensitivity of 4.10 $\pm$0.06 divs./cm. A sample calibration is given in Fig. 4.

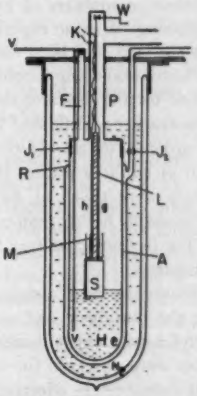

FIG. 3. Sectional view of the helium cryostat.

[14] R. Bowers and K. Mendelssohn, Proc. Phys. Soc. (London) A63, 1318 (1950).

[15] J. J. Beaver and D. J. Beaver, J. Ind. Eng. Chem. 15, 359 (1923).

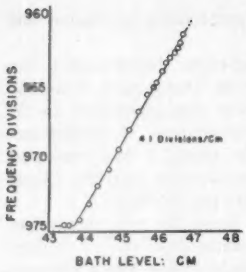

FIG. 4. Typical depth gauge calibration curve.

To verify that the rf field within the capacitor had no effect on the transport rate, the oscillator signal was interrupted for a short time during the course of the transport. The result of such a check is shown in Fig. 5. No indication of rf disturbance was found in any of the many checks which were made.

Optical determinations of transport rate over the auxiliary containers of Pyrex glass were made at the beginning of each experiment to determine whether the surfaces had been contaminated with solid air. If contamination had occurred, measurements were abandoned for the day and the apparatus warmed to room temperature and flushed thoroughly with pure He gas. In order to detect the possible progressive contamination of surfaces during the course of a run, measurements were taken at successively lower and then at successively higher temperatures. Transport rates taken at the beginning and at the end of the run were then compared.

Flow rates were obtained both for filling and emptying the containers and were compared in order to correct for evaporation losses. No significant differences in rates were observed for these two conditions. This result indicated the effectiveness of the radiation shield.

RESULTS

The dependence of transport rate on the position of the liquid level below the container rim was found to correspond qualitatively with the results of other investigators.[3,4,16] The emptying curve in Fig. 6 shows this initial rate as varying while the liquid level is near the lip of the container, and a constant rate thereafter. Transport rates plotted in the figures correspond to the constant rates determined from the straight portions of the curves.

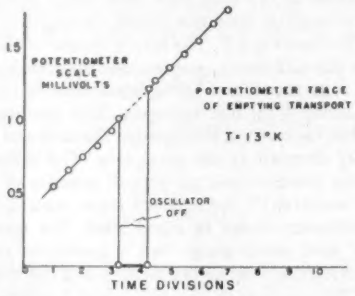

FIG. 5. Effect of capacitor excitation on transport rate.

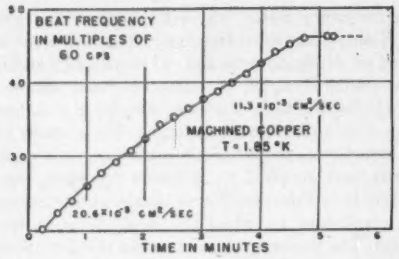

FIG. 6. Typical emptying curve for a machined copper container.

COPPER

Initial measurements with a carefully machined copper vessel yielded a maximum film transport rate approximately twice that previously published for glass. To verify this result, a number of measurements were made with containers of varying dimensions, the annular liquid spaces ranging from 0.005 in. to 0.090 in. Within the experimental error, the containers all gave the same value; results of a typical run are shown in Fig. 7. As a check on these measurements, the transport at 1.3° from a Pyrex glass container was studied by the depth gauge technique. The result was identical with that of Daunt and Mendelssohn.[2]

A machined copper container that had yielded transport rates as shown in Fig. 7 was etched for two minutes in 0.1 N nitric acid and then reinstalled in the cryostat. This container gave the high rates shown in Fig. 8. Owing to an insufficient amount of liquid He in the bath during this experiment, only three rate determinations could be made at temperatures below 1.89°.

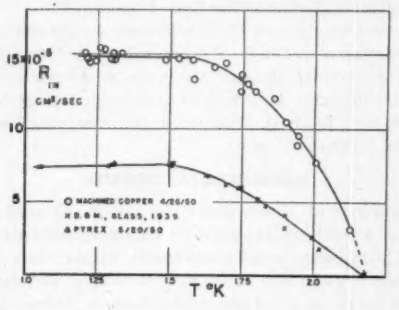

FIG. 7. HeII film transport rates over machined copper (typical curve).

[16] Webber, Fairbank, and Lane, Phys. Rev. **76**, 609 (1949).

The shape of the curve cannot therefore be determined with the same certainty as the other two in this figure; nevertheless, it appears that all three are similar in showing an increasing rate at the lowest temperatures reached.

Microscopic examination of this etched surface indicated considerable surface roughness, and this may contribute to the high transport rate. Attempts were made to determine the increase in perimeter by photographing the container edges under high magnification, but the results were not considered reliable for comparison purposes.

The etched container was then allowed to oxidize in air for two days at room temperature. The result of this treatment, also given in Fig. 8, shows a large decrease in rate, together with some change in temperature dependence.

In order to observe additional effects of copper surface preparation, measurements were made on a burnished copper container. The effect of burnishing, i.e., the production of an amorphous surface layer by high

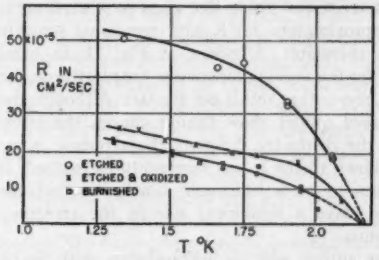

FIG. 8. HeII film transport rates over variously treated copper surfaces.

local temperature and pressure during polishing, is seen from Fig. 8 to reduce the rate still further but to produce a temperature dependence similar to the etched and oxidized material.

STAINLESS STEEL

The results of a single run on machined 18–8 stainless steel are presented in Fig. 9. The structure of this curve resembles the results for burnished copper, there being a continued increase in rate with decline in temperature.

LUCITE

It was considered desirable to determine the transport rate over the surface of a dielectric other than glass; owing to its machinability, Lucite was chosen. The container surfaces were polished with rouge after machining. This vessel showed the unusual temperature dependence exhibited in Fig. 9. Numbers alongside the experimental points refer to the chronological order in which the data were taken; it thus appears that the peak at 1.5° was reproduced. The singular nature of

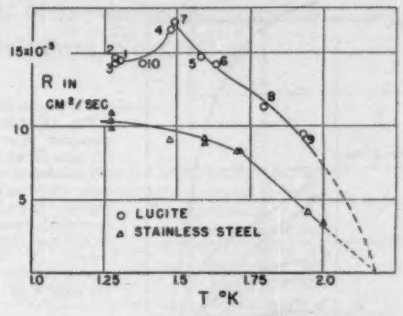

FIG. 9. HeII film transport rates over Lucite and stainless steel.

the curve is noteworthy. The results, however, are submitted as tentative, pending further investigation.

LEAD AND IRON

An exploratory investigation was made of the possible effects of ferromagnetic and superconducting substrates on the transport rate using, respectively, cold-rolled steel and lead vessels. The data for these two materials are given in Fig. 10.

If a transfer of heat plays a part in determining the transport rate, it might be expected that an abrupt change in the thermal conductivity of the container material would disclose this effect. It is rather striking to realize that such an abrupt change can be brought about by applying a magnetic field of sufficient strength to a superconductor, the thermal conductivity in the superconducting state being usually much smaller than in the normal state at the same temperature. Lead, for instance, at 2°K shows conductivities[17] differing by 900 percent.

A lead container was therefore constructed and measurements of the transport rate were made with the metal in the superconducting and in the normal state; as Fig. 10 shows, no appreciable difference in the rate was observed. It should be remarked, however,

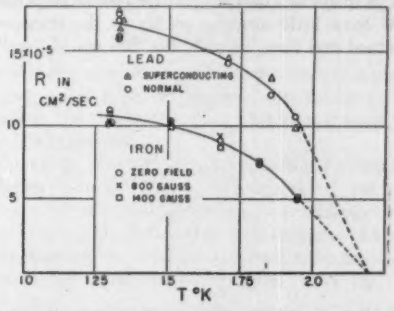

FIG. 10. HeII film transport rates over lead and iron.

[17] W. J. de Haas and A. Rademakers, Physica 7, 992 (1940).

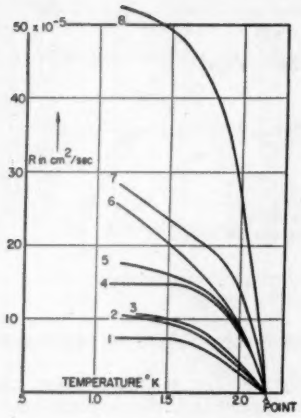

FIG. 11. HeII film transport rates for: (1) glass (D and M), (2) stainless steel, (3) iron, (4) machined copper, (5) lead, (6) burnished copper, (7) etched and oxidized copper, (8) etched copper (all drawn to the same scale).

that the experiment was carried out after a dark oxide layer had formed on the surface of the material. Although it seems unlikely that this circumstance should have completely masked an effect if it were present, further investigation is planned.

Measurements of the transport rate over a magnetized and unmagnetized ferromagnetic surface were made using cold-rolled steel. Although the fields applied in this case (up to 1400 oersteds) were not sufficient to produce saturation, here again the absence of any perceptible effect makes it seem unlikely that any effect exists.

DISCUSSION OF RESULTS

All experiments on the transport of the He film have led to the conclusion that other conditions being the same, the transfer of liquid from a container to the bath is limited by the narrowest part of the containing surface located above the upper liquid level. Under the conditions prevailing in these experiments, this narrowest part is the inner perimeter of the transfer vessel *B* of Fig. 1. Since the film is of the order of 10^{-6} cm thick, it might be expected that the geometric perimeter would have little meaning as far as the transport is concerned and that, instead, the film would "see" the microscopic perimeter and its flow would be adjusted accordingly.

If this were true, it would appear reasonable to expect that a given glass vessel would not maintain its rate with age or with extreme temperature cycling over a period of months; microscopic surface cracks could increase in depth or in number or both; alternatively, it might be argued that a microscopic deposit from whatever source would in time tend to reduce the surface roughness. In any event such changes would be apparent as an altered transport rate. It appears, however, that no effect of this kind has ever been found. This suggests that the microscopic perimeter is not the effective perimeter for transport, a view that is supported by the agreement of the transport rates obtained from the various machined copper containers (Fig. 7).

An extension of this argument against the effectiveness of the microscopic perimeter may be made by noting that if the transport were a function of the temperature and the microscopic perimeter and nothing else, then *all* substances should show rates which, while differing from each other, should exhibit the common characteristic of rising like glass to a maximum value at approximately 1.5°K and remaining sensibly constant thereafter. A glance at Fig. 11, in which the rates for the various substances are plotted on the same scale, shows that this is not the fact. Although glass and *machined* copper show similar curves, the others display the distinctly different characteristic of a rising rate down to the lowest temperatures reached. It thus appears to be a legitimate conclusion that the substrate plays a significant role in the transport phenomenon.

The author wish to acknowledge, with thanks, assistance from the Research Corporation and the Linde Air Products Company. They are also indebted to Messrs. Albert Brown, Sheldon Datz, Leonard Lesensky, and Bernard Smith for assistance during the course of the investigation. Mr. Joseph Leon of Professor T. I. Taylor's laboratory in the Department of Chemistry, Columbia University, assisted with the microscopic examination of the copper surfaces; finally, it is a pleasure to thank Dr. Donald B. Cook and Professor Mark W. Zemansky for their active interest and fruitful suggestions.

Cosmic Radiation and Cosmic Magnetic Fields. I. Origin and Propagation of Cosmic Rays in our Galaxy

A. UNSÖLD
Institut für theoretische Physik und Sternwarte, Kiel, Germany
(Received October 11, 1950)

The radiofrequency radiation of the galaxy is shown to be analogous not to the "quiet" but to the "disturbed" radiation of the sun (produced by plasma oscillations). Many arguments point toward its origin on stars with an "activity" qualitatively similar to that of the sun but several billion times stronger. It is assumed that in these stars the relation between radiofrequency radiation and the emission of cosmic rays is similar to that observed for the sun by Forbush and Ehmert. In the magnetic field of the galaxy this primary cosmic radiation is "stored" by a factor 10^3 to 10^4, each particle describing a complicated path until it is killed by a nuclear collision, and directional isotropy established. The cutoff of the energy spectrum at small energies, hitherto mostly ascribed to a solar magnetic dipole, is attributed to the stopping power of interstellar matter. Some other theories concerning the origin of cosmic rays are reviewed critically.

I. INTRODUCTION

THE old problem of the origin of cosmic rays has acquired a new aspect through the discovery of quite a different radiation coming from the universe, the radiofrequency radiation discovered by Jansky in 1932. Recently, it has been proved that the sun emits "bursts" of both types of radiation in connection with violent solar "flares" (bright H_α eruptions). Even if we do not yet understand in every detail how the production of solar radiofrequency and cosmic-ray bursts on the sun is accomplished, it is very tempting to assume that the corresponding cosmic radiations are generated in a similar way on stars of our galaxy.

This hypothesis has hitherto met with many objections and in fact has mostly not even received serious consideration. We intend, however, to demonstrate that all these objections are unfounded and that, on the contrary, our idea has very interesting astrophysical consequences which are corroborated by extensive observational material.

II. SOLAR AND GALACTIC RADIOFREQUENCY RADIATION[1]

A

It is well known that the sun emits two kinds of radiofrequency radiations:

(a) The *"quiet" solar radiation*, which can be explained by free-free transitions of electrons in the solar corona ($T \approx 10^6$ °K) and the chromosphere ($T \approx 6000$°K). For quantitative details we may refer to earlier publications.

(b) The *"disturbed" solar radiation* whose intensity may, at times of violent "solar activity," especially during solar flares, surpass by many powers of ten that of the "quiet" radiation always present. Recent theoretical studies by various authors point towards an explanation in terms of plasma oscillations excited by turbulent streams of ionized gases penetrating into each other with high velocities.

Denoting the order of magnitude of these velocities by v_s, it is evident that coherent oscillations with frequency ν producing radiation with a wavelength $\lambda = c/\nu$ can be excited only over domains whose size D is

$$D < \lambda v_s/2\pi c. \tag{1}$$

On the other hand, "plasma" oscillations are only possible if an electron, whose velocity is v_s, cannot leave the domain during unit phase change. That is,

$$D > v_s/2\pi\nu. \tag{2}$$

The conditions (1) and (2) are only compatible, if $v_s \gtrsim v_s$. In a magnetic field, however, the path of an electron is coiled up, and condition (2) may lose considerably in importance, so that excitation of plasma oscillations becomes possible also for $v_s < v_s$.

Putting*

$$v_s \approx v_s = \left(\frac{8}{\pi}\cdot\frac{kT}{m}\right)^{\frac{1}{2}}, \tag{3}$$

where T is the temperature, k and m have the usual meaning, and, following Langmuir,

$$(2\pi\nu)^2 = 4\pi e^2 N/m, \tag{4}$$

where N is the number of electrons per cm³; it is easily seen that, apart from the unimportant factor $(8/\pi)^{\frac{1}{2}} = 1.6$, D is the "Debye length" well known from the theory of electrolytes.

For $\lambda = 3$ m, $T = 10^6$ °K, and $v_s \approx 6000$ km/sec, an "oscillating domain" has a diameter $D \approx 1$ cm and contains $\sim 10^8$ electrons performing synchronous oscillations. It is easily verified that such domains can well account even for the strongest observed radio emissions (On the other hand, for wavelengths <0.1 cm, the

[1] For detailed references see the following recent reports: M. E. Stahr, Radio Astronomy Report No. 2, 4, and 10 (Cornell University, Ithaca, New York, 1948, 1950); J. S. Hey, Monthly Notices Roy. Astron. Soc. **109**, 179 (1949); G. Reber and J. L. Greenstein, Observatory **67**, 15 (1947); A. Unsöld, Naturwiss. **34**, 194 (1947) and Z. Astrophys. **26**, 176 (1949).

* The velocity of sound waves propagated mainly by the electrons is also $\sim v_s$; that of the particles exciting auroras and magnetic storms is only about one-fourth the size.

number of electrons in an oscillating domain becomes so small, according to Eqs. (1) and (4), that only a weak "disturbed" radiation can be emitted.) Self-absorption plays no appreciable role, because the plasma does not contain "preformed" D-domains. Since, without magnetic field, every electron stays during only about one oscillation within a domain, its emission should exhibit a bandwidth $\Delta\nu$ of the order of the frequency ν itself. The damping constant of the emission, as various authors have noted,[2,3] should be determined by the number of collisions per sec (e.g. ~ 1 sec^{-1} in the solar corona).

Apart from consideration of theoretical details we emphasize that the "quiet" solar radiation is emitted thermally, i.e., in accordance with Kirchhoff's law, while the "disturbed" radiation is typically nonthermal.

B

The *galactic radiofrequency radiation* has, following Henyey and Keenan,[4] been interpreted mostly (in analogy with the "quiet" solar radiation) as free-free radiation of the interstellar gas. At first this hypothesis seemed quite consistent with the observations, even quantitatively. Recently, however, better observations in connection with a more detailed theoretical analysis have shown that the interstellar hypothesis can explain only a small fraction of the galactic radiation, the major part being produced in analogy with the "disturbed" solar radiation.[2,5]

Let us consider the main arguments for this thesis:

(a) *Intensity of galactic radiation in the 10 to 15 m range.* Since the intensity of thermal radiation must always be inferior to that of a blackbody having the temperature of the emitting gas, we can use absolute intensity measurements for deriving a lower limit for the electron temperature of the interstellar gas, assuming that the latter emits the radiation. Following this idea Townes and Unsöld independently arrived at temperatures higher than 100,000°K. Such excessive temperatures, however, are incompatible with our astrophysical knowledge of the interstellar gas. Even in planetary nebulae whose central stars do have temperatures of more than 100,000°, the electron temperature reaches only 6000 to 10,000°, since the fast photoelectrons lose their energy by collisions with oxygen ions.

(b) *Intensity of interstellar H_α radiation.* If the galactic radiofrequency radiation were mostly due to free-free transitions in the interstellar hydrogen gas (other elements being considerably less abundant), it should be accompanied by H_α recombination-radiation whose relative intensity can easily be computed and proves to be almost independent of the assumed temperature. The result of such calculations which were made by Unsöld and later, but independently, by Lambrecht[6] is that the observed radiofrequency radiation of the galaxy is too strong in comparison with the intensity of the H_α radiation measured by Struve and Elvey.

(c) *Spectral intensity distribution of the galactic radiation.* For the quasithermal emission of the interstellar gas by free-free transitions, theory leads us to expect a spectral intensity distribution $I_\nu \approx$ const. for optically thin layers, while optically thick layers should give blackbody radiation with $I_\nu \sim \nu^2$.

Observations (see reference 2) over the frequency range from 25 to 200 Mc/sec indicate that on the average $I_\nu \sim \nu^{-0.4}$, in definite disagreement with the above predictions but in good agreement with measurements of the disturbed solar radiation, whose I_ν also decreases mostly toward higher frequencies. Solar observations by Ryle and Vonberg for 80 and 175 Mc/sec give on the average $I_\nu \sim \nu^{-0.05}$ and for violent disturbances exponents up to -1.5 (the "quiet" solar radiation in the same frequency range corresponding to $I_\nu \sim \nu^{+0.92}$).

(d) *Cosmic centers of radiofrequency radiation.* We need hardly emphasize that the high intensity of the radiating centers discovered by Hey and others certainly cannot be explained on a quasithermal basis.[7] It must be due to some sort of plasma oscillations. Recent observations by Bolton, Stanley, and Slee[8] seem to identify some discrete sources of radiofrequency radiation with known nebulae (one being the Crab nebula produced by a supernova which exploded A.D. 1054). However, even if other discrete sources should be identified with similar astronomical objects, it does not seem possible to ascribe the general galactic radiofrequency radiation to plasma oscillations of the interstellar medium:

1. The Langmuir frequency of the interstellar gas, 9 kc/sec for 1 electron/cm^3, is far below the "astronomical" frequency range.

2. The concentration of galactic radiofrequency radiation in galactic longitude towards the galactic center $l = 325°$ is considerably stronger, and that in galactic latitude much less, than might be expected if it originated from the interstellar medium, which is known to exhibit little concentration in longitude but a strong concentration towards the galactic plane.

(e) *Stellar origin of the galactic radiofrequency radiation.* All the evidence discussed so far points toward the idea that the galactic radiofrequency radiation originates like the disturbed solar radiation in "active" stellar atmospheres, where plasma oscillations are

[2] A. Unsöld, Z. Astrophys. **26**, 176 (1949) (concerning literature see this paper).
[3] J. C. Jaeger and K. C. Westfold, Austr. J. Research (A) **2**, 322 (1950).
[4] L. G. Henyey and P. C. Keenan, Astrophys. J. **91**, 625 (1940).
[5] A. Unsöld, Nature **163**, 489 (1949).
[6] H. Lambrecht, Astr. Nachr. **277**, 223 (1949).
[7] The "variability" of these centers has recently been proved by Smith, Little, and Lovell [Nature **165**, 422 (1950)] to be mainly by ioniospheric origin. The sizes and velocities of the required "ionospheric striae" agree quite well with those of the "luminous night clouds" observed by Jesse, Störmer, Publ. Oslo Univ. Observ. **1**, No. 6 (1933); Astrophys. Norv. **1**, 87 (1934); and others.
[8] Bolton, Stanley, and Slee, Nature **164**, 101 (1949).

excited by turbulence, sometimes perhaps in conjunction with magnetic fields.

This hypothesis, however, has usually met with one weighty objection: the ratio of the average radiofrequency radiation at 64 Mc/sec to the visual radiation is $\sim 2\times 10^9$ times higher for the galaxy than it is for the sun.

We propose[2,5] to interpret this ratio as indicating that our sun is only a very poor radiofrequency transmitter and that other stars show an "activity" qualitatively like our sun, but quantitatively several billion times stronger.

Even so, the total energy radiated by the stars in the range of radiofrequencies is still a minute fraction of their total light and heat radiation.

An increase of the ratio of radio to visual radiation by a factor $\sim 10^9$ to 10^{11} compared with the average sun can be understood without difficulty, considering the tremendous increase of the solar radiofrequency radiation observed during solar flares. On July 25, 1946, Lovell and Banwell observed at 72 Mc/sec the solar radiation (compared with the quiet one) increasing by a factor $\sim 5\times 10^5$ during a flare whose total area was only 1/800 of the visible hemisphere while the actually radiating part probably was still smaller. Moreover, it should be remembered that for cool stars the visual radiation per unit surface is much smaller than for the sun; for M stars by a factor ~ 90. Combining these factors, 10^{10} is reached quite easily.

In this connection it is very remarkable that astrophysicists have found numerous spectroscopic indications of "stellar activity" vastly superior but qualitatively similar to that of our sun.

1. On the sun, "active" areas are indicated by bright reversals of the Ca II H and K lines and of hydrogen H_α. These emissions, however, are barely visible in the integrated solar spectrum.

Recently, Joy and Wilson[9] have collected all the evidence, beginning from Eberhard and Schwarzschild's discovery in 1913, concerning bright H and K lines in stellar spectra, mostly of types later than the sun. These spectra indicate that the surface of such stars quite frequently exhibits an average activity superior to that within spot groups on the sun which occupy only a minute fraction of the solar surface.

2. In the variable M-type giant Mira Ceti, Joy[10] discovered bright hydrogen lines with superposed metallic absorption lines of the reversing layer. Quite a similar structure was observed by Ellermann[11] in the so-called "solar bombs," indicating a very high degree of local activity. Again, the average stellar spectrum corresponds to the most active areas on the sun.

3. Recently, Luyten, Kron, Joy, and Humason[12] have detected in several late-type dwarf stars most violent variations of light and spectrum, which can be interpreted almost only as "flares" similar to those familiar on the sun. Kron,[13] moreover, detected regular light variations of $0^m.06$ with a period of 115 days for Ross 248, which point towards an explanation in terms of a rotating star with a patchy or spotted surface.

Other objects like Babcock's "magnetic" variables, Struve's close binaries emitting prominence-like gaseous streams, and the Wolf-Rayet stars with their enormous doppler effects should perhaps be mentioned also in this connection. Statistical evidence, which however cannot yet be considered as definitive, seems to indicate that late-type stars produce the largest part of galactic radiofrequency radiation.

III. ORIGIN OF COSMIC RAYS IN THE ATMOSPHERES OF HIGHLY ACTIVE STARS

The ratio of the average solar radiation to the radiation flux coming from the universe or the galaxy is,[2] for visual light, 4×10^8; for cosmic rays (according to Ehmert), 0.7×10^{-3}; and for radiofrequency radiation at 64 Mc/sec $\sim 10^{-1}$. It seemed, therefore, quite hopeless to try to ascribe the general cosmic radiation to stars as long as it was compared with visual light. The work of Forbush[14] and Ehmert,[15] as well as that of Clay, Jongen, and Dijker[16] and others, however, has shown that solar cosmic-ray bursts occur always in connection with large solar flares which also give strong radiofrequency bursts. Accepting our hypothesis that the galactic radiofrequency radiation and cosmic rays both originate in stars, whose "activity" surpasses that of the sun by a factor of $\sim 10^{10}$, in qualitatively the same way and the same ratio as they do in the sun, we are able to explain the great intensity of cosmic rays up to a factor 10^{-1}: $0.7\times 10^{-3}\approx 140$. In the following section we show that a factor of this order of magnitude or probably somewhat larger can, together with other important features of cosmic radiation, be accounted for by a galactic magnetic field. For the present we note that we do not presume that cosmic rays and radiofrequency radiation originate exactly together, but that they are connected statistically within the general frame of solar and stellar activity.

IV. PROPAGATION OF COSMIC RAYS IN THE GALAXY

It is well known that the energy of cosmic radiation is about equivalent to the total light plus heat flux from all the stars. This fact in connection with the second law of thermodynamics would preclude a stellar origin of the cosmic radiation, and it is, in this connexion, also not astonishing that our hypothesis of superactive stars by itself explains only a fraction of the observed inten-

[9] A. H. Joy and R. E. Wilson, Astrophys. J. **109**, 231 (1949); and A. H. Joy, Astrophys. J. **110**, 424 (1949).
[10] A. H. Joy, Astrophys. J. **108**, 288 (1947).
[11] F. Ellermann, Astrophys. J. **46**, 298 (1912).
[12] See numerous notes in Publ. Astron. Soc. Pacific **61** (1949); etc.
[13] Kron, Sky and Telescope **9**, 161 (1950).
[14] S. E. Forbush, Phys. Rev. **70**, 771 (1946).
[15] A. Ehmert, Z. Naturforsch. **3a**, 264 (1948).
[16] Clay, Jongen, and Dijker, Proc. Acad. Sci. Amsterdam **52**, 899, 906, and 923 (1949).

sity. As various authors, especially Alfvén and Fermi,[17] have pointed out, this difficulty, together with the observed isotropy of cosmic rays, can be accounted for by the assumption of a turbulent interstellar magnetic field.

It is evident that such a field will at once establish directional isotropy of cosmic rays.

By "coiling" the paths of the primary cosmic-ray particles the magnetic field will "store" the cosmic radiation in the galaxy. An upper limit of this effect can at once be derived, essentially following Fermi's ideas: A fast particle can at most wander through the galaxy until it hits an atom of interstellar matter so closely that a meson shower is produced whose secondaries "degenerate" rapidly. Taking the density of interstellar matter $\sim 2.5\times10^{-24}$ g/cm^3, the mean free path Λ, determining the "life" of a cosmic-ray particle corresponding to ~ 100 g/cm^2,† becomes 4×10^{24} cm $=1.3\times10^7$ parsec. If the particles were not deflected by a magnetic field (as, for instance, the accompanying radiofrequency waves) they would come from an average distance of only $r_1\approx 1000$ pc (half the thickness of the galaxy being $z_0\approx 150$ pc, and our distance from its center $R\approx 10{,}000$ pc). Thus, the "storage-factor" can at most amount to $\sim 10^4$. Evidently the factor ~ 140 (or more likely $\sim 10^3$) missing in our previous considerations can, together with the directional isotropy, be well explained by an interstellar magnetic field.

Let us now consider the propagation of cosmic rays in our galaxy in somewhat greater details.

(A) Scattering by Magnetic Turbulence Elements

Following Fermi,[17] we might assume that a cosmic-ray particle can be scattered (isotropically) by magnetic turbulence elements in interstellar space with a mean free path $l \ll \Lambda$. A total path r_2 corresponds then to $n=r_2/l$ free paths. According to a well-known theorem, the distance towards a fixed direction reached after n random steps of length l is $l(n/3)^{\frac{1}{2}}$. On the other hand, a particle should leave the galaxy after having permeated about half its thickness $z_0\approx 150$ pc. Therefore, the total path of a particle within the galaxy will be

$$r_2=3z_0^2/l=7\times10^4/l. \tag{5}$$

(B) Reflection at the Boundary of the Galaxy

Having arrived at the boundary of the galaxy, a particle may either be "reflected" or escape into intergalactic space. Ascribing formally to the galactic boundary a reflexion coefficient $\rho=1-\zeta$, a particle will still be present after 1, 2$\cdots$ reflections with a probability ρ, $\rho^2\cdots$. The distance $\approx 4z_0$, which it must on the average permeate until it reaches the boundary of the galaxy, is therefore effectively extended by a factor

$$1+\rho+\rho^2+\cdots=1/(1-\rho)=1/\zeta. \tag{6}$$

i.e., we obtain a total average path r_3,

$$r_3\approx 4z_0/\zeta=600/\zeta. \tag{7}$$

Let us now *summarize* our results:[17a]

A particle will migrate within the galaxy over a distance

$r_1\approx 1000$ pc in the case of straight motion.

$r_2\approx 7\times10^4/l$ pc in the case of scattering by turbulence elements with an average size $\sim l$.

$r_3\approx 600/\zeta$ pc in the case of reflexion at the boundary of the galaxy to which a transmission coefficient ζ is ascribed.

$\Lambda\approx 1.3\times10^7$ pc if its path is very coiled.

Scattering should become important if $r_2\gg r_1$, i.e. $l<10$ pc, and reach its full effect if $r_2>\Lambda$, i.e., $l<5\times10^{-3}$ pc. In galactic gaseous nebulae, good photographs show details down to at least 10^{-2} pc, but recent evidence makes us feel doubtful whether these structural elements can be considered as "magnetic turbulence elements." If the observations of Hiltner[18] and Hall[19] on the polarization of starlight by cosmic clouds are interpreted in terms of a magnetic field, this must be rather uniform over dimensions of at least 200 pc. Also, theoretical considerations by Biermann and Schlüter[19a] indicate that only turbulence elements $\gtrsim 200$ pc can be magnetized, while small scale motion should be considerably restricted by the magnetic field of the larger turbulence elements.

Cosmic radiation, once generated, should then spread chiefly along the magnetic lines of force. Since the intensity at such points in space, which can be reached at all, is the same according to the generalized Liouville theorem,[20] we expect that, in general, a tube of force will be filled with cosmic radiation rather uniformly. In order to make the storage within extended tubes of force efficient, $r_3=600/\zeta$ must reach the order of magnitude of $\Lambda=1.3\times10^7$ pc; i.e., the transmission coefficient ζ must be $<1/20000$.

One might ask first whether the magnetic field of the galaxy could produce totally reflecting torus surfaces of the kind familiar from Störmer's theory of the aurora. It is easily seen, however, using the dynamics of a charged particle in a magnetic field in the form developed, for example, by Alfvén,[21] that such surfaces are only encountered moving towards increasing field strength. A cosmic-ray particle intending to leave the galaxy, however, is moving for the most part just the other way.

[17] E. Fermi, Phys. Rev. **75**, 1169 (1949).

† We are indebted to Dr. Haxel, Göttingen, Germany, for his kind advice on this problem.

[17a] A more detailed mathematical analysis of the discussed items has been made, following closely the methods developed for radiative equilibrium problems in stellar atmospheres, by A. S. Eddington, *The Internal Constitution of the Stars* (University Press, Cambridge, England, 1930), chapter 12. For the present purpose it is hardly worthwhile to present it in detail.

[18] W. A. Hiltner, Astrophys. J. **109**, 471 (1949).

[19] J. S. Hall and A. H. Mikesell, Astron. J. **54**, 187 (1949).

[19a] L. Biermann and A. Schlüter, Phys. Rev. **82**, 863 (1951).

[20] W. Heisenberg, *Kosmische Strahlung* (Berlin, 1943), contribution by J. Meixner, p. 148.

[21] H. Alfvén, Arkiv Mat. Astron. Fysik **27A**, 22 (1941).

Nevertheless, an extremely small ζ is not as unreasonable as it might appear, offhand. A particle can leave the galaxy only under the following conditions: 1. If its Larmor radius R becomes large compared with the geometrical dimensions of the field. For $H=10^{-5.5}$ gauss, however, 10^{19} ev give $R=3.4\times10^{-6}$ pc only; i.e., such an escape is practically impossible. 2. If the pressure (resp. energy density) of the accumulated cosmic radiation becomes larger than that of the magnetic field $H^2/8\pi$ and of the interstellar matter $\rho v^2/2$. The well-known observational evidence that the three mentioned pressures are of the same order of magnitude indicates that probably cosmic radiation is accumulated in the galaxy until it begins to escape under its own pressure gradient together with magnetized interstellar matter.

Our present estimates of the rate of production of primary cosmic radiation are not yet accurate enough to judge the possible cosmogonical importance of this process. However, we can feel fairly sure that the storage factor of cosmic radiation in our galaxy is near its upper boundary value 10^4.

Apart from a storage factor $\sim10^4$, our considerations automatically account for the observed high degree of isotropy of cosmic radiation.

Since, according to our present ideas, cosmic radiation is connected with interstellar matter through the magnetic field of the galaxy, and since the solar system almost shares the galactic rotation of the latter, we should even expect no "Compton-Getting effect."

As Professor Bagge kindly pointed out to us, observational evidence concerning this effect seems not yet convincing. While the recent measurements by Hogg,[22] comparing the sidereal period in the northern and southern hemispheres, as well as a previous comparison of north and south absolute intensities by Compton[23] and his collaborators, appear unfavorable for the existence of the effect; the old investigation by Rau,[24] measuring only the hardest component under very good conditions, is more in favor of a positive effect. A clear decision can probably only be gained by repeating Rau's experiment simultaneously on the northern and southern hemispheres over an interval of several years.

Concerning the energy spectrum of the cosmic radiation we can make the following comments: Since an average cosmic-ray particle before reaching the earth has traversed some 50 g/cm² of interstellar matter, most particles with energies below about 5×10^8 ev should have been removed from the primary cosmic radiation simply by ionization.[25] In order to explain the cutoff of the cosmic-ray spectrum for small energies it is, therefore, not necessary to appeal to the action of a general magnetic field of the sun, whose existence has become very doubtful through recent observations by Babcock and Thiessen.[26] In connection with our theory it would be important to observe the low energy limit more accurately by high altitude flights (with less than 50 g/cm² air mass) near the geomagnetic poles.[27]

As to the *chemical composition* of the cosmic radiation observed at high altitudes, certain difficulties pointed out by Bradt and Peters[28] concerning the light nuclei cannot yet be explained in a satisfactory way. This point should be investigated in greater detail.

The well-known 2.9 power law governing the energy distribution of cosmic rays is, in our theory, more or less a consequence of similar power laws determining the number of turbulence elements (e.g. sunspots) of various sizes in stellar atmospheres. The sun is known to produce particles up to about $5\cdot10^9$ ev; a supergiant with a surface area 10^8 times larger and correspondingly larger spots may well produce particles up to 10^{14} ev. The observed energy spectrum of cosmic rays should roughly reflect the frequency distribution of various

$$\oint (\mathbf{E}, d\mathbf{s}) = -\frac{1}{c}\frac{d}{dt}\int \mathbf{B}_n d\sigma$$

(in the notations usual for Maxwell's theory). Since the small whirls are produced by subdivision of larger ones, they are more abundant, as we observe with sunspots. Smaller spots will have smaller fields and faster changes; these two factors operate against each other. Finally, small stars are more frequent than large ones. It is not yet possible to make detailed statistics concerning all these factors, but we may expect, offhand, that something like an inverse power of the observed order of magnitude will turn out.

V. OTHER THEORIES CONCERNING THE ORIGIN OF COSMIC RAYS

Let us now review critically the theories of cosmic radiation recently advanced by Fermi[17] as well as those of Richtmyer and Teller.[29] On the other hand, we shall not deal with theories attempting to connect cosmic radiation with the beginnings of the universe some 5×10^9 years ago.

(A) Fermi's Theory

Fermi assumes that cosmic-ray particles gain an essential part of their energy on their way through the galaxy by collisions with magnetic turbulence elements. The exponent $n=2.9$ in the law of energy distribution has, according to Fermi, the meaning

$$n=1+(l/\Lambda)(c/v)^2, \tag{8}$$

where again Λ and l, respectively, are the mean free paths for absorption by nuclear collisions and for

[22] A. R. Hogg, Nature 162, 613 (1948).
[23] A. H. Compton, Revs. Modern Phys. 11, 136 (1939).
[24] W. Rau, Z. Physik 114, 165 (1939).
[25] See, for example, H. Bethe, *Handbuch der Physik* (Verlag. Julius Springer, Berlin, 1933), 24/2.
[26] G. Thiessen, Z. Astrophys. 26, 16 (1949).
[27] Compare also M. A. Pomerantz, Phys. Rev. 77, 830 (1950).
[28] H. L. Bradt and B. Peters, Phys. Rev. 77, 54 (1950).
[29] R. D. Richtmyer and E. Teller, Phys. Rev. 75, 1729 (1949); and several subsequent papers.

scattering by turbulence elements. Here v is the average relative velocity of the scattering turbulence elements, and c is the velocity of light. Numerically, Fermi takes $\Lambda=2.3\times10^7$ pc and $l=0.4$ pc. For the velocity of the turbulence elements he assumes $v=30$ km/sec or $v/c=10^{-4}$, and thus obtains the required $n=2.9$.

An observational average value of the velocity of interstellar matter can be derived in the first place from its density distribution in the gravitational field of the galaxy.

The acceleration which the galaxy exerts at a distance z [cm] from its central plane in our neighborhood is, according to Oort[30] for $z<200$ pc

$$K(z)=-0.57\cdot10^{-20}z\ [\text{cm sec}^{-2}]. \tag{9}$$

Let the velocity component of matter perpendicular to the galactic plane be Z. Then (as in an isothermal atmosphere of temperature $kT=\mu\overline{Z^2}$) the density distribution $\rho(z)$ is determined by

$$(1/\rho)d\rho(z)/dz=-K(z)/\overline{Z^2} \tag{10}$$

or

$$\rho(z)/\rho(0)=\exp\left\{-\frac{0.57\times10^{-20}z^2}{2\overline{Z^2}}\right\}. \tag{11}$$

On the observational side van Rhijn,[31] summarizing also earlier evidence, describes the density distribution of interstellar "smoke" (grains) by the formula,

$$\rho(z)/\rho(0)=e^{-z/\frac{1}{e}} \text{ with } \tfrac{1}{e}=120 \text{ pc}. \tag{12}$$

Equating (11) and (12) for $\rho(z)/\rho(0)=1/e$ we get immediately[31a]

$$[\langle Z^2\rangle_{Av}]^{\frac{1}{2}}=6.3 \text{ km/sec}. \tag{13}$$

This velocity refers to turbulence elements filling approximately the cross section of the galaxy or having a diameter of ~250 pc. Since the velocity distribution of galactic turbulence will probably be not far from isotropy, we compare it with the turbulent velocities derived from Mt. Wilson measurements of interstellar sodium and calcium lines by Jentzsch and Unsöld.[32] They find for a distance of 250 pc that $[\langle Z^2\rangle_{Av}]^{\frac{1}{2}}=v_D/\sqrt{2}$ (using the notation of that paper):

$$[\langle Z^2\rangle_{Av}]^{\frac{1}{2}}=\begin{cases}7.1 \text{ km/sec for Ca II } H+K\\ 4.4 \text{ km/sec for Na } D.\end{cases} \tag{14}$$

It is not known how the difference between the Ca^+ and Na velocities should be explained, but, in any case, their average value, 6.6 km/sec, agrees well with Eq. (13). The limits of uncertainty may be estimated to be ±2.5 km/sec.

Passing to smaller turbulence elements, we should be aware that according to v. Weizsäcker[33] and Heisenberg[34] the velocities decrease about as the cube root of their diameters. For the interstellar gas the determination of turbulent velocity as a function of distance between $D=100$ and 2000 pc by Jentzsch and Unsöld (reference 32, Fig. 8) agrees well with this law. For elements 0.4 pc in diameter we should then expect a $[\langle Z^2\rangle_{Av}]^{\frac{1}{2}}=6.3(0.4/250)^{\frac{1}{3}}=1.2$ km/sec and relative velocities v (in analogy with well-known formulas of kinetic theory) $4/\sqrt{\pi}$ times greater, i.e.,

$$v=2.7 \text{ km/sec}. \tag{15}$$

This would give a "theoretical" exponent $n\approx200$, according to Fermi's Eq. (8), which means that we get practically no additional acceleration in the interstellar gas.

One might try to remedy the matter by reducing in Eq. (8) the diameter l of the turbulence elements, about which our knowledge is still admittedly meager. Then however, v decreases again. It is easily seen that no reasonable choice[34a] of l can remove the difficulty which, indeed, proves fatal for the theory of interstellar acceleration even if one should be inclined to disregard the aforementioned objections concerning the magnetization of the small turbulence elements.

Finally, it appears rather unsatisfactory that according to Fermi's theory the existence of a cosmic radiation is connected with quite definite properties of interstellar turbulence, i.e., that it is almost a matter of chance.

(B) The Richtmyer-Teller Theory

Let us now examine the hypothesis advanced by Richtmyer and Teller,[35] that the cosmic radiation is really solar radiation entrapped by a magnetic field surrounding the sun. Denote by $I_\odot$ the average intensity (per unit surface, time, and solid angle) of the cosmic rays emitted by the sun, by I the average intensity of the general cosmic radiation. Then, the average ratio of the observed fluxes due to the sun and space is $I_\odot\Delta\omega/\pi I$, where $\Delta\omega=6.8\times10^{-5}$ is the solid angle of the solar disk. As the observational value of our ratio, according to Ehmert, is $\sim7\times10^{-4}$, we find $I_\odot/I\approx32$.

Since the mean free path of a cosmic-ray particle in galactic space is $\Lambda=1.3\times10^7$ pc, it may at most keep going during a time $T=\Lambda/c\approx4\times10^7$ years. During this time interval the sun (radius $R_\odot$) emits altogether

$$\pi I_\odot\cdot4\pi R_\odot{}^2\cdot T. \tag{16}$$

If the space to which cosmic-ray particles are confined is a sphere $4\pi\bar{R}^3/3$, the average density of cosmic radia-

[30] J. H. Oort, Bull. Astr. Inst. Netherlands No. 238 (1932).
[31] P. J. v. Rhijn, Publ. Kapteyn Astr. Inst. (Groningen) No. 50 (1946); No. 53 (1949).
[31a] If the pressure of the magnetic field and of cosmic radiation should be important in addition to the dynamic pressure, this velocity would become still smaller.
[32] Ch. Jentzsch and A. Unsöld, Z. Physik **125**, 370 (1948).
[33] C. F. v. Weizsäcker, Physik **124**, 614 (1947).
[34] W. Heisenberg, Z. Physik **124**, 628 (1947).
[34a] The free paths of atoms in the interstellar gas are $\sim0.3\times10^{-4}$ pc.

tion inside will be $4\pi I/c$ and its total content

$$(4\pi\bar{R}^3/3)\cdot(4\pi I/c). \tag{17}$$

Equating (16) and (17), we get

$$\bar{R}^3=\tfrac{3}{4}(I_\odot/I)R_\odot^2\Lambda \tag{18}$$

or

$$\bar{R}=5.4\times10^{-3}\text{ pc}=1.1\times10^3\text{ astr. units}. \tag{19}$$

Assuming a larger than average density of interstellar matter in our neighborhood, Λ and $\bar{R}$ would become smaller.

It seems quite impossible that the sun can maintain a systematic magnetic field of the strength required to deflect hard cosmic rays appreciably within dimensions of the order $\bar{R}$. If we return, however, to the previous assumption that the magnetic field originates in the interstellar matter, there will always be "channels" allowing cosmic-ray particles produced by the sun to escape into galactic space. Then, however, the observed intensity of the general cosmic radiation can again only be explained by combining the theory of the "storage factor" with our idea of the existence of superactive stars all over the galaxy.

I am indebted to Professor Biermann and Dr. Schlüter for many interesting and stimulating discussions on problems of plasma physics and cosmic magnetic fields.

PHYSICAL REVIEW VOLUME 82, NUMBER 6 JUNE 15, 1951

Cosmic Radiation and Cosmic Magnetic Fields. II. Origin of Cosmic Magnetic Fields

LUDWIG BIERMANN AND ARNULF SCHLÜTER
Max Planck Institut für Physik, Göttingen, Germany
(Received October 11, 1950)

The equations governing the behavior of a wholly or partly ionized gas moving in the presence of a magnetic field are given. It is emphasized that the electric conductivity is independent of the magnetic field strength in many cases of actual interest. The stationary case of a magnetic field arising from the nonrigid rotation of a gaseous body is considered. Such a field is of the toroidal type. Fields of poloidal type may arise by the contraction of magnetized interstellar matter towards a star. The increase of strength of a magnetic field in turbulent conducting matter (stellar or interstellar) is considered. The conclusion is reached that the turbulence of every order of magnitude leads finally to a magnetic field, the energy density of which corresponds roughly to the energy density of the turbulence considered. If the magnetic field was weak in the beginning, this state was reached at first by the turbulence of smallest scale and smallest velocity, and then by the turbulence of higher orders; hence, the magnetic field strength must change secularly, as long as this process goes on. If our galaxy had only weak fields in its earlier stages, the present magnetic field should correspond to the turbulent velocity associated with distances of the order of 10^6 light years (between 10^{-6} and 10^{-5} gauss), and these fields should be more or less homogeneous over distances of this order. If there were already fields in the beginning, the present fields might be somewhat stronger.

INTRODUCTION

THE problem of the origin of stellar magnetic fields has caused considerable interest since Hale[1] communicated his measurements of the sun's general field. Although these results have not been confirmed lately, the discovery by Babcock[2] of highly magnetized stars has renewed this interest. No definite theory of the origin of these fields has as yet been proposed. We will show that one has to expect that differential rotation and other internal motions inside the stars will quite naturally cause magnetic fields, since electrons and ions will not move in exactly the same way just because of the different masses.

The existence of interstellar magnetic fields has been derived[3] from the properties of cosmic rays. If the cosmic rays occupied the whole universe with the energy density observed in our immediate neighborhood, their total energy would exceed that of light, and it would not be easy to escape the conclusion that more energy is continuously being transformed into that of cosmic rays than into that of heat radiation. Barring this possibility, it has to be assumed that the cosmic rays observed by us are continuously being produced within the galactic system or within a part of it. The approximate isotropy of their intensity is then explained by assuming interstellar magnetic fields of sufficient energy density to overcome the pressure of the cosmic-ray particles (10^{-5}–10^{-6} gauss). In this case the required production of cosmic rays would become much smaller than in the case of the first assumption; as discussed in detail by Unsöld[3a] in the preceding paper, it would be sufficient to assume that only a small fraction of the energy output of the stars is converted into cosmic-ray energy.

Here, of course, the question imposes itself of whether there are independent reasons for assuming galactic

[1] Hale, Seares, v. Maanen, and Ellermann, Astrophys. J. 47, 206 (1918).
[2] H. W. Babcock, Astrophys. J. 105, 105 (1947).
[3] H. Alfvén, Arkiv. Mat. Astron. Fysik 25B, No. 29 (1937); Z. Physik 107, 579 (1937); E. Fermi, Phys. Rev. 75, 1169 (1949). See also H. Alfvén, *Cosmical Electrodynamics* (Oxford, 1950).

[3a] A. Unsöld, Phys. Rev. 82, 857 (1951).

magnetic fields of the required order of magnitude. Alfvén showed that the interstellar gas, owing to its partial or complete ionization and especially because of the large dimensions involved, behaves in some respects like a conductor without resistivity: The Joule losses of electromagnetic fields are very small, and kinetic energy may be transformed by induction effects into magnetic energy until the densities of both have become comparable. The kinetic energy available is that of the interstellar gas, which, according to observation, is concentrated for the most part in clouds and shares the nonrigid rotation around the center of the galaxy of the stars, with irregular components of about 5 km/sec for normal compact clouds (but of up to 100 km/sec for the less compact ones). The growth of magnetic fields in turbulent conductive fluids has been studied further by Batchelor,[4] and by the present authors.[5] Reference should be made also, to the work of Elsasser and to that of Bullard on similar problems arising in the theory of the earth's magnetic field and its secular variations.[6]

The present authors have been especially concerned with the origin of the primary magnetic fields which are afterwards increased by induction effects. One mechanism, which operates as well in interstellar matter as inside stars, arises from the accelerations and pressure gradients because of the different masses of ions and electrons. The equations of the problem have been used in a form given by one of us (A.S.),[7] which takes explicit account of the "plasma" properties of the interstellar gas. This is rather essential in the presence of a magnetic field, especially with regard to the electric conductivity. By defining the original state of the magnetic fields, it becomes possible to draw definite conclusions regarding their rate of growth. The present state is probably not a stationary one, but the magnetic field still increases secularly.

THE PROPERTIES OF A QUASINEUTRAL IONIZED GAS ("PLASMA")

We restrict ourselves to the case in which the relative separation of electric charges is so small that the convection currents arising from mass motions can always be neglected.[8] Then, the following equation holds for the electric current density $\mathbf{j}$ in the presence of a magnetic field of strength $\mathbf{H}$, if the medium is moving with the mass velocity $\mathbf{v}$.

$$\mathbf{j}/\sigma=\mathbf{E}+(\mathbf{v}/c)\times\mathbf{H}-(\mathbf{j}\times\mathbf{H})(m_i-m_e)/e\rho c +(m_i\,\mathrm{grad}\,p_e-m_e\,\mathrm{grad}\,p_i)/e\rho. \quad (1)$$

Here, σ denotes the ordinary conductivity (esu), m_i and m_e the masses of the ions and electrons, respectively, p_i and p_e their partial pressures, ρ the mass density of the plasma, and $+e$ the charge of an ion. Here, $\mathbf{E}+(\mathbf{v}/c)\times\mathbf{H}=\mathbf{E}^c$ is the electric field as measured by an observer moving with the velocity of the plasma. It is evident that the field in this co-moving coordinate system is responsible for the relative diffusion of electrons and ions. The next term, containing the vectorial product of $\mathbf{j}$ and $\mathbf{H}$, is the one responsible for the diminution of conductivity in the presence of a magnetic field. The last terms indicate that, in addition to the electromagnetic causes, gradients of the partial pressures of the constituents tend to generate diffusion, i.e., electric current.

Equation (1) has been derived in a former paper[7] by a simple momentum balance for the single constituents. It is also contained essentially in the book by Chapman and Cowling.[8a] It has been used, without the pressure terms, by a great many authors.

Equation (1) is not sufficient for determining the current in a given electromagnetic field, because the current acts by the Lorentz force on the motion of the plasma. The equation of motion of the plasma

$$\rho d\mathbf{v}/dt=\mathrm{grad}\,p-(\mathbf{j}/c)\times\mathbf{H} \qquad (d\mathbf{v}/dt\equiv\partial\mathbf{v}/\partial t+(\mathbf{v}\cdot\mathrm{grad})\mathbf{v};\ p=p_i+p_e) \quad (2)$$

must be solved simultaneously with Eq. (1). It is advisable to eliminate by virtue of Eq. (2) the term $\mathbf{j}\times\mathbf{H}$ in Eq. (1). So one arrives at

$$\mathbf{j}=\sigma(\mathbf{E}^c+\mathbf{E}^i), \quad (3)$$

where

$$e\mathbf{E}^i=(m_e\,\mathrm{grad}\,p_e-m_i\,\mathrm{grad}\,p_i)/\rho+(m_i-m_e)d\mathbf{v}/dt. \quad (4)$$

$\mathbf{E}^i$ may be called an "impressed" electromotive field; it summarizes the effects of the nonelectrical forces (we have taken into account only pressure and inertia) on diffusion in terms of an equivalent electric field.

While of course Eqs. (3) and (2) are still interdependent, Eq. (3) no longer contains $\mathbf{j}$ explicitly on the right side. Thus, there is no explicit influence (except by the term $\mathbf{v}\times\mathbf{H}$ in $\mathbf{E}^c$) of the magnetic field on the current density. The formulation in Eqs. (3) and (4) is obviously superior to that of Eq. (1) in stationary cases (more precisely, if $d\mathbf{v}/dt=0$), when the elimination of the $\mathbf{j}\times\mathbf{H}$ term is achieved by a modification of the pressure terms (which often lead only to space charges compensating the resulting $\mathbf{E}^i$); but it is also useful in nonstatic cases. It shows that in many cases of actual interest it is the ordinary electric conductivity which determines the dynamical state of the plasma.

Equations (1) and (3) show that the electric phenomena are especially simple when viewed by a co-moving observer. We, therefore, also transform Faraday's law. First, we define[9] an operator D/Dt which, when operated on a vector field $\mathbf{A}$, measures the flux of $\mathbf{A}$ through a surface element, the boundaries of

[4] G. K. Batchelor, Proc. Roy. Soc. (London) (A) **201**, 405 (1950).
[5] A. Schlüter and L. Biermann, Z. Naturforsch. **5a**, 237 (1950).
[6] An account of this work has just been given by W. M. Elsasser Revs. Modern Phys. **22**, 1 (1950).
[7] A. Schlüter, Z. Naturforsch. **5a**, 72 (1950).
[8] This will be allowed in practically all cosmic applications.
[8a] S. Chapman and T. G. Cowling, *The Mathematical Theory of Non-Uniform Gases* (Cambridge, 1939).
[9] Abraham-Becker, *Theorie der Elektrizität* (B. G. Teubner, Leipzig, Germany), Vol. I, Sec. 19; Vol. II, Sec. 45.

which are moved and distorted by the velocity field $\mathbf{v}$. According to the rules of vector analysis, this operator can be expressed by

$$D\mathbf{A}/Dt=\partial\mathbf{A}/\partial t+\mathbf{v}\,\mathrm{div}\mathbf{A}-\mathrm{curl}[\mathbf{v}\times\mathbf{A}].$$

When operating on the magnetic field it yields, because of $\partial\mathbf{H}/\partial t=-c\,\mathrm{curl}\mathbf{E}$ and the definition of $\mathbf{E}^e$,

$$D\mathbf{H}/Dt=-c\,\mathrm{curl}\mathbf{E}^e \tag{5}$$

or, from Eq. (3)

$$D\mathbf{H}/Dt=c\,\mathrm{curl}\mathbf{E}^i-c\,\mathrm{curl}(\mathbf{j}/\sigma).$$

The last term shows that the free decay of a magnetic field is determined by the unchanged value of the conductivity and is therefore extremely slow for fields of cosmic dimensions. The first term describes the production (and annihilation) of magnetic lines of force by the impressed fields.

The preceding results can be generalized on several ways. It is easily possible to take into account other forces beside pressure and inertia. The general form of Eq. (4) is

$$e\mathbf{E}^i=(m_i\mathbf{f}_i-m_e\mathbf{f}_e)/(m_i+m_e), \tag{6}$$

where $\mathbf{f}_i$ and $\mathbf{f}_e$ represent all nonelectromagnetic forces on a particle (ion or electron, respectively), including pressure gradients, inertial forces, radiative pressure, thermodiffusion, and so on.

If neutral atoms are present in considerable number, the exact equations become more complicated.[10] The result is, however, that to a sufficient approximation, if the Lorentz-force is small compared with $\mathrm{grad}p$ in the equation of motion, Eq. (2), the impressed force is given by

$$N_e(\alpha_{in}+\alpha_{en})e\mathbf{E}^i=\alpha_{in}\,\mathrm{grad}p_e-\alpha_{en}\,\mathrm{grad}p_i, \tag{7}$$

where N_e is the numerical density of electrons; α_{en} and α_{in}(g cm^{-3} sec^{-1}) measure the transfer of momentum between the neutral atoms and the electrons and ions, respectively. Since α_{in} happens to be very large compared with α_{en} because of the mass difference, we can write

$$e\mathbf{E}^i\approx(1/N_e)\mathrm{grad}p_e. \tag{8}$$

In all cases we can assume the order of magnitude of $\mathbf{E}^i$ to be given by

$$e\mathbf{E}^i=\bar{m}d\mathbf{v}/dt, \tag{9}$$

where $\bar{m}$ is a certain mean value of the masses of the constituents. In the case of Eq. (4) this is clearly a reasonable approximation. For an *HI* region, Eq. (9) gives a lower limit, since all local differences of the degree of ionization and of electron temperature give higher impressed forces than that given by Eq. (9).

The value of the conductivity may be taken from the work of Chapman and Cowling,[8a] under astrophysical conditions it is roughly proportional to $T^{\frac{1}{2}}$ and depends only to a small degree upon the density. In interstellar space its value may be assumed to be 10^{11} sec^{-1} in *HI* regions, and between 10^{12} and 10^{13} in *HII* regions, but up to 10^{15} in the interior of the sun.

The time scale of the free decay of a magnetic field or of its growth under the influence of a steady impressed electric field is of the order of magnitude $Q\sigma/c^2$ (where Q is a representative cross section), as follows from Eq. (5) and from $\mathrm{curl}\mathbf{H}=4\pi\mathbf{j}$, if one puts approximately $\mathrm{curl}\,\mathrm{curl}\approx 4\pi/Q$. If the time available is small compared with $Q\sigma/c^2$, $\mathbf{E}^i$ is always very nearly equal to $-\mathbf{E}^e$. In interstellar space the smallest distances of interest are of order 10^{16} cm (1/100 light year), and the corresponding time scale is of order $\sigma\times10^{11}$ sec or $\geqslant 10^{14.5}$ years.

STELLAR MAGNETIC FIELDS

We consider first the stationary magnetic field produced by nonrigid rotation of a gaseous body.[11] A magnetic field is maintained if the impressed force $\mathbf{E}^i$ arising from the inertia of the rotating masses cannot be compensated for by a suitable distribution of space charges, that is if $\mathrm{curl}\mathbf{E}^i\neq 0$. If $\mathbf{E}^i$ is due to rotation, this means $\partial\omega/\partial z\neq 0$ (ω is the angular velocity of rotation z the axis of rotation).

As an example, we assume the vector $\boldsymbol{\omega}$ proportional to $\mathbf{a}(R/|\mathbf{r}|)$ ($\mathbf{a}$ is a constant vector parallel to z, $\mathbf{r}$ the radius vector, R the radius of body). Furthermore, the conductivity inside the body is taken equal to a constant σ_0; outside the body it is equal to zero. The solution is

$$\mathbf{H}=6\pi\sigma_0(\bar{m}/ec)[(R^2-r^2)/r^2][\mathbf{a}\times\mathbf{r}](\mathbf{a}\cdot\mathbf{r}) \tag{10}$$

inside the body, and $\mathbf{H}=0$ outside of it. If we put $\sigma_0=10^{17}$ esu, $\bar{m}=1.66\times10^{-24}$ g, and ω equal to the equatorial angular velocity of the sun, we get (φ latitude)

$$H=0.94\cdot10^3[(R^2-r^2)/R^2]\sin2\varphi\quad\text{(gauss)}. \tag{11}$$

Since there is no reason to expect $\partial\omega/\partial z=0$ in actual stars, and the time scale considered above is comparable with the age of most of the normal stars, it appears that the magnetic fields directly created by diffusion effects in the interior of stars may be quite considerable.

The geometrical properties of the simple model discussed above—two toroidal fields of opposite direction symmetrical to the axis of rotation, one in each hemisphere—do not lead to fields observable at the surface; but it has been long recognized[12] that, for instance, the sunspot fields must be carried to the surface by induction effects.

In this special model the magnetic field is not disturbed by convection, since $\mathbf{v}\times\mathbf{H}$ vanishes everywhere.

[10] A. Schlüter, Z. Naturforsch. **6a**, 73 (1951).

[11] L. Biermann, with an appendix by A. Schlüter, Z. Naturforsch. **5a**, 65 (1950).

[12] T. G. Cowling, Monthly Notices Roy. Astron. Soc. **94**, 39 (1934).

This does not hold, of course, in more complicated types of motion.

The problem of how magnetic fields of poloidal types can arise by convection has been treated by Elsasser and by Bullard[6] for the case of the earth's magnetic field. It appears difficult to understand fields of this type and of their observed strength on stars.

If the existence of *interstellar* magnetic fields (which will be discussed in the following section) is assumed, another explanation suggests itself. These fields are supposed to be rather homogeneous over distances comparable with those between neighboring stars.

It seems very plausible to assume that stars of early spectral type augmented their mass to some extent by accretion of interstellar matter within the last 10^8 or 10^9 years. We consider the simple case of a homologous contraction towards the star. Then, it follows from $D\mathbf{H}/dt=0$, that

$$d(\mathbf{H}\rho^{-1})/dt=0; \quad d/dt=\partial/\partial t+\mathbf{v}\cdot\text{grad}; \qquad (12)$$

this may also be seen intuitively. If the original field has a strength of 10^{-6} gauss, a contraction by 10^{24} in the density would give a field of 10^{10} gauss. In this case the magnetic forces would overcome gravitation by several powers of 10. This means that the contraction must be nonisotropic; the matter will be attracted by the star mainly along the magnetic lines of force. The result will be a magnetized star with a field of poloidal type. It is difficult to estimate its probable strength, and only an upper limit can be given. Since the mean value of $\mathbf{H}^2/4\pi$ must be small compared with GM^2/R^4 (M is the mass, R the radius of the star), it follows that

$$H\ll 10^8 \text{ gauss}.$$

Furthermore, the relatively small conductivity in the outer layers has as a consequence that their currents maintaining the field decay much faster than in the interior, where the time scale $Q\sigma/c^2$ is of the order 10^9–10^{10} years. Hence, at the surface one would expect a field smaller by perhaps two powers of ten than in the far interior. The smaller density of these layers works in the same direction. Therefore, fields above 10^6 gauss at the surface would not be expected from this argument.

MAGNETIC FIELDS IN A TURBULENT FLUID

At the end of the last section, we considered the increase of a given magnetic field by a regular motion. Now the influence of irregular motions will be treated.

At first we study the consequence of the assumption $D\mathbf{H}/Dt=0$. It may be seen intuitively that any line of force is on the average continuously lengthened as long as the magnetic forces do not react on the motion. This is the case when the energy density of the magnetic field becomes comparable with that of the motion. The increase is essentially exponential with time until this limit has been reached.[13] This can be shown in the following way:

From $D\mathbf{H}/Dt=0$ and the equation of continuity, it follows that

$$\rho d(\mathbf{H}/\rho)/dt=(\mathbf{H}\cdot\text{grad})\mathbf{v} \qquad (13)$$

(ρ is the mass density, and d/dt is the time derivative). If there are no substantial changes in the density and if the velocity field is essentially constant during a certain time τ, the magnetic field strength will therefore change exponentially (increase or decrease) during this time. Denoting a characteristic length of the irregular motion by L, a relation of the kind

$$\ln\{H(t+\tau)/H(t)\}=\alpha(v/L) \qquad (14)$$

will be valid, where α represents a positive or negative number of order of magnitude 1. According to the usual assumptions in the theory of turbulent motion, the time τ during which the state of motion remains essentially unchanged is just of the order v/L. If we, furthermore, assume that at any instant $t+T$ the velocity field is no longer correlated with that at the time t, where $T>\tau$, the value of $\ln\{H(t+T)/H(t)\}$ (which we shall denote by ξ) will be a statistical sum of T/τ numbers α of order of magnitude 1. For $T\gg\tau$, the probability of arriving at a certain value of ξ will be given by a gaussian distribution

$$\omega(\xi)=\omega_0\exp\{-2\xi^2/(T/\tau)\}, \qquad (15)$$

where we have taken $\alpha=\pm 1$. The expectation value of H^2 will then be given by

$$\langle H^2(t+T)\rangle_{Av}=H^2(t)\frac{\int\omega(\xi)e^{2\xi}d\xi}{\int\omega(\xi)d\xi} \qquad (16)$$

$$=H^2(t)\exp\{T/2\tau\}.$$

The exponential growth of the mean magnetic field strength in a turbulent fluid on which the magnetic field does not react, is characterized by a doubling time of the order of the lifetime of the turbulence elements. This increase, of course, takes place only if the time constant of the exponential decay by Joule losses is greater than this doubling time. In this way we arrive at the criterion

$$L^2\sigma/c^2>\tau, \qquad (17)$$

or, using again the relation between the characteristic

[13] This was first pointed out by G. K. Batchelor (reference 4), to whom we are indebted for valuable remarks. However, the conclusions arrived at by us regarding interstellar fields differ from those of Dr. Batchelor. *Note added in proof:* The result, that ultimately equilibrium between turbulent and magnetic energy density is reached in *every* order of magnitude, is supported by Elsasser's result (Phys. Rev. **79**, 183 (1950)), that (for an incompressible fluid) the hydromagnetic equations are symmetrical with respect to $\mathbf{H}(4\pi\rho)^{-\frac{1}{2}}$ and $\mathbf{v}$.

quantities of turbulence $\tau = L/v$,

$$Lv\sigma/c^2 > 1. \tag{18}$$

If this condition is satisfied, any magnetic field will grow to the limit given by the reaction of the field on the motion. The properties of the original field, e.g., its local derivations, do not enter into the discussion and are therefore quite inessential.

The field reacts on the motion when the term $(\mathbf{j}/c) \times \mathbf{H} \equiv (1/4\pi)[\mathrm{curl}\mathbf{H} \times \mathbf{H}]$ in the equation of motion, Eq. (2), becomes comparable with the other terms. This amounts to saying that the magnetic energy density will finally reach the energy density of the turbulence considered (if the time scale permits this to happen).[14]

In the interior of all stars, electromotive forces are to be expected if there are any internal motions. These will generate magnetic fields, as discussed in the preceding section, and these magnetic fields will be amplified wherever turbulent motions exist. Let us consider for instance the sun. In that region below the surface where the hydrogen is just partly ionized, convection will take place up and down, and it will cause a kind of turbulent motion. The granulas are the outermost part of this hydrogen-convection zone. If we follow Schwarzschild's recent analysis,[15] the typical velocity in the most energetic elements is of the order 2 km/sec; they are too small to be directly visible, but their diameter has been estimated to some 100 km. The mean lifetime of these elements should be of the order 1 min, as compared with the time constant for spontaneous decay of 10 days. ($\sigma \approx 10^{13}$ esu). Therefore, our criterion for turbulent amplification is fulfilled. The doubling time being extremely short as compared with the age of the sun, any original magnetic field will have grown to the upper limit given by the energy density of the motion. This, in the granulas, is of the order 10^3 erg/cm,^{3} so that a magnetic field of order 10^2 gauss would result. This discussion is rather superficial, because we see only the outermost part of the hydrogen convection zone, which is perhaps not typical. On the other hand, the density gradient will cause a diminution of the magnetic field somewhat similar to the $\rho^{\frac{1}{2}}$-law of the preceding section. It is not yet known how rapidly the density increases inward within the zone; a value of 10^{-7} gr/cm^3 has been adopted before, which is probably a lower limit for the interior of the zone.

In the same way in all other stellar convection zones, magnetic fields should be present (e.g., in the central convective core of the sun, if this core exists) but not enough is known about their extension and state of motion to draw any definite conclusion.

[14] The variations of **H** over smaller distances tend to average out in Eq. (2). For the detailed argument see Sec. VIII of our paper (reference 5).

[15] R. S. Richardson and M. Schwarzschild, Astrophys. J. **111**, 351 (1950).

INTERSTELLAR MAGNETIC FIELDS

The same principles apply also to the matter between the stars. But the situation is rather different in several respects. Let us take for instance $L \approx 300$ to 400 parsec $\approx 10^{21}$ cm as a characteristic length, and the corresponding irregular velocity as $v = 5$ km/sec. That value of the velocity is an approximate mean of the peculiar velocities of the heavy interstellar gas clouds, the absorption lines of which have been observed with great accuracy by Adams.[16] It follows that the doubling time is of the order L/v $10^{15.3}$ or $10^{15.4}$ sec or 1/50 to 1/40 of the age of the galaxy, if the latter is assumed to be 10^{17} sec $= 3 \times 10^9$ years. During the existence of the galaxy, any weak original magnetic field will have grown by a factor 10^{12}–10^{15}. The most conservative estimate of the present field strength is obtained in the following way. We assume that in the earliest stages of the galaxy, during which its state of motion was already similar to the present one, no magnetic fields were present except those which were produced by the electromotive forces of the galaxy itself. The order of magnitude of these is given, according to Eq. (4), by

$$eE' \approx m_H dv/dt \approx m_H v^2/L \tag{19}$$

(m_H = mass of a proton) or by

$$|D\mathbf{H}/Dt| \approx (cm_H/e)(v^2/L^2). \tag{20}$$

Then, after the first characteristic time of the turbulence, we arrive at a magnetic field of the order

$$H_0 \approx (cm_H/e)(v/L), \tag{21}$$

since during the time v/L the creation of magnetic flux will be in the same sense. Inserting the values for v and L used above, Eq. (21) yields

$$H_0 \approx 10^{-19} \text{ gauss.}$$

This we take as the starting field of the amplification process, and we arrive at a present magnetic field of

$$H \approx 10^{12} \cdots 10^{15} \cdot H_0 \approx 10^{-7} \cdots 10^{-4} \text{ gauss,}$$

the energy density of which is roughly of the order of the kinetic energy of the turbulent motion considered (10^{-13} erg/cm^{-3}). The latter is the upper limit for the magnetic energy density which can be produced by the turbulence of this characteristic velocity.

Had we taken a smaller value for the characteristic length, the starting field as well as the amplification factor would have been greater. Then the limit given by the turbulent energy density would have been reached in the past. When this was the case, the turbulence of this order of magnitude was no longer able to lengthen the magnetic lines of force. We may assume that the kinetic energy of turbulence associated with turbulence of a certain characteristic length L is greater, the

[16] W. S. Adams, Astrophys. J. **97**, 105 (1943); **109**, 354 (1949); see also A. Schlüter and P. Stumpff, Z. Astrophys. (to be published).

greater the value of L.[17] Then the turbulence of greater scale is not much changed by the magnetic field belonging to turbulence of a smaller scale.

The motions which bring about the amplification in the largest dimension considered take place mainly in the plane of the galaxy. Hence, it must be concluded that the magnetic lines of force also run more or less parallel to this plane. Furthermore, for the reasons given above, the magnetic field should be rather homogeneous over distances comparable with this same L. Local differences are to be expected, especially in places where the mass density is above average.

The magnetic term in the equation of motion, Eq. (2), acts in the direction perpendicular to the plane of the galaxy—on the average as a force directed away from the plane. Also, the pressure exerted by the cosmic-ray particles acts in the same direction. Both must be compensated for by the gravitational force. It now seems likely that these are the most essential factors governing the lateral extension of interstellar matter.

The interstellar gas clouds commonly observed with high dispersion[16] should be strongly affected by the magnetic field. Components of motion perpendicular to H are not prohibited, but they must be of such character that no permanent lengthening of the lines of force results (e.g., oscillatory).

[17] This is equivalent to the statement that the mean square of the (irregular) velocity difference v between two points, whose separation is L, increases with increasing L. The Kolmogoroff-Weizsäcker theory of isotropic statistical turbulence predicts $v \sim L^{\frac{1}{3}}$ for an incompressible fluid.

The influence of the non-ionized part of the gas has been considered in detail in our paper.[5] It is shown there that it does not lead to any essential modification of this picture, because the relative motion of the ionized and the non-ionized part of the gas ("ambipolar diffusion") is rather slow (probably $\lesssim 1$ km/sec). If the dissipation of turbulent energy corresponds to the values of v and L used above (from which results 10^{-4} erg/g sec), the ambipolar diffusion would provide a comparatively important mechanism converting turbulent into thermal energy. The dissipation of energy may be higher if the relatively fast moving clouds are frequent enough.

It follows from the analysis outlined before that the age of the galaxy determines essentially the value of L/v of the largest elements whose motion is just affected by the magnetic field. Their kinetic energy determines the magnetic field strength and their extension (namely, L) the approximate radius of curvature. On the other hand, the present field depends very little (by a logarithmic term) on the initial field.

From these considerations it seems likely that in other galaxies conditions may be fairly different, either in the sense that the dynamics of the interstellar gas are more greatly affected by the magnetic field or in the opposite sense.

The authors wish to express their indebtedness to Professor von Weizsäcker, Göttingen, Professor Schwarzschild, Princeton, and especially to Professor Unsöld, Kiel, for important remarks and suggestions concerning the topics treated in this paper.

PHYSICAL REVIEW VOLUME 82, NUMBER 6 JUNE 15, 1951

Electron Removal in Mercury Afterglows*

P. DANDURAND† AND R. B. HOLT
Department of Physics, Harvard University, Cambridge, Massachusetts

(Received February 16, 1951)

Observations of the electron density, visible and near ultraviolet light intensity, and spectrum associated with a 2800-Mc pulsed electrodeless discharge through mercury vapor have been made. Our results indicate ambipolar diffusion as the principal mechanism of electron removal at low pressure, with attachment becoming increasingly important at higher pressure. The data also yield a considerable amount of information regarding electron temperatures, recombination coefficient, and other parameters necessary to a detailed description of the processes taking place in the discharge.

I. INTRODUCTION

As part of a general program of studying the mechanism of the disappearance of electrons from gas discharge plasmas, an investigation of mercury afterglows has been made. The method used includes simultaneous spectroscopic and electron density measurements together with relative and absolute light intensity measurements.

Previous work on metallic vapors has been confined largely to mercury and cesium. Mohler and Boeckner[1] and Mohler[2] have investigated cesium afterglows after cut-off of an intense direct current discharge at a pressure of 0.1 mm with electron densities of the order of 10^{12} electrons/cm^3. Electron temperatures in the afterglow were of the order of 1200°K. The spectrum was

* Assisted by the ONR.
† Present address: 52 rue Vancau, Paris 7, France.

[1] F. L. Mohler and C. Boeckner, Natl. Bur. Standards J. Research 2, 489 (1929).
[2] F. L. Mohler, J. Research Natl. Bur. Standards 19, 446 (1937).

found to consist of lines with about the same intensity distribution as in the discharge, plus a continuous spectrum beyond the series limit which had less wavelength spread in the afterglow than in the discharge. Mohler[2] has also used a probe to measure electron density after cut-off and found a value for the recombination coefficient α (defined by the equation for electron density, n, as a function of time, t, as follows: $dn/dt = -\alpha n^2$) of 3.4×10^{-10} cm³/ion-sec in the pressure range 0.01 to 0.03 mm. Using the same technique in mercury at 0.27-mm pressure for 2000°K electrons, Mohler[3] found a recombination coefficient of 2.3×10^{-10} cm³/ion-sec. Mierdel,[4] however, has found that the relation between electron density and time under very similar conditions in mercury indicates an ambipolar diffusion-type electron loss rather than recombination. The electron temperature was found to be 2000°K and almost independent of pressure in this work, a fact which is attributed to collisions of the second kind between metastable mercury atoms and electrons.

II. METHOD AND APPARATUS

The method used is the same as the one described in previous papers by one of the authors,[5,6] and it will be enough to recall briefly how we measure the different variables of the experiment. The electron density is given by the frequency shift of a microwave (2800 Mc) resonant cavity. The conditions of the experiment are such that the electron density is directly proportional to the frequency shift observed. A gated photomultiplier, which is on for 40 microseconds at an adjustable time after cut-off, gives values of the light intensity as a function of time. A calibration of the photomultiplier is made in order to relate the signal of the photomultiplier to the *absolute* light intensity. A rotating disk provided with slits is used to observe the spectrum of the discharge and of the afterglow. The synchronization between the modulation of the microwave oscillator (which initiates the discharge in the quartz bottle) and the rotation of the disk is obtained with a continuous light source and a photomultiplier which generates the initial trigger a few hundred microseconds before the slit passes the discharge tube. Calibrated delay circuits are used to measure times between cut-off and the instant at which the measurement is made.

A block diagram of the apparatus is shown in Fig. 1. A two-chamber oven (Fig. 2) is used around the entire cavity and discharge tube. The pressure is determined by the temperature of the region containing the reservoir of metal; dimensions of the tube are chosen to avoid difficulties in pressure determination due to thermal transpiration. The temperature of the gas is determined by the temperature (independently varied)

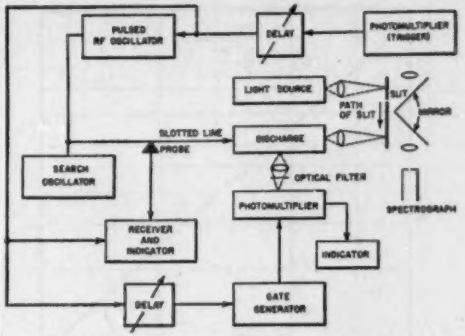

FIG. 1. Block diagram of the electron density and high speed spectroscopic apparatus.

of the other half of the oven. The electron temperature is not measured directly in this investigation. Theoretical calculations can be made, including the effect of collisions of the second kind between metastable mercury atoms and electrons and of the Ramsauer effect.[7] Taking into account available experimental values, the electron temperature would be expected to decrease very rapidly to 2000°K, where it is kept fairly constant by collisions of electrons with metastable atoms. For pressures above 3 mm, however, the disappearance of metastables in the plasma may be fairly rapid, and thermal energies are probably reached in 1 millisecond or so.

III. RESULTS

Because of the great care taken in the purification of the gas, very pure samples were obtained. The only

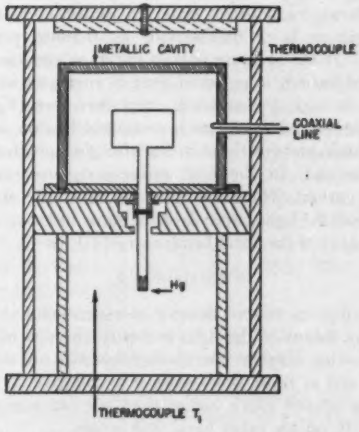

FIG. 2. Double-chamber oven used for varying pressure and temperature.

[2] F. L. Mohler, J. Research Natl. Bur. Standards **19**, 559 (1937).
[4] G. Mierdel, Z. Physik **121**, 574 (1943).
[5] Holt, Richardson, Howland, and McClure, Phys. Rev. **77**, 239 (1950).
[6] McClure, Johnson, and Holt, Phys. Rev. **80**, 376 (1950).
[7] W. Allis and P. Morse, Z. Physik. **70**, 567 (1931).

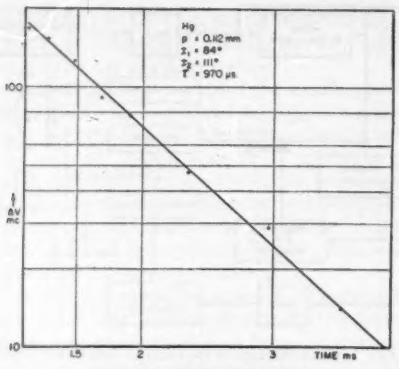

FIG. 3. Electron density as a function of time (case 1). The electron density is in arbitrary units.

lines observed on prolonged spectroscopic observation of the discharge are mercury atomic lines.

The simplest way to describe the experimental results is to distinguish four ranges of pressure and temperature.

Case 1. Pressures from 0.08 to 0.5 mm; Temperature below 120°C

The electron density n can be measured between approximately 1 and 5 milliseconds after cut-off. In this range, it is found that an exponential law of the type

$$n = n_0 \exp(-t/\tau_1) \tag{1}$$

is very closely verified (Fig. 3). The time constant τ_1 is of the order of 1 millisecond and, if the temperature is kept constant, is found to increase not quite proportionately with pressure. For a temperature of 112°C, for instance, τ_1 increases from 0.8 millisecond at 0.08 mm-pressure to 2 milliseconds at 0.5-mm pressure (Fig. 4). If the pressure is kept constant and the temperature varied, it is found that τ_1 increases at first, passes through a maximum, then decreases (Fig. 5). Light intensity *versus* time is a straight line on a semilogarithmic plot for times in the afterglow greater than 1 millisecond. In the first millisecond, however, the line is curved. The time constant τ_2 of the straight portion of the light curve is of the same order as τ_1, the mean value of the ratio being $\tau_1/\tau_2 = 1.1$, or

$$I = \text{constant} \cdot n^{1.1}. \tag{2}$$

An attempt to extend density measurements to short times by means of the light intensity curve is made in the following manner. The above relation is not thought to be valid at short times since it would give an initial electron density much higher than one can reasonably expect. If, on the other hand, one writes

$$I = An^2 + Bn,$$

it is possible to find A and B such that Eq. (2) is closely verified for t greater than 1 millisecond. Such a calculation shows that the quadratic terms would be more important at very short times. This would indicate that recombination-type electron removal is playing an important role. Our data indicates a value of the order 5×10^{-9} cm³/ion-sec for α at these pressures. An estimate of the absolute light intensity emitted at 2537A can also be made. At 1.1 milliseconds in the afterglow the intensity radiated is of the order of 10^{-6} watt. If we assume that this emission comes only from recombination, thus neglecting the possible transitions from a metastable state to the 2^3P_1 state or the dissociation of molecules with 2^3P_1 excited atoms as one of the dissociation products, and also assume that only approximately one-fifth of the recombinations will eventually give rise to the 2537A line, we find that there are only 5×10^{-2} ev of light emitted per electron disappearing. This is not surprising, since we expect most of the electrons to be lost by diffusion to the walls. Spectrograms of the discharge show an intense atomic line spectrum of HgI both in the discharge and in the afterglow. The relative intensity of high members of the series ($2p_1-6d_1$, for instance) are very high in the discharge and immediate afterglow. At 400 microseconds in the afterglow, these lines have disappeared, whereas other lines are still visible. This suggests that the enhancement of high members of the $2p-md$ series as observed by Hayner[8] is associated with extremely high densities. A continuous spectrum is also conspicuous from about 4900A to 2547A. In the discharge the maxima of intensity are approximately located at 4500A (very strong), 3300A (strong), and 2650A (weak). A narrow and intense continuum extends on both sides of the 2537 line with two band heads at 2469A and 2476A visible. In the afterglow, the continuum intensity is well maintained in the neighborhood of the resonance line, at 3300A and especially at 4500A, and it has a higher relative intensity than the

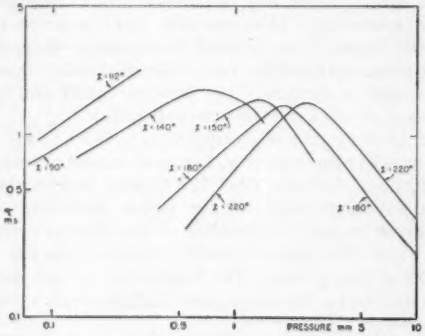

FIG. 4. Variation of electron density decay time constant with pressure.

[8] L. Hayner, Z. Physik 35, 365 (1925).

atomic lines. Four band heads at 3070, 3095, 3450, and 3480A appear in the afterglow.

Case 2. Pressure from 0.1 to 0.5 mm; Temperature above 130°C

At low pressures, electron density decay becomes more rapid with increasing temperature. Exponential decay is found for times greater than 1 millisecond, and τ_1 for a given pressure is smaller than in case 1. At constant temperature (e.g., 140°C), however, τ_1 is found to increase with pressure as in case 1. Light intensity measurements (Fig. 6) show that the initial curved portion of the plot is not very much affected by the increase in temperature, whereas the straight portion of the curve progressively disappears. Spectrograms show that the atomic lines have about the same intensity as in case 1, both in the discharge and the afterglow, with the same change in relative intensity. The continuum, on the other hand, is considerably weaker. In the afterglow, the continuum at 4500A shows up very weakly, while no continuous spectrum is observed at other wavelengths. This indicates that the straight portion of the light intensity curve corresponds to the continuous emission, particularly to the emission of the 4500A continuum, which is the strongest observed in this region.

Case 3. Pressure from 0.5 mm to 4 mm; Temperature below 190°C

The electron density measurement becomes more difficult under these conditions, since the real component of the complex conductivity of the gas is no longer negligible compared with the imaginary component. Nevertheless, exponential decay is found, the time constant τ_1 going through a maximum and then decreasing almost proportionately with pressure. At 140°C, the maximum value of τ_1 is 1.5 milliseconds, which occurs at about 0.8-mm pressure. As seen on Fig. 6, the straight portion of the light intensity curve extends to rather short times. The intensity in the afterglow is very high, and is about 10 times greater at 1 millisecond for 3.6 mm than for 0.19-mm pressure. The time constant associated with the light curve is found to go through a maximum at about the same pressure as the electron density time constant. After the maximum, it decreases faster with pressure, behaving very closely like the time constant found by Alpert and others[9] in experiments on imprisonment of resonance radiation. Simultaneous spectrograms show the reappearance of a very strong, continuous spectrum. Both in the discharge and the afterglow, maxima of light intensity are found at 3300A and 4500A. The maximum at 3300A is relatively much stronger than in case 1. Band heads at 3070, 3095, 3450, 3480A appear in the afterglow.

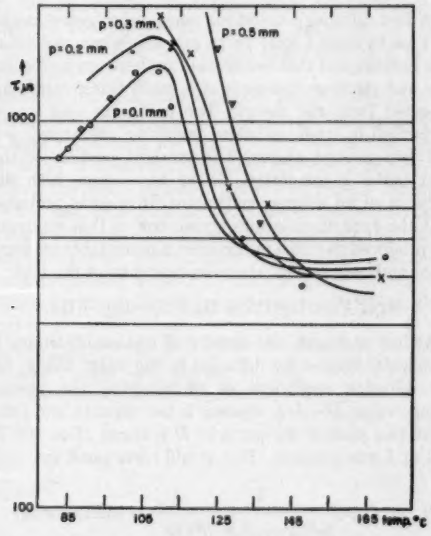

FIG. 5. Variation of electron density decay time constant with temperature.

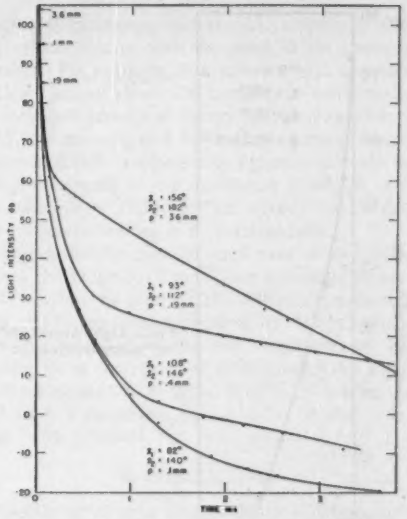

FIG. 6. Light intensity in the afterglow (case 2).

Case 4. Pressures 4 mm to 10 mm; Temperature below 230°C

In this region the real and imaginary part of the conductivity are of the same order of magnitude. This introduces some uncertainty about the absolute value of the electron density; however, once again exponential

[9] Alpert, McCoubrey, and Holstein, Phys. Rev. 76, 1257 (1949).

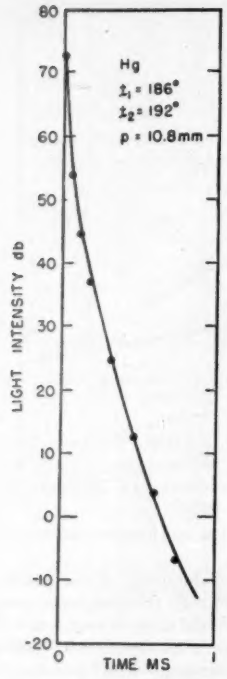

FIG. 7. Light intensity in the afterglow (case 4).

decay is found. The value of the time constant (which depends only on the ratio of two values of the electron density) is probably not too much in error. Electron density time constants are found to decrease almost proportionately with pressure. The light intensity is found to decrease very rapidly, giving time constants of the order of 100 microseconds (Fig. 7). In the spectrograms of the afterglow, an extremely intense band spectrum is observed together with persistent atomic lines. The band heads, although very diffuse, can be identified. Their wavelengths agree with values published by previous workers.[10-12]

IV. DISCUSSION

For pressures under 0.5 mm, the electron-density decay follows fairly well the predictions of ambipolar diffusion theory. The formula giving the time constant of the electron decay is

$$\tau_1=\frac{1}{(\pi^2/a^2)+(5.8/R^2)}\frac{e}{k}\frac{273}{300K_0}\frac{p}{T^+(T^++T_e)},$$

where a is the tube height; R is the tube radius; k is the Boltzmann constant; e is the electronic charge in esu; K_0 is the mobility of Hg^+ at 1-mm pressure, 0°C in cm/sec/volts/cm; p is the pressure in mm; T^+ is the positive ion temperature in °K; and T_e is the electron temperature in °K. If we use for K_0 the value given by Mierdel[4] of 220 cm/sec/volt/cm, and if we consider experiments where the gas temperature is nearly equal to the temperature of the liquid mercury, we consistently find values around 2000°K for the electron temperature, as calculated from the above expression using our measured values of τ_1 (see Table I). With the same pressures but higher temperatures, on the other hand, we observe an unexpected increase of the time constant, which results in a smaller value of T_e (e.g., $p=0.1$ mm, $T^+=380$°K gives $T_e=1000$). This is presumably owing to the effect of heating, which reduces the density of metastables in the afterglow. Metastables would diffuse faster to the walls at higher temperature, thus increasing the probability of transitions $2^3P_0\rightarrow 2^3P_1$.

TABLE I.

p	T^+	T_e (calculated)
0.1 mm	355	2100
0.2 mm	371	2170
0.3 mm	388	1930

As we have previously stated, we can estimate the recombination coefficient as about 5×10^{-9} from the curved portion of the light intensity curve. This value is higher than the theory of such processes would predict for a radiative recombination of the type

$$Hg^++e\rightarrow Hg+h\nu.$$

This fact, although noted for many other gases, might lead us to expect that there are also some molecular ions present and that recombination between molecular ions and electrons proceeds at a much faster rate than expected from the theory. The molecular ions would be formed in triple collisions involving one atomic ion and two neutral atoms. The straight portion of the light curve is associated, as we have seen, with the emission of an intense continuum. It is quite probable that the excited molecules giving rise to this spectrum are produced in collisions between a metastable mercury atom and two neutral atoms in reactions of the type

$$Hg(2^3P_0)+Hg(1^1S)+Hg(1^1S)\rightarrow Hg_2'+Hg.$$

At low pressures, the density of metastable atoms is principally limited by diffusion to the walls. Using, for the diffusion coefficient of metastables, the kinetic theory value $D=cl/3$, where c is the velocity and l the mean free path of the particle, D is about 25 at 400°K and at 1 mm pressure. This would correspond to

$$\tau_{\text{metastables}}=\frac{1}{(\pi^2/a^2)+(5.8/R^2)}\frac{1}{D}=12 \text{ milliseconds}.$$

At pressures of about 0.1 mm, the time constant should

[10] Lord Rayleigh, Proc. Roy. Soc. (London) **A116**, 702 (1927).
[11] H. Hamada, Phil. Mag. **12**, 56 (1931).
[12] J. Stark and G. Wendt, Physik. Z. **14**, 564 (1913).

be about 1 millisecond, which is closely equal to the observed time constant for light intensity decay. This value is not very different from the value corresponding to electron density decay at the same pressure.

When the pressure is increased above 1 mm, the electron decay becomes faster. Since the electron density curve is found to be exponential, the possibility of recombination as the process responsible for electron removal is excluded. The hypothesis of attachment of electrons to neutral mercury atoms seems to explain the data fairly well. If η is the attachment coefficient, the electron density n satisfies the following equation:

$$dn/dt = -\eta n_a n,$$

where n_a is the density of neutral atoms. The associated time constant

$$\tau_1 = 1/(\eta n_a)$$

should decrease proportionately with pressure at constant temperature. This is found experimentally. At constant pressure, an increase with temperature is expected and is also observed. From our measured τ_1, we calculate

$$\eta = 1/(\tau_1 n_a) = 2\times 10^{-14}.$$

Attachment loss is often described in terms of the attachment probability per collision, which in this case would be about 2×10^{-7}. The appropriate quantum computation[13] shows that the attachment probability in Hg should increase with decreasing electron energies below 1 ev. The calculated attachment probability is of the order of 10^{-6}, using an electron affinity of 1.79 ev which had been found[14] by a semi-empirical method. Our results indicate that this value of the electron affinity is too high, a fact already suggested by the failure of some observers to find negative ions in mercury vapor.[15]

We find that the time constant associated with the light intensity decay goes through a maximum at about the same pressure as the one at which the slowest electron decay is observed. When the pressure is increased further, the light intensity decays extremely rapidly (Fig. 7) and time constants are about those observed by Alpert and others.[9] This is explained by the competition between two processes for the destruction of metastable atoms in the 2^3P_0 state. The first of these is diffusion to the walls, which becomes negligible as the pressure is increased; the second, transitions $2^3P_0 \rightarrow 2^3P_1$, which become more frequent as the pressure is increased. For example, at a pressure of 3 mm and at 50°C, we expect about 100 times more collisions with the necessary amount of energy for this transition than at 0.1-mm pressure and 80°C. Consequently, the continuum at 3300A is expected to become relatively more intense compared to the continuum at 4800A, a fact that we observed and which has already been noticed[16] after moderate heating of a discharge tube.

Electron density data becomes poor as the pressure reaches the range 5–10 mm. This is related to an increase of the real part of the complex conductivity. From the recent results obtained by Adler,[17] who observed a maximum of the real component at 9-mm pressure for a frequency of 8400 megacycles and an electron temperature of about 8000°K, it can be calculated that a maximum should occur in our case at about 7-mm pressure.

V. CONCLUSIONS

The rate of electron density decay is determined at low pressure by ambipolar diffusion and at higher pressures by attachment. Some recombination is present and probably accounts for the line spectrum and part of the band spectrum in the afterglow (especially the bands at 3448A and 3480A). The greatest part of the light intensity, however, probably comes from formation of excited molecules in collisions between neutral and metastable atoms. The density of metastable atoms, upon which the light intensity depends, is determined in the afterglow by diffusion at low pressures and by collision processes at higher pressures.

Interpretation of the results is made complex by the presence of metastables in the plasma. These are the source of many effects which are coexistent with the processes involving electrons and ions. The fact that in the pressure range studied recombination loss was not found to become predominant is quite remarkable. Our assumption that the high pressure decay is mainly due to attachment needs to be substantiated by other investigations; in particular, by introducing mass spectrography in the afterglow to identify the ions present.

One of the authors (P. D.) is greatly indebted to the Centre National de la Recherche Scientifique for the award of a generous scholarship, which made this work possible.

[13] H. S. W. Massey and R. A. Smith, Proc. Roy. Soc. (London) A155, 472 (1936).
[14] George Glockler, Phys. Rev. 46, 11 (1934).
[15] U. Stille, An. Physik 17, 635 (1933).
[16] W. M. Nielsen, Phys. Rev. 38, 888 (1931).
[17] Fred Adler, J. Appl. Phys. 20, 1115 (1949).

Electron Removal in Argon Afterglows*

A. REDFIELD† AND R. B. HOLT
Department of Physics, Harvard University, Cambridge, Massachusetts
(Received February 16, 1951)

Ambipolar diffusion and recombination occurring in argon after the cut-off of a pulsed microwave discharge have been studied. The electron density and spectroscopic data obtained indicated that ambipolar diffusion is operative at low pressures, supplemented by recombination which is characterized by a relatively low recombination coefficient. At high pressures, electron removal is principally by recombination which is characterized by a relatively high value of recombination coefficient.

I. INTRODUCTION

ESSENTIALLY the same techniques as those described in the preceding paper[1] have been applied to the investigation of the various electron removal processes in argon afterglows. The reader is referred to this previous paper for a discussion of the method, definition of terms, etc.

The previous work bearing most directly on the present investigation[2] found a value of 3×10^{-7} cm³/ion-sec for the recombination coefficient, α, between positive ions and electrons in argon. This value, along with those reported for several other gases, is considerably in excess of theoretical values[3] for direct radiative recombination. This fact makes detailed investigation of the *mechanism* of electron removal processes particularly important.

Earlier work[4] using probe techniques after the cut-off of a direct current discharge gave values of 2×10^{-10} cm³/ion-sec for the recombination coefficient, but with low probable accuracy owing to a number of uncertainties in the measurements, the nature of which is discussed in the original paper. These measurements included a number of observations concerning the qualitative behavior of the spectrum of the afterglow as a function of time. As will be pointed out, many of these are in agreement with the present work. The recent work on the use of double probes rather than single ones for following plasma decays[5] makes it clear that it is necessary to be very careful in the interpretation of single-probe measurements after excitation has been removed.

II. HIGH PRESSURE MEASUREMENTS

In the pressure range above approximately 10 mm, electron removal from an argon plasma of moderate density (about 10^9 electrons/cm³) is practically entirely by a recombination-type mechanism. The plots of $1/n$ *vs* t are very good, straight lines. With moderate power input to the microwave discharge (10 microsecond pulses, a few hundred-watts peak power), the recombination coefficient was found to be 1.1×10^{-6} cm³/ion-sec independent of pressure over the range 20 to 30 mm.

In this same pressure range, an anomalous effect occurs with high input power (on the order of 1 kw peak). Two separate and distinct values of the recombination coefficient can be observed, depending on the excitation conditions, for the same sample of gas. This phenomenon is reproducible (at least with a spread of values on the order of ±15 percent), and gives values of 1.1×10^{-6} cm³/ion-sec and 0.65×10^{-6} cm³/ion-sec for moderate and high input power, respectively. The existence of these two distinct values for the recombination coefficient at short (250–600 microseconds) and long (greater than 1 millisecond) times in the same afterglow can be observed under proper excitation conditions; the electron decay curve (plotted as $1/n$ *vs* t) shows two straight portions separated by a curved transition region in this case. This effect has been observed only at the highest pressure studied (30 mm). It is thought that the existence of the lower value of the recombination coefficient associated with higher power excitation may be caused by the formation of a second type of ion (possibly a metastable; possibly a different molecular species) which recombines with its own characteristic coefficient. This explanation, although not entirely satisfactory, seems preferable, to us, to explanations based on variations of electron density across the discharge, etc. A similar effect has been noted in nitrogen.[6]

Our values should be compared with those of Biondi and Brown,[2] who obtained 0.3×10^{-6} cm³/ion-sec. In general, these results certainly agree in order of magnitude with ours. Biondi and Brown expressed doubt, also, as to the purity of their argon. We took normal precautions in the preparation of our argon samples; spectroscopic observations of the discharge produced by microwave breakdown revealed only the singly ionized argon spectrum. Prolonged exposures with the discharge excited by a cw 2.5-mc oscillator showed traces of CO bands. In one bottle in which traces of nitrogen were detected, no differences as regards elec-

* Assisted by the ONR.
† Present address: Department of Physics, University of Illinois, Urbana, Illinois.
[1] P. Dandurand and R. B. Holt, Phys. Rev. **82**, 868 (1951).
[2] M. A. Biondi and S. C. Brown, Phys. Rev. **76**, 1697 (1949).
[3] E. C. G. Stueckelberg and P. M. Morse, Phys. Rev. **36**, 16 (1930).
[4] C. Kenty, Phys. Rev. **32**, 624 (1928).
[5] E. O. Johnson and L. Malter, Phys. Rev. **80**, 58 (1950).
[6] R. Bryan, paper presented at the 1950 Conference on Gaseous Electronics.

tron removal were noted. Biondi and Brown used higher excitation power and longer breakdown pulses than we did. It should be pointed out that many of our measurements cover two orders of magnitude in time and in electron density, which gives us considerable confidence in the results.

Figure 1 shows a plot of light intensity (plotted as $1/I^{\frac{1}{2}}$ *vs* t) and electron density (plotted as $1/n$ *vs* t) data for a typical case. In all cases, the light intensity decay curve was found to approach an exponential behavior with a time constant of about 8 milliseconds at long times in the afterglow. This is owing to fluorescence of the quartz containers; this effect has also been noted in hydrogen afterglows.[7] Subtraction of the fluorescence background indicates that a two-body process is responsible for the radiation observed, since $1/I^{\frac{1}{2}}$ is then proportional to t. The fluorescence limited the range of observation, but the proportionality between light intensity and the square of electron density was found to be valid for a variety of pressures, ion densities, and excitation powers. Measurement of the total radiated energy in the visible and near ultraviolet spectrum gave an average value of 0.05 ev per electron removed; this indicates that a considerable number of the electrons are removed by radiative capture, but that this is probably not the primary process responsible for the electron density decay. These measurements, of course, apply only to the total intensity radiated. The qualitative changes in the spectrum as a function of various conditions will be discussed in a later section.

III. LOW PRESSURE MEASUREMENTS

Electron removal in the pressure range 0.5 to 1.5 mm agrees very well with amnipolar diffusion theory at low electron densities; plots of $\log n$ *vs* t are good straight lines. A value of the product of ambipolar diffusion coefficient and pressure, $D_a p$, of 150 mm Hg·cm²/sec, corresponding to a value for the mobility, μ_0, of 1.4 cm²/volt sec (at 0°C, 760 mm), were obtained. These values were reproducible within ±10 percent. Recent work[8] has shown the existence of both atomic and molecular ions with differing mobilities in argon under certain conditions. Since we did not employ a mass spectrometer in this investigation, we are unable to state positively which type of ion the above measurements refer to; however, the spectroscopic data which we did obtain suggest that we were probably dealing largely with atomic ions.

In this pressure range, it is also possible to get a good estimate of the recombination coefficient by measuring the perturbing effect of recombination on electron-density decay due to ambipolar diffusion. The approximate equation under these conditions is

$$-dn_0/dt = 0.54\alpha n_0^2 + D_a n_0/\Lambda^2,$$

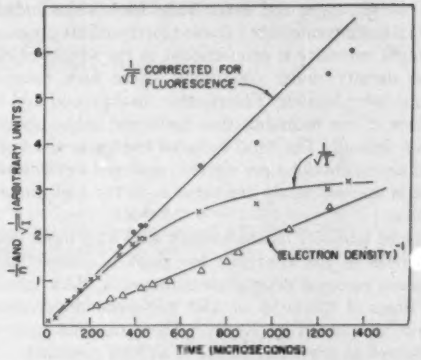

FIG. 1. Typical electron density and light intensity data at 20 mm pressure. Although not shown in this figure, the electron density data fall on the straight line out to 13 milliseconds.

where n_0 is the density of electrons at the center of a cylindrical container (with a bessel function radial and sinusoidal vertical distribution), and $1/\Lambda^2$ is $(\pi/h^2) + 2.4/r^2$ (h is height, r is radius of container). This equation is derived in the Appendix. The exact solution of this equation is

$$n_0/(1+0.54\alpha\tau n_0) = \text{const} \times \exp(-t/\tau),$$

where τ is Λ^2/D_a. The recombination coefficient α is evaluated by choosing $\alpha\tau$ so as to obtain the best fit of the experimental data with the above equation. Data from a typical run is shown in Fig. 2. The actual treatment of the data involves plotting $n_0/(1+0.54\alpha\tau n_0)$ on a logarithmic scale *vs* t for several values of the parameter $\alpha\tau$, selecting the best straight line, and evaluating τ (and thus α) from the slope of this line. This method gives an average value of 4×10^{-8} cm³/ion-sec for α in this pressure range. This is considerably lower than the value obtained at higher pressure.

Evaluation of the recombination coefficient from electron removal data at intermediate pressures is difficult because of the competition of the two electron removal processes on an almost equal basis; however,

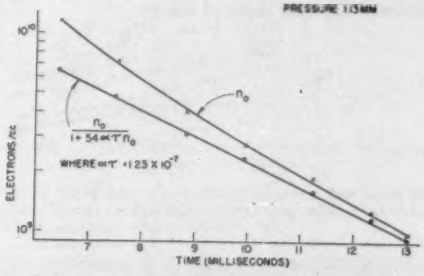

FIG. 2. Typical electron density data at low pressure, showing the method of estimating the recombination coefficient α.

[7] J. M. Richardson and R. B. Holt, Phys. Rev. **81**, 153 (1951).
[8] J. A. Hornbeck, Phys. Rev. **80**, 297 (1950).

we can set upper and lower limits for α which indicate that it has intermediate values at intermediate pressures.

Light intensity is proportional to the square of electron density under conditions where such measurements were feasible. Fluorescence background and low values of the recombination coefficient make observations difficult. The total radiated energy in the visible and near ultraviolet per electron removed *by recombination* is approximately the same as in the high pressure region.

Light intensity measurements, with high input power at times in the afterglow too short to permit simultaneous electron density measurements, show maxima at times of the order of 150 microseconds. A similar effect was noted by Kenty.[4] These maxima were not observed at low input power or at high pressures.

IV. SPECTROSCOPIC RESULTS

Analysis of the spectra obtained yields the following results (Paschen notation used): *In the visible*, at low pressures, the $2p-ms$ and $2p-md$ transitions are enhanced in the afterglow relative to the $1s-2p$ and $1s-3p$ transitions; also, the $1s-3p$ are enhanced relative to the $1s-2p$. This is in accord with Kenty's results;[4] he also reports that the higher term transitions within the $2p-ms$ and $2p-md$ are enhanced. Our data show only slight evidence of this enhancement; it is not so striking as in Kenty's experiment.

At higher pressures, the situation is reversed (!). The $1s-2p$ and $1s-3p$ transitions are definitely enhanced in the afterglow over the $2p-ms$ and mp transitions. Comparing the spectra during the discharge at different pressures, the $1s-2p$ and $1s-3p$ transitions are enhanced with increasing pressure.

Our data in the ultraviolet are incomplete. There seems, in general, to be little change in the spectrum between the discharge and the afterglow, although faint bands degraded to the ultraviolet with heads at about 3370 and 3578A were observed in the afterglow, in one case, at 18 mm pressure.

At high pressures, a continuum, in addition to a many-line spectrum, is observed during the discharge and in the afterglow, with no striking enhancement in the afterglow. This continuum contains an appreciable fraction of the total radiated energy.

V. CONCLUSIONS

At high pressures, electron removal in argon afterglows is principally by a recombination-type mechanism. Total light intensity measurements indicate that while radiative type capture probably plays some part in the removal, it is probably not the principal effect operative. Detailed analysis of the spectra observed does not suggest to us any very definite conclusions concerning the mechanism of either the radiative or the nonradiative part of this removal.

At low pressures, ambipolar diffusion is operative, supplemented by recombination which is characterized by a coefficient considerably smaller than that obtained at higher pressures. The spectrum emitted shows some qualitative difference from that at high pressures, but does not lead us to any definite conclusions regarding the explanation for the observed difference in recombination coefficients.

APPENDIX

The exact equation governing the electron removal process is

$$(-\partial n/\partial t)=\alpha n^2+D_a\nabla^2 n, \tag{1}$$

where n is the electron density as a function of space and time, and α and D_a are defined above. The boundary conditions are that $n=0$ on the surface of the container, which is cylindrical. This equation and boundary conditions cannot easily be solved exactly or by a straightforward perturbation method in α.

If α equals zero, the solution to the equation is a sum of cylindrical harmonics with different exponential decays in time. We make our measurements at a time long enough in the afterglow so that the high order solutions have decayed and we have essentially a first-order distribution:

$$n=n_0\sin(\pi z/h)J_0(2.4r/R), \tag{2}$$

where $n_0=\text{const}\times\exp(-t/\tau)$, and τ is defined above.

When α is dufficiently large to perturb the solution, the approximation we make is to assume that the spatial distribution of the electrons is the same as in the unperturbed case. Then substituting Eq. (2) into Eq. (1) and integrating over the volume of the container, we get

$$(-dn_0/dt)=0.54\alpha n_0^2+(n_0/\tau).$$

We feel that this approximation is somewhat preferable to that of Biondi and Brown,[2] who assume that the recombination process behaves as if the distribution were uniform, with a density equal to the average density of the unperturbed distribution. This approximation gives

$$(-dn_0/dt)=0.27\alpha n_0^2+(n_0/\tau).$$

The Stark Effect of the Ammonia Inversion Spectrum*

D. K. Coles and W. E. Good
Westinghouse Research Laboratories, East Pittsburgh, Pennsylvania

and

J. K. Bragg and A. H. Sharbaugh
General Electric Research Laboratory, Schenectady, New York

(Received February 26, 1951)

A detailed study of the Stark effect of certain transitions in the inversion spectrum of ammonia has been made. The hyperfine structure due to quadrupole and electric field effects is in agreement with theory. The value 1.468±0.009D has been obtained for the dipole moment. Consideration has been given to possible second-order effects; their influence is shown to be negligible.

I. INTRODUCTION

In this paper we shall report the results of a detailed study of the Stark effect for the $J,K=1,1$; 2,2; and 3,3 transitions in the inversion spectrum of $N^{14}H_3$. In these experiments the combined effects of the electric field and the quadrupole moment of the nitrogen nucleus have been observed and accounted for. The experimental results from the 1,1 and 2,2 transitions in the intermediate and strong-field regions have been compared with exact solutions of the appropriate secular equations. The strong-field behavior of the 3,3 line is in agreement with the calculation of Jauch.[1] A precise value of the dipole moment of ammonia has been obtained from the strong-field measurements of the three lines.

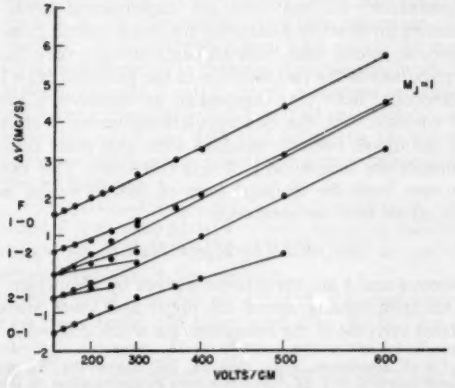

FIG. 1. Stark effect for $J,K=1,1$ ammonia line. Solid lines were computed; circles denote experimentally observed points.

II. EXPERIMENTAL

Measurements of the Stark effect were made using both straight detection[2] and Stark modulation;[3] however, better resolution was obtained with the former method. The constant used in conversion of the voltage applied to the wave guide electrode to electric field strength was checked by a measurement of the dipole moment of OCS. Our value of 0.712±0.005D is in agreement with the careful determinations of Shulman and Townes.[4]

The solid lines of Figs. 1–3 show the computed Stark effect as a function of the electric field for the $J,K=1,1$; 2,2; and 3,3 ammonia lines, respectively. The experimentally determined values, represented by the circles, are seen to be in excellent agreement with theory. In the case of unresolved lines, the observed resultant line falls at the approximate center of gravity of the group. A photograph of the triplet characteristic of the $M_J=1$ transition is shown in Fig. 4. The data given in Fig. 3 for the $J,K=3,3$ line were taken with a

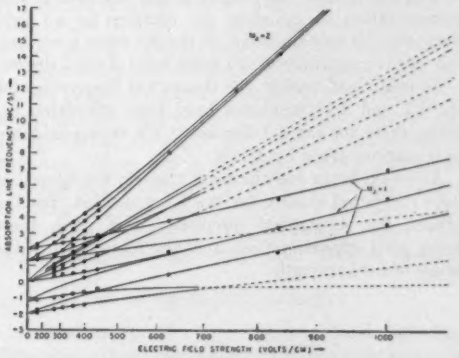

FIG. 2. Stark effect for $J,K=2,2$ ammonia line. Lines shown partially dotted are forbidden at high field strengths. Circles denote experimentally observed points.

* The work reported in this paper was done independently in the Research Laboratories of the General Electric Company and the Westinghouse Electric Corporation. When it was discovered that duplication had occurred, it was decided to publish the results jointly.

[1] J. M. Jauch, Phys. Rev. **72**, 715 (1947). The separation of the two satellites of the $M_J=1$ component is just half that given by Jauch; in his quantity Ω, given just after Eq. (18) in this reference, the factor 2 should not appear. This had no effect on the strong field frequencies of the other Stark components.

[2] See, for example, W. E. Good, Phys. Rev. **70**, 213 (1946).

[3] R. H. Hughes and E. B. Wilson, Jr., Phys. Rev. **71**, 562 (1947).

[4] R. G. Shulman and C. H. Townes, Phys. Rev. **77**, 500 (1950).

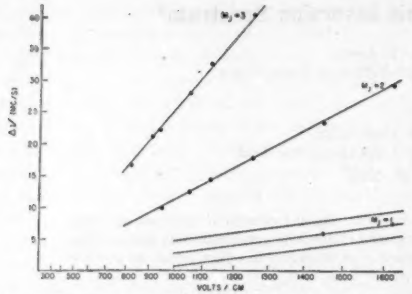

FIG. 3. Stark effect for $J,K=3,3$ ammonia line. Solid lines were computed; circles denote experimentally observed points.

Stark modulation spectrograph, and this triplet structure was not resolved.

The dipole moment was calculated from measurements taken at field strengths of 1150 to 2500 volts per cm, using the strong-field approximation

$$\Delta\nu=(2\mu^2E^2/\Delta h^2)[K^2M_J^2/J^2(J+1)^2]\times10^{-12},$$

where μ is the dipole moment in esu, E is the field strength in esu, Δ is the frequency in mc/s of the J,K ammonia line, and $\Delta\nu$ is the Stark splitting in mc/s. Within the experimental error, the dipole moments obtained from measurements of the three transitions were the same. An extended series of measurements of the $M_J=2$ component of the 2,2 line yielded the value 1.468±0.009D.

III. THEORETICAL

(a) Calculation of the Spectrum

The calculation of the energy levels of ammonia in an electric field has been discussed in detail by Jauch.[1] It was found most convenient to use the strong field representation to calculate the energies for all field strengths; for any transition in the inversion spectrum, this leads to equations which are at most of third degree.

As mentioned earlier, the theoretical frequencies for the 1,1 and 2,2 transitions have been calculated exactly, those for the 3,3 line being the strong-field approximations given by Jauch.

As an aid in the identification, the relative intensities were computed exactly for the 1,1 transition. For the others, the strong-field intensities were used, these being good approximations over the major part of the range of field strengths.

FIG. 4. Photograph of the Stark effect pattern characteristic of the $M_J=1$ transition in ammonia.

The strong-field Stark spectrum of any transition shows the characteristic triplet structure of the $M_J=1$ component owing to the fact that the quadrupole hamiltonian couples the states $M_J=1$, $M_I=-1$ and $M_J=-1$, $M_I=1$ which remain degenerate in the electric field. All other components ($|M_J|\neq1$) are single in the strong field approximation.

(b) Possible Corrections to the Energies

There are several small corrections to our computed energies which have been ignored as smaller than the experimental uncertainties. First, the Stark term was taken as $(\pm\mu^2E^2/\Delta)[K^2M_J^2/J^2(J+1)^2]$, where Δ is the separation of the two components of the inversion doublet in question. The contribution of interaction terms between levels of different J can easily be calculated for the 1,1 transition to be less than 0.1 percent of the principal Stark term; for transitions involving higher J, the correction becomes steadily less important.

Second, the first-order quadrupole hamiltonian was used; for nitrogen, the quadrupole coupling is so small that second-order corrections are negligible.

Third, the slight deviations from the quadrupole rule due to magnetic interaction of the nuclear spin with off-diagonal terms of the electronic orbital angular momentum[5] are less than the experimental uncertainties involved in measuring the Stark splitting; indeed, at strong field, such an effect changes only the separations of the two satellites of the principal $M_J=1$ component from that component, an influence it has in common with the quadrupole hamiltonian. Values of the dipole moment obtained from any other components are independent of this correction. This can be seen from the diagonal term of this correction in the strong field representation,

$$2\{[aK^2/J(J+1)]+b\}M_IM_J,$$

where a and b are the constants given by Henderson.[5] This term equally affects the upper and lower Stark states involved in the transitions for which $\Delta M_J=0$.

[5] R. S. Henderson, Phys. Rev. 74, 107, 626 (1948). We are much indebted to J. H. Van Vleck for a communication on this subject.

Luminous Fronts in Pulsed Gas Discharges

RICHARD G. FOWLER, JACK S. GOLDSTEIN,* AND BERYL E. CLOTFELTER†
University of Oklahoma, Norman, Oklahoma
(Received January 11, 1951)

Recent experiments in which an intense luminosity was observed in side tubes connected to an electrodeless discharge ring have been duplicated using a discharge with electrodes. It is concluded that a large part of the luminosity observed is the result of a moving front of disturbance rather than the decay of an ejected tongue of excited gas. Measurements made of the velocity of advance of this front and its dependence on gas parameters show that the front advances into the side tube with a speed proportional to the estimated velocity of sound in the hot gas of the main discharge. Intense continua accompany discrete spectra in the fronts, particularly in hydrogen, indicating that recombination may play a large part in producing the luminosity observed.

I. INTRODUCTION

IN a previous paper[1] a description has been given of recent investigations of the phenomenon termed by Rayleigh[2] "the long lifetime of the Balmer lines in hydrogen." The fingers of luminosity which can be observed in side tubes connected to an electrodeless discharge tube have been shown to arise from excited systems created at or near the point at which the luminosity is observed. Earlier theories[3] had considered the luminosity to be of the nature of an afterglow in a thermally ejected jet of luminous gas.

Rayleigh observed that the effect found in hydrogen with his apparatus was not present in nitrogen. Further investigation of this limitation seemed desirable. It was suspected that the failure to observe these effects in nitrogen was in some way associated with insufficient energy transfer resulting from the rather poor coupling present in the electrodeless discharge apparatus. Accordingly, more effective means were sought for supplying pulsed energy to the tube. A simple and successful arrangement was found in which a charged condenser was connected abruptly to a pair of metal electrodes sealed into the tube. With this apparatus, the experiments described before[1] have been largely verified and greatly extended.

The apparatus employed in this investigation consisted of three main parts: a vacuum system of standard design, an electrical discharge circuit, and an optical system for studying the discharge.

While some variations in discharge tube construction have been made, the tubes used thus far had many common features. They were constructed of Pyrex glass, with cylindrical aluminum alloy electrodes 1.5 cm in diameter and 1.5 cm long sealed in opposite ends of a tube 15 cm long and 1.7 cm in diameter. Midway between these electrodes a side tube was sealed onto the main discharge tube and connected to the vacuum system.

The discharge is initiated by connecting a charged condenser to the tube through a vacuum switch, using a circuit in which inductance and resistance have been reduced to a low value by means of short heavy leads. Capacitors of 6 to 12 μfd capacitance have been used, charged to potentials ranging from a minimum value of around 800 volts up to 5000 volts. Oscillatory frequency and decrement measurements indicate total distributed inductances of approximately one microhenry and mean total resistances of the order of a tenth of an ohm in a typical circuit. Estimates of the maximum current in the discharge lie in the neighborhood of 10^4 amperes.

The optical system was arranged to give simultaneous photographs of the advance of the luminosity down the side tube with a rotating mirror, and of the spectral composition at every point along its course with a spectrograph. The entire discharge tube was masked, except for a slit 1-mm wide down the length of the side tube. This slit served jointly for the mirror and for the spectrograph; the latter was operated with an open collimator at a distance of several meters. The mirrors used were turned at various measured speeds up to 60 rps. Some of the data reported in Table I are less satisfactory than others because they were taken with an inferior mirror used in the early stages of the investigation.

Since no attempt was made to control the position of the slit image at the instant of discharge, a film holder was constructed as a section of a one-meter circle, center at the mirror, on which three 4″×5″ films could be mounted. Three photocells were arranged using an adjacent face of the mirror, so that when light struck any film, it also struck the corresponding one of the three photocells and thus tripped one of three glow tubes as a tell-tale, indicating which film had been exposed.

II. EXPERIMENTAL RESULTS

Studies conducted with the apparatus described above have duplicated qualitatively and quantitatively the results obtained previously in the electrodeless ring discharge.[1,2] Because of the better coupling which existed in the discharge between electrodes, the range of pressures over which the phenomenon could be observed was greatly extended. It was also found possible to

* Now at Cornell University, Ithaca, New York.
† Now at Ohio State University, Columbus, Ohio.
[1] R. J. Lee and R. G. Fowler, Phys. Rev. 81, 457 (1951).
[2] R. J. Strutt, Proc. Roy. Soc. (London) 183, 26 (1944).
[3] H. Zanstra, Proc. Roy. Soc. (London) 186, 236 (1946).

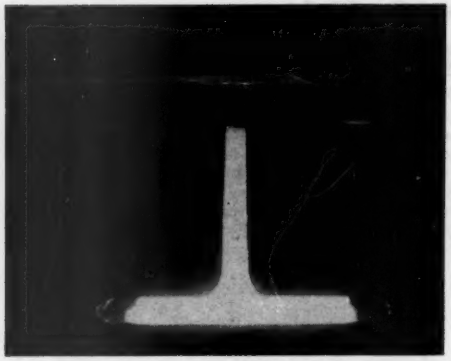

FIG. 1. Abrupt condenser discharge through a tube with side arm. Luminosity is sharply terminated by constriction.

produce fronts in every kind of gas examined, even nitrogen, in contrast to the results of Rayleigh. A direct photograph of a typical discharge is shown in Fig. 1. As would be expected, the discharge is extremely brilliant, related as it is to the well-known photoflash lamp. Two remarkable things which are indicated by the figure are, first, that the intensity in the sidearm is not a trivial luminosity, but is fully as bright as the discharge in the main tube, and second, that the luminosity has a definite point of termination. This point of termination coincided with a constriction in the tube, and is definitely related to it, since it was found impossible to force the luminosity past the constriction.

TABLE I. Measured velocities of luminous fronts under various conditions.

Gas	Pressure (mm Hg)	Condenser potential (volt)	Front velocity ($\times 10^{-5}$) (cm/sec)
Hydrogen[a]	0.2	5000	18
Hydrogen	1.0	2000	10.5
Hydrogen	1.0	3000	12.5
Hydrogen	1.0	4000	10.5
Hydrogen	1.0	5000	17.0
Hydrogen	5.0	3000	8.0
Hydrogen	5.0	4000	9.0
Hydrogen	5.0	5000	10.0
Hydrogen	11.5	5000	7.0
Hydrogen	25.0	5000	3.0
Hydrogen[b]	5.0	2000	7.0
Hydrogen	5.0	3000	8.0
Helium	0.9	2300	12.0
Helium	0.9	4200	15.0
Helium	1.2	3000	13.0
Helium	1.4	3000	10.0
Helium	2.5	2000	5.5
Helium	5.0	2000	6.0
Helium	9.0	2000	7.5
Neon	1.2	2500	5.0
Neon	4.0	2000	4.5
Neon	0.9	2800	9.0
Nitrogen	0.9	2800	9.0
Nitrogen	2.5	2500	7.5
Argon	0.7	2300	6.5
Argon	9.0	1900	3.5
Argon	10.0	2500	2.0

[a] At 6.0 μfd capacitance.
[b] These and all subsequent data at 12.0 μfd capacitance.

A summary of measurements of front velocity is given in Table I. Velocity measurements were made in the following manner. The discharge was photographed with the slit over the tube and the rotating mirror stationary in order to establish a vertical reference on the film. When the discharge was photographed with the mirror in motion, it was observed that the slit image was inclined to the vertical. The angle of inclination was related through the geometry of the optical system to the velocity of advance of the luminosity. Frontal velocities will be seen from Table I to increase directly with condenser energy, inversely with molecular mass, and inversely with pressure.

Two special aspects of frontal behavior were noted. The fronts, especially in heavy gases, decelerate as they advance. Figure 2 shows the curvature of front which accompanies this. Curvature of the fronts is one effect which has made velocity measurements uncertain thus far. Figure 2 is not a typical mirrorgram, since it shows an infrequently observed phenomenon which we have terms an "echo" front. A return front is seen to come up the tube after the primary front had gone down it. This effect is observed only in tubes in which the course of the primary front is impeded by a constriction, and represents a reflection of the front at and by the constriction. It is related to the termination of the luminosity seen in Fig. 1. The velocity of the echo will be seen to be greater than that of the primary front. Little is known yet about the echo fronts. They have been observed in argon, neon, and air; but so far, not in helium, hydrogen, or nitrogen. However, no special effort was made to produce them at the time they were first encountered. They were not consistently observed even in argon where they were most common. In the belief that this phenomenon contains a clue to the mechanism of the discharge, a careful investigation of it is currently under way.

It has been previously reported[1] that the fronts were observed to have a greater range in tubes of large diameter than in small ones. An attempt was made to measure this effect. Three tubes of different diameters were joined like spokes of a wheel to a main discharge tube of a larger diameter. By photographing the discharge tube from one end, it was possible to determine how far the fronts moved down each tube before reaching the same level of luminosity. A list of such ranges is given in Table II, taken at 5000 volts potential difference across a 6 μfd capacitor. As might be expected, an intensity function of the form $I=A(r_0^2-r^2)\times\exp(-\alpha z)$ fits the data to a fair degree.

Examination of Fig. 2 shows that the discharge is not completely described by the term "front," since other luminosity is observed in the side tube subsequent to the front. Frequently, photographs show belated extra fronts which travel with a great variety of speeds. Tests have shown that this later luminosity can be markedly

affected by varying the discharge circuit constants, without any great effect on the primary fronts. The equipment used for these experiments heretofore has been inadequate to resolve these luminosities, if such resolution be possible. Far more precise equipment, freed from optical aberrations and uncertainties in the discharge circuit, is currently being set up for pursuit of this problem under sponsorship of the Office of Naval Research.

The spectra taken of the discharges showed a high level of excitation. HeII, NII, and NIII have been observed. Such a degree of excitation might well have been expected in the main discharge tube, since the discharge there is probably little more than a low pressure spark, on which a number of studies have already been made.[4] To find it, in what amounts to a backwater, off from the main stream of the discharge current is surprising and further evidence that this phase of the discharge cannot be regarded as a mere afterglow.

Spectra taken of the hydrogen discharges present an intense continuum setting in around H_ϵ, and extending beyond 3000A. The Balmer series is not complete, but terminates near H_θ, going beyond that point into a pure continuum. The suppression of the series at this point is probably caused by the intense local fields of the ion cloud from within which the atoms are radiating.

The continuum was observed to be little abated at 0.2 mm Hg pressure, and no trace of the multiline spectrum was detected at any pressure. We have concluded, therefore, that we were dealing with an atomic continuum enhanced by the intense local fields of the surrounding ion cloud. On this assumption, an experiment was performed to ascertain in what manner the continuous radiation and discrete radiation contributed individually to mirrorgrams made using the entire radiation. A mirrorgram taken through an NiO_2 filter which transmitted the entire continuum and the series members above H_θ was compared with a mirrorgram taken through a sodium nitrite solution which eliminated the continuum and series members above H_θ. No significant difference in form was noted between these mirrograms.

It was next undertaken to determine whether there was any appreciable difference between the times of emission of the quantized and unquantized radiation. The upper-half of the discharge tube slit was covered with the one filter and the lower half with the other. No appreciable relative displacement of the two segments of the trace could be distinguished. It was concluded that the quantized and unquantized radiations are therefore related in being emitted at each successive point of the tube within the same brief time interval. From the lateral breadth of trace on the mirrorgrams, it was estimated that the duration of emission is not over 1 or 2 microseconds. From the complete absence of dislocation of the trace in the two filter experiment, we estimate that the interval between emission of the continuous and discrete transitions cannot be more than 10^{-7} second, or roughly the mean relaxation time of an atomic system.

[4] L. B. Loeb, *Fundamental Processes of Electric Discharge in Gases* (John Wiley and Sons, Inc., New York), p. 476.

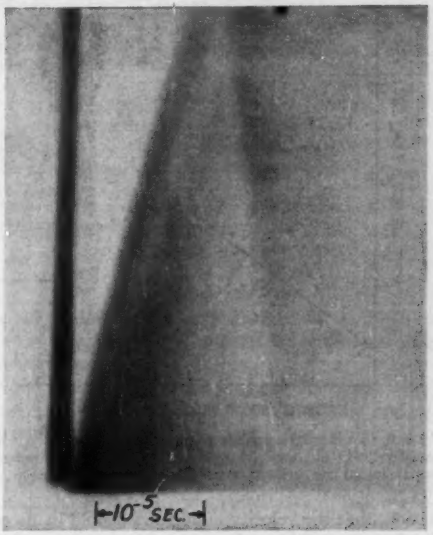

FIG. 2. Rotating mirror photograph of side arm of tube shown in Fig. 1. Stationary reference image at left. Lines parallel with stationary trace give instantaneous distributions of luminosity along side arm.

III. DISCUSSION

There seems little reason to believe that the phenomenon of the ejected luminosity is an afterglow, as suggested by Rayleigh and Zanstra. Rather, the evidence shows that it should be regarded as an active exciting process of considerable overall significance in the disposal of the energy supplied to the discharge. The near-sonic nature of the velocities observed, the reflection of an echo pulse returning at higher speed as if into a hotter gas, the general frontal character of the discharge, all combine to suggest kinship with shock waves and high amplitude acoustical effects.

A descriptive theory of the fronts is easily obtained. Treating them as shock waves shows, in first approxi-

TABLE II. Range of the luminosity in helium.

Pressure mm Hg	Tube diameters 3.30 mm	5.0 mm	8.9 mm
3.00	— cm	6.6 cm	9.6 cm
0.80	2.4	6.0	6.0
0.60	2.4	4.8	5.4
0.35	1.7	3.6	4.8
0.12	1.1	3.0	3.6

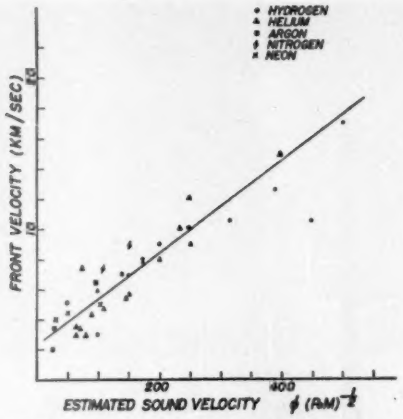

FIG. 3. Plot of front velocities of luminosity against an estimated sound velocity obtained by combination of capacitor potential (volts), initial gas pressure (mm Hg), and molecular weight.

mation, that the velocity of advance should be proportional to the velocity of sound in the hot gas which is advancing down the tube. That is,

$$V \propto p^{\frac{1}{2}} D^{-\frac{1}{2}}.$$

But if the pressure p is identified with the mean kinetic energy per unit volume in the hot gas, it can be approximately expressed as proportional to the initial condenser energy divided by the volume of the tube. The density D is jointly proportional to the pre-discharge gas pressure p_0 and the molecular weight m. It is therefore to be expected that if ϕ is the initial condenser potential,

$$V \propto \phi (p_0 m)^{-\frac{1}{2}}.$$

Within the experimental error, this expression accounts for the observed data of Table I. A graph of these results is given in Fig. 3. On a basis of this agreement it seems evident that the descriptive theory that has been suggested, i.e., that the frontal luminosity is a concommittant of a shock wave resulting from the abrupt discharge of the condenser, has merit. The problem of the mechanism by which the condenser energy is actually delivered to the front by the gas is not covered. Neither is the question of the radiative mechanism in the front, on which point the experimental indications are that recombination plays a major role. Answers to both of these questions will probably hinge on studies of the deceleration and reflection of the fronts and on improved spectrograms of the discharge. It seems unlikely that better measurements of the initial velocity can do anything more than confirm the results of Fig. 3, and hence assure us that the front is caused by an abruptly expanding hot gas. Although it has been necessary, owing to the experimental misapprehension on which it was based, to reject the theory of Zanstra as applying in its present form to this side-tube luminosity; nevertheless, a modification of it seems likely to be ultimately successful, since the level of excitation is so high in this luminosity that volume recombination appears to be an important process in the fronts themselves. This conclusion is based on the interpretation we place on the experiments, which show that the observed Balmer continuum, although extraordinarily intense, is properly associated with the atomic ion. This conclusion is strengthened by the fact that the radiation of these continuous quanta occurs at essentially the same spot as the radiation of the discrete quanta. Thus far this viewpoint is the simplest one which we have found to be qualitatively consistent with all observations.

IV. CONCLUSIONS

Extension of the studies of the Rayleigh afterglow phenomenon have verified earlier conclusions that the luminosity is not an afterglow but is excited *in situ*.

Volume recombination is in all probability a major process in radiative disposal of gas energy in the phenomenon of Rayleigh luminosity. Large ion concentrations and a high degree of excitation have been found to exist, and must be contributing factors.

A major part of the luminosity moves as a front or wave of decreasing speed, for which the initial value has been shown to be related to the velocity characteristic of sound in the gas of the main discharge tube after adiabatic heating with the energy of the condenser.

Whatever mechanical process acts to advance the luminosity, it must be one capable of undergoing reflection at discontinuities in the tube.

Gravitational Transverse-Transverse Waves

ADRIAN E. SCHEIDEGGER
Department of Physics, Queen's University, Kingston, Ontario, Canada
(Received October 6, 1950)

It has been stated in earlier papers that no system of masses subject to their gravitational field alone can radiate gravitational waves, if the approximation procedure of Einstein, Infeld, and Hoffman is adopted. However, this result was proved explicitly only for radiation of purely longitudinal and transverse-longitudinal waves.

In this paper a new deduction of that fact for the types of waves mentioned above, is given. Furthermore, the case of transverse-transverse waves is extensively investigated, and it is shown explicitly that there cannot be any radiation of such waves either.

IT has been stated in several earlier papers by Infeld and the present author[1,2] that no system of masses subject to their gravitational field alone can radiate gravitational waves. This result, as contained in the paper mentioned first[1] was announced at a meeting of the American Physical Society[3] and gave rise to a considerable flow of discussion. I am particularly grateful to Professor P. G. Bergmann of Syracuse for having drawn my attention to some points which need further clarification, which I shall try to give here.

It is known[1] that the Einstein, Infeld, and Hoffmann (EIH) solution[4] of the gravitational field equations is ambiguous to the extent of containing or not containing a certain set of terms which heretofore have been interpreted as representing radiation by earlier authors working in this field. In our last papers,[1,3] however, it was pointed out that these terms can be created or annihilated by appropriate coordinate transformations, and, thus, that they cannot have a physical meaning. Specifically, it was shown that if a "radiation" term was inserted for γ_{0s} (0=time, s=space coordinates)[5] in the lowest approximation, no physical effects can be expected to arise from it. This gave the explanation of why many earlier calculations (for instance, that of Hu[6]) for detecting radiation effects from γ_{0s}-terms have never yielded any sensible results.

However, it has been consistently overlooked by all people working in this field, and it actually should have been anticipated, that γ_{0s}-terms can be annihilated by suitable coordinate transformations, for it is well known that one can set up a linear approximation to Einstein's field theory; the ensuing equations have solutions of the wave type. In this linearized theory only the waves where $\gamma_{st}\neq 0$ have a physical meaning, as the others can be annihilated by coordinate transformations. This fact is contained, for example, in Bergmann's book[7] (p. 188). The only waves that cannot be wiped out in the linear approximation refer to $\gamma_{st}\neq 0$ and are commonly called transverse-transverse waves.

Now, it should be noted that the linearized theory mentioned above should be identical to the first approximation of the exact theory, thus implying that radiation terms of the type $\gamma_{0s}\neq 0$ can be wiped out by a suitable coordinate transformation in the lowest approximation of the EIH method. Hence, it follows that such terms cannot represent any real physical effects.

In this instance the example chosen in reference 1 for demonstrating the application of the general theory actually yielded no new results. The only gravitational waves for which the possibility of annihilation by a coordinate transformation is not so obvious beforehand are thus the transverse-transverse waves. It may be worthwhile, therefore, to demonstrate here explicitly that transverse-transverse waves, too, are physically nonexistent; i.e., that they can be wiped out by choosing a suitable coordinate system.

The way the approximation procedure works is that starting from ${}_2\gamma_{00}$ (Newtonian expressions) the higher terms of the expansion of the γ's are calculated in the following sequence:

$$ {}_{2k}\gamma_{00},\ {}_{2k+1}\gamma_{0s},\ {}_{2k+2}\gamma_{st},\ {}_{2k+2}\gamma_{00},\ \cdots, \tag{1a} $$

$$ {}_{2k+1}\gamma_{st},\ {}_{2k+1}\gamma_{00},\ {}_{2k+2}\gamma_{0s},\ {}_{2k+3}\gamma_{st},\ \cdots. \tag{1b} $$

By analogy with electrodynamics[8] we call the first row (1a) "nonradiative" terms, the second one (1b) "radiative" terms. For the calculation of any one term, only terms to the left of it in either row are needed. This is an important feature of this theory and has not been emphasized properly in the earlier publications. It is due to the fact that the "interaction" between radiative and nonradiative terms takes place only through nonlinear combinations of the previous terms. It is consistent to assume that all the radiative terms are equal to zero; then one obtains the ordinary stationary solution of EIH.

The way to introduce transverse-transverse waves into the approximate procedure is to choose

$$ {}_{2k+1}\gamma_{st}=f_{st}(x^0), \tag{2} $$

[1] L. Infeld and A. E. Scheidegger, Can. J. Math. 3, in press.
[2] A. E. Scheidegger, Proc. 2nd Can. Math. Congr. Vancouver (1949).
[3] A. E. Scheidegger and L. Infeld, Phys. Rev. 79, 201 (1950).
[4] A. Einstein and L. Infeld, Can. J. Math. 1, 209 (1949).
[5] For the definition of the gravitational potentials $\gamma_{\mu\nu}$, see Bergmann, reference 7, p. 182.
[6] N. Hu, Proc. Roy. Irish Acad. 51A, 87 (1947).
[7] P. G. Bergmann, *Introduction to the Theory of Relativity* (Prentice-Hall Inc., New York, 1947).
[8] L. Infeld, Phys. Rev. 53, 836 (1938).

where f_{st} is an arbitrary function of time. It should be noted that such a choice is compatible with the general requirements of the approximation procedure, since both the field equations and the usual coordinate conditions are satisfied at the stage of the approximation concerned. Hence, a term of the form (2) can always be inserted, and the question is whether any physical effects do arise from it. Setting $k=1$ in (2) corresponds to the solution of the linearized gravitational field equations representing transverse-transverse waves.

Similarly, one can choose other radiative terms for starting a radiation expansion, but we have dealt with them in our earlier publications.

If we want to investigate how an assumption of a term of the form of Eq. (2) will alter the higher order terms, we may observe that an alteration can only occur in terms that are in (1) to the right of the newly inserted radiation term (2). Therefore, if we can set up a coordinate transformation that wipes out the value for ${}_{2k+1}\gamma_{st}$ chosen by (2) and furthermore affects only γ's to the right of the latter in (1), then it is clear that in the new coordinate system the solution of the field equation is the nonradiative solution.

This, however, can be done in the present case. It has been demonstrated in our earlier papers[1,2] that the effect of a transformation of the order k in the approximation parameter λ

$$x^s = x^{s*} + \lambda^k \, {}_kT^s \tag{3}$$

is

$$\left.\begin{aligned} {}_k\gamma_{st}{}^* &= {}_k\gamma_{st} + \delta_{st}\,{}_kT^r{}_{,r} - {}_kT^s{}_{,t} - {}_kT^t{}_{,s}, \\ {}_k\gamma_{00}{}^* &= {}_k\gamma_{00} - {}_kT^r{}_{,r}, \\ {}_{k+1}\gamma_{0s}{}^* &= {}_{k+1}\gamma_{0s} - {}_kT^s{}_{,0}. \end{aligned}\right\} \tag{4}$$

Similarly, for a transformation

$$x^0 = x^{0*} + \lambda^k \, {}_kT^0 \tag{5}$$

we have obtained

$$\left.\begin{aligned} {}_{k+1}\gamma_{st}{}^* &= {}_{k+1}\gamma_{st} + \delta_{st}\,{}_kT^0{}_{,0}, \\ {}_{k+1}\gamma_{00}{}^* &= {}_{k+1}\gamma_{00} + {}_kT^0{}_{,0}, \\ {}_k\gamma_{0s}{}^* &= {}_k\gamma_{0s} + {}_kT^0{}_{,s}. \end{aligned}\right\} \tag{6}$$

In these formulas the comma denotes differentiation with respect to the coordinates following after it, the time coordinate being replaced by λx^0 according to the well-known rules of the EIH procedure. Equations (4) and (6) were obtained straightforwardly by substituting (3) and (5) into the EIH procedure.

It is easy to see that an appropriate choice of ${}_{2k+1}T^s$ in Eq. (3) will reduce the term (2) to zero, affecting otherwise only terms to the right of ${}_{2k+1}\gamma_{st}$ in (1). All one has to do is to choose ${}_{2k+1}T^s$ such that

$$-f_{st} = \delta_{st}\,{}_{2k+1}T^r{}_{,r} - {}_{2k+1}T^s{}_{,t} - {}_{2k+1}T^t{}_{,s}. \tag{7}$$

This can always be done.

This procedure is in accordance with the general rules outlined above. One can, however, raise some objections to it from a more phenomenological standpoint, for it will be noted that by formula (7) there will be induced a change in ${}_{2k+1}\gamma_{00}$ which, although it is to the right of ${}_{2k+1}\gamma_{st}$ in (1), is of the same order as the latter. Furthermore, it is evident that in this particular case ${}_{2k+1}\gamma_{st}$ is not needed for calculating ${}_{2k+1}\gamma_{00}$, so that one could argue that it is not possible to get rid of the radiation term ${}_{2k+1}\gamma_{st}$, but only to shift it into ${}_{2k+1}\gamma_{00}$. This argument is, of course, unsound, because, as should be noted, in solving the equation leading to ${}_{2k+1}\gamma_{00}$ an arbitrary time function can be added which may be chosen so that the term ${}_{2k+1}\gamma_{00}$ again vanishes.

However, this treatment may not seem entirely satisfactory, and, therefore, it will be shown that a coordinate transformation can be set up which annihilates (2) without introducing new expressions into terms of the same order. This can be achieved by taking Eqs. (4) and (6) together; then the change induced by transforming x^μ into $x^{\mu*}$ (the Greek index denoting both space and time coordinates) is

$$\left.\begin{aligned} {}_{2k+1}\gamma_{st}{}^* &= {}_{2k+1}\gamma_{st} + \delta_{st}\,{}_{2k+1}T^r{}_{,r} - {}_{2k+1}T^s{}_{,t} \\ &\quad - {}_{2k+1}T^t{}_{,s} + \delta_{st}\,{}_{2k}T^0{}_{,0}, \\ {}_{2k+1}\gamma_{00}{}^* &= {}_{2k+1}\gamma_{00} - {}_{2k+1}T^r{}_{,r} + {}_{2k}T^0{}_{,0}. \end{aligned}\right\} \tag{8}$$

In these equations T^s and T^0 must be chosen so that

$$\left.\begin{aligned} \delta_{st}({}_{2k+1}T^r{}_{,r} + {}_{2k}T^0{}_{,0}) - {}_{2k+1}T^s{}_{,t} - {}_{2k+1}T^t{}_{,s} &= -f_{st}, \\ {}_{2k+1}T^r{}_{,r} &= {}_{2k}T^0{}_{,0}. \end{aligned}\right\} \tag{9}$$

This can always be done, as may be checked by a straightforward calculation.

Thus, we see that, apart from the results obtained in earlier papers, transverse-transverse waves also, cannot have a physical meaning within the scope of the EIH approximation procedure.

Furthermore, the deduction of the meaninglessness of all other types of waves except transverse-transverse waves given here by comparison with the linearized theory provides one more strong indication that calculations of the type made by Hu[6] will never yield any sensible results.

In conclusion, I should like to emphasize once more that the notion of "gravitational radiation" is used in the present paper in the same sense as it was used when introduced by Infeld[8] into the EIH procedure.

Thus, it may well be that solutions of Einstein's field equations exist which describe a wave, but those solutions cannot be obtained by the approximation procedure which is under consideration here. If a series expansion of such a wave solution is made in terms of powers of $1/c$, then it is seen[1] that it either can be transformed away, or else contains singular terms which are not permitted by the prescriptions of EIH. It is interesting to compare these facts with a similar situa-

tion in electromagnetic theory, where one can "disguise" a retarded Lienard-Wiechert potential in such a manner that no one will recognize it by its odd terms; i.e., one can carry out a gauge transformation that gets rid of the odd terms. Nevertheless, this solution leads to a net loss of energy in the system.

The difference between electromagnetic and gravitational theory, however, is that the motion of the sources of the electromagnetic field is completely arbitrary. Therefore, there is no objection against introducing singular terms in the Lienard-Wiechert solution, so long as Maxwell's equations are satisfied. In the gravitational case, however, the motion of the sources is contained in the field equations—at least as long as one deals with a system which is only subject to its own gravitational field. Thus, when talking about possible solutions of Einstein's field equations, one has to observe the prescriptions of the EIH method as well. The latter stands or falls with the assumption that no arbitrary singularities be introduced at higher stages of the method than the first one. Therefore, "disguised" retarded potentials have to be excluded.

Thus, it should be kept in mind that neither the question of the existence of gravitational waves as possible solutions of Einstein's field equations under the assumption of weird sources, nor the secular behavior of a double star, is discussed here. But we do state that there are no physically different solutions than the EIH one if a system of masses subject to their own gravitational field is considered.

PHYSICAL REVIEW VOLUME 82, NUMBER 6 JUNE 15, 1951

The Solution of the Boltzmann Equation for a Shock Wave

H. M. MOTT-SMITH
Atomic Energy Commission Staff, Washington, D. C.
(Received January 22, 1951)

It is pointed out that the distribution of molecular velocities in a strong shock wave in a gas is bimodal. Assuming the distribution function to consist of a sum of two maxwellian terms with temperatures and mean velocities corresponding to the subsonic and supersonic streams, it is found that the space distribution, as determined by the solution of a transport equation, is appropriate to describe a shock wave. Comparison of the solutions of two different transport equations shows that the assumed distribution changes relatively slowly with time and so is an approximate stationary solution of the Boltzmann equation for strong shocks. The shock thickness found is considerably greater than that given by previous theories. The nominal thermal conduction coefficient is negative in the after part of the shock.

I. INTRODUCTION

THE calculation of the thickness of a shock wave in a gas, and of the distribution of density and velocity within it, is an interesting and challenging problem because of the failure of all standard methods of attack. In treatments of this problem by the equations of fluid mechanics, it was early recognized[1–3] that the effect of viscosity and of heat conduction must be taken into account. Solutions of the Navier-Stokes equation for a special case were obtained by Becker,[4] who treated the coefficients of viscosity and of thermal conduction as constants. This solution was improved by Thomas,[5] who allowed for the temperature variation of these quantities. The thickness calculated for strong shock waves by the Becker and Thomas theories are very different, and they show the importance of correct estimation of the dissipative effects in a shock wave. At the same time, the thickness obtained even by the Thomas theory is of the order of only a few mean free paths. This throws doubt on the validity of the Navier-Stokes equations in a shock wave, for, according to the kinetic theory, these equations are only valid if the physical quantities defining the state of the gas change only by a small fractional amount in the distance of a mean free path.

In the kinetic theory of gases, the equations of fluid flow are obtained by solving the Boltzmann equation for the space and velocity distribution of the molecules by the Enskog-Chapman (E-C) method. This is a series solution for the distribution function, in which the expansion parameter is effectively $l/\Delta x$, where l is the mean free path and Δx the distance in which the distribution function changes by an appreciable fraction of itself.[6] The first, or zero-order terms give the equations of flow of a frictionless fluid, the first-order terms give the Navier-Stokes equation, and the second-order terms the so-called Burnett equation.[7] Thomas[5] made some estimate of the effect of the Burnett terms, but since the value of $l/\Delta x$ for a shock wave indicated by

[1] W. V. M. Rankine, Trans. Roy. Soc. (London) **160**, 277 (1870).
[2] Lord Raleigh, Proc. Roy. Soc. (London) **A84**, 247 (1910).
[3] G. I. Taylor, Proc. Roy. Soc. (London) **A84**, 371 (1910).
[4] R. Becker, Z. Physik **8**, 321 (1923).
[5] L. H. Thomas, J. Chem. Phys. **12**, 449 (1944).

[6] For an exposition of this theory, see, for instance, Chapman and Cowling, *The Mathematical Theory of Non-Uniform Gases* (Cambridge University Press, Teddington, England, 1939).
[7] D. Burnett, Proc. Math. Soc. (London) **40**, 382 (1935).

the Thomas theory is not small, it is doubtful whether the whole E-C theory is applicable to a shock wave, as pointed out by Thomas and by Burnett himself. This question has apparently been settled by Wang-Chang,[8] who made a thoroughoing treatment of the shock-wave problem on the Enskog-Chapman theory, taking into account the effect of the third-order terms in the distribution function. She shows that the E-C theory yields expressions for the velocity distribution function in a shock wave and for its reciprocal thickness, which are series in powers of $M-1$, where M is the Mach number, and that these series converge so slowly that it is doubtful whether they have any validity unless N is only very slightly greater than 1, perhaps about 1.2. We must therefore conclude that the whole E-C theory is inapplicable to strong shocks.

In the E-C theory, the distribution function is represented as a "skewed" maxwellian one, the function having only one strong maximum. Now, in a strong shock wave, whose thickness is only a few mean free paths, we can expect that a considerable number of the maxwellian molecules of the bounding supersonic and subsonic streams penetrate into the center of the shock. This suggests that what characterizes the velocity distribution in a strong shock is the existence of two maxima of comparable magnitudes, i.e., that the distribution is bimodal in the sense of the theory of statistics. To represent such a distribution, a series of monocentric orthogonal functions such as is used in the E-C theory is inappropriate, since, for instance, the series of Sonine polynomials representing a bimodal sum of two maxwellian terms is only asymptotically convergent, as can easily be verified. To use orthogonal function theory, it would seem to be necessary to define and employ orthogonal functions of a two center variety, analogous to the molecular orbitals of quantum theory.

Instead of this, an approximate solution of the Boltzmann equation for a strong shock is here obtained by a method which can be regarded as the first step in an iterative scheme. For the initial solution, the distribution function is assumed to be the sum of two maxwellian terms with different temperatures and mean velocities but with unassigned space densities. The densities are obtained from the solution of a transport equation for u^n, where n is an integer and u is the component of molecular velocity in the stream direction. This choice is made for mathematical convenience. The calculations are carried out for $n=2$ and $n=3$. Comparison of the results gives some indication of the adequacy of the assumed distribution function. The agreement is not too close, the difference between shock-wave thickness calculated from the two cases amounting to 5 percent to 25 percent, depending on the Mach number. Nevertheless, the discrepancy for strong shocks is far less than that between the Becker and Thomas formulas. One can expect, perhaps, that for M greater than about 2, the present solution gives a better picture of conditions in a shock wave than any of the hydrodynamical theories. On the other hand, while the solution makes the reciprocal of the shock thickness proportional to $M-1$ for $M-1$ small, as found by existing theories, the constant of proportionality is wrong. Thus, the present solution stands in need of correction for weak shocks.

The thicknesses found are considerably greater than those predicted by the Thomas theory. The thickness approaches a limit for infinite Mach number, but this limit is about twice as great as that given by the Thomas formula. It is interesting that previous treatments, as they improved their basic assumptions, have successively given increasing estimates for shock-wave thickness and so probably still err in defect. Probably the thickness given by the present treatment errs in excess and so provides an upper limit to the thickness; for the velocity distribution function used represents about the maximum in difference from "quasi-equilibrium" types of distribution, such as are assumed in the E-C theory underlying hydrodynamical treatments.

Since the space density, mean velocity, and all other macroscopic quantities are obtained directly from the distribution function, the solution involves only the Mach number and collision cross sections derivable from the intermolecular laws of force. It circumvents any use of fluid flow equations, or of the concepts of temperature, viscosity, and thermal conduction. It is evident *a priori* that these latter quantities here have only a nominal significance, for, because of the bimodal distribution, averages over the distribution lose their physical importance as defining the flow. For instance, very few molecules have the average velocity, few have a random component of velocity corresponding to the "temperature," and so on. Nevertheless, temperature, coefficient of heat conduction, etc. are still formally definable, and it is interesting to examine how they behave in the present model of a shock wave. It turns out that the heat flow vector is constant in direction throughout the shock, being always directed from the subsonic to the supersonic stream as expected. But for M greater than about 2, the "temperature" reaches a maximum within the shock, so that the gradient changes sign. Thus, the nominal thermal conduction coefficient is actually negative in the after part of the shock. Since the calculated thermal conduction coefficient is a second-order quantity sensitive to small errors in the assumed velocity distribution, too much significance cannot be given to the quantitative aspects of these results. Qualitatively, however, we can give them some significance, and they illustrate drastically the reason for failure of treatments of the shock-wave problem based on concepts of macroscopic fluid flow.

The calculations can be interpreted in a different way, as determining the time rate of change of an initially given distribution. From the time-dependent

[8] C. S. Wang-Chang, *On the Theory of Thickness of Weak Shock Waves*, University of Michigan, Dept. of Engineering Report UMH-3-F (APL/JHU CM-503), August 19, 1948 (unpublished).

transport equations for u^2 and u^3, one can calculate the life (i.e., the time for e-fold change) of the assumed velocity distribution considered as established initially. This life turns out to be of the order of ten to a hundred times the mean free time between molecular collisions, depending on the Mach number. Since, for an arbitrary initial distribution, the life, in general, would be of the order of the mean free time itself, the assumed distribution is something of an approximation to a steady-state solution.

It is to be noted that, for polyatomic gases, the treatment of the shock-wave problem by the ordinary Boltzmann equation, as here, is only an approximation due to relaxation effects. In a strong shock we must expect lack of equipartition of energy between translation and vibrational modes. An accurate treatment of this effect would require, at the same time, the consideration of the effect of the internal degrees of freedom in modifying the laws of collision. To the extent that laws of collisions between spheres are adequate, a treatment like the present one takes some account of relaxation effects by assuming the ratio of specific heats γ to have a value greater than the normal one. A comparison of the theory with experimental results would determine the effective γ and so permit an estimate of the importance of relaxation effects. The present theory is scarcely accurate enough to make such a comparison very significant, but it does give a dependence of shock-wave thickness on γ different from that given by the Thomas theory, and may be closer to the facts for strong shocks.

Finally, the concept of a double distribution, here used for a shock wave, may be appropriate in other cases, such as those of flame fronts, detonation fronts, and in the analysis of the interaction between a boundary layer and a shock front. Physically, the picture given is that of a mixture of two gases of different temperatures and mass motions. The Boltzmann equation describes the interaction between these two components and plays the role of an equation of chemical reaction. The reaction is a "bimolecular" one, corresponding to the fact that linearized solutions of the Boltzmann equation do not apply here and that its essentially quadratic character must be taken into account. In tring to set up such a theory, for instance for the two dimensional case applicable to analysis of boundary layer-shock-wave interaction, we would have eight variables to deal with for each of the two gas components; namely, the molecular density, temperature, and two space components of mass velocity. It would be natural to assume that in each volume element the directions of the mass velocities of the two gas components lay in the same line to a first approximation. As will be seen in the following, this provides two equations of a Rankins-Hugoniot character, relating the mass velocities and temperatures, and reducing the number of independent variables to six. The transport equation for mass, momentum, and energy would provide four more equations, linear in the space densities, and there would be left two more relations to be obtained from the Boltzmann equation, quadratic in the space densities, which might be taken to be two more transport equations for judiciously selected quantities. Such an analysis naturally would be complicated, but it would be required if the transition from boundary layer to shock wave is only a few mean free paths in thickness, which may well be the case.

III. THE TRANSPORT EQUATION

If $\mathbf{c}$ is the vector velocity of a molecule, u its x-component, t the time, and $f(x, \mathbf{c})$ the distribution function, the one-dimensional transport equation for an arbitrary $\Phi(\mathbf{c})$ is

$$\frac{\partial}{\partial t}\int \Phi f d\mathbf{c}+\frac{\partial}{\partial x}\int u\Phi f d\mathbf{c} = \int\int\int (\Phi'-\Phi) f f_1 g d\Omega d\mathbf{c}_1 d\mathbf{c}, \quad (1)$$

where g is the magnitude of the relative velocity $\mathbf{g}$ of a colliding pair:

$$\mathbf{g}=\mathbf{c}_1-\mathbf{c}. \quad (2)$$

Also, f_1 means $f(\mathbf{c}_1)$, and Φ' means $\Phi(\mathbf{c}')$, where $\mathbf{c}'$ is the velocity of the first molecule after collision; $d\Omega$ is a differential cross section.[9] We now assume f to be of the form

$$f=f_\alpha+f_\beta, \quad (3)$$

with

$$f_\alpha=n_\alpha(x)(m/2\pi kT_\alpha)^{\frac{1}{2}}\exp\{-(m/2kT_\alpha)(\mathbf{c}-\mathbf{i}u_\alpha)^2\}, \quad (4)$$

and similarly for f_β with α replaced by β throughout. Here $\mathbf{i}$ is a unit vector in the x direction; m, the mass of a molecule; and k, Boltzmann's constant. The parameters T_α, c_α, T_β, c_β are assumed independent of x and t. Substitution of Eqs. (3) and (4) in Eq. (1) gives an equation of the form

$$\frac{\partial}{\partial t}\int \Phi f d\mathbf{c}+\frac{\partial}{\partial x}\int u\Phi f_\alpha d\mathbf{c}+\frac{\partial}{\partial x}\int u\Phi f_\beta d\mathbf{c} = I_{\alpha\alpha}+I_{\alpha\beta}+I_{\beta\alpha}+I_{\beta\beta}, \quad (5)$$

where

$$I_{\alpha\beta}=\int\int\int (\Phi'-\Phi) f_\alpha f_{\beta 1} g d\Omega d\mathbf{c}_1 d\mathbf{c}. \quad (6)$$

If in Eq. (6) we interchange $\mathbf{c}_1$ and $\mathbf{c}$ (which does not change the value of the integral), and also interchange α and β, throughout, the integral is restored to its original form, except that $\mathbf{c}_1$ and $\mathbf{c}$ must be interchanged in $\Phi'-\Phi$. Thus we get $I_{\beta\alpha}$ by effecting the last change alone in the integral in Eq. (6). Also, since f_α and f_β are maxwellian,

$$f_\alpha' f_{\alpha 1}'=f_\alpha f_{\alpha 1}, \quad f_\beta' f_{\beta 1}'=f_\beta f_{\beta 1},$$

[9] The notation conforms generally to that of reference 6.

and from this, it follows[10] that

$$I_{\alpha\alpha}=I_{\beta\beta}=0. \tag{6a}$$

First take Φ in turn equal successively to the collisional invariants **1**, u, and $c^2+(2/m)E_i$, where E_i is the internal energy of a molecule. For these, the right-hand side of Eq. (5) vanishes; and for the steady state $\partial f/\partial t=0$, we obtain the following equations expressing the conservation of matter, momentum, and energy:

$$\begin{gathered} n_\alpha u_\alpha+n_\beta u_\beta=R, \\ n_\alpha(u_\alpha{}^2+c_\alpha{}^2)+n_\beta(u_\beta{}^2+c_\beta{}^2)=P, \\ n_\alpha u_\alpha(u_\alpha+ac_\alpha{}^2)+n_\beta u_\beta(u_\beta{}^2+ac_\beta{}^2)=Q, \end{gathered} \tag{7}$$

in which R, P, Q are constants of the flow,

$$c_\alpha{}^2=kT_\alpha/m, \quad c_\beta{}^2=kT_\beta/m, \tag{8}$$

$$a=N_i+5=2\gamma/(\gamma-1), \tag{9}$$

where N_i is the number of internal degrees of freedom, and γ is the ratio of specific heats. The last of Eq. (7) assumes equipartition of energy between internal and translational degrees of freedom. In accordance with the introductory remarks, we can expect a for polyatomic gases to have an effective value less than the normal one because of relaxation effects.

In order that Eq. (7) be consistent when regarded as determining n_α, n_β, we must have

$$(u_\alpha{}^2+c_\alpha{}^2)/u_\alpha=(u_\beta{}^2+c_\beta{}^2)/u_\beta, \quad u_\alpha{}^2+ac_\alpha{}^2=u_\beta{}^2+ac_\beta{}^2.$$

These equations, when solved for u_β and c_β, give

$$\begin{gathered} u_\beta=[u_\alpha{}^2+ac_\alpha{}^2]/[(a-1)u_\alpha], \\ c_\beta{}^2=[u_\alpha{}^2+ac_\alpha{}^2]/[(a-1)^2u_\alpha{}^2][(a-2)u_\alpha{}^2-c_\alpha{}^2]. \end{gathered} \tag{10}$$

Equations (10), together with the first of Eqs. (7), are equivalent to the Rankine-Hugoniot equations giving the density, velocity, and temperature of the subsonic stream in terms of those of the supersonic stream.[11] Thus, only two parameters in Eq. (3) are independent.

To determine the space densities $n_\alpha(x)$, $n_\alpha(x)$, we need a choice which does not make the right-hand side of Eq. (5) vanish. The simplest choice is $\Phi=u^n$, for which the integrations can be carried out with relative ease. Let $\mathbf{K}$ be the change in the velocity of the first molecule due to the collision, so that

$$\mathbf{K}=\mathbf{c}'-\mathbf{c}=\mathbf{c}_1-\mathbf{c}_1'.$$

Let ψ be the angle between $\mathbf{g}$ and $\mathbf{K}$, θ the angle between $\mathbf{g}$ and $\mathbf{i}$ (the x axis), ϵ the angle between the plane of $\mathbf{g}$ and $\mathbf{K}$, and the plane of $\mathbf{g}$ and $\mathbf{i}$. Then from the laws of collision,

$$\begin{gathered} u'-u=K(\cos\theta\cos\psi+\sin\theta\sin\psi\cos\epsilon), \\ u_1-u=g\cos\theta, \quad K=g\cos\psi, \end{gathered} \tag{11}$$

where u', u_1 are the x-components of $\mathbf{c}'$, $\mathbf{c}_1$. Also if $\mathbf{g}'=\mathbf{c}_1'-\mathbf{c}'$ and χ is the angle between $\mathbf{g}$ and $\mathbf{g}'$, χ is the angle of deflection in the center-of-gravity system and is related to ψ by

$$\psi=\tfrac{1}{2}(\pi-\chi). \tag{12}$$

Let b be the usual collision parameter, which for elastic spheres of diameter σ is given by

$$b=\sigma\sin\psi. \tag{13}$$

Then, for the $d\Omega$ in Eq. (1) we can write

$$d\Omega=bdbd\epsilon. \tag{14}$$

III. THE CASE $\Phi=u^2$

Putting $\Phi=u^2$ in Eq. (6) and using Eqs. (11) and (14), we find

$$\begin{aligned} \int(u'^2-u^2)d\Omega&=\int_0^\infty\int_0^{2\pi}(u'^2-u^2)gbdbd\epsilon db \\ &=2\pi\int_0^\infty\{2u(u_1-u)\cos^2\psi+(u_1-u)^2\cos^4\psi \\ &\quad+\tfrac{1}{2}[g^2-(u_1-u)^2]\cos^2\psi\sin^2\psi\}gbdb. \end{aligned}$$

By the rule under Eq. (6), the corresponding expression in $I_{\alpha\beta}+I_{\beta\alpha}$ is obtained by interchanging u_1 and u in the above and adding the result to the original expression. Doing this, we get

$$\begin{aligned} 2\pi\int_0^\infty&[g^2-3(u_1-u)^2]\cos^2\psi\sin^2\psi gbdb \\ &=\tfrac{1}{2}\pi\psi_{11}{}^{(2)}(g)[g^2-3(u_1-u)^2], \end{aligned} \tag{15}$$

where χ is given by 12 and

$$\phi_{11}{}^{(l)}(g)=\int_0^\infty(1-\cos^l\chi)gbdb \tag{16}$$

is the elementary cross section defined by Chapman and Cowling.[12] Substitution of Eqs. (4) and (15) in Eq. (6) gives

$$\begin{aligned} &I_{\alpha\beta}+I_{\beta\alpha}=n_\alpha n_\beta(m/2\pi kT_\alpha{}^{\frac{1}{2}}T_\beta{}^{\frac{1}{2}})^3 \\ &\times\int\int\exp\{-(m/2kT_\alpha)(\mathbf{c}-\mathbf{i}u_\alpha)^2-(m/2kT_\beta)(\mathbf{c}_1-\mathbf{i}u_\beta)^2\} \\ &\qquad\times\tfrac{1}{2}\pi\phi_{11}{}^{(2)}(g)\{g^2-3(u_1-u)^2\}d\mathbf{c}_1d\mathbf{c}. \end{aligned}$$

Make the transformation

$$\mathbf{c}=\mathbf{i}u_\alpha+\mathbf{F}-\mathbf{G}T_\alpha/(T_\alpha+T_\beta)$$

and

$$\mathbf{c}_1=\mathbf{i}u_\beta+\mathbf{F}+\mathbf{G}T_\beta/(T_\alpha+T_\beta)$$

and express the new coordinate vectors $\mathbf{F}$, $\mathbf{G}$ in terms of spherical polar coordinates F, θ_F, ϕ_F, G, θ_G, ϕ_G, so that $d\mathbf{c}_1d\mathbf{c}=F^2\sin\theta_Fd\theta_Fd\phi_FdF\cdot G^2\sin\theta_Gd\theta_Gd\phi_GdG$. The

[10] See reference 6, pp. 66, 70.

[11] It is to be noted, however, that Eqs. (10) are more general than the Rankine-Hugoniot equations, since they must be satisfied at each point within a shock wave, in case u_α, u_β, c_α, c_β are considered functions of position. Compare remarks in the introduction.

[12] See reference 6, p. 157.

integrations with respect to θ_F, ϕ_F, F, ϕ_G can then be carried out, with the result

$$n_\alpha n_\beta[m/2k(T_\alpha+T_\beta)]^{\frac{1}{2}}\pi^{\frac{1}{2}}\int\int \exp\{-mG^2/2k(T_\alpha+T_\beta)\}$$
$$\times\phi_{11}^{(2)}(\{G^2+2G(u_\beta-u_\alpha)\cos\theta_G+(u_\beta-u_\alpha)^2\}^{\frac{1}{2}})$$
$$\times\{G^2-2G(u_\alpha-u_\beta)\cos\theta_G+(u_\beta-u_\alpha)^2$$
$$-3(G\cos\theta_G+u_\beta-u_\alpha)^2\}\sin\theta_G d\theta_G G^2 dG.$$

Introduce the dimensionless quantities G_0, $u_{\alpha\beta}$ defined by

$$G=[(2k/m)(T_\alpha+T_\beta)]^{\frac{1}{2}}G_0, \tag{17}$$

$$u_\alpha-u_\beta=[(2k/m)(T_\alpha+T_\beta)]^{\frac{1}{2}}u_{\alpha\beta}. \tag{18}$$

Also put

$$r=G_0/u_{\alpha\beta} \tag{19}$$

and replace θ_G by a new variable of integration Z given by

$$r^2-2r\cos\theta_G+1=Z^2. \tag{20}$$

The limits of integration for Z are $|1+r|$ and $|1-r|$, corresponding to $\theta_G=+\pi$ and $\theta_G=0$, the absolute values occurring because Z is proportional to the relative geometry g of a colliding pair, which is always taken to be a positive quantity. Substitution from Eqs. (17)–(20), in the integral yields an expression for $I_{\alpha\beta}+I_{\beta\alpha}$ of the form

$$I_{\alpha\beta}+I_{\beta\alpha}=n_\alpha n_\beta[(2k/m)(T_\alpha+T_\beta)]^2\pi^{\frac{1}{2}}$$
$$\times\int_0^\infty \exp(-G_0^2)H(G_0,u_{\alpha\beta})G_0^2dG_0, \tag{21}$$

where

$$H(G_0,u_{\alpha\beta})=-[(2k/m)(T_\alpha+T_\beta)]^{-\frac{1}{2}}(u_{\alpha\beta}/4r)$$
$$\times\int_{|1-r|}^{|1+r|}\{3z^4+2(1-3r^2)z^2+3(1-r^2)^2\}$$
$$\times\phi_{11}^{(2)}\{u_{\alpha\beta}(2k/m)^{\frac{1}{2}}(T_\alpha+T_\beta)^{\frac{1}{2}}z\}\cdot zdz. \tag{22}$$

The integrations in Eq. (22) can be carried out for any of the laws of intermolecular force for which $\phi_{11}^{(2)}$ has been evaluated. For instance, for elastic spheres of diameter σ,

$$\phi_{11}^{(2)}(g)=\tfrac{1}{4}g\sigma^2$$

(see reference 6, p. 197), and we find

$$H(G_0,u_{\alpha\beta})=H_0(G_0,u_{\alpha\beta}),$$

with

$$H_0(G_0,u_{\alpha\beta})=-(4/105)\sigma^2u_{\alpha\beta}^3(35+35r^2-7r^4+r^6), \quad r<1$$
$$=-(4/105)\sigma^2u_{\alpha\beta}^3(8r^{-1}+56r). \quad r>1 \tag{23}$$

For Sutherland's model of elastic spheres with an attractive field of force, we have (see reference 6, p. 182)

$$\phi_{11}^{(2)}(g)=\tfrac{1}{4}g\sigma^2+(\sigma^2/g)(kS/m),$$

where S is Sutherland's constant, which has the dimensions of a temperature. This gives

$$H=H_0+H_s, \tag{24}$$

where H_0 is given by Eq. (23) and

$$H_s(G_0u_{\alpha\beta})=-\frac{2}{15}\sigma^2u_{\alpha\beta}\frac{S}{T_\alpha+T_\beta}(15-10r^2+3r^4), \quad r<1$$
$$=-\frac{16}{15}\sigma^2u_{\alpha\beta}\frac{S}{T_\alpha+T_\beta}\cdot\frac{1}{r}. \quad r>1 \tag{25}$$

Substituting from Eqs. (24), (23), (25), (19) in Eq. (21) and carrying out the integration, we find, for Sutherland's model,

$$I_{\alpha\beta}+I_{\beta\alpha}=-\tfrac{1}{2}\pi^{\frac{1}{2}}\sigma^2n_\alpha n_\beta\left[\frac{2k}{m}(T_\alpha+T_\beta)\right]^{\frac{1}{2}}$$
$$\times\left[A(u_{\alpha\beta})+\frac{S}{T_\alpha+T_\beta}A_s(u_{\alpha\beta})\right], \tag{26}$$

where

$$A(u)=\left(\frac{1}{u}+\frac{1}{u^3}-\frac{3}{4u^5}\right)\exp(-u^2)$$
$$+\left(2u+\frac{3}{u}-\frac{3}{2u^3}+\frac{3}{4u^5}\right)\operatorname{erf}u, \tag{27}$$

$$A_s(u)=\left(\frac{3}{2}-\frac{9}{4u^2}\right)\exp(-u^2)$$
$$+\left(3u^2-3+\frac{9}{4u^2}\right)\frac{1}{u}\operatorname{erf}u, \tag{28}$$

with

$$\operatorname{erf}u=\int_0^u \exp(-s^2)ds.$$

In Eq. (5), we put $\partial f/\partial t=0$, use Eq. (6a), substitute from Eq. (26) in the right-hand side, and evaluate the integrals on the left for f_α, f_β given by Eq. (4). Introducing the notation (8), the result is

$$u_\alpha(u_\alpha^2+3c_\alpha^2)(dn_\alpha/dx)+u_\beta(u_\beta^2+3c_\beta^2)(dn_\beta/dx)$$
$$+\tfrac{1}{2}\pi^{\frac{1}{2}}\sigma^2(2c_\alpha^2+2c_\beta^2)^{\frac{1}{2}}n_\alpha n_\beta$$
$$\times[A(u_{\alpha\beta})+S(T_\alpha+T_\beta)^{-1}A_s(u_{\alpha\beta})]=0. \tag{29}$$

This is a differential equation determining the densities $n_\alpha(x)$, $n_\beta(x)$ for the steady state. We assume the α stream to be the supersonic one and take the direction of flow to be positive. Then u_α, u_β, and $u_{\alpha\beta}$ are all positive. Let $n_0=n_\alpha(-\infty)$ be the density of the supersonic stream a long way from the shock. The first of Eqs. (7) can then be written

$$n_\alpha u_\alpha+n_\beta u_\beta=n_0u_\alpha. \tag{30}$$

If M is the Mach number of the supersonic stream, then

TABLE I. Values of B_0, B_s, and B_1 as functions of the Mach number, for $\gamma=5/3$ and 7/5.

	$\gamma=5/3$			$\gamma=7/5$		
M	B_0	B_s	B_1	B_0	B_s	B_1
1.0	0	0	0	0	0	0
1.1	0.1204	0.0171	0.0999	0.1122	0.0214	0.0923
1.2	0.2388	0.0568	0.2122	0.2108	0.0477	0.1872
1.3	0.3648	0.0793	0.3163	0.3169	0.0704	0.2835
1.4	0.4640	0.0943	0.4194	0.4196	0.0901	0.3805
1.6	0.6562	0.1202	0.6184	0.6106	0.1211	0.5688
1.8	0.8202	0.1350	0.8040	0.7825	0.1423	0.7575
2.0	0.9583	0.1417	0.9738	0.9346	0.1556	0.9318
2.5	1.2144	0.1381	1.3262	1.2385	0.1646	1.3092
3.0	1.3824	0.1226	1.5872	1.4561	0.1551	1.6028
5.0	1.6758	0.0652	2.1078	1.9586	0.0928	2.2264
10.0	1.8218	0.0195	2.4009	2.1227	0.0297	2.6016
∞	1.8740	0	2.5117	2.2147	0	2.7488

from Eqs. (8) and (9), the fact that u_α is the velocity of the supersonic stream, and the definition of the Mach number, we find that

$$M^2=[(a-2)/a]\cdot(u_\alpha^2/c_\alpha^2). \tag{31}$$

Using Eqs. (30) and (10) to express n_β, u_β, and c_β in terms of n_α, u_α, and c_α, and using the results to eliminate the first three quantities from Eq. (29), we find that everything remaining can be expressed in terms of the Mach number as given by Eq. (31). Equation (29) is finally reduced to the form

$$dv_\alpha/dx+(B/l)v_\alpha(1-v_\alpha)=0, \tag{32}$$

where

$$v_\alpha=n_\alpha/n_0, \quad \text{and} \quad l=\tfrac{1}{2}/\sqrt{2}\pi n_0\sigma^2, \tag{33}$$

so that l is the maxwell mean free path in the supersonic stream.

$$B=\frac{2}{3(a-3)}\left(\frac{a-2}{\pi a}\right)^{\frac{1}{2}} \times\frac{[aM^4+2a(a-2)M^2-a+2]^{\frac{1}{2}}}{[M^2-1][M^2+a-1][aM^2+a-2]} \times\left\{A(u_{\alpha\beta})+\frac{S/T_\alpha}{1+T_\beta/T_\alpha}A_s(u_{\alpha\beta})\right\}, \tag{34}$$

$$u_{\alpha\beta}=[M^2-1][\tfrac{1}{2}a(a-2)]^{\frac{1}{2}} \times[aM^4+2a(a-2)M^2-a+2]^{-\frac{1}{2}}, \tag{35}$$

and

$$T_\beta/T_\alpha=(M^2+a-2)(aM^2-1)/(a-1)^2M^2. \tag{36}$$

The solution of Eq. (32) is

$$v_\alpha=1/(1+e^{Bx/l}), \tag{37}$$

where the constant of integration is determined by choosing the origin $x=0$ as the point where $v_\alpha=\frac{1}{2}$. Solving Eq. (30) for n_β, substituting from Eq. (38), and defining $v_\beta=n_\beta/n_0$, we find

$$v_\beta=(u_\alpha/u_\beta)(1-v_\alpha)=(u_\alpha/u_\beta)/(1+e^{-Bx/l}). \tag{38}$$

Here u_α/u_β can be expressed in terms of the Mach number and a. Equations (37) and (38) complete the solution of the problem. It is seen that v_α decreases from 1 at $x=-\infty$ to 0 at $x=+\infty$, while v_β increases from 0 to u_α/u_β. As we proceed from $x=-\infty$ to $x=+\infty$, one density grows at the expense of the other, and it is apparent that the solution is appropriate to represent a shock wave in which f_α is the velocity distribution in the supersonic stream and f_β that in the subsonic stream. The shock-wave thickness is determined by the quantity B defined by Eq. (34), in which the functions $A(u_{\alpha\beta})$, $A_s(u_{\alpha\beta})$ are defined by Eqs. (27) and (28), and $u_{\alpha\beta}$ is defined by Eq. (35), a by Eq. (9).

IV. THE CASE $\Phi=u^3$

The calculations for this case will only be summarized briefly. The integration over all types of collisions give for the contribution to

$$I_{\alpha\beta}+I_{\beta\alpha}\left[\int_0^\infty\int_0^\pi(u'^3-u^3)gbdedb\right]_{\alpha\beta+\beta\alpha} =\tfrac{3}{4}\pi[u_1+u][g^2-3(u_1-u)^2]\varphi_{11}^{(2)}(g).$$

From this point on, only the case of elastic spheres will be given. Carrying out the integrations by the same methods as before, we find

$$I_{\alpha\beta}+I_{\beta\alpha}=\tfrac{1}{2}\pi^{\frac{1}{2}}\sigma^2n_\alpha n_\beta[(2k/m)(T_\alpha+T_\beta)]^2 \times\int_0^\infty\exp(-G_0^2)K(G_0,u_{\alpha\beta})G_0^2dG_0,$$

where

$$K(G_0,u)=-\frac{4}{35}\frac{aM^2+a-2}{(a-2)(M^2-1)}\{35u^4+35u^2G_0^2 -7G_0^4+G_0^6u^{-2}+(2/3a)(105u^4G_0^2 +21u^2G_0^4+3G_0^6-G_0^8u^{-2})\}, \quad G_0<u$$

$$=-\frac{4}{35}\frac{aM^2+a-2}{(a-2)(M^2-1)}\{8u^5G_0^{-1}+56u^3G_0 -(8/3a)(-u^7G_0^{-1}+12u^5G_0+21u^3G_0^3)\}, \quad G_0>u.$$

Ultimately, an equation of the same form as Eq. (32) is obtained, with B replaced by B_1 given by

$$B_1=\frac{4}{35\pi^{\frac{1}{2}}}\frac{a(a-2)(aM^2+a-2)}{M^2+a-2} \cdot(1C)[aM^4+2a(a-2)M^2-a+2]A_1(u_{\alpha\beta}), \tag{39}$$

$$C=a^2(a^2-4a+1)M^4+2a(a-2)(2a^2-7a+3)M^2 +(a-2)^2(a^2-6a+3), \tag{40}$$

$$A_1(u)=\frac{35}{2}u^2\left[1+\frac{3}{2u^2}-\frac{3}{4u^4}-\frac{3}{a}\left(1+\frac{1}{2u^2}+\frac{1}{4u^4}-\frac{3}{8u^6}\right)\right]\operatorname{erf}u+u^3\left[\frac{1}{2}+\frac{21}{2u^2}+\frac{105}{8u^4}-\frac{1}{a}\left(\frac{105}{4u^2}+\frac{315}{16u^6}\right)\right]\times\exp(-u^2). \quad (40)$$

V. RESULTS

The molecular density n at any point in space is given by $n=n_\alpha+n_\beta=(\nu_\alpha+\nu_\beta)n_0$. Substituting from Eqs. (37) and (38), and expressing u_α/u_β in terms of the Mach number by the use of Eqs. (31) and (10), we find

$$\frac{n}{n_0}=\frac{M^2+a-2+M^2(a-1)e^{Bx/l}}{(M^2+a-2)(1+e^{Bx/l})}. \quad (41)$$

The stream velocity $\bar{u}$ is found by averaging u over the distribution, or more directly from the equation of continuity $n\bar{u}=n_0u_a$. Following the usual practice, we can define the density thickness of the shock wave as equal to $[n(+\infty)-n(-\infty)]/|dn/dx|_{\max}$, and the velocity thickness as $[\bar{u}(-\infty)-\bar{u}(+\infty)]/|d\bar{u}/dx|_{\max}$. Here $|dn/dx|_{\max}$ and $|d\bar{u}/dx|_{\max}$ are, respectively, the maximum absolute value of the density gradient and of the velocity gradient. It turns out that here the two thicknesses are the same and are given by

$$X=4l/B. \quad (42)$$

The reciprocal thickness $1/X$ is therefore, proportional to the quantity B given by Eq. (34) or Eq. (39), according to whether u^2 or u^3 is used in the transport equation.

If we write Eq. (34) in the form

$$B=B_0+B_s(S/T_a), \quad (43)$$

B_0 determines the shock-wave thickness for the elastic sphere model and B_s the correction to this to account for the attractive forces of the Sutherland model. Table I gives B_0, B_s, and B_1 as a function of the Mach number M, where B_1 is defined by Eq. (39), for $\gamma=5/3$ and $\gamma=7/5$. Figure 1 shows a plot of l/x for air and for helium, where x is the calculated shock-wave thickness and l the mean free path in the gas before the shock. The thicknesses calculated by using B of Eq. (34) and B_1 of Eq. (39) are both shown, and for comparison, the thickness given by the Thomas theory. For air, γ has been assumed to be 1.4, although a larger value should probably be used to allow for relaxation effects. It is seen that the thicknesses calculated from the u^2 and the u^3 transport equations are in good agreement for intermediate Mach numbers, but there is some discrepancy for the higher Mach numbers, particularly for monatomic gases.

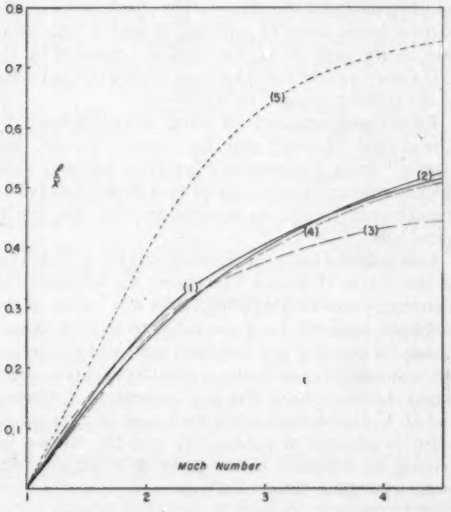

FIG. 1. Ratio of mean free path l to shock-wave thickness X as function of Mach number M. (1) Air at 300°K intake temperature, using u^2 transport equation with Sutherland model. (2) Air at 300°K using u^3 transport equation with elastic sphere model. (3) Helium at 300°K from u^2 equation with Sutherland model. (4) Helium at 300°K from u^3 equation with elastic sphere model. (5) Thomas curve for air.

TABLE II. Half-life of the distribution for various Mach numbers.

M	1.1	2	3	5	10	∞
Half-life	69	144	37	26	17	16

In the time-dependent transport equation, (5), let us assume that f has the form (3) at $t=0$, where $n_\alpha(x)$, $n_\beta(x)$ are chosen to make $(\partial/\partial t)\int f\Phi d\mathbf{c}=0$ for $\Phi=u^2$. Then $n_\alpha(x)$, $n_\beta(x)$ are given by Eqs. (37) and (38). Putting now $\Phi=u^3$, we get an equation for $\partial f/\partial t$ at time $t=0$, from which we can get an equation for say $\partial n_\alpha/n_\alpha\partial t$ at time $t=0$, measuring the fractional change with time of the supersonic component. It turns out that, if we express time in terms of the mean free time $t_{\alpha\beta}$ between collisions of α- and β-molecules, this quantity is independent of position and is given, for $\gamma=7/5$, by

$$\left(\frac{\nu_\alpha}{t_{\alpha\beta}}\frac{\partial t}{\partial\nu_\alpha}\right)_{t=0}=2\left(\frac{5}{2\pi}\right)^{\frac{1}{2}}\frac{M^2(5M^2+3)}{25M^4+90M^2+3}\cdot\frac{4M^2}{M^2+3}\left(5+\frac{30}{M^2}-\frac{3}{M^4}\right)^{\frac{1}{2}}D(u_{\alpha\beta})\cdot\frac{1}{B_0-B_1},$$

where

$$D(u)=(u+1/2u)\int_0^u\exp(-G^2)dG+\tfrac{1}{2}\exp(-u^2).$$

The half-life of the ν_α component, equal to ln2 times the above quantity, measures the half-life of the dis-

TABLE III. Distribution of nominal temperature T and nominal thermal conduction coefficient in the shock wave, for $\gamma=7/5$.

	$M=\sqrt{2}$		$M=2$		$M=\infty$	
ν_α	T/T_β	λ/λ_β	T/T_β	λ/λ_β	T/T_β	λ/λ_β
0	1.000	48.20	1.0000	−155	1.0000	−92.8
0.05	0.998	42.20	1.0002	−459	1.0058	−92.3
0.10	0.995	37.40	1.0002	+354	1.0112	−92.2
0.15	0.992	33.23	0.9997	115.5	1.0178	−92.5
0.20	0.988	29.57	0.9990	64.2	1.0240	−93.5
0.25	0.984	26.31	0.9974	42.2	1.0305	−95.3
0.30	0.979	23.48	0.9956	29.9	1.0380	−98.5
0.40	0.968	18.62	0.9876	16.94	1.0500	−113.5
0.50	0.953	14.76	0.9650	10.26	1.0612	−163.2
0.60	0.935	11.42	0.9526	8.31	1.0667	$\mp\infty$
0.70	0.910	9.08	0.9394	5.09	1.0560	74.1
0.75	0.897	7.99	0.9172	4.05	1.0370	46.6
0.80	0.880	6.99	0.8585	2.42	1.0000	20.6
0.85	0.862	6.11	0.8183	1.834	0.9305	11.28
0.90	0.842	5.31	0.7608	1.350	0.8000	5.80
0.95	0.818	4.06	0.6892	0.958	0.5465	2.53
1.00	0.792	3.89	0.5928	0.658	0	0.664

tribution in terms of $l_{\alpha\beta}$ and is shown in Table II for various Mach numbers. This indicates the degree to which the solution obtained from the transport equation for u^2 is a steady-state solution.

If $\bar{u}$ is the mass velocity, T the temperature defined in terms of the translational energy of the molecules, and q the heat transport vector, the standard formulas of the kinetic theory give $n\bar{u}=n_\alpha u_\alpha+n_\beta u_\beta$, $3nkT/m=n_\alpha\langle(\mathbf{c}-\mathbf{i}\bar{u})^2\rangle_{\alpha h}+n_\beta\langle(\mathbf{c}-\mathbf{i}\bar{u})^2\rangle_{\beta h}$, and $q=n_\alpha\langle(u-\bar{u})E_r\rangle_{\alpha h}+n_\beta\langle(u-\bar{u})E_r\rangle_{\beta h}$, where $\langle\ \rangle_{\alpha h}$ indicates an average over the α distribution, $\langle\ \rangle_{\beta h}$ one over the β-distribution, and $E_r=(m/2)(\mathbf{c}-\mathbf{i}\bar{u})^2+E_i$ is the sum of the kinetic energy relative to the mass motion and the internal energy for a molecule. Evaluating the averages we find

$$kT/m=(1/n)(n_\alpha c_\alpha{}^2-n_\beta c_\beta{}^2)+\tfrac{1}{3}(n_\alpha n_\beta/n^2)(u_\alpha-u_\beta)^2,$$
$$2nq/m=n_\alpha n_\beta[u_\alpha-u_\beta]\times[a(c_\alpha{}^2-c_\beta{}^2)+(u_\alpha-u_\beta)^2(n_\alpha-n_\beta)/n],$$

where c_α, c_β are given by Eqs. (8). We can go on to define a thermal conduction coefficient λ by the usual formula $q=-\lambda\partial T/\partial x$. The resulting formulas for T and λ can be expressed in terms of the Mach number of the use of Eq. (31), and the values of n_α, n_β are given by Eqs. (37) and (38). In this way we get formulas showing the values of T and of λ as functions of position in the shock wave. The results are shown in Table III, where the ratios T/T_β, λ/λ_β are shown as functions of ν_α for $M=\sqrt{2}$, 2 and ∞, and for $\gamma=7/5$. Here T_β is the temperature in the subsonic stream, λ_β the thermal conduction coefficient calculated for the conditions in the subsonic stream by the standard kinetic theory formulas for the elastic sphere model, and ν_α is given by Eq. (37). $\nu_\alpha=1$ corresponds to the supersonic edge of the shock wave, $\nu_\alpha=0$ to the subsonic edge.

As the table illustrates, for Mach numbers of 2 and greater, the temperature T reaches a maximum within the shock wave; and between this point of maximum T and the subsonic edge of the shock, λ is negative. This nominal λ is seen to differ by orders of magnitude from the ordinary kinetic theory value. Of course we cannot expect the present crude approximation to the distribution function to give correct results for λ, and, in any case, the simple formula $q=-\lambda\partial T/\partial x$ should be corrected, as for instance in the Burnett theory; but the anomalous values of λ give some indication of how far the flow in a shock wave differs from that described by equations of the Navier-Stokes type, if the distribution function here used is any approximation to the actual distribution.

In seeking to improve the present theory, it is natural to attempt an iterative solution of the Boltzmann equation itself, taking as initial solution the f given by Eqs. (3) and (4). The collision integral can be evaluated, at least in powers of $M-1$, and this has been done; but the results suffer from the defect that they do not vanish identically for $u=0$, as the Boltzmann equation requires. This makes carrying out of the next step difficult because of the occurrence of a $1/u$ singularity, although the integrals of the second step are finite in spite of this. But more appropriate would be the introduction, in the initial function, of "skew" terms of the type $f_\alpha{}^{(0)}[(\mathbf{c}-\mathbf{i}u_\alpha)^2-5kT_\alpha/m][u-u_\alpha]$, $f_\alpha{}^{(0)}[(u-u_\alpha)^2-\frac{1}{3}(\mathbf{c}-\mathbf{i}u_\alpha)^2]$, where $f_\alpha{}^{(0)}$ is given by Eq. (4), and similar β terms. Such terms occur in the first-order solution of the E-C theory. The coefficients of the various terms could be adjusted in such a way as to give, in the limit $M\to1$, the form of f required by the E-C theory and, at the same time, to give the vanishing of the collision integral for $u=0$.

Recent measurements of shock wave thickness by Cowan and Hornig[13] and by Greene, Cowan, and Hornig[14] using the optical reflectivity method, show thicknesses significantly greater than those predicted by the Thomas theory, in accordance with the results found here.

I am indebted to Dr. H. Polichek and Dr. A. Van Tuyl of the Naval Ordnance Laboratory for checking the manuscript and for preparing tables and curves of the functions involved; I am also indebted to C. S. Wang-Chang for carrying out computations and for pointing out a numerical error in the original formulation of the theory. I wish to thank Drs. E. F. Greene, G. R. Cowan, and D. F. Hornig for sending me a copy of their manuscript in advance of publication, and Dr. Greene for keeping me informed of the progress of experimental measurements in Brown University.

[13] G. R. Cowan and D. F. Hornig, J. Chem. Phys. **18**, 1008 (1950).

[14] Greene, Cowan, and Hornig, J. Chem. Phys. **19**, 427 (1951).

On Fluctuations and the General Distribution Problem in Electron Cascades*

W. T. Scott
Brookhaven National Laboratory, Upton, New York, and Smith College, Northampton, Massachusetts
(Received February 15, 1951)

Recent developments of Bhabha, Friedman, and Jánossy are applied to the general probability distribution problem of electron cascades (cosmic-ray showers). In particular, it is shown that the master function giving the probability of any number of particles with any given energy distribution at a depth t in a shower is determined, in principle, by the average energy spectrum. Certain theorems connecting the various functions are derived, and a discussion is given of the as yet unsolved problem of getting satisfactory analytic or numerical results from the formalism. Only the simplified model originated by Furry has been discussed, but the theorems embody many properties of the actual electron-photon multiplication process.

I. INTRODUCTION

RECENTLY Bhabha[1] has published a general theory of stochastic processes involving a continuously varying parameter, that is directly suited to the theory of electron cascades.[1a] It is the purpose of this article to present certain further results in this field, with the hope that although these results are preliminary, they may be of interest and help to others.

The idea of using the energy as a continuously varying parameter and constructing a master equation for a cascade occurred to the writer in 1945, and part of the development here presented dates from that time. However, no results of any finality were achieved; the work has been developed to its present point through the use of certain ideas recently proposed by Jánossy[2] and Friedman.[3]

The problems we are here concerned with deal with the distribution-in-number of particles at depth t in a shower-producing material, when one particle of energy E_0 is incident on the layer, as well as with their distribution-in-energy. This problem, although clearly of extreme interest in the interpretation of high energy experiments, is very complex, and for simplicity we shall discuss it here only for the simplified model of a cascade introduced by Furry.[4,4a] Many of the basic features of the cascade problem are present in this model, and the generalization to the actual electron-photon case is not essentially difficult.

II. THE FURRY MODEL

We consider a shower process in which particles produce pairs of like particles, and also lose energy by collision loss at a rate β per unit track length. (Energy is conserved but not charge!) Hence we can expect multiplication, division of the initial energy among progressively more particles, the final dissipation of all energy in ionization, and the removal of all particles from the shower. We shall take the total pair production or "splitting" cross section to be independent of energy, and assume a symmetrical spectrum of energy for the two "daughter" particles (the parent is considered to die at the birth of the pair). For simplicity, we may take this spectrum to be uniform, and the rate of energy loss per unit track length to be independent of the energy, but neither simplification is required for the arguments that follow.

Let us then denote by $q(E,u)dudt$ the probability that a particle of energy E split in thickness dt, producing a particle of energy u to $u+du$ and another of energy $E-u$ to $E-u-du$. We shall choose our unit of length ("radiation length") so that $\int_0^E q(E,u)du=1$. The homogeneity property thus indicated may be represented by writing $q(E,u)=E^{-1}\chi(u/E)$. The rectangular spectrum is given by $\chi=1$. No angular or lateral spread of the shower is considered.

III. THE MASTER EQUATION

All information desired about the cascades described is contained in the function $P_N(E_0;E_1,E_2,E_3,\cdots E_N;t)\times dE_1dE_2\cdots dE_N$, which signifies the probability that at depth t there be exactly N particles, *and* that one has energy E_1 to E_1+dE_1, the second E_2 to E_2+dE_2, and so on. E_0 represents the energy of the incident particle that started the shower at $t=0$. P_N is symmetric in the N E's. We can derive an equation for P_N if we ask for its value at $t+dt$. By straightforward reasoning we obtain

$$\frac{\partial}{\partial t}P_N(E_0;E_1,E_2,\cdots E_N;t)=-NP_N(E_0;E_1,E_2,\cdots E_N;t)$$
$$+2\sum_{i=2}^{N}\sum_{j=1}^{i-1}P_{N-1}(E_0;E_1,\cdots E_i+E_j,\cdots E_N;t)\times q(E_i+E_j,E_i)$$
$$+\beta\left(\frac{\partial}{\partial E_1}+\frac{\partial}{\partial E_2}+\cdots+\frac{\partial}{\partial E_N}\right)P_N(E_0;E_1,\cdots E_N;t)$$
$$+\beta P_{N+1}(E_0;0,E_1,E_2,\cdots E_N;t), \quad (1)$$

* Work performed, in part, at the Brookhaven National Laboratory, under the auspices of the AEC.
[1] H. J. Bhabha, Proc. Roy. Soc. (London) **A202**, 301 (1950).
[1a] This method represents a fundamental improvement over the so-called "general" treatment of N. Arley, *Stochastic Processes and Cosmic Radiation* (John Wiley and Sons, Inc., New York, 1948).
[2] L. Jánossy, Proc. Phys. Soc. (London) **A363**, 241 (1950).
[3] F. Friedman, M.I.T. Lab. for Nuclear Sci. and Eng., Tech. Rpt. 31 (1949) (unpublished).
[4] W. H. Furry, Phys. Rev. **52**, 569 (1937).
[4a] Nordsieck, Lamb, and Uhlenbeck, Physica **7**, 344 (1940).

with

$$P_N(E_0; E_1, \cdots E_N; 0)=\delta_{N1}\delta(E_1-E_0). \quad (1a)$$

This is the master equation. The first term on the right represents the reduction in P_N due to production of $N+1$ particles by one splitting; the second represents the gain from $N-1$ to N particles; the third represents the shift in the N-fold spectrum due to the continuous loss of energy; and the last represents the change from $N+1$ to N particles accompanying the removal of a particle from the shower when it gets to energy zero.

If P_N is known, the probability $P(E_0, N, t)$ of finding N particles of any energy may be found from

$$P(E_0, N, t)=\frac{1}{N!}\int_0^\infty dE_1\cdots\int_0^\infty dE_N \times P_N(E_0; E_1, \cdots E_N; t). \quad (2)$$

The factor $N!$ represents the number of times the N particles are counted by letting each energy variable range from 0 to ∞. We must have, of course,

$$\sum_{N=0}^{\infty} P(E_0, N, t)=1. \quad (2a)$$

Unfortunately, an equation for $P(E_0, N, t)$ that does not involve other unknown functions cannot be obtained by integrating (1), unless $\beta=0$. In this case, it is readily seen that

$$(\partial/\partial t)P(E_0, N, t)=-NP(E_0, N, t) +(N-1)P(E_0, N-1, t), \quad (3)$$

$$P(E_0, N, 0)=\delta_{N1}, \quad (3a)$$

which is Furry's original equation. The solution is easy to obtain, but will be found below in another way. However, as Bhabha and Chakrabarty[5] pointed out, the behavior of a shower with $\beta=0$ is radically different from that with any finite β (in the former case, the total number of particles increases indefinitely), so that the various shower functions are certainly not all analytic functions of β for $\beta=0$. This is the source of the difficulty in using the solutions for $\beta=0$ to build solutions for $\beta>0$.[5a]

We shall use Eq. (1) in a different way. Let us define, for $N\geqslant M$,

$$W_M(E_0; E_1, \cdots E_M; N; t) =\frac{1}{(N-M)!}\int_0^\infty dE_{M+1}\cdots\int_0^\infty dE_N \times P_N(E_0; E_1, \cdots E_N; t), \quad (4)$$

with

$$W_M(E_0; E_1, \cdots E_M; M; t)=P_M(E_0; E_1, \cdots E_M; t)$$

and

$$W_0(E_0; N; t)=P(E_0, N, t).$$

W_M represents the probability of finding N particles at t, with M of them lying within prescribed differential energy ranges and the remaining $M-N$ having any energy whatsoever.

An equation for the W_M can now be obtained from (1) if we multiply by $dE_{M+1}\cdots dE_N/(N-M)!$ and integrate. The result is (omitting E_0 for convenience):

$$\begin{aligned}\frac{\partial}{\partial t}&W_M(E_1, \cdots E_M; N; t)= \\ &-NW_M(E_1, \cdots E_M; N; t) \\ &+(N-M-1)W_M(E_1, \cdots E_M; N-1; t) \\ &+2\int_{E_1}^\infty duq(u, E_1)W_M(u, E_2, \cdots E_M; N-1; t) \\ &+2\int_{E_2}^\infty duq(u, E_2)W_M(E_1, u, \cdots E_M; N-1; t)+\cdots \\ &+2\int_{E_M}^\infty duq(u, E_M)W_M(E_1, E_2, \cdots u; N-1; t) \\ &+\sum_{i=2}^{M}\sum_{j=1}^{i-1} q(E_i+E_j, E_i) \times W_{M-1}(E_1, E_2, \cdots E_i+E_j, \cdots E_M; N-1; t) \\ &+\beta\left(\frac{\partial}{\partial E_1}+\frac{\partial}{\partial E_2}+\cdots+\frac{\partial}{\partial E_M}\right)W_M(E_1, \cdots E_M; N; t) \\ &-\beta W_{M+1}(0, E_1, \cdots E_M; N; t) \\ &+\beta W_{M+1}(0, E_1, \cdots E_M; N+1; t), \end{aligned} \quad (5)$$

with

$$W_M(E_0; E_1, \cdots E_M; N; 0) =\delta_{M1}\delta_{N1}\delta(E_1-E_0)+\delta_{M0}\delta_{N1}. \quad (5a)$$

This equation appears not less complex than (1), and indeed still contains terms where the argument must be set equal to zero. But, if we sum over N from M to infinity, these last terms all cancel. (The term in $W_{M+1}(0, E_1\cdots E_M; N; t)$ does not appear if $N=M$.) Therefore, we define

$$K_n(E_0; E_1, \cdots E_n; t)=\sum_{N=n}^{\infty} W_n(E_0; E_1, \cdots E_n; N; t) \quad (6)$$

as the probability of finding n particles at t, each in preassigned differential energy ranges, without regard to the possible existence of further particles of other energies. We note that K_n may also be interpreted as the average product of the numbers of particles in dE_1,

[5] H. J. Bhabha and S. K. Chakrabarty, Proc. Roy. Soc. (London) A181, 267 (1943).

[5a] If an attempt is made to solve the diffusion equations (Eqs. (11) and (23) below) in powers of β, a series expression for the Laplace-Mellin transform results that is divergent for *all* values of β. See reference 7 to follow.

$dE_2\cdots dE_n$, as long as no two of the energies $E_1\cdots E_n$ are equal. Bhabha[1] discusses the singularities that occur in a "complete" average product that includes the cases for two or more energies equal. The functions K_n are derived from such "complete" average product functions in an earlier publication.[6] We now show that $\langle N(N-1)\cdots(N-n+1)\rangle_{Av}$, which function we denote by $M_n(E_0, t)$, is given by an integral over K_n:

$$M_n(E_0, t)=\langle N(N-1)\cdots(N-n+1)\rangle_{Av}$$
$$=\sum_{N=0}^{\infty}[N!/(N-n)!]P(E_0, N, t)$$
$$=\sum_{N=n}^{\infty}\frac{1}{(N-n)!}\int_0^{\infty}dE_1\cdots\int_0^{\infty}$$
$$\times dE_N P_N(E_0; E_1, \cdots E_N; t)$$
$$=\int_0^{\infty}dE_1\cdots\int_0^{\infty}dE_n K_n(E_0; E_1, \cdots E_n; t), \quad (7)$$

by (4) and (6).

In particular, $K_1(E_0; E; t)\equiv F(E_0, E, t)$ is the probability of finding one particle per unit energy range at E; that is, it represents the average energy spectrum for the cascade, and is the analog for the Furry model of the usual distribution functions of shower theory. We can thus calculate

$$\langle N\rangle_{Av}=\int_0^{\infty}F(E_0, E, t)dE=M_1(E_0, t) \quad (8)$$

and for calculating the "fluctuation" $\langle N^2\rangle_{Av}-\langle N\rangle_{Av}^2$ we can find

$$\langle N^2-N\rangle_{Av}=\int_0^{\infty}dE_1\int_0^{\infty}dE_2 K_2(E_0; E_1, E_2; t)$$
$$=M_2(E_0, t). \quad (9)$$

We now derive the equation for K_n and show that all the K_n's may be found by iteration if $K_1\equiv F$ is known. Performing the summation (6) on Eq. (5), we find readily (omitting E_0):

$$\frac{\partial}{\partial t}K_n(E_1, \cdots E_n; t)=-nK_n(E_1, \cdots E_n; t)$$
$$+2\int_{E_1}^{\infty}duq(u, E_1)K_n(u, E_2, \cdots E_n; t)+\cdots$$
$$+2\int_{E_n}^{\infty}duq(u, E_n)K_n(E_1, E_2, \cdots u; t)$$
$$+2\sum_{i,j}q(E_i+E_j, E_i)K_{n-1}(E_1, \cdots E_i+E_j, \cdots E_n; t)$$
$$+\beta\left(\frac{\partial}{\partial E_1}+\cdots+\frac{\partial}{\partial E_n}\right)K_n(E_1, \cdots E_n; t), \quad (10)$$

with

$$K_n(E_1, \cdots E_n; 0)=\delta_{n1}\delta(E_1-E_0). \quad (10a)$$

For $n=1$ we have

$$\frac{\partial F(E_0, E, t)}{\partial t}+F(E_0, E, t)-\beta\frac{\partial F(E_0, E, t)}{\partial E}$$
$$=2\int_E^{\infty}q(u, E)F(E_0, u, t), \quad (11)$$

with

$$F(E_0, E, 0)=\delta(E-E_0). \quad (11a)$$

As shown in a previous paper,[6] we may solve (10) by using $F(E_0, E, t)$ as a Green's function. In fact, the solution of (10) is

$$K_n(E_0; E_1, \cdots E_n; t)=2\int_0^t d\tau\int_0^{\infty}du_1\cdots\int_0^{\infty}du_n$$
$$\times\Big\{F(u_1, E_1, t-\tau)F(u_2, E_2, t-\tau)\cdots$$
$$\times F(u_n, E_n, t-\tau)\sum_{i=2}^{n}\sum_{j=1}^{i-1}q(u_i+u_j, u_i)$$
$$\times K_{n-1}(E_0; u_1, u_2, \cdots u_i+u_j, \cdots u_n; \tau)\Big\}. \quad (12)$$

Next we show that if the K_n are known, the master functions $P_N(E_0; E_1, \cdots E_N; t)$ are also determined. We assert that

$$P_N(E_0; E_1, \cdots E_N; t)$$
$$=\sum_{n=N}^{\infty}\frac{(-1)^{n-N}}{(n-N)!}\int_0^{\infty}dE_{N+1}\cdots$$
$$\times\int_0^{\infty}dE_n K_n(E_0; E_1, \cdots E_n; t), \quad (13)$$

where the term for $n=N$ involves no integrations. Using (6) and (4), we obtain for the right side of (13)

$$\sum_{n=N}^{\infty}\frac{(-1)^{n-N}}{(n-N)!}\int_0^{\infty}dE_{N+1}\cdots\int_0^{\infty}dE_n\sum_{j=n}^{\infty}\frac{1}{(j-n)!}$$
$$\times\int_0^{\infty}dE_{n+1}\cdots\int_0^{\infty}dE_j P_j(E_0; E_1, \cdots E_j; t)$$
$$=\sum_{j=N}^{\infty}\int_0^{\infty}dE_{N+1}\cdots\int_0^{\infty}dE_j P_j(E_0; E_1, \cdots E_j; t)$$
$$\times\sum_{n=N}^{j}\frac{(-1)^{n-N}}{(n-N)!(j-n)!}.$$

The n-summation in the last line may be recognized as $1/(j-N)!$ times the binomial expansion of $(1-1)^{j-N}$,

[6] W. T. Scott and G. E. Uhlenbeck, Phys. Rev. 62, 407 (1942).

and hence is zero unless $j=N$. Thus the only remaining term of the j-summation is the first one, and we have proved our assertion.

To find $P(E_0, N, t)$, integrate Eq. (13) according to (2) and (7):

$$P(E_0, N, t)=\sum_{n=N}^{\infty}\frac{(-1)^{n-N}}{N!(n-N)!}M_n(E_0, t). \quad (14)$$

Equation (2a) will be satisfied provided we take $M_0=1$. This result was obtained in the earlier publication[6] by a less direct method, and is valid for any distribution, if M_n signifies $\langle N!/(N-n)!\rangle_{Av}$.

Convergence of the series in (6), (7), (13), and (14) will not be discussed here in detail, but it seems clear from physical considerations that all the functions given must go to zero rapidly for large N.

We see that, in principle, all information about a one-dimensional shower is "contained" in the functions $F(E_0, E, t)$. The equation for F can be solved by the method of integral transforms,[7] but we have not yet found a satisfactory method for calculating $M_2(E_0, t)$ using the F obtained by this method.

One may ask if it is possible to solve Eq. (1) directly. If $\beta\neq 0$, there does not seem to be any transform method which will make the equations amenable. One can develop a solution in powers of t, which is tedious, slowly convergent, and involves successively higher derivatives of the initial condition (δ-function). This corresponds to the method of successive collisions[8] which yields a slowly convergent series, of value only when the series can be summed.

However, if $\beta=0$, one can solve Eq. (1) successively for $N=1, 2, 3\cdots(P_0(E_0, t)\equiv 0$ in this case). We take here the case of the rectangular spectrum $\chi=1$. In fact, if one writes p_N for the laplace transform of P_N:

$$p_N(E_0; E_1, \cdots E_N; s)=\int_0^{\infty} e^{-st}dtP_N(E_0; E_1, \cdots E_N; t), \quad (15)$$

we find

$$p_N=2^{N-1}\delta(E_1+E_2+\cdots+E_N-E_0)r_N(E_1, \cdots E_N)\times[(s+1)(s+2)\cdots(s+N)]^{-1}, \quad (16a)$$

with

$$r_N=\sum_{i=2}^{N}\sum_{j=1}^{i-1}r_{N-1}(E_1, \cdots E_i+E_j, \cdots E_N)/(E_i+E_j);\qquad r_2=1/(E_1+E_2). \quad (16b)$$

The r_N are symmetric algebraic functions which may be found successively. A general formula for r_N does not seem possible to find, but the symmetry properties are related to the "trees" discussed by Polyà in his work on the counting of isomers of organic compounds.[9]

[7] W. T. Scott, Phys. Rev. **80**, 611 (1950).
[8] H. J. Bhabha and W. Heitler, Proc. Roy. Soc. (London) A159, 432 (1937).
[9] G. Polyà, Acta. Math. **68**, 145 (1937).

The only usefulness of this solution would seem to lie in the possibility of making a "cut-off" calculation —finding the distribution in the number of particles above a certain energy ϵ, which can be related to β so as to include approximately the effects of ionization while setting $\beta=0$ in the equations. However, this involves integration and summing over expressions r_N involving all possible numbers of particles of energy less than ϵ, and does not appear useful. A cut-off can be applied to Eq. (1) by defining a suitable new set of functions, but the results are too complicated to develop here.

IV. ADJOINT THEORY

A more hopeful approach lies in the use of generating functions recently proposed by Jánossy.[2] It will be convenient first to introduce the adjoint theory of Friedman.[3] We start with the equation for F and use again the laplace transform in t as a convenience in writing the formulas.

Let

$$f(E_0, E, s)=\int_0^{\infty} e^{-st}F(E_0, E, t)dt. \quad (17)$$

Multiplying (11) by $e^{-st}dt$, integrating both sides and using (11a), we obtain on rearrangement

$$(s+1)f(E_0, E, s)-\beta\frac{\partial f}{\partial E}-2\int_E^{E_0} f(E_0, u, s)q(u, E)du=\delta(E_0-E), \quad (18a)$$

which we write compactly as

$$L_E f(E_0, E, s)=\delta(E_0-E). \quad (18b)$$

We have set the upper limit in the integral equal to E_0, since F and f are zero for $E>E_0$; all particles have energy less than the incident. As a matter of fact, F must vanish in this model when $E>E_0-\beta t$, but a similar property does not hold in the cosmic-ray case.

The behavior of f as $E\to E_0$ may be found from the fact that it depends only on values of f for t small. A zero-order approximation for F is, clearly, $e^{-st}\delta(E_0-E-\beta t)$, representing the energy distribution associated with the "unsplit" incident particles. The transform is $\beta\exp[-(s+1)(E_0-E)/\beta]$. Thus as $E\to E_0^-$, $f\to\beta$, we write

$$\left.\begin{aligned} f(E_0, E_0^-, s)&=f(E^+, E, s)=\beta\\ f(E_0, E, s)&=0, \quad E>E_0\end{aligned}\right\}. \quad (19)$$

Now, let $\phi(E_0, E)$ be an arbitrary function that satisfies the conditions (19). In (18a), let us write $E=v$, multiply both sides by $\phi(v, E)$ and integrate over v from 0 to ∞. (We may replace E_0 by ∞ in the integral in (18a) by using (19).) After an integration by parts and a change of order of integration, we find

$$\phi(E_0, E)=\int_0^{\infty} du f(E_0, u, s)L_u^{\dagger}\phi(u, E), \quad (20a)$$

where[10]

$$L_{E_0}^{\dagger}\phi(E_0, E)=(s+1)\phi(E_0, E)+\beta\partial\phi/\partial E_0 - 2\int_0^{E_0}\phi(v, E)q(E_0, v)dv. \quad (20b)$$

$L_{E_0}^{\dagger}$ is called the adjoint operator to L_E. If we now let $\phi(E_0, E)=f(E_0, E, S)$, we see that

$$f(E_0, E, s)=\int_0^{\infty} du f(E_0, u, s)L_u^{\dagger}f(u, E, s). \quad (21)$$

$L_u^{\dagger}f(u, E, S)$ acts like $\delta(u-E)$ in (21) for all values of E_0. We conclude that

$$L_{E_0}^{\dagger}f(E_0, E, s)=\delta(E_0-E). \quad (22)$$

This equation is the adjoint equation for f.

The corresponding equation for F is, obviously

$$\left(\frac{\partial}{\partial t}+1+\beta\frac{\partial}{\partial E_0}\right)F(E_0, E, t) = 2\int_0^{E_0} q(E_0, v)F(v, E, t)dv. \quad (23)$$

If the methods of reference 7 are applied to this equation with $q=1/E_0$, a solution is obtained that is identical to that obtained from (11). Equation (23) may be derived from physical considerations if one considers the shower at $t+dt$ as derived from the two showers that start from a splitting in the first dt, plus the shower resulting from incident particles that do not split in the first dt. All equations in cascade theory derived from considerations concerning the start of the shower will here be called "adjoint equations."

The average number of particles, $\langle N\rangle_{av}=M_1(E_0, t)$ is of course of particular interest. If we integrate (11) over E, we obtain

$$\partial M_1/\partial t-M_1(E_0, t)=-\beta F(E_0, 0, t), \quad (24)$$

which cannot be used directly to get M_1. If we integrate (23), however, we obtain the adjoint equation for M_1:

$$\frac{\partial M_1}{\partial t}+M_1+\beta\frac{\partial M_1}{\partial E_0}=2\int_0^{E_0} M_1(u, t)q(E_0, u)du, \quad (25)$$

together with the boundary condition

$$M_1(E_0, 0)=1. \quad (25a)$$

We find now that (25a) does not determine the correct solution to (25). If we develop a solution in powers of t starting with (25a), we find that all coefficients are, like (25a), *independent of* E_0. In fact, if we assume M_1 to be independent of E_0, (25) becomes $dM_1/dt=M_1$, yielding $M_1=e^t$, which is the correct solution for the Furry model with $\beta=0$ (see below).

[10] Equation (19) allows the limits of the integrals in both (20a) and (20b) to read E and E_0.

We can correct this difficulty by noting that no shower develops if $E_0<0$. Introducing the unit step-function $\eta(E_0)$:

$$\left.\begin{aligned}\eta(E_0)&=1, \quad E_0>0\\ &=0, \quad E_0<0\end{aligned}\right\}, \quad (26)$$

we can write the boundary condition

$$M_1(E_0, 0)=\eta(E_0), \quad (25b)$$

and use as first approximation

$$M_1(E_0, t)\simeq e^{-t}\eta(E_0-\beta t). \quad (25c)$$

Even so, the resulting series is very slowly convergent. The transform methods of reference 7 cannot be used with (25a) or (25b). Thus it still seems necessary to solve (23) or (11), with (11a) in either case, to arrive at a result for $M_1(E_0, t)$.

V. GENERATING FUNCTIONS

Let us now write the adjoint equation for $P(E_0, N, t)$. As in the case of M_1, the adjoint equation is self-contained whereas the equation derived from the end of the shower is not. We have

$$\left(\frac{\partial}{\partial t}+1+\beta\frac{\partial}{\partial E_0}\right)P(E_0, N, t) = \int_0^{E_0} q(E_0, v)dv\sum_{n=0}^{N} P(v, n, t)P(E_0-v, N-n, t), \quad (27)$$

subject to

$$P(E_0, N, 0)=\delta_{N1}\eta(E_0) \quad (27a)$$

using (26).

Thus beginning with $P(E_0, 0, t)$ we could determine P successively for all N. However, since $P(E_0, 0, 0)=0$, we see from (27) with $N=0$,

$$\left(\frac{\partial}{\partial t}+1+\beta\frac{\partial}{\partial E_0}\right)P(E_0, 0, t) = \int_0^{E_0} q(E_0, v)dvP(v, 0, t)P(E_0-v, 0, t), \quad (27b)$$

that all the derivatives of $P(E_0, 0, t)$ with respect to E_0 and t vanish when $t=0$, so that no analytic development near $t=0$ is possible. This is physically evident, since the vanishing of the shower occurs for large t and should have a probability of vanishing near $t=0$, which is zero in very high order.

Let us now write a generating function for $P(E_0, N, t)$:

$$G(E_0, t, U)=\sum_{N=0}^{\infty} U^N P(E_0, N, t), \quad (28a)$$

with the initial condition

$$G(E_0, 0, U)=(U-1)\eta(E_0)+1=\begin{cases}U, & E_0>0\\ 1, & E_0<0.\end{cases} \quad (28b)$$

The vanishing property referred to following Eq. (18b) implies that

$$G(E_0, t, U)=1 \text{ when } \beta t > E_0. \tag{28c}$$

The normalization (2a) yields

$$G(E_0, t, 1)=1 \text{ for all } t. \tag{28d}$$

We may obtain $M_n(E_0, t)$ from G by differentiating n times with respect to U and then setting $U=1$:

$$M_n(E_0, t)=\left(\frac{\partial^n G}{\partial U^n}\right)_{U=1}, \tag{29}$$

and hence we may write

$$G(E_0, t, U)=\sum_{n=0}^{\infty}\frac{(U-1)^n M_n(E_0, t)}{n!}. \tag{30}$$

We may now obtain (14) by expanding $(U-1)^n$ in (30) in powers of U.

We find readily from (27) an adjoint equation for G:

$$\left(\frac{\partial}{\partial t}+1+\beta\frac{\partial}{\partial E_0}\right)G(E_0, t, U)$$
$$=\int_0^{E_0} q(E_0, v)dv G(v, t, U)G(E_0-v, t, U). \tag{31}$$

Just as for (25), (31) has a solution independent of E_0, corresponding to the case $\beta=0$. We would then have

$$\frac{\partial G}{\partial t}+G=G^2, \tag{32a}$$

and must replace (28b) by

$$G(t, U)=U, \text{ when } t=0. \tag{28b'}$$

The solution of (32a) is

$$G=\frac{Ue^{-t}}{1-U(1-e^{-t})}=Ue^{-t}\sum_{N=1}^{\infty}U^{N-1}(1-e^{-t})^{N-1}. \tag{32b}$$

Thus we find Furry's solution for his problem A:[4]

$$\left.\begin{aligned} &P(N, t)=e^{-t}(1-e^{-t})^{N-1};\ N\geq 1\\ &P(0, t)=G(E_0, t, 0)=0.\end{aligned}\right\} \tag{33}$$

Equation (28d) is satisfied, and we can find $M_1=\langle N\rangle_{Av}$ from $(\partial G/\partial U)_{U=1}=e^t$, as was found from (25).

We note, however, that (32b) does not satisfy any condition similar to (28c). As $t\to\infty$, $G\to 0$, showing that the coefficient of each U^N goes to zero, as the number of particles steadily increases. We must take into account the step-function behavior of G for $E_0=0$, just as for Eq. (25). Hence the condition (28c) is in some way essential to the determination of a solution to (31) when $\beta\neq 0$.

Equivalent integral equations may be obtained from (31) in various ways. Two of interest are given here. First, we may treat the right side of (31) as the inhomogeneous part of a linear partial differential equation. The solution of this equation, subject to (28b), is

$$G(E_0, t, U)=e^{-t}[(U-1)\eta(E_0-\beta t)+1]$$
$$+\int_0^t d\tau e^{\tau-t}\int_0^{E_0-\beta t+\beta\tau} dv q(E_0-\beta t+\beta\tau, v)$$
$$\times G(v, \tau, U)G(E_0-\beta t+\beta\tau-v, \tau, U). \tag{34}$$

This equation may be used to derive (28c) from the boundary condition (28b).

We may solve Eq. (34) by the method of iteration (Liouville-Neumann series), starting with the inhomogeneous part as first approximation and substituting successive approximations into the integrand. A solution in powers of $(U-1)$ results; however, each iteration continues to change the coefficients of all the lower powers of $(U-1)$.

If we use (28b') instead of (28b), we obtain again (32b), and (28c) is of course not satisfied.

A second integral equation for G may be obtained by setting $G(E_0, t, U)=g(E_0, t, U)+1$ with $g(E_0, 0, U)=(U-1)\eta(E_0)$, $g(E_0, t, 1)=0$, and $g(E_0, t, U)=0$ if $\beta t>E_0$. We find for g:

$$\left(\frac{\partial}{\partial t}+1+\beta\frac{\partial}{\partial E_0}\right)g(E_0, t, U)$$
$$=2\int_0^{E_0} dv q(E_0, v)g(v, t, U)$$
$$+\int_0^{E_0} dv q(E_0, v)g(v, t, U)g(E_0-v, t, U). \tag{35}$$

We may now treat this equation as an inhomogeneous variation of (23), for which $F(E_0, E, t)$ is a Green's function. Thus (35) may be transformed into

$$g(E_0, t, U)=(U-1)M_1(E_0, t)$$
$$+\int_0^t d\tau\int_0^{E_0} dv F(E_0, v, t-\tau)\int_0^v dw q(v, w)$$
$$\times g(w, \tau, U)g(v-w, \tau, U). \tag{36}$$

This equation is compatible with all the conditions given above. The initial value $(U-1)M_1(E_0, t)$ satisfies these conditions, and thus an iterated solution will satisfy them. In contrast to (34), we now get the n'th iteration leaving unaffected the n'th and lower powers of $(U-1)$.

In fact, the iterated solution is just (30). This can be shown by comparing the results of the substitution with the recursion relation for the M_n. This could be derived from (12), but it is better found from the adjoint

equation for the M_n derived most readily from (29) and (31):

$$\left(\frac{\partial}{\partial t}+1+\beta\frac{\partial}{\partial E_0}\right)M_n(E_0,t)$$

$$=2\int_0^{E_0}dvq(E_0,v)M_n(v,t)+\sum_{j=1}^{n-1}\frac{n!}{j!(n-j)!}\int_0^{E_0}$$

$$\times dvq(E_0,v)M_{n-j}(v,t)M_j(E_0-v,t). \quad (37)$$

These equations may also be transformed by use of the Green's function F:

$$M_n(E_0,t)=\int_0^t d\tau\int_0^{E_0}dvF(E_0,v,t-\tau)\sum_{j=1}^{n-1}\frac{n!}{j!(n-j)!}$$

$$\times\int_0^v dwq(v,w)M_{n-j}(w,\tau)M_j(v-w,\tau). \quad (38a)$$

In particular we find

$$M_2(E_0,t)=2\int_0^t d\tau\int_0^{E_0}dvF(E_0,v,t-\tau)$$

$$\times\int_E^v q(v,w)M_1(w,\tau)M_1(v-w,\tau). \quad (38b)$$

Jánossy[2] generalizes our definition of the generating function. One form he gives corresponds to inserting another variable E: $G(E_0,E,t,U)$ is the generating function for the probability $P(E_0,E,N,t)$ of finding N particles of energy E *or more*. We have, of course, $G(E_0,0,t,U)=G(E_0,t,U)$. Equation (27) holds true for $P(E_0,E,N,t)$, but (27a) becomes

$$P(E_0,E,N,t)=\delta_{N1}\eta(E_0-E). \quad (39)$$

Using the same definition (28a), we find the same Eq. (31):

$$\left(\frac{\partial}{\partial t}+1+\beta\frac{\partial}{\partial E_0}\right)G(E_0,E,t,U)$$

$$=\int_0^{E_0}dvq(E_0,v)G(v,E,t,U)G(E_0-v,E,t,U). \quad (40a)$$

The conditions (28b), (28c), and (28d) become, respectively,

$$G(E_0,E,0,U)=(U-1)\eta(E_0-E)+1; \quad (40b)$$

$$G(E_0,E,t,U)=1 \text{ if } E>E_0-\beta t; \quad (40c)$$

$$G(E_0,E,t,1)=1. \quad (40d)$$

We may also write analogous expressions to (29) and (30). Equation (35) holds for $g(E_0,E,t,U)=G-1$ with the appropriate boundary condition. The transformation corresponding to (36) yields

$$g(E_0,E,t,U)=(U-1)\int_E^{E_0}F(E_0,v,t)dv$$

$$+\int_0^t d\tau\int_0^{E_0}dvF(E_0,v,t-\tau)$$

$$\times\int_0^v dwq(v,w)g(w,\tau,U)g(v-w,\tau,U). \quad (41)$$

A development in powers of $(U-1)$ corresponding to (30) may be found for (41).

We note that

$$(\partial G(E_0,E,t,U)/\partial U)_{U=1}=\int_E^{E_0}F(E_0,u,t)du,$$

and hence according to our general theory, the function $G(E_0,E,t,U)$ contains essentially all the information about the longitudinal development of a shower.

VI. CONCLUDING REMARKS

It has been hoped in the present work that some analytic way would be found either of treating the series (30) or of finding solutions for (31) or (38a) with a different type of expansion in U. Attempts have also been made to give a semi-analytic treatment of these equations so that the work of numerical integration would be reduced to amenable proportions. Even a qualitative idea of the behavior of $P(E_0,N,t)$ would be of considerable interest.

The solution for F obtained as a triple complex integral by the methods of reference 7 has been applied to (38b) for M_2, but a satisfactory method for obtaining even purely numerical results has not yet presented itself. It was hoped, in fact, to check results quoted in reference 6 for the Furry model using the cut-off method, but even this fluctuation calculation seems difficult.

Consequently, a numerical use of the results for F and M_1 is not too promising for numerical work on the equations for G.

Two other approaches deserve mention here. An attempt was made to find "correlation" theorems related to integrals of the type found in (12) and (38b). The only two relations found are not connected with these integrals, but are reproduced here for reference:

$$F(E_0,E,t)=\int_0^\infty duF(E_0,u,t')F(u,E,t-t');$$

$$0\leqslant t'\leqslant t, \quad (42)$$

$$F(E_0,E,t)=F(E_0,E+\beta t-\beta t',t')e^{t'-t}$$

$$+2\int_0^{t-t'}d\tau e^{-\tau}\int_0^\infty du\int_0^u dvq(u,v)$$

$$\times F(E_0,u+\beta\tau,t')F(v,E,t-t'-\tau);$$

$$0\leqslant t'\leqslant t. \quad (43)$$

Equations (42) and (43) may both be shown to satisfy (11) and (23); they may also be derived directly from physical considerations.

The second approach lies in the use of the "extra" boundary condition (28c) or (40c). In Eq. (35), for instance, if we consider the region in the E_0-t plane determined by $\beta t<E_0<2\beta t$, then not more than one of the two factors g in the integral can differ from 0 for any v. We thus have a homogeneous, linear equation, which may be solved by using the Green's function F. We may then use this solution to study the region $2\beta t<E_0<3\beta t$, obtaining an inhomogeneous equation involving the previous solution, and so forth. The boundary condition (28b) must be introduced by letting $\bar{E}_0\to 0$ and $t\to 0$ with $E_0/\beta t$ between 1 and 2, or 2 and 3, etc. Successive applications of this method are quite cumbersome, and of course an infinite series is needed for a complete solution.

It may be, however, that a numerical integration procedure can be started satisfactorily with this approach.

Finally, it should be remarked that Friedman[3] has developed variational-iterational methods for F which, however, we have been unable to apply to the nonlinear equations for G.

PHYSICAL REVIEW VOLUME 82, NUMBER 6 JUNE 15, 1951

Temperature Dependence of the Energy Gap in Semiconductors*

H. Y. Fan
Purdue University, Lafayette, Indiana
(Received January 8, 1951)

The problem treated is the effect of lattice vibrations in producing a shift of the energy levels which results in a temperature dependent variation of the energy gap in semiconductors. Calculations for silicon and germanium give results of the same order of magnitude as the observed temperature dependent shift of the absorption band edge. The effect of lattice vibrations on the energy gap has been treated previously on the basis of broadening rather than shifting of the energy levels. The effect was found to be negligible for nonpolar crystals, whereas according to our treatment it should be much larger. For polar crystals our result turns out to be essentially the same as was given by the previous treatment.

I. INTRODUCTION

RECENT measurements on germanium and silicon show that the long wavelength limit of the optical absorption band shifts toward shorter wavelength with decreasing temperature.[1] The steeply rising edge of the absorption band shifts without changing its shape. The position of the band edge corresponds approximately to the width of the forbidden energy gap determined from resistivity and Hall coefficient measurements. The shift thus indicates a variation of the energy gap with temperature. An alternative explanation is that the absorption edge should actually be at a higher energy, the close agreement with the energy gap being due to deviations in the crystal from perfect periodicity which allow the violation of selection rules for optical transitions. The shift in absorption could then be attributed to the change in the degree of deviation from periodicity due to the temperature variation of the lattice vibrations.[2] However, this does not seem to be the explanation for our case, since the band edge is very sharp and shifts without changing shape. Moreover, for a given temperature samples differing in resistivity by several orders of magnitude, thus having different concentrations of impurity and different degrees of deviation from periodicity, show no appreciable difference in the position and the shape of the absorption edge. Thus, temperature variation of the energy gap is the more likely explanation. Temperature variation of the photoelectric threshold for germanium and silicon p–n junctions have also been observed.[3] Furthermore, analysis of the temperature variation of carrier concentrations determined by Hall and resistivity measurements also indicate such a dependence of the energy gap in these materials.[4]

The shift of absorption limit with temperature has been known for polar crystal insulators. Möglich and Rompe[5] pointed out the effect of lattice expansion on the energy gap and made rough estimations showing that it could account for only a small part of the observed temperature shift, although their work cannot be regarded as quantitative. Recently, Höhler measured the shift of absorption edge in CdS with pressure. Using his result, Seiwert[6] found that thermal expansion

* Supported by a Signal Corps contract.

[1] M. Becker and H. Y. Fan, Phys. Rev. **76**, 1531 (1949); H. Y. Fan, Phys. Rev. **78**, 808 (1950); H. Y. Fan and M. Becker, report at Conference of Semiconducting Materials, July, 1950, to be published soon; unpublished work of H. B. Briggs, see reference 9.

[2] The author is indebted to Professor F. Seitz for raising this point in a private discussion.

[3] Unpublished work by F. S. Goucher and H. B. Briggs, see reference 9.

[4] G. L. Pearson and J. Bardeen, Phys. Rev. **75**, 865 (1949); V. Johnson and H. Y. Fan, Phys. Rev. **79**, 899 (1950).

[5] F. Möglich and R. Rompe, Z. tech. Physik **119**, 472 (1942).

[6] R. Seiwert, Ann. Physik **6**, 241 (1949).

effect accounts for only one-sixth of the observed temperature shift.

Möglich, Riehl, and Rompe[7] have also considered the effect of lattice vibrations as a cause for broadening the energy levels and thereby changing the energy gap. This approach was followed later by Radkowsky,[8] who showed that the effect is large for polar crystals, the result agreeing quite well with experimental data. For nonpolar crystals, of which germanium was chosen for consideration, the effect was found to be negligible.

Bardeen and Shockley[9] have recently treated the effect of lattice expansion on the energy gap for nonpolar crystals. We shall reexamine the effect of lattice vibrations, all evidence indicating that thermal expansion cannot fully account for the observed shift of absorption edge in silicon and germanium. Rather than treat the lattice vibrations as producing a broadening of the energy levels, we consider them as causing a shift of the energy levels. A crystal with vibrating lattice not only has an additional vibrational energy of the ions, but also has a different electron-lattice interaction energy as compared with a stationary lattice. Two states of different electron distributions in a vibrating crystal will not, therefore, necessarily differ by the same amount of energy as the corresponding states in the stationary lattice, since the difference in electron-lattice interaction energy for the two states may not be the same in both cases. The energy gap is the difference in the energy of the crystal when an electron is excited from the top of the valence band up to the bottom of the conduction band. Our problem is to determine the change in the electron-lattice interaction energy of the crystal which accompanies such excitation. This change depends upon the lattice vibrations and therefore on the temperature.

The difference between our approach and the energy level broadening concept will be clear from the following discussion. The vibrating crystal in the absence of external perturbations has stationary states corresponding to various energy levels as does a vibrating molecule. As in the treatment of molecular absorption, we consider an external perturbation to produce transitions between various energy levels of the vibrating crystal. If we have only solutions for the lattice fixed, then the problem is to obtain the energy levels of the vibrating crystal by approximation methods. On the other hand, if it is specifically given that the vibrating crystal is not in one of its stationary states but is in a state which would be stationary had the lattice been fixed, then the state of the crystal will change with time. Under such conditions the crystal can be regarded as having approximately the energy computed for the fixed lattice, with an uncertainty proportional to the rate of transition of the state to other states. This is the basis of the energy level broadening treatment. Since we have no reason to deal with such nonstationary states, our approach seems to be more reasonable.

We wish to mention still another way of treating the effect of lattice vibrations on absorption, used by Muto[10] for metals. This method is based on the idea of simultaneous photon absorption and the absorption or emission of a lattice vibrational quantum. As in the energy level broadening treatment, it also starts with the crystal in a state which would be stationary if the lattice were fixed; but it deals with the change of this state due to the simultaneous actions of the lattice vibrations and the radiation field, instead of considering first the effect of lattice vibrations separately. In the case of semiconductors this treatment will give a small absorption extending beyond the direct absorption limit by a frequency range corresponding to the maximum energy of a phonon, unless simultaneous absorption of several phonons is considered. According to the point of view of dealing with stationary states of the vibrating crystal, such an effect is analogous to a change of the vibrational state of a molecule which accompanies an electron transition and should be treated along the same line. In the treatment given below this effect is not taken into account.

The results of the following treatment show that the lattice vibrations give a much larger temperature dependence of the energy gap in nonpolar crystals than that obtained by Radkowsky. The effect is comparable with the effect of thermal expansion and should help to explain the observed shift of absorption edge for silicon and germanium. These results have been discussed previously without the details of the treatment.[11] In the case of polar crystals our results turn out to be essentially the same as those obtained by Radkowsky.

II. ELECTRON-LATTICE INTERACTION ENERGY

The change in electron-lattice interaction energy due to a lattice distortion is to the first approximation proportional to the displacement of the ions. The vibrations of the ions can be analyzed into normal modes, and the change in the interaction energy for an electron can usually be written in the following form:

$$\Delta U=\sum_{\mathbf{q}}[a(\mathbf{q})\exp(i\mathbf{q}\cdot\mathbf{r})+a^*(\mathbf{q})\exp(-i\mathbf{q}\cdot\mathbf{r})]f(\mathbf{q}), \quad (1)$$

where $\mathbf{r}$ represents the coordinates of the electron and $a(\mathbf{q})$ is the time dependent amplitude of the normal mode having wave-number vector $\mathbf{q}$. Although there is more than one mode having the same $\mathbf{q}$, we will be interested in only one of them. For nonpolar crystals $f(\mathbf{q})$ is a periodic function of $\mathbf{r}$ with the periodicity of the lattice. For polar crystals it is independent of $\mathbf{r}$. The Bloch wave function for electrons in a periodic lattice

[7] Möglich, Riehl, and Rompe, Z. tech. Physik **21**, 6, 128 (1940).
[8] A. Radkowsky, Phys. Rev. **73**, 749 (1948).
[9] J. Bardeen and W. Shockley, Phys. Rev. **80**, 72 (1950).
[10] T. Muto, Sci. Papers Inst. Phys. Chem. Research **27**, 179 (1935).
[11] The second and third works mentioned in reference 1. *Note added in proof:*—A similar treatment has since been reported by T. Muto and S. Oyama independently, Prog. Theor. Phys. **5**, 833 (1950).

ψ can be characterized by a reduced wave number vector $\mathbf{k}$ and an index σ indicating the energy band to which the wave function belongs. The wave function of the ions χ is a product of harmonic oscillator wave functions, one for each normal mode. It can be specified by a set of quantum numbers n for the various modes. It is well known that with such ΔU, ψ, and χ the matrix components of ΔU in the representation of $\psi\chi$ vanish except when

$$\mathbf{k}'=\mathbf{k}\pm\mathbf{q}, \text{ and } n'=n \text{ except } n_q'=n_q\mp 1. \quad (2)$$

Thus, the nonvanishing elements are

$$[\psi(\mathbf{k}\pm\mathbf{q};\sigma)\chi(n_q\mp 1)|\Delta U|\psi(\mathbf{k},\sigma)\chi(n_q)]. \quad (3)$$

It is understood that the two ψ's have the same spin.

Treating ΔU as a perturbation, the interaction energy is zero in the first order of approximation, since the diagonal elements of ΔU vanish. In the second-order approximation the interaction energy for the whole crystal is[12]

$$\Delta E=\sum_{\mathbf{k},\sigma}\sum_{\mathbf{q},\sigma'}\frac{|[\psi(\mathbf{k}\pm\mathbf{q},\sigma')\chi(n_q\mp 1)|\Delta U|\psi(\mathbf{k},\sigma)\chi(n_q)]|^2}{\epsilon(\mathbf{k},\sigma)-[\epsilon(\mathbf{k}\pm\mathbf{q},\sigma')\mp\hbar\omega_q]}, \quad (4)$$

where ϵ is the electron energy in the undistorted lattice and ω_q is the angular frequency of the normal mode $\mathbf{q}$. The summation over $\mathbf{k}$ and σ (spin) covers all the occupied states, whereas the summation over $\mathbf{q}$ and σ' is limited by the requirement that $(\mathbf{k}\pm\mathbf{q},\sigma')$ must be an unoccupied state. This limitation is imposed by the Pauli principle. If we apply the perturbation theory to the crystal as a whole, using $\sum_i \Delta U_i$ summed over all the electrons as the perturbation, and assume the electronic part of the crystal wave function to be a determinant of single electron wave functions, then we get just Eq. (4), with the limitation in summation following from the antisymmetrical nature of the crystal wave function. However, the validity of the perturbation method when applied to the crystal as a whole is questionable. Equation (4) is to be preferably regarded as approximating the interaction energy of the crystal by summing the interaction energy of individual electrons.

In Eq. (4) the difference between two ϵ's in the denominator is large if σ' is different from σ, that is, if the two states belong to different energy bands. We shall therefore take only σ' identical with σ. We shall see later that in the usual approximation the matrix elements of ΔU are independent of $\mathbf{k}$. Thus, we can write

$$\Delta E=\sum_{\mathbf{k},\sigma}\sum_{\mathbf{q}}\frac{|\Delta U(\sigma,\pm\mathbf{q})|^2}{\epsilon(\mathbf{k},\sigma)-\epsilon(\mathbf{k}\pm\mathbf{q},\sigma)\pm\hbar\omega_q}. \quad (5)$$

When an electron is shifted from a state near the top of the valence band $(\mathbf{k}_t, v)$ to a state near the bottom of the conduction band $(\mathbf{k}_b, c)$, the change in the interaction energy is

$$\Delta E_G=\sum_{\mathbf{q}}\frac{|\Delta U(c,\pm\mathbf{q})|^2}{\epsilon(\mathbf{k}_b,c)-\epsilon(\mathbf{k}\pm\mathbf{q},c)\pm\hbar\omega_q}-\sum_{\mathbf{k}}\frac{|\Delta U(c,\pm\mathbf{q})|^2}{\epsilon(\mathbf{k},c)-\epsilon(\mathbf{k}\pm\mathbf{q}=k_b,c)\pm\hbar\omega_q}-\sum_{\mathbf{q}}\frac{|\Delta U(v,\pm q)|^2}{\epsilon(\mathbf{k}_t,v)-\epsilon(\mathbf{k}_t\pm\mathbf{q},v)\pm\hbar\omega_q}+\sum_{\mathbf{k}}\frac{|\Delta U(v,\pm\mathbf{q})|^2}{\epsilon(\mathbf{k},v)-\epsilon(\mathbf{k}\pm\mathbf{q}=\mathbf{k}_t,v)\pm\hbar\omega_q}. \quad (6)$$

The first two terms are due to the introduction of an extra electron into the state $(\mathbf{k}_b, c)$, and the last two terms are due to the removal of an electron from the state $(\mathbf{k}_t, v)$. In a semiconductor only a few of the states in the conduction band are occupied, and we can let $\mathbf{q}$ take all values in the first summation. For the same reason there are few terms in the second summation over the occupied $\mathbf{k}$, which can therefore be neglected. The valence band on the other hand is practically filled. The third summation, connecting $(\mathbf{k}_t, v)$ with the unoccupied states, will thus have few terms and will therefore be negligible, whereas in the fourth summation $\mathbf{k}$ can take practically all possible values.

For the lattice undistorted by the vibrations the change in crystal energy due to shifting an electron from state $(\mathbf{k}_t, v)$ to state $(\mathbf{k}_b, c)$ is

$$E_{G_0}=\epsilon(\mathbf{k}_b,c)-\epsilon(\mathbf{k}_t,v). \quad (7)$$

The energy gap in a vibrating lattice is thus

$$E_G=E_{G_0}+\Delta E_G=\epsilon(\mathbf{k}_b,c)-\epsilon(\mathbf{k}_t,v)+\sum_{\mathbf{q}}\frac{|\Delta U(c,\pm\mathbf{q})|^2}{\epsilon(\mathbf{k}_b)-\epsilon(\mathbf{k}_b\pm\mathbf{q})\pm\hbar\omega_q}+\sum_{\mathbf{q}}\frac{|\Delta U(v,\pm q)|^2}{\epsilon(\mathbf{k}_t\mp q)-\epsilon(\mathbf{k}_t)\pm\hbar\omega_q}. \quad (8)$$

The last term on the right is the last term in Eq. (6), where the summation over $\mathbf{k}$ has been changed to the summation over $\mathbf{q}$ which can take all possible values. The first and third terms correspond to the energy required to introduce an electron into state $(\mathbf{k}_b, c)$. The second and fourth terms give the energy required to remove an electron or to introduce a hole into the state $(\mathbf{k}_t, v)$. Thermal expansion affects the energy gap through E_{G_0}, which depends on the equilibrium distance between the ions. We are concerned with the temperature dependence of the last two terms.

Equation (8) applies only when the two states, the energy difference of which defines the energy gap, have lifetimes long compared with the periods of lattice vibrations. In optical absorption the lifetime of the

[12] H. Fröhlich, Phys. Rev. **79**, 845 (1950).

excited state is of the order 10^{-8} sec. Actually, the lifetime of the states may be shorter than this, since the crystal is also perturbed by the thermal radiation. However, the maximum frequency of the acoustic vibrations is of the order 10^{13} sec^{-1}. It should be possible to take into account the effect of most of the vibrational modes by Eq. (8). Acoustic vibrations of very long wavelengths with periods longer than the lifetimes should not be included in Eq. (8). The proper way to calculate the effect of these is to determine the energy levels for each instantaneous pattern of the lattice distorted by these slow vibrations. This should result in a broadening of the absorption band edge. The effect being limited to very long waves should be negligible. It is unnecessary to determine accurately the low frequency limit for the applicability of Eq. (8). In the result obtained for nonpolar crystals, Eq. (22), cutting off at any frequency makes a negligible difference so long as the frequency is much lower than the maximum. The question does not arise in the case of polar crystals, since there only the optical modes are of consequence.

III. NONPOLAR CRYSTALS

There are various assumptions used in estimating the electron-lattice interaction potential for nonpolar crystals. The frequently used deformable-atom idea of Bloch assumes that the electronic potential in a vibrating crystal is

$$V(\mathbf{r}+\mathbf{R})=V_0(\mathbf{r}), \tag{9}$$

where $V_0(\mathbf{r})$ is the potential at point $\mathbf{r}$ if the lattice is at rest and $\mathbf{R}$ is the "displacement" of the point $\mathbf{r}$ due to the vibrations. The displacement of the αth ion in the pth unit cell can be written[12]

$$\mathbf{R}_{\alpha,p}=(M_\alpha N)^{-\frac{1}{2}}\sum_{\mathbf{q},l}[a(\mathbf{q},l)\boldsymbol{\xi}(\mathbf{q},l)\exp(i\mathbf{q}\cdot\mathbf{r}_{\alpha p}) +a^*(\mathbf{q},l)\boldsymbol{\xi}^*(\mathbf{q},l)\exp(-i\mathbf{q}\cdot\mathbf{r}_{\alpha p})], \tag{10}$$

where M_α is the mass of the ion, N is the total number of unit cells in the lattice, $a(\mathbf{q},l)$ is the time-dependent amplitude of the lth normal mode having wave number vector $\mathbf{q}$, and $\boldsymbol{\xi}$ is the polarization vector normalized according to

$$\sum_\alpha \boldsymbol{\xi}_\alpha(\mathbf{q},l)\boldsymbol{\xi}_\alpha^*(\mathbf{q},l')=\delta_{l,l'}, \tag{11}$$

$\boldsymbol{\xi}$ is real if the waves are plane polarized. In the case of one atom per unit cell, there is just one α and we have a single expression for the displacement of all the ions. We can then take $\mathbf{R}$ to be given by Eq. (10) with the variable $\mathbf{r}$ in place of the ion coordinates

$$\mathbf{R}(\mathbf{r})=(MN)^{-\frac{1}{2}}\sum_{\mathbf{q},l}\mathbf{i}(\mathbf{q},l)[a(\mathbf{q},l)\exp(i\mathbf{q}\cdot\mathbf{r}) +a^*(\mathbf{q},l)\exp(-i\mathbf{q}\cdot\mathbf{r})], \tag{12}$$

where $\mathbf{i}$ is a unit vector, since according to Eq. (11) $\boldsymbol{\xi}$ is a unit vector when there is only one α. For every $\mathbf{q}$ there are in this case three modes ($l=1,2,3$), one longitudinal and two transverse vibrations. The matrix elements (3) of

$$\Delta U=V(\mathbf{r})-V_0(\mathbf{r})=-\mathbf{R}\cdot\operatorname{grad}V_0 \tag{13}$$

are well known in the theory of conductivity. Only the displacement due to longitudinal vibrations gives nonvanishing matrix elements. These are given by[14]

$$[\psi(\mathbf{k}\pm\mathbf{q},\sigma)\chi(n_q\mp1)|\Delta U|\psi(\mathbf{k},\sigma)\chi(n_q)] =\mp(MN)^{-\frac{1}{2}}\frac{2i}{3}qC_\sigma\left(\frac{\hbar}{2\omega_q}\right)^{\frac{1}{2}}\begin{vmatrix}(n_q)^{\frac{1}{2}}\\(n_q+1)^{\frac{1}{2}}\end{vmatrix}, \tag{14}$$

where C_σ is an interaction parameter independent of $\mathbf{k}$. In the theory of metallic conduction only electrons in one energy band have to be considered. Since we have to deal with both valence and conduction bands, we have to use two different C's, one for each band σ.

When there are two atoms per unit cell, the displacements of which are given by different expressions the question arises what expression to take for $\mathbf{R}(\mathbf{r})$. If we limit the values of $\mathbf{q}$ to the first Brillouin zone, then there will be six modes for each $\mathbf{q}$; three of which, having relatively low frequencies, form the acoustic branch, the other three constitute the optical branch. In the acoustic vibrations of long wavelength (small $\mathbf{q}$) the two atoms in a unit cell move approximately in the same directions with equal amplitudes. For such modes[15]

$$\xi_1(\mathbf{q},l)/M_1^{\frac{1}{2}}=\xi_2(\mathbf{q},l)M_2^{\frac{1}{2}}. \tag{15}$$

In view of the normalization condition we have

$$\begin{aligned}\xi_1(\mathbf{q},l)&=\mathbf{i}(\mathbf{q},l)(M_1/M_1+M_2)^{\frac{1}{2}},\\ \xi_2(\mathbf{q},l)&=\mathbf{i}(\mathbf{q},l)(M_2/M_1+M_2)^{\frac{1}{2}}.\end{aligned} \tag{16}$$

The displacements of all ions caused by such a mode of vibration are given then by one expression

$$[(M_1+M_2)N]^{-\frac{1}{2}}\mathbf{i}(\mathbf{q},l)[a(\mathbf{q},l)\exp(i\mathbf{q}\cdot\mathbf{r}_{\alpha p}) +a^*(\mathbf{q},l)\exp(-i\mathbf{q}\cdot\mathbf{r}_{\alpha p})],$$

and we can again take the displacement of any point $\mathbf{r}$ to be given by this expression with $\mathbf{r}$ replacing $\mathbf{r}_{\alpha p}$. We shall assume that $R(r)$ due to all the acoustic modes is given by Eq. (12) with (M_1+M_2) replacing M. Thus, for germanium and silicon we use twice the atomic mass for M. For these substances the optical modes do not seem to play a significant part in determining the electron scattering in conduction problems. It might be inferred that the interaction with these modes is small compared with that with acoustic modes.[16] We shall not consider the effect of these modes.

To use Eq. (8) we have to know the difference between any energy level $(\mathbf{k},c)$ of the conduction band and the bottom level $(\mathbf{k}_b,c)$ of the band, and the difference

[12] F. Seitz, *The Modern Theory of Solids* (McGraw-Hill Book Company, Inc., New York, 1940). His Eq. (23), p. 131, omits the second term on the right-hand side of Eq. (12). For the case of one atom per unit cell see reference 14, p. 503.

[14] A. Sommerfeld and H. Bethe, *Handbuch der Physik* 24/2 (1933).

[15] L. Brillouin, *Wave Propagation in Periodic Structures* (McGraw-Hill Book Company, Inc., New York and London, 1946), p. 52.

[16] F. Seitz, Phys. Rev. **73**, 549 (1948).

TABLE I. Temperature coefficient of the energy gap in silicon and germanium.

	$\lvert C_c\rvert$ ev	$\lvert C_v\rvert$ ev	β degree^{-1}	$\partial E_G/\partial T$ (10^{-4} ev/°K) (24)	(23)	(23+24)	$\partial E_G/\partial T$ (10^{-4} ev/°K) experimental
Si	9.75[a]	16.9[a]	10×10^{-6} [b]	−1.78	−1.8[c]	−3.58	−3 to −5[d]
Ge	2.55[a]	3.6[a]	23×10^{-6} [b]	−0.95	−0.11[c]	−1.06	∼−4[d]

[a] Value given by Bardeen and Shockley (reference 9).
[b] Slightly different values were used by Bardeen and Shockley: 9×10^{-6} for Si and 19×10^{-6} for Ge.
[c] The values given in the first work of reference 11 were in error by a factor 2.
[d] Absorption measurements by M. Becker. These measurements are being repeated with greater accuracy.

between any energy level $(\mathbf{k}, v)$ and the top level $(\mathbf{k}_t, v)$ of the valence band. We shall assume that in both cases the difference is equal in magnitude to

$$\hbar^2|\Delta\mathbf{k}|^2/2m^*, \tag{17}$$

where m^* is the absolute value of the effective mass. The summations in Eq. (8) will as usual be replaced by integrations

$$\Sigma_q=[N\Omega/(2\pi)^3]\int_0^{q_{\max}}\int_0^{\pi}\int_0^{2\pi} q^2\sin\theta dq d\theta d\varphi, \tag{18}$$

where Ω is the volume of the unit cell and $q_{\max}/2\pi$ is the radius of a sphere with volume equal to a unit cell in the reciprocal lattice

$$q_{\max}=2\pi\Omega^{-\frac{1}{3}}(3/4\pi)^{\frac{1}{3}}. \tag{19}$$

Substituting Eqs. (14), (17), and (18) into Eq. (8) we get with

$$\Delta E_G=-\frac{1}{(2\pi)^3}\frac{4}{9}\frac{\hbar\Omega}{2Mu}$$
$$\times\left[\frac{2m_c^*}{\hbar^2}C_c^2\int\int\int\left(\frac{n_q}{q-K_c}+\frac{n_q+1}{q+K_c}\right)q^2\sin\theta dq d\theta d\varphi\right.$$
$$\left.+\frac{2m_v^*}{\hbar^2}C_v^2\int\int\int\left(\frac{n_q}{q-K_v}+\frac{n_q+1}{q+K_v}\right)q^2\sin\theta dq d\theta d\varphi\right], \tag{20}$$

where the subscripts c and v refer to the conduction and valence bands, respectively, u is the sound velocity in the crystal, and $K=2m^*/\hbar^2$. If the temperature is high enough so that $kT>(\hbar\omega_q)_{\max}$ we can use the approximation,

$$n_q=1/[\exp(\hbar\omega_q/kT)-1]\sim kT/\hbar\omega_q. \tag{21}$$

The first term in each integrand has a denominator that goes through zero at $q=K$. Taking the principal value for the integrals of these, we get

$$\Delta E_G=-\frac{1}{(2\pi)^3}\frac{4}{9}\frac{\Omega}{\hbar Mu}(m_c^*C_c^2+m_v^*C_v^2)$$
$$\times\left(\frac{kT}{\hbar u}8\pi q_{\max}+2\pi q_{\max}\right). \tag{22}$$

In this equation we have neglected K compared with $q_{\max}$, since K is of the order 10^6 cm^{-1}, whereas $q_{\max}$ is of the order 10^8 cm^{-1}. In view of Eq. (19) we get

$$\partial\Delta E_G/\partial T=-(8/9\pi)(3/4\pi)^{\frac{1}{3}}(k\Omega^{\frac{1}{3}}/\hbar^2Mu^2)$$
$$\times(m_c^*C_c^2+m_v^*C_v^2). \tag{23}$$

To check this equation with the experimentally observed temperature dependence of E_G, the variation of E_{G0} with temperature has to be taken into account. According to Bardeen and Shockley[9]

$$|\partial E_{G0}/\partial\Delta|=\tfrac{2}{3}(|C_c|\pm|C_v|),$$

where Δ is the dilation of the lattice. They conclude on the basis of experimental evidence that for germanium and silicon $\partial E_{G0}/\partial\Delta$ is negative and that on the right hand side the positive sign should be taken. Thus,

$$\partial E_{G0}/\partial T=-\tfrac{2}{3}(|C_c|+|C_v|)\beta, \tag{24}$$

β being the volume coefficient of expansion. The parameters C_c and C_v can be estimated from the mobilities of conduction electrons and holes, using the well-known equation of mobility due to lattice scattering[17]

$$\mu=3(\pi/2)^{1/2}e\hbar^4Mu^2/\Omega(kT)^{3/2}m^{*5/2}C^2. \tag{25}$$

Although the mobilities have been accurately measured, the effective masses have not been reliably determined. The smaller the effective masses the larger will be both Eqs. (23) and (24). Table I gives the results of numerical calculations for silicon and germanium using the free electron mass for the effective masses.[11] Fair agreement with the experimental data is obtained for silicon. For germanium the calculated value is too small; however, if the effective masses were about one-third of the free electron mass, good agreement would have been obtained.[18] Only experimental data of the optical measurements are given in the table. There are other measurements giving information on $\partial E_G/\partial T$ as we have mentioned at the beginning. A detailed discussion of these results has been presented elsewhere.[11]

Strictly speaking, each effective mass in Eq. (23)

[17] NDRC Report 14-585, Purdue University, 1945 (unpublished).

[18] Recently, J. H. Taylor reported measurements on the pressure dependence of the resistance of germanium, Phys. Rev. **80**, 919 (1950). Attributing the effect entirely to a variation of the energy gap, it was found that the results agree with Eq. (24) if free electron mass are used for the effective masses. The interpretation of the effect could, however, be more complicated. The author is indebted to Professor P. H. Miller, Jr. for seeing the manuscript before publication.

should be a suitable average for the band with which it is associated and will not be the same as the effective mass in Eq. (25) which applies near the band edge. In fact our assumption (17) is a good approximation only near the band edges. However, the order of magnitude of the result should not depend on the form of Eq. (17), and the brief discussion shows that the lattice vibration effect is not negligible and that its order of magnitude is compatible with experimental results. According to Radkowsky's treatment this effect would be about 10^3 times smaller.

IV. POLAR CRYSTALS

In polar crystals strong electron-lattice interaction results from the polarization of the lattice which is produced mainly by the longitudinal optical modes. The polarization in a unit cell is

$$e^*(\mathbf{R}_1-\mathbf{R}_2), \tag{26}$$

where $\mathbf{R}_1$ and $\mathbf{R}_2$ are the displacements of the positive and negative ions, respectively, and e^* is the effective charge of the ions, which differs from the true charge by the effect of the polarization of the ions as a result of their displacements. For optical modes of small $\mathbf{q}$[15]

$$\mathbf{R}_1/\mathbf{R}_2=-M_2/M_1. \tag{27}$$

The normalization condition (11) gives in conjunction with Eq. (27)

$$\begin{aligned}\xi_1(\mathbf{q})&=i(\mathbf{q})(M_2/M_1+M_2)^{\frac{1}{2}},\\ \xi_2(\mathbf{q})&=-i(\mathbf{q})(M_1/M_1+M_2)^{\frac{1}{2}}.\end{aligned} \tag{28}$$

Thus, for small q the polarization of a cell with center at $\mathbf{r}_p$ is, according to Eqs. (10) and (26),

$$e^*(MN)^{-\frac{1}{2}}i(\mathbf{q})[a(\mathbf{q})\exp(i\mathbf{q}\cdot\mathbf{r}_p)+a^*(\mathbf{q})\exp(-i\mathbf{q}\cdot\mathbf{r}_p)],$$

where $M=M_1M_2/(M_1+M_2)$ is the reduced mass. Assuming that the optical modes give a combined polarization (per unit volume) wave

$$\frac{e^*}{2a^3}\frac{1}{(MN)^{\frac{1}{2}}}\sum_q i(\mathbf{q})[a(\mathbf{q})\exp(i\mathbf{q}\cdot\mathbf{r})+a^*(\mathbf{q})\exp(-i\mathbf{q}\cdot\mathbf{r})], \tag{29}$$

where a is the interionic distance, Fröhlich[19] has shown that the matrix elements of the interaction potential are given by

$$\frac{1}{(MN)^{\frac{1}{2}}}\frac{2\pi ee^*}{a^3q}\left(\frac{\hbar}{2\omega_0}\right)^{\frac{1}{2}}\begin{Bmatrix}(n_q)^{\frac{1}{2}}\\(n_q+1)^{\frac{1}{2}}\end{Bmatrix}. \tag{30}$$

The frequencies of the longitudinal optical modes are approximately constant and are related to the ω_t of the transverse optical modes (Reststrahl frequency) by[20]

$$\omega^2=\omega_t^2(\epsilon_s/\epsilon_0), \tag{31}$$

where ϵ_s is the static dielectric constant and ϵ_0 is the contribution to the dielectric constant from the polarizability of the ions, i.e. the dielectric constant at frequencies too high for ion displacements to follow. The frequency ω_t itself is related to ϵ_s and ϵ_0 by

$$\omega_t^2=2\pi e^{*2}\epsilon_0/Ma^3(\epsilon_s-\epsilon_0), \tag{32}$$

from which the effective charge e^* can be determined. In view of Eqs. (31) and (32) the matrix elements of interaction potential (30) can also be written

$$\frac{4\pi e}{V^{\frac{1}{2}}}\frac{1}{q}\left[\frac{\hbar\omega}{8\pi}\left(\frac{1}{\epsilon_s}-\frac{1}{\epsilon_0}\right)\right]^{\frac{1}{2}}\begin{Bmatrix}(n_q)^{\frac{1}{2}}\\(n_q+1)^{\frac{1}{2}}\end{Bmatrix}, \tag{33}$$

where $V=2Na^3$ is the volume of the crystal. This is the same expression derived by Fröhlich, Pelzer, and Zienau.[21]

Using Eq. (30) we get from Eq. (8)

$$\begin{aligned}\Delta E_G=&-\frac{(2\pi ee^*)^2}{a^6}\frac{\hbar}{2MN\omega}\frac{2Na^3}{(2\pi)^3}\\ &\times\left[\frac{2m_e^*}{\hbar^2}\int\int\int\left(\frac{n_q}{q^2-J_e^2}+\frac{n_q+1}{q^2+J_e^2}\right)\sin\theta dqd\theta d\varphi\right.\\ &\left.+\frac{2m_v^*}{\hbar^2}\int\int\int\left(\frac{n_q}{q^2-J_v^2}+\frac{n_q+1}{q^2+J_v^2}\right)\sin\theta dqd\theta d\varphi\right],\end{aligned} \tag{34}$$

where $J^2=2m^*\hbar\omega/\hbar^2$. Since ω is approximately constant, n_q is independent of $\mathbf{q}$ according to Eq. (21). Taking principal values for the integrals of the first term in each integrand, we get

$$\Delta E_G=-\frac{\pi(ee^*)^2\hbar^{\frac{1}{2}}}{a^3M\omega^{\frac{1}{2}}}\left[\left(\frac{2m_e^*}{\hbar^2}\right)^{\frac{1}{2}}+\left(\frac{2m_v^*}{\hbar^2}\right)^{\frac{1}{2}}\right](n+1), \tag{35}$$

where we have neglected J compared with $q_{\max}$, since $\hbar^2q_{\max}^2/2m^*$ is of the order of several electron-volts, whereas $\hbar\omega$ is of the order 10^{-1} to 10^{-2} ev. This equation gives the same dependence of ΔE_G on n (or temperature) as obtained by Radkowsky. Because of this coincidence we can refer to his discussion of the result, which shows that it is in general agreement with the experimental data on the shift of absorption edge in polar crystals.

The author wishes to express his indebtedness to Professor H. Fröhlich, Professor H. M. James, and Professor K. Lark-Horovitz for helpful discussions.

[19] H. Fröhlich, Proc. Roy. Soc. (London) **160**, 230 (1937). In this paper e was used instead of e^* and $2N$ was used instead of N. See H. B. Callen, Phys. Rev. **76**, 1394 (1949).

[20] Lyddane, Sachs, and Teller, Phys. Rev. **59**, 673 (1950).

[21] Fröhlich, Pelzer, and Zienau, Phil. Mag. **41**, 221 (1950).

Radioactive Decay of Cs^{137}

M. A. WAGGONER*
Departments of Physics, State University of Iowa, Iowa City, Iowa
(Received January 24, 1951)

The spins of the ground states of Cs^{137} and Ba^{137} are known to be 7/2 and 3/2, respectively. The shape of the 518-kev beta-ray spectrum has been measured and found to correspond to the correction factor $G'=(W_0-W)^3+A(W^2-1)$ in agreement with previous work. This is the shape predicted by the Fermi theory of beta-ray decay and the Gamow-Teller selection rules for a transition for which $\Delta I=\pm 2$ and there is a parity change. The internal conversion coefficient of the 663-kev gamma-ray has been measured and found to be 0.097, which is in agreement with the theoretical value for magnetic 2^4-pole radiation.

IN the isotope Cs^{137} we have a means of testing the Fermi theory of beta-ray decay and the selection rules involved therein as well as the theory of internal conversion and the recent calculations of internal conversion coefficients.

An experiment designed for these purposes is as follows.

I. KNOWN

It is known that the spins[1] of the ground states of Cs^{137} and Ba^{137} are 7/2 and 3/2, respectively, and that the Cs^{137} isotope decays by beta-ray emission either to the ground state of Ba^{137} or to a metastable excited state of Ba^{137}, which then decays by single gamma-ray emission to the ground state of Ba^{137}. This gamma-ray is highly internally converted.

The decay scheme of Cs^{137} is shown in Fig. 1. For convenience we assume that the ground state of Ba^{137} has even parity as predicted by the nuclear shell model.[2] The energy of the high energy beta-ray given in Fig. 1 is that given by Osaba,[3] whose results indicate

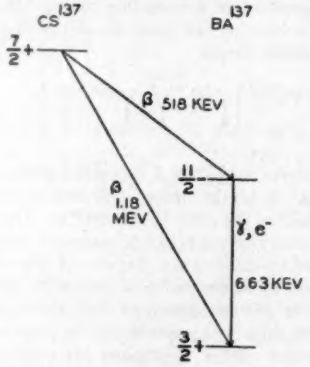

FIG. 1. Decay scheme of Cs^{137} and assignment of spins and parities to the nuclear levels involved in its decay.

that two to five percent of the decay processes proceed in this manner. All other energy values given in Fig. 1 are those obtained in the present experiment and are in agreement with previous results.[3] The half-life of the metastable excited state of Ba^{137} is known to be 158 ± 5 seconds.[4]

Langer and Moffat[5] have recently investigated the shape of the high energy beta-ray spectrum in detail and found that it is the shape predicted by the Fermi theory of beta-ray decay and the Gamow-Teller selection rules for a transition for which $\Delta I=\pm 2$ and there is no parity change. The shape of the low energy beta-ray spectrum has been investigated carefully by several different research groups[3,6,7] and found to have the shape predicted by the Fermi theory of beta-ray decay and the Gamow-Teller selection rules for a transition for which $\Delta I=\pm 2$ and there is a parity change. (Correction factor G'.)

The internal conversion coefficient for the K shell (α_K) and the α_K/α_L ratio for the 663-kev gamma-ray have been measured by Osaba[3] and by Mitchell and Peacock.[8] Their results were $\alpha_K=0.081$, $\alpha_K/\alpha_L=5.0$ and $\alpha_K=0.118$, $\alpha_K/\alpha_L=4.8$, respectively. These results do not permit an unambiguous classification of the multipole order of the gamma-ray.

II. APPARATUS

The beta-ray spectrometer used in this experiment is the double-coil thin-lens magnetic spectrometer described in a recent paper by Waggoner, Moon, and Roberts.[9] The adjustment of the spectrometer for this experiment is the same as that described in the paper referred to, namely, 2.40 percent transmission, line width of about 3.0 percent, energy calibration with respect to the Co^{60} internal conversion lines, and the crystal spectroscopy values for the energies of these lines.[10] The source mounting, counters, and external conversion absorbers and converters used in this experiment are as described in that paper.

* Present address: Department of Physics, Vassar College, Poughkeepsie, New York.

[1] L. Davis, Phys. Rev. **76**, 435 (1949); Davis, Nagle, and Zacharias, Phys. Rev. **76**, 1069 (1949); R. Hays, Phys. Rev. **60**, 75 (1941); O. Arroe, Phys. Rev. **77**, 745A (1950).

[2] E. Feenberg and K. C. Hammack, Phys. Rev. **75**, 1877 (1949).

[3] J. S. Osaba, Phys. Rev. **76**, 345 (1949).

[4] Townsend, Cleland, and Hughes, Phys. Rev. **74**, 499 (1948).

[5] L. M. Langer and R. J. D. Moffat, Phys. Rev. **82**, 333 (1951).

[6] C. Peacock and A. Mitchell, Phys. Rev. **75**, 1272 (1949).

[7] L. Langer and H. Price, Jr., Phys. Rev. **76**, 641 (1949).

[8] A. Mitchell and C. Peacock, Phys. Rev. **75**, 197 (1949).

[9] Waggoner, Moon, and Roberts, Phys. Rev. **80**, 420 (1950).

[10] Lind, Brown, and DuMond, Phys. Rev. **76**, 591, and 1838 (1949).

III. MEASUREMENTS

A. Shape of the 518-kev Beta-Ray Spectrum

The uncorrected Fermi plot of the 518-kev beta-ray spectrum is shown in Fig. 2, curve A. Curve B of Fig. 2 shows the Fermi plot of the same spectrum when corrected with the correction factor[11] $G'=(W_0-W)^2+A(W^2-1)$, where W is the electron energy in units of m_0c^2, W_0 is the total energy available for the beta-ray transition in units of m_0c^2, and A is a function of the atomic number and the electron energy W.

The fit of the correction factor G' is in agreement with previous results[3,6,7] and indicates that the interaction is of either the tensor or axial vector form and that the selection rule obeyed in this beta-ray transition is

$$\Delta I=\pm 2;\ \text{change in parity.}$$

B. Internal Conversion Coefficient of the Cs^{137} Gamma-Ray First Method

The methods by which the internal conversion coefficient can be measured have been discussed fully in the paper by Waggoner, Moon, and Roberts.[9] The first method which we used to measure the internal conversion coefficient of the Cs^{137} gamma-ray is method A of that paper, i.e.,

$$\alpha=r_a/(N_\gamma t), \tag{1}$$

where α = internal conversion coefficient of the gamma-ray = number of internal conversion electrons/number of gamma-rays, $N\gamma$ = number of gamma-rays per minute from the source, and r_a = counting rate per minute at the peak of the internal conversion line as observed with a spectrometer of transmission t when using an infinitely thin source.

Owing to the fact that the excited state of Ba^{137} is metastable with a half-life of 158 seconds, the number of gamma-rays could not be determined by coincidence counting techniques, and we determined N_γ by means of external conversion comparison methods. That is, using identical converters, we compared the external conversion line of a source of Cs^{137} with the external conversion line of a source which could be calibrated by coincidence counting techniques. The converter used consisted of an aluminum absorber ($\frac{1}{16}$" thick) and a lead converter (0.001" thick) placed directly in front of the radioactive source. Because of the dependence of the photoelectric cross section on energy and the effects of anisotropy and scattering of the photoelectrons, it is advisable to use sources such that the energies of the gamma-rays being compared are as nearly alike as possible in order that the errors due to the above effects may be small. It is often difficult to obtain such sources, however.

The gamma-rays used for comparison measurements

[11] E. J. Konopinski and G. E. Uhlenbeck, Phys. Rev. **60**, 308 (1941); E. J. Konopinski, Revs. Modern Phys. **15**, 226 (1943); J. S. Osaba, Phys. Rev. **76**, 345 (1949).

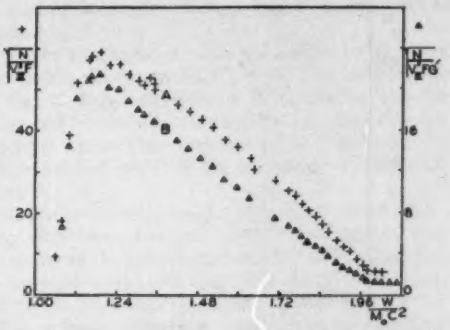

FIG. 2. A: The uncorrected Fermi plot of the 518-kev beta-ray spectrum from Cs^{137} (left scale). B: The Fermi plot of the 518-kev beta-ray spectrum from Cs^{137} when corrected with the correction factor G' (right scale).

were the 880-kev gamma-ray from Sc^{46} and the 1.117- and 1.332-Mev gamma-rays from Co^{60}. These sources could be calibrated by coincidence counting techniques and the external conversion lines obtained quite accurately with the spectrometer. The empirical formula of Gray[12] was used to obtain the dependence of the photoelectric cross section on energy. The probable errors given for the values of α obtained by this method do not include possible errors caused by uncertainty in the dependence of the photoelectric cross section on energy or the effects of anisotropy or scattering of the photoelectrons.

A typical example of the data obtained for the determination of r_a, i.e., the internal conversion line of Cs^{137}, is shown in Fig. 3.

The values of α obtained by this method ($\alpha=r_a/N_\gamma t$, N_γ obtained by external conversion comparison measurements) are given in Table I. The average of the values obtained by this method is $\alpha=0.097\pm0.003$.

It should be noted that this method of determining the internal conversion coefficient of the gamma-ray is entirely independent of all of the other decay processes of Cs^{137} and in particular does not make any use of the Fermi theory of beta-ray decay.

C. Internal Conversion Coefficient of the Cs^{137} Gamma-Ray Second Method

The second method of determining the internal conversion coefficient of the Cs^{137} gamma-ray which we used is the method B discussed in the paper of Waggoner, Moon, and Roberts,[9] i.e.,

$$\alpha=[(A/r_a\omega)-1]^{-1}=[(A/A_a)-1]^{-1}, \tag{2}$$

where A is the area under the beta-ray spectrum for the beta-ray which leads to the excited state, which then decays by the emission of the gamma-ray whose internal conversion coefficient is to be measured, A_a is

[12] L. H. Gray, Proc. Cambridge Phil. Soc. **27**, 103 (1931).

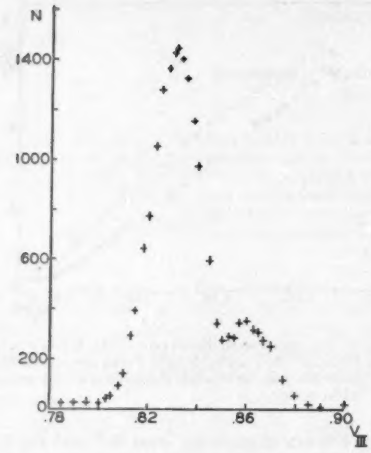

FIG. 3. The K and $L+M+N$ internal conversion lines for the gamma-ray involved in the decay of Cs^{137}.

the area under the internal conversion line, and w is the line width for the particular source and spectrometer adjustment, $w=A_a/r_a$. Equation (2) assumes that the same source is used to obtain both A and A_a and that the spectrometer has the same adjustment for both measurements.

In order to obtain A for the Cs^{137} sources the momentum plot of the beta-ray spectrum was reconstructed from the corrected Fermi plot of that spectrum. This reconstruction procedure was necessary, since the thickness of the counter window did not permit us to obtain valid data below about 120 kev. Thus, points for the momentum plot in this energy region were obtained by extrapolating to zero the straight corrected Fermi plot (correction factor G') observed at higher energies.

The values for the internal conversion coefficient of the Cs^{137} gamma-ray obtained by this method are given in Table I. The average of the values of α obtained by this method is $\alpha=0.097\pm0.005$. The probable error given includes possible error due to the high energy beta-ray spectrum which was not of sufficient abundance[9] to be accurately corrected for otherwise.

TABLE I. Experimental values of the internal conversion coefficient of the gamma-ray involved in the decay of Cs^{137}. Value obtained for ratio of number of K conversion electrons to number of $L+M+N$ conversion electrons=4.7.

Method of measurement	Cs^{137} source number		$\alpha_K\times10^3$
External conversion comparison against			
Sc^{46}	7		9.20
	19		10.15
		Average	9.7±0.3
Co^{60}	7		9.69
	19		9.72
		Average	9.7±0.3
Comparison of areas A_a/A	7		9.86
	19		9.52
		Average	9.7±0.5

IV. CONCLUSIONS

A. The 518-kev beta-ray spectrum has an energy dependence which can be associated with the correction factor[11] G'. This is the shape predicted by the Fermi theory of beta-ray decay and the Gamow-Teller selection rules for a beta-ray transition for which the spin changes by two units ($\Delta I=\pm2$) and there is a change in parity.

B. The above results indicate that the selection rule obeyed in the 518-kev beta-ray transition is $\Delta I=\pm2$; change in parity and thus that the spin of the metastable excited state of Ba^{137} is 3/2 or 11/2, and the parity of this state is different from that of the ground state of Cs^{137}. Since the spin of the Ba^{137} ground state is known to be 3/2, in order to account for the low abundance of the 1.8-Mev beta-ray and the 158-second half-life of the metastable excited state of Ba^{137} we must, on the basis of beta-ray theory alone, assign the latter of these two values, 11/2, as the spin of the Ba^{137} metastable excited state.

TABLE II. Comparison of the experimental and theoretical (reference 13) values for the internal conversion coefficient for the Cs^{137} gamma-ray.

Experimental value of α_K	Theoretical values (reference 13) for α_K				
	$E(2^4)$	$E(2^5)$	$M(2^5)$	$M(2^4)$	$M(2^6)$
0.097±0.005	0.025	0.053	0.045	0.094	0.25

C. Since the results obtained for the value of the internal conversion coefficient as measured by the two different methods agree, it appears that the theory of beta-ray decay and the correction factor G' for the 518-kev beta-ray spectrum, in so far as they were used in one of these methods of determining the internal conversion coefficient and to the extent that the value of the internal conversion coefficient depends on this use, are in agreement with experiment.

D. The experimental value of the internal conversion coefficient of the Cs^{137} gamma-rays agrees unambiguously with the theoretical value[13] for magnetic 2^4-pole radiation, $M(2^4)$, as indicated in Table II. This agreement constitutes another experimental verification of the theory of internal conversion.[9,14]

E. Since the gamma-ray is $M(2^4)$-pole radiation, the selection rule obeyed in the gamma-ray transition must be

$$|I-I'|\leqslant4\leqslant|I+I'|\text{; change in parity;}$$

i.e., the parity of the Ba^{137} metastable excited state must

[13] Rose, Goertzel, Spinrad, Harr, and Strong Phys. Rev. **76**, 184 (1949).

[14] Moon, Waggoner, and Roberts, Phys. Rev. **79**, 905 (1950).

be odd and the spin I satisfy the condition

$$|I-\tfrac{1}{2}| \leqslant 4 \leqslant |I+\tfrac{1}{2}|.$$

Thus, the spin I of the Ba^{137} metastable excited state must be 11/2. An assignment of a lower value, e.g., 9/2, would permit $E(2^8)$-pole radiation as a competing process of much higher probability (half-life[15] of less than 10^{-7} seconds) and internal conversion coefficient much different from the experimental value.

F. The value predicted for the spin of the Ba^{137} metastable state from the results on the 518-kev beta-ray transition (conclusion B) and the results on the internal conversion of the gamma-ray (conclusion E) agree, and thus, if we assume the theory of internal conversion is correct, as seems indicated, we may consider this agreement a verification of the Fermi theory of beta-ray decay and the Gamow-Teller selection rules. (It is of interest to recall here that the theory of internal conversion does not depend on any particular knowledge of nuclear structure nor is it based on any nuclear model.)

G. The assignment of spins and parities to the states involved in the decay of Cs^{137} would thus be as shown in Fig. 1. This assignment is in agreement with the shape and relative abundance of the 1.18-Mev beta-ray spectrum indicated by previous results[3,5] and with the 158-second half-life[3,15] of the metastable excited state of Ba^{137}.

H. The predicted spins and parities are also in agreement with the nuclear shell model,[3] which predicts that the parity of the ground state of Ba^{137} and Cs^{137} should be the same (even) and that there should be an 11/2, odd excited state near the ground state of Ba^{137}.

The radioactive isotopes used in this investigation were obtained from the Oak Ridge National Laboratory, Union Carbide and Carbon Corporation.

The author wishes to express her sincere thanks to Dr. A. Roberts for many helpful discussions and to Mr. M. L. Moon, who assisted in the construction and maintenance of the apparatus used.

[15] E. Segrè and A. C. Helmholz, Revs. Modern Phys. **21**, 280 (1949); H. Bethe, Revs. Modern Phys. **9**, 226 (1937).

PHYSICAL REVIEW VOLUME 82, NUMBER 6 JUNE 15, 1951

Effect of Turbulence in Thermal Diffusion Columns*

JOHN DONALDSON† AND W. W. WATSON
Sloane Physics Laboratory, Yale University,‡ New Haven, Connecticut

(Received January 16, 1951)

A certain amount of controlled turbulence improves markedly the separation factor and transport of thermal diffusion isotope separation columns. Measurements on this effect are reported for hot-wire columns 3 meters long, operating on argon gas, and with power input about 725 watts. At pressures three times that for onset of gene ral turbulence the separation factor q_e is still 1.5. Spacers made of pairs of cross-wires of 40-mil Ni wire attached to the hot wire every 10 cm along its length raise the separation factor q_e for optimum pressure from 9.1 to 27.2. If these spacers are attached every 5 cm, q_e rises further to 36. The optimum pressure increases from 0.17 atmos (no spacers) to 0.28 atmos. Identical operation of a similar column with a plain hot wire but with slight constrictions every 15 cm in the cold wall gives $q_e=26.6$. Introduction of these regularly spaced interruptions to the lamellar convective flow of the gas also increases the transport of the A^{36} isotope to the top of the column. Some analysis of these effects is given.

I. INTRODUCTION

IN the treatment of the thermal diffusion column by Furry, Jones, and Onsager,[1] and by others[2] it is specified that the vertical convective flow of the gas is lamellar, and that if any horizontal convective mixing does occur the separation of the isotopes is thereby reduced. There have been several reports,[3–7] however, that upon introduction of some turbulence, either by increasing the gas pressure sufficiently or by placing at regular intervals in the column partial obstructions to the gas flow, increases in the separation of the gas components result. Furthermore, recent thermal diffusion column work[8,9] with binary gas mixtures at high pressure, hence surely somewhat turbulent, has produced separations greater than the values predicted by the laminar-flow theory.

In their first long paper giving details of their simple

* Part of a dissertation submitted by John Donaldson in partial fulfillment of the requirements for the degree of Doctor of Philosophy at Yale University.

† Now with California Research and Development Co. at Radiation Laboratory, Berkeley, California.

‡ Assisted by the AEC.

[1] Furry, Jones, and Onsager, Phys. Rev. **55**, 1083 (1939).

[2] R. C. Jones and W. H. Furry, Revs. Modern Phys. **18**, 151 (1946). This review article contains references to most of the earlier work on thermal diffusion.

[3] A. K. Brewer and A. Bramley, Science **90**, 165 (1939); Phys. Rev. **55**, 590A (1939).

[4] A. Bramley and A. K. Brewer, J. Chem. Phys. **7**, 553 and 972 (1939).

[5] A. Bramley, Phys. Rev. **57**, 359A (1940).

[6] K. Clusius and G. Dickel, Z. physik. Chem. **B44**, 451 (1939).

[7] R. Simon, Phys. Rev. **69**, 596 (1946).

[8] E. W. Becker, Z. Naturforsch. **2a**, 447 (1947).

[9] Drickamer, Mellow, and Tung, J. Chem. Phys. **18**, 945 (1950); Giller, Duffield, and Drickamer, J. Chem. Phys. **18**, 1027 (1950).

but most successful method of cascading the thermal diffusion effect in a vertical column with a hot wire along its axis, Clusius and Dickel state that spacers used to keep the wire centered not only do not reduce the separation effect but that the introduction of more spacers actually increases the separation of HCl^{35} and HCl^{37} in a given length of column.[10] Their spacers were circular disks of platinum, 0.2 mm thick, perforated to allow for gas flow, and gold soldered onto the platinum wire. These were originally spaced at 60-cm intervals along their column. For some columns they found that installation of even more spacers nearly doubled the isotope separation produced by the column, but no details are given.

Brewer and Bramley[2–5] found that the insertion of various types of partial obstruction to smooth, laminar gas flow at regular intervals along short concentric-cylinder columns increased somewhat the separation of a CH_4-NH_3 gas mixture. One of their most interesting observations was that well-defined swirls existed in the gas between the brass washers used as spacers in their column producing the largest gas separation factor. We, too, have demonstrated the existence of such gas swirls in our most successful isotope-separating column of the hot-wire type with many spacers regularly spaced along the wire.

Our experiments have been carried out to determine more exactly how the introduction of some turbulence into the gas betters the performance of a hot-wire thermal diffusion column for isotope separation. We have both extended the observations of Simon[7] for the condition of general turbulence and have operated with various arrangements of spacers and with regularly spaced constrictions of the outer cold wall at optimum gas pressure for maximum isotope separation factor.

II. APPARATUS

The construction of the glass hot-wire columns is similar to those described in previous publications from this laboratory.[11] The cold wall is a glass cylinder of 2 cm i.d., the hot wire is 20-mil tungsten, and the column length is 3 meters. A 130 cm^3 end volume is convectively connected to the bottom of the column, but at the top the sampling outlet is attached directly to the column. The top end of the column itself of course acts as an end volume, and by the process of analyzing several samples taken one after another we estimate it to be effectively about 20 cm^3. Our second column has these same dimensions except that the cold wall is indented every 15 cm along its length. These constrictions are about 2 mm deep.

We have used as spacers two nickel wires, either 20 mil or 40 mil, attached perpendicularly to the tungsten wire and perpendicular to each other to form a cross. The smaller Ni wires are spot-welded to the tungsten wire, each pair covering about 5 percent of the cross-sectional area of the column. Holes are drilled through the larger Ni wires so that they may be just slipped on to the tungsten wire, and they are then welded on at the proper points along the main wire. Since they cover 10 percent of the column cross-section, the heavier cross-wire pairs cause more blocking of the vertical convective gas flow, and they also more effectively lower the wire temperature by conduction and radiation at each spacer position. No appreciable effect on the isotope separation can be detected when spacing wires are used at 1-meter intervals along the hot wire.

All of these measurements have been made with cylinder argon gas, freed of most of its nitrogen impurity by storage over calcium metal chips at 400°C. This gas when taken from the top of the column after equilibrium is attained shows at the most a 1 percent nitrogen content. The ratio of the A^{36}/A^{40} ratio at the top to that at the bottom of the column at equilibrium, effectively 6 hours under these operating conditions, measures the separation factor q_e of the column.

The isotope ratios have been determined with our 60° mass spectrometer which is based on the design of Graham, Harkness, and Thode.[12] A Brown recording potentiometer is used as the detecting device. Since our data consist mostly of the ratios of two A^{36}/A^{40} ratios, we minimize the effect of mass discrimination and other systematic errors by analyzing the two samples of a pair successively and as quickly as possible. The errors shown in our figures are all just probable errors. These are the largest for the cases of large separation factor because then the samples from the bottom of the column contain only about 0.05 percent A^{36}. The measurement of such a small relative abundance nears the sensitivity limit of our spectrometer. These too-large probable errors do not vitiate our conclusions, however, for the variations in separation factor we observe are large.

III. EXPERIMENTAL RESULTS

The large radius, 1 cm, of the cold wall of our first column was deliberately chosen so that turbulence would begin at relatively low pressures. We have employed the method of Onsager and Watson[13] to determine the critical pressure for onset of turbulence. Figure 1 is a plot of the temperature of the hot wire as a function of the pressure of the argon gas for constant power input. It is obvious that turbulence begins at 0.4 atmos and becomes increasingly more prominent the higher the pressure above this critical value, as evidenced by the greater heat transfer through the gas. This pressure of 0.4 atmos corresponds to a Reynolds number of 14. The peculiar drop in the curve where the pressure is decreasing at about 0.2 atmos and the anomalous fluctuations in the range from 0.4 atmos to

[10] See reference 6, p. 472.
[11] See for example, A. Zucker and W. W. Watson, Phys. Rev. **80**, (1950), Fig. 2.
[12] Graham, Harkness, and Thode, J. Sci. Instr. **24**, 119 (1947).
[13] L. Onsager and W. W. Watson, Phys. Rev. **56**, 474 (1939).

0.65 atmos are reproducible effects whose cause we have not yet investigated.

In Fig. 2 are plotted the experimentally determined values of the equilibrium separation factor q_e of this column as a function of the pressure, and with the power input held constant at 795±10 watts. Since these observations were made rather randomly over a period of about a month and yet lie near the smooth curve, it is obvious that the mass spectrometer was quite consistent in determining the A^{36}/A^{40} abundance ratios. These data represent a considerable extension of the earlier work of Simon[7] who made just two measurements with turbulent conditions in his column.

It is instructive to see how well the equation

$$\ln q_e = LH/(K_c+K_d) \tag{1}$$

of the Furry, Jones, and Onsager theory agrees with these experimental values. Here $L=295$ cm, H is the transport coefficient concerned with thermal diffusion, and K_c and K_d are the coefficients for the remixing by vertical convection and diffusion respectively. These transport coefficients may be evaluated from the relations given by Jones and Furry,[2] using $\alpha=0.0146$, $T_2/T_1=1680/280=6.0$, and $r_1/r_2=1.0/0.0262=38$. This calculation gives

$$\begin{aligned} H &= H'p^2 = 1.53\times10^{-4}p^2, \\ K_c &= K_c'p^4 = 2.69\times10^{-2}p^4, \\ K_d &= K_d' = 2.02\times10^{-3}. \end{aligned} \tag{2}$$

Substitution of these values into (1) gives a relationship indicating a maximum q_e of 20.4 at $p=0.53$ atmos, while for $p=0.20$ atmos it predicts q_e to be 2.3. The agreement with the observations plotted in Fig. 2 is poor, for the maximum of the experimental curve comes at $q_e=6.9$, $p=0.16$ atmos, while for $p=0.20$ atoms the experimental $q_e=6.0$.

Jones and Furry suggest that in practice a so-called parasitic convection coefficient K_p should be included to account for the remixing effect arising from inevitable asymmetries in the column. Then

$$\ln q_e = LH/(K_c+K_d+K_p). \tag{3}$$

We assume that $K_p=K_p'p^n$, where K_p' is independent of the pressure and n is an integer. Then taking the experimental values for three points in the range of laminar flow, and with $n=2$, we find that Eq. (3) fits this portion of the experimental curve well if the coefficients have the following numerical values:

$$\ln q_e = L(0.828)p^2/(1593p^4+1+46.8p^2). \tag{4}$$

But as indicated in Fig. 2 this calculated curve lies well below the (dotted) experimental curve in the higher pressure range where some turbulence exists in the column. Thus the separation factor is larger when the gas flow is somewhat turbulent than it would be if the flow remained strictly laminar for $p>0.4$ atmos.

When the hot wire in this column carried a pair of cross-wire spacers of 20-mil Ni every 15 cm along its length, the separation factors for pressures near that for the maximum of the q_e *vs* p curve were increased by

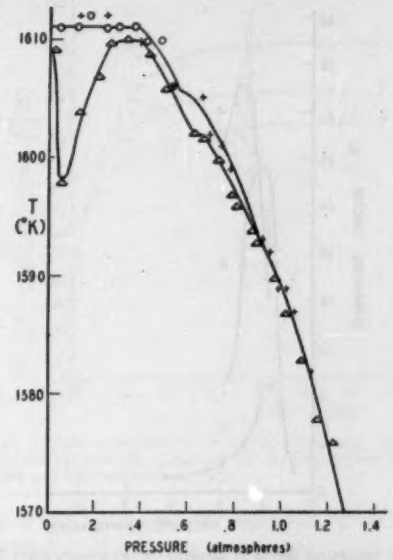

FIG. 1. Variation of the temperature of the hot wire of the thermal diffusion column with pressure of the argon gas for constant power consumption of 756 watts. Circles represent p decreasing from 0.52 atmos, crosses p increasing from 0.04 to 1.29 atmos, and triangles p decreasing from 1.29 to 0.01 atmos. Temperature determined from extension of wire.

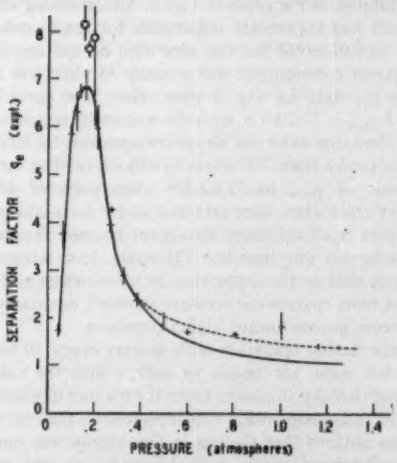

FIG. 2. Separation factor *vs* pressure for $T=1680\pm20$°K, power $=795\pm10$ watts. Crosses give observations for wire with spacers every 100 cm, circles are q_e values for wire with spacers every 15 cm. Strictly laminar flow ends at 0.4 atmos. Solid curve drawn by fitting Eq. (3) to three experimental points in range of laminar flow. Dotted curve averages the observed values in the pressure range where turbulent flow exists.

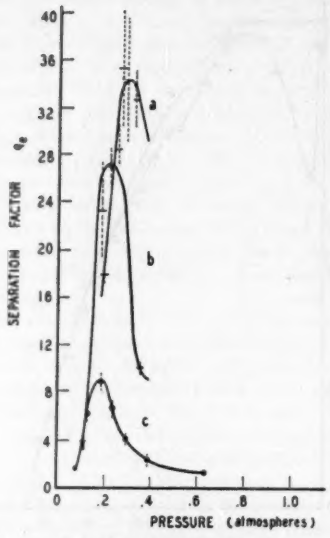

FIG. 3. Separation factor *vs* pressure for (a) spacers every 5 cm along wire, (b) spacers every 10 cm, (c) no spacers.

about 15 percent as indicated in Fig. 2. Then, after some repairing of the glass column, including the straightening of a slight bow in the cold-wall tube, operation was carried out with pairs of 40-mil Ni wire spacers every 10 cm and every 5 cm along the hot wire. The astonishing improvement in the separation factor is exhibited in the plots of Fig. 3. Straightening of the column was apparently responsible for the increase in q_{max} to 9.07 ± 0.81 for the wire with no spacers, since the power consumption was actually 35 watts less than when the data for Fig. 2 were taken. For curve *b* of Fig. 3 q_{max} is 27.2 ± 1.6, with the mean wire temperature kept the same as for the no-spacer operation by increase of the power from 760 watts to 830 watts. The further increase of q_{max} to 35.8 ± 4.9 when pairs of 40-mil spacer cross-wires were attached every 5 cm along the hot wire is all the more significant because the power consumption was then but 721 watts. It is interesting to note that as the separation factor increases with the use of more spacers the pressure at which the maximum q_e occurs moves toward higher pressures.

Once during operation with spacers every 10 cm on the hot wire, air began to diffuse into the column through a leaky stopcock. From the manner in which the resulting tungsten oxide was deposited on the cold wall, it was obvious that the gas in the column was moving in well-defined swirls, each beginning at one set of spacers and ending at the next. This observation is similar to that reported by Brewer and Bramley.[4] These swirls could arise partly from the partial blocking of the smooth lamellar flow and partly from variations in the temperature of the wire near the spacers.

To interrupt the smooth vertical convective flow of the gas in a different manner, our second glass column with the constrictions every 15 cm along the cold wall was operated with the hot wire carrying no spacers and, judging by its color, running at constant temperature throughout its length. The separation factors produced by this column are plotted in Fig. 4. For almost exactly the same power as used for the first column when its wire carried spacers every 5 cm, the maximum separation factor is 26.6 ± 0.08. This is three times the maximum factor developed for identical operation of the first column without spacers.

Finally, we have measured the rate of increase of the amount of A^{38} at the "light" end of the column to determine whether the increase in separation factor was accompanied by a change in the efficiency of operation. These measurements were made for the first column both with no spacers and with the spacers at 5-cm intervals on its hot wire, and also for the column with indentations in its cold wall. In each case the apparatus was filled to the argon gas pressure for which q_e had proved to be a maximum. The power consumption throughout was maintained at 720 ± 5 watts. Since the fraction of the total A^{36} in the column taken in each sample was not negligible, the method was to evacuate the column after each sampling and then start once again, under identical conditions, a run for a different time of operation. The results are shown in Fig. 5.

In each case the column reached equilibrium in about 6 hours. For the first hour of operation the transport, or rate of increase of the amount of A^{38} at the "light" end, was actually about 20 percent greater when the hot wire carried spacers at 5 cm intervals than when it had no spacers. Therefore the large gain in separation factor upon introduction of regular swirls in the gas by

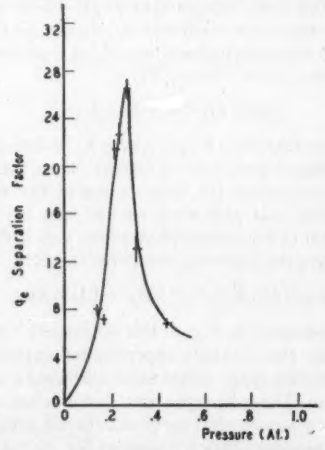

FIG. 4. Separation factor *vs* pressure for similar hot-wire column with 2-mm-deep constrictions every 15 cm along the cold wall. Wire has no spacers, $T=1640\pm10^{\circ}$K, power$=725\pm10$ watts.

means of many spacers on the hot wire or constrictions in the cold wall is accompanied by improvement in the efficiency of operation.

IV. DISCUSSION

It is of some interest to compare the representation of curves *b* and *c* of Fig. 3 by Eq. (3). We again assume $K_p = K_p' p^2$ and choose for each case three experimental points for a fit. There results for the column with spacing wires every 10 cm along the not wire

$$\log_{10} q_e = 51.9p^2/(375p^4+1-2.82p^2), \qquad (5)$$

while for the same column with no cross-wire spacers

$$\log_{10} q_e = 63.2p^2/(1130p^4+1-1.69p^2). \qquad (6)$$

The chief effect of the introduction of the spacers is apparently the considerable reduction of the ratio K_c'/K_d. Now K_d should be almost the same for the two cases, for these spacers are surely too small to affect appreciably the remixing by diffusion. Therefore the spacers mainly just alter the convective flow of the gas in the column.

In this connection we should recall that for a hot-wire column K_c depends on the eighth power of the radius of the cold wall. One might argue then that the introduction of a considerable number of spacers into the gap space of such a colum decreases the effective gap width enough to produce the observed effects. However, it is difficult to see how the cross-wire type of spacers we have employed could have solely this effect. We have observed fairly well-defined swirls in the gas of length equal to the interval between spacers. Such partial interruption of the vertical lamellar gas flow may be considered as multiple recycling which improves the amount of cascading in a given length of column of the horizontal thermal diffusion separation. Also the many spacing wires may increase somewhat the average temperature of the gas, with consequent increase in α, the thermal diffusion constant. Most probably the improved performance occurs in part for each of these reasons, and for others too. No single, simple explanation will suffice.

As to the K_p' values in Eqs. (5) and (6) it is only significant that they are small, effectively zero. For the same column before it was straightened K_p' was 46.8 (Eq. (4)), showing that a slight bend in a long thermal diffusion column can increase markedly parasitic remixing and hence lower the separation factor of the column.

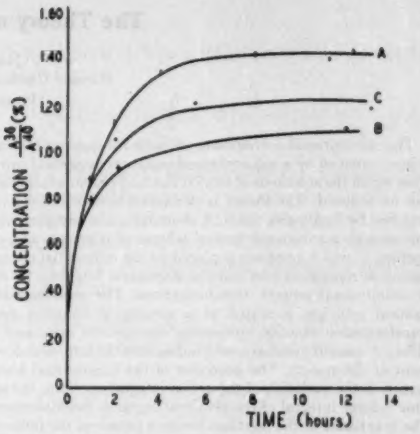

FIG. 5. Rate of increase of A^{36} at top of column; (A) 5 cm spacers on hot wire, (B) no spacers, (C) indentations every 15 cm in cold wall but no spacers on wire.

Because of the fairly high temperature of our hot wires the convection rate is high. Then, as Drickamer, Mellow, and Tung[9] point out, with some general turbulence at high gas pressures only a fraction of the gap between hot and cold walls is available for horizontal diffusion and thermal diffusion. The mixing due to turbulence should be at first confined to the central region of the gap. The effect of this would be to increase the temperature gradient in the non-turbulent part and to decrease the distance the molecules must traverse through thermal diffusion. These changes could increase the thermal diffusion more than they increase the remixing, and thus increase the transport and the separation factor.

The practical application of the increase in separation factor produced by controlled turbulence is obvious. By these simple means columns can be made to yield greater separations for the same power input. Further design studies are necessary in order to maximize the effect, and a theoretical treatment of turbulence in thermal diffusion columns would of course be of great help.

The Theory of Quantized Fields. I*

JULIAN SCHWINGER
Harvard University, Cambridge, Massachusetts
(Received March 2, 1951)

The conventional correspondence basis for quantum dynamics is here replaced by a self-contained quantum dynamical principle from which the equations of motion and the commutation relations can be deduced. The theory is developed in terms of the model supplied by localizable fields. A short review is first presented of the general quantum-mechanical scheme of operators and eigenvectors, in which emphasis is placed on the differential characterization of representatives and transformation functions by means of infinitesimal unitary transformations. The fundamental dynamical principle is stated as a variational equation for the transformation function connecting eigenvectors associated with different spacelike surfaces, which describes the temporal development of the system. The generator of the infinitesimal transformation is the variation of the action integral operator, the space-time volume integral of the invariant lagrange function operator. The invariance of the lagrange function preserves the form of the dynamical principle under coordinate transformations, with the exception of those transformations which include a reversal in the positive sense of time, where a separate discussion is necessary. It will be shown in Sec. III that the requirement of invariance under time reflection imposes a restriction upon the operator properties of fields, which is simply the connection between the spin and statistics of particles. For a given dynamical system, changes in the transformation function arise only from alterations of the eigenvectors associated with the two surfaces, as generated by operators constructed from field variables attached to those surfaces. This yields the operator principle of stationary action, from which the equations of motion are obtained. Commutation relations are derived from the generating operator associated with a given surface. In particular, canonical commutation relations are obtained for those field components that are not restricted by equations of constraint. The surface generating operator also leads to generalized Schrödinger equations for the representative of an arbitrary state. Action integral variations which correspond to changing the dynamical system are discussed briefly. A method for constructing the transformation function is described, in a form appropriate to an integral spin field, which involves solving Hamilton-Jacobi equations for ordered operators. In Sec. III, the exceptional nature of time reflection is indicated by the remark that the charge and the energy-momentum vector behave as a pseudoscalar and pseudovector, respectively, for time reflection transformations. This shows, incidentally, that positive and negative charge must occur symmetrically in a completely covariant theory. The contrast between the pseudo energy-momentum vector and the proper displacement vector then indicates that time reflection cannot be described within the unitary transformation framework. This appears most fundamentally in the basic dynamical principle. It is important to recognize here that the contributions to the lagrange function of half-integral spin fields behave like pseudoscalars with respect to time reflection. The non-unitary transformation required to represent time reflection is found to be the replacement of a state vector by its dual, or complex conjugate vector, together with the transposition of all operators. The fundamental dynamical principle is then invariant under time reflection if inverting the order of all operators in the lagrange function leaves an integral spin contribution unaltered, and reverses the sign of a half-integral spin contribution. This implies the essential commutativity, or anti-commutativity, of integral and half-integral field components, respectively, which is the connection between spin and statistics.

I. INTRODUCTION

DESPITE extensive developments in the concepts and techniques of the theory of quantized fields, quantitative success has been achieved thus far only in the restricted domain of quantum electrodynamics. Furthermore, the existence of divergences, whether concealed or explicit, serves to emphasize that the present quantum theory of fields must, in some respect, be incomplete. It is not our purpose to propose a solution of this basic problem, but rather to present a general theory of quantum field dynamics which unifies several independently developed procedures and which may provide a framework capable of admitting fundamentally new physical ideas.

Quantum mechanics involves two distinct sets of hypotheses—the general mathematical scheme of linear operators and state vectors with its associated probability interpretation and the commutation relations and equations of motion for specific dynamical systems. It is the latter aspect that we wish to develop, by substituting a single quantum dynamical principle for the conventional array of assumptions based on classical hamiltonian dynamics and the correspondence principle.[1] We shall find it useful, however, first to review briefly some aspects of the mathematical formalism that find repeated application in the construction of our theory.

The simultaneous eigenvectors of some complete set of commuting hermitian operators, $\Psi(\alpha')$, provide a description of the arbitrary state Ψ by means of the representative

$$(\alpha'|)=(\Psi(\alpha'),\Psi), \tag{1.1}$$

which has the interpretation of a probability amplitude. Two such representations, associated with different complete sets of commuting operators, are related by

$$(\alpha'|)=\int(\alpha'|\beta')d\beta'(\beta'|), \tag{1.2}$$

where $\int d\beta'$ indicates integration and summation over

* The author wishes to acknowledge the hospitality of the Brookhaven National Laboratory, which is under the auspices of the AEC. The general program of this series was initiated there during the early summer of 1949, and the present paper was largely written at this Laboratory during the summer of 1950.

[1] Although our attention will be focused on field dynamics, the analogous development of particle quantum dynamics should be evident.

the totality of eigenvalues β', and

$$(\alpha'|\beta')=(\Psi(\alpha'),\Psi(\beta')) \tag{1.3}$$

is the transformation function. As a special example of Eq. (1.2), we have

$$(\alpha'|\gamma')=\int(\alpha'|\beta')d\beta'(\beta'|\gamma'), \tag{1.4}$$

the multiplicative composition law of transformation functions.

The set of commuting hermitian operators

$$\bar{\alpha}=U\alpha U^{-1}, \tag{1.5}$$

which is obtained from α with the aid of the arbitrary unitary operator U, has the property that its eigenvalues are identical with those of α, and that its eigenvectors are given by

$$\Psi(\bar{\alpha}')=U\Psi(\alpha'), \tag{1.6}$$

where $\bar{\alpha}'$ and α' are the same set of eigenvalues. Conversely, two sets of operators that possess the same eigenvalue spectrum are related by a unitary transformation. Note that the transformation function $(\bar{\alpha}'|\alpha'')$ may also be viewed as the matrix of U^{-1} in the original eigenvector system,

$$\begin{aligned}(\bar{\alpha}'|\alpha'')&=(U\Psi(\alpha'),\Psi(\alpha''))=(\Psi(\alpha'),U^{\dagger}\Psi(\alpha''))\\&=(\alpha'|U^{-1}|\alpha'').\end{aligned} \tag{1.7}$$

The unitary operator

$$U=1-(i/\hbar)F,\quad U^{-1}=1+(i/\hbar)F, \tag{1.8}$$

in which F is an infinitesimal hermitian operator, induces an infinitesimal transformation in the commuting set of operators,

$$\bar{\alpha}=U\alpha U^{-1}=\alpha-\delta\alpha, \tag{1.9}$$

where

$$i\hbar\delta\alpha=\alpha F-F\alpha=[\alpha,F]. \tag{1.10}$$

If the system is such that it is possible to obtain operators $\delta\alpha$ that commute with the complete set α, one can treat the $\delta\alpha$ as arbitrary, infinitesimal numbers, and $\Psi(\bar{\alpha}')$ provides an eigenvector of α with the eigenvalue set $\alpha'+\delta\alpha$. This evidently corresponds to the special circumstance of α having a continuous eigenvalue spectrum.

The concept of infinitesimal unitary transformation can be used to provide a differential characterization for the representative of a state, or for a transformation function. The change in the representative $(\alpha'|)$ when the commuting set of operators is altered by the unitary transformation generated by the infinitesimal hermitian operator F, is given by

$$\delta(\alpha'|)=((\alpha-\delta\alpha)'|)-(\alpha'|)=(\delta\Psi(\alpha'),\Psi), \tag{1.11}$$

where

$$\delta\Psi(\alpha')=U\Psi(\alpha')-\Psi(\alpha')=-(i/\hbar)F\Psi(\alpha'). \tag{1.12}$$

Therefore,

$$\delta(\alpha'|)=(i/\hbar)(\Psi(\alpha'),F\Psi)=(i/\hbar)(\alpha'|F|), \tag{1.13}$$

or

$$(\hbar/i)\delta(\alpha'|)=\int(\alpha'|F|\alpha'')d\alpha''(\alpha''|), \tag{1.14}$$

which is a differential equation for the representative $(\alpha'|)$. In a similar manner, we can characterize the transformation function $(\alpha'|\beta')$ by the effect of altering the two commuting sets α and β into $\alpha-\delta\alpha$ and $\beta-\delta\beta$, as induced by the two infinitesimal generating operators F_α, and F_β. Thus,

$$\begin{aligned}\delta(\alpha'|\beta')&=(\delta\Psi(\alpha'),\Psi(\beta'))+(\Psi(\alpha'),\delta\Psi(\beta'))\\&=(i/\hbar)(\alpha'|(F_\alpha-F_\beta)|\beta'),\end{aligned} \tag{1.15}$$

or

$$\begin{aligned}(\hbar/i)\delta(\alpha'|\beta')&=\int(\alpha'|F_\alpha|\alpha'')d\alpha''(\alpha''|\beta')\\&\quad-\int(\alpha'|\beta'')d\beta''(\beta''|F_\beta|\beta').\end{aligned} \tag{1.16}$$

II. QUANTUM DYNAMICS OF LOCALIZABLE FIELDS

A localizable field is a dynamical system characterized by one or more operator functions of the space-time coordinates, $\phi^a(x)$. Contained in this statement are the assumptions that the operators x_μ, representing position measurements, are commutative,

$$[x_\mu,x_\nu]=0, \tag{2.1}$$

and furthermore, that they commute with the field operators,

$$[x_\mu,\phi^a]=0, \tag{2.2}$$

so that

$$(x|\phi^a|x')=\delta(x-x')\phi^a(x). \tag{2.3}$$

The difficulties associated with current field theories may be attributable to the implicit hypothesis of localizability. However, our development of quantum field dynamics will be confined to such fields. It remains to be seen whether other systems can be included within its scope.

The problem of constructing a complete set of commuting operators, that is, of simultaneously measurable physical quantities, necessarily involves specific properties of the fields. Nevertheless, as a general principle associated with relativistic requirements, we must expect such mutually commuting operators to be formed from field quantities at physically independent space-time points, that is, points which cannot be connected even by light signals. A continuous set of such points form a spacelike surface, which is a geometrical concept independent of the coordinate system. Therefore, a base vector system, $\Psi(\zeta',\sigma)$, will be specified by a spacelike surface σ and by the eigenvalues ζ' of a complete set of commuting operators constructed from field quantities attached to that surface. A change of representation will correspond, in general, to the intro-

duction of another set of commuting operators on a different spacelike surface. Of particular importance is the transformation $\zeta_2, \sigma_2 \rightarrow \zeta_1, \sigma_1$, in which ζ_1 and ζ_2 are similarly constructed operator sets which possess the same eigenvalue spectrum and are therefore related by a unitary transformation [Eqs. (1.5) and (1.6)],

$$\zeta_1 = U_{12}\zeta_2 U_{12}^{-1},$$
$$\Psi(\zeta_1', \sigma_1) = U_{12}\Psi(\zeta_2', \sigma_2), \quad \zeta_1' = \zeta_2', \tag{2.4}$$

so that [Eq. (1.7)]

$$(\zeta_1', \sigma_1|\zeta_2'', \sigma_2) = (\zeta_2', \sigma_2|U_{12}^{-1}|\zeta_2'', \sigma_2). \tag{2.5}$$

A description of the temporal development of a system is evidently accomplished by stating the relationship between eigenvectors associated with different spacelike surfaces, or, in other words, by exhibiting the transformation function (2.5). Accordingly, we may expect that the quantum dynamical laws will find their proper expression in terms of the transformation function. A differential formulation of this type will now be constructed.

The operator U_{12}^{-1} describes the development of the system from σ_2 to σ_1 and involves, not only the detailed dynamical characteristics of the system in this space-time region, but also the choice of commuting operators, ζ_1 and ζ_2, on the surfaces σ_1 and σ_2. Any infinitesimal change in the quantities on which the transformation function depends induces a corresponding alteration in U_{12}^{-1},

$$\delta(\zeta_1', \sigma_1|\zeta_2'', \sigma_2) = (\zeta_2', \sigma_2|\delta U_{12}^{-1}|\zeta_2'', \sigma_2). \tag{2.6}$$

Now it is a consequence of the unitary property that $iU_{12}\delta U_{12}^{-1}$ must be hermitian. Accordingly, we write

$$\delta U_{12}^{-1} = (i/\hbar)U_{12}^{-1}\delta W_{12}, \tag{2.7}$$

where δW_{12} is an infinitesimal hermitian operator, and obtain

$$\delta(\zeta_1', \sigma_1|\zeta_2'', \sigma_2) = (i/\hbar)(\zeta_1', \sigma_1|\delta W_{12}|\zeta_2'', \sigma_2). \tag{2.8}$$

The composition law of transformation functions [Eq. (1.4)],

$$(\zeta_1', \sigma_1|\zeta_3''', \sigma_3) = \int (\zeta_1', \sigma_1|\zeta_2'', \sigma_2)d\zeta''(\zeta_2'', \sigma_2|\zeta_3''', \sigma_3), \tag{2.9}$$

imposes a restriction on δW, the generating operator of infinitesimal transformations. Thus,

$$(\zeta_1', \sigma_1|\delta W_{13}|\zeta_3''', \sigma_3) = \int (\zeta_1', \sigma_1|\delta W_{12}|\zeta_2'', \sigma_2)d\zeta''(\zeta_2'', \sigma_2|\zeta_3''', \sigma_3) + \int (\zeta_1', \sigma_1|\zeta_2'', \sigma_2)d\zeta''(\zeta_2'', \sigma_2|\delta W_{23}|\zeta_3''', \sigma_3), \tag{2.10}$$

or

$$\delta W_{13} = \delta W_{12} + \delta W_{23}; \tag{2.11}$$

the infinitesimal generating operators satisfy an additive law of composition.

Our basic assumption is that δW_{12} is obtained by variation of the quantities contained in a hermitian operator W_{12}, which must have the general form

$$W_{12} = (1/c)\int_{\sigma_2}^{\sigma_1}(dx)\mathfrak{L}[x], \tag{2.12}$$

according to the additive requirement (2.11). Individual systems are described by stating $\mathfrak{L}$ as an invariant hermitian function of the fields and their coordinate derivatives,

$$\mathfrak{L}[x] = \mathfrak{L}(\phi^\alpha(x), \phi_\mu{}^\alpha(x)), \quad \phi_\mu{}^\alpha(x) = \partial_\mu\phi^\alpha(x). \tag{2.13}$$

In conformity with their classical analogs, we shall call W and $\mathfrak{L}$ the action integral and lagrange function operators, respectively. The invariance of the lagrange function, and therefore of the action integral, guarantees that our fundamental dynamical principle,

$$\delta(\zeta_1', \sigma_1|\zeta_2'', \sigma_2) = (i/\hbar)(\zeta_1', \sigma_1|\delta W_{12}|\zeta_2'', \sigma_2) = (i/\hbar c)(\zeta_1', \sigma_1|\delta\int_{\sigma_2}^{\sigma_1}(dx)\mathfrak{L}|\zeta_2'', \sigma_2), \tag{2.14}$$

is unaltered in form by a change in the coordinate system. An exception must be made, however, for those coordinate transformations that include a reversal in the positive sense of time, which require a separate discussion. We shall see that the requirement of invariance under time reflection imposes a general restriction upon the commutation properties of fields, which is simply the connection between the spin and statistics of elementary particles.

If the parameters of the system are not altered, the variation of the transformation function in Eq. (2.14) arises only from infinitesimal changes of ζ_1, σ_1 and ζ_2, σ_2. Such transformations may be characterized by infinitesimal generating operators, $F(\sigma_1)$ and $F(\sigma_2)$, which act on the eigenvectors $\Psi(\zeta_1', \sigma_1)$ and $\Psi(\zeta_2'', \sigma_2)$, and are therefore expressed in terms of operators associated with the surfaces σ_1 and σ_2, respectively. On referring to Eq. (1.15), we obtain for such variations,

$$\delta W_{12} = F(\sigma_1) - F(\sigma_2). \tag{2.15}$$

This is the operator principle of stationary action, for it states that the action integral operator is unaltered by infinitesimal variations of the field quantities in the interior of the region bounded by σ_1 and σ_2, being dependent only on operators attached to the boundary surfaces. The equations of motion for the field are contained in this principle.[2]

[2] In the following discussions, one should keep in mind that the lagrange functions of the simple systems usually considered are no more than quadratic in the components of individual fields.

The evaluation of δW_{12} involves adding the independent effects of changing the field components at each point by $\delta_0\phi^\alpha(x)$, and of altering the region of integration by a displacement δx_μ of the points on the boundary surfaces. Thus,

$$\delta W_{12}=(1/c)\int_{\sigma_2}^{\sigma_1}(dx)\delta_0\mathfrak{L} +(1/c)\left(\int_{\sigma_1}-\int_{\sigma_2}\right)d\sigma_\mu\delta x_\mu\mathfrak{L}, \quad (2.16)$$

where

$$\delta_0\mathfrak{L}=(\partial\mathfrak{L}/\partial\phi^\alpha)\delta_0\phi^\alpha+(\partial\mathfrak{L}/\partial\phi_\mu{}^\alpha)\partial_\mu\delta_0\phi^\alpha$$
$$=[(\partial\mathfrak{L}/\partial\phi^\alpha)-\partial_\mu(\partial\mathfrak{L}/\partial\phi_\mu{}^\alpha)]\delta_0\phi^\alpha +\partial_\mu[(\partial\mathfrak{L}/\partial\phi_\mu{}^\alpha)\delta_0\phi^\alpha]. \quad (2.17)$$

This expression for $\delta_0\mathfrak{L}$ is to be understood symbolically, since the order of the operators in $\mathfrak{L}$ must not be altered in the course of effecting the variation. Accordingly, the commutation properties of $\delta_0\phi^\alpha$ are involved in obtaining the consequences of the stationary requirement on the action integral. For simplicity, we shall introduce here the explicit assumption that the commutation properties of $\delta_0\phi^\alpha$ and the structure of the lagrange function must be so related that identical contributions are produced by terms that differ fundamentally only in the position of $\delta_0\phi^\alpha$. We may now infer the equations of motion

$$\partial_\mu(\partial\mathfrak{L}/\partial\phi_\mu{}^\alpha)=\partial\mathfrak{L}/\partial\phi^\alpha. \quad (2.18)$$

From the resulting form of δW_{12} we obtain the infinitesimal generating operator $F(\sigma)$, which acts on eigenvectors associated with the surface σ,

$$F(\sigma)=(1/c)\int_\sigma d\sigma_\mu[(\partial\mathfrak{L}/\partial\phi_\mu{}^\alpha)\delta_0\phi^\alpha+\mathfrak{L}\delta x_\mu]. \quad (2.19)$$

The total variation, $\delta\phi^\alpha(x)$, is composed additively of the variation $\delta_0\phi^\alpha(x)$ at the point x, and of the change in $\phi^\alpha(x)$ produced by moving from the point x on σ to $x+\delta x$ on $\sigma+\delta\sigma$. In evaluating the latter, we shall take into account that the field components $\phi^\alpha(x)$, although stated in terms of some fixed coordinate system, are most advantageously considered in relation to the local coordinate system provided by σ at the point x. Only such motions are contemplated that correspond to a local rigid displacement of the surface σ. This restriction is expressed by

$$\partial_\mu\delta x_\nu=-\partial_\nu\delta x_\mu, \quad (2.20)$$

being the condition that an infinitesimal space vector on σ be mapped into one of equal length on $\sigma+\delta\sigma$. The displacement induced change in $\phi^\alpha(x)$ may be obtained by an alteration in the coordinate system that reduces, in the neighborhood of x, to the equivalent local coordinate transformation. Thus, under the infinitesimal coordinate transformation

$$x_\mu'-x_\mu=-\delta x_\mu, \quad (2.21)$$

where

$$\delta x_\mu=\epsilon_\mu-\epsilon_{\mu\nu}x_\nu, \quad \epsilon_{\mu\nu}=-\epsilon_{\nu\mu}=\partial_\mu\delta x_\nu, \quad (2.22)$$

the field components suffer a linear transformation, as expressed by

$$\phi^{\alpha\prime}(x')-\phi^\alpha(x)=(i/\hbar)\tfrac{1}{2}\epsilon_{\mu\nu}S_{\mu\nu}{}^{\alpha\beta}\phi^\beta(x). \quad (2.23)$$

Therefore,

$$\phi^{\alpha\prime}(x)-\phi^\alpha(x)=\partial_\mu\phi^\alpha(x)\delta x_\mu+(i/\hbar)\tfrac{1}{2}\epsilon_{\mu\nu}S_{\mu\nu}{}^{\alpha\beta}\phi^\beta(x), \quad (2.24)$$

and

$$\delta\phi^\alpha(x)=\delta_0\phi^\alpha(x)+\phi_\mu{}^\alpha(x)\delta x_\mu +(i/\hbar)\tfrac{1}{2}\partial_\mu\delta x_\nu S_{\mu\nu}{}^{\alpha\beta}\phi^\beta(x). \quad (2.25)$$

With the introduction of the total variation, the infinitesimal generating operator $F(\sigma)$ assumes the form

$$F(\sigma)=\int_\sigma d\sigma_\mu[\Pi_\mu{}^\alpha\delta\phi^\alpha+(1/c)\mathfrak{L}\delta x_\mu-\Pi_\mu{}^\alpha\phi_\nu{}^\alpha\delta x_\nu -(i/2\hbar)\Pi_\mu{}^\alpha S_{\lambda\nu}{}^{\alpha\beta}\phi^\beta\partial_\lambda\delta x_\nu], \quad (2.26)$$

where

$$c\Pi_\mu{}^\alpha=\partial\mathfrak{L}/\partial\phi_\mu{}^\alpha. \quad (2.27)$$

To simplify the last term of Eq. (2.26), we define

$$f_{\mu\lambda\nu}=-f_{\lambda\mu\nu}=(i/2\hbar)[\Pi_\mu{}^\alpha S_{\lambda\nu}{}^{\alpha\beta}\phi^\beta+\Pi_\nu{}^\alpha S_{\lambda\mu}{}^{\alpha\beta}\phi^\beta +\Pi_\lambda{}^\alpha S_{\nu\mu}{}^{\alpha\beta}\phi^\beta], \quad (2.28)$$

and obtain

$$(i/2\hbar)\Pi_\mu{}^\alpha S_{\lambda\nu}{}^{\alpha\beta}\phi^\beta\partial_\lambda\delta x_\nu=f_{\mu\lambda\nu}\partial_\lambda\delta x_\nu =\partial_\lambda(f_{\mu\lambda\nu}\delta x_\nu)+\partial_\lambda f_{\lambda\mu\nu}\delta x_\nu, \quad (2.29)$$

since the last two terms of $f_{\mu\lambda\nu}$ are symmetrical in λ and ν, and therefore do not contribute to Eq. (2.29), in view of Eq. (2.20). We now remark that, in virtue of $f_{\mu\lambda\nu}=-f_{\lambda\mu\nu}$,

$$\int_\sigma d\sigma_\mu\partial_\lambda(f_{\mu\lambda\nu}\delta x_\nu)=0, \quad (2.30)$$

provided $f_{\mu\lambda\nu}\delta x_\nu$ effectively approaches zero, with sufficient rapidity, at infinitely remote points[3] on σ. Finally then,

$$F(\sigma)=\int_\sigma d\sigma_\mu[\Pi_\mu{}^\alpha\delta\phi^\alpha+(1/c)T_{\mu\nu}\delta x_\nu], \quad (2.31)$$

where

$$(1/c)T_{\mu\nu}=(1/c)\mathfrak{L}\delta_{\mu\nu}-\Pi_\mu{}^\alpha\phi_\nu{}^\alpha-\partial_\lambda f_{\lambda\mu\nu} \quad (2.32)$$

is the stress tensor operator. As we shall demonstrate, this tensor has the property of being symmetrical,

$$T_{\mu\nu}=T_{\nu\mu}. \quad (2.33)$$

[3] All such characterizations of a spatially closed system, in terms of an operator approaching zero at infinity, are to be understood as a restriction to states for which the matrix elements of the operator have this property.

as an expression of the conservation of angular momentum.

Conservation laws are associated with variations that leave the action integral unchanged, since

$$\delta W_{12}=F(\sigma_1)-F(\sigma_2)=0 \tag{2.34}$$

implies the constancy of the corresponding generating operator. The mechanical conservation laws for an isolated system are derived by considering a rigid displacement of the entire field, or equivalently, of the coordinate system, which is described by a common infinitesimal translation and rotation of the surfaces σ_1 and σ_2,

$$\delta x_\mu=\epsilon_\mu-\epsilon_{\mu\nu}x_\nu, \quad \epsilon_{\mu\nu}=-\epsilon_{\nu\mu}, \tag{2.35}$$

combined with the field variation $\delta\phi^\alpha=0$. The displacement generating operator is then given by

$$F_{\delta x}(\sigma)=\epsilon_\mu P_\mu(\sigma)+\tfrac{1}{2}\epsilon_{\mu\nu}J_{\mu\nu}(\sigma), \tag{2.36}$$

where

$$P_\nu(\sigma)=(1/c)\int_\sigma d\sigma_\mu T_{\mu\nu}, \tag{2.37}$$

and

$$J_{\mu\nu}(\sigma)=(1/c)\int d\sigma_\lambda M_{\lambda\mu\nu},$$
$$M_{\lambda\mu\nu}=x_\mu T_{\lambda\nu}-x_\nu T_{\lambda\mu}. \tag{2.38}$$

Accordingly,

$$P_\nu(\sigma_1)-P_\nu(\sigma_2)=0, \tag{2.39}$$

and

$$J_{\mu\nu}(\sigma_1)-J_{\mu\nu}(\sigma_2)=0, \tag{2.40}$$

which are the conservation laws for the energy-momentum vector, and the angular momentum tensor, respectively. Since the surfaces σ_1 and σ_2 are arbitrary, we infer the corresponding differential conservation laws,

$$\partial_\mu T_{\mu\nu}=0, \tag{2.41}$$

and

$$\partial_\lambda M_{\lambda\mu\nu}=0, \tag{2.42}$$

which, in conjunction, imply the symmetry of the stress tensor:

$$\partial_\lambda M_{\lambda\mu\nu}=T_{\mu\nu}-T_{\nu\mu}=0. \tag{2.43}$$

The conservation law of charge can be obtained from the required invariance of the hermitian lagrange function under constant phase transformations—the multiplication of mutually hermitian conjugate pairs of field components by $\exp(\pm i\gamma)$. We consider infinitesimal phase transformations and, for convenience, write

$$\gamma=(e/\hbar c)\delta\lambda. \tag{2.44}$$

Thus, we postulate the invariance of $\mathfrak{L}$ under the infinitesimal transformation

$$\delta\phi^\alpha=-(ie/\hbar c)\epsilon^\alpha\delta\lambda\phi^\alpha, \tag{2.45}$$

where ϵ^α is characteristic of the field component ϕ^α, and may assume the values 0, or ±1. The associated generating operator is

$$F_{\delta\lambda}(\sigma)=-(ie/\hbar c)\int_\sigma d\sigma_\mu\Pi_\mu{}^\alpha\epsilon^\alpha\phi^\alpha\delta\lambda$$
$$=(1/c)Q(\sigma)\delta\lambda, \tag{2.46}$$

where

$$Q(\sigma)=(1/c)\int_\sigma d\sigma_\mu j_\mu \tag{2.47}$$

and

$$j_\mu=-(iec/\hbar)\Pi_\mu{}^\alpha\epsilon^\alpha\phi^\alpha. \tag{2.48}$$

The implied conservation law,

$$Q(\sigma_1)-Q(\sigma_2)=0, \tag{2.49}$$

is that of the total charge in the system.

It is important to notice the ambiguity in the lagrange function that is associated with given equations of motion. Thus, two lagrange functions that are related by

$$\overline{\mathfrak{L}}(\phi^\alpha,\phi_\mu{}^\alpha)=\mathfrak{L}(\phi^\alpha,\phi_\mu{}^\alpha)+c\partial_\nu f_\nu(\phi^\alpha,\phi_\mu{}^\alpha) \tag{2.50}$$

provide action integral operators that differ by surface integrals:

$$\overline{W}_{12}=W_{12}+\left(\int_{\sigma_1}-\int_{\sigma_2}\right)d\sigma_\nu f_\nu. \tag{2.51}$$

Therefore, the principle of stationary action for $\overline{W}_{12}$ is automatically satisfied by the equations of motion deduced from W_{12}, and

$$\delta\overline{W}_{12}=\overline{F}(\sigma_1)-\overline{F}(\sigma_2), \tag{2.52}$$

where

$$\overline{F}=F+\delta w, \quad w=\int d\sigma_\nu f_\nu. \tag{2.53}$$

Hence, augmenting a lagrange function by the divergence of an arbitrary vector does not affect the equations of motion, but modifies the infinitesimal generating operator associated with a given surface σ. However, this ambiguity of the lagrange function corresponds precisely to the possibility of subjecting the commuting set of operators on σ to an arbitrary unitary transformation.

We verify this statement by specializing the general transformation theory to unitary transformations on a given surface. Let us introduce ξ, a new set of commuting operators on σ, which are obtained from ζ by a unitary transformation,

$$\Psi(\xi',\sigma)=\mathfrak{U}\Psi(\zeta',\sigma), \tag{2.54}$$

where $\mathfrak{U}$ is characterized by an infinitesimal hermitian generating operator δw, according to

$$\delta\mathfrak{U}^{-1}=(i/\hbar)\mathfrak{U}^{-1}\delta w. \tag{2.55}$$

As the analog of Eq. (2.8) we have, therefore,

$$\delta(\xi',\sigma\,|\,\zeta'',\sigma)=(i/\hbar)(\xi',\sigma\,|\,\delta w\,|\,\zeta'',\sigma); \tag{2.56}$$

but

$$\delta w = \bar{F} - F, \tag{2.57}$$

where $\bar{F}$ and F are, respectively, the operators generating infinitesimal transformations of $\bar{\zeta}$ and ζ. This is just of the form (2.53); and conversely, by employing a particular w we obtain from Eq. (2.56) a differential equation to determine the transformation function that defines the new representation.

The commutation relations of our theory are implicit in the significance of F as an infinitesimal generating operator. We shall consider first those transformations that do not alter the surface σ, so that $\delta x_\nu = 0$. It is convenient to write

$$d\sigma_\mu = n_\mu d\sigma, \tag{2.58}$$

where n_μ is a unit timelike vector and $d\sigma$ is the numerical measure of the surface element. To avoid irrelevant geometrical complications in the following discussion, we shall henceforth restrict σ to be a plane surface, so that n_μ is constant on σ. Note, incidentally, that coordinate derivatives can be decomposed into components normal and tangential to σ,

$$\begin{aligned} &\partial_\mu = n_\mu \partial_n + \partial_{t\mu}, \\ &\partial_n = -n_\mu \partial_\mu, \quad \partial_{t\mu} = (\delta_{\mu\nu} + n_\mu n_\nu)\partial_\nu, \end{aligned} \tag{2.59}$$

and that the equations of motion read

$$\partial_n \Pi^\alpha = (1/c)(\partial \mathfrak{L}/\partial \phi^\alpha) - \partial_{t\mu} \Pi_\mu{}^\alpha. \tag{2.60}$$

We have here introduced the notation

$$\Pi^\alpha = n_\mu \Pi_\mu{}^\alpha \tag{2.61}$$

for a quantity which, more precisely, should be written $\Pi^\alpha(x, \sigma)$.

The generating operator F now becomes

$$F_{\delta\phi} = \int d\sigma \Pi^\alpha \delta\phi^\alpha. \tag{2.62}$$

Another significant form, associated with a different base vector system, is obtained from Eq. (2.53) with

$$f_\nu = -\Pi_\nu{}^\alpha \phi^\alpha. \tag{2.63}$$

Indeed, we have

$$\begin{aligned} \delta \int d\sigma_\nu f_\nu &= -\delta \int d\sigma \Pi^\alpha \phi^\alpha \\ &= -\int d\sigma (\Pi^\alpha \delta\phi^\alpha + \delta\Pi^\alpha \phi^\alpha), \end{aligned} \tag{2.64}$$

so that

$$\bar{F} = F_{\delta\Pi} = -\int d\sigma \delta\Pi^\alpha \phi^\alpha. \tag{2.65}$$

It should be emphasized again that these operator expressions are symbolic in the sense that the actual positions in which $\delta\phi^\alpha$ and $\delta\Pi^\alpha$ appear depend upon the structure of the lagrange function.

To obtain the proper interpretation of $F_{\delta\phi}$ or $F_{\delta\Pi}$, it is necessary to recognize that some of the Π^α can be identically equal to zero. This expresses the possibility that derivatives in timelike directions of some of the ϕ^α may not occur in the lagrange function. Accordingly, we shall divide the quantities ϕ^α and Π^α into two sets: ϕ^α and Π^α, called the canonical variables, and ϕ^A, Π^A, termed the constraint variables, in which the second set is characterized by

$$\Pi^A \equiv 0. \tag{2.66}$$

The name ascribed to the ϕ^A refers to the fact that, for these quantities, the equations of motion (2.60) degenerate into equations of constraint,

$$(1/c)(\partial \mathfrak{L}/\partial \phi^A) = \partial_{t\mu} \Pi_\mu{}^A, \tag{2.67}$$

that is, relations among the variables on σ. The nature of these relations can be made more apparent by exploiting the requirement that Eq. (2.66) be independent of the coordinate system. We shall later show that the implied restriction on the structure of $\mathfrak{L}$ is expressed by

$$n_\mu \Pi_\nu{}^A - n_\nu \Pi_\mu{}^A = (i/\hbar) \Pi^\alpha S_{\mu\nu}{}^{\alpha A}. \tag{2.68}$$

On multiplication with n_ν, we obtain from this equation that

$$\Pi_\mu{}^A = (i/\hbar) \Pi^\alpha S_{\mu\nu}{}^{\alpha A} n_\nu, \tag{2.69}$$

which enables the constraint equations to be written

$$(1/c)(\partial \mathfrak{L}/\partial \phi^A) = (i/\hbar) \partial_\mu \Pi^\alpha S_{\mu\nu}{}^{\alpha A} n_\nu. \tag{2.70}$$

We shall now assume that it is possible to solve the left side of Eq. (2.70) for ϕ^A, thus exhibiting explicitly the constraint variables as functions of the canonical variables. This excludes systems for which the ϕ^A are fundamentally ambiguous in consequence of the existence of gauge transformations. The latter situation will be discussed subsequently in terms of the familiar example provided by the electromagnetic field.

It is evident from these considerations, and from the structure of the generating operators,

$$\begin{aligned} F_{\delta\phi} &= \int d\sigma \Pi^\alpha \delta\phi^\alpha, \\ F_{\delta\Pi} &= -\int d\sigma \delta\Pi^\alpha \phi^\alpha, \end{aligned} \tag{2.71}$$

that only the canonical variables are dynamically independent on σ. Accordingly, $F_{\delta\phi}$ is to be interpreted as the generator of that infinitesimal transformation of the commuting operator set ζ on σ which is produced by changing ϕ^α into $\phi^\alpha - \delta\phi^\alpha$. Similarly, $F_{\delta\Pi}$ is regarded as generating the infinitesimal transformation of ζ in which Π^α is replaced by $\Pi^\alpha - \delta\Pi^\alpha$. Thus, ϕ^α and Π^α are special examples of a set of independent field coordi-

nates, and the most general possibility is implicit in the transformation (2.53). Associated with any such set of operators is the conjugate set appearing in F, as Π^a is conjugate to ϕ^a, and $-\phi^a$ to Π^a.

We shall now examine the change in the matrix of G, an arbitrary function of field variables on σ, which is produced by the infinitesimal transformation generated by $F_{\delta\phi}$, say. Thus, we have

$$\begin{aligned}\delta(\zeta',\sigma|G|\zeta'',\sigma)&=(\Psi(\zeta',\sigma),G\delta\Psi(\zeta'',\sigma))\\&\quad+(\delta\Psi(\zeta',\sigma),G\Psi(\zeta'',\sigma))\\&=-(i/\hbar)(\zeta',\sigma|[G,F_{\delta\phi}]|\zeta'',\sigma).\end{aligned}\tag{2.72}$$

On the other hand, we have

$$\delta(\zeta',\sigma|G|\zeta'',\sigma)=(\zeta',\sigma|\delta_\phi G|\zeta'',\sigma),\tag{2.73}$$

where $\delta_\phi G$ means the change in G produced on increasing ϕ^a by $\delta\phi^a$. This simply expresses the fact that replacing ϕ^a by $\phi^a-\delta\phi^a$ in both G and ζ leaves the relation between them, and therefore the matrix, unaltered. We thereby infer the commutation relation,

$$[G,F_{\delta\phi}]=i\hbar\delta_\phi G,\tag{2.74}$$

with its evident generalization in regard to the field coordinates, including, in particular,

$$[G,F_{\delta\Pi}]=i\hbar\delta_\Pi G.\tag{2.75}$$

Of special importance are the results obtained from Eqs. (2.74) and (2.75) with $G=\phi^a$ and Π^a:

$$\begin{aligned}\left[\phi^a(x),\int_\sigma d\sigma'\Pi^b(x')\delta\phi^b(x')\right]&=i\hbar\delta\phi^a(x),\\\left[\Pi^a(x),\int_\sigma d\sigma'\Pi^b(x')\delta\phi^b(x')\right]&=0,\end{aligned}\tag{2.76}$$

and

$$\begin{aligned}\left[\int_\sigma d\sigma'\delta\Pi^b(x')\phi^b(x'),\Pi^a(x)\right]&=i\hbar\delta\Pi^a(x),\\\left[\int_\sigma d\sigma'\delta\Pi^b(x')\phi^b(x'),\phi^a(x)\right]&=0,\end{aligned}\tag{2.77}$$

in which we have invoked the dynamical independence of the ϕ^a and the Π^a.

To extract explicit commutation relations among the ϕ^a and Π^a we must know the operator properties of $\delta\phi^a$ and $\delta\Pi^a$. The requirement that the formalism be invariant with respect to time reflection supplies the desired information. It will be shown in Sec. III that $\delta\phi^b(x')$ and $\delta\Pi^b(x')$ commute with all field quantities $\phi^a(x)$ and $\Pi^a(x)$, on σ, except when both a and b designate components of fields that possess half-integral spin, in which event they anti-commute. Accordingly, the commutation relations of Eqs. (2.76) and (2.77) become

$$\begin{aligned}\int_\sigma d\sigma'[\phi^a(x),\Pi^b(x')]_\pm\delta\phi^b(x')&=i\hbar\delta\phi^a(x),\\\int_\sigma d\sigma'[\Pi^a(x),\Pi^b(x')]_\pm\delta\phi^b(x')&=0,\\\int_\sigma d\sigma'\delta\Pi^b(x')[\phi^b(x'),\Pi^a(x)]_\pm&=i\hbar\delta\Pi^a(x),\\\int_\sigma d\sigma'\delta\Pi^b(x')[\phi^b(x'),\phi^a(x)]_\pm&=0,\end{aligned}\tag{2.78}$$

where

$$[A,B]_-=AB-BA\tag{2.79}$$

and

$$[A,B]_+=AB+BA.\tag{2.80}$$

Since the $\delta\phi^a$ and $\delta\Pi^a$ are quite arbitrary, we have derived the fundamental commutation relations,

$$\begin{aligned}[\phi^a(x),\Pi^b(x')]_\pm&=i\hbar\delta_{ab}\delta_\sigma(x-x'),\\[\phi^a(x),\phi^b(x')]_\pm&=[\Pi^a(x),\Pi^b(x')]_\pm=0.\end{aligned}\tag{2.81}$$

Here $\delta_\sigma(x-x')$ denotes the three-dimensional delta-function, which is defined by

$$\int_\sigma d\sigma'\delta_\sigma(x-x')f(x')=f(x),\tag{2.82}$$

where $f(x)$ is an arbitrary function. The commutation properties of the ϕ^A can then be obtained from their explicit expression in terms of the canonical variables. Thus, according to Eq. (2.70),

$$(1/c)[\partial\mathfrak{L}/\partial\phi^A(x),\phi^a(x')]_\pm=\partial_\mu\delta_\sigma(x-x')S_{\mu\nu}{}^{aA}n_\nu,\tag{2.83}$$

and

$$[\partial\mathfrak{L}/\partial\phi^A(x),\Pi^a(x')]_\pm=0.\tag{2.84}$$

In the requirement that commutators be employed, for components of an integral spin field, and anti-commutators for components of a half-integral spin field, we have the connection between the spin and statistics of particles. We shall note here that the commutation properties of a Bose-Einstein system, that is, an integral spin field, can be represented by means of differential operators. According to Eq. (1.13), a suitable representative of an arbitrary state obeys

$$\begin{aligned}\delta(\zeta',\sigma|)&=(i/\hbar)(\zeta',\sigma|F_{\delta\phi}|)\\&=(i/\hbar)\left(\zeta',\sigma\left|\int_\sigma d\sigma\Pi^a\delta\phi^a\right|\right),\end{aligned}\tag{2.85}$$

in which σ is not altered. Now the characteristic property of an integral spin field is that $\delta\phi^a$ commutes with all dynamical variables and can therefore be treated as a number. The representation involved in

Eq. (2.85) is evidently that which is labeled by the continuous eigenvalues of the $\phi^a(x)$ at all points of σ. In terms of the notation

$$\delta(\phi', \sigma|) = \int_\sigma d\sigma \delta\phi^{a\prime}(x)(\delta/\delta\phi^{a\prime}(x))(\phi', \sigma|), \quad (2.86)$$

we obtain

$$(\hbar/i)(\delta/\delta\phi^{a\prime}(x))(\phi', \sigma|) = (\phi', \sigma|\,\Pi^a(x)|), \quad (2.87)$$

and similarly,

$$i\hbar(\delta/\delta\Pi^{a\prime}(x))(\Pi', \sigma|) = (\Pi', \sigma|\,\phi^a(x)|). \quad (2.88)$$

We shall make further application of the general commutation relations (2.74) and (2.75) by successively placing $G = P_\nu$, $J_{\mu\nu}$, and Q. According to Eq. (2.30), the last term of Eq. (2.32) makes no contribution to P_ν, so that

$$P_\nu = -\int d\sigma \Pi^a \partial_\nu \phi^a + (1/c)\int d\sigma_\nu \mathfrak{L}. \quad (2.89)$$

In the evaluation of δP_ν we encounter

$$(1/c)\int d\sigma_\nu \delta\mathfrak{L} = \int d\sigma_\nu \partial_\mu(\Pi_\mu{}^a \delta\phi^a) = \int d\sigma_\mu \partial_\nu(\Pi_\mu{}^a \delta\phi^a)$$

$$= \int d\sigma \partial_\nu(\Pi^a \delta\phi^a), \quad (2.90)$$

whence

$$\delta P_\nu = \int d\sigma(\partial_\nu \Pi^a \delta\phi^a - \delta\Pi^a \partial_\nu \phi^a). \quad (2.91)$$

The rearrangements of Eq. (2.90) have involved Eq. (2.17), as simplified by the equations of motion, and the assumption that the system is spatially closed. We thereby obtain

$$\begin{aligned}[\phi^a(x), P_\nu] &= (\hbar/i)\partial_\nu \phi^a(x),\\ [\Pi^a(x), P_\nu] &= (\hbar/i)\partial_\nu \Pi^a(x),\end{aligned} \quad (2.92)$$

in virtue of the commutativity of P_ν with $\delta\phi^a$ and $\delta\Pi^a$, which is a consequence of the fact that half-integral spin field components must appear paired in the vector P_ν. Incidentally, a commutator $[F^{(1)}, F^{(2)}]$, which has been evaluated by considering the effect on $F^{(2)}$ of the transformation generated by $F^{(1)}$, can equally well be viewed from the reverse standpoint. Thus, the relations (2.92) also exhibit P_ν in the role of the translation generator.

The angular momentum tensor $J_{\mu\nu}$ is easily brought into a form analogous to (2.89),

$$J_{\mu\nu} = -\int d\sigma \Pi^a[(x_\mu \partial_\nu - x_\nu \partial_\mu)\phi^a + (i/\hbar) S_{\mu\nu}{}^{ab}\phi^b]$$

$$+ (1/c)\int (d\sigma_\nu x_\mu \mathfrak{L} - d\sigma_\mu x_\nu \mathfrak{L}). \quad (2.93)$$

The contribution of the second term to $\delta J_{\mu\nu}$ is evaluated as follows,

$$\delta(1/c)\int (d\sigma_\nu x_\mu \mathfrak{L} - d\sigma_\mu x_\nu \mathfrak{L})$$

$$= \int [d\sigma_\nu x_\mu \partial_\lambda(\Pi_\lambda{}^a \delta\phi^a) - d\sigma_\mu x_\nu \partial_\lambda(\Pi_\lambda{}^a \delta\phi^a)]$$

$$= \int d\sigma_\lambda (x_\mu \partial_\nu - x_\nu \partial_\mu)(\Pi_\lambda{}^a \delta\phi^a)$$

$$+ \int (d\sigma_\mu \Pi_\nu{}^a - d\sigma_\nu \Pi_\mu{}^a)\delta\phi^a$$

$$= \int d\sigma[(x_\mu \partial_\nu - x_\nu \partial_\mu)(\Pi^a \delta\phi^a)$$

$$+ (n_\mu \Pi_\nu{}^a - n_\nu \Pi_\mu{}^a)\delta\phi^a]. \quad (2.94)$$

Therefore,

$$\delta J_{\mu\nu} = -\int d\sigma \delta\Pi^a[(x_\mu \partial_\nu - x_\nu \partial_\mu)\phi^a + (i/\hbar) S_{\mu\nu}{}^{ab}\phi^b]$$

$$+ \int d\sigma[(x_\mu \partial_\nu - x_\nu \partial_\mu)\Pi^a - (i/\hbar)\Pi^b S_{\mu\nu}{}^{ba}$$

$$+ n_\mu \Pi_\nu{}^a - n_\nu \Pi_\mu{}^a]\delta\phi^a. \quad (2.95)$$

We have thus derived the commutation relations

$$\begin{aligned}[\phi^a, J_{\mu\nu}] &= (x_\mu(\hbar/i)\partial_\nu - x_\nu(\hbar/i)\partial_\mu)\phi^a + S_{\mu\nu}{}^{ab}\phi^b,\\ [\Pi^a, J_{\mu\nu}] &= (x_\mu(\hbar/i)\partial_\nu - x_\nu(\hbar/i)\partial_\mu)\Pi^a - \Pi^b S_{\mu\nu}{}^{ba}\\ &\quad + (\hbar/i)(n_\mu \Pi_\nu{}^a - n_\nu \Pi_\mu{}^a),\\ 0 &= -\Pi^a S_{\mu\nu}{}^{aA} + (\hbar/i)(n_\mu \Pi_\nu{}^A - n_\nu \Pi_\mu{}^A),\end{aligned} \quad (2.96)$$

which exhibit $J_{\mu\nu}$ in the role of the rotation generator and illustrate the formation of $J_{\mu\nu}$ as the superposition of orbital and spin angular momenta. The third equation of Eq. (2.96), the statement that $\Pi^A \equiv 0$ is a property independent of the coordinate system, has already been employed in Eq. (2.68).

According to Eqs. (2.47) and (2.48), the charge operator is given by

$$Q = -(ie/\hbar)\int d\sigma \Pi^a \epsilon^a \phi^a. \quad (2.97)$$

Therefore, we have

$$\delta Q = -(ie/\hbar)\int d\sigma(\delta\Pi^a \epsilon^a \phi^a + \Pi^a \epsilon^a \delta\phi^a), \quad (2.98)$$

from which we obtain the commutation relations

$$[\phi^a, Q] = e\epsilon^a \phi^a, \quad [\Pi^a, Q] = -e\epsilon^a \Pi^a. \quad (2.99)$$

These indicate the significance of e as the elementary charge, and exhibit Q in the role of the phase transformation generator. Note, however, that the derivation of Eq. (2.99) from the latter viewpoint is not restricted to the canonical variables, although nothing new is obtained thereby.

The general infinitesimal operator (2.31) describes the transformation from the commuting operator set ζ, σ to $\zeta-\delta\zeta$, $\sigma+\delta\sigma$, as indicated by

$$\Psi((\zeta-\delta\zeta)',\ \sigma+\delta\sigma)=[1-(i/\hbar)F]\Psi(\zeta',\ \sigma). \quad (2.100)$$

The operator F is additively composed of two parts,

$$F=F_{\delta\phi}+F_{\delta x}, \quad (2.101)$$

where $F_{\delta\phi}$ induces, via $\delta\phi^\alpha$, a change in the commuting operator set defined in relation to the local coordinate system provided by a fixed σ,

$$\Psi((\zeta-\delta\zeta)',\ \sigma)=[1-(i/\hbar)F_{\delta\phi}]\Psi(\zeta',\ \sigma), \quad (2.102)$$

while

$$F_{\delta x}=(1/c)\int d\sigma_\mu T_{\mu\nu}\delta x_\nu \quad (2.103)$$

generates the change in σ described by δx_ν, for a fixed set of commuting operators defined relative to σ,

$$\Psi(\zeta',\ \sigma+\delta\sigma)=[1-(i/\hbar)F_{\delta x}]\Psi(\zeta',\ \sigma). \quad (2.104)$$

Consistent with our restriction to plane surfaces, we consider only rigid displacements of σ, for which the generating operator has already been given in Eq. (2.36).

Differential equations that describe the change in the representative of an arbitrary state, as produced by rigid displacements, are inferred from

$$\delta_x(\zeta',\ \sigma|)=(\delta_x\Psi(\zeta',\ \sigma)_t\Psi)=(i/\hbar)(\zeta',\ \sigma|F_{\delta x}|). \quad (2.105)$$

In terms of the notation

$$\delta_x(\zeta',\ \sigma|)=\epsilon_\mu\delta_\mu(\zeta',\ \sigma|)+\tfrac{1}{2}\epsilon_{\mu\nu}\delta_{\mu\nu}(\zeta',\ \sigma|), \quad (2.106)$$

we obtain generalized Schrödinger equations[4] for translations,

$$(\hbar/i)\delta_\mu(\zeta',\ \sigma|)=(\zeta',\ \sigma|P_\mu(\sigma)|)$$
$$=\int(\zeta',\ \sigma|P_\mu(\sigma)|\zeta'',\ \sigma)d\zeta''(\zeta'',\ \sigma|), \quad (2.107)$$

and rotations,

$$(\hbar/i)\delta_{\mu\nu}(\zeta',\ \sigma|)=(\zeta',\ \sigma|J_{\mu\nu}(\sigma)|)$$
$$=\int(\zeta',\ \sigma|J_{\mu\nu}(\sigma)|\zeta'',\ \sigma)d\zeta''(\zeta'',\ \sigma|). \quad (2.108)$$

An operator $G(\sigma)$, which is constructed from field quantities on σ, has a matrix $(\zeta',\ \sigma|G(\sigma)|\zeta'',\ \sigma)$ that is independent of σ, since the relation between $G(\sigma)$ and the ζ on σ is unchanged by an alteration of the surface. The components of $P_\mu(\sigma)$ referred to axes based on σ are of this nature; and, consequently, the matrix of $P_\mu(\sigma)$ in Eq. (2.107) involves the orientation of σ relative to the coordinate system, but is otherwise independent of σ. Commutation relations between P_μ, $J_{\mu\nu}$ and $G(\sigma)$ follow from this property of the $G(\sigma)$ matrix. Thus, we have

$$0=\delta_x G(\sigma)-(i/\hbar)[G(\sigma),\ F_{\delta x}], \quad (2.109)$$

whence

$$[G(\sigma),\ P_\mu]=(\hbar/i)\delta_\mu G(\sigma), \quad (2.110)$$

and

$$[G(\sigma),\ J_{\mu\nu}]=(\hbar/i)\delta_{\mu\nu}G(\sigma). \quad (2.111)$$

As the first of several illustrations of these commutation relations, we choose $G(\sigma)=\phi^\alpha(x)$. According to Eq. (2.25), we have

$$[\phi^\alpha(x),\ P_\mu]=(\hbar/i)\partial_\mu\phi^\alpha(x), \quad (2.112)$$

and

$$[\phi^\alpha(x),\ J_{\mu\nu}]=(x_\mu(\hbar/i)\partial_\nu-x_\nu(\hbar/i)\partial_\mu)\phi^\alpha(x)$$
$$+S_{\mu\nu}{}^{\alpha\beta}\phi^\beta(x), \quad (2.113)$$

which is in agreement with Eqs. (2.92) and (2.96), but without the restriction of the latter to the components ϕ^a. A particularly simple example is provided by $G(\sigma)=Q$, the total charge. Since this operator is independent of σ, we have

$$[Q,\ P_\mu]=[Q,\ J_{\mu\nu}]=0, \quad (2.114)$$

which state, inversely, that P_μ and $J_{\mu\nu}$ are unaffected by phase transformations. The effect of a displacement of σ on the quantity $G(\sigma)=P_\lambda e_\lambda(\sigma)$, where $e_\lambda(\sigma)$ is an arbitrary vector that is rigidly attached to σ, comes entirely from the rotation of the vector $e_\lambda(\sigma)$,

$$\delta_x(P_\lambda e_\lambda(\sigma))=-\epsilon_{\mu\nu}P_\mu e_\nu(\sigma). \quad (2.115)$$

Therefore, we have

$$[P_\mu,\ P_\nu]=0, \quad (2.116)$$

and

$$[P_\lambda,\ J_{\mu\nu}]=i\hbar(\delta_{\nu\lambda}P_\mu-\delta_{\mu\lambda}P_\nu). \quad (2.117)$$

Our last example, $G(\sigma)=J_{\lambda\kappa}e_\lambda{}^{(1)}(\sigma)e_\kappa{}^{(2)}(\sigma)$, where both $e_\lambda{}^{(1)}(\sigma)$ and $e_\kappa{}^{(2)}(\sigma)$ are arbitrary vectors rigidly attached to σ, is actually an extension of the type of operator under consideration, since

$$J_{\lambda\kappa}e_\lambda{}^{(1)}e_\kappa{}^{(2)}=(1/c)\int d\sigma_\mu[x_\lambda e_\lambda{}^{(1)}T_{\mu\kappa}e_\kappa{}^{(2)}$$
$$-x_\kappa e_\kappa{}^{(2)}T_{\mu\lambda}e_\lambda{}^{(1)}] \quad (2.118)$$

involves space-time coordinates, in addition to field variables. The necessary revision of Eq. (2.109) is

$$\delta_x G(\sigma)=(i/\hbar)[G(\sigma),\ F_{\delta x}]+\partial_x G(\sigma), \quad (2.119)$$

where $\partial_x G(\sigma)$ denotes the displacement induced change in $G(\sigma)$, associated with the explicit appearance of space-time coordinates. In the example provided by

[4] Note that these Schrödinger equations have been obtained from the Heisenberg picture, in which the arbitrary state vector is fixed. P. A. M. Dirac, *The Principles of Quantum Mechanics* (The Clarendon Press, Oxford, 1947), third edition, Sec. 32.

Eq. (2.118), $\partial_\sigma G(\sigma)$ arises from the translation (but not rotation) of σ,

$$\partial_\sigma(J_{\lambda\kappa}e_\lambda^{(1)}e_\kappa^{(2)})=(\epsilon_\lambda P_\kappa-\epsilon_\kappa P_\lambda)e_\lambda^{(1)}e_\kappa^{(2)}. \quad (2.120)$$

On combining this with

$$\delta_\sigma(J_{\lambda\kappa}e_\lambda^{(1)}e_\kappa^{(2)})=-\epsilon_{\mu\nu}J_{\mu\kappa}e_\nu^{(1)}e_\kappa^{(2)}-\epsilon_{\mu\nu}J_{\lambda\mu}e_\lambda^{(1)}e_\nu^{(2)}, \quad (2.121)$$

we again obtain Eq. (2.117), and

$$[J_{\lambda\kappa}, J_{\mu\nu}]=ih(\delta_{\lambda\nu}J_{\mu\kappa}+\delta_{\lambda\mu}J_{\kappa\nu}+\delta_{\kappa\nu}J_{\lambda\mu}+\delta_{\kappa\mu}J_{\nu\lambda}). \quad (2.122)$$

We may remark, as an example of a general procedure for constructing representations of operator commutation properties, that the identity

$$[[\phi^\alpha, J_{\lambda\kappa}], J_{\mu\nu}]-[[\phi^\alpha, J_{\mu\nu}], J_{\lambda\kappa}] =[\phi^\alpha, [J_{\lambda\kappa}, J_{\mu\nu}]] \quad (2.123)$$

leads to analogous commutation relations for the representatives of orbital and spin angular momentum in Eq. (2.113).

In a final comment concerning commutation relations, we observe that the commutators of generating operators are of significance in connection with integrability conditions for the infinitesimal transformations generated by these operators.[8] If $F^{(1)}$ and $F^{(2)}$ are two such generators of infinitesimal transformations, we have

$$\begin{aligned}\delta^{(1)}\Psi(\zeta', \sigma)&=\Psi((\zeta-\delta^{(1)}\zeta)', \sigma+\delta^{(1)}\sigma)-\Psi(\zeta', \sigma)\\ &=-(i/\hbar)F^{(1)}\Psi(\zeta', \sigma),\\ \delta^{(2)}\Psi(\zeta', \sigma)&=\Psi((\zeta-\delta^{(2)}\zeta)', \sigma+\delta^{(2)}\sigma)-\Psi(\zeta', \sigma)\\ &=-(i/\hbar)F^{(2)}\Psi(\zeta', \sigma).\end{aligned} \quad (2.124)$$

Now, the difference between the results of the two ways in which these transformations can be successively applied may be regarded as the effect of a third, related transformation,

$$\begin{aligned}&(\delta^{(1)}\delta^{(2)}-\delta^{(2)}\delta^{(1)})\Psi(\zeta', \sigma)\\ &\quad=\Psi((\zeta+(\delta^{(1)}\delta^{(2)}-\delta^{(2)}\delta^{(1)})\zeta)', \sigma+(\delta^{(1)}\delta^{(2)}-\delta^{(2)}\delta^{(1)})\sigma)\\ &\qquad\qquad-\Psi(\zeta', \sigma)\\ &\quad=-(i/\hbar)F^{[12]}\Psi(\zeta', \sigma).\end{aligned} \quad (2.125)$$

Therefore,

$$[F^{(1)}, F^{(2)}]=ihF^{[12]} \quad (2.126)$$

is a condition necessary to the integrability of Eq. (2.124). A simple illustration of this viewpoint is provided by rigid displacements:

$$\begin{aligned}\delta^{(1,2)}x_\mu&=\epsilon_\mu^{(1,2)}-\epsilon_{\mu\nu}^{(1,2)}x_\nu,\\ F_{\delta x}^{(1,2)}&=\epsilon_\mu^{(1,2)}P_\mu+\tfrac{1}{2}\epsilon_{\mu\nu}^{(1,2)}J_{\mu\nu},\end{aligned} \quad (2.127)$$

since

$$\begin{aligned}(\delta^{(1)}\delta^{(2)}-\delta^{(2)}\delta^{(1)})x_\mu&=-\epsilon_{\mu\nu}^{(1)}\epsilon_\nu^{(2)}+\epsilon_{\mu\nu}^{(2)}\epsilon_\nu^{(1)}\\ &\quad-(-\epsilon_{\mu\lambda}^{(1)}\epsilon_{\lambda\nu}^{(2)}+\epsilon_{\mu\lambda}^{(2)}\epsilon_{\lambda\nu}^{(1)})x_\nu\\ &=\epsilon_\mu^{[12]}-\epsilon_{\mu\nu}^{[12]}x_\nu\end{aligned} \quad (2.128)$$

is another rigid displacement. The ensuing commutation relations are just Eqs. (2.116), (2.117), and (2.122).

In our discussions of the variational principle (2.14), we have dealt with the properties of a given dynamical system. The principle is also applicable, however, to variations in which the system is altered, as characterized by a change in the structure of the lagrange function. For a variation of this type, we have

$$\delta(\zeta_1', \sigma_1|\zeta_2'', \sigma_2)=(i/\hbar c)\int_{\sigma_2}^{\sigma_1}(dx)(\zeta_1', \sigma_1|\,\delta\mathfrak{L}[x]\,|\zeta_2'', \sigma_2), \quad (2.129)$$

or

$$\delta(\zeta_1', \sigma_1|\zeta_2'', \sigma_2)=(i/\hbar c)\int_{\sigma_2}^{\sigma_1}(dx)\int(\zeta_1', \sigma_1|\zeta^a, \sigma)d\zeta^a(\zeta^a, \sigma|\,\delta\mathfrak{L}[x]\,|\zeta^b, \sigma)d\zeta^b(\zeta^b, \sigma|\zeta_2'', \sigma_2), \quad (2.130)$$

where the surface σ contains the point x. If two independent variations of this nature are applied successively we obtain

$$\begin{aligned}\delta^{(2)}\delta^{(1)}(\zeta_1', \sigma_1|\zeta_2'', \sigma_2)&=(i/\hbar c)\int_{\sigma_2}^{\sigma_1}(dx)\Big[\int\delta^{(2)}(\zeta_1', \sigma_1|\zeta^a, \sigma)d\zeta^a(\zeta^a, \sigma|\,\delta^{(1)}\mathfrak{L}[x]\,|\zeta_2'', \sigma_2)\\ &\qquad+\int(\zeta_1', \sigma_1|\,\delta^{(1)}\mathfrak{L}[x]\,|\zeta^b, \sigma)d\zeta^b\delta^{(2)}(\zeta^b, \sigma|\zeta_2'', \sigma_2)\Big]\\ &=(i/\hbar c)^2\int_{\sigma_2}^{\sigma_1}(dx)\Big[\int_\sigma^{\sigma_1}(dx')(\zeta_1', \sigma_1|\,\delta^{(2)}\mathfrak{L}[x']\delta^{(1)}\mathfrak{L}[x]\,|\zeta_2'', \sigma_2)\\ &\qquad+\int_{\sigma_2}^{\sigma}(dx')(\zeta_1', \sigma_1|\,\delta^{(1)}\mathfrak{L}[x]\delta^{(2)}\mathfrak{L}[x']\,|\zeta_2'', \sigma_2)\Big].\end{aligned} \quad (2.131)$$

We shall introduce here a notation for chronologically ordered operators,

$$(A(x)B(x'))_+=\begin{cases}A(x)B(x'), & x_0>x_0'\\ B(x')A(x), & x_0'>x_0,\end{cases} \quad (2.132)$$

[8] See, for example, H. Weyl, *The Theory of Group and Quantum Mechanics* (E. P. Dutton and Company, Inc., New York, 1931), p. 177.

which is an invariant concept provided that the operators involved commute when $x-x'$ is a spacelike interval and that the positive sense of time is preserved. Thus we may write Eq. (2.131) more compactly as

$$\delta^{(1)}\delta^{(2)}(\zeta_1', \sigma_1|\zeta_2'', \sigma_2)=\delta^{(2)}\delta^{(1)}(\zeta_1', \sigma_1|\zeta_2'', \sigma_2)$$
$$=(i/\hbar c)^2\int_{\sigma_2}^{\sigma_1}(dx)\int_{\sigma_2}^{\sigma_1}(dx')(\zeta_1', \sigma_1|(\delta^{(1)}\mathfrak{L}[x]\delta^{(2)}\mathfrak{L}[x'])_+|\zeta_2'', \sigma_2). \quad (2.133)$$

These results will find frequent application in later work.

We shall conclude this section by indicating, in connection with a Bose-Einstein field, a method for constructing the transformation function $(\zeta_1', \sigma_1|\zeta_2'', \sigma_2)$, which has as its classical analog the Hamilton-Jacobi theory of field mechanics. The actual motion of the system is implicit in the form assumed by the variation of the action integral,

$$\delta W_{12}=\left[\int_\sigma d\sigma\Pi^a\delta\phi^a+\epsilon_\mu P_\mu(\sigma)+\tfrac{1}{2}\epsilon_{\mu\nu}J_{\mu\nu}(\sigma)\right]_{\sigma_2}^{\sigma_1}, \quad (2.134)$$

in which we continue the restriction to plane spacelike surfaces. It is implied by Eq. (2.134) that W_{12} can be exhibited as a function of σ_1, σ_2, and of the ϕ^a on these surfaces, and therefore that the Π^a, P_μ and $J_{\mu\nu}$ associated with each surface can also be so exhibited. With the aid of commutation relations between the ϕ^a on σ_1 and on σ_2, it will be possible to order the operators in Eq. (2.134) so that the ϕ^a on σ_1 everywhere stand to the left of the ϕ^a on σ_2. The differential expression, thus ordered, shall be denoted by $\delta\mathcal{W}(\phi_1, \sigma_1; \phi_2, \sigma_2)$, from which we obtain differential equations connecting the various ordered operators,

$$(\delta/\delta\phi^a(x_1))\mathcal{W}=\Pi^a(x_1), \quad (\delta/\delta\phi^a(x_2))\mathcal{W}=-\Pi^a(x_2),$$
$$\delta_\mu{}^{(1)}\mathcal{W}=P_\mu(\sigma_1), \quad \delta_\mu{}^{(2)}\mathcal{W}=-P_\mu(\sigma_2), \quad (2.135)$$
$$\delta_{\mu\nu}{}^{(1)}\mathcal{W}=J_{\mu\nu}(\sigma_1), \quad \delta_{\mu\nu}{}^{(2)}\mathcal{W}=-J_{\mu\nu}(\sigma_2),$$

where x_1 and x_2 are arbitrary points on σ_1 and σ_2, respectively. In conjunction with the commutation relations (2.81), these Hamilton-Jacobi operator equations serve to determine the ordered operator $\mathcal{W}(\phi_1, \sigma_1; \phi_2, \sigma_2)$, to within an additive constant.

It is important to recognize that $\mathcal{W}\neq W_{12}$, and indeed, that $\mathcal{W}$ is a non-hermitian operator.[6] This is a consequence of the noncommutativity of the ϕ^a on σ_1 and on σ_2 in a manner which depends upon the location of these surfaces. Thus, if the operator W_{12} is first ordered and then varied, the result will differ from what is obtained by ordering δW_{12}. We now turn to the differential characterization of the transformation function labelled by eigenvalues of ϕ^a on σ_1 and σ_2,

$$\delta(\phi', \sigma_1|\phi'', \sigma_2)$$
$$=(i/\hbar)(\phi', \sigma_1|\delta\mathcal{W}(\phi_1, \sigma_1; \phi_2, \sigma_2)|\phi'', \sigma_2), \quad (2.136)$$

and observe that, in virtue of the ordering in $\delta\mathcal{W}$, the operators ϕ^a on σ_1 and on σ_2 act directly on their respective eigenvectors and can be replaced by the associated eigenvalues:

$$\delta(\phi', \sigma_1|\phi'', \sigma_2)$$
$$=(i/\hbar)\delta\mathcal{W}(\phi', \sigma_1; \phi'', \sigma_2)(\phi', \sigma_1|\phi'', \sigma_2). \quad (2.137)$$

The transformation function is thereby obtained as[7]

$$(\phi', \sigma_1|\phi'', \sigma_2)=\exp[(i/\hbar)\mathcal{W}(\phi', \sigma_1; \phi'', \sigma_2)], \quad (2.138)$$

where the constant of integration, which is additively contained in $\mathcal{W}$, can be determined from the condition

$$\lim_{\sigma_1\to\sigma_2}(\phi', \sigma_1|\phi'', \sigma_2)=\delta(\phi'-\phi''). \quad (2.139)$$

III. TIME REFLECTION

The general physical requirement of invariance with respect to coordinate transformations applies not only to translations and rotations of the coordinate system, but also to reflections of the coordinate axes. Among

[6] The elementary example of a one-dimensional free particle will suffice to illustrate this. The Hamilton-Jacobi equations for the construction of $\mathcal{W}(x(t_1), x(t_2), t)$, $t=t_1-t_2$, are

$$(\partial/\partial x(t_1))\mathcal{W}=-(\partial/\partial x(t_2))\mathcal{W}=p, \quad -(\partial/\partial t)\mathcal{W}=p^2/2m.$$

According to the solution of the equations of motion,

$$x(t_1)-x(t_2)=(t/m)p,$$

we have

$$[x(t_1), x(t_2)]=-i\hbar t/m,$$

whence

$$-(\partial/\partial t)\mathcal{W}=(m/2t^2)(x(t_1)-x(t_2))^2$$
$$=(m/2t^2)[x^2(t_1)-2x(t_1)x(t_2)+x^2(t_2)]-i\hbar/2t.$$

The solution of the Hamilton-Jacobi operator equations is

$$\mathcal{W}=(m/2t)[x^2(t_1)-2x(t_1)x(t_2)+x^2(t_2)]+\tfrac{1}{2}i\hbar\log(At),$$

which should be compared with the hermitian action integral

$$W_{12}=\tfrac{1}{2}mv^2t=(m/2t)(x(t_1)-x(t_2))^2$$
$$=(m/2t)[x^2(t_1)-2x(t_1)x(t_2)+x^2(t_2)]-\tfrac{1}{2}i\hbar.$$

Incidentally, the analog of Eq. (2.138) is

$$(x', t_1|x'', t_2)=\exp[(i/\hbar)\mathcal{W}(x', x'', t)]$$
$$=(At)^{-\frac{1}{2}}\exp[(im/2\hbar t)(x'-x'')^2],$$

where the constant A is determined to be

$$A=2\pi i\hbar/m$$

from the analog of Eq. (2.139),

$$\lim_{t\to 0}(x', t_1|x'', t_2)=\delta(x'-x'').$$

[7] The exponential form of Eq. (2.138) is familiar as a basis for establishing a correspondence connection with classical Hamilton-Jacobi particle mechanics. Dirac employed this form in a discussion of unitary transformations and recognized, in part, that the Hamilton-Jacobi equations are rigorous as relations among ordered operators (see the end of the section quoted in reference 4). In Feynman's version of quantum mechanics [R. P. Feynman, Revs. Modern Phys. **20**, 367 (1948)], the exponential form is employed for infinitesimal time intervals, with the real part of $\mathcal{W}$ defined as the classical action integral.

the latter transformations, time reflection has a singular position. Its special nature can be indicated by the transformation properties of some integrated physical quantities. Thus, the expectation value of the energy-momentum vector,

$$\langle P_\nu\rangle=(1/c)\int_\sigma d\sigma_\mu\langle T_{\mu\nu}\rangle, \tag{3.1}$$

is actually a pseudovector with respect to time reflection. With the plane surface σ chosen perpendicular to the time axis, the components of $\langle P_\nu\rangle$ are obtained as three-dimensional volume integrals,

$$\langle P_0\rangle=(1/c)\int d\sigma\langle T_{00}\rangle,$$
$$\langle P_k\rangle=(1/c)\int d\sigma\langle T_{0k}\rangle, \quad k=1,2,3, \tag{3.2}$$

and the time reflection $x_0\rightarrow -x_0$, $x_k\rightarrow x_k$ induces $\langle P_0\rangle\rightarrow\langle P_0\rangle$, $\langle P_k\rangle\rightarrow -\langle P_k\rangle$, according to the transformation properties of tensors. This differs in sign from a proper vector transformation. In particular, the energy does not reverse sign under time reflection. More generally, this property of $\langle P_\nu\rangle$ is obtained from the pseudovector character of $d\sigma_\mu$, which expresses the pseudoscalar nature of a four-dimensional volume element with respect to time reflection. Similarly, the expectation value of the charge

$$\langle Q\rangle=(1/c)\int d\sigma_\mu\langle j_\mu\rangle=(1/c)\int d\sigma\langle j_0\rangle \tag{3.3}$$

behaves as a pseudoscalar under time reflection. Hence, this transformation interchanges positive and negative charge, and both signs must occur symmetrically in a covariant theory. Indeed, for some purposes the requirement of charge symmetry can be substituted for the more incisive demand of invariance under time reflection.

The significant implication of these properties is that time reflection cannot be included within the general framework of unitary transformations. Thus, on referring to the Schrödinger equation for translations (2.107), or the analogous operator equation (2.110), we encounter a contradiction between the transformation properties of the proper vector translation operator δ_μ and of the pseudovector P_μ. This difficulty appears most fundamentally in our basic variational principle (2.14). With $\mathfrak{L}$ behaving as a scalar and (dx) as a pseudoscalar, reflection of the time axis introduces a minus sign on the right side of this equation. However, it is important to notice that the scalar nature of $\mathfrak{L}$ cannot be maintained for that part of the lagrange function which describes half-integral spin fields. Indeed, such contributions to $\mathfrak{L}$ behave like pseudoscalars with respect to time reflection.[8] If we were to consider only such a half-integral spin field, the basic dynamical equation would preserve its structure under time reversal, but at the expense of violating the general transformation properties of all physical quantities; charge would remain unaltered, and energy would reverse sign under time reflection. The latter difficulty simply indicates that, on inclusion of the contributions of integral spin fields, the various parts of $\mathfrak{L}$ would transform differently, thus emphasizing again the general failure of Eq. (2.14) to admit time reflection as a unitary transformation.

To aid in investigating the extended class of transformations that is required to include time reflection we shall introduce some notational developments. The scalar product of two vectors, Ψ_a and Ψ_b, can be written

$$(a|b)=\Psi_a^*\Psi_b=\Psi_b\Psi_a^*, \tag{3.4}$$

thereby being regarded as the invariant combination of a vector Ψ_b with the dual, complex conjugate vector Ψ_a^* We allow operators to act both on the left and on the right of vectors, Ψ and Ψ^*. Thus, an operator associated with A, the transposed operator A^T, is defined by[9]

$$A\Psi=\Psi A^T, \quad \Psi^*A=A^T\Psi^*, \tag{3.5}$$

or by

$$(a|A|b)=\Psi_a^*A\Psi_b=\Psi_bA^T\Psi_a^*. \tag{3.6}$$

We also define the associated complex conjugate operator A^*,

$$(A\Psi)^*=A^*\Psi^*. \tag{3.7}$$

The connection with the hermitian conjugate operator $A^\dagger$ is obtained from the definition of the latter,

$$(A\Psi)^*=\Psi^*A^\dagger, \tag{3.8}$$

---

[8] The fundamental invariant of a spin $\frac{1}{2}$ field is $\bar\psi\psi=\psi^\dagger\gamma_0\psi$. The transformation that represents time reflection, $\psi'=R\psi$, can be obtained from its equivalence with a rotation through the angle π in the (45) plane; $R=\exp[i\pi\frac{1}{2}\sigma_{45}]=i\sigma_{45}$. Accordingly,

$$\bar\psi'\psi'=\psi^\dagger R^{-1}\gamma_0R\psi=-\bar\psi\psi,$$

which indicates the pseudoscalar character of the spin $\frac{1}{2}$ field lagrange function, with respect to time reflection. The corresponding behavior of fields with other spin values can be obtained from the observation that a spinor of rank n contains fields of spin $\frac{1}{2}n$, $\frac{1}{2}n-1$, $\cdots$. The basic invariant and time reflection operator for a spinor of rank n are

$$\bar\psi\psi=\psi^\dagger\prod_{k=1}^{n}\gamma_0^{(k)}\psi,$$

and

$$R=\exp\left[i\pi\tfrac{1}{2}\sum_{k=1}^{n}\sigma_{45}^{(k)}\right]=\prod_{k=1}^{n}i\sigma_{45}^{(k)}.$$

Therefore,

$$\bar\psi'\psi'=\psi^\dagger R^{-1}\prod_{k=1}^{n}\gamma_0^{(k)}R\psi=(-1)^n\bar\psi\psi,$$

which shows the pseudoscalar nature of the lagrange function for all half-integral spin fields.

[9] Note how the familiar property of transposition, $(AB)^T=B^TA^T$, follows from this definition: $AB\Psi=A(\Psi B^T)=\Psi B^TA^T$.

namely,

$$A^\dagger = A^{*T}. \tag{3.9}$$

Conventional quantum mechanics contemplates transformations only within the Ψ vector space, and contragradient transformations within the dual Ψ^* space. We shall now consider transformations that interchange the two spaces, as in

$$\Psi_a \rightarrow \Psi_{\bar{a}} = \Psi_a^*. \tag{3.10}$$

The effect of Eq. (3.10) is indicated by

$$(a|b) = \Psi_a^* \Psi_b = \Psi_{\bar{a}} \Psi_{\bar{b}}^* = (\bar{b}|\bar{a}), \tag{3.11}$$

and

$$(a|A|b) = \Psi_a^* A \Psi_b = \Psi_{\bar{a}} A \Psi_b^* = (\bar{b}|A^T|\bar{a}). \tag{3.12}$$

More generally, if

$$\Psi_{\bar{a}}^* = R\Psi_a, \tag{3.13}$$

where R is a unitary operator, we have

$$(a|b) = (\bar{b}|\bar{a}), \quad (a|A|b) = (\bar{b}|\bar{A}|\bar{a}), \tag{3.14}$$

in which

$$\bar{A} = (RAR^{-1})^T. \tag{3.15}$$

Now, we have

$$\overline{AB} = (RABR^{-1})^T = (RBR^{-1})^T (RAR^{-1})^T = \bar{B}\bar{A}, \tag{3.16}$$

and therefore

$$(a|[A, B]|b) = -(\bar{b}|[\bar{A}, \bar{B}]|\bar{a}). \tag{3.17}$$

We have here precisely the sign change that is required to preserve the structure of equations like Eq. (2.110) under time reflection.

We now examine whether it is possible to satisfy the requirement of invariance under time reflection by means of transformations of the type (3.13). When we introduce the coordinate transformation

$$\bar{x}_0 = -x_0, \quad \bar{x}_k = x_k, \quad k = 1, 2, 3, \tag{3.18}$$

in conjunction with the eigenvector transformation

$$\Psi^*(\bar{\zeta}', \sigma) = R\Psi(\zeta', \sigma), \tag{3.19}$$

the fundamental dynamical equation (2.14) becomes

$$\delta(\bar{\zeta}_2'', \sigma_2|\bar{\zeta}_1', \sigma_1) = (i/\hbar c)(\bar{\zeta}_2'', \sigma_2|\delta \int_{\sigma_1}^{\sigma_2} (d\bar{x})\overline{\mathfrak{L}}|\bar{\zeta}_1', \sigma_1), \tag{3.20}$$

where

$$\overline{\mathfrak{L}} = (R\mathfrak{L}R^{-1})^T = \mathfrak{L}^T((R\phi^\alpha R^{-1})^T, \pm\bar{\partial}_\mu(R\phi^\alpha R^{-1})^T). \tag{3.21}$$

In the last statement, the $\pm$ sign indicates the effect of the coordinate transformation (3.18) on the components of the gradient vector, while the notation $\mathfrak{L}^T(\ )$ symbolizes the reversal in the order of all factors induced by the operation of transposition. The operator R will now be chosen to produce that linear transformation of the ϕ^α,

$$R\phi^\alpha R^{-1} = R^{\alpha\beta}\phi^\beta, \tag{3.22}$$

which compensates the effect of the gradient vector transformation. Thus. we have

$$\overline{\mathfrak{L}} = (\pm)\mathfrak{L}^T(\phi^{\alpha T}, \bar{\partial}_\mu \phi^{\alpha T}), \tag{3.23}$$

where the $(\pm)$ sign here refers to the fact that the structure of the lagrange function, for half-integral spin fields, can be maintained only at the expense of a change in sign. We now see that if

$$\overline{\mathfrak{L}} = \mathfrak{L}(\phi^{\alpha T}, \bar{\partial}_\mu \phi^{\alpha T}), \tag{3.24}$$

the form of our fundamental dynamical equation will have been preserved under time reflection, since Eq. (3.20) will then differ from Eq. (2.14) only in the substitution of $\phi^{\alpha T}$ for ϕ^α as the appropriate field variable, and in the interchange of σ_1 and σ_2, which simply reflects the reversed temporal sense in which the dynamical development of the system is to be traced.

Invariance under time reflection thus requires that inverting the order of all factors in the lagrange function leave a scalar term unchanged, and reverse the sign of a pseudoscalar term. This can be satisfied, of course, by an explicit symmetrization or antisymmetrization of the various terms in $\mathfrak{L}$. When the lagrange function, thus arranged, is employed in the principle of stationary action, the variations $\delta_0\phi^\alpha$ will likewise be disposed in a symmetrical or antisymmetrical manner. We must now recall that the equations of motion (2.18), which do not depend explicitly on the nature of the field commutation properties, have been obtained by postulating the equality of terms in $\delta_0\mathfrak{L}$ that differ basically only in the location of $\delta_0\phi^\alpha$. Since such terms appear with the same sign in scalar components of $\mathfrak{L}$, and with opposite signs in pseudoscalar components, we deduce a corresponding commutativity, or anticommutativity, between $\delta_0\phi^\alpha$ and the other operators in the individual terms of $\delta_0\mathfrak{L}$.

The information concerning commutation properties that has thus been obtained is restricted to operators at common space-time points, since this is the nature of the terms in $\mathfrak{L}$. Commutation relations between field quantities located at distinct points of a space-like surface are implied by the general compatibility requirement for physical quantities attached to points with a spacelike interval. Components of integral spin fields, and bilinear combinations of the components of half-integral spin fields, are the basic physicial quantities to which this compatibility condition applies. By considering the general possibilities of coupling between the various fields, we may draw from these two expressions of relativistic invariance the consequence that the variations $\delta\phi^b(x')$, and therefore the conjugate varia-

tions $\delta\Pi^b(x')$, commute or anticommute with $\phi^a(x)$, $\Pi^a(x)$ for all x and x' on a given σ, where the relation of anticommutativity holds when both a and b refer to components of half-integral spin fields. The consistency of this statement with the general commutation relations that have already been deduced from it is easily verified. By subjecting the canonical variables in Eq. (2.81) to independent variations, we obtain

$$[\phi^a(x), \delta\phi^b(x')]_\pm = [\Pi^a(x), \delta\phi^b(x')]_\pm = 0,$$
$$[\phi^a(x), \delta\Pi^b(x')]_\pm = [\Pi^a(x), \delta\Pi^b(x')]_\pm = 0, \quad (3.25)$$

which is valid for all x, x' on σ. In addition, Eq. (2.81) properly states that all physical quantities commute at distinct points of σ.

We conclude that the connection between the spin and statistics of particles is implicit in the requirement of invariance under coordinate transformations.[10]

[10] The discussion of the spin and statistics connection by W. Pauli [Phys. Rev. **58**, 716 (1940)] is somewhat more negative in character, although based on closely related physical requirements. Thus, Pauli remarks that Bose-Einstein quantization of a half-integral spin field implies an energy that possesses no lower bound, and that Fermi-Dirac quantization of an integral spin field leads to an algebraic contradiction with the commutativity of physical quantities located at points with a spacelike interval. Another postulate which has been employed, that of charge symmetry [W. Pauli and F. J. Belinfante, Physica **7**, 177 (1940)], suffices to determine the nature of the commutation relations for sufficiently simple systems. As we have noticed, it is a consequence of time reflection invariance. The comments of Feynman on vacuum polarization and statistics [Phys. Rev. **76**, 749 (1949)] appear to be an illustration of the charge symmetry requirement, since a contradiction is established when the charge symmetrical concept of the vacuum is applied to a Bose-Einstein spin $\frac{1}{2}$ field, or to a Fermi-Dirac spin 0 field.

PHYSICAL REVIEW VOLUME 82, NUMBER 6 JUNE 15, 1951

Diffusion of High Energy Gamma-Rays through Matter. III. Refinement of the Solution of the Diffusion Equation*

L. L. FOLDY
Case Institute of Technology, Cleveland, Ohio

(Received February 19, 1951)

In Part I of the present series of papers an approximate equation was derived governing the diffusion of high energy gamma-rays through matter. In Part II an approximate solution of this diffusion equation was obtained in the energy region where the total gamma-ray cross section was substantially independent of energy. In the present paper, by consideration of the methods employed in obtaining the solution in II, a refinement of the solution is carried out which reduces the errors introduced by the approximations made both in the energy distribution and the angular distribution of the multiply-scattered gamma-rays. The solution is also modified to take into partial account the effect of small variations of the total gamma-ray cross section with energy. An upper and lower bound on the solution is obtained when the cross section is independent of energy.

I. INTRODUCTION

IN the first (I) of the present series of papers,[1] an approximate equation governing the diffusion of gamma-rays through matter was derived. The gamma-ray energies for which the equation is valid extends from a few Mev up to energies (depending on the material) where the radiation of gamma-rays by the secondary electrons (photoelectrons, Compton recoils, and pairs) produced by the primary gamma-rays becomes important. In the second (II) paper of the series, the solution of the diffusion equation was considered in the energy range where the total cross section for gamma-rays was practically independent of energy. In all materials this latter energy range coincides practically with the energy range over which the diffusion equation itself is valid. However, in order to obtain a solution to the equation, even with this restriction, it was necessary to make a rather poor approximation to the Klein-Nishina formula; and this last approximation leads to rather large errors, especially for gamma-rays whose energy lies far below the energy of the incident gamma-rays. The present paper is directed towards refining the approximation somewhat, making certain corrections to the solution to improve its accuracy, and studying the magnitudes of the remaining errors. The notation used is the same as in I and II, and reference should be made to these papers for the meaning of symbols not sufficiently defined below.

* Supported by the AEC and by a grant-in-aid from the Scientific Research Society of America.

[1] L. L. Foldy, Phys. Rev. **81**, 395 (1951), hereinafter referred to as I, and L. L. Foldy and R. K. Osborn, Phys. Rev. **81**, 400 (1951), hereinafter referred to as II.

II. APPROXIMATIONS TO THE KLEIN-NISHINA FORMULA FOR WHICH THE DIFFUSION EQUATION CAN BE SOLVED

The equation governing the diffusion of gamma-rays derived in I is

$$\partial f(\sigma, \xi, \eta, \zeta)/\partial\zeta + \phi_T f(\sigma, \xi, \eta, \zeta)$$
$$= (1/\pi)\int_{-\infty}^{\infty}\int_{-\infty}^{\infty} K(\sigma'/\sigma) f(\sigma', \xi', \eta', \zeta) d\xi' d\eta', \quad (1)$$

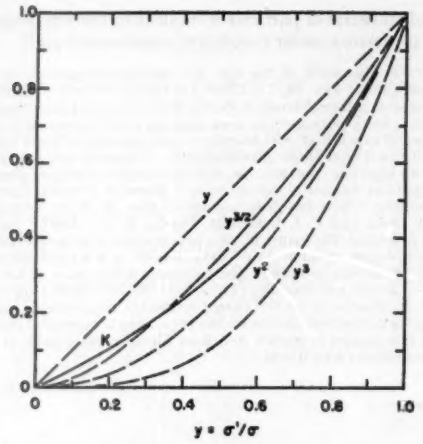

FIG. 1. The function $K(\sigma'/\sigma)$ together with several power law approximations to this function.

where f is the distribution function for the gamma rays in softness σ (reciprocal of the gamma-ray energy measured in units of the electron rest energy = gamma-ray wavelength measured in electron Compton wavelengths), and angle (as specified by the "rectangular" orientation variables ξ and η), at a depth ζ (dimensionless depth parameter) in the material. ϕ_T is the (constant) total gamma-ray cross section,

$$\sigma'=\sigma-\tfrac{1}{2}\{(\xi-\xi')^2+(\eta-\eta')^2\}, \tag{2}$$

and the kernel,

$$K(\sigma'/\sigma)=\tfrac{1}{2}(\sigma'/\sigma)[1+(\sigma'/\sigma)^2], \tag{3}$$

represents (apart from a constant dimensional factor) the Klein-Nishina cross section for scattering of a gamma-ray from a softness σ' to a softness σ.

We wish to note first that a solution of Eq. (1) can easily be obtained if the kernel K can be approximated by any power of σ'/σ, say $(\sigma'/\sigma)^n$. For, if one replaces K by this factor, then by the substitution,

$$f(\sigma, \xi, \eta, \zeta)=(\sigma_0/\sigma)^n g(\sigma, \xi, \eta, \zeta), \tag{4}$$

Eq. (1) can be reduced to the form

$$[\partial g(\sigma, \xi, \eta, \zeta)/\partial\zeta]+\phi_T g(\sigma, \xi, \eta, \zeta)$$

$$=(1/\pi)\int_{-\infty}^{\infty}\int_{-\infty}^{\infty} g(\sigma', \xi', \eta', \zeta)d\xi' d\eta'. \tag{5}$$

This is the equation whose solution corresponding to monoenergetic gamma-rays of softness σ_0 incident normally on the surface of the material was found in II to be

$$g(\sigma, \xi, \eta, \zeta)=[\sum_{m=0}^{\infty} g_m(\sigma, \xi, \eta, \zeta)]\exp(-\phi_T\zeta), \tag{6}$$

where

$$\begin{aligned} g_0&=\delta(\sigma-\sigma_0)\delta(\xi)\delta(\eta),\\ g_1&=(\zeta/\pi)\delta[\sigma-\sigma_0-\tfrac{1}{2}(\xi^2+\eta^2)],\\ g_m&=\frac{(m-1)(2\zeta)^m}{2\pi(m!)^2}\left(\sigma-\sigma_0-\frac{\xi^2+\eta^2}{2m}\right)_*^{m-2}, \quad m\geq 2. \end{aligned} \tag{7}$$

In the above, the asterisk subscript on the parentheses indicates that if the quantity contained in parentheses is negative, then the parentheses is to be replaced by zero. The distribution function f is then given simply by g multiplied by $(\sigma_0/\sigma)^n$. In II, the solution for the choice $n=1$ was examined.

In Fig. 1, we have plotted K as a function of (σ'/σ) together with several power law approximations ($n=1$, $\frac{3}{2}$, 2, and 3) to it. It can be seen that $n=1$ is not a very satisfactory approximation, being everywhere too high, but it is the only power law approximation behaving correctly for small σ'/σ. Since physically K determines the probability of a Compton scattering of a gamma-ray of softness σ' to a softness σ, this means that in this approximation we predict too many scattered gamma-rays at all energies, particularly at low energies. It will be noted further that the choice $n=2$ is a rather good approximation for $\sigma'/\sigma>0.5$; and, hence, the solution obtained with this choice will give quite accurate results for the distribution of gamma-rays in the range from half the incident energy to the incident energy ($\sigma_0<\sigma<2\sigma_0$), but it will predict far too few gamma-rays at the lower energies. On the other hand, the choice $n=\frac{3}{2}$ is a fair approximation over the range from $\sigma'/\sigma=0.2$ to $\sigma'/\sigma=1$ (better than 15 percent), and so might be relied on to give good results over the softness range (σ_0 to $5\sigma_0$). It represents probably the best power law approximation to the Klein-Nishina formula but will predict too many scattered gamma-rays at high energies at the expense of too few at low energies.

Now the fact that a change in the power by which the Klein-Nishina formula is approximated leads only to a change in the power of (σ_0/σ) by which g is multiplied to give the distribution function suggests that a still better approximation to the solution can be obtained by "interpolation" on the coefficient of g. The natural choice here is to take this coefficient to be just $K(\sigma_0/\sigma)$:

$$f(\sigma, \xi, \eta, \zeta)=\tfrac{1}{2}(\sigma_0/\sigma)[1+(\sigma_0/\sigma)^2]g(\sigma, \xi, \eta, \zeta), \tag{8}$$

since this decreases the number of high energy gamma-rays slightly and brings it into accord with what one obtains by a good approximation ($n=2$) for this energy region and at the same time increases the number of low energy gamma-rays substantially so as to give a number much closer to what one would anticipate on the basis of the results from the choice $n=1$. Hence, we would expect Eq. (8) to be superior to any solution obtained by a simple power law approximation to K.

Actually the approximate solution (8) has a very simple interpretation. The problem to which we are

trying to find a solution corresponds to the diffusion of gamma-rays which are Compton scattered with a probability proportional to $K(\sigma'/\sigma)=\frac{1}{2}(\sigma'/\sigma)[1+(\sigma'/\sigma)^2]$. If we replace this problem by one in which the incident gamma-rays are divided into two equal groups, one group being scattered with a probability proportional to σ'/σ and the other with a probability proportional to $(\sigma'/\sigma)^3$, so that the average probability is given by K, then Eq. (8) would be the exact solution to this latter problem.

III. IMPROVEMENT OF THE SOLUTION

As we pointed out in II, the series (6) has the interpretation that the first term represents gamma-rays reaching the depth ζ unscattered, while the second, third, fourth, etc., terms represent, respectively, the gamma-rays reaching the depth ζ after having been scattered once, twice, three times, etc. Actually, the solution for a power law approximation to K given by Eq. (4) could have been obtained by an iteration procedure on the original diffusion equation. One is led to inquire why one can easily obtain a solution to the diffusion equation when K is approximated by a power law and yet a solution is difficult to obtain when the correct expression for K is used. By investigating the iteration method of solution the reason for this difference is found to be the following: Consider a gamma-ray scattered m times and as a result having its softness modified from σ_0 to σ. If $\sigma_1, \sigma_2, \cdots\sigma_{m-1}$ are the softnesses of the gamma ray after the first, second, $\cdots(m-1)$th, scatterings, then when K is approximated by $(\sigma'/\sigma)^n$, the probability that this sequence of scattering takes place is proportional to

$$(\sigma_0/\sigma_1)^n(\sigma_1/\sigma_2)^n\cdots(\sigma_{m-1}/\sigma)^n=(\sigma_0/\sigma)^n. \tag{9}$$

The fact that this expression is independent of the sequence of intermediate softnesses is what makes the simple solution possible, and the fact that it is independent of m (the number of scatterings) is what allows the factor $(\sigma_0/\sigma)^n$ to be factored out of the expression and appear as the coefficient of g in Eq. (4). If K had these same simple properties, then the solution of Eq. (1) could be written in the form (8).

Actually, K does not have these properties; but we can show that it does not deviate too greatly from having these properties. If we define the functions

$$\begin{aligned}K_m(\sigma_0/\sigma;\,&\sigma_1,\sigma_2,\cdots\sigma_{m-1})\\&=K(\sigma_0/\sigma_1)K(\sigma_1/\sigma_2)\cdots K(\sigma_{m-1}/\sigma)\\&=K_{m-1}(\sigma_0/\sigma_{m-1})K(\sigma_{m-1}/\sigma),\end{aligned} \tag{10}$$

then we must show first that K_m is not very sensitive to variations of $\sigma_1, \sigma_2, \cdots\sigma_{m-1}$. In the appendix we give a proof that K_m is always bounded from above by K and from below by $(\sigma_0/\sigma)^2$ for any values of the intermediate softnesses.[2] Referring to Fig. 1 we see that this confines K_m to a relatively narrow range, particularly for $\sigma_0/\sigma>0.5$. Insofar as K_m may be approximated by K, Eq. (8) will be the solution to our problem.

Actually, however, it is possible to improve on the solution given by Eq. (8), since a tractable form can still be obtained even when the K_m are approximated by functions which are different for different m. Statistically, we would expect that a gamma-ray would reach the softness σ from an initial softness σ_0 in m scatterings far more frequently through those sequences of intermediate softnesses which are uniformly distributed between σ_0 and σ_m than by such sequences which include one or more large changes in softness and many small ones. This in turn would lead one to expect that if one had to pick an *effective* K_m for scattering independent of $\sigma_1, \sigma_2, \cdots\sigma_{m-1}$, the best choice would lie close to that K_m, which we shall denote as $\bar{K}_m(\sigma_0/\sigma)$, for which $\sigma_1, \sigma_2, \cdots\sigma_{m-1}$ are uniformly spaced between σ_0 and σ. We have plotted these for $m=1$, 2, 3, and 4 in Fig. 2a. The exact expressions for $\bar{K}_m(\sigma_0/\sigma)$ are quite complicated, but one can approximate them closely by the series of functions,

$$W_m(\sigma_0/\sigma)=(\sigma_0/\sigma)\{(\sigma_0/\sigma)+(m+1)^{-1}[1-(\sigma_0/\sigma)^2]\}, \tag{11}$$

which have a simple analytical form. These have been plotted in Fig. 2b for comparison with the curves in Fig. 2a. W_m is slightly larger than $\bar{K}_m$ for small values of (σ_0/σ); but this is fortuitous, since we would expect the best effective value for K_m to lie above $\bar{K}_m$ in this region.

We shall now show that to within the error made in replacing $W_m(\sigma_0/\sigma')K(\sigma'/\sigma)$ by $W_{m+1}(\sigma_0/\sigma)$, the function

$$\begin{aligned}&f(\sigma,\xi,\eta,\zeta)\\&\quad=[\sum_{m=0}^{\infty}W_m(\sigma_0/\sigma)g_m(\sigma,\xi,\eta,\zeta)]\exp(-\phi_T\zeta),\end{aligned} \tag{12}$$

with the g_m given by Eq. (7), is a solution of Eq. (1). The proof rests on the fact that

$$\begin{aligned}&\partial g_{m+1}(\sigma,\xi,\eta,\zeta)/\partial\zeta\\&\quad=(1/\pi)\int_{-\infty}^{\infty}\int_{-\infty}^{\infty}g_m(\sigma',\xi',\eta',\zeta)d\xi'd\eta',\end{aligned} \tag{13}$$

as can be seen by substituting Eq. (6) in Eq. (5). If one substitutes Eq. (12) in Eq. (1), one obtains easily

$$\begin{aligned}&W_{m+1}(\sigma_0/\sigma)\partial g_{m+1}(\sigma,\xi,\eta,\zeta)\,\partial\zeta\\&\quad=(1/\pi)\int_{-\infty}^{\infty}\int_{-\infty}^{\infty}K(\sigma'/\sigma)W_m(\sigma_0/\sigma')\\&\qquad\times g_m(\sigma',\xi',\eta',\zeta)d\xi'd\eta',\end{aligned}$$

which establishes our contention. On the basis of the discussion above, it is unlikely that the errors in the solution (12) are large at any depth and for any softness.

[2] From this it follows by elementary arguments that $(\sigma_0/\sigma)^3g(\sigma,\xi,\eta,\zeta)\leqslant f(\sigma,\xi,\eta,\zeta)\leqslant\frac{1}{2}(\sigma_0/\sigma)[1+(\sigma_0/\sigma)^2]g(\sigma,\xi,\eta,\zeta)$.

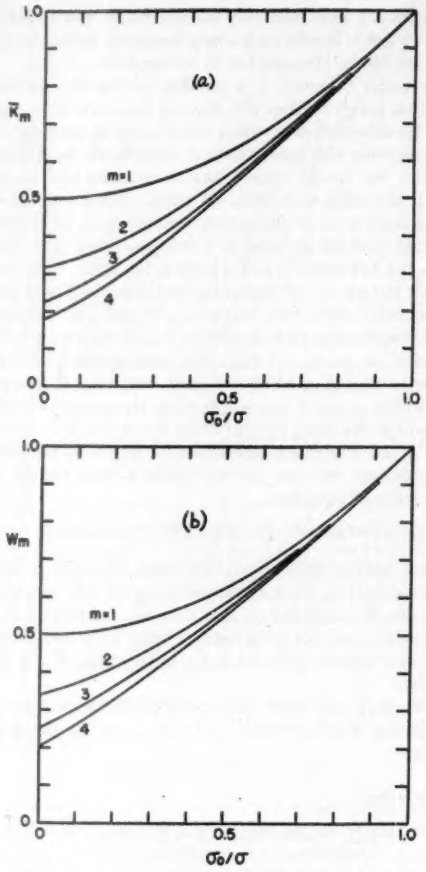

FIG. 2(a) The function $\bar{K}_m(\sigma_0/\sigma)$ for $m=1, 2, 3, 4$; (b) the functions $W_m(\sigma_0/\sigma)$ for $m=1, 2, 3, 4$, representing approximations to the corresponding functions $\bar{K}_m$.

Absolute, but rather wide, limits on the errors are provided by the inequality in reference 2.

IV. FURTHER REFINEMENTS IN THE SOLUTION

The best solution we have obtained so far for our diffusion problem is given by Eq. (12). In this section we shall make some small modifications of this solution to ameliorate the effects of some of the other approximations we have been forced to make.

(a) Improvement in the Angular Distribution

In the solution (12) each term for $m \geqslant 2$ cuts off at an angle $\vartheta=[2m(\sigma-\sigma_0)]^{\frac{1}{2}}$ because of the asterisk on the parentheses in g_m. One can easily show that the rigorous cut off in angle for an m-fold scattered gamma-ray of softness σ actually occurs at the angle ϑ fixed by the equation: $m\{1-\cos(\vartheta/m)\}=\sigma-\sigma_0$. Hence, we might expect an improvement in the angular distribution represented by Eq. (8) if the factor $(\sigma-\sigma_0-\vartheta^2/2m)_*$ is replaced by the factor $(\sigma-\sigma_0/m\{1-\cos(\vartheta/m)\})_*$.

(b) Correction of the Term for Single Scattering

One can easily show that the correct form for the term in Eq. (8) representing a single scattering of a gamma-ray when employing the rigorous Klein-Nishina formula should be

$$(2\pi)^{-1}\zeta(\sigma_0/\sigma)[1+(\sigma_0/\sigma)^2-(\sigma_0/\sigma)\sin^2\vartheta] \times\delta(\sigma-\sigma_0-\{1-\cos\vartheta\}).$$

Hence, we can employ this correct term in place of the result obtained above for the single-scattering term in the series (8).

(c) Correction of the Exponential Absorption Factor

It has been assumed in the work above that the total gamma-ray cross section is independent of softness in the range of energies in which we are working. Actually this cross section varies somewhat with energy. Since the exponential factor $\exp(-\phi_T\zeta)$ represents simply the over-all absorption of the gamma-rays in penetrating to the depth ζ and since a gamma-ray with softness σ at a depth ζ has generally filtered down to this softness through a series of intermediate softness values, some improvement of the solution would be anticipated if one replaced the constant ϕ_T in the exponential by the average value of ϕ_T over the softness range from σ_0 to σ. We shall represent this average value by $\bar{\phi}_T(\sigma_0, \sigma)$.

Making all of the above corrections, our "best" solution of the diffusion problem now takes the form

$$f(\sigma, \xi, \eta, \zeta)=[\sum_{m=0}^{\infty} f_m]\exp[-\bar{\phi}_T(\sigma_0, \sigma)\zeta],$$

$$f_0=\delta(\sigma-\sigma_0)\delta(\xi)\delta(\eta),$$

$$f_1=(2\pi)^{-1}\zeta(\sigma_0/\sigma)[1+(\sigma_0/\sigma)^2-(\sigma_0/\sigma)\sin^2\vartheta] \times\delta(\sigma-\sigma_0-\{1-\cos\vartheta\}),$$

$$f_m=\frac{\sigma_0}{\sigma}\left\{\frac{\sigma_0}{\sigma}+\frac{1}{m+1}\left(1-\frac{\sigma_0}{\sigma}\right)^2\right\}\frac{(m-1)(2\zeta)^m}{2\pi(m!)^2} \times(\sigma-\sigma_0-m\{1-\cos(\vartheta/m)\})_*^{m-2}, \quad m\geqslant 2. \quad (14)$$

V. SPECIAL CASES

In certain special cases, the solution given by Eq. (14) can be made to take simpler forms by the use of methods such as those employed in II. In particular, for the special cases where $\vartheta^2\ll 2(\sigma-\sigma_0)$ or where $\rho=[8\zeta(\sigma-\sigma_0)]^{\frac{1}{2}}\gg\vartheta^2/2(\sigma-\sigma_0)$, the series in Eq. (14)

may be summed to give the closed form:

$$f=[\delta(\sigma-\sigma_0)\delta(\xi)\delta(\eta)+(\zeta/2\pi)(\sigma_0/\sigma)\times[1+(\sigma_0/\sigma)^2-(\sigma_0/\sigma)\sin^2\vartheta]\delta(\sigma-\sigma_0-\{1-\cos\vartheta\})+(4/\pi)\zeta^2(\sigma_0/\sigma)^2(\{[1-I_0(\rho)+\tfrac{1}{2}\rho I_1(\rho)]/\rho^4\}+\{(\sigma/\sigma_0)(1-\sigma_0/\sigma)^2[\rho-2I_1(\rho)+\rho I_2(\rho)]/\rho^5\})\times\exp[-\vartheta^2/2(\sigma-\sigma_0)]]\exp[-\tilde{\phi}_T(\sigma_0,\sigma)\zeta]. \quad (15)$$

To obtain the distribution function at any depth integrated over all angles for the gamma-rays, it was found necessary to omit the slight improvement in the angular distribution, resulting from the replacement of $\vartheta^2/2m$ by $m[1-\cos(\vartheta/m)]$ in order to carry out the integration. Once this is done, the series can be summed to give for the integral distribution function

$$F(\sigma,\zeta)=\int\int f(\sigma,\xi,\eta,\zeta)d\xi d\eta$$
$$=\{\delta(\sigma-\sigma_0)+[4\zeta(\sigma_0/\sigma)^2I_1(\rho)/\rho]+8\zeta(\sigma_0/\sigma)(1-\sigma_0/\sigma)^2I_2(\rho)/\rho^2\}\times\exp[-\tilde{\phi}_T(\sigma_0,\sigma)\zeta]. \quad (16)$$

For convenience in calculations the functions

$$[1-I_0(\rho)+\tfrac{1}{2}\rho I_1(\rho)]/\rho^4,\ [\rho-2I_1(\rho)+\rho I_2(\rho)]/\rho^5,$$

$I_1(\rho)/\rho$, and $I_2(\rho)/\rho^2$, occurring in the above formulas, have been plotted as a function of ρ in Fig. 3.

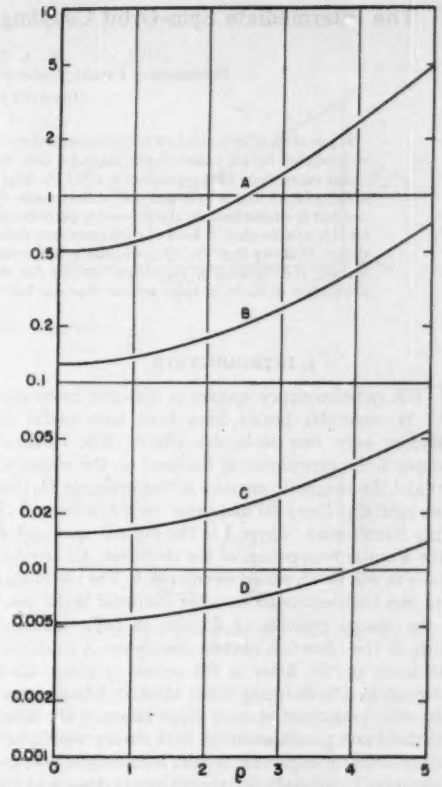

FIG. 3. Plots of the functions entering Eqs. (15) and (16). (A) The function $I_1(\rho)/\rho$; (B) the function $I_2(\rho)/\rho^2$; (C) the function $[1-I_0(\rho)+\frac{1}{2}\rho I_1(\rho)]/\rho^4$; (D) the function $[\rho-2I_1(\rho)+\rho I_2(\rho)]/\rho^5$.

APPENDIX

We wish to establish that

$$(\sigma_0/\sigma)^2\leqslant K_m(\sigma_0/\sigma;\sigma_1,\sigma_2,\cdots\sigma_{m-1})\leqslant K_1(\sigma_0/\sigma)=K(\sigma_0/\sigma). \quad (A\text{-}1)$$

We shall use the method of mathematical induction based on the fact that

$$K(\sigma_0/\sigma)\geqslant(\sigma_0/\sigma)^2. \quad (A\text{-}2)$$

We have first that if

$$K_m(\sigma_0/\sigma)\geqslant(\sigma_0/\sigma)^2, \quad (A\text{-}3)$$

then

$$K_{m+1}(\sigma_0/\sigma)=K_m(\sigma_0/\sigma_m)K(\sigma_m/\sigma)\geqslant(\sigma_0/\sigma_m)^2(\sigma_m/\sigma)^2=(\sigma_0/\sigma)^2, \quad (A\text{-}4)$$

which combined with Eq. (A-2) is sufficient to establish the inferior limit in Eq. (A-1).

Secondly, we shall show that if

$$K_m(\sigma_0/\sigma)\leqslant K(\sigma_0/\sigma),$$

then

$$K_{m+1}(\sigma_0/\sigma)\leqslant K(\sigma_0/\sigma),$$

which combined with Eq. (A-2) is sufficient to establish the superior limit in Eq. (A-2). We have

$$K_{m+1}(\sigma_0/\sigma)=K_m(\sigma_0/\sigma_m)K(\sigma_m/\sigma)\leqslant K(\sigma_0/\sigma_m)K(\sigma_m/\sigma),$$
$$K(\sigma_0/\sigma_m)K(\sigma_m/\sigma)=\tfrac{1}{2}(\sigma_0/\sigma_m)[1+(\sigma_0/\sigma_m)^2]\cdot\tfrac{1}{2}(\sigma_m/\sigma)[1+(\sigma_m/\sigma)^2]$$
$$=\tfrac{1}{2}(\sigma_0/\sigma)[1+(\sigma_0/\sigma)^2]\cdot\{\tfrac{1}{2}[1+(\sigma_m/\sigma)^2][1+(\sigma_0/\sigma_m)^2]/[1+(\sigma_0/\sigma)^2]$$
$$=K(\sigma_0/\sigma)\cdot\{\tfrac{1}{2}+\tfrac{1}{2}[(\sigma_m/\sigma)^2+(\sigma_0/\sigma_m)^2]/[1+(\sigma_0/\sigma)^2]\}\leqslant K(\sigma_0/\sigma).$$

The last inequality follows from the fact that $(\sigma_m/\sigma)^2+(\sigma_0/\sigma_m)^2$ has its maximum value for σ_m equal to σ_0 or σ, this maximum value being just $1+(\sigma_0/\sigma)^2$.

The Intermediate Spin-Orbit Coupling for Large Rotational Quantum Number

W. A. NIERENBERG
Department of Physics, University of California, Berkeley, California
(Received January 19, 1951)

If a nucleus of spin one-half is cosine-coupled to the molecular rotation, its molecular beam spectrum can be predicted for all values of the magnetic field from the Zeeman to the Paschen-Back region with one, closed expression. This expression is valid for large values of rotational quantum number and small rotational g-factor and is averaged over a Boltzmann distribution of rotational states. The special case of spin one-half is simple because the symmetry permits cosine coupling only, and the energy levels are well known for this hamiltonian. A kind of correspondence principle can be developed for this example which does two things. It shows that the other nucleus in a diatomic molecule has little effect on the spectrum of the first because the coupling of the second nucleus due to the rotation. Second, it permits the extension of the calculation to nuclei of spins greater than one-half when the coupling is predominantly cosinelike.

I. INTRODUCTION

THE radiofrequency spectra of diatomic molecules in molecular beams have been very useful in analyzing very fine molecular effects. The classical example is the experiment of Ramsey[1] on the magnetic field and the magnetic moment of the molecule H_2 due to its rotation. This field manifests itself in a term $c\mathbf{I}\cdot\mathbf{J}$ in the hamiltonian, where $\mathbf{I}$ is the nuclear spin and $\mathbf{J}$ is the angular momentum of the molecule. All angular momenta will be expressed in units of h. The use of this term can been extended to other diatomic molecules.[2] In the special example of fluorine in LiF, the large width of the observed nuclear resonance is explained completely on the basis of the cosine coupling, since the quadripole broadening is not allowed. The observations were performed at very large values of the magnetic field and good agreement with theory was found. At zero field, the experiments were inconclusive because of the large "nonadiabatic" transitions that masked the effect. The magnitude of c for fluorine in LiF was found to be 8.9×10^{-23} erg and this was considered to be too large by an order of magnitude at the time on the basis of the rather naive picture of a diatomic molecule as a revolving rigid dumbbell.

A theory for the magnitude of c in H_2 had been worked out by Wick[3] in an early paper; and the discussions were carried forward in later papers by Wick[4] and Foley[5] with the conclusion that, while the observed interaction was large, it was not incompatible with the calculations. This interaction has since been observed by other investigators in other molecules.[6-8]

The expected line shape for a nucleus of spin one-half, cosine coupled to $\mathbf{J}$, in a magnetic field strong enough to Paschen-Back the coupling was calculated in reference 2 and compared with experiment. However, neither the experiments nor the line shape were done for intermediate and weak values of the field. The purpose of this paper is to obtain a closed expression for the line shape for spin one-half for all values of the magnetic field. As a corollary, a useful kind of correspondence method is justified which extends the result to any value of nuclear spin and gives a good physical picture of the motion of the spin vectors.

II. QUANTUM-MECHANICAL TREATMENT OF SPIN ONE-HALF

The starting point of the calculation is the hamiltonian. If only terms involving the nucleus of spin one-half are included (the justification for ignoring the other nucleus is based on the large value of J and will be discussed in a later paragraph), then the hamiltonian is

$$\mathcal{H}=-\mu_N g_I \mathbf{I}\cdot\mathbf{H}-\mu_N g_J \mathbf{J}\cdot\mathbf{H}-c\mathbf{I}\cdot\mathbf{J}, \tag{1}$$

μ_N is the nuclear magneton, and g_I and g_J are the g-factors corresponding to $\mathbf{I}$ and $\mathbf{J}$, respectively. The energy levels when $I=\frac{1}{2}$ are well known and are given by the Breit-Rabi formula:[9]

$$\begin{aligned} W_{J+\frac{1}{2},m} &= -(\Delta W/2I+1)-g_J\mu_N Hm \\ &\quad -\tfrac{1}{2}\Delta W[1+(4mx/2J+1)+x^2]^{\frac{1}{2}}, \\ W_{J-\frac{1}{2},m} &= -(\Delta W/2I+1)-g_J\mu_N Hm \\ &\quad +\tfrac{1}{2}\Delta W[1+(4mx/2J+1)+x^2]^{\frac{1}{2}}. \end{aligned} \tag{2}$$

$\Delta W=c(J+\frac{1}{2})$, $x=(g_I-g_J)\mu_N H/\Delta W$, m is the total magnetic quantum number and $J+\frac{1}{2}$, $J-\frac{1}{2}$ are the values of the total angular momentum for very weak fields. The selection rules are $\Delta F=\pm1$, 0 and $\Delta m=\pm1$, 0 in weak fields and $\Delta m_I=\pm1$, 0, $\Delta m_J=\pm1$, 0, $\Delta m=\pm1$, 0 in strong fields. Not all these transitions are observable, however. Transitions which result in changes of m_J only in the strong deflecting fields are not observable in present apparatus. (H_2 is an exceptional case because of its large g_J.) The only important transitions are those for which $\Delta m_I=\pm1$. Therefore, we need consider only transitions where the total angular momentum goes from $J+\frac{1}{2}$ to $J-\frac{1}{2}$. There is

[1] N. F. Ramsey, Jr., Phys. Rev. **58**, 226 (1940).
[2] W. A. Nierenberg and N. F. Ramsey, Phys. Rev. **72**, 1075 (1947).
[3] G. C. Wick, Z. Physik **85**, 25 (1933).
[4] G. C. Wick, Phys. Rev. **73**, 51 (1948).
[5] H. M. Foley, Phys. Rev. **72**, 504 (1947).
[6] J. W. Trischka, Phys. Rev. **74**, 718 (1948).
[7] A. Roberts, Phys. Rev. **76**, 1723 (1949).
[8] L. Grabner and V. Hughes, Phys. Rev. **79**, 819 (1950).
[9] G. Breit and I. I. Rabi, Phys. Rev. **38**, 2082 (1931).

one exception. In the transitions

$$(J+\tfrac{1}{2}, J-\tfrac{1}{2}) \leftrightarrows (J+\tfrac{1}{2}, J+\tfrac{1}{2})$$

or

$$(J+\tfrac{1}{2}, -J+\tfrac{1}{2}) \leftrightarrows (J+\tfrac{1}{2}, -J-\tfrac{1}{2})$$

there is a difference in that a large change in magnetic moment occurs. In the present analysis $J \sim 50$. Therefore, this exceptional transition is statistically negligible. It follows that the observable frequencies are

$$\nu = (\Delta W/h)(1+2zx+x^2)^{\frac{1}{2}}. \quad (3)$$

The approximations $|g_J| \ll |g_I|$ and $J \gg 1$ are used, and $z = m/J$. Thus, for each value of z, $-1 \leqslant z \leqslant 1$, there is a corresponding resonance; and, therefore, a spectrum is observed for a range of frequencies corresponding to $-1 \leqslant z \leqslant 1$. If the method of Feld and Lamb[10] is followed, the density of states is calculated from $dz/d\nu$, since it is assumed that all values of m are equally probable in the beam. The number of states per unit frequency interval is

$$dN/d\nu = |dz/d\nu| = \tfrac{1}{2}(\nu/\nu_I)(h/cJ), \quad -1 \leqslant z \leqslant 1, \quad (4)$$

where $\nu_I = cJx/h = g_I \mu_N H/h$, the Larmor frequency for the uncoupled nucleus. The factor $\frac{1}{2}$ is to normalize the range of z. Therefore, for a given (large) value of J, the spectrum is a trapezoid centering about ν_I if $x>1$ and centering about cJ/h if $x<1$. (See Fig. 1.) This is the line shape for a given value of J. In the molecular beam apparatus there is no separation of different J states; and, therefore, the contributions from all states J to a given frequency are summed with a weight $2a^2J \exp(-a^2J^2)dJ$ for each interval dJ, $a^2 = h^2/8\pi^2KT$, where K is the moment of inertia of the molecule. There are two regions of ν for which the summation is different. First, consider $\nu \leqslant \nu_I$:

$$\frac{dN}{d\nu} = \int_{h(\nu_I-\nu)/c}^{h(\nu+\nu_I)/c} \frac{1}{2}\frac{\nu}{\nu_I}\frac{1}{(cJ/h)} 2a^2J \exp(-a^2J^2)dJ. \quad (5)$$

Second, consider $\nu \geqslant \nu_I$:

$$\frac{dN}{d\nu} = \int_{h(\nu-\nu_I)/c}^{h(\nu+\nu_I)/c} \frac{1}{2}\frac{\nu}{\nu_I}\frac{1}{(cJ/h)} 2a^2J \exp(-a^2J^2)dJ. \quad (6)$$

By an appropriate change of variables and the use of an absolute value bracket, the two cases can be combined into a single expression for the spectrum:

$$dN/dy = \tfrac{1}{2}\pi^{\frac{1}{2}}(y/y_I)[\mathrm{erf}(y+y_I) - \mathrm{erf}|y-y_I|], \quad (7)$$

where

$$y = (ha/c)\nu, \quad y_I = (ha/c)\nu_I$$

and

$$\mathrm{erf}\, y = (2/\pi^{\frac{1}{2}}) \int_0^y \exp(-\xi^2)d\xi.$$

[10] B. T. Feld and W. E. Lamb, Jr., Phys. Rev. 67, 15 (1945).

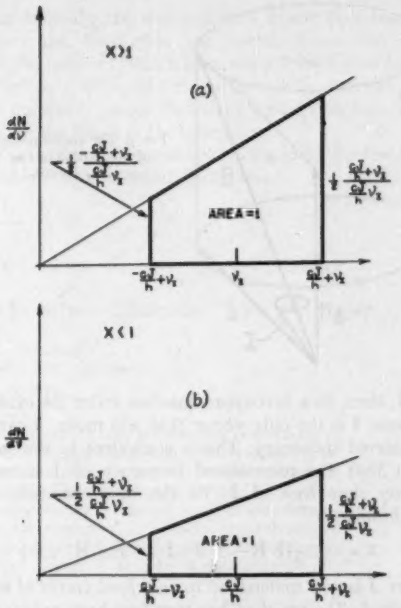

FIG. 1(a and b). The density of states for a fixed value of J *versus* the reduced frequency.

In the limits of large field ($\nu_I \to \infty$) and zero field ($\nu_I \to 0$) the expression (7) reduces to those previously found.[2] Figure 2 displays the calculated spectral curves for different values of the parameter y_I which may be used as a measure of the cosine coupling. The largest value of y_I used, $y_I = 5$, is equivalent to ∞, in so far as the term $\mathrm{erf}(y+y_I) = 1.00$ over the range where the spectrum is appreciably different from zero but an appreciable asymmetry still exists because of the factor y/y_I. The transition of the spectrum between the two limits is clearly exhibited.

III. SEMICLASSICAL APPROXIMATION AND EXTENSION TO HIGHER SPIN

Within the range of validity of the result, $|g_J| \ll |g_I|$ and $J \gg 1$, the same result can be obtained from a more classical picture which gives some insight to the motion of the angular momentum vectors. If $|g_J| \ll |g_I|$ and

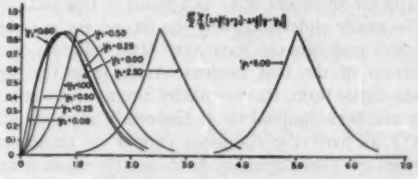

FIG. 2. The complete spectrum for different values of magnetic field. The parameter y_I is proportional to the magnetic field.

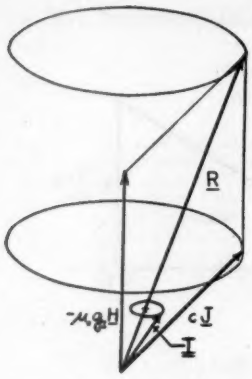

FIG. 3. The vector model of the motion of the angular vectors.

$J \gg 1$, then, to a first approximation under the existing torques, **I** is the only vector that will move, **J** can be considered stationary. This is equivalent to the statement that the precessional frequency of **I** is much greater than that of **J**. To this approximation, the hamiltonian is

$$\mathcal{H} = -\mu_N g_I \mathbf{I}\cdot\mathbf{H} - c\mathbf{I}\cdot\mathbf{J} = \mathbf{I}\cdot(-\mu_N g_I \mathbf{H} - c\mathbf{J}), \quad (8)$$

where **J** is now understood to be a *fixed* vector of magnitude J. The problem has therefore been reduced to the space quantization of the spin vector **I** with respect to the vector resultant **R**:

$$\mathbf{R} = -\mu_N g_I \mathbf{H} - c\mathbf{J}, \quad (9)$$

whose magnitude is

$$R = [(\mu_N g_I H)^2 + (cJ)^2 + 2\mu_N g_I H c J \cos\vartheta]^{\frac{1}{2}} \quad (10)$$

and θ is the angle between **J** and **H**. The energy levels are

$$W_{m_I} = -m_I R, \quad m_I = -I, -I+1, \cdots, I, \quad (11)$$

and the Larmor frequency of precession of I about **R** is

$$\nu = R/h; \quad (12)$$

and this agrees with Eq. (3) if $z = \cos\theta$, an obvious correspondence. A good physical picture can be obtained (Fig. 3), by picturing **I** processing rapidly about **R** with frequency R/h and **R** itself precessing slowly about **H**. Therefore, the motion of **I** can be approximately described as conical with the axis of the cone itself moving in a cone. This answer, to this approximation, is valid for all values of I. As a result of this picture, it can be easily understood why the second nucleus of the diatomic molecule can have very little influence on the spectrum of the first nucleus. Aside from the small dipole-dipole term, the two nuclei interact only because they are both coupled to J. Since this approximation sees J as fixed the couplings cannot be transmitted through J. This argument holds for the most general form of the coupling function as well as for cosine coupling, and for all values of the magnetic field.

IV. APPARATUS RESOLVING POWER AND TRANSITION PROBABILITIES

The spectrum, to this point, has only included the density of states factor. A complete calculation should include the transition probability as a factor in Eq. (4) before summing contributions from all J. In addition, the natural line width of the apparatus has to be "folded in" to get the true spectrum.

In any practical application, the line width is $\sim$5000–25,000 sec^{-1} and is much smaller than the width of the spectrum. Therefore, the shape will not be appreciably changed but an estimate can be made of the expected intensity. The resolution function can be chosen rectangular,[2]

$$F(\nu', \nu) = K_1 K_2, \quad \nu - \Delta\nu \leqslant \nu' \leqslant \nu + \Delta\nu; \quad (13)$$

K_1 and K_2 are constant apparatus factors less than unity and $\Delta\nu$ is the effective half-width of the natural line. For all other ν', $F(\nu', \nu) = 0$. Then the true spectrum is given by the total number of transitions per resolution interval of frequency:

$$N(\nu) = \int_0^\infty F(\nu', \nu)(dN/d\nu')d\nu'; \quad (14)$$

$dN/d\nu$ is considered a function of ν' in the integrand. Since $F(\nu', \nu)$ is a narrow function, $dN/d\nu'$ may be taken from the integrand as a constant factor with $\nu = \nu'$. The integration is performed with the result that

$$N(\nu) = \Delta\nu K_1 K_2 (ha/c)\pi^{\frac{1}{2}}(y/y_I) \times [\mathrm{erf}(y+y_I) - \mathrm{erf}|y-y_I|]. \quad (15)$$

Referring to Fig. 2, it is clear that the greatest fractional reduction of the beam is approximately equal to $2\Delta\nu K_1 K_2 (ha/c)$ and is roughly constant for all fields.

The transition probability factor is more complicated, and no calculation will be made chiefly because the oscillating magnetic field is always set at a high value when observing broad spectra. By a high value is meant a value such that the average molecule undergoes several transitions while in the field. This would, at first sight, seem to make matters worse; but then the temperature distribution of velocities of the beam molecules prevents complete transition for the average molecule, and the reduction in beam intensity can be taken as a constant factor K_2. It can be argued that this factor, despite the large perturbing field can still depend slightly on frequency and therefore should be included before summing over J. That this is not so can be understood by considering the first-order transition probabilities which will give a maximum estimate of the effect. On one hand, the transition probability is independent of z for strong fields; and for weak fields where the transition probability varies rapidly with z the trapezoid of Fig. 1 is very narrow, and the line shape is determined primarily by the variation in J and is again unaffected. Therefore, it is concluded the Eq. (13) should describe the observed line shape quite well.

IV. CONCLUSION

As a result of the calculation, a closed expression is given for the line shape for all values of the magnetic field. This suggests the experiment of following the fluorine resonance structure in LiF and CsF down in field to nearly zero field to corroborate the existence of the assumed cosine interaction. As for spins greater than one-half, the omission of a quadrupole coupling makes the calculation less useful. There still exist spectra, however, which have not yet been interpreted, particularly Cl^{35} and Cl^{37} in the alkali chlorides; and the possibility exists that large cosine coupling might explain the shape of the resonance.

The author expresses his gratitude to Professor R. Serber for several useful discussions.

PHYSICAL REVIEW VOLUME 82, NUMBER 6 JUNE 15, 1951

The Mobility of Electrons in Silver Chloride

J. R. Haynes and W. Shockley
Bell Telephone Laboratories, Murray Hill, New Jersey

(Received February 20, 1951)

Techniques are described which utilize the "print out effect" to obtain both the direction and velocity of photoelectrons in silver chloride crystals in an electric field. Hall mobility of the electrons is calculated from their change in direction produced by crossed electric and magnetic fields. Drift mobility of the electrons is obtained by measurement of their velocity in known electric fields. The value obtained for the Hall mobility ($R\sigma$) multiplied by $8/3\pi$ is 51 cm²/volt sec at 25°C. The values obtained for the drift mobility are shown to be a function of temperature. A value of 49.5 cm²/volt sec was obtained at 25°C, which is within experimental error of $(8/3\pi)R\sigma$, indicating that acoustical scattering is the principal mechanism and that temporary trapping is unimportant. A summary of the behavior of conduction electrons in silver chloride, calculated from the results of these experiments, is included.

I. INTRODUCTION

THE measurements of the mobility of electrons in silver chloride described in this paper are a continuation of earlier experiments which were originally undertaken to furnish definite evidence of the role of electrons in certain photographic processes in this material. Not only were these early experiments successful in their primary objective, but they have also led to the development of new techniques for the study of the motion and trapping of electrons in silver halides.

The results of the early experiments, dealing largely with the trapping of electrons in silver chloride, were published by the authors in the Report of a Conference on the Strength of Solids.[1] The present paper presents later studies of mobility.

II. THEORY OF THE "PRINT OUT EFFECT"[2]

The original object of this investigation was to establish the mechanism of the "print out effect," which is very closely related to latent image formation (see Mott and Gurney[3] for a general discussion on this topic). It is observed that if a photographic emulsion is exposed to strong light for a long time, it becomes dark. Microscopic examination of the small (10^{-4}–10^{-5} cm in diameter) single crystals of the salt in the emulsion shows that the darkening is localized in the form of a number of small specks within the grain. Further research has shown that these specks are colloidal metallic silver[4] and that the total amount of metallic silver produced in the grain is approximately that which would be expected if every photon absorbed added one atom of silver to the colloidal specks.[5] Since the photons are absorbed in all parts of the grain, there must, therefore, be a transport mechanism by which the absorbed energy is made effective at the silver speck.

The transport mechanism proposed by Mott and Gurney involves the fact that silver chloride is an ionic conductor at room temperature and that its conductivity is due to the motion of silver ions. An illustration of how this conductivity occurs is shown in Fig. 1. Thermal agitation causes some silver ions to move from normal sites to interstitial positions B, thus leaving a vacant lattice point C in the normal lattice. A series of exhaustive experiments by Koch and Wagner[6] and by Tubandt and Eggert[7] has shown that both the vacant lattice points and positive interstitial silver ions are mobile and both contribute significantly to the conductivity, the negative chlorine ions making a negligible contribution.[7a]

[1] Conference on Strength of Solids, University of Bristol, July, 1947 (The Physical Society, London, England, 1948), pp. 151, 157.

[2] The following description of the "print out effect" is largely reproduced from the original article.

[3] N. F. Mott and R. W. Gurney, *Electronic Processes in Ionic Crystals* (Oxford University Press, New York, 1940), p. 122. For a recent review article see J. H. Webb, Phys. Today **3**, No. 5, 8 (1950).

[4] R. Hilsch and R. W. Pohl, Z. Physik **77**, 421 (1932).

[5] J. Eggert and W. Noddack, Z. Physik **20**, 299 (1923); Handb. Wissenschaftlichen Angewandten Photographie **5**, 132 (1932).

[6] E. Koch and C. Wagner, Z. physik. Chem. **B38**, 295 (1937).

[7] C. Tubandt and S. Eggert, Z. anorg. Chem. **110**, 196 (1920).

[7a] It has been proposed by J. W. Mitchell that conduction by chlorine vacancies plays an important role in the photographic

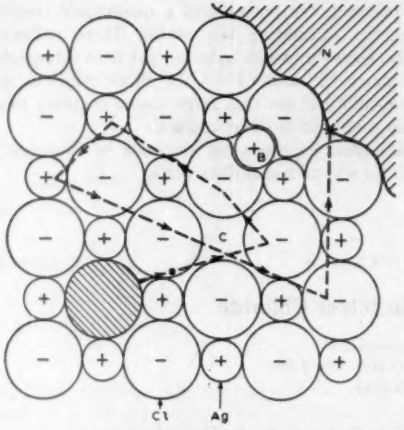

FIG. 1. Schematic representation of the Gurney and Mott theory of the print out effect.

The "print out effect" is supposed to occur as follows: A photon of light ejects an electron from a chlorine ion; this electron moves about in the crystal under the influence of thermal agitation, leaving the neutral chlorine behind. In the course of its wanderings it becomes trapped on a particle of metallic silver N. This produces a net negative charge on the metallic silver which is neutralized by silver ion conductivity. When the silver ion reaches the speck of silver, it can combine with it, neutralizing the negative charge and adding one atom of metal to the speck. Thus, the theory of Mott and Gurney supposes that thermally diffusing photoelectrons constitute the connecting link between the absorption of a photon at one point and the addition of a silver atom to a silver at another point.

A definite experimental prediction, which is a consequence of the above theory, is that it should be possible to displace the darkening in the "print out effect" by deflecting the photoelectrons with electric fields. The practical realization of this prediction, however, requires careful control of the experimental conditions.

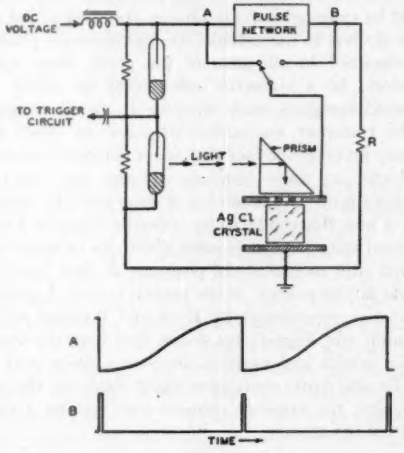

FIG. 2. Schematic diagram of equipment used to generate repetitive pulses of light and synchronized voltage waves.

III. EXPERIMENTAL CONDITIONS AND APPARATUS

It is impracticable to maintain a constant electric field of suitable magnitude in a silver halide crystal because the resulting steady ionic current would lead to decomposition. For this reason, the average current through the crystal must be zero, a result which can be ensured by applying all voltages through condensers which will not pass direct current.

The ionic conductivity imposes further conditions on the voltage wave form to be applied to the condenser plates. For the geometrical arrangement used it is found that the relaxation time for the field in silver chloride is 5×10^{-4} second. In other words, if a voltage were suddenly applied to the condenser, thus producing a field in the silver chloride, this field would drop to $1/e$ of its value in this time. Thus, it is necessary to set up conditions in which it suffices to have the field available for the order of only a few hundred microseconds.

Techniques suitable for operation in this time range have become generally available as a result of the development of radar. The apparatus used for these experiments was designed for testing fixed spark gap modulator tubes.[8] A schematic circuit diagram of this equipment is shown in Fig. 2. When the triggering voltage is applied, the pulse shaping network is discharged through the spark tubes and resistance load R. Networks designed to produce voltage pulses of 1 and 5 microseconds were used. The spark tubes consist simply of a mercury pool above which is suspended at a distance of 6 mm a perpendicular rod of molybdenum in an atmosphere of hydrogen at a pressure of 90 cm of mercury. During the time of discharge (network time) these tubes are an intense source of light ($>10^8$ candle power), which is largely that of excited mercury vapor.[9] This light is used to produce photoelectrons in a sample of silver chloride placed between condenser plates. The voltage wave forms at points A and B in the circuit are for convenience also shown below. Both of these waves have been applied to the condenser plates to create an electric field in the sample at the time of the light pulse and so move the photoelectrons.

process (Phil. Mag. **40**, 249 (1949)). Recent experiments by C. H. Berry (Phys. Rev. **82**, 422 (1951)) indicate that interstitial silver ions predominate over bromide vacancies in AgBr by a factor of at least 10.

[8] Goucher, Haynes, Depp, and Ryder, Bell System Tech. J. **25**, 563 (1946).

[9] J. R. Haynes, Phys. Rev. **73**, 891 (1948).

The experimental condenser arrangement used for simultaneously applying the light pulse and electric field to the silver chloride crystal is shown in Fig. 3. A large single crystal block[10] 5 mm×12 mm×15 mm was placed between the condenser plates with the field in the long direction. Between the condenser plates and the crystal were placed thin glass plates coated on the side in contact with the condenser electrodes with 25 percent transmission platinized film having a high conductance. The light entered through the upper film along an axis parallel to the field and illuminated three rectangles on the end of the crystal. In this way an equipotential surface was maintained across the crystal faces, and at the same time the relaxation time of the field was increased to several hundred microseconds through the introduction of the high capacitance produced across the glass plates.

When the voltage wave applied across the plates of the condenser arrangement was taken from the point *A* in the circuit, the electric field applied to the crystal was nearly constant during the time that the photoelectrons are free to move. When the voltage wave was taken from the point *B*, the field was on for a period less than this time.

Light pulses of one and five microseconds duration were used at repetition rates of 1000 and 500 per second. Under these conditions the charge of the trapped electron in a given pulse was neutralized by ionic conductivity before the next pulse of light was applied.[11] In order to avoid space charge effects in the individual pulse, the illumination intensity was reduced until 10^9 electrons/cm^2 per pulse were produced in the illuminated area of the crystal (as measured at liquid air temperature by the charge through a ballistic galvanometer). Under these conditions exposures of 16 hours or more were required to obtain satisfactory amounts of colloidal silver.

IV. SOME RESULTS OF EARLY EXPERIMENTS[12]

The early experiments showed at once that the darkening could be displaced from the illuminated region as if the connecting link were a negatively charged particle with a mobility of about 50 cm^2 per volt sec. This result may be regarded as an unambiguous confirmation of the basic assumption of the Gurney and Mott theory.

It was also found that the darkening could be reduced to negligible amounts by filtering the light through 10^{-3} cm of silver chloride, which shows that for practical purposes all of the photoelectrons in the experiments were produced within this distance of the surface.

[10] The block was cut on a circular milling saw from cylinders of silver chloride about 3 in. in diameter and 2 in. long obtained from the Harshaw Chemical Company of Cleveland, Ohio.

[11] The time of neutralization of the charge of a trapped electron is $K/4\pi\sigma$ (esu), where σ is the conductivity of silver chloride and K is its dielectric constant (see reference 3, page 232).

[12] For a more complete description see reference 1.

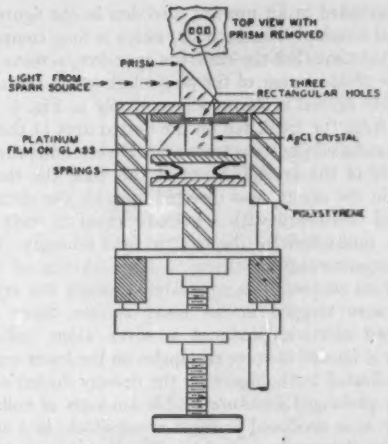

FIG. 3. Experimental condenser arrangement used for the simultaneous application of pulses of light and electric field to single crystals of silver chloride. [Pt. film on opposite side of glass from that in contact with AgCl.]

Since the colloidal silver is formed at points where electrons are trapped, a study of the distribution of darkening produced in an electric field reveals the location of these traps. This study shows that colloidal silver, crystal grain boundaries, and slip bands are all efficient electron traps. It was found, however, that the density of these traps could be greatly reduced by carefully annealing the crystals[13] so that the mean life of the photoelectrons could be increased in this way from 2 to 10 microseconds.

With this increased lifetime, the displacement of the electrons was sufficient to permit large numbers of them to pass completely through a crystal of silver chloride 15 mm long, using electric fields easily attained.

The experimental procedure was to connect the upper plate of the condenser arrangement, shown in Fig. 2, to the point *A* and to ground the lower plate. This resulted in the application of an electric field to the crystal which reversed at the time of the light pulse

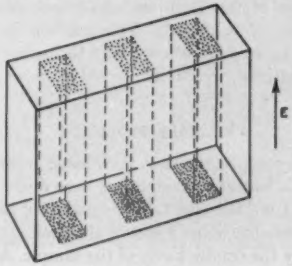

FIG. 4. Schematic diagram of displacement of photoelectrons by the electric field.

[13] J. R. Haynes, Rev. Sci. Instr. **19**, 51 (1948).

and persisted in an upward direction in the figure for several hundred microseconds, which is long compared with the time that the electrons were free to move.

The displacement of the photoelectrons in the silver chloride crystal is shown schematically in Fig. 4. The light from the spark fell on the dotted area at the top and produced photoelectrons at, and very near, the top surface of the crystal. Since at this time the electric field in the crystal was directed upward, the electrons moved downward with a velocity equal to their mobility multiplied by the electric field intensity. With our experimental conditions, a large fraction of these electrons succeeded in completely crossing the crystal and were trapped at the lower surface. Since each trapped electron produced a silver atom, colloidal silver is formed in three rectangles on the lower surface as indicated in the figure by the densely dotted areas. With prolonged exposure visible amounts of colloidal silver were produced in these areas which, in a sense, are the electron images of the illuminated areas at the top surface of the crystal.

We will show how these techniques and experimental results may be utilized to provide new ways of measuring the mobility of conduction electrons in silver chloride.

V. DEFINITIONS OF MOBILITY

It has been pointed out[14] that the values of mobility determined in various ways will not necessarily agree. For the purposes of this paper, therefore, we need to clearly distinguish between three kinds of mobility as follows:

Microscopic mobility, μ_m; this is the mobility of a charge carrier in the conduction band of energies and is the conventional concept.

Drift mobility, μ_D; this is the velocity of drift of a charge carrier in unit electric field. The value of drift mobility will not agree with that of microscopic mobility if the carriers spend appreciable time in temporary traps. Thus, if the carriers spend half their time in traps and half in the conduction band, the result is that $\mu_D=\frac{1}{2}\mu_m$.

Hall mobility, μ_H; this is the experimentally determined value of the Hall coefficient multiplied by the conductivity of a sample. The relation between μ_H and either μ_m or μ_D is known only for certain simplifying assumptions which are considered in the next section.

VI. HALL MOBILITY

Most of our present day knowledge concerning the mobility of electrons in solids has been derived through the use of the Hall effect. The usual way of obtaining the Hall mobility is to measure the Hall constant and multiply by the conductivity of the sample. Alternately, the Hall mobility may be calculated from the Hall angle (angle between current and electric field) of a sample in a known magnetic field. In order for the significance of our results to be appreciated, the philosophy of the derivation of the Hall angle should be clearly in mind.[15] To that end we indicate the reasoning, neglecting the random motion of the electrons and considering that each electron after a collision starts its new path in the opposite direction to that of the applied electric field and suffers a collision after moving on the average for the relaxation time t'.

According to statistical theory, an electron has on the average been subject to the field for a time t' since its last collision and has therefore acquired a drift velocity equal to its acceleration Ee/m times t', or

$$\bar{v}=Eet'/m=\mu_m E.$$

Owing to the drift motion in the magnetic field, the electron has been subjected to a side thrust and has acquired a transverse velocity:

$$\theta\bar{v}=\omega t'\bar{v}=(eHt'/mc)\bar{v}=\mu_m H\bar{v}/c.$$

In this formula θ is the Hall angle and is equal to the circular frequency ω of an electron in a magnetic field times the mean free time t'. The Hall mobility $R\sigma$ defined above can also be expressed in terms of the Hall angle and reduces to

$$R\sigma\equiv\mu_H=\theta c/H=\mu_m.$$

For the idealized assumptions represented by the above equations, the relationship $\mu_H=\mu_m$ results.

It will be observed that the value assigned to the Hall mobility depends on the effects produced by crossed electric and magnetic fields on a *moving* charge carrier and will therefore be entirely unaffected by the time which the carrier may spend in shallow traps. In this sense, the Hall mobility should give a value in accord with the microscopic mobility μ_m but not necessarily with that of the drift mobility μ_D.

A rigorous derivation shows that for spherical energy surfaces in the Brillouin zone and for degenerate statistics as in a metal, $\mu_m=\mu_H$. For the nondegenerate case, such as conduction electrons in silver chloride, it seems fair to assume a maxwellian distribution of velocities and a mean free path which is independent of direction and energy.[15a] The value of the constant relating the Hall mobility to the microscopic mobility then depends only on the shape assumed for the energy surfaces. If the customary assumption of spherical energy surfaces[16] is made, the velocities average to obtain the result,

$$\mu_m=(8/3\pi)\mu_H=(8/3\pi)(\theta c/H)\ \text{cm}^2/\text{esu volt sec},$$

[14] Pearson, Haynes, and Shockley, Phys. Rev. 78, 295 (1950).

[15] A rigorous derivation along the lines discussed below is given in W. Shockley, *Electrons and Holes in Semiconductors* (D. Van Nostrand Company, Inc., New York, 1950).

[15a] If the mean free path is proportional to velocity, as indicated in reference 22 the factor $8/3\pi\doteq 0.85$ becomes unity. We shall return to this point in Sec. VIII, retaining the factor $8/3\pi$ in the meantime in order to stress the distinction between μ_m and μ_H.

[16] For a case where the energy surfaces are apparently not spherical, see reference 14.

or

$$\mu_m = (10^8)(8/3\pi)(\theta/H) \text{ cm}^2/\text{volt sec.}$$

for H measured in oersteds.

Since silver chloride is an ionic conductor, it would certainly be very difficult to measure the Hall mobility of electrons in this material using the usual procedure. However, by employment of new techniques a direct measure of the Hall angle of these carriers was obtained as follows:

A single crystal of silver chloride was inserted in the condenser arrangement which was then connected to apply an electric field of long duration, thereby moving a large fraction of the photoelectrons generated at the top surface all the way through the crystal as described in Sec. IV. In this experiment, however, two changes were made. The top surface was masked so that light was allowed to fall on only half of each of the rectangles at the top surface, and a magnetic field was applied in a direction perpendicular to the large surfaces of the crystal, as shown in Fig. 5a. The crystal was then exposed to one-microsecond light pulses and synchronized electric fields for 24 hours. During this time a large fraction of the photoelectrons produced by each light pulse in the illuminated areas at the top (dotted in the figure) was drawn through the crystal by the electric field before being trapped. In the absence of the magnetic field these electrons would have produced colloidal silver in the dotted areas at the lower surface. In the presence of the magnetic field, however, the paths of the electrons were turned through the Hall angle; and, in consequence of this, the rectangles of colloidal silver produced at the bottom surface were displaced to the left as indicated in Fig. 5a. The mask at the top was then moved so that the opposite half of the top of the crystal was illuminated, and the direction of the magnetic field was also reversed as shown in Fig. 5b. The crystal was then exposed for an additional 24 hours. During this second exposure the photoelectrons produced at the top surface were again deflected through the Hall angle but in the opposite direction. As a result the rectangles of colloidal silver formed at the lower surface were displaced toward the right and offset from the rectangles produced in the first exposure as indicated.

A photograph of a crystal exposed in this way is shown in Fig. 6. The offset in the rectangles of colloidal silver produced at the bottom surface is clearly visible. The distance of this offset divided by the length of the crystal gives a number which is very close to twice the Hall angle in radians.[17]

Six measurements of the distance of the offset were obtained with this single sample, the average value

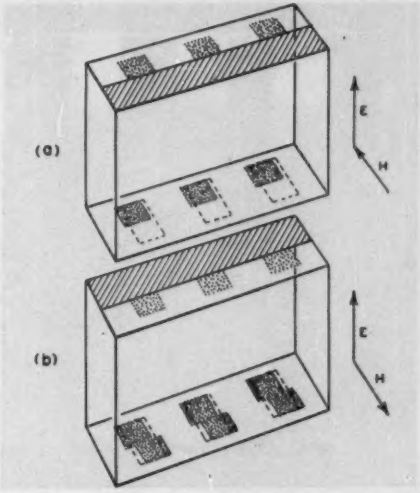

FIG. 5. Schematic diagram of procedure used for measuring the Hall angle of photoelectrons in silver chloride. (a) First exposure. (b) Second exposure.

obtained being $(22\pm1)\times10^{-3}$ cm. Since the crystal was 1.48 cm long, the measured Hall angle $\theta=7.5\times10^{-3}$ radian. The magnetic field used during the exposure had an intensity of 12.5×10^3 oersteds, so that the microscopic mobility of the photoelectrons as measured by the Hall angle on the above assumptions of spherical

FIG. 6. Photograph of silver chloride crystal used to measure the Hall angle, showing displacement of colloidal silver (dark areas) by magnetic field. Bottom surface of crystal appears greatly compressed due to high index of refraction of crystal.

[17] It is worthwhile pointing out that in previous Hall angle determinations the change in direction of the electric field is measured, while the direction of the current remains fixed. Here the reverse is true because of the absence of space charge effects.

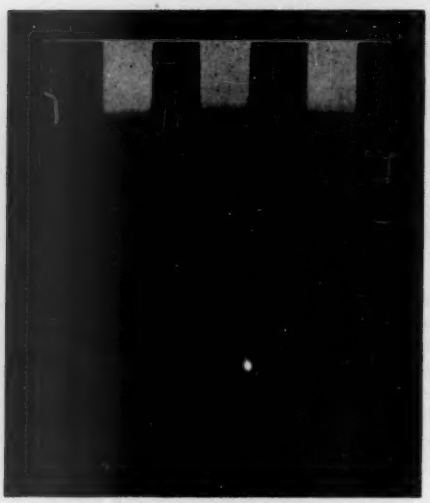

FIG. 7. Photograph of a crystal of silver chloride used to measure drift mobility of photoelectrons, showing columns of colloidal silver (light areas) produced by the electric field.

energy surfaces is

$$\mu_m = (8/3\pi)(7.5\times10^{-3}/12.5\times10^{3})(10^{8})$$
$$= 51 \text{ cm}^2/\text{volt sec.}$$

It will be shown that the electron mobility in silver chloride is a function of temperature. The temperature of the sample during this experiment was 25±3°C. Taking this uncertainty in sample temperature into account, as well as the uncertainty in the distance of offset, we have, finally, that the microscopic mobility of electrons in silver chloride at 25°C as determined by direct measurement of the Hall angle, is

$$\mu_m = (8/3\pi)\mu_H = 51\pm3 \text{ cm}^2/\text{volt second.}$$

VII. DRIFT MOBILITY

The drift mobility of electrons in silver chloride has also been determined by means of the new techniques and the following experimental procedure: A well-annealed single crystal of silver chloride was placed in the condenser arrangement (Fig. 3) and the bottom plate was connected to ground as before. The top plate of the condenser was now connected to the point B in the circuit shown in Fig. 2. Under these conditions simultaneous pulses of light and an electric field were applied to the crystal. At the start of each light pulse an electric field was suddenly applied to the crystal and maintained nearly constant for a time approximately equal to the nominal pulse network time. The photoelectrons produced by the light at the top surface of the crystal in the three rectangles drift downward in the crystal with a velocity $\mu_D E$, where E is the electric field intensity in the crystal. At the end of the light and electric field pulse the electrons stop their systematic drift and are trapped locally, producing colloidal silver. Repeated pulses of light electric field results in the production of visible amounts of colloidal silver.

A photograph of a crystal exposed in this way for 16 hours is shown in Fig. 7. This photograph was taken in a direction perpendicular to the large surface of the crystal, with the illuminated areas in which the photoelectrons originated at the top of the photograph. In order to increase the contrast, the crystal was photographed against a dark background with a transverse beam of light so that regions containing colloidal silver are made visible by scattered light. In the photograph, therefore, the light regions are those containing colloidal silver. The colloidal silver is seen to extend in three columns from the top surface, corresponding to the illuminated areas, to a depth which is an appreciable fraction of the length of the crystal (1.4 mm). The colloidal silver produced at the maximum depth below the illuminated surface is due to electrons produced at the start of the light pulse, and therefore those that were able to move for the entire time that the electric field was applied. The colloidal silver lying nearer the surface is due in part to photoelectrons which had a range much less than the average, but it is chiefly due to photoelectrons produced at later times.

It will be observed that the density of the colloidal silver in each column decreases sharply at its lower boundary,[18] permitting the maximum displacement of the electrons from the surface to be measured with considerable accuracy. This is the expected result, since the diffusion distance of electrons is small compared with the distance which they are moved by the electric field.[19]

The distance of electron displacement is given by $l=\mu_D E t$, or $\mu_D = l/Et$. One can, therefore, make a good estimate of the drift mobility of the electrons by simply measuring the electric field and substituting for t the nominal pulse network time. Since, however, the voltage pulse applied to the crystal is a square wave pulse only

[18] When viewed with a microscope from a direction exactly perpendicular to the crystal surface, these boundaries appear even sharper.

[19] The relative effects of diffusion and electric field displacement may be deduced from the following considerations: The distance which an electron diffuses in the time which it is free to move, τ, is given by the usual diffusion formula,

$$d^2 = D\tau = kT\mu_D\tau/e,$$

where D is the diffusion constant of conduction electrons, k is Boltzmann's constant, T is the absolute temperature, and e is the electron charge. On the other hand, the electric field acting for a time t displaces the electron a distance $l=\mu_D Et$, so that $l^2=\mu Elt$. Therefore, the ratio of the distance which the electron diffuses to the distace which is translated to the electric field is $d/l=(kT\tau/eElt)^{\frac{1}{2}}$. At room temperature $kT/e=1/40$ ev. The mean life, τ, of a conduction electron in these crystals has been shown to be ~10 microseconds (see reference 1). The electric field intensity used was ≐8 kv/cm. Thus, for an electric field applied for 1 microsecond ≐ network time ≐ t, l ≐ 0.2 cm and the ratio of the diffusion distance to the electric field displacement is given by

$$d/l = 1\times10^{-2}.$$

to a first approximation, appreciable errors are introduced. While these errors can be reduced by analysis of oscillograms of the voltage pulse as a function of time, a more accurate calculation of drift mobility can be made from other considerations in which this function enters only as a small correction factor.

The considerations which make it possible to neglect the voltage pulse time are easily understood with the aid of the equivalent circuit shown in Fig. 8. In this circuit the spark tubes are represented by a switch, the pulse network by its capacitance C, and the silver chloride crystal, mounted in the condenser arrangement, by three condensers and a resistance. The condensers C_1 have a value equal to the capacitance formed across the evaporated platinum films on the thin glass plates at either end of the crystal. The condenser C_2 has a value equal to that of a parallel plate condenser having an area equal to a cross section of the silver chloride crystal, a separation equal to its length, and a dielectric constant equal to the dielectric constant of silver chloride. The resistance R_1 is included to take account of the ionic conductivity of the silver chloride crystal.[20] The action of the spark tubes may be likened to the closing of the switch for a short period of time, long enough to permit discharge of the network capacitance C but not long enough to permit appreciable current to flow through the choke coil.

With these considerations we now proceed to derive the required equation for μ_D using the notation:

Q = quantity of electricity (coulombs) stored in the pulse network,
V = voltage to which the network is charged at the time of closing the switch,
C = capacitance of the network,
R = load resistance in ohms,
i = current flowing through R when switch is closed,
V_1 = voltage across R,
t_1 = time of current flow (of the order of the network time),
E = electric field intensity in the AgCl crystal,
V_2 = voltage across the crystal,
L = length of the crystal,
l = distance that the photoelectrons are displaced by the electric field,
G = thickness of glass plates at either end of the crystal,
K_G = dielectric constant of glass plates,
K_C = dielectric constant of AgCl,
σ = conductivity of AgCl.

When the switch is closed, the electricity stored in the condenser flows around the circuit and through the load resistance, a negligible fraction flowing through the equivalent crystal network. Under these conditions,

$$Q=CV=\int_0^{t_1} i dt.$$

Multiplying by R gives

$$RCV=\int_0^{t_1} Ri dt=\int_0^{t_1} V_1 dt.$$

[20] The conductivity produced by the photoelectrons is negligible compared with the ionic conductivity over the temperature range and light intensity used.

During time T_1 the photoelectrons travel a distance l with a velocity $E=f(l)$, or

$$l=\mu_D \int_0^{t_1} E dt.$$

The electric field E is V_2/L; however, the voltage V_2 across the crystal will be less than V_1 because then condensers $C_1C_2C_1$ form a voltage divider of ratio

$$\alpha=C_1/(2C_2+C_1)=1/[1+(2GK_C/LK_G)]$$

and because of decay of the voltage across C_2 due to R_2; the reduction due to this factor, called β, is evaluated below. In terms of these correction factors we may write $E=\alpha\beta V_1/L$, so that,

$$l=(\alpha\beta\mu_D/L)\int_0^{t_1} V_1 dt=\alpha\beta\mu_D RCV/L,$$

and

$$\mu_D=Ll/\alpha\beta RCV,$$

which is the required equation for drift mobility in which the pulse time does not appear. In order to use this equation, however, the small correction factors α and β must be evaluated.

The corection factor β is a constant only for a particular voltage pulse shape and time. Since, however, β introduces only a small correction to μ_D ($\sim$1 percent), very little error is introduced if the voltage pulses used of 1 and 5 microseconds are considered to be ideal square top voltage pulses persisting for exactly the nominal network time. With this assumption, $\beta=\bar{V}_2/\alpha V_1$, where $\bar{V}_2$ is the average value of V_2 over time t_1 and we can proceed to calculate β as follows:

Owing to the ionic conduction in the crystal the voltage V_2 decays exponentially with a time constant λ, so that

$$V_2=\alpha V_1 \epsilon^{-t/\lambda}.$$

The average value of V_2 during pulse time t_1 is,

$$\bar{V}_2=(\alpha/t_1)\int_0^{t_1} V_1 \epsilon^{-t/\lambda} dt,$$

or

$$\bar{V}_2=(\alpha V_1\lambda/t_1)(1-\epsilon^{-t_1/\lambda})=\alpha V_1\beta.$$

Therefore, we have

$$\beta=(\lambda/t_1)[1-\exp(-t_1/\lambda)],$$

or, since β is very close to unity, $\beta=1-(t_1/2\lambda)$.

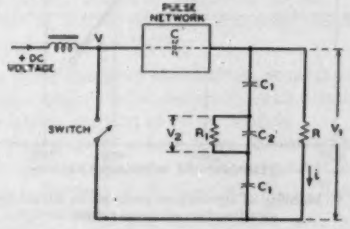

FIG. 8. Equivalent circuit used to derive equation for drift mobility.

TABLE I. Drift mobility of electrons in silver chloride.[a]

Crystal length L (cm)	Electron displacement l (cm)	Pulse time t_1 (μs)	Network capacitance C (μf)	Correction factor $\alpha\beta$	Temperature in degrees centigrade	Drift mobility (cm²/volt sec)
1.45	0.874	5	0.0508	0.962	40	45.5
1.45	0.172	1	0.00980	0.971	38	45.6
1.42	0.195	1	0.00980	0.972	20	50.6
1.45	0.131	1	0.00980	0.960	100	35.1
1.45	0.128	1	0.00980	0.960	100	34.3
1.48	0.121	1	0.00980	0.960	113	33.1
1.44	0.252	1	0.00980	0.972	−25.5	66.4
1.45	0.253	1	0.00980	0.972	−26.5	66.9

[a] For all data: the network voltage $V=11.1$ kv, the load resistance $R=51.5$ ohms, the thickness of the glass plates $G=0.012$ cm, the dielectric constant of the glass plates $K_G=7.0$, and the dielectric constant of silver chloride $=12$.

The decay constant λ is equal to[21]

$$R_1(\tfrac{1}{2}C_1+C_2) = [1/4\pi(9)(10^{11})](K_G/\sigma)[(K_C/K_G)+L/2G],$$

where σ is the conductivity of silver chloride in ohm^{-1} cm^{-1}.

The conductivity of these silver chloride crystals has been measured as a function of temperature. The results can be expressed to a high order of accuracy as

$$\sigma=0.038e^{-3960/T} \text{ ohm}^{-1} \text{ cm}^{-1}.$$

By means of this analysis the electron drift mobility can be accurately determined, since its value depends to a first order only on quantities which can easily be measured (l, L, R, C, and V), while G, K_C, K_G, σ, and t_1 enter only to provide a small correction term.

The drift mobility of electrons in silver chloride has been measured in this way over a temperature range of from −26 to 113°C. Temperatures above room temperature were achieved by placing the sample in a thermostatically controlled electric oven provided with a glass window. Temperatures below room temperature were obtained by placing the sample in a transparent Dewar flask cooled by thermostatically controlled air flow through a copper coil immersed in a toluene and dry ice mixture.

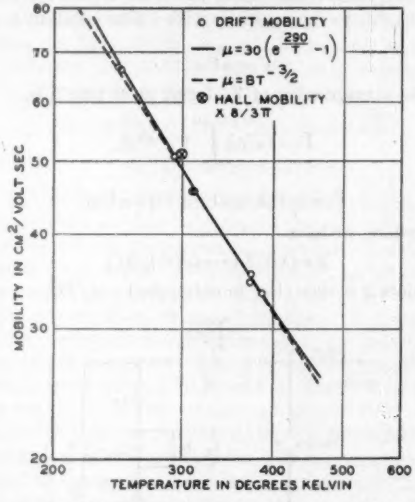

FIG. 9. Mobility of conduction electrons in silver chloride as a function of temperature.

The results are shown in Table I. It may be observed that the electron displacement due to the applied electric field, l, varies from a little over a millimeter (1 microsecond pulse network at 113°C) to nearly a centimeter (5 microsecond pulse network at 40°C) and that the correction factor $\alpha\beta$ is near unity in all cases.

The sample used to obtain the data tabulated in the last line of Table I was cut from an ingot of silver chloride produced by the Harshaw Chemical Company more than six months after the ingots from which the rest of the samples were produced, and it was visibly clearer. No significant difference, however, is observed in the measured mobility. This result is interpreted as evidence that impurity scattering and trapping play a negligible roll in these crystals at temperatures at least as low as −26°C.

The values of mobility of Table I plotted as a function of temperature are shown in Fig. 9. The data can be fitted within experimental error by the theory of Fröhlich and Mott[22] in which it is assumed that the conduction electrons are scattered by optical vibrations of the ions. The mobility expressed in practical units, based on the mean free time (Eq. (6.10) of the second paper) is[22]

$$\mu_m=(1/300)3(2k\theta m^*)^{-\frac{1}{2}}ea_0(e^{\theta/T}-1)KK_0/(K-K_0)$$

where $\theta=(hc/\lambda k)(K/K_0)^{\frac{1}{2}}=290$°K is the characteristic temperature for longitudinal polarization waves, λ being the wavelength for infrared absorption=87 microns for AgCl[24], c the speed of light, k Boltzmann's constant, $K=12.3$ and $K_0=4.01$ the low and high frequency dielectric constants,[25] m^* the effective mass, and $a_0=\hbar^2/m^*e^2$. Substituting these values and assuming $m^*=0.70$ m, where m is the mass of the free electrons, gives

$$\mu_m=30(e^{290/T}-1).$$

This function is plotted in Fig. 9 (solid line).

An equally good fit of the data, however, may be obtained using a theoretical equation first derived by

[21] See E. Frank, *Pulsed Linear Networks* (McGraw-Hill Book Company, Inc., New York, 1940), p. 141.

[22] H. Fröhlich and N. F. Mott, Proc. Roy. Soc. (London) **171A**, 496 (1939). Some corrections to the original theory have been presented by Fröhlich, Pelzer, and Zienau, Phil. Mag. **41**, 221 (1950).

[23] This formula may be too large by a factor of 2, see footnote at the end of the second paper of reference 22. According to C. Herring, on the other hand, this factor should be 3 but is partially counterbalanced by a factor of 2 in the other direction due to numerical error.

[24] H. Rubens, Preuss. Akad., Wiss. Physik. Math. Klass., p. 513 (1913), as quoted by R. Hofstadter, Nucleonics 4, No. 5, 29 (1949).

[25] The values of dielectric constant of silver chloride are taken from Mott and Gurney's book (see reference 3).

Wilson[26] on the assumption that the conduction electrons are scattered by acoustic vibrations,

$$\mu_m = BT^{-1}.$$

This equation, with $B=2.54\times10^5$, is also plotted in Fig. 9 (dotted line).

It is therefore impossible to determine from the data alone whether the scattering is due principally to the acoustic or to the optical vibration of the crystal. From theoretical considerations, however, it appears likely that the optical vibrations should be largely responsible for the electron scattering, and that the close fit of the data to T^{-1} is pure coincidence. It should be noted, however, that the mobility values obtained by Hofstadter[27] fit the acoustic scattering equation at low temperatures much better than the optical scattering equation. Hofstadter's values for the mobility of electrons in silver chloride at 77°K range from 114 to 400 cm²/volt second. The acoustic scattering equation gives a value of mobility of 376 cm²/volt second at this temperature, while the optical scattering equation yields a value of 1230 cm²/volt second.

VIII. COMPARISON OF HALL MOBILITY AND DRIFT MOBILITY

If we assume that the conduction electrons are scattered principally by acoustical modes, the mean free path is independent of velocity and $\mu_m=(8/3\pi)\mu_H$, as indicated in Sec. IV. The value of the microscopic mobility calculated on this assumption from the experimentally measured value of the Hall angle is plotted in Fig. 9. It is seen to lie within experimental error of the drift mobility values. This result may be interpreted in two ways:

(1) $\mu_D=(8/3\pi)\mu_H<\mu_m$. If the conduction electrons spend part of their time in temporary traps, $\mu_D<(8/3\pi)\mu_H$. On the other hand,[14] if the energy surfaces in the Brillouin zone are re-entrant, $\mu_m>\mu_H$. The possibility therefore exists that although the energy surfaces are re-entrant, the amount of temporary trapping was, in this case, just sufficient to compensate, so that although $\mu_D=(8/3\pi)\mu_H$, both are less than μ_m.

(2) $\mu_D=(8/3\pi)\mu_H=\mu_m$. This is the expected result if the energy surfaces are spherical and if the electrons spend a small fraction of their mean free time in temporary traps.

Temporary traps could be produced either by lattice imperfections or by impurities. In either case the density of these traps should have varied widely in the samples used in the drift mobility experiments.[28] It is observed, however, that all of the drift mobility values obtained fall on a smooth curve so that temperature appears to be the only variable. We therefore conclude that temporary trapping is an unimportant process and that $\mu_D=(8/3\pi)\mu_H=\mu_m$ if the electrons are scattered largely by acoustical vibrations of the ions.

If, on the other hand, we assume that the electrons are scattered principally by optical modes we are led to a mean free time independent of velocity resulting in $\mu_m/\mu_H=1$ instead of $8/3\pi$. The microscopic mobility calculated from our experimentally determined Hall angle would then have the value of 60 ± 3 cm²/volt second and consequently be definitely outside of the experimental error of the drift mobility.[29]

This discrepancy cannot easily be explained since we have shown experimentally that temporary trapping is unimportant. Complex energy bands can, of course, change the value of μ_m/μ_H; in general, however, deviations from a spherical form appear to produce ratios greater than unity and thus increase the disagreement. On the theoretical grounds also one would expect the conduction band to arise from $5s$ wave functions on silver and hence to be a simple nondegenerate band with a single effective mass.

It appears probable that, over the temperature range considered, both the acoustical and optical modes play some role in scattering the conduction electrons so that $1>\mu_m/\mu_H>8/3\pi$ and $m^*/m<0.7$. However, in order to make the drift mobility values agree with either the Hall mobility results or Hofstadter's low temperature mobility values it appears necessary to assume that acoustical scattering predominates.

IX. SUMMARY OF BEHAVIOR OF ELECTRONS IN SILVER CHLORIDE

In the early experiments reported at the Conference on Strength of Solids[1] the mean range ($\mu_D E\tau$) of photoelectrons in these annealed crystals was found to be approximately 1.5 cm with a field of 3.2×10^4 volts/cm at room temperature. Combining this information with the measured mobility values, one can calculate the following concerning the behavior of conduction electrons in silver chloride at room temperature (298°K):

drift mobility, $\mu_D=49.5$ cm²/volt sec,
mobility from Hall effect, $(8/3\pi)\mu_H=51\pm3$ cm²/volt sec,
relaxation time, $\mu_m m/e=2.8\times10^{-14}$ sec,
mean free path, $\mu_m mv/e=33$A,
mean free lifetime, $\tau=W/\mu_D E\approx10$ microseconds,
total uncoiled length of path $=v\tau=110$ cm,
number of lattice constants traversed before final trapping $=v\tau/a=2\times10^6$,

where e is the charge of the electron, m is its mass, W is its mean range, v is its average thermal velocity, and a is the lattice constant of silver chloride.

It is a pleasure to acknowledge the advice and assistance of many persons in this organization, particularly J. Bardeen, F. S. Goucher, W. L. Bond, and R. A. Chegwidden.

[26] A. H. Wilson, *Theory of Metals* (Cambridge University Press, Cambridge, 1934), p. 211.
[27] R. Hofstadter, Nucleonics 4, No. 5, 29 (1949).
[28] The samples used were cut from a variety of crystals obtained from two different melts. These melts certainly contained different amounts of impurities (see Sec. VII). Also, some of the samples used had acquired considerable strain subsequent to annealing, so that the permanent trap density was greatly increased locally as judged by the change in density of colloidal silver..
[29] It is very difficult to see how the drift mobility measurements can be in error by more than a few percent.

Radiochemical and Spectrometer Studies of Several Neutron-Deficient Zirconium Isotopes and Their Decay Products*

EARL K. HYDE AND GROVER D. O'KELLEY
Radiation Laboratory and Department of Chemistry, University of California, Berkeley, California

(Received February 7, 1951)

Radioactive zirconium isotopes of mass number <90 have been prepared by bombardment of niobium with 100-Mev protons. These isotopes and their decay products have been extensively studied in the beta-ray spectrometer and by radiochemical methods. Zr^{87} is shown to be a 94±6-minute activity, emitting positrons of 2.10±0.02-Mev energy and decaying into Y^{87m}. Accompanying its 14-hour decay into Y^{87}, Y^{87m} has a complex gamma-ray spectrum. The most prominent conversion electrons correspond to a 0.389±0.004-Mev gamma-ray. Y^{87} decays by orbital electron capture into Sr^{87m} which decays by emission of a 0.394±0.004-Mev gamma-ray with a 2.80±0.03 hour half-life into stable Sr^{87}. Zr^{86} is a 17±2-hour orbital electron capturing isotope decaying into Y^{86}, which in turn disintegrates into stable Sr^{86} with a half-life of 14.6±0.2 hours by the emission of positrons. This positron spectrum is complex, with two components of approximately equal intensity. The energies are 1.80 ±0.02 and 1.19±0.02 Mev. The latter appears to have a forbidden Fermi-Kurie plot corresponding to a first-forbidden transition with a spin change of two units and a change of parity.

The energy of the Zr^{89} positron is redetermined as 0.910±0.010 Mev. Conversion electrons corresponding to previously unreported gamma-rays of energy 0.027, 0.396, 0.917, and 1.27 Mev are observed. Preliminary evidence for Zr^{88} is presented which indicates that this isotope decays, by the capture of orbital electrons with a half-life of the order of 150 days, into 105-day Y^{88}. Conversion electrons of a 0.406-Mev gamma-ray are prominent in the decay of Zr^{88}.

I. INTRODUCTION

A NUMBER of the lighter neutron-deficient isotopes of zirconium have been prepared by bombarding high purity niobium metal with 100-Mev protons in the 184-inch synchrocyclotron. The lightest molybdenum and niobium isotopes produced by (p, xn) and (p, pxn) nuclear reactions decay quickly by orbital electron capture or positron emission to isotopes of zirconium. In addition, zirconium isotopes are produced directly by spallation reactions of the type $Nb^{93}(p, 2pxn)Zr^{<93}$. This is a convenient method of preparation of radioactive isotopes of zirconium of mass number 89 or less, free of interference from higher mass zirconium activities. The mass numbers of the stable isotopes of zirconium are 90, 91, 92, 94, and 96, so that the isotopes to be discussed all lie on the neutron deficient side of stability.

During the course of extensive radiochemical and spectrometer studies on the zirconium activities thus prepared and on their decay products, we have assembled information on the decay of Zr^{89}, Zr^{88}, Zr^{87}, and Zr^{86}. Much of this information is new; part of it is to be compared with the previous work of others, with which it does not always agree. After a description of the chemical procedures employed, the detailed studies on each isotope are presented separately.

II. CHEMICAL SEPARATIONS

Thin strips of spectrographically pure niomium metal were bombarded for periods of from 5 to 20 minutes with 100-Mev protons in the 184-inch cyclotron. Such bombardments produced $\sim 10^9$ disintegrations per minute of total zirconium activity. Numerous bombardments were carried out in the course of the research.

The niobium target foils were dissolved immediately by dropping them into a mixture of concentrated HNO_3 and concentrated HF. Ten milligrams of lanthanum nitrate were added, with stirring, to precipitate LaF_3. All the zirconium activities in solution were coprecipitated with the LaF_3 and cleanly separated from the niobium, a separation which has been studied by Ballou[1] and by Gest, Burges, and Davies.[2] The coseparation is believed to be caused by the surface adsorption of $ZrF_6^{=}$ ion on LaF_3. The LaF_3 precipitate was contacted with strong KOH to metathesize the fluoride to the hydroxide compound. Then the hydroxide was dissolved in $2M$ $HClO_4$. In order to scavence out any traces of niobium which might remain, manganese dioxide was precipitated from the resulting solution by adding in turn Mn^{++} and $KMnO_4$.

The zirconium was extracted from the $HClO_4$ solution by contacting it intimately for 15 minutes with an equal volume of a $0.2M$ solution of α-thenoyltrifluoroacetone (hereinafter referred to as TTA) in benzene. Aluminum nitrate was added to the aqueous phase to complex any traces of fluoride ion which might remain from the metathesis step, since the fluoride ion interferes with the TTA extraction. The work of Connick and McVey[3] and of Huffman and Beaufait[4] was used as a guide in this purification step. The zirconium-TTA complex in benzene solution was thoroughly scrubbed of possible traces of extraneous activities by contact with $2M$ $HClO_4$ wash solution. Then the benzene solution was diluted 10-fold and contacted with one-tenth its

* This work was carried out under the auspices of the AEC.

[1] N. Ballou, *National Nuclear Energy Series, Plutonium Project Record*, "Radiochemical Studies: The Fission Products" (McGraw-Hill Book Co., Inc., New York, to be published 1951), Vol. 9B, Paper No. 824.4.

[2] Gest, Burges, and Davies, U. S. Atomic Energy Commision Declassified Document, AECD-2560 (April 18, 1949) (unpublished).

[3] R. E. Connick and W. H. McVey, J. Am. Chem. Soc. 71, 3182 (1949).

[4] E. H. Huffman and L. J. Beaufait, J. Am. Chem. Soc. 71, 3179 (1949).

volume of concentrated HCl to effect the return of the zirconium to an aqueous medium.

This zirconium fraction was quite pure both chemically and radioactively; but to be absolutely certain of its purity, it was subjected to an additional purification step, capable in itself of effecting excellent decontamination from most other elements. The HCl solution was slowly passed through a short column (2 cm×4 mm) of Dowex-1 anion exchange resin[4a] which had been pre-equilibrated with concentrated HCl. Unpublished research results of this laboratory[5] have shown that from solutions 10*M* or higher in HCl concentration, negatively charged chloride complex ions of zirconium adsorb strongly on Dowex anion resin. From solutions of concentration less than 6*M*, they do not adsorb. Niobium forms even stronger complexes, but the other elements which could possibly be present are not adsorbed. Hence, by passing the concentrated HCl solution through the resin column and rinsing it well with more concentrated HCl solution, the zirconium was quantitatively and cleanly adsorbed. The zirconium could be immediately desorbed by passing a 4*M* HCl solution through the column. In some experiments, the zirconium activity was left on the column and periodically milked of its yttrium daughter activity by rinsing the column with 10–12*M* HCl at the proper time. The zirconium was retained quantitatively and the yttrium quantitatively removed by this step.

This isolation procedure has several advantages over some previous methods commonly used for radiochemical isolation of zirconium such as co-precipitation on barium fluozirconate. A principal one is that the zirconium is isolated in a carrier free state.

III. ZIRCONIUM 87

The decay scheme which best fits our information for Zr^{87} is presented in Fig. 1, while the detailed chemical and physical evidence on which it is based is presented below. The Y^{87m}, Y^{87}, and Sr^{87m} isotopes were observed many years ago by DuBridge and Marshall,[6] who measured the decay constants and established the genetic relationship of Sr^{87m} to Y^{87}. They did not establish experimentally the relationship of Y^{87} to Y^{87m} but suggested it correctly. During the course of our investigation, a report on Zr^{87} appeared by Robertson, Scott, and Pool.[7] These authors prepared Zr^{87} by helium ion bombardment of separated strontium isotopes and reported it to be a 2.0±0.1-hour activity decaying by the emission of 2.0±0.1-Mev positrons and by emission of x-rays and gamma-rays.

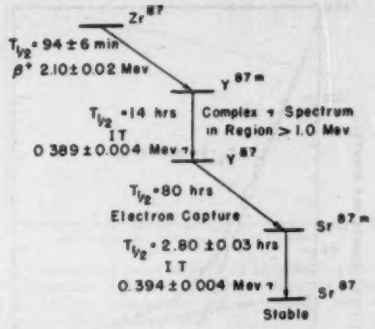

FIG. 1. Decay scheme of Zr^{87}.

HALF-LIFE OF Zr^{87}

The decay curve of the zirconium fraction followed through no absorber with an ordinary Geiger counter starting at a time about 1.5 hours after bombardment appears as in Fig. 2. Inspection of the curve indicates a prominent activity with a half-life of about 90 minutes, but a reliable resolution of the curve is difficult because of the complexity of the mixture. The growth and decay of yttrium and strontium daughter activities is superimposed on the straight decay of 78-hour Zr^{89}, 17-hour Zr^{88}, and 94-minute Zr^{87}. The nature and energies of the radiations involved did not allow a simplification of the resolution by following the decay through properly selected absorbers. The half-life of Zr^{87} was measured by placing a sample in a high resolution beta-ray spectrometer and following the decay of positrons of a specific energy in the high energy region.[7a] Other positron activity was present (principally 0.910-Mev Zr^{89}), but by choosing an energy beyond the Zr^{89} positron end point, the interference from it and from

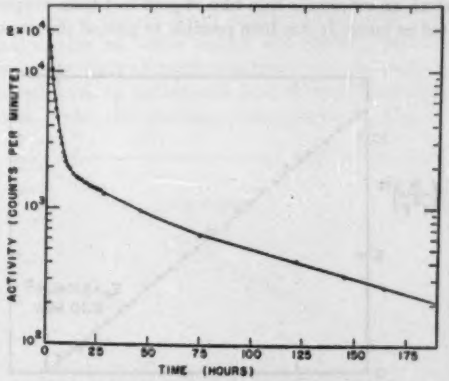

FIG. 2. Gross no-absorber decay of radioactivity in zirconium fraction starting 1.5 hours after bombardment.

[4a] Manufactured by Dow Chemical Company, Midland, Michigan; purchased from Microchemical Specialties Company, Berkeley, California.

[5] D. A. Orth and K. Street, Jr., preliminary report on unpublished work, University of California Radiation Laboratory Memorandum MB-IP-451 (January 27, 1950).

[6] L. A. DuBridge and J. Marshall, Phys. Rev. 58, 7 (1940).

[7] Robertson, Scott, and Pool, Phys. Rev. 76, 1649 (1949).

[7a] We wish to thank C. I. Browne, Jr., for assistance in this experiment.

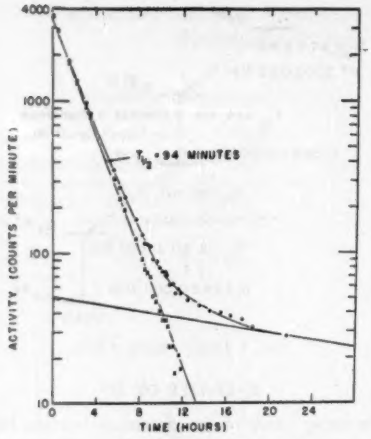

FIG. 3. Half-life of Zr^{87} determined by measuring decay of monoenergetic positrons of 1.47 Mev in spectrometer.

other causes was reduced to a minimum. A typical decay curve is shown in Fig. 3. The points shown have been corrected for the normal counter background of 38 counts per minute. As the result of several determinations, we obtain a value of 94±6 minutes for the half-life. Our value is somewhat shorter than the 120±6-minute value found by Robertson *et al.*[7]

ENERGY OF Zr^{87} POSITRON

The positron spectrum of the zirconium fraction was run, within a few hours after bombardment, at a time when Zr^{87} was the predominant positron activity, the ratio of Zr^{87} to Zr^{89} being 4 to 1. A carrier-free sample was mounted on a thin tygon film (<30 $\mu g/cm^2$) onto which an extremely thin film of gold had been evaporated *in vacuo*. It was then possible to ground the source

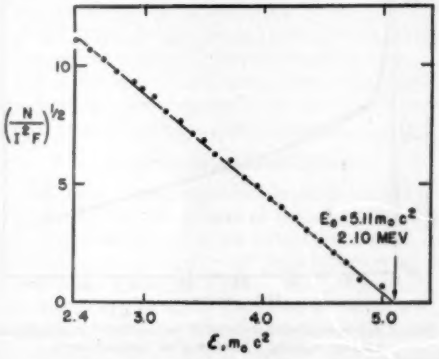

FIG. 4. Fermi-Kurie plot of high energy part of Zr^{87} positron spectrum.

to the frame of the spectrometer by means of the aluminum holder and to avoid source charging effects.

The 25-cm radius of curvature beta-ray spectrometer used in these investigations is of the double-focusing type proposed by Svartholm and Siegbahn[8] and by Shull and Dennison.[9] The focusing angle is $\pi\sqrt{2}$, or approximately 255 degrees, and the inhomogeneous field varies approximately as $1/\sqrt{r}$. For a resolution of 1.3 percent, the theoretical transmission is about 1 percent; in practice, the machine is usually baffled down, which reduces the transmission considerably.

The spectrometer was calibrated with the conversion line[10] of Cs^{137}, and the calibration was checked by determining the energy of the P^{32} beta-particle. A value of 1.685±0.01 Mev was obtained, in excellent agreement with recent values of others.[11] Our resolution was usually 1.5 percent, with resolution defined for a monoenergetic electron as the full half-width of the electron line in momentum units divided by the momentum of the line and expressed in percent. Our electron detector was a Geiger tube filled to a regulated pressure of 8.8 cm with a 10 percent ethylene, 90 percent argon mixture. The tube window was a grid-supported Formvar film of approximately 30 μg per cm^2 thickness. The magnet power supply was electronically regulated to better than 0.1 percent.

The Fermi-Kurie plot of the Zr^{87}-Zr^{89} mixture was resolvable into the 2.10±0.02-Mev component of Zr^{87} and the 0.910±0.010-Mev component of Zr^{89} and no others. The portion of the plot beyond the Zr^{89} end point is shown in Fig. 4. Our value agrees with the value obtained by Robertson *et al.*[7] by aluminum absorption measurements, within their experimental error.

An examination of the electron spectrum showed no prominent conversion electrons which could be assigned to Zr^{87}, nor could evidence by found for Zr^{87} gamma-radiation by lead absorption measurements on the freshly purified zirconium, but we are not able to set very low limits on the possible presence of unconverted gamma-radiation. Robertson *et al.*[7] found gamma-rays of 0.35- and 0.65-Mev energy and x-radiation accompanying the decay of Zr^{87}.

IDENTIFICATION OF DECAY PRODUCTS OF Zr^{87}

If an yttrium fraction is milked from the purified zirconium, by the HCl-anion exchange method outlined above, within two or three hours after the bombardment, the yttrium fraction is nearly 100 percent Y^{87m} with a nearly undetectable trace of Y^{86} and Y^{88}. If the decay of this activity is followed with a thin window Geiger tube using no absorber, the resulting decay curve is as shown by the experimental points in Fig. 5.

[8] N. Svartholm and K. Siegbahn, Arkiv. Mat. Astron. Fysik 33A, No. 21 (1946); see also Hedgran, Siegbahn, and Svartholm, Proc. Phys. Soc. (London) 63A, 960 (1950).
[9] F. Shull and D. Dennison, Phys. Rev. 71, 681 (1947); 72, 256 (1947).
[10] L. M. Langer and R. D. Moffatt, Phys. Rev. 78, 74 (1950).
[11] L. M. Langer and H. C. Price, Jr., Phys. Rev. 76, 641 (1949).

What is represented by this curve is principally the decay of 14-hour Y^{87m} and the growth and decay of the conversion electrons of the 2.80-hour Sr^{87m} granddaughter. The contribution to the counting rate of the gamma-radiation of Y^{87m} and Sr^{87m} and of the x-radiation of 80-hour Y^{87} is relatively small. Shown on Fig. 5 is a theoretical curve drawn for the case of a 14-hour parent decaying to an 80-hour daughter with undetectable radiation, and a 2.80-hour granddaughter whose radiation is detected with the same efficiency as that of its grandparent. It is seen that the experimental points follow the theoretical curve except for a leveling off on a line 18 percent below the theoretical curve. This difference may be attributed to a difference in the conversion coefficients of the 0.389-Mev gamma-ray of Y^{87m} and the 0.394-Mev gamma-ray of Sr^{87m}, the latter being slightly lower.

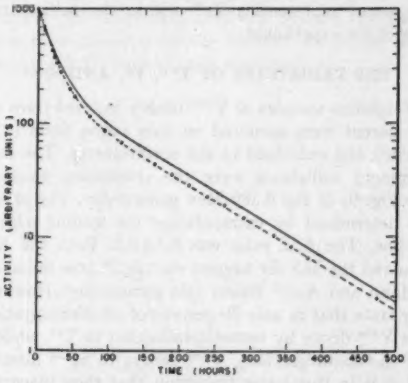

FIG. 5. Decay of an initially pure Y^{87m} sample. Points and dotted line are experimental. Solid curve is the theoretical decay of an initially pure 14-hour activity decaying to an 80-hour daughter and a 2.8-hour granddaughter when the parent and granddaughter activities are assumed to count with equal efficiencies and the radiation of the daughter is undetected.

Convincing auxiliary proof that the decay chain is as represented by Fig. 1 was obtained by establishing that the growth and decay of the Sr^{87} nuclide occurred quantitatively as indicated. A pure sample of Y^{87m} was prepared as described in the last experiment; and at intervals of many hours, the Sr^{87m}, which was in transient equilibrium with it, was isolated and measured with a Geiger counter.

The chemical procedure was the following. One milligram of yttrium and of strontium were added to the Y^{87m} solution in 1 ml of dilute HCl. Then 0.5 ml of a solution of 8-hydroxyquinoline (660 mg dissolved in 50 ml acetone and diluted to 200 ml with water) was added. Yttrium 8-hydroxyquinolinate was precipitated by adding concentrated NH_4OH dropwise until the precipitate just failed to redissolve. After the precipitate was heated in boiling water five minutes,

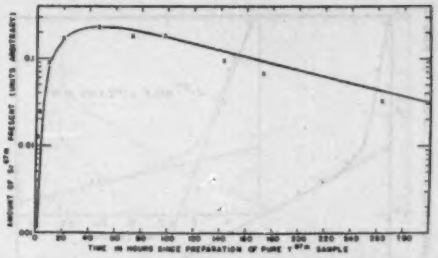

FIG. 6. Growth and decay of Sr^{87m} in an initially pure sample of Y^{87m}. Points are experimental. Line is theoretical curve for growth of 2.8-hour grandaughter of an initially pure 14-hour activity and its 80-hour daughter.

centrifuged, and separated, it was redissolved in dilute HCl and set aside until the time of the next milking. To the original supernate, four drops of saturated sodium oxalate solution were added, followed by one drop of dilute ammonia, to precipitate strontium oxalate. This precipitate was evaporated on a platinum disk and counted. In several cases the decay of the strontium sample activity was followed to establish the identity of the activity. All counts were taken on the same counter, using identical conditions, and the counts were extrapolated back to the time of separation from yttrium. This chemical procedure is based on one given by DuBridge and Marshall.[6]

Ten milkings were carried out on three separate samples. The results for one sample are shown in Fig. 6. The crosses are the experimental points. The line is the theoretical growth and decay curve for a 2.80-hour granddaughter of an initially pure 14-hour parent when the daughter half-life is 80 hours. It is concluded that the genetic relationships are correctly stated in Fig. 1.

HALF-LIFE OF Sr^{87m}

In one of the strontium separations discussed in the last section, an active sample was carefully repurified from any trace of yttrium activity and its decay followed down to background in a chlorine filled Geiger tube. From the resulting curve shown in Fig. 7, a

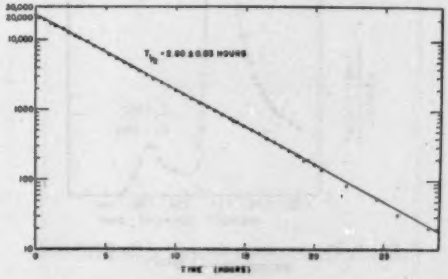

FIG. 7. Half-life of Sr^{87m}.

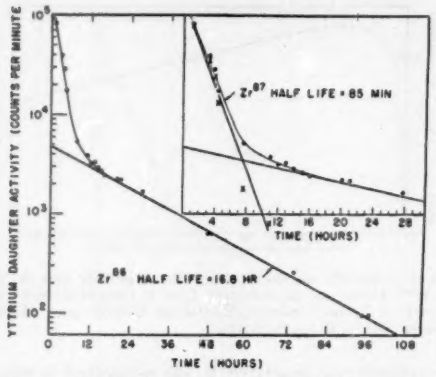

FIG. 8. The rate of formation of yttrium daughter activity in the zirconium fraction as a function of time, starting three hours after bombardment. Resolution of shorter-lived component plotted on expanded time scale in insert. Resolved components represent half-lives of Zr^{86} and Zr^{87}.

half-life of 2.80±0.03 is determined, in excellent agreement with the recent results of Mann and Axel.[12]

PARENT-DAUGHTER RELATIONSHIPS OF $Zr^{87}-Y^{87m}$

This relationship was established in an experiment which also served to measure the half-life of Zr^{86}. Three hours after bombardment, a purified zirconium fraction was adsorbed on a short Dowex-1 resin column from concentrated HCl solution. A constant slow flow of pure concentrated HCl was maintained through the column. Under the conditions used no detectable amount of zirconium activity stripped off the column, while the yttrium daughter activity appeared in the elutriant solution as soon as it was formed. The amount of yttrium activity appearing in a definite period of time was determined at frequent intervals by counting the activity under standardized conditions. The samples were counted within a half-hour of the time the yttrium was formed. In the early samples, the predominant activity was 14-hour Y^{87m} identified by the conversion electron of the 0.389-Mev gamma-ray and by its half-life, but as its 94-minute parent Zr^{87} disappeared, the percentage of 14.6-hour Y^{86}, identified by its positron radiation, steadily rose. This gave rise to the two-component curve seen in Fig. 8 where the initial counts of yttrium activity collected in a standardized time interval are plotted against time. This curve may be resolved into a 16.8 hour component representing Zr^{86}, which we round off to 17±2 hours, and an 85-minute component representing Zr^{87} within the rather large error of the experiment.

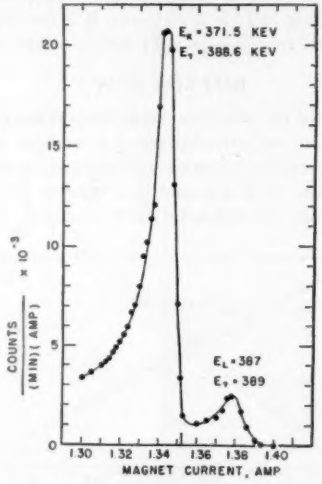

FIG. 9. The conversion electrons of the 0.389-Mev gamma-ray of Y^{87m}.

THE RADIATIONS OF Y^{87m}, Y^{87}, AND Sr^{87m}

Weightless samples of Y^{87m} freshly isolated from the Zr^{87} parent were mounted on thin tygon films (<30 $\mu g/cm^2$) and examined in the spectrometer. The most prominent radiations were the conversion electrons (see Fig. 9) of the 0.389-Mev gamma-ray. The energy was determined by extrapolating the leading edge of the line. The K/L ratio was 8.3±0.5. Both the K/L ratio and the half-life suggest electric 2^5 pole radiation.

Mann and Axel[12] report this gamma-ray. However, they state that in only 50 percent of its disintegrations does Y^{87m} decay by isomeric transition to Y^{87}, while in half the disintegrations, Y^{87m} decays to Sr^{87m} directly, and it is in this latter transition that they place this gamma-ray. We find it difficult to fit our experimental results to this decay scheme.

Robertson *et al.*[13] report that 14-hour Y^{87m} decays by positron emission and not by isomeric transition to Y^{87}, and they state that Y^{87m} and Y^{87} decay independently to Sr^{87m}. From the evidence given in the present paper, this clearly cannot be the case. Possibly what Robertson and co-workers were measuring was the 14.6-hour yttrium activity which we have assigned to Y^{86} (see below), which in their bombardments would have appeared through the $Sr^{84}(\alpha, pn)Y^{86}$ reaction.

As the Y^{87m} conversion electrons decay out, the conversion electrons of the Sr^{87m} grandaughter grow in as shown by the plots in Fig. 10. Figures 9 and 10 represent the same sample examined approximately 3 hours, 28 hours, and 45 hours after preparation of a pure Y^{87m} sample. The Sr^{87m} gamma-ray energy is 0.394 ±0.004 Mev. The K/L ratio is 7.2 which, within our experimental error, is in agreement with Mann and Axel's[12] value, 6.9. The K-line of the Sr^{87m} gamma-ray falls between the K and L lines of the Y^{87m} gamma-ray.

[12] L. G. Mann and P. Axel, Phys. Rev. **80**, 759 (1950).

[13] Robertson, Scott, and Pool, Phys. Rev. **78**, 318 (1950).

Our value for the Sr^{87m} gamma-ray energy may be compared to Helmholtz's[14] 1941 value of 0.386 and to Mann and Axel's[12] recent value of 0.390 Mev.

Within experimental error, the area under the Y^{87m} K-line peak decayed with the proper 14-hour half-life, while the sum of the areas under all four peaks decayed in a manner similar to the experimental points of Fig. 5, thus indicating that the observed conversion lines are correctly assigned.

In addition to these prominent lines, an examination of the electron spectrum of freshly prepared Y^{87m} showed six conversion electron lines in the region above 1 Mev.

No detailed study has yet been made of these electrons, but they decayed with a 14-hour half-life. Auger electrons were observed but not studied. No negative beta-particles were observed, and the total number of positrons was <0.001 times the number of conversion electrons. No conversion electrons beyond the Auger region were observed for the 80-hour Y^{87} or the Sr^{87m} except the Sr^{87m} lines already discussed.

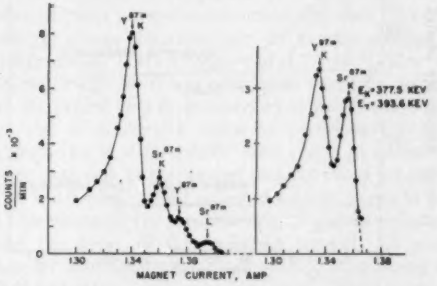

FIG. 10. The conversion electron spectrum 28 hours and 46 hours after preparation of pure Y^{87m} sample, showing growth of conversion electrons of 0.394-Mev gamma-ray of Sr^{87m}.

Lead absorption curves were determined on these isotopes to obtain evidence supplementary to the spectrometer results. A lead absorption curve on a sample of Y^{87m} is shown in Fig. 11. Another curve for a sample of Y^{87}, in equilibrium with its daughter Sr^{87m} but nearly free of Y^{87m}, is shown in the same figure. Figure 11 shows that considerable hard gamma-radiation of energy >1.0 Mev accompanies the decay of Y^{87m}, but is not present in the decay of Y^{87} or Sr^{87m} which supports the assignment of the group of energetic conversion electrons mentioned above to Y^{87m}. The gamma-ray component of the lower curve is believed to represent the 0.394-Mev gamma-ray of Sr^{87m}. Robertson *et al.*[13] report conversion electrons of a 0.5-Mev gamma-ray of Sr^{87m}, and Mann and Axel report that the K-capture decay of 80-hour Y^{87} is immediately followed by emission of a 0.485-Mev gamma-ray. We failed to see these conversion electrons in our spectrometer studies, but the conversion coefficient measured by these authors is

[14] A. C. Helmholtz, Phys. Rev. **60**, 422 (1941).

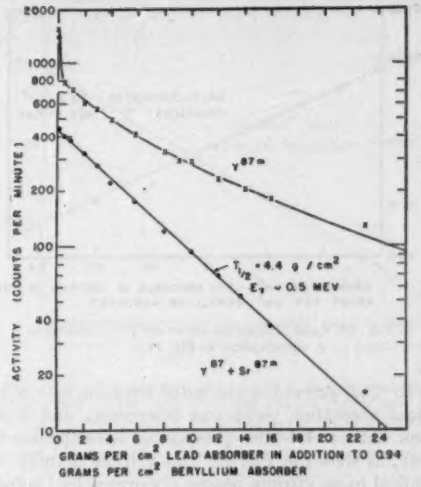
ACTIVITY (COUNTS PER MINUTE)
Y87m
T1/2 = 4.4 g / cm²
Eγ ~ 0.5 MEV
Y87 + Sr87m
GRAMS PER cm² LEAD ABSORBER IN ADDITION TO 0.94
GRAMS PER cm² BERYLLIUM ABSORBER

FIG. 11. Lead absorption curve on Y^{87m} (no Y^{87} or Sr^{87m} present) and on an equilibrium mixture of Y^{87} and Sr^{87m} (no Y^{87m} present). Samples mounted on platinum 3.6 cm from the window of commercial chlorine filled Amperex Geiger tube, housed in aluminum-lined lead shield. 0.94 g per cm² perylium absorber immediately below window. Lead absorbers immediately below beryllium.

small enough that we could have overlooked them. If this 0.485-Mev gamma-ray is correctly assigned, the absorption curve of Fig. 11 represents a 1/1 mixture of a 0.485- and 0.394-Mev gamma-ray.

IV. YTTRIUM 86

When a purified zirconium fraction was allowed to decay for 24 hours after bombardment and then stripped of its yttrium daughters, no more of the mass 87 chain daughters were formed. If a fresh yttrium fraction was then separated after a few hours, or a day or two, considerable positron activity was found. The activity decayed, as shown in Fig. 12, with a half-life of 14.6 ± 0.2 hours. The small amount of long-lived activity amount-

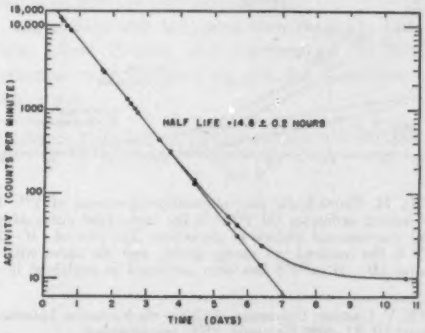

FIG. 12. Half-life of Y^{86}.

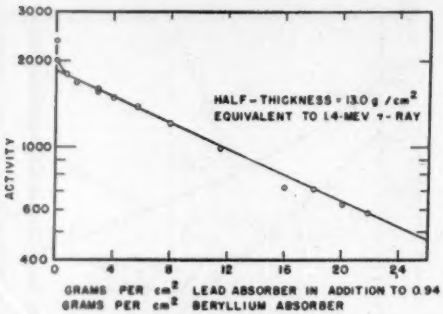
HALF-THICKNESS = 13.0 g/cm²
EQUIVALENT TO 1.4-MEV γ-RAY
ACTIVITY
GRAMS PER cm² LEAD ABSORBER IN ADDITION TO 0.94
GRAMS PER cm² BERYLLIUM ABSORBER

FIG. 13. Lead absorption curve on Y^{86}. Conditions equivalent to Fig. 11.

ing to <0.1 percent of the initial counting rate is Y^{88}. A lead absorption curve was determined, and it was found that a 1.4-Mev gamma-ray accompanies the decay, as shown in Fig. 13. This yttrium activity was identical to an yttrium isotope discovered by Castner[15] in bombardments of strontium isotopes and assigned by him to mass number 86. Castner found, through relative yields of this nuclide from bombardments of strontium isotopes of different isotopic enrichments with proton beams of differing energies, that the most probable mass assignment was 86, but this is not certain.

A carrier-free sample of this activity was studied in the spectrometer with interesting results. A Fermi-Kurie plot of the positron spectrum, corrected for instrumental distortion according to Owen and Primakoff,[16] is shown in Fig. 14. Two components are present in about equal intensity, with maximum energies of 1.80±0.02 Mev and 1.19±0.02 Mev. There are not sufficient data on the high energy component to establish any deviation from linearity, but the low energy group appears to be forbidden. The comparative half-life of the low energy positron ($ft \sim 10^6$) indicates a first forbidden transition, while the spectral shape

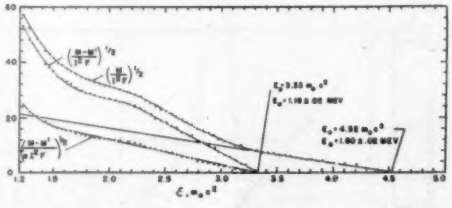

FIG. 14. Fermi-Kurie plot of positron spectrum of Y^{86}. The plot having ordinates $(M/PF)^{\frac{1}{2}}$ is the unresolved curve after a small instrumental distortion correction. The plot of $(M-M'/PF)^{\frac{1}{2}}$ is the resolved low energy group, and the curve with ordinates $(M-M'/aP^2F)^{\frac{1}{2}}$ has been corrected as explained in the text.

[15] S. V. Castner, University of California Radiation Laboratory Report UCRL-1099 (January, 1951) (unpublished).
[16] G. E. Owen and H. Primakoff, Phys. Rev. **74**, 1406 (1948).

suggests a spin change of two units and a change of parity. According to the theory of forbidden spectra,[17,18] dividing the ordinates of the plot of the low energy component in Fig. 14 by $a^{\frac{1}{2}}$ should yield a straight line if the transition is of this type. The factor $a=(\epsilon^2-1)+(\epsilon_0-\epsilon)^2$, with ϵ the energy in units of m_0c^2, arises from the unique energy dependence of this transition. Figure 14 shows such a corrected plot, and it is seen that a straight line does indeed result.

The factor $C=(\epsilon^2-1)^2+(10/3)(\epsilon^2-1)(\epsilon_0-\epsilon)^2+(\epsilon_0-\epsilon)^4$ gave a poor fit. Conformity to this factor would have indicated a second forbidden transition with a spin change of 3 units and no change in parity.

Internal conversion lines were sought, but none were seen. However, the samples were of comparatively low intensity, and the presence of gamma-radiation other than the hard 1.4-Mev gamma-ray cannot be ruled out.

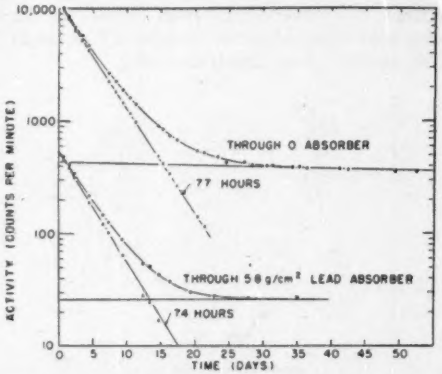

FIG. 15. Decay of Zr^{89} in a sample repurified one week after bombardment through no absorber and through 5.8-g per cm² lead absorber. Long-lived background is Zr^{88}.

V. ZIRCONIUM 89

The previously reported[6,19] 78–80 hour nuclide, Zr^{89}, was the prominent activity in our zirconium fractions when repurified several days after bombardment. By this time the other zirconium activities had decayed out, with the exception of Zr^{88}, discussed below, which, because of its long half-life and inefficiently counted x-radiation, contributed only a few percent to the total radiation at this time. A decay curve for such a zirconium sample counted in a chlorine filled Geiger tube through no absorber is shown in Fig. 15. The long-lived component is Zr^{88}; the 77-hour component is Zr^{89}.

Carrier-free samples of this activity mounted on thin tygon films were examined in the spectrometer. The Zr^{89} positron energy, redetermined by a Fermi-Kurie

[17] E. J. Konopinski and G. E. Uhlenbeck, Phys. Rev. **60**, 308 (1941).
[18] E. J. Konopinski, Revs. Modern Phys. **15**, 209 (1943).
[19] Overstreet, Jacobson, and Hamilton, as reported in Manhattan Project Metallurgical Laboratory Report CH-498 (February 15, 1943) (unpublished).

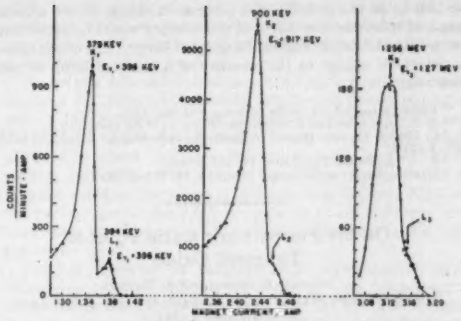

FIG. 16. Conversion electrons of Zr^{89}.

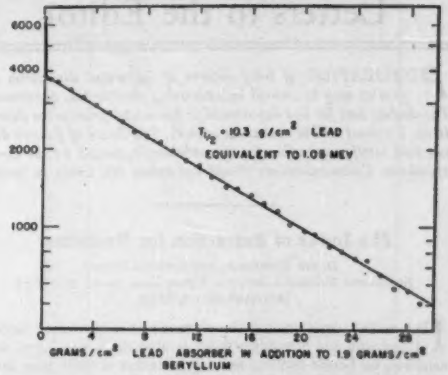

FIG. 17. Lead absorption curve for Zr^{89}. Sample mounted on platinum was 5.2 cm away from end window Geiger tube filled with argon-alcohol mixture. 1.9 g beryllium absorber immediately below counter window. Lead absorbers immediately above sample. One half-inch lead around tube. Tube and sample unhoused.

plot of our data, gave a value of 0.910±0.010 Mev. Our new value is somewhat lower than the value of 1.07 Mev determined by Overstreet, Jacobson, and Hamilton[16] by aluminum absorption.

The original communication[6] on Zr^{89} stated that no gamma-radiation accompanied its decay; however, we observed four groups of conversion electrons. The high energy groups corresponding to gamma-energies of 0.396±0.004, 0.917±0.005, and 1.27±0.01 Mev are shown in Fig. 16. It was established that they decayed at the proper rate to be assigned to Zr^{89}. In addition, K and L conversion electrons corresponding to a gamma-ray of 0.027±0.001 Mev and Auger electrons were observed. It is apparent that the decay scheme of Zr^{89} is complex. A lead absorption curve shown in Fig. 17 corroborated the presence of hard gamma-radiation, and the decay of this radiation through 5.8 grams per cm² lead absorber, plotted on Fig. 15, followed the Zr^{89} half-life.

VI. ZIRCONIUM 86

The parent of the 14.6-hour Y^{86} was looked for, but no clear cut direct evidence for its radiations could be found. This in itself is good evidence that Zr^{86} is an orbital electron capturing nuclide. Positron activity would have contributed a prominent component to the gross decay shown in Fig. 2 and, in particular, would have been seen in the many zirconium samples studied in the spectrometer during the course of this work. It seems clear then that this isotope decays predominantly by orbital electron capture and that its inefficiently counted x-rays are unobserved in the presence of interfering Zr^{89} and Zr^{87} activity. Its half-life was determined indirectly in the manner discussed above and presented in Fig. 8, namely, by determining the amount of Y^{86} formed in the zirconium fraction as a function of time.

VII. ZIRCONIUM 88

Zirconium fractions repurified months after bombardment still retained considerable radioactivity. This activity was found to consist of x-radiation, gamma-radiation, and conversion electrons. The x-rays were identified as yttrium x-rays by analyzing them with a proportional counter coupled to a multi-channel differential pulse analyzer, a technique described by Hanna, Kirkwood, and Pontecorvo.[20] The conversion electrons were measured in our spectrometer, and the gamma-ray energy was determined to be 0.406±0.004 Mev The mass assignment of 88 is made on the basis of the isolation of the Y^{88} daughter identified by its 105-day half-life and by its x- and gamma-radiation. The half-life of Zr^{88} is approximately 150 days. These results on Zr^{88} are only preliminary.

The authors wish to express their thanks to James T. Vale, Lloyd Houser, and members of the 184-inch cyclotron crew for carrying out the numerous bombardments.

[20] Hanna, Kirkwood, and Pontecorvo, Phys. Rev. 75, 985 (1950).

Letters to the Editor

PUBLICATION of brief reports of important discoveries in physics may be secured by addressing them to this department. The closing date for this department is five weeks prior to the date of issue. No proof will be sent to the authors. The Board of Editors does not hold itself responsible for the opinions expressed by the correspondents. Communications should not exceed 600 words in length.

The Index of Refraction for Neutrons*

DAVID KLEINMAN AND GEORGE SNOW
Brookhaven National Laboratory, Upton, Long Island, New York
(Received May 1, 1951)

IN a recent paper on variational principles in scattering theory, Lippmann and Schwinger[1] have treated the scattering of slow neutrons by bound protons as an application of their time independent formulation, which they obtain from time dependent scattering theory by means of several devices including the adiabatic reduction of the interaction to zero at $t=\pm\infty$. The merits of this formulation are (a) the exact transition rate is obtained in the form $\omega_{ba}=2\pi\delta(E_b-E_a)|T_{ba}|^2$, where T is an operator which in Born approximation is the interaction energy; (b) a variational principle is given for the T-matrix; (c) a sum rule is given which states that the total rate of transition out of the initial state Φ_a is $-2\,\mathrm{Im}T_{aa}$.

By a simple generalization from the neutron scattering by one bound proton we have considered the scattering by a thin slab of material containing many nuclei. The Φ_a component of the final state $S\Phi_a$, where S is the Heisenberg S-matrix, is $[1-i(m\lambda/2\pi)T_{aa}]\Phi_a$. When the sum rule is invoked, the imaginary part of T_{aa} gives the customary amplitude extinction factor $(1-\frac{1}{2}N\sigma x)\approx\exp(-\frac{1}{2}N\sigma x)$, where x is the thickness of the slab, and N is the nuclear density. Similarly, the real part of T_{aa} represents a phase shift, which one might interpret as due to the index of refraction of the slab. When the Fermi approximation to T_{aa} is used, the phase shift is in agreement with the usual formula for the index of refraction, $n=1-N\lambda^2a_c/2\pi$, where a_c is the isotopic average of the *bound* coherent scattering amplitudes of the nuclei.

One cannot expect an actual derivation of the index of refraction to follow from time dependent scattering theory, because from the time dependent viewpoint $S\Phi_a$ is the final state after the interaction has been adiabatically reduced to zero, and it is not clear why the phase shift in $S\Phi_a$ should necessarily be the same as that which the interaction would produce in a stationary wave function. To overcome this objection we have found a formal solution to the stationary eigenvalue problem identical with the $\Psi_a^{(+)}$ of Lippmann and Schwinger, which we show represents an incoming plane wave and an outgoing scattered wave. This stationary formulation is similar to that of Moller,[2] who introduced the S-matrix into stationary scattering theory. The connection between the S-matrix and the wave function is that the outgoing part of $(S-1)\Phi_a$ is identical with the scattered wave. On the basis of this theory we arrive at a general derivation of the index of refraction for gases, liquids, and solids.

This derivation of the index clearly shows that there is no doppler effect due to the motion of the individual nuclei, because the λ in the formula is the neutron wavelength relative to the boundary of the slab. The variational principle gives, besides the Fermi approximation, a temperature dependent correction to the simple formula, thereby taking into account the effect of virtual inelastic interactions of the neutron with the material. We have not as yet evaluated the correction in a specific case, but Lippmann[3] finds a correction of 0.2–0.3 percent to the scattering cross section of parahydrogen in its lowest rotational state for neutrons of zero energy. In liquids or solids at fairly high temperature and for neutrons of nonzero energy it would seem possible for the correction to be of the order of 1 percent. A change in the critical angle of reflection of a mirror of this amount would be significant in the experiment of Hughes, Burgy, and Ringo,[4] and might cause a detectable change in the intensity of a reflected beam of pile neutrons.

* Research carried out under contract with the AEC.
[1] B. A. Lippmann and J. Schwinger, Phys. Rev. **79**, 469 (1950).
[2] C. Moller, D. Kgl. Danske Vidensk. Selskab, Mat-fys. Medd. XXIII, Nr. 1 (1945).
[3] B. A. Lippmann, Phys. Rev. **79**, 481 (1950).
[4] Hughes, Burgy, and Ringo, Phys. Rev. **77**, 291 (1950).

On the Ferroelectric Curie Point of Tungsten Oxide

S. SAWADA, R. ANDO, AND S. NOMURA
Institute of Science and Technology, University of Tokyo, Tokyo, Japan
(Received April 9, 1951)

SINCE Nagasawa[1] pointed out the possible existence of ferroelectric phenomena in tungsten oxide, the physical properties of this substance have been studied extensively at several laboratories in Japan. Matthias[2] also reported independently the experimental investigations of the ferroelectric properties of tungsten oxide. According to the preceding investigators, this substance was found to have many of the properties peculiar to ferroelectrics, i.e., the very high value of permittivity, the characteristic variation with a biasing field, the hysteresis loop, the domain structure, and the sensitive variation with external stress. On the other hand, the domain structure has not been influenced by an electric field, and its transition temperature has not been discovered up to about 550°C, which state of affairs makes us hesitate to conclude that tungsten oxide has ferroelectric properties. In order to clarify this situation, we have recently extended our experimental observations to higher temperatures and have found that tungsten oxide really has a spontaneous polarization with the Curie point at about 710°C. In the following the results of our observations are reported briefly.

The domain structure of a single crystal of area 0.01 mm² and thickness 0.01 mm was observed, up to 950°C, by a polarized-light microscope, using a very small electric furnace. On heating the crystal, the domain structure did not vary at all up to about 710°C, at which temperature the domain patterns vanished with the field of view becoming dark almost suddenly, and at still higher temperatures the birefringence was no longer discernible. On cooling, the domain patterns appeared almost suddenly at about 685°C, and the original features were approximately realized again at room temperature.

Next we prepared a rectangular crystal (0.4×0.2×0.02 mm) with a few bands inclined by 45° to the edges, which had two fired-on silver paste electrodes separated by 0.1 mm along the longest direction of the crystal. It was then connected to the 100-v terminals of a battery through a 20-kΩ rheostat, the resistance of the crystal being 2.5 kΩ. On account of the rather high conductivity, the temperature of the crystal is raised by the Joule's heat by decreasing the resistance of the rheostat, and at about 550°C the new 45° bands begin to appear. As the temperature is raised more new bands appear, and finally at about 700°C the whole crystal becomes dark suddenly. The successive disappearance of the 45° bands is observed as the temperature is lowered, i.e., as the resistance of the rheostat is increased, although nearly half of the newly-appeared 45° bands still remain at room temperature. It is shown by x-ray analysis that the a- and b-axes of a plate crystal lie parallel or perpendicular to the edges in the plane of the plate, and hence the abovementioned results can be clearly understood by assuming that tungsten oxide has a spontaneous polarization with Curie point at 710°C in the direction of the b-axis, and further by taking into account the generally accepted fact that the coersive field decreases with increasing temperature. The results of the x-ray analysis of the crystal structure suggest to us that the spontaneous polarization does not lie along the direction

of the a-axis, while that along the c-axis may perhaps exist. We have been unable to ascertain clearly the c-axis polarization, since any plate crystal with the c-axis lying in the plane of the plate can, unfortunately, not be prepared.

By using a differential dilatometer, we made relative measurements of the thermal expansion of tungsten oxide with respect to that of barium titanate, both samples being ceramic rods, and found that a contraction of volume of tungsten oxide was clearly observed at about 710°C on heating, and at about 685°C on cooling, respectively. Furthermore, by cooling ceramic powder of tungsten oxide, an anomaly was distinctly observed near 700°C on the cooling curve, which fact suggests to us the existence of a latent heat or a λ-type anomaly of the specific heat at this temperature.

The low resistance of tungsten oxide makes the dielectric measurements quite difficult, especially at high temperatures. Although any decisive result, therefore, has not yet been obtained from our measurements of both the permittivity and the hysteresis loop, an anomaly of the permittivity in the neighborhood of 700°C and the almost linear variation of polarization with applied field above this temperature have been qualitatively observed to exist.

From these observations we may conclude that the tungsten oxide actually has ferroelectric properties and that its Curie point is situated at about 710°C. Quantitative observations are now in progress, the results of which will be reported shortly.

The authors wish to thank Professor T. Muto for his kind criticism and advice.

[1] S. Nagasawa, Denki-kagaku 16, 13, 57 (1948); 17, 174 (1949).
[2] B. T. Matthias, Phys. Rev. 76, 430 (1949).

Gamma-Rays Emitted in the Disintegration of the 36-Hour Rh^{105}

C. E. MANDEVILLE AND E. SHAPIRO
Bartol Research Foundation of the Franklin Institute, Swarthmore, Pennsylvania*
(Received May 2, 1951)

THE radiations of the 36-hour Rh^{105} have been examined by several groups of investigators,[1] and more recently by the writers.[2] Subsequent to all of the abovementioned measurements, more precise data have been obtained by Duffield and Langer.[3] They did not, however, find any evidence of the gamma-ray at ~0.3 Mev which had been observed by Sullivan, Sleight, and Gladrow[1] and by the writers.[2] Accordingly, a second quantity of metallic ruthenium has been irradiated by slow neutrons for ten hours in the Oak Ridge pile. The 36-hour rhodium was thus grown from its 4.5-hour ruthenium parent element.

The ruthenium used for pile irradiation was purified before exposure by distillation of RuO_4 from a perchloric-sulfuric acid solution of chemically pure $RuCl_3$. Irradiated Ru was dissolved in a mixture of 10 parts conc. HCl, 1 part conc. HNO_3, at 160°C. Rhodium carrier was added to the Ru solution and RuO_4 was distilled from a perchloric-sulfuric acid solution. Inactive $RuCl_3$ was added to the residue and another RuO_4 distillation effected. The residue in the distillation flask was diluted to 1 M in acid and treated while hot with magnesium powder to precipitate rhodium. After dissolving excess magnesium in HCl, the suspension was filtered, the rhodium washed with HCl, hot water, alcohol, and ether, then dried.

The purified source of Rh^{105} was placed between two blocks of aluminum, each having a surface density of 1.7 g/cm^2. This thickness was more than sufficient to stop all of the beta-rays of Rh^{105}, because they have a maximum energy of only 0.570±0.005 Mev.[4] Adjacent to either aluminum block was placed a G-M tube, having glass walls of thickness 0.1 cm and copper cathodes of wall thickness 0.013 cm. In one counter, the half-period of the quantum radiations being emitted by the source of Rh^{105} was measured; with the other, absorption curves in lead of the gamma-rays were

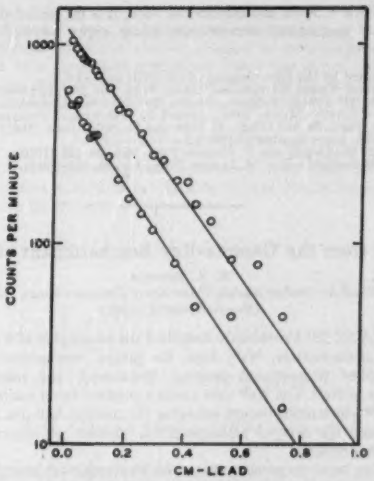

FIG. 1. Absorption in lead of the quantum radiations emitted in the disintegration of rhodium (105). The two curves, separated in time by forty hours, indicate a quantum energy of 0.3 Mev.

obtained. The decay curve of the gamma-ray activity of Rh^{105} was followed for three half-periods, and its slope gave a half-period of 35±1 hours. Two lead absorption curves for the gamma-rays of Rh^{105} are shown in Fig. 1. The first of these curves was taken at the beginning of the decay curve, and the second curve was obtained forty hours later. The quantum energy taken from the slope of the curves is 0.3 Mev.

The question arose whether the presence of quantum radiations might be accounted for by bremsstrahlung effects. This seemed to be an unlikely explanation for the presence of the gamma-rays, because the mean energy of the beta-rays from Rh^{105} is only 0.2 Mev.[5] However, to show positively that the results are not in any way related to the presence of bremsstrahlung, comparative measurements were carried out, using the beta-spectrum of RaE. The source of Rh^{105}, the gamma-ray activity of which had been followed for three half-periods, was placed before a thin window "bubble" counter. The beta-ray counting rate was observed, and after 0.1 cm of lead had been placed before the counter, the gamma-ray activity was likewise noted. The source of Rh^{105} was removed; a source of Ra($D+E+F$) was positioned to give the same beta-ray counting rate as was previously observed for Rh^{105}, and the same sheet of lead was placed over the counter to observe the residual counting rate. The data are given in Table I, where it is clear that

TABLE I. Gross counting rates (per minute).

Background	Ra($D+E+F$)	Rh^{105}
37.5±3	39±4.5	116±4

although the counting rate from Ra($D+E+F$) did not exceed the background count, that of Rh^{105} was three times greater. Were the quantum radiations which were detected in the counter originating from bremsstrahlung production in the lead sheet, the counting rate from Ra($D+E+F$) should have been the larger, because the beta-rays of RaE have a maximum energy of 1.17 Mev.

As previously reported,[2] beta-gamma coincidences have actually been observed in the disintegration of Rh^{105}. In conclusion, it can be stated that data taken with two different sources of Rh^{105}, produced at different times and from different samples of target material, indicate that gamma-rays are present in the disintegra-

tion of Rh^{103}. From the coincidence data, it is estimated that the 0.3-Mev gamma-ray accompanies about eight percent of the beta-rays.

* Assisted by the joint program of the ONR and AEC.

[1] Nishina, Yasaki, Kimura, and Ikawa, Phys. Rev. 59, 323 (1941); Phys. Rev. 59, 677 (1941). Sullivan, Sleight, and Gladrow, Plutonium Project Report CC-1493 (March, 1944), quoted by Seaborg and Perlman, Revs. Modern Phys. 20, 585 (1948). E. Bohr and N. Hole, Arkiv. Mat., Astron. Fysik 32A, paper number 15 (1948).

[2] C. E. Mandeville and E. Shapiro, Phys. Rev. 80, 125 (1950).

[3] R. B. Duffield and L. M. Langer, Phys. Rev. 81, 203 (1951).

Na^{20} from the Gamma-Ray Bombardment of NaF

R. K. Sheline
Institute for Nuclear Studies, University of Chicago, Chicago, Illinois
(Received April 23, 1951)

ALVAREZ[1] has recently described the production of a delayed alpha-emitter, Na^{20}, from the proton bombardment of a neon-filled proportional counter. Presumably the reaction is $Ne^{20}(p, n)Na^{20}$. The Na^{20} then emits a positron to an excited state of Ne^{20} which alpha decays following the positron half-life. Alvarez observed the delayed alpha-particles, whereas we observed the positron directly.

Using betatron gamma-rays of 76-Mev maximum energy it has been possible to produce Na^{20} from NaF. For this purpose a solid cylinder of NaF 8 inches long and ¾ inches in diameter was placed directly in the beam. It was counted in place immediately after turning off the beam with a Geiger tube two inches off the center of the beam but parallel to both the beam and the sample. The Geiger tube was shielded from the beam by 6 inches of lead. The betatron and the high voltage supply of the Geiger tube were controlled by a motor-driven timing switch which executed a duty cycle: Betatron—on 3 sec, off 5 sec, on 3 sec, etc., synchronous with counter off 3 sec, on 5 sec, off 3 sec, etc. The scaler pulse was fed directly to one pen of a two-channel Brush recorder. The other pen was fed 60-cycle ac to act as a timer. In this way it was possible to bombard the NaF sample for 3 sec and then count it within milliseconds after the beam was turned off for a period of 5 sec. Since the activity of the Na^{20} produced was so weak, it was necessary to sum a number of such runs in order to obtain better statistics. A series of consecutive runs summed is shown in Fig. 1. The half-life, 0.23±0.08 sec, agrees well with the value 0.25 sec reported by Alvarez.

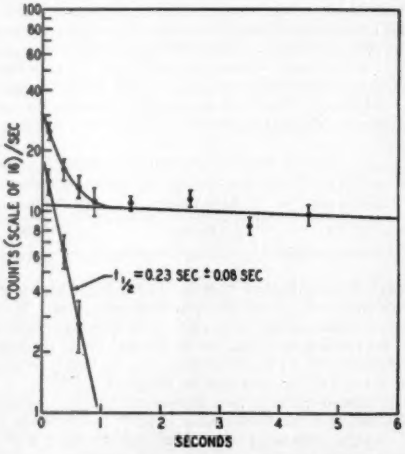

FIG. 1. Decay curve of NaF after bombardment with 0- to 76-Mev gamma-rays.

Using the mass 20.015 for Na^{20} one calculates 42.5 Mev as the threshold for the reaction $Na^{23}(\gamma, 3n)Na^{20}$. However, it was not possible to check this threshold. A series of runs using gamma-rays of 48-Mev maximum energy showed no Na^{20} activity. This is understandable in view of the diminution of total energy of the betatron beam with lower maximum energy and the much lower fraction of gamma-rays with energy sufficient to initiate the reaction in the lower maximum energy beam because of the shape of the gamma-ray spectrum.

Because of the low intensity of this second-order reaction it was not possible to measure accurately the energy of the Na^{20} activity. However, using the data of Alvarez, it is possible to put limits on the end point of the positron spectrum of 3.5 to 7.3 Mev.

The interest and advice of Professor Willard F. Libby throughout this work was deeply appreciated.

[1] L. Alvarez, Phys. Rev. 80, 519 (1950).

Microwave Resonance Absorption in Manganese Sulfates

H. Kumagai, K. Ōno, I. Hayashi, H. Abe, H. Shōno, S. Tachimori,* H. Ibamoto,† and J. Shimada
Institute of Science and Technology, Tokyo University, Tokyo, Japan
(Received April 5, 1951)

THE microwave resonance absorption in manganese sulfates was measured by Cummerow and others,[1] who observed strong and sharp resonance absorption. Recently we have repeated the experiment, using single crystals of $MnSO_4 \cdot 4H_2O$ and $MnSO_4 \cdot 5H_2O$ prepared by one of us (H. I.). These crystals are transparent with light pink color, while tetrahydrates are monoclinic ($\beta = 90° 53'$—P. Groth, Chem. Krystal Teil 2, 413) and pentahydrates are triclinic, very similar to $CuSO_4 \cdot 5H_2O$.

The half-value width of tetrahydrate is 920 oersteds when the direction of the static magnetic field is (100), 1310 oersteds at (010), and 1180 oersteds at (001), and that of pentahydrate is 1380 oersteds in the (001) direction. The g-value is about 2.05 in all these cases.

We then measured the absorption at different state of hydration in the following way. A single crystal of tetrahydrate is crushed to powder and the width is measured. Then, by heating the powder in air at 60~90°C for about an hour, we obtain monohydrate, which is very stable below 200°C and can be checked by weighing. After the width measurement by the powder, it is heated at 280~300°C to obtain anhydrate.

The absorption curves of polycrystals by the four states are shown in Fig. 1, and the half-widths are shown in Table I with some results in copper sulfates. The widths were reproducible within ±5 oersteds.

If Cummerow's sample was an ordinary commercial one, the measured value may be ascribed to something like monohydrate. In both cases of tetrahydrate and anhydrate, our widths are larger than those of Zavoisky, which may be, according to Van Vleck's considerations,[2] explained by widening action by the crystalline Stark effect which gives wide breadth in high microwave frequency; but it is doubtful whether Van Vleck's considerations can

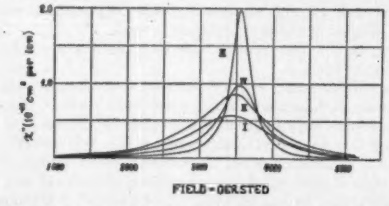

FIG. 1. Microwave resonance absorption curves for four polycrystalline states of manganese sulfate. I—$MnSO_4 \cdot 5H_2O$; II—$MnSO_4 \cdot 4H_2O$; III—$MnSO_4 \cdot H_2O$; IV—$MnSO_4$.

TABLE I. Half-width in polycrystals.

	Present paper $\lambda=3.0$ cm	Cummerow[1] $\lambda=3.2$ cm	Zavoisky (in Van Vleck's paper)	Calc. width by dipolar broadening (Van Vleck)
$MnSO_4\cdot 5H_2O$	1250 oersteds	...	...	...
$MnSO_4\cdot 4H_2O$	1140	415	400	1500
$MnSO_4\cdot H_2O$	305	...	...	...
$MnSO_4$	655	...	300	3500
$CuSO_4\cdot 5H_2O$	300	318		
$CuSO_4\cdot H_2O$	310	...		
$CuSO_4$	no absorption			

be applied here because the measured g-values in single crystals of tetrahydrates are almost constant in all orientations.

It is noticeable that, although the half-width of $MnSO_4\cdot 5H_2O$ is about four times larger than that of $CuSO_4\cdot 5H_2O$, they are almost equal in the case of $MnSO_4\cdot H_2O$ and $CuSO_4\cdot H_2O$. These differences may be ascribed to the different states of Mn^{++} and Cu^{++} ions, as the corresponding crystals have almost the same crystal structure.

The value of maximum χ'' per ion in the four states are shown in Table II.

TABLE II.

	$MnSO_4\cdot 5H_2O$	$MnSO_4\cdot 4H_2O$	$MnSO_4\cdot H_2O$	$MnSO_4$
χ''/ion	0.56×10^{-25}	0.84×10^{-25}	1.97×10^{-25}	0.98×10^{-25}

The microwaves were generated by a demountable klystron continuously evacuated by an oil diffusion pump. The absorption was measured by the change of transmitted power through a resonant cavity containing the sample, the cavity being always kept at resonance. The incident power was monitored by a directional coupler, and the magnetic field was measured by proton resonance. Our thanks are due to Professor T. Mutô and Professor M. Kotani for valuable discussions.

* Now at Department of Physics, Faculty of Science, Kanazawa University.
† Department of Chemistry, Faculty of Science, Osaka University, Osaka, Japan.

[1] Cummerow, Halliday and Moore, Phys. Rev. 72, 1233 (1947).
[2] J. H. Van Vleck, Phys. Rev. 74, 1168 (1948).

Forbidden Beta-Ray Spectra

A. M. SMITH
Department of Natural Philosophy, University of Aberdeen, Aberdeen, Scotland

(Received April 12, 1951)

RECENT developments in the study of shapes of forbidden beta-ray spectra have indicated that the interaction responsible for beta-decay may involve some linear combination of the five relativistically invariant forms which have hitherto been used.[1] (S, V, T, A, and P in the usual notation.) These developments are:

(a) The explanation of the shape of the spectrum of Cl^{36} using a combination of interactions.[2]

(b) The explanation of the shapes of a number of spectra, (e.g., Sr^{89}, Sr^{90}, Y^{90}, Y^{91}) using the α-factor.[3] This implies a first-forbidden transition with the tensor or axial vector form of interaction, and would not be affected by using a combination of interactions. (It would be affected by a combination of the tensor and axial vector forms, but this combination is already excluded on other grounds.)[4]

(c) The explanation of the shape of the spectrum of Be^{10} using the D_3 factor,[5] and of K^{40} using the C factor.[6] Neither of these would be affected by a combination of interactions.

In view of this, the cross correction factors for first- and second-forbidden transitions, which arise due to squaring of terms in the interaction, have been worked out and are given here, as they may be of interest to others who are engaged in comparing observed spectra with theoretical predictions. Fierz[4] has shown from consideration of the effect on the allowed spectrum that combinations of S with V and T with A must be excluded. We take as the invariant

$$I=\lambda_S S+\lambda_V V+\lambda_T T+\lambda_A A+\lambda_P P$$

with the understanding that $\lambda_S\lambda_V=\lambda_T\lambda_A=0$. Using the same notation and method as in reference (1), the first-forbidden cross correction factors are:

$$C_{ST}{}^1=i\lambda_S\lambda_T\Big[\Big\{\Big(\int\tau\Big)^*\cdot\int\sigma\times\mathbf{r}-\text{c.c.}\Big\}(L_1-M_0)$$
$$-\Big\{\Big(\int\tau\Big)^*\cdot\int\alpha-\text{c.c.}\Big\}(\tfrac{1}{3}KL_0+N_0)\Big],$$

$$C_{SA}{}^1=-i\lambda_S\lambda_A\Big[\Big\{\Big(\int\tau\Big)^*\cdot\int\sigma\times\mathbf{r}-\text{c.c.}\Big\}(\tfrac{1}{3}KN_0{}^-+L_1{}^-+M_0{}^-)\Big],$$

$$C_{VT}{}^1=\lambda_V\lambda_T\Big[i\Big\{\Big(\int\tau\Big)^*\cdot\int\alpha-\text{c.c.}\Big\}(\tfrac{1}{3}KL_0{}^--N_0{}^-)$$
$$+i\Big\{\Big(\int\tau\Big)^*\cdot\int\sigma\times\mathbf{r}-\text{c.c.}\Big\}(\tfrac{1}{3}KN_0{}^--L_1{}^-M_0{}^-)$$
$$-\Big\{\Big(\int\alpha\Big)^*\cdot\int\sigma\times\mathbf{r}+\text{c.c.}\Big\}$$
$$\times(\tfrac{1}{3}KL_0{}^--N_0{}^-)+2L_0{}^-\Big|\int\alpha\Big|^2\Big],$$

$$C_{VA}{}^1=\lambda_V\lambda_A\Big[i\Big\{\Big(\int\tau\Big)^*\cdot\int\sigma\times\mathbf{r}-\text{c.c.}\Big\}(L_1-M_0)$$
$$+\Big\{\Big(\int\alpha\Big)^*\cdot\int\sigma\times\mathbf{r}+\text{c.c.}\Big\}(\tfrac{1}{3}KL_0+N_0)\Big],$$

$$C_{TP}{}^1=-i\lambda_T\lambda_P\Big[\Big\{\Big(\int\sigma\cdot\mathbf{r}\Big)^*\int\gamma_5-\text{c.c.}\Big\}(\tfrac{1}{3}KL_0+N_0)\Big],$$

$$C_{AP}{}^1=\lambda_A\lambda_P\Big[i\Big\{\Big(\int\sigma\cdot\mathbf{r}\Big)^*\int\gamma_5-\text{c.c.}\Big\}$$
$$\times(\tfrac{1}{3}KL_0{}^--N_0{}^-)+2L_0{}^-\Big|\int\gamma_5\Big|^2\Big].$$

The second-forbidden cross correction factors are:

$$C_{ST}{}^2=i\lambda_S\lambda_T[\{\textstyle\sum_{ij}R_{ij}{}^*T_{ij}-\text{c.c.}\}\{\frac{1}{3}K^2(L_1-M_0)+\frac{1}{3}(L_2-M_1)\}$$
$$-\{\textstyle\sum_{ij}R_{ij}{}^*A_{ij}-\text{c.c.}\}$$
$$\times\{(1/30)K^2L_0+\tfrac{1}{3}K^2N_0+\tfrac{1}{3}KL_1+\tfrac{1}{3}N_1\}],$$

$$C_{SA}{}^2=-i\lambda_S\lambda_A[\{\textstyle\sum_{ij}R_{ij}{}^*T_{ij}-\text{c.c.}\}\{(1/15)K^2N_0{}^-$$
$$+\tfrac{1}{3}K^2(L_1{}^-+M_0{}^-)+KN_1{}^-+\tfrac{1}{3}(L_2{}^-+M_1{}^-)\}],$$

$$C_{VT}{}^2=\lambda_V\lambda_T[i\{\textstyle\sum_{ij}R_{ij}{}^*T_{ij}-\text{c.c.}\}$$
$$\times\{(1/15)K^2N_0{}^--\tfrac{1}{3}K^2(L_1{}^-+M_0{}^-)$$
$$+KN_1{}^--\tfrac{1}{3}(L_2{}^-+M_1{}^-)\}+i\{\textstyle\sum_{ij}R_{ij}{}^*A_{ij}-\text{c.c.}\}$$
$$\times\{(1/30)K^2L_0{}^--\tfrac{1}{3}K^2N_0{}^-+\tfrac{1}{3}KL_1{}^--\tfrac{1}{3}N_1{}^-\}$$
$$-\tfrac{1}{3}\{\textstyle\sum_{ij}A_{ij}{}^*T_{ij}+\text{c.c.}\}$$
$$\times\{(1/15)K^2L_0{}^--\tfrac{1}{3}K^2N_0{}^-+KL_1{}^--3N_1{}^-\}$$
$$+\textstyle\sum_{ij}|A_{ij}|^2\{\frac{1}{3}K^2L_0{}^-+\frac{1}{3}L_1{}^-\}],$$

$$C_{VA}{}^2=\lambda_V\lambda_A[i\{\textstyle\sum_{ij}R_{ij}{}^*T_{ij}-\text{c.c.}\}\{\frac{1}{3}K^2(L_1-M_0)+\frac{1}{3}(L_2-M_1)\}$$
$$+\tfrac{1}{3}\{\textstyle\sum_{ij}A_{ij}{}^*T_{ij}+\text{c.c.}\}$$
$$\times\{(1/15)K^2L_0+\tfrac{1}{3}K^2N_0+KL_1+3N_1\}],$$

$$C_{VP}{}^2=-i\lambda_V\lambda_P\Big[\Big\{\Big(\int\alpha\times\mathbf{r}\Big)^*\cdot\int\gamma_5\mathbf{r}-\text{c.c.}\Big\}$$
$$\times\{\tfrac{1}{3}KN_0{}^-+L_1{}^-+M_0{}^-\}\Big].$$

The L, M, and N functions are as given in reference 1, but because of the presence of the Dirac matrix β in some of the interactions and not in others, further functions L^-, M^-, and N^- have to be introduced. These are given below, and following the arrow in each case is an approximation good for $\alpha Z \ll 1$.

$$L_0^- = \left(\frac{2\pi}{F\rho^3}\right)\frac{g_0^3 - f_{-2}^3}{4\pi} = \frac{S+S^3}{2W} \rightarrow \frac{1}{W},$$

$$L_1^- = \left(\frac{2\pi}{F\rho^3}\right)\frac{g_1^3 - f_{-1}^3}{4\pi\rho^2} = \frac{F_1}{F}\frac{p^2}{9W}\frac{2S_1+S_1^3}{8} \rightarrow \frac{p^2}{9W},$$

$$L_2^- = \left(\frac{2\pi}{F\rho^3}\right)\frac{g_2^3 - f_{-1}^3}{4\pi\rho^4} = \frac{F_2}{F}\frac{p^4}{225W}\frac{3S_2+S_2^3}{18} \rightarrow \frac{p^4}{225W},$$

$$M_0^- = \left(\frac{2\pi}{F\rho^3}\right)\frac{f_0^3 - g_{-2}^3}{4\pi\rho^3}$$

$$= \frac{1}{W}\left[\frac{S-S^3}{2\rho^2} - \frac{\alpha ZW}{\rho}(1-S) + \frac{1}{(2S+1)^2}\{p^2(4S^4-7S^2+2) - \alpha^2Z^2(4S^3-S-2)\}\right]$$

$$\rightarrow \frac{1}{W}\left[\frac{\alpha^2Z^2}{4\rho^2} - \frac{p^2}{9}\right],$$

$$M_1^- = \left(\frac{2\pi}{F\rho^3}\right)\frac{f_1^3 - g_{-1}^3}{4\pi\rho^4}$$

$$= \frac{F_1}{F}\frac{p^2}{36W}\left[\frac{2S_1-S_1^3}{2\rho^2} - \frac{\alpha ZW}{\rho}(2-S_1) - \frac{1}{(2S_1+1)^2(1+S_1)}\left\{\frac{p^2}{2}(1+S_1)(4+4S_1+3S_1^2-2S_1^3) + \frac{\alpha^2Z^2}{2}(1+S_1) + \frac{\alpha^2Z^2W^2}{2}(8S_1^3-2S_1^2-21S_1-11)\right\}\right]$$

$$\rightarrow \frac{p^2}{36W}\left[\frac{\alpha^2Z^2}{4\rho^2} - \frac{4p^2}{25}\right],$$

$$N_0^- = \left(\frac{2\pi}{F\rho^3}\right)\frac{f_0g_0 + f_{-2}g_{-2}}{4\pi\rho} = -\left[\frac{\alpha ZS}{2\rho W} - \alpha^2Z^2\right] \rightarrow -\frac{\alpha Z}{2\rho W},$$

$$N_1^- = \left(\frac{2\pi}{F\rho^3}\right)\frac{f_1g_1 + f_{-1}g_{-1}}{4\pi\rho^3} = -\frac{F_1}{F}\frac{p^2}{36}\left[\frac{\alpha ZS_1}{2\rho W} - \alpha^2Z^2\right] \rightarrow -\frac{p^2}{36}\frac{\alpha Z}{\rho W}.$$

Work in connection with the comparison of complete correction factors with experimental spectra is proceeding.

[1] E. J. Konopinski and G. E. Uhlenbeck, Phys. Rev. 60, 308 (1941).
[2] Longmire, Wu, and Townes, Phys. Rev. 76, 693 (1949).
[3] L. M. Langer and H. C. Price, Phys. Rev. 76, 641 (1949).
[4] M. Fierz, Z. Physik 104, 553 (1936).
[5] H. W. Fulbright and J. C. D. Milton, Phys. Rev. 76, 1271 (1949).
[6] D. E. Alburger, Phys. Rev. 78, 629 (1950).

Magneto-Optics of an Electron Gas with Guided Microwaves*

L. Goldstein, M. Lampert, and J. Heney
Federal Telecommunication Laboratories, Inc., Nutley, New Jersey

(Received April 17, 1951)

In recent years the magneto-optics of electromagnetic wave propagation have been extended to guided propagation at microwave frequencies. In particular, Faraday-effect experiments have been made[1-3] in which the plane of maximum E-field of the TE_{11} mode in a circular wave guide is rotated by propagation through a section of the guide filled with a liquid or solid dielectric and located in an axial dc magnetic field. In all the published work to date, very small angles of rotation are obtained per guide wavelength, even at the gyromagnetic resonant field.

We have performed magneto-optic propagation experiments in circular wave guide in the range of frequencies 4600–5500 Mc/sec, employing as the dielectric the decaying plasma from a pulsed dc gas discharge. The main results are as follows:

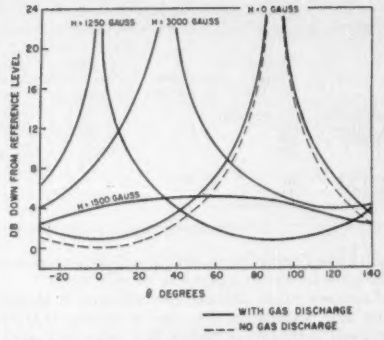

FIG. 1. Relative rf electric field distribution over periphery of circular wave guide. (Signal frequency: 5500 Mc/sec, Gas: Ne+1% at 1 mm Hg.) The reference plane for θ and the reference level for the E-field measurements are the plane and amplitude, respectively, of the maximum E-field with no discharge. Signal pulse 50 sec after 5 sec dc discharge pulse. Pulse voltage: 1050-v peak. Pulse current: 135-ma peak.

(1) Very large angles of rotation, on the order of 90° or more per guide wavelength, exhibiting a pronounced resonance behavior in the region where the gyromagnetic frequency of the electrons approaches the signal frequency.

(2) Departure from linear polarization as resonance is approached. Polarization becomes more broadly elliptical and finally almost purely circular at resonance.

(3) Demonstration of an analogue, for guided microwaves, of the crossed Nicol prisms experiment.

The anisotropic electron gas is produced by a pulsed dc discharge in a hot-cathode tube containing a rare gas, which completely fills a five-inch long section of guide which is enveloped by a solenoid. A signal pulse ten microseconds wide, with variable time delay after the dc discharge pulse, is sampled by a probe in a following section of guide, which can be mechanically rotated about the guide axis.

In Fig. 1 the rf electric field at the guide periphery is plotted as a function of angle for several values of magnetic field. In Fig. 2 the angle of rotation of the plane of maximum E-field is plotted as a function of magnetic field. The experimental conditions are

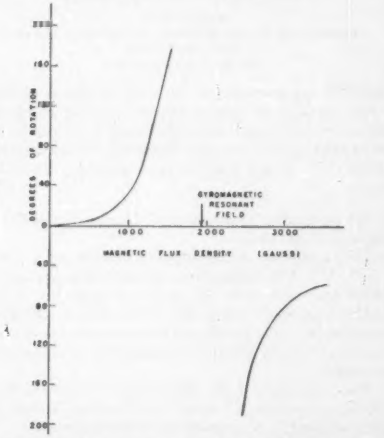

FIG. 2. Rotation of plane of maximum E-field vs magnetic field. The experimental conditions are the same as for Fig. 1.

indicated on the graphs. Measurements were made at 4600, 4900, 5200, and 5500 Mc/sec in a guide with cutoff at 4430 Mc/sec, over a range of gas pressures from 0.5 to 100 mm Hg, and at various dc pulse currents and voltages.

The results obtained are readily explained in terms of decomposition of the "linear" TE_{11} wave into two oppositely-rotating circularly-polarized waves, an "anomalous" and a "normal" wave. The "anomalous" wave exhibits, in the region of gyromagnetic resonance, very strong attenuation and a reversal of the sign of its phase shift with respect to propagation in vacuum. The "normal" wave is only slightly attenuated in this region and accounts for the circular polarization observed at gyromagnetic resonance.

The roles of "anomalous" and "normal" waves are interchanged if the sense of the magnetic field is reversed. Consequently, each of the circularly-polarized waves is heavily attenuated by one or the other of two opposing magnetic fields, both at gyromagnetic resonance. This fact enabled the construction, with two independent solenoids, of a microwave analogue of crossed Nicol prisms.

The circularly-polarized waves are not true propagating modes through the plasma in these experiments. Our interpretation remains, however, valid because a short section of plasma was employed. The theoretical details have been worked out for the case of the unbounded anisotropic plasma, including electron collision effects. Further theoretical work remains for the wave guide case.

These results hold promise as a tool for the study of gas discharge phenomena. They are applicable also to switching, amplitude, phase or frequency modulation, and polarization control in an electronically controllable medium.

* This work was sponsored by the Signal Corps Engineering Laboratories of the United States Army.

[1] P. Keck, Ann. Phys. 5, 15, 903 (1932).
[2] M. C. Wilson and G. F. Hull, Jr., Phys. Rev. 74, 711 (1948). R. G. Barnes and G. F. Hull, Jr., Phys. Rev. 82, 341 (1951).
[3] Mme. Soutif-Guichert and M. M. Lambinet, Compt. rend. 231, 1460 (1950).

Evidence for Ionosphere Currents from Rocket Experiments Near the Geomagnetic Equator*

E. Maple and W. A. Bowen, Jr.†
Naval Ordnance Laboratory, White Oak, Maryland
and
S. F. Singer‡
Applied Physics Laboratory, Johns Hopkins University, Silver Spring, Maryland
(Received April 19, 1951)

RECORDS of magnetic field as a function of altitude have been obtained from total-field magnetometers mounted in two Aerobee sounding rockets which were fired from the seaplane tender USS Norton Sound in March, 1949, off the west coast of Peru. The flights were made 60 miles apart at 89° west longitude, 11° south latitude or geomagnetic longitude 341°, geomagnetic latitude −1°.

The purpose of the flights was to obtain experimental evidence concerning the existence of an ionosphere current system. Harmonic analysis of the diurnal variation of the earth's magnetic field recorded at the earth's surface has shown that it could be represented as the field produced by a current system and that it was largely produced by an external source. It has been generally accepted, although not experimentally verified, that the source was a current system in the upper atmosphere. Several theories of the origin of such a current system have been proposed.[1]

A previous flight at White Sands, New Mexico, had shown the feasibility of the method and instrumentation.[2] The location at the geomagnetic equator was most favorable for detection of the ionosphere currents with a total-field magnetometer which measures the scalar value of the field without regard to direction. The field of the predicted currents in this region is parallel to the main field of the earth; also, the diurnal variation is anomalously large at Huancayo, Peru.

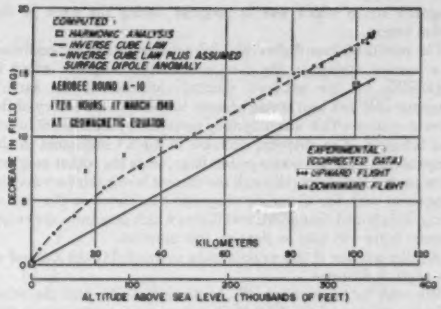

FIG. 1. Decrease of earth's magnetic field (from actual field at sea level) vs altitude above sea level for Aerobee A-10 flight.

Aerobee Round A-10 was fired on March 17, at 1720 hours 90th meridian time. Figure 1 shows that the field decreased between 20 km and 105 km, in accordance with the simple dipole field. At that time of day surface measurements show a small value for the diurnal variation, and no evidence of a current layer was obtained in the altitude range covered.

Aerobee A-11 was fired on March 22, at 1120 hours 90th meridian time when the diurnal variation at the surface is near a maximum. Figure 2 shows, in addition to the decrease of the main field of the earth, a decrease of about 4 milligauss between 93 km and 105 km. This decrease at the top of the flight could not be accounted for by sources inside the earth and is attributed to penetration of a current layer by the magnetometer.

Both flights show effects at low altitudes which are attributed to assumed dipole surface anomalies. No other information about surface anomalies in this region is available. The results are, however, consistent with anomalies observed on aerial surveys in other parts of the Pacific.[3]

The estimated accuracy of the decrease in field for the A-10 flight and for the A-11 flight up to 93 km is ±1 milligauss. The decrease in field for the A-11 Flight between 93 km and 105 km is placed at 4±0.5 milligauss.

The expected field discontinuity, if the magnetometer passed completely through the current layer, would be about twice the diurnal variation as measured at the earth's surface. The results of these flights are in reasonable agreement with the magnetograms from the observatory at Huancayo, Peru, for the days of the flights, although accurate correlation is difficult because of a

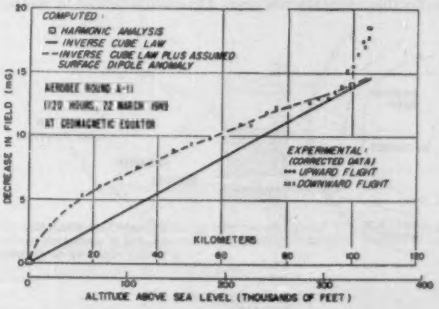

FIG. 2. Decrease of earth's magnetic field (from actual field at sea level) vs altitude above sea level for Aerobee A-11 flight.

magnetic storm which was in progress during the week of the rocket firings.

The results of these flights establish experimentally the existence of a current system in the *E*-region of the ionosphere which is responsible for the sea-level diurnal variation of the earth's magnetic field and lend strong support to the dynamo theory of the current system which was originally proposed by Balfour, Stewart, and Schuster. The observed decrease of 4 ± 0.5 milligauss in the range of 93 to 105 km seems rather large, since the rocket may not have passed completely through the current layer; this fact may be connected with the disturbed magnetic conditions on the day of firing. It is hoped that additional flights which penetrate the entire current layer will help to clear up this question.

A fuller account of this work is being submitted to the *Journal of Geophysical Research*.

We wish to thank Capt. T. A. Ahroon, USN, and the other officers and men of the USS Norton Sound who were responsible for the conduct of the expedition and the rocket firings. We would like to express our appreciation to our associates at the Naval Ordnance Laboratory, Mr. L. R. Alldredge, Dr. E. A. Schuchard, and Mr. C. J. Aronson, and at the Applied Physics Laboratory to Dr. J. A. Van Allen and Messrs. L. W. Fraser and A. V. Gangnes.

We are indebted to Dr. E. H. Vestine of the Department of Terrestrial Magnetism, Carnegie Institution of Washington, for advice on problems of the geomagnetic field.

* Supported by the U. S. Navy Bureau of Ordnance and the ONR.

† Now at the U. S. Naval Civil Engineering Research Laboratory, Port Hueneme, California.

‡ Now with the ONR, London Branch, London, England.

[1] For a discussion of the problems of the geomagnetic field and the upper atmosphere, see, for example, Terrestrial Magnetism and Electricity (McGraw-Hill Book Company, Inc., New York, 1939).

[2] Maple, Bowen, and Singer, J. Geophys. Research **55**, 115 (1950); Singer, Maple, and Bowen, Phys. Rev. **77**, 398 (1950).

[3] Alldredge and Keller, Trans. Am. Geophys. Union **30**, 494 (1949).

Total Cross Sections of π-Mesons on Protons and Several Other Nuclei*

C. CHEDESTER, P. ISAACS, A. SACHS, AND J. STEINBERGER
Columbia University, New York, New York

(Received April 20, 1951)

THE interaction of mesons with nuclei has previously been studied in photographic emulsions[1-3] and, to a lesser extent, in the cloud chamber.[4] As the first step in a study of the scattering and absorption of mesons by means of counter techniques, we have measured the total cross section of mesons in various elements, including hydrogen. The results are still preliminary, but their interest may warrant their release at this time. We studied the attenuation of a 100-Mev meson beam in the various absorbing materials, in a geometry (Fig. 1) which is poor enough so that the contribution of coulomb scattering to the measured cross section is smaller than the statistical error. The beam is defined by means of a time of flight telescope of sufficient time resolution to reject electrons and protons from the beam of mesons which travel with a velocity of $0.82c$. Actually a comparison of the shapes of the time resolution curves at various distances between the counters shows that the electron and proton components of the beam are negligibly small. The only other possible contamination in the beam consist of mesons with the wrong range, and μ-mesons produced by $\pi-\mu$-decay in flight. The μ-meson flux has been studied as a function of range by means of $\mu-e$-decay, and is 5 percent, concentrated chiefly at the high energy tail of the range curve (Fig. 2). The meson range has been studied by observing the counting rate, demanding a pulse which is several times minimum ionizing in the last counter. This selects mesons nearing the end of their range in this counter. The small counting rate in the short-

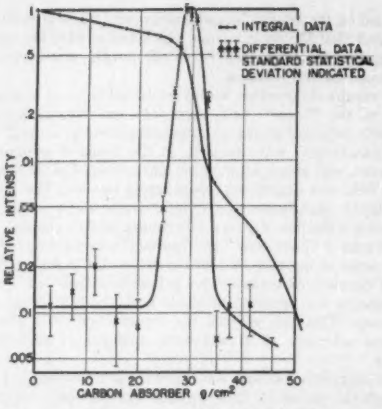

FIG. 2. Counting rate as a function of the delay time between the two beam defining counters.

TABLE I. Total cross sections of various nuclei for 85-Mev π^- mesons.

Nucleus	Mean free path g/cm²	Cross section in cm²	Nuclear area $\pi A^{\frac{2}{3}}\left(\frac{\hbar}{\mu c}\right)^2$ cm²
H	125 ± 10	$1.33 \pm 0.11 \times 10^{-24}$	6.1×10^{-26}
Li	48 ± 2	24.2 ± 1	22.6
Be	59 ± 4	25.3 ± 2	26.5
C	58 ± 2	34.4 ± 1.3	31.9
O	57 ± 2	46.6 ± 1.8	38.9
Al	72 ± 3	62.3 ± 2.5	55.1
Cu	106 ± 5	99 ± 5	98
Cd	117 ± 5	159 ± 7	142
Pb	143 ± 6	240 ± 11	214

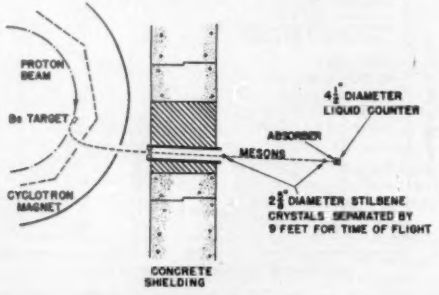

FIG. 1. Experimental arrangement.

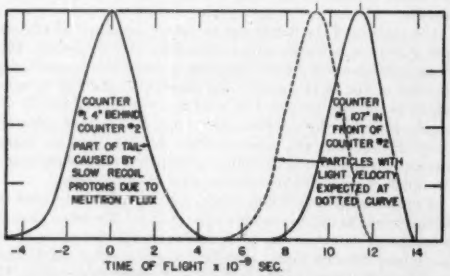

FIG. 3. Integral and differential range of the meson beam in carbon.

range region of this differential range curve (Fig. 2) is chiefly due to nuclear interaction of the mesons in the last counter, as can be calculated from the cross sections we obtain.

The results are listed in Table I. The hydrogen cross section is obtained by $C-CH_2$ subtraction. It will be noted that the hydrogen cross section is about 5 times smaller than $\pi(\hbar/\mu c)^2$. The heavier nuclei, however, all have geometrical cross sections. In the case of hydrogen, three reactions can occur:

$$\pi^-+P\rightarrow\pi^-+P \text{ scattering}, \quad (1)$$
$$\pi^-+P\rightarrow\pi^0+N \text{ charge exchange scattering}, \quad (2)$$
$$\pi^-+P\rightarrow N+h\nu \text{ radiative absorption}. \quad (3)$$

The last reaction has a cross section $\sim10^{-28}$ cm[2], as is known from the inverse reaction,[5] and so is small compared to the other two, which combine to a total cross section of $\sim1.33\pm0.11\times10^{-26}$ cm^2. It seems therefore that the interaction of the meson with the nucleon is not as strong as would be required for the success of strong coupling theories or the statistical considerations of Fermi.[6] Neither is it so weak that perturbation theory can be expected to be valid. (The total calculated cross section in the various perturbation theories is of the order $g^4(\hbar/\mu c)^2$; g^2 would have to be ~0.45 on the basis of this experiment.)

In the case of complex nuclei, in addition to being scattered it is possible for the meson to be absorbed. The work of Bernardini *et al.*[3] shows that at these energies meson absorption is the most probable process ($\sim$60 percent). This accounts for the fact that the cross sections of complex nuclei are geometrical, despite the small elementary scattering cross sections.

The absorption must be accompanied by an elastic diffraction scattering, which, however, is concentrated at such small angles to the beam direction that it makes only a very small contribution to the measured attenuation.

The small hydrogen cross section does rule out those interpretations of the meson interaction in heavy elements which are based on the idea that mesons scatter violently inside nuclei before either being absorbed or finally reemitted.

* Research assisted by the ONR and AEC.
[1] P. H. Fowler, Phil. Mag. **41**, 169 (1950).
[2] Bernardini, Booth, Lederman, and Tinlot, Phys. Rev. **80**, 924 (1950).
[3] H. Bradner and B. Rankin, Phys. Rev. **80**, 916 (1950).
[4] Camac, Corson, Littauer, Shapiro, Silverman, Wilson, and Woodward, Phys. Rev. **82**, 335 (1951).
[5] Bishop, Steinberger, and Cook, Phys. Rev. **80**, 291 (1950).
[6] E. Fermi, Prog. Theor. Phys. **5**, 570 (1950).

On the Cross Section for Photomeson Production

GENTARO ARAKI
Faculty of Engineering, Kyoto University, Yosida, Kyoto, Japan
(Received December 12, 1950)

THE observed values of the cross section for the production of positively charged photomesons have recently been published by Bishop, Steinberger, and Cook.[1] Their experiment will be compared with the meson theory in the following.

The exact expressions for the cross section were first derived by the present writer[2,3] on the scalar and pseudoscalar meson theories, and later by Brueckner[4] including the vector and pseudovector theories. The differential cross section for the positive-meson production by photons incident on a proton at rest are given by[5-7] (s: scalar theory; ps: pseudoscalar theory)

$$d\sigma_s=a_s\phi_s d\epsilon/\epsilon_0^2 \qquad d\sigma_{ps}=a_{ps}\phi_{ps}d\epsilon/\epsilon_0^2 \quad (1)$$
$$a_s=(\pi/2)(eg/M)^2 \qquad a_{ps}=(\pi/2)(ef_3/M)^2 \quad (2)$$
$$\phi_s=v+\{2-(b^2/2)\}w \qquad \phi_{ps}=v-(b^2/2)w \quad (3)$$
$$v=\{\epsilon-(b^2/2)\}/\epsilon_0 \qquad w=(\epsilon^2-b^2)\sin^2\theta/[\epsilon_0+(b^2/2)-\epsilon]^2 \quad (4)$$

where f_3 stands for $f_1+(2Mf_3/\mu)$, and g, f_1, and f_3 are the constants for scalar, pseudoscalar, and pseudovector couplings of mesons with nucleons, μ and M are masses of a meson and a proton, respectively, b denotes μ/M, ϵ_0 and ϵ are energies of the incident photon and the emitted meson in units of M, respectively ($\hbar=c=1$), and θ is an angle between directions of the incident photon and the emitted meson. The relation between θ, ϵ, and ϵ_0 is given by

$$\epsilon_0(\epsilon^2-b^2)^{\frac{1}{2}}\cos\theta=(1+\epsilon_0)\epsilon-\epsilon_0-(b^2/2). \quad (5)$$

We first compute the differential cross section per steradian at $\theta=90°$ for various photon-energies from Eqs. (1)–(5). The result is compared with the experiment of Bishop, Steinberger, and Cook[1] in Fig. 1. The values of constants used in this computation are $\mu=286m$, $M=1840m$ (m=electron mass), $g^2=1.5$, and $(\mu f_3/2M)^2=0.2$. The last value of the coupling constant for pseudoscalar mesons was determined from the binding energy of the deuteron by the writer and Mori.[8] We find a rough agreement of the pseudoscalar theory with the experiment. The scalar theory shows a good energy dependence, but this does not imply its agreement with the experiment because the value of g is adjusted so as to fit the experiment. Moreover, it has an angular inconsistency, as was pointed out by these experimenters.[1]

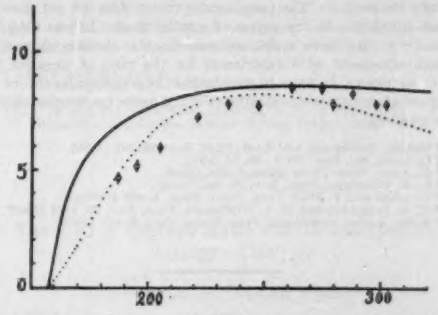

FIG. 1. Energy dependence at 90°. Abscissa: energy of incident photons in Mev. Ordinate: cross section in 10^{-30} cm^2/steradian. Circles: experimental results of Bishop, Steinberger, and Cook. Full curve: pseudoscalar theory $[f_3+(\mu/2M)f_1]^2=0.2$. Dotted curve: scalar theory $g^2=1.5$.

We next transform the above expressions to those in the center-of-mass system. The angular dependence, in this system, of the cross section per steradian for photon-energy of 250 Mev (in the laboratory system) is compared with the experiment of the abovementioned authors[1] in Fig. 2. We see that the scalar theory is

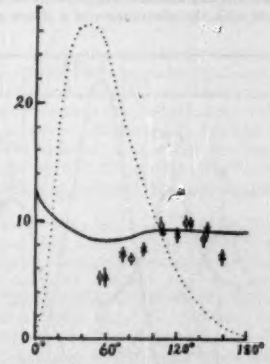

FIG. 2. Angular dependence for photon energy of 250 Mev. Abscissa: angle of emission in the center-of-mass system in degrees. Ordinate: cross section in 10^{-30} cm^2/steradian.
Circles } : experimental results of Bishop,
Crosses }
Steinberger, and Cook for {liquid hydrogen / carbon-paraffin.
Full curve: pseudoscalar theory $[f_3+(\mu/2M)f_1]^2=0.2$. Dotted curve: scalar theory $g^2=1.5$.

fatally inconsistent. The pseudoscalar theory does not yet show a good agreement in the region of smaller angle. It was already found[3,4,6,7] that both scalar and pseudoscalar theories showed a rough agreement with experiment for the ratio of negative to positive mesons. In order to see whether the pseudoscalar theory is in good agreement with experiment or not, more exact experiments are required.

[1] Bishop, Steinberger, and Cook, Phys. Rev. **80**, 291 (1950).
[2] G. Araki, Sci. Pap. IPCR. **39**, 14 (1941).
[3] G. Araki, Prog. Theor. Phys. **5**, 307 (1950).
[4] K. A. Brueckner, Phys. Rev. **79**, 641 (1950).
[5] G. Araki and Y. Mori, Prog. Theor. Phys. **5**, 505 (1950).
[6] K. A. Brueckner and M. L. Goldberger, Phys. Rev. **76**, 1725 (1949).
[7] Koba, Kotani, and Nakai, Prog. Theor. Phys. **5**, 137 (1950).

The Radioactive Decay of Ca^{41}

V. L. Sailor and J. J. Floyd
Brookhaven National Laboratory, Upton, Long Island, New York
(Received April 27, 1951)

THE threshold of the $K^{41}(p,n)Ca^{41}$ reaction[1] indicates that Ca^{41} should decay by electron capture to K^{41}. The half-life of Ca^{41} has previously been listed as approximately 10 days;[2,3] however, several unsuccessful attempts to verify this result make it subject to doubt.[4,5]

We have observed x-rays resulting from the decay of Ca^{41} by using a proportional counter x-ray spectrometer of the type described by Bernstein *et al.*[6] X-rays from the source entered a high multiplication proportional counter through a thin Be window. Most of the x-rays were absorbed in the counter gas and produced pulses proportional to the x-ray energy. The pulse distribution was obtained with a sliding channel pulse-height analyzer. A homogeneous x-ray gave a single peak having a full width at half-maximum of about 20 percent. The resolution of the instrument permitted the K_α x-rays of adjacent elements to be distinguished.

The analyzer was calibrated with Fe^{55}, V^{49}, and A^{37} (Fig. 1).[7] Table I lists the energies of the characteristic x-rays in the vicinity of calcium and a few isotopes which emit these x-rays.

The calcium sample was listed as item No. 13A of the "Irradiated Units" in the AEC Isotopes catalog.[8] It had been irradiated in a neutron flux of about 10^{13} from June 13, 1949, to July 11, 1949. The measurements were made in July, 1950, more than a year after the irradiation. The sample contained some Ca^{45}, which emits β-particles with a 152-day half-life. The presence of the β-particles did not interfere with the observation of a 3-kev x-ray because most of the β-particles lost 12 to 15 kev in the counter, and consequently produced much larger pulses. The β-background at 3 kev was about 30 percent. X-rays produced by β-particles striking the counter walls, neighboring atoms of calcium, etc., were found to be negligible for such a weak source by taking measurements with P^{32} sources of various strengths.

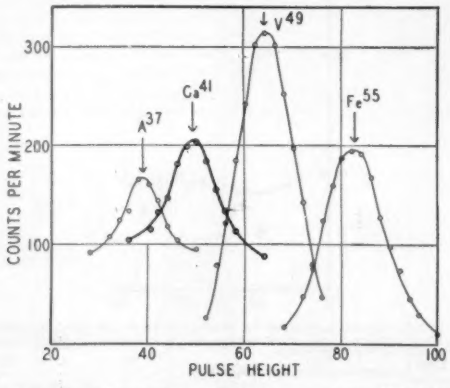

FIG. 1. X-rays from electron capture. The x-ray peaks are obtained by a proportional counter x-ray spectrometer. The relative amplitudes of the peaks have no significance.

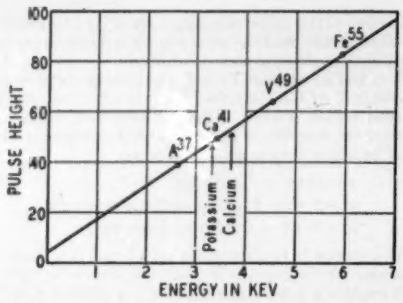

FIG. 2. Calibration curve of pulse-height analyzer. A plot of the K_α x-ray energy *vs* the analyzer setting at the peak shows the linearity of the analyzer. The peak from the calcium sample falls at a position which corresponds to a potassium K_α x-ray.

TABLE I. K_α x-rays and some radioactive isotopes decaying by electron capture.

Radioactive isotope	Characteristic x-ray	K_α x-ray energy
A^{37}	17 chlorine	2.625 kev
K^{40}	18 argon	2.96
Ca^{41}	19 potassium	3.316
	20 calcium	3.694
	21 scandium	4.092
V^{49}	22 titanium	4.512
Fe^{55}	25 manganese	5.898

The x-ray emitted by the irradiated calcium had an energy of 3.40 ± 0.15 kev (Fig. 2). This apparently is a potassium K_α x-ray (3.31 kev), which indicates that some isotope of calcium is decaying by electron capture. Examination of the isotope tables shows that Ca^{41} is the only reasonable choice, as none of the other calcium isotopes can be associated with electron capture.

It appears, therefore, that Ca^{41} decays by electron capture and has a half-life of the order of several months. At present a sample of enriched Ca^{40} is being irradiated in the Brookhaven reactor. It will be used for a more precise measurement of the half-life of Ca^{41}.

[1] H. T. Richards and R. V. Smith, Phys. Rev. **74**, 1257 (1948).
[2] K. Way and G. Haines, AECD 2138 (1948).
[3] Walke, Thompson, and Holt, Phys. Rev. **57**, 177 (1940).
[4] R. Overstreet and L. Jacobson, Phys. Rev. **72**, 349 (1947).
[5] D. E. Matthews and M. L. Pool, Phys. Rev. **72**, 163 (1947).
[6] Bernstein, Brewer, and Rubinson, Nucleonics **6**, No. 2, 30 (1950).
[7] The V^{49} source was kindly furnished by Professor E. C. Pollard at Yale University.
[8] "Isotopes," Catalog and Price List No. 3, July 1949, USAEC.

Magnetic Analysis of the $B(\alpha, p)C$ Reaction

G. M. Frye[*] and M. L. Wiedenbeck
Department of Physics, University of Michigan, Ann Arbor, Michigan
(Received April 30, 1951)

THE two most recent reports on the $B(\alpha, p)C$ reaction by Perkin[1] and Creagan[2] have given the following Q values: 4.07, 0.85, 0.31, 0.07, −0.31, −1.57, −1.76, and 4.08, 3.35, 0.65, 0.15, −0.57 Mev, respectively. Use of a separated isotope target by Creagan identified the 0.85 group as belonging to B^{11}, the others to B^{10}.

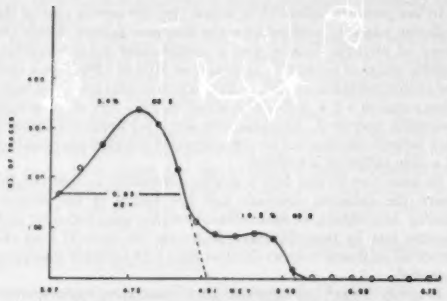

FIG. 1. High energy proton groups. The ratio of peak No. 3 to the background is approximately 170.

In this investigation a semicircular focusing magnetic spectrograph was used to analyze the protons produced by a polonium alpha-particle source. The source and target were $1\frac{1}{2}\times\frac{1}{4}$ in. with a separation of $\frac{1}{4}$ in. between them. This "poor" geometry was necessary to give an appreciable proton intensity and resulted in a broad line for each group (Fig. 1). However, Q may be determined from the value of the high energy cutoff, since, for observation in the direction of the alpha-beam, the most energetic protons are those formed on the surface of the target nearest the source by alphas striking the target normally. Adding the energy loss in the target to the cutoff value gives the total proton energy.

NTA plates, inclined at an angle to the proton beam, were employed as the detector. They were covered with an 8-mg/cm² layer of collodion to screen off stray Po alpha-tracks. This layer was soaked off with a 9 to 1 acetone-water solution before developing. By counting only tracks of the right direction and length, the effect of background radiation and particles scattered in the chamber was eliminated. This enabled one to make long exposures without accumulating appreciable background. The actual exposure times ranged from 37 to 199 hr. The targets were either of pressed boron powder or B_2O_3 evaporated onto a tin foil, and varied in thickness from 1.1 to 2.2 cm of air. This air equivalent was determined by measuring in the spectrometer the energy loss of Po alphas in passing through the target. The magnet used had a maximum usable radius of 26 cm at a field of 18,200 gauss. Current regulation was achieved by a circuit of the type described by Lawson and Tyler.[3]

The energy of each proton group was determined by comparing its radius of curvature with that of the Po 5.300-Mev line. Thus for protons of energy 4–6 Mev (groups 2 and 3 below), the effect of small inhomogeneities in the field are greatly reduced.

Results (See Table I):

$Q\sim3.8$ Mev. Evidence was found for a high energy proton group, but the intensity was too low to give an accurate value.

$Q_2=0.75$ Mev. Using an enriched B^{10} target confirmed the assigning of this group to B^{11}. Five determinations gave a mean deviation of 0.01 Mev. Using mass values from Mattauch's[4] tables, this gives the mass of C^{14} as 14.007824 amu.

$Q_3=0.24$ Mev. Six determinations gave a mean deviation of 0.02 Mev. This larger uncertainty is due to the fact that groups 2 and 3 were not completely resolved, and thus the high energy cutoff of group 3 was partially masked.

TABLE I. Summary of Q values found in this work.

Q Values	
B^{10}	B^{11}
~3.8 Mev	0.75±0.01
0.24±0.02	
−0.22	

$Q_4=-0.22$ Mev. This group was observed only for the run where the protons were observed at 90° to the alpha-beam.

* AEC Predoctoral Fellow.
† J. L. Perkin, Phys. Rev. **79**, 175 (1950).
‡ R. J. Creagan, Phys. Rev. **76**, 1769 (1949).
[3] J. L. Lawson and A. W. Tyler, Rev. Sci. Instr. **10**, 304 (1939).
[4] J. Mattauch and S. Flugge, Nuclear Physics Tables (1946).

The L to K Capture Ratio and Disintegration Energy of $^{113}_{49}$In^{113}

D. A. THOMAS,*† S. K. HAYNES, AND C. D. BROYLES*
Vanderbilt University,‡ Nashville, Tennessee
AND
H. C. THOMAS
Mississippi State College,‡ State College, Mississippi
(Received April 30, 1951)

THE decay scheme of Sn^{113} based on the work of Barnes[1] and of Lawson and Cork[2] is given by the latter to consist of orbital capture to an excited state of In^{113} which then reaches its ground state by successive 85-kev and 390-kev transitions. The properties of the latter transition were found to be: half-life 104 minutes, $\alpha=2.3\pm0.3$ or 0.7 ± 0.1,[3] $\alpha_K/\alpha_L=5.4$. Later Coleman and Poole[4] failed to find the 85-kev gamma-ray.

In order to examine the possibility of direct transitions to the 390-kev state and to the ground state, we have made the following measurements on this activity. (a) With a counter of known beta- and gamma-ray sensitivity, α for the 390-kev transition was found to be 0.35 ± 0.1. The 85-kev gamma-ray, if present, was found to have an intensity of less than one percent of the 390-kev gamma-ray. (b) With a low energy compensated magnetic lens spectrometer,[5] a very thin electroplated source, and two thin Nylon windows (36 and 18 μg/cm²) the intensity of the K Auger electrons relative to the total conversion electrons of the 390-kev transition was found to be 0.61 ± 0.01. The thinness of the source is indicated by the almost complete absence of low energy tail on the 20-kev Auger line. The transparency of the counter window is indicated by the fact that the thinner window increased the 20-kev Auger-line intensity by only 3.8 percent. Correction for window loss is included in the above ratio. The conversion electrons of the 85-kev transition, if present, were found to have an intensity less than one percent of the conversion electrons of the 390-kev transition. All other measurements, where made, were in agreement with previous values.

According to Weisskopf[6] a half-life of 105 minutes for a 390-kev transition is consistent with a magnetic 2^4-pole radiation; therefore the spin of In^{113*} is probably $\frac{1}{2}$. Using a value of $\alpha_K=0.45$, as found in Rose's tables,[7] together with the measured value of α_K/α_L, the theoretical conversion coefficient is 0.53. Although the accuracy of our value is not sufficient to show that the theoretical value is wrong, it is apparent that the previous value was considerably too high. In the following argument the conversion coefficient will be assumed to be 0.53.

From the values of α_K/α_L, α, the Auger coefficient (one minus the fluorescence yield), and the Auger-conversion electron ratio, it can be shown that a negligible number of transitions direct to the ground state can occur and that more than normal L capture occurs. The chief uncertainty in the ratio of L capture to K capture as determined above is the Auger coefficient for indium. The theory of Massey and Burhop[8] gives 0.216, while the experimental results for $Z>40$ almost all give larger values than theory.[9,10] It is therefore assumed that the most probable value of the Auger coefficient for indium is 0.25 and that 0.20 and 0.30 represent outside limits. Using these values the most probable ratio of L capture to K capture is 0.81 with extreme values of 0.31 and 1.43. The ratio normally expected is only 0.115.[11]

Using the theoretical results of Marshak[12] and Rose and Jackson,[11] it can be shown that the orbital capture to the 390-kev

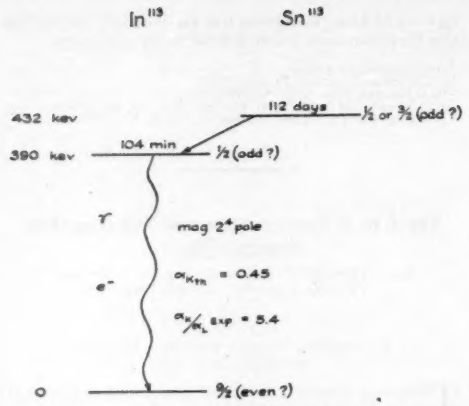

FIG. 1. Proposed decay scheme of Sn^{113}.

state is allowed. By use of these results the most probable value of disintegration energy is computed to be 42 kev with outside limits of 65 kev and 37 kev.

Since the orbital capture transition is allowed, the spin of Sn^{113} is $\frac{1}{2}$ or $\frac{3}{2}$. The transition to the ground state of In^{113} is therefore at least second- and probably third-forbidden. The transition to a state 85 kev above the 390-kev state is energetically forbidden. The proposed decay scheme is shown in Fig. 1. Further measurements on the conversion coefficient of the 390-kev transition and on the Auger coefficient for indium are being made to improve the accuracy of these results.

* AEC Predoctoral Fellow.
† Now at the University of the South, Sewanee, Tennessee.
‡ This work was supported by the Research Corporation, the Carnegie Foundation for the Advancement of Teaching, the Natural Science Research Fund of Vanderbilt University, and a contract with the AEC.

[1] S. W. Barnes, Phys. Rev. **56**, 414 (1939).
[2] J. L. Lawson and J. M. Cork, Phys. Rev. **57**, 982 (1940).
[3] The statement "Conversion coefficient of 70 percent" made in 1939 might well imply that 70 percent of all transitions were converted.
[4] K. D. Coleman and H. L. Poole, Phys. Rev. **72**, 1070 (1947).
[5] S. K. Haynes and J. W. Wedding, Rev. Sci. Instr. **22**, 97 (1951).
[6] R. D. Hill, Phys. Rev. **81**, 470 (1951).
[7] M. E. Rose *et al.*, *Tables of K-shell Conversion Coefficients*.
[8] H. S. S. Massey and E. H. S. Burhop, Proc. Roy. Soc. (London) **153**, 661 (1936).
[9] Steffen, Huber, and Humbel, Helv. Phys. Acta **22**, 222 (1949). The values given here when corrected for even the minimum L capture are greater than theoretical.
[10] L. S. Germain, Phys. Rev. **80**, 937 (1950).
[11] M. E. Rose and J. L. Jackson, Phys. Rev. **76**, 1540 (1949).
[12] R. E. Marshak, Phys. Rev. **61**, 431 (1942).

Concerning the Mechanism of Electron-Ion Recombination

MANFRED A. BIONDI AND T. HOLSTEIN
Westinghouse Research Laboratories, East Pittsburgh, Pennsylvania
(Received April 23, 1951)

MICROWAVE studies of electron-ion recombination[1,2] have yielded recombination coefficients 10^3 to 10^5 times larger than those predicted by quantum theory for radiative capture of electrons by ions. In an effort to determine the capture mechanism occurring in these experiments, we have simultaneously measured the electron density and radiation emitted from the ionized gas. Measurement of the electron density was accomplished by microwave techniques,[3] while a gated photomultiplier and a shuttered spectrograph were used to determine the intensity and spectral distribution of the radiation emitted from the recombination process.

In low pressure helium (1 to 5 mm Hg) the square root of the radiation intensity emitted from the afterglow follows closely the decay of electron density over a considerable range.[4] Spectrographic plates covering the interval from 3700 to 7200A show that the visible radiation consists of line spectra originating from high-lying states ($n=3, 4, 5, 6$) which are all within 1.5 ev of the atomic ionization potential. Absolute intensity measurements indicate that for each electron lost by recombination, roughly one quantum of visible radiation is emitted.

In neon ($p=10$ mm Hg) a similar correlation is observed between the radiation intensity and the square of the electron density. In addition, we again observe roughly one photon for each electron lost by recombination. However, the spectral lines observed all originate from levels more than 0.85 ev below ionization potential.

Recently Bates[6] has suggested that dissociative recombination between electrons and molecular ions is responsible for the large capture cross sections. The process is illustrated for helium in Fig. 1. Thermal electrons are captured by molecular ions in electronic state A; the system then attains a nearby electronic state B, which is presumed repulsive, leading to the dissociation of the unstable excited helium molecule into a normal and an excited atom. If the molecular ion is assumed to be in its ground vibrational state,[6] the energy of the final excited atom can be at most equal to the atomic ionization potential, V_I, minus the dissociation energy, D, of the molecular ion.

For the case of Ne_2^+, this energy limitation might well explain the absence of lines originating from higher states (within 0.85 ev of V_I); unfortunately lack of knowledge of $D(Ne_2^+)$ does not permit a quantitative check.

In the case of helium, however, $D(He_2^+)$ has been computed[7,8] and experimentally estimated[9] to lie between 2.2 and 3.1 ev. Hence our observation of lines originating from atomic levels which are only 0.3 to 1.5 ev below V_I (see C of Fig. 1) presents difficulties for the dissociation hypothesis which, it appears, can be resolved only by the presumption that He_2^+ ions are present in sufficiently high vibrational states. At the pressures employed in our experiments (1–5 mm Hg) the collision frequency of He_2^+ ions with helium atoms is $\sim 10^7$–10^8 sec^{-1}. In order that He_2^+ ions remain in high vibration states for $\sim$5 milliseconds (the duration of observations) it is necessary that the probability of vibrational de-excitation be $\lesssim 10^{-6}$ per collision.

A discussion of the lifetime of vibration states is contained in a recent review article by Massey.[10] Experimental results vary greatly from gas to gas; however there are cases reported in which the vibration excitation persists for $\sim 10^6$ collisions. A theoretical estimate for helium (from formulas in reference 10) indicates that the probability of de-excitation of vibration for a molecular ion in a vibration state 0.3 ev below V_I (state X of Fig. 1) is of the order of 10^{-8} per collision. Thus the metastability of high vibration states, while a somewhat extreme hypothesis, must be considered; on this

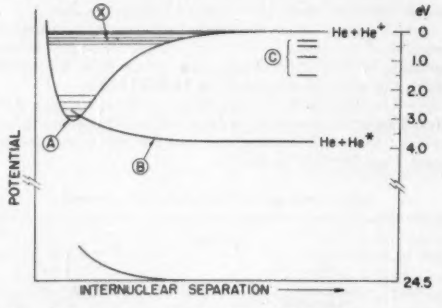

FIG. 1. Dissociative recombination for He_2^+. Some of the vibration levels are omitted.

basis dissociative recombination is still capable of describing our observations.

In order to study the recombination under conditions which rule out the dissociative process, it is necessary to insure the absence of molecular ions during our measurements. Consequently, studies using helium-argon and neon-argon mixtures are planned in which there is sufficient argon to permit rapid ionization of argon atoms by helium or neon metastables, but insufficient concentration to permit formation of molecular argon ions.[11] Since previous work[1] has shown that argon gas also exhibits a large recombination coefficient, the proposed experiments should demonstrate whether atomic or molecular ions are responsible for the large electron capture cross sections.

The authors wish to thank A. O. McCoubrey, who designed the gated photomultiplier circuits.

[1] Biondi and Brown, Phys. Rev. **75**, 1700 (1949); **76**, 1697 (1949).
[2] Johnson, McClure, and Holt, Phys. Rev. **80**, 376 (1950).
[3] M. A. Biondi, (to be published).
[4] If the radiation originates from recombination, its intensity should follow the rate of change of electron density, which is proportional to the square of the electron density.
[5] D. R. Bates, Phys. Rev. **77**, 718 (1950); **78**, 492 (1950).
[6] D. R. Bates, Phys. Rev. **82**, 103 (1951).
[7] L. Pauling, J. Chem. Phys. **1**, 56 (1933).
[8] S. Weinbaum, J. Chem. Phys. **3**, 547 (1935).
[9] G. Herzberg, *Spectra of Diatomic Molecules* (D. Van Nostrand Company, Inc., New York, 1950), second edition, p. 536.
[10] H. S. W. Massey, Rep. Prog. Phys. **12**, 262 (1948–49).
[11] The existence of stable HeA$^+$ (or NeA$^+$) ions seems quite unlikely; in particular the one-electron "resonance" interaction responsible for the formation of homonuclear diatomic ions is nonoperative by virtue of the discrepancy in the ionization potentials of the constituent atoms.

The Energy and Angular Distribution of the Gamma-Rays from the Reaction $Li^7(p, \gamma)Be^8$

H. Narholz, P. Stoll, and H. Wäffler*
Federal Institute of Technology, Zürich, Switzerland
(Received April 23, 1951)

During the last years, spectroscopy of high energy gamma-rays has been performed mainly by the use of pair spectrometers.[1] Instead of applying the pair creation process to the determination of quantum energies, one can, in principle, also use suitable (well-known Q-values) photonuclear reactions which give rise to particles of exactly measurable energies. Examples of such reactions are: the photodisintegration of the deuteron, the photofission of C^{12} into three alpha-particles, the (γ, p)-reaction on O^{16}. We have chosen the $C^{12}(\gamma, \alpha)2\alpha$-reaction for analyzing the gamma-rays emitted from the 17.6-Mev state of the Be^8 nucleus. This highly excited state is created by protons of 440-kev energy in a resonance capture process on Li^7. Nuclear track plates (English Kodak NT 1a, emulsion thickness 200 microns) have been irradiated for 60 hours with gamma-rays from a thick target of pure lithium at proton energies of 450–500 kev. The gelatin of the emulsion contains sufficient carbon to give rise to about 40 stars per cm,[2] formed by the three emitted alpha-particles, without overly strong background fogging. Since the Q-value of this reaction is -7.35 ± 0.12 Mev, gamma-rays with quantum energies greater than about 12 Mev can be determined by this method. Errors which arise from the microscopic measurement of the alpha-track length may be corrected to some extent by a check of the momentum balance of the reaction. In Fig. 1 the number of stars as a function of the total energy of the three alpha-particles is given. The two groups at 10.3 and 7.4 Mev are those associated with the well-known gamma-lines of 17.6 and 14.7 Mev, which correspond to transitions to the ground state and the first excited state of Be^8, respectively. In addition to these, a very weak third group at about 5.2 Mev appears. It would correspond to a gamma-line of about 12.6 Mev, which in turn relates to a 5-Mev state of Be^8. Since a state at 4.9 Mev in Be^8 is already known, and the gamma-rays leading from it to the ground state have been observed,[3] it seems reasonable that, corresponding to the figure, approximately 10 percent of the transitions from the resonant 17.6-Mev state would lead to the 4.9-Mev state of Be^8. Since the

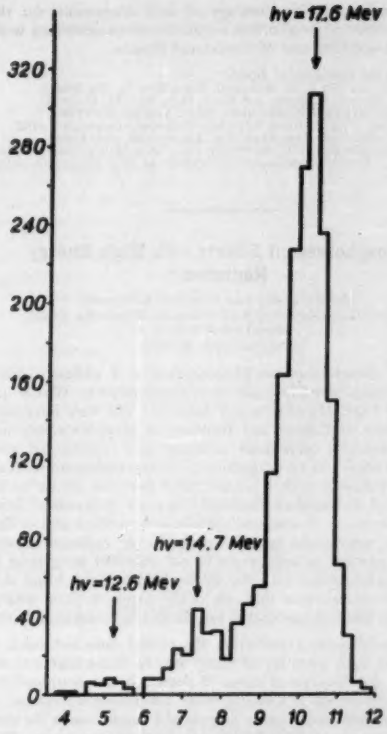

Fig. 1. Energy distribution of carbon stars. Abscissa: total energy of the three alpha-particles. Ordinate: number of stars per 0.25-Mev interval.

frequency of stars is proportional to the number of the corresponding quanta times the cross section of the $C^{12}(\gamma, \alpha)2\alpha$-reaction, Fig. 1 does not give directly the energy distribution of the gamma-rays. From the work of Walker and McDaniel[4] who give for the resonant radiation a ratio of 2:1 for the number of quanta at 17.6 and 14.7 Mev, respectively, one can estimate a $C^{12}(\gamma, \alpha)2\alpha$ cross-section ratio of 4:1 for 17.6 and 14.7 Mev, respectively.

By simultaneously irradiating plates which were positioned at various angles with respect to proton beam and the emitted gamma-rays, we were also able to measure their angular distribution. In a preliminary communication, isotropy of the 17.6-Mev line together with a remarkable asymmetry of the 14.7-Mev component were reported.[5,4] Meanwhile, two investigations concerning the angular distribution of the lithium gamma-rays have appeared.[6,4] In both of them the resonant gamma-rays, 17.6 as well as 14.7 Mev, have been found to be isotropic within the limits of error. A thorough reinvestigation of our measurements has shown that the first reported result[5] was erroneous. Our revised measurements give us, from a statistics of 2200 stars, the following intensity ratios:

$$\left[\frac{J(14.7)}{J(17.6)}\right]_{\vartheta=0^\circ} \Big/ \left[\frac{J(14.7)}{J(17.6)}\right]_{\vartheta=45^\circ} = 1.04\pm0.30;$$

$$\left[\frac{J(14.7)}{J(17.6)}\right]_{\vartheta=0^\circ} \Big/ \left[\frac{J(14.7)}{J(17.6)}\right]_{\vartheta=90^\circ} = 1.14\pm0.25;$$

$$\left[\frac{J(14.7)}{J(17.6)}\right]_{\vartheta=0^\circ} \Big/ \left[\frac{J(14.7)}{J(17.6)}\right]_{\vartheta=135^\circ} = 1.02\pm0.25.$$

This, therefore, signifies isotropy of both components for the resonant radiation in accordance with the abovementioned work of Devons and Hine and McDaniel and Stearns.

* Now at the University of Zürich.
[1] R. L. Walker and B. D. McDaniel, Phys. Rev. **74**, 315 (1948).
[2] Benett, Bonner, Richards, and Watt, Phys. Rev. **71**, 11 (1947).
[3] Nabholz, Stoll, and Wäffler, Helv. Phys. Acta **23**, 858 (1950).
[4] H. Wäffler, Proc. of Harwell Nuclear Conference (September 1950).
[5] Devons and Hine, Proc. Phys. Soc. (London) **63**, 1202 (1950).
[6] M. B. Stearns and B. D. McDaniel, Phys. Rev. **82**, 450 (1951). We are indebted to Professor McDaniel for sending us this manuscript before publication.

Phosphorescent Effects with High Energy Radiation*

MILTON FURST AND HARTMUT KALLMANN
Physics Department, New York University, Washington Square, New York, New York
(Received April 26, 1951)

THE fluorescence and phosphorescence of sodium chloride crystals have previously been investigated by Glasser and Beaseley[1,2] and Mandeville and Albrecht.[3] The very interesting observations of Glasser and Beaseley on phosphorescence and light stimulation have been extended and investigated more quantitatively. Our investigations have been conducted on NaCl crystals activated with 1 percent AgCl provided for us by the courtesy of the Harshaw Chemical Company. An essential difference between our crystals and theirs may be a much greater light efficiency, since under gamma-irradiation our activated crystals were as efficient as anthracene in our standard integrating intensity arrangement with the 1P28 photomultiplier,[4] and since after light stimulation they are easily visible to dark adapted eyes after first being subjected to sufficient high energy radiation.

(1) Under gamma-irradiation the crystal does not reach its maximum light intensity at once, but the fluorescent intensity shows a slow increase of about 25 percent in one hour and then remains essentially at a steady value. The emission spectrum obtained for gamma-excitation consists of 2 bands: one in the ultraviolet from about 2350–2600A and another from about 3200–4500A.

(2) Upon removal of the gamma-source, the luminescence of the crystal drops immediately to about 1/4 to 1/2 of the original intensity and then decays rather slowly. This immediate drop and the following decay diminish with increasing total of gamma-irradiation (doses). With a dose of 60 roentgens, for example, after two days, more than 5 percent of the original fluorescent intensity still remained.

(3) Irradiating the crystals with visible or near ultraviolet light (about 3600A) produced no luminescence if the crystals were not first exposed to high energy radiation. However, if the crystals are first excited by high energy radiation and then exposed to visible or near ultraviolet light (light stimulation), a tremendous increase in luminescent light output is observed; this is the case even after the original high energy induced luminescence has decayed to a very low level.

(4) The luminescent output, for the same amount of near ultraviolet radiation, was found to be roughly proportional to the total amount of gamma-excitation (doses) received by the crystal.

(5) A variation of the rate of excitation by a factor of 100 for a total gamma-excitation of 1 roentgen produced no difference in luminescent output after ultraviolet irradiation of one minute.

(6) A dose of 10 milliroentgens could easily be detected by light stimulation within one hour after gamma-irradiation and was still barely detectable after one day.

(7) A dose of 1 roentgen could be detected visibly with dark-adapted eyes and an ultraviolet intensifying screen. Only about a quarter of the total emitted light is visible.

(8) After a dose of about 500 roentgens over 20 hours of irradiation, stimulation by a tungsten lamp produced a light intensity 450 times larger than the original light intensity after the immediate drop in intensity. The stimulation was applied one hour after removal of the gamma-source.

(9) The light-stimulated luminescence also decays slowly and amounts to about 10 percent after 5 minutes; it does not seem to depend on the gamma-dose. It is faster than the phosphorescence decay after direct excitation by high energy radiation, especially when high gamma-doses are applied.

(10) Under continuous light stimulation, with wavelengths up to about 7500A, the luminescent intensity rises, goes through a maximum, and then slowly decays depending on the strength and spectral distribution of the stimulating light. Most effective light stimulation occurs around 3600A. A certain difficulty in removing the last traces of gamma-excitation exists. Strong and extended light irradiation must be applied.

(11) Light stimulation can be applied intermittently with ever-decreasing amplitudes of luminescence.

(12) The process of luminescent stimulation by light can be initiated after delays of three days and very likely much longer. The intensities obtained after such long delays with strong excitation were essentially the same as after short delays.

(13) Excitation with alpha-particles similarly gave a large luminescent output. The decay was, however, considerably faster after the removal of the exciting alpha-source than after gamma-irradiation. After use of a 5-millicurie alpha-source, there was an almost immediate drop to about 10 percent of the original value and then a further drop in 10 minutes of 85 percent. The light stimulating effect after alphas was not as high as that after gamma-irradiation, probably as a consequence of the alpha-particle irradiation being a surface effect and causing an increased density of excitation.

(14) Under fast electron bombardment strong phosphorescence was also observed. The effects were very similar to those after gamma-irradiation. Three days after the removal of the beta-source, the intensity was still several percent of the original decay luminescence. If after this length of time the crystal was irradiated with light, the intensity was of the same order as the initial luminescence.

These properties make activated NaCl crystals very suitable for detection of all types of high energy radiation. Experiments with cosmic rays were not yet conclusive, since crystals which were completely de-excited show a small increase in luminescence after being in darkness for several days. Whether this effect is due to cosmic rays or to a natural recovery of the crystal has not been yet ascertained.

A rough estimate of the amount of stored energy that can be expelled by light stimulation shows that about 20 percent of the total energy which can be emitted as light is stored and can be released by the light stimulation.

* This work was supported by the Signal Corps Engineering Laboratories, Fort Monmouth, New Jersey, Contract No. DA36-039sc-5487.
[1] O. Glasser and I. E. Beaseley, Phys. Rev. **47**, 570 (1935).
[2] O. Glasser and I. E. Beaseley, Phys. Rev. **47**, 789 (1935).
[3] C. E. Mandeville and H. O. Albrecht, Phys. Rev. **80**, 299 (1950).
[4] H. Kallmann and M. Furst, Phys. Rev. **79**, 857 (1950).

Pressure-Induced Absorption in Hydrogen

J. VAN KRANENDONK AND R. B. BIRD
Institute for Theoretical Physics, University of Amsterdam, Amsterdam, The Netherlands
(Received April 30, 1951)

CRAWFORD, *et al.*[1–3] observed in compressed hydrogen and hydrogen foreign gas mixtures an absorption at the frequency of the usually forbidden 0—1 vibrational band of hydrogen. From the pressure dependence of this absorption they concluded that molecular distortions induced during binary collisions are responsible for this pressure activation of the vibrational band. Detailed calculations have now been made of this pressure-induced absorption in H_2. It is assumed that the absorption coefficient may be obtained by first calculating the absorption due to one interacting pair of molecules (1 and 2) at

fixed distance R, and then adding the contributions of all pairs of molecules. The absorption due to a pair 1,2 is obtained by considering 0−1 vibrational transitions in molecule 1 or 2, accompanied by rotational transitions in either or both of the molecules. These radiational transitions result from the dipole moment arising from the mutual distortion of 1 and 2 which is the sum of:

(i) The distortion due to the overlapping of the wave functions of 1 and 2; this distortion, which decreases exponentially with R, has been calculated using a variational method and Rosen type wave functions.[4] This effect is primarily responsible for the Q-branch ($\Delta J=0$), contributing but slightly to the S- and O-branches ($\Delta J=+2, -2$).

(ii) The distortion due to the permanent quadrupole moments of 1 and 2, which is present even when 1 and 2 do not overlap and which decreases as R^{-4}. This effect is primarily responsible for the S-branch. Let Q^0 and α^0 be the quadrupole moment and polarizability of the H_2 molecule in its equilibrium position, and Q' and α' the derivatives with respect to the internuclear distance r. Then the contribution to the absorption coefficient due to effect (ii) contains two terms, proportional to $(Q'\alpha')^2$ and $(Q'\alpha^2)^2$, respectively. The first of these two terms has also been considered by Mizushima in his examination of the absorption in oxygen.[5,6] If we consider 0−1 vibrational transitions taking place in molecule 1, then this term corresponds to the Q^0 of molecule 2 polarizing molecule 1, giving it a dipole moment which depends on r_1 because α_1 depends on r_1 (i.e., on α'). The second term proportional to $(Q'\alpha^0)^2$, however, is as important as the first one, and results from the fact that the Q of molecule 1 induces a dipole in molecule 2 which also depends on r_1 because Q_1 depends on r_1 (i.e., on Q').

The total dipole moment of a pair of molecules at a fixed distance R and mutual orientations ω_1 and ω_2 ($\omega=\vartheta, \varphi$ where ϑ, φ are polar angles with R as polar axis), produced by the effects (i) and (ii) can be expanded in a Taylor series in the internuclear distances r_1 and r_2 about their equilibrium values r_1^0 and r_2^0:

$$\mu(R, r_1, r_2, \omega_1, \omega_2)=\mu^0(R, \omega_1, \omega_2)+(r_1-r_1^0)\cdot\mu_1'(R, \omega_1, \omega_2)+(r_2-r_2^0)\cdot\mu_2'(R, \omega_1, \omega_2)+\cdots. \quad (1)$$

The first term in (1) gives no contribution to the 0−1 vibrational transition elements, and the second and third terms give identical contributions to the absorption coefficient. The contribution to the total absorption coefficient of one pair of molecules undergoing vibrational transitions 0−1 and rotational transitions from $\rho(=J_1, m_1, J_2, m_2)$ to ρ' is:

$$a_{\rho\rho'}(R)=[4\pi(\nu/\nu_0)/3m_H c]P_\rho|(\mu_1')_{\rho\rho'}|^2 \quad (2)$$

in which $\nu=\nu_0+(E_{\rho'}-E_\rho)/h$, ν_0=fundamental vibration frequency, m_H=mass of H atom, and P_ρ is essentially the population of the initial rotational state ρ. $(\mu_1')_{\rho\rho'}$ is still a function of R. Adding the contributions of all pairs of molecules gives:

$$A_{\rho\rho'}=(N^2/2V)[4\pi(\nu/\nu_0)/3m_H c]P_\rho \times\int_0^\infty|(\mu_1')_{\rho\rho'}|^2\exp[-\varphi(R)/kT]4\pi R^2dR \quad (3)$$

where for $\varphi(R)$ we have used the average experimental intermolecular field from second virial coefficients.[7] N is the number of molecules, V the volume.

TABLE I. Values of $A_{\rho\rho'}$.

Branch	H_2-H_2	H_2-He
$O(3)$	0.067	0.013
$O(2)$	0.072	0.014
Q	2.74	2.76
$S(0)$	0.466	0.089
$S(1)$	1.51	0.289
$S(2)$	0.241	0.047
$S(3)$	0.181	0.035
$A_{theor.}$(total)	5.28	3.25
$A_{exp.}$(total)	10.5	7.44

TABLE II. Ratio of intensities, $Q:S:O$.

	H_2-H_2	H_2-He
Theoretical	1:0.87:0.05	1:0.17:0.01
Experimental	1:0.8 :0.04	1:0.2 :0.02

In the accompanying table is given the total calculated absorption for pure H_2, in (cm^{-1} sec^{-1})(per molecule)(per molecule per cm^2)$\times10^{22}$. The enhancement of the H_2-absorption due to the adding of He has also been calculated, and the results for this enhancement are given in Table I, in (cm^{-1} sec^{-1})(per molecule H_2)(per atom He per cm^2)$\times10^{22}$. From this table it may be seen that the calculated values of $A_{\rho\rho'}$ are too small but are of the right order of magnitude. The discrepancy may easily result from our use of over-simplified wave functions and variational methods in the calculation of the distortions due to effects (i) and (ii). Such simplifications are necessary, however, in order to avoid unreasonably complicated calculations.

The calculated relative intensities of the Q-, S-, and O-branches are in close agreement with the corresponding experimental values, as is shown in Table II. The experimental ratios have been estimated from the graphs given by Crawford, *et al.*[3]

A detailed account of this work will appear in *Physica*. We wish to thank Professor J. de Boer for suggesting this problem and for many helpful discussions. One of the authors (RBB) wishes to acknowledge the opportunity for foreign study made possible by the Fulbright Exchange Program.

[1] Crawford, Welsh, and Locke, Phys. Rev. **75**, 1607 (1949).
[2] Welsh, Crawford, and Locke, Phys. Rev. **76**, 580 (1949).
[3] Crawford, Welsh, MacDonald, and Locke, Phys. Rev. **80**, 469 (1950).
[4] N. Rosen, Phys. Rev. **38**, 2099 (1931).
[5] M. Mizushima, Phys. Rev. **76**, 1268 (1949).
[6] M. Mizushima, Phys. Rev. **77**, 149 (1950).
[7] J. de Boer and A. Michels, Physica **5**, 945 (1938).

Dipolar Domains in Paramagnetic Crystals at Low Temperatures

C. KITTEL
Bell Telephone Laboratories, Murray Hill, New Jersey
(Received April 25, 1951)

A THEORY of dipolar paramagnetic domains can be constructed similar to the theory[1] of ferromagnetic domains. At very low temperatures ($T\ll T_c\approx\mu^3/ka^3\approx0.1°K$), according to the classical theory of dipolar interactions,[2,3] crystals bearing spins on b.c.c. and f.c.c. lattices will be magnetically saturated, if demagnetizing effects are neglected. Domains may then form to lower the demagnetization energy of a bounded crystal. Previous workers overlooked the possibility of domain formation, and some of their conclusions must accordingly be modified. The present discussion is limited to 0°K.

Wall energy.—An upper limit to the surface energy density σ of the boundary between domains saturated in opposite directions is given by supposing the transition occurs abruptly, between two adjacent planes of dipoles. Then $\sigma\approx(\mu/a^3)\mu(1/a^2)\approx M_s^2a$; for a saturation magnetization $M_s\approx500$ and lattice constant $a\approx4\times10^{-8}$ cm, $\sigma\approx10^{-2}$ erg/cm^2. The form of the estimate may be checked against the results of Luttinger and Tisza for alternating planes of dipoles.

Wall thickness.—Measured in lattice constants, the thickness of the transition layer is, according to FD Eq. (3.2.6), $\approx$(dipolar energy per ion/anisotropy energy per ion)$^{\frac{1}{2}}\approx1$, since the anisotropy energy is $\approx\mu^3/a^3$ as discussed below.

Dipolar energy.—Within a domain, or in an infinitely long specimen, the classical dipolar energy density is calculated from the Lorentz field and is $(2\pi/3)M_s^2\approx5\times10^8$ ergs/cc.

Anisotropy energy.—Classically there is no anisotropy energy in a saturated cubic crystal, but in quantum mechanics the zero-point motion prevents complete saturation and anisotropy arises

from the dipolar interaction in the second order. The results of Van Vleck[4] for ferromagnetic anisotropy may be carried over approximately if we set the local field $H=4\pi M_s/3$. Then the anisotropy constant at $T=0°K$ is, apart from a numerical constant of the order of unity,

$$K_1\approx -M_s^2/S\approx -2\times 10^5 \text{ ergs/cc};$$

here $S(\approx 1)$ is the spin quantum number; for classical spins ($S\to\infty$) the effect vanishes. Anisotropy of this magnitude may also occur as the result of an anisotropic g-value, as in some cobalt salts.

Magnetostriction.—On Becker's classical calculation (FD Eqs. (B.5) and (2.3.16)) we estimate the magnetostriction

$$\lambda\approx\kappa M_s^2\approx 10^{-7},$$

where κ denotes the compressibility ($\approx 10^{-12}$ cm^2/dyne). This may be modified by quantum effects.

Domain dimensions.—Except in properly bounded cubic crystals the domain width D in a slab of thickness $L(\approx 1$ cm) is given approximately by FD Eq. (4.1.6) or (4.2.5). As now $K\approx M_s^2$, both equations give approximately the same result:

$$D\approx[\sigma L/M_s^2]^{\frac{1}{2}}\approx[aL]^{\frac{1}{2}}\approx 2\times 10^{-4} \text{ cm}.$$

The energy density of the domain structure is $w\approx[M_s^2\sigma L]^{\frac{1}{2}}\approx 10^{-4}M_s^2$. If one has a flux closure arrangement without anisotropy energy FD Eq. (4.2.11) applies, and

$$D\approx[\sigma L\lambda^2]^{\frac{1}{3}}\approx 0.2 \text{ cm}$$

and a correspondingly low energy. It is in either case economical to form domains for particles larger than a few unit cells, as is seen from FD Sec. 6.1.

The transition from a nonmagnetic dipole array to a saturated array, predicted by Sauer to occur for prolate spheroid axial ratios in excess of certain values, is not according to domain theory expected to take place. Instead, domains will be expected for almost every conceivable size and shape, if the lattice is appropriate.

Magnetization curves.—The results of Luttinger and Tisza must be modified. In a polycrystalline specimen or in a single crystal in a hard direction of magnetization a field $H_s\approx M_s/S$ will be required for saturation in the direction of the field, provided that the specimen is very long. In other cases H_s is probably determined largely by the demagnetizing factor N of the specimen, so that the magnetization curve is given by $M\approx H/N$, and the saturation field is $H_s=NM_s$.

[1] For a review see C. Kittel, Revs. Modern Phys. 21, 541 (1949); this will be referred to as FD.
[2] J. A. Sauer, Phys. Rev. 51, 142 (1940); J. A. Sauer and A. N. V. Temperley, Proc. Roy. Soc. (London) 176, 203 (1940).
[3] J. M. Luttinger and L. Tisza, Phys. Rev. 70, 954 (1946).
[4] J. H. Van Vleck, Phys. Rev. 52, 1178 (1937).

The Diamagnetism of Free Electrons in Finite Systems

R. B. Dingle
Royal Society Mond Laboratory, Cambridge, England
(Received March 12, 1951)

It has recently been suggested[1] that free electrons contained in a finite box show "almost perfect diamagnetism up to a critical field, and then a triple-valued transition (similar to the condensation of a van der waals gas) to a non-diamagnetic state. This behavior is provisionally identified with the perfectly diamagnetic behavior of a superconductor. . . ."

In the course of a detailed investigation of the magnetic properties of metals I have obtained results[2] which do not support this suggestion. When the magnetic field is sufficiently weak for the bulk of the electron orbits to be of greater radius than the specimen (for most metals this requires that $HR<5$ gauss cm, where R is the radius of the specimen), the volume susceptibility is given by[3]

$$\kappa=-\frac{xe^2R^{1/3}\zeta^{2/3}}{(2m)^{1/2}c^2h^{4/3}}\left\{1-\frac{5}{54}\left(\frac{\pi kT}{\zeta}\right)^2\cdots\right\},$$

where ζ is the Fermi energy at absolute zero, and x a numerical factor equal to 0.0333 for an infinite cylinder (axis parallel to field) and 0.00717 for a sphere. This diamagnetic susceptibility at very low fields is greater than the Landau value (valid for large fields or large specimens) by a factor of the order $(R/d)^{1/3}$, where d is the mean spacing of the electrons. The Landau value is, however, so minute (10^{-6} cgs units for most metals) that the susceptibility at low fields only approaches the value necessary for perfect diamagnetism ($-1/4\pi$) for specimens of several hundred miles radius—and then only fields less than $\sim 10^{-7}$ gauss would be excluded.

[1] M. F. M. Osborne, Phys. Rev. 81, 147 (1951).
[2] To be published in detail elsewhere.
[3] There are also some complicated terms periodic in the magnetic field. These are somewhat analogous to the periodic terms which give rise to the de Haas-van Alphen effect at high fields and, like them, are appreciable only at very low temperatures.

A Modification of the Isotopic Lead Method for Determination of Geological Ages*

C. B. Collins,† J. R. Freeman, and J. T. Wilson
Geophysics Laboratory, Department of Physics, University of Toronto, Toronto, Canada
(Received April 12, 1951)

The method of determining geological ages from isotopic analyses of radiogenic lead samples was developed by A. O. Nier.[1,2] He used the formula,

$$\frac{N(Pb^{207})}{N(Pb^{206})}=\frac{N(U^{235})}{N(U^{238})}\cdot\frac{\{\exp[\lambda(U^{235})t]-1\}}{\{\exp[\lambda(U^{238})t]-1\}},$$

where $N(Pb^{207})$ etc., refer to numbers of atoms of the indicated isotopes in the sample, $\lambda(U^{235})$ and $\lambda(U^{238})$ are decay constants, and t is the age of the sample in years.

Nier determined the ratio $N(Pb^{207})/N(Pb^{206})$, or more simply Pb^{207}/Pb^{206}, by mass spectrometer analysis of lead iodide (PbI_2). Because PbI_2 is a solid, both source and tube must be heated to about 350°C. Free lead is deposited on the inside of the mass spectrometer tube, which causes electrical leakage and necessitates frequent and troublesome cleaning. These experimental difficulties, together with the need for a mass spectrometer of high resolving power, have resulted in few isotopic lead ages being determined.

To assist in interpreting the geology of the Canadian Shield by age determinations, a mass spectrometer of high resolving power (better than one mass unit in 275) has been constructed in this laboratory and a new technique for analysis has been evolved.

Lead tetramethyl has been found satisfactory as a source of ions. It has sufficient vapour pressure at room temperature and does not contaminate the mass spectrometer tube. A method of preparing it from samples of lead chloride as small as 50 mg has been developed by Professor G. F. Wright and Mr. H. L. Cohen of the Department of Chemistry, University of Toronto.

The mass spectrograms obtained from lead tetramethyl are complex, but they can easily be divided into groups associated with Pb^+, $Pb(CH_3)^+$, $Pb(CH_3)_2^+$, and $Pb(CH_3)_3^+$ ions. The full interpretation cannot be discussed here, but values for the isotopic constitution of lead determined by examining the several ion groups agree with one another and with previous determinations, when corrections are made for the occurrence of such ions as PbH^+, $Pb(CH_2)^+$, $Pb(CH)^+$, and $Pb(CH_3)_2(CH_2)^+$, and for the occurrence of C^{13}. The $Pb(CH_3)_3^+$ ions are the most abundant, and the only related ions found to occur with them are $Pb(CH_3)_2(CH_2)^+$ ions (1 percent). With a mass spectrometer of high resolving power the small ion currents due to $Pb(CH_3)_2(CH_2)^+$ ions can be measured accurately, and the corrections for them and for C^{13} atoms are easily made. For these reasons analyses are being based upon the lead trimethyl ion group.

Several radiogenic lead samples extracted from pitchblende have been analyzed. The results appear in Table I. Isotopic constitution of leads from Katanga and Great Bear Lake agree with determinations by Nier of samples from the same areas although the samples were obtained independently.

TABLE I. Isotopic analysis of several radiogenic lead samples.

1 Mineral and source	2 Pb^{207}/Pb^{204} (Toronto) %	3 Pb^{207}/Pb^{204} (Nier) %	4 Age (Toronto) millions of years	5 Age (Nier) millions of years
1. Pitchblende, Katanga, Belgium Congo	6.07±0.06	6.00 to 6.13 (7 specimens)	640	610 to 655
2. Pitchblende, Port Radium, Great Bear Lake	8.82±0.18	8.88	1400	1420
3. Pitchblende, Lake Athabaska	8.74±0.17	—	1380	—

Note: In column 2 the errors given are mean deviations of observations.

Geological age calculations based on the formula in the first paragraph of this paper depend on the values of the half-lives of U^{235} and U^{238}.

In 1939, Nier[1] chose a value of 7.07×10^8 years for the half-life of U^{235} in order to make age determinations based on the Pb^{207}/Pb^{206} ratio agree with those obtained by the Pb^{206}/U^{238} method. Some recent investigations[2,4,5] give a higher value for the half-life of U^{235}.

If a higher value than 7.07×10^8 years is adopted then all the ages in the geological time scale which are based on Nier's work must be increased; similarly, the estimates of the age of the earth calculated by Holmes' method[6] will also be increased.

* This research has been supported by the National Research Council of Canada and by the Research Council of Ontario.
† Holder of National Research Council of Canada Fellowship.
[1] A. O. Nier, Phys. Rev. 55, 150 (1939).
[2] A. O. Nier, Phys. Rev. 60, 112 (1941).
[3] British Atomic Energy Report—BR-522 (1944).
[4] Perlman, Ghiorso, and Seaborg, Phys. Rev. 77, 26 (1950).
[5] C. A. Kienberger, Phys. Rev. 76, 1561 (1949).
[6] A. Holmes, Nature 162, 822 (1948).

The Specific Alpha-Activity of U^{235}

E. H. FLEMING, JR., A. GHIORSO, AND B. B. CUNNINGHAM
Radiation Laboratory and Department of Chemistry, University of California, Berkeley, California*
(Received April 30, 1951)

THE half-life of U^{235} has been the subject of several recent experimental investigations. Clark, Spencer-Palmer, and Woodward[1] reported a value of 8.91×10^8 years, derived from their alpha-pulse analyses of natural and enriched mixtures of U^{238}, U^{235}, and U^{234}. Kienberger,[2] after remeasuring the specific activity and U^{234} content of normal uranium, computed the specific activity of U^{235} by subtraction and obtained a half-life of $(8.8\pm1.1)\times10^8$ years. Knight[3] obtained $(7.53\pm0.22)\times10^8$ years for the half-life of U^{235} from specific activity measurements on highly enriched material and a crude pulse analysis for U^{234} and U^{235} alpha-particles. All of these values are substantially higher than Nier's[4,5] recalculated[6] figure of 7.07×10^8 years.

Because of the rather wide divergence among these various values, and also because of the general interest in the exact value of the U^{235} half-life, which enters into the computation of geological time, we have carried out several measurements of the specific alpha-activity of U^{235} in this laboratory.

The uranium used for this purpose was highly purified (99.9 percent) U^{235}, supplied to us as U_3O_8 from Dr. C. E. Larson, Y-12 Plant, Carbide and Carbon Chemicals Division, Oak Ridge National Laboratory. Careful spectrographic analysis established that the chemical purity of this material was better than 99.95 percent.

Differential pulse analysis showed that (65.3±0.7) percent of the alpha-activity was due to U^{235}, and (34.7±0.3) percent to U^{234}. The details of this measurement are contained in another publication by Ghiorso.[7]

Samples of the oxide were weighed to ±0.1 percent, and were then dissolved in concentrated nitric acid and diluted to volume. Accurate volume aliquots of these solutions were taken and the uranium electrodeposited quantitatively onto platinum disks. Thin, uniform films resulted of the order of 100–200 micrograms per sq cm. The highly enriched U^{235} depositions were counted in a specially constructed, helium filled, medium geometry counter [counting yield (8.313±0.016) percent], which was calibrated with mixtures of U^{238} and U^{234} against a low geometry counter of accurately known counting yield. We believe that use of the medium geometry counter for the U^{235} samples reduced to negligible magnitude any errors arising from backscattering or self-absorption, since analysis of the pulses from this chamber showed an extremely flat plateau.

The specific activity of U^{238}, as determined from five separate U^{235} depositions, was found to be 4774±72 disintegrations per minute per milligram, with a corresponding decay constant of $(9.80\pm0.15)\times10^{-10}$ per year, and a corresponding half-life of $(7.07\pm0.11)\times10^8$ years.

Our value for the half-life agrees with the 7.07×10^8 year value reported by Nier.[4,5,6] The value reported by Clark and co-workers, 8.91×10^8 years, differs from ours by about 25 percent. A partial explanation lies in the fact that these workers were unable to detect the high and low energy alpha-groups,[7] comprising about 15 percent of the total disintegrations from U^{235}, in their pulse analysis of slightly enriched U^{235} samples. However, it is difficult to account for the other 10 percent discrepancy.

The use of our value in the computation of the age of the earth as carried out by Holmes,[6] reduces his figure of 3350 million years by about 3 percent.

A more precise value and a detailed description of this work are to be reported at a later date.

* This work was performed under the auspices of the AEC.
[1] Clark, Spencer-Palmer, and Woodward, British Atomic Energy Report BR-522 (1944) (unpublished).
[2] C. A. Kienberger, Phys. Rev. 76, 1561 (1949).
[3] G. B. Knight, Oak Ridge National Laboratory Report K-663 (1950) (unpublished).
[4] A. O. Nier, Phys. Rev. 55, 150 (1939).
[5] A. O. Nier, Phys. Rev. 55, 153 (1939).
[6] G. T. Seaborg and I. Perlman, Revs. Modern Phys. 20, 585 (1948).
[7] A. Ghiorso, Phys. Rev. 82, 979 (1951).
[8] A. Holmes, Nature 157, 680 (1946).

Hyperfine Structure of Sm^{149}, Sm^{147}, Nd^{145}, and Nd^{143}

KIYOSHI MURAKAWA AND JOHN S. ROSS
*Department of Physics, University of Wisconsin, Madison, Wisconsin**
(Received April 23, 1951)

THE hyperfine structure of the spectra of samarium and neodymium was studied, using the separated isotopes[1] of Sm^{149}, Sm^{147}, Nd^{146}, and Nd^{145}, respectively. The hollow-cathode light source[2] which was used contained about 25 milligrams of the sample. The cathode was made of aluminum and liquid-air or water cooling was used. The carrier gas was neon at a few mm Hg pressure. The fine structure was examined with a silvered Fabry-Pérot etalon and a Hilger constant deviation prism spectrograph.

The maximum number of hyperfine components of any samarium line[3] with a flag pattern was observed to be six, from which it follows that both Sm^{149} and Sm^{147} have spin 5/2.

The splitting of the ground term of Sm II for Sm^{147} was determined from the structure of the line[4] λ4704 ($4f^6 6s\ {}^9F_1 - 4f^6 6p\ 1^0_4$)

TABLE I. Nuclear spins and magnetic moments.

Isotope	Spin	Magnetic moment (nm)
Sm^{149}	5/2	-0.25 ± 0.04
Sm^{147}	5/2	-0.30 ± 0.05
Nd^{145}	7/2	-0.62 ± 0.09
Nd^{143}	7/2	-1.0 ± 0.2
$\mu(Sm^{147})/\mu(Sm^{149}) = 1.177 \pm 0.015$		
$\mu(Nd^{145})/\mu(Nd^{143}) = 1.60 \pm 0.06$		

and, neglecting the splitting of the initial term, that of the final term was found to be -0.120 cm^{-1}. Since the term $4f^6 6s\ ^8F_{\frac{1}{2}}$ can be regarded as due to a $4f^6\ ^7F_0$ configuration plus a $6s$ electron, we get the splitting factor $a(6s) = -0.040$ cm^{-1}. Using the Fermi-Segrè-Goudsmit formula

$$\mu = a(s) I n^{*3} \times 118.5/[Z Z_0^2 F dn^*/dn]$$

and putting $I = 5/2$, n^* (effective quantum number) $= 2.18$, $dn^*/dn = 1.08$, F (relativity correction factor) $= 1.54$, $Z = 62$, $Z_0 = 2$, we get the value of μ^{147} listed in Table I.

The Sm II line λ4515 classified by us as due to a transition $J = \frac{1}{2} \rightarrow J' = \frac{1}{2}$ was observed to have three components 0 (26), 0.1149 (21), 0.1904 (26) cm^{-1} for Sm^{147}, where numbers in parentheses represent relative intensities. Similarly for Sm^{149} the components 0 (26), 0.0974 (21), 0.1618 (26) cm^{-1} were obtained. Taking the ratio of the distances of the outermost components, μ^{147}/μ^{149} and hence the value of μ^{149} (since the value of μ^{147} is known) were obtained (see Table I).

In the case of Nd^{143} or Nd^{145}, the line[5] Nd II λ4303 ($4f^4 6s\ ^6I_{1/2} - 4f^4 6p\ ^6K^0_{3/2}$) was observed to consist of at least six components, and the intensity distribution was in harmony only with the assumption of $I = 7/2$, neglecting the splitting of the initial term. The total splitting of the final term was found to be $+0.2604$ cm^{-1} and $+0.1623$ cm^{-1} for Nd^{143} and Nd^{145}, respectively. The ratio μ^{143}/μ^{145} is listed in Table I. The spins of Nd^{143} and Nd^{145} and the ratio of the nuclear magnetic moments (μ^{143}/μ^{145}) given here are in good agreement with the recent work of Bleaney and Scovil.[6]

The usual formula[7] for coupling of quantum vectors gives the relation for the splitting factor

$$A[4f^4(^5I_4)6s\ ^6I_{7/2}] = \frac{4}{63}\left[\frac{35}{2}a(4f^4\ ^5I_4) - \frac{7}{4}a(6s)\right],$$

which, when we neglect any contribution of the $4f$ electrons, yields $A = -\frac{1}{4}a(6s)$. Putting $a(6s) = 0.0837$ cm^{-1} for Nd^{143} and $I = 7/2$, $Z = 60$, $Z_0 = 2$, $F = 1.491$, $n^*(6s) = 2.23$, $dn^*/dn = 1.08$ into the Fermi-Segrè-Goudsmit formula, we obtained the value of $\mu(Nd^{143})$, and hence that of $\mu(Nd^{145})$, listed in Table I.

* Supported by the ONR.
[1] Loaned by Union Carbide and Carbon Corporation, Oak Ridge.
[2] O. H. Arroe and J. E. Mack, J. Opt. Soc. Am. 40, 386 (1950).
[3] With respect to a summary of the previous work on the displacement effect of even isotopes of samarium, see D. D. Smith and J. R. McNally, Jr., J. Opt. Soc. Am. 40, 878 (1950). A similar effect in the spectrum of Nd I was observed by P. F. A. Klinkenberg, Physica 11, 327 (1945).
[4] The Sm II spectrum was classified by W. Albertson, Astrophys. J. 84, 26 (1936).
[5] The Nd II spectrum was classified by Albertson, Harrison, and McNally, Phys. Rev. 61, 167 (1942).
[6] B. Bleaney and H. E. D. Scovil, Proc. Phys. Soc. (London) 63, 1369 (1950).
[7] P. Güttinger and W. Pauli, Z. Physik 67, 743 (1931).

Gamma-Transitions in the Disintegration of Cerium 144

W. S. EMMERICH, G. JOHN, AND J. D. KURBATOV
Ohio State University, Columbus, Ohio
(Received April 19, 1951)

CERIUM 144, with a half-life of ~300 days, was obtained from the Oak Ridge National Laboratory and aged for nine months to allow cerium 141 to decay. The sample was chemically separated from all other rare earth elements and other elements, the active isotopes of which may have been present. Cerium nitrate, without addition of carrier, was oxidized with permanganate and filtered with the manganese dioxide precipitated in acid solution. The manganese was reduced to divalent ion, and cerium was separated by adsorption of the latter on filter paper.

A sample of cerium 144 was prepared by evaporating the radioactive solution on a strip of zapon. A study of internal conversion electrons was made in a permanent magnet spectrograph set at 104 and 179 gauss, covering an energy range from 10 kev to 400 kev. Calibration of the instrument was obtained with the radiations of iodine 131.

TABLE I. Conversion electrons identified in praseodymium 144.

Electron energy in kev		Relative intensity	Gamma-ray energy in kev
38.2	*K*	medium	80.2 ± 0.5
73.5	*L*	weak	80.3
78.8	*M*	very weak	80
92.0	*K*	strong	134.0 ± 0.5
127.1	*L*	medium	133.9
132.5	*M*	weak	134

Table I gives the energies and relative intensities of those internally converted electron groups for which identification of the corresponding gamma-ray energies has been established with certainty. Binding energies of the *K*, *L*, and *M* electrons of praseodymium and neodymium were considered in these cases. The agreement in energy values for the gamma-rays found were within 0.3-kev experimental error when the monoenergetic electron groups were attributed to transitions in praseodymium. On the contrary, when the binding energies of neodymium were used for calculation of the gamma-ray energies, discrepancies became as large as 1.2 kev. Thus the energy difference between the conversion electrons corresponds more closely to the difference in binding energy in praseodymium, and the transitions are ascribed to this element.

TABLE II. Indirectly identified conversion electrons in praseodymium 144.

Electron energy in kev		Gamma-ray energy in kev
26.8	*L*	33.6
34.2	*L*	41.0
46.1	*L*	53.0
52.8	*K*	94.8
57.6	*K*	99.6
28.5	Auger	

Independently, the *K* and *L* conversion electrons of the 134-kev transition were observed with a beta-spectrometer and found to have an experimental K/L intensity ratio of about seven. The 134-kev transition is described in the literature as following the disintegration of Pr^{144}.

Other internal conversion electrons observed with the spectrograph are listed in Table II. Identification of these electron groups is less certain than those of Table I.

The electron groups of 26.8 kev and 34.2 kev are tentatively assigned to *L* conversion and the 52.8-kev and 57.6-kev groups to *K* conversion. The weakest electron line is that of 46.1 kev. If it is interpreted from experimental considerations as *L* conversion, then the gamma-rays of 53 kev would be due to a transition from the 134-kev level to 80 kev. This would account in part for the smaller experimental intensity of the 94.8-kev transition as compared to that of the 80.2-kev transition.

The energy balance for all observed levels in praseodymium up to 175 kev has been considered. One branch disintegrates by the consecutive transitions of 94.8 kev and 80.2 kev. The other branch disintegrates by the transitions of 41.0 kev, 99.6 kev, and 33.6 kev. The predominant transition, 134.0 kev, is a crossover of the 99.6-kev and the 33.6-kev transitions.

A Grant in Aid of the Industrial Research Foundation received from the Graduate School of the Ohio State University is greatly appreciated by the authors.

The Inelastic Scattering of Fast Neutrons

M. A. GRACE, L. E. BEGHIAN, G. PRESTON, AND H. HALBAN
Clarendon Laboratory, Oxford, England
(Received April 26, 1951)

IN a previous communication[1] we have given the values of the energy levels and cross sections for the inelastic scattering of 2½-Mev neutrons by fluorine, magnesium, and sulfur. The absolute γ-ray yield from the excited nuclei due to a known fast neutron flux was investigated with a pair of calibrated Geiger-Müller counters operated in coincidence. The energy of the γ-radiation was determined by the method of Bleuler and Zunti[2] from the absorption in aluminium of the secondary electrons produced by a polystyrene radiator. The absolute value of the neutron flux was measured with a proton recoil ionization chamber.[3] In this way the elements, beryllium, copper, chromium, and iron have also been investigated.

The method of Bleuler and Zunti permits the γ-ray energy to be found both from the form of the absorption curve and from the range of the secondary electrons. When the values of energy obtained in these two ways agree the γ-radiation is homogeneous, thus indicating the excitation of a single nuclear level only. Such homogeneity was found for the γ-radiation from chromium, magnesium, fluorine, and sulfur.

If the radiation is complex, agreement between the two values will not be obtained. However, the method of Bleuler and Zunti can be extended to the analysis of γ-ray spectra when two components are present. The high energy component is found from the range of the secondary electrons, and this value then enables the low energy component to be determined from the form of the absorption curve. Copper and iron both exhibited complex spectra.

TABLE I. Gamma-ray energies and inelastic scattering cross sections.

Element	γ-ray energy (Mev)	Inelastic scattering cross section
Beryllium	...	$<0.014\times10^{-24}$ cm²
Chromium	1.4 ±0.1	1.2 ±0.4
Copper	1.1 ±0.1 2.2 ±0.1	1.2 ±0.6 0.34±0.12
Fluorine	1.3 ±0.1	0.52±0.18
Iron	0.8 ±0.1 2.2 ±0.2	1.8 ±1.3 0.14±0.05
Magnesium	1.4 ±0.1	0.75±0.23
Sulfur	2.35±0.15	0.38±0.1

The copper spectrum could be resolved into two components: that of iron could be accounted for by two components but statistical uncertainty did not exclude the possible presence of γ-rays of intermediate energy. The analysis of the iron spectrum has been made on the basis of these two components. From considerations of the available energy it appears that these levels are separately excited.

The earlier results for fluorine, magnesium, and sulfur have been revised and are included in Table I. The cross sections given are for the naturally occurring elements.

[1] Beghian, Grace, Preston, and Halban, Phys. Rev. **77**, 286 (1950).
[2] E. Bleuler and W. Zunti, Helv. Phys. Acta **19**, 375 (1946).
[3] L. E. Beghian and H. Halban, Proc. Phys. Soc. (London) **62A**, 395 (1949).

On the Theory of Beta-Decay

R. J. BLIN-STOYLE AND J. A. SPIERS
Clarendon Laboratory, Oxford, England
(Received April 26, 1951)

IT has been found possible to write the matrix elements of standard beta-decay theory[1] in a way which not only gives the beta-spectra and angular distributions for arbitrary degree of forbiddenness, but also yields very simply the selection rules appropriate to any chosen type of interaction.

TABLE I. Degrees of forbiddenness f of transitions creating the system electron plus neutrino in states ^{2S+1}L. Even values of f refer to parity change no, odd values (underlined) to parity change yes. An * denotes that the term vanishes.

Dirac operators and values of S		$J=0$ $L=0,\ 1$	1 0, 1, 2	2 1, 2, 3	3 2, 3, 4	4 3, 4, 5
1, β	(0)	0, *	*, 1, *	*, 2, *	*, 3, *	*, 4, *
α, $\beta\alpha$	(1)	*, 2	1, 2, 3	2, 3, 4	3, 4, 5	4, 5, 6
σ, $\beta\sigma$	(1)	*, 1	0, 1, 2	1, 2, 3	2, 3, 4	3, 4, 5
γ_5, $\beta\gamma_5$	(0)	1, *	*, 2, *	*, 3, *	*, 4, *	*, 5, *

Thus, to anticipate, Table II enables the degree of forbiddenness of any emission with nuclear spin change $J_i \to J_f$ and parity change "yes" or "no" to be read off, for the three commonly used interactions.

States of the system $e+\nu$ (electron plus neutrino) are expressed as superpositions of wave functions $\psi(JM, j_e j_\nu)$ specified by the following quantities: total angular momentum J of the system as a whole, with z-component M, angular momentum j_e of the electron, angular momentum j_ν of the neutrino. J, of course, can have any integral value 0, 1, 2, etc. . . .

The magnitudes of the individual orbital angular momenta are not constants of the motion owing to relativistic effects. However an expansion of the form

$$\psi(JM, j_e j_\nu) = \sum_{L,S} A(L, S; j_e, j_\nu)\phi(JM, LS)$$

is possible, each term of which may be regarded as representing a state of the system $e+\nu$ having a definite total orbital angular momentum L and total spin $S=0$ or 1 ("spins anti-parallel" or "parallel"), combined vectorially to yield the resultant J, M.

The matrix element of a beta-emission can now be expressed as a sum of "matrix terms," each of which contains (besides nuclear functions) one function $\phi(JM, LS)$ and one of the Dirac operators of the chosen interaction.

Such a "matrix term" gives the probability of a transition in which the system $e+\nu$ is created in the state JM, LS, by the operator concerned. Inspection shows that the nonvanishing terms can be picked out, and each one classified with a "degree of forbiddenness" f (see Table I), by the following rules:

1. $S=0$ or 1 according to the operator (Table I, column 2).
2. For given J and S, $L=|J-S|$ to $J+S$ in integral steps.
3. $f=L$ for terms containing the operators 1, β, σ, $\beta\sigma$; while $f=L+1$ for α, $\beta\alpha$, γ_5, $\beta\gamma_5$. Allowed transitions are denoted by $f=0$, first forbidden by $f=1$, etc.
4. If there is (is not) a nuclear parity change on emission, only terms with odd (even) f are nonvanishing.
5. If the nuclear spin change is $J_i \to J_f$, the possible values of J are $|J_i-J_f|$ to J_i+J_f in integral steps.

Thus from Table I, using rule 5 and selecting the Dirac operators of the chosen interaction, we can enumerate the f-values of all terms contributing to the beta-emission; the least f-value among

TABLE II. Degrees of forbiddenness f of transitions creating the system electron plus neutrino with total angular momentum J. For nuclear spin change $J_i \to J_f$, J ranges from $|J_i-J_f|$ to J_i+J_f. The degree of forbiddenness F of the emission as a whole is the least (even or odd) value of f in this range (for parity change no or yes, respectively). 0 = allowed. * = completely forbidden.

	$J=0$	1	2	3	4
Fermi (1, α)	0, *	1, 2	2, 3	3, 4	4, 5
Tensor ($\beta\sigma$, $\beta\alpha$)	2, 1	0, 1	1, 2	2, 3	3, 4
Axial vector (σ, γ_5)	*, 1	0, 1	1, 2	2, 3	3, 4

these gives the degree of forbiddenness F of the emission as a whole.[2]

Table II is constructed from Table I for use where only the F of the emission as a whole is required. Thus, e.g., for a nuclear spin change $0\rightarrow 0$, $J=0$ only, and Table II shows that on the Fermi interaction $F=0$ ("allowed") for parity change "no," and completely forbidden ("yes"); for $1\rightarrow 1$, $J=0, 1, 2$, and on Fermi interaction $F=0$ (no) and 1 (yes), etc.

In a forthcoming paper it will be shown how this formalism can be used to derive the energy spectra and the angular distribution properties of beta-emissions of arbitrary degree of forbiddenness.

[1] E. J. Konopinski and G. E. Uhlenbeck, Phys. Rev. **60**, 308 (1941); C. L. Critchfield, Phys. Rev. **63**, 417 (1943); D. L. Falkoff and G. E. Uhlenbeck, Phys. Rev. **79**, 334 (1950).

[2] Except that for the pure pseudoscalar interaction $\beta\gamma_5$, F is one unit less, owing to the absence of any terms with $f=0$.

Failure of Paschen's Law and Spark Mechanism at High Pressure

F. Llewellyn Jones and C. G. Morgan
Department of Physics, University College of Swansea, Swansea, Great Britain
(Received May 2, 1951)

THE use of air at high pressures as an insulating medium as, for example, with power cables and high voltage apparatus in nuclear physics, has aroused considerable interest in the electric breakdown of gases at high pressure. Investigations have been made by Howell,[1] and more recently by Skilling,[2] Skilling and Brenner,[3] Trump, Safford, and Cloud,[4] and Trump, Cloud, Mann, and Hanson.[5] These investigations have all revealed a pronounced failure of Paschen's law when the gas pressure p was very high, as was the case when working with high voltage and short gap distances. These conditions involved very high fields F at the electrodes.

The recent investigators[2–5] agree that the failure of Paschen's law was due to the significant occurrence of a source of ionization which did not depend on the discharge parameter F/p, being instead a function of F and the nature of the cathode surface. It follows that the electron emission from the cathode must play an important and significant part in the breakdown mechanism, which cannot then be accounted for in terms of gas processes alone. The results of Skilling and Brenner,[3] and those of Trump *et al.*[5] all indicated that the electron emission from the cathode contributed strongly (exponentially in the case of an aluminium cathode) to the prebreakdown current, and this emission became, in fact, the controlling secondary process at the very highest pressures investigated. The mechanism of cathode emission suggested was the field emission of electrons from the cathode at high values of F, but no estimates of the magnitude of the field current under such circumstances have been given.

Prebreakdown cold emission of electrons from the cathode in spark gaps at atmospheric pressure in air has been studied during recent years in this laboratory.[6,7] The effect of different surface conditions was examined when the macroscopic electric intensity at the cathode was $\sim 10^6$ volts/cm, corresponding to breakdown, and it was shown that the surface condition and the previous treatment of the cathode exerted a considerable influence on the rates of electron emission. The electron emission was found to follow the Fowler-Nordheim[8] field law which gives the number of electrons emitted per second i in terms of the electric field F by the relation

$$r=i/F^2=A\exp(-6.8\times 10^7\phi^{\frac{3}{2}}/F),$$

where ϕ is the work function of the cathode surface in volts, and F is the field in volts/cm. From this equation estimates of ϕ for the emitting surface and of the emitting area for various values of F and i were made. Cold emission currents of the order of 10^4 and 10^5 electrons/sec were readily produced in the prebreakdown phase. If a value of $\phi\sim 4.5$ ev for the common metals such as nickel is taken, the above equation shows that fields of at least 3×10^7 volts/cm are required to produce the observed emission. However, such emission was obtained with values of the macroscopic field in the gap as low as 10^6 volts/cm. Clearly then, either the microscopic field F at the cathode surface is much greater than the measured macroscopic field in the gap (gap voltage/gap distance), or the work function of the region from which the electrons were extracted is much less than 4.5 ev. Allowing for possible local intensification (up to 10 times[9]) of the field at microscopic points on the surface, estimates of ϕ lay within the range 0.1 ev to 0.5 ev, the emitting area was estimated $\sim 10^{-14}$ cm^2. These values appear to suggest that the electrons were obtained from the surface oxide layer (which is always present on electrodes in air). This result shows that high electron emission is possible by field extraction processes from cathodes in air. For breakdown in very small gaps and high air pressures, this process would be very important, and could predominate as a source of ionization when extremely high pressures (and therefore fields) are employed, just as indicated by measurements in air at high pressures.[1–5] Further, this ionization process depends on the field F and also on the nature of the surface which itself to a certain extent might depend on the air pressure. However, the far most important factor in the mechanism is certainly the field F, so that this ionization process is bound to lead to deviations from Paschen's law, which holds only for processes dependent, not on F, but on F/p.

It is now of interest to consider whether such field processes can influence the secondary ionization mechanism[10] in such a way as to produce a modification of Paschen's law. Trump *et al.*[5] have suggested that the high fields employed in small gaps at high gas pressures may enhance the secondary ionization coefficient γ, and that such enhancement would lead to a lowering of the sparking potential V_s and to failure of Paschen's law. In this connection Germer and Haworth,[11] and Newton[12] have already shown how greatly the efficiency of positive ion electron extraction from metal surfaces is increased in the presence of high electric surface fields, and it is likely that this process of electron extraction would be greatly enhanced if electrons were available from regions of low work function, such as oxide layers.[6,7]

However, there is another aspect of this question. It has been established that considerable field emission is obtainable from oxide layers on a cathode surface, and it is interesting to consider whether the presence of positive ions on such layers could produce an enhancement of the microscopic field there and thus produce increased field emission in accordance with the equation above. The net result of this would be a comparatively high electron emission due to the incidence of the positive ions on the cathode or, in other words, an enhancement of the effective value of γ as compared with the (very low) values found in low pressure work when the field F is low. Our previous results[6,7] have shown how rapidly the electron emission i increases with the field F, so that an enhancement of F due to the presence of positive ions on cathode surface layers could lead to greatly increased electron emission. It should be noticed that such a mechanism outlined above would be taking place during the whole prebreakdown process and would appear as a greatly enhanced γ.

Support for this view has been found from the results of recent work in this laboratory on the enhancement of prebreakdown field emission from the cathode due to the presence of positive ions on the surface. In these experiments, residual ions from a previous spark were swept on to the cathode surface and the resulting emission measured. Owing to the difficulties involved in estimating quantitatively the positive ion concentration at the cathode, it is difficult at present to give an accurate estimate of the degree of enhancement obtained in these measurements. It is not, however, unreasonable to consider that the efficiency of the effective γ-process would be considerably increased by a factor $\sim 10^4$ by the enhanced field emission produced by the presence of the positive ions on thin surface cathode layers. This would be especially the case when there was considerable prebreakdown concentration of positive ions in the gap during the time when the sparking potential was being measured.

This effect could lead to an enhancement of γ of about the order required to account for the observed deviation from Paschen's law.

Owing to the large spread observed in measurements of V_s by Trump *et al.*,[5] and indeed of all other observers in this region,[2-4] it is difficult to make reliable estimates of the values of the γ which were effective in these measurements by applying the Townsend sparking criterion to their values of V_s. This spread probably indicates the extremely high dependence of the total emission on the nature of the electrode surface in the presence of oxide films. However, an approximate estimate indicates that on the basis of the Townsend breakdown criterion, the value of γ must have been enhanced by a factor of at least 10^4 to account for the observed deviations in V_s.

It is, however, significant to note that cold electron emission $\sim 10^4$ times greater than would be expected for clean surfaces has been obtained with macroscopic fields of $\sim 10^6$ volts/cm in the presence of oxide films, so that an effective enhancement of this order of the coefficient γ due to the presence of positive ions of the gas on this oxide layer on the cathode would appear to be not impossible.

[1] A. H. Howell, Trans. Am. Inst. Elec. Engrs. **58**, 193 (1939).
[2] H. H. Skilling, Trans. Am. Inst. Elec. Engrs. **58**, 161 (1939).
[3] H. H. Skilling and W. C. Brenner, Trans. Am. Inst. Elec. Engrs. **60**, 112 (1941).
[4] Trump, Safford, and Cloud, Trans. Am. Inst. Elec. Engrs. **69**, 132 (1941).
[5] Trump, Cloud, Mann, and Hanson, Trans. Am. Inst. Elec. Engrs. **69**, 961 (1950).
[6] F. Llewellyn Jones, Nature **157**, 298, 371 (1946); Proc. Phys. Soc. (London) **62B**, 366 (1949).
[7] Jones, de la Perrelle, and Morgan, Compt. rend. **232**, 572 (1951).
[8] Stern, Gossling, and Fowler, Proc. Roy. Soc. (London) **A124**, 699 (1929).
[9] W. Schottky, Z. Physik **14**, 63 (1923).
[10] F. L. Jones and A. B. Parker, Nature **165**, 960 (1950).
[11] L. H. Germer and F. E. Haworth, Phys. Rev. **73**, 1121 (1948).
[12] R. R. Newton, Phys. Rev. **73**, 1122 (1948).

Microwave Spectrum of NO_2

K. B. McAfee, Jr.*
Harvard University, Cambridge, Massachusetts†
(Received April 19, 1951)

THE microwave absorption spectrum of gaseous nitrogen dioxide has been observed at approximately 26,660 Mc. The spectrograph employed has been described elsewhere.[1] Stark effect modulation was used throughout. The Zeeman effect was measured by winding a coil of approximately 5000 turns of No. 18 wire on a 4-inch diameter coil form. The coil was centered on a $\frac{1}{2}\times 1$-in. wave guide such that only 10 percent of the guide was subject to a fringing field. The direction of the static magnetic field was perpendicular to that of the microwave E vector, giving rise to Zeeman transitions of the type $\Delta M=\pm 1$. A slight splitting of one of the lines was observed in the absence of the applied dc field due to the component of the gravitational field parallel to the guide axis.

The observed spectrum of nitrogen dioxide is shown in Table I. The frequency range of the apparatus was from 18,000 to 31,000 Mc. The relative intensities were measured to approximately ± 10 percent. The intensities shown do not indicate the temperature coefficient of any of the lines, but only the relative intensities at each temperature. The fact that both of the sets of triplets arise from the same energy level to within 40 wave numbers was established by the constancy of the relative intensities at the two temperatures. The last column of Table I shows the measurements of the Zeeman effect in weak fields. $\Delta\nu$ represents the splittings of the centers of gravity of the two symmetrically displaced components. These measurements were made with the simultaneous application of Stark and Zeeman effects. The effect of varying the Stark voltages upon each magnetic field splitting was determined, and an extrapolation to zero voltage was made when necessary.

TABLE I. Observed spectrum of NO_2.

Line freq. (Mc)	Rel. int. (30°C)	Rel. int. (−75°C)	$\Delta\nu$(Mc/gauss)
26,647.17	147	143	
26,633.83	149	153	0.217
26,619.38	178	183	0.440
26,603.65	6	—	
26,577.02	176	184	0.471
26,569.21	176	184	0.233
26,563.25	144	151	

The NO_2 molecule has a magnetic moment of one Bohr magneton arising from one uncompensated electron spin and an electrical polarity of approximately $\frac{1}{3}$ Debye unit. The lines observed are interpreted as arising from the electric rather than the magnetic moment of the molecule. The various angular momenta involved in the molecule include the angular momentum due to motion of the nuclear framework denoted by $\mathbf{L}$, and the electron and nuclear spin momenta $\mathbf{S}$ and $\mathbf{I}$, respectively. The hamiltonian may be written as

$$H=\left[\frac{L_a^2}{2I_a}+\frac{L_b^2}{2I_b}+\frac{L_c^2}{2I_c}\right]+A\mathbf{L}\cdot\mathbf{S}+2g_I\beta_I\beta[\mathbf{I}\cdot\mathbf{S}-3r^{-2}(\mathbf{S}\cdot\mathbf{r})(\mathbf{I}\cdot\mathbf{r})]$$
$$+[(16\pi/3)\beta g_I\beta_I]|\psi(0)|^2+2\beta\mathbf{S}\cdot\mathbf{H}. \quad (1)$$

The electronic and nuclear magnetons are denoted by β and β_I, respectively. A is a constant, while $\mathbf{r}$ is the radius vector from the N^{14} nucleus to the free electron spin. The proportionality constant A is a function of L and of K, the axial component of L. This hamiltonian does not include the interaction between the electrical moment of the molecule and the applied electric field giving rise to the Stark effect. The first term is the familiar energy of an asymmetrical top. The second member of (1) represents the interaction between the electron spin and the magnetic field produced by the rotation of the molecule. The third member is the dipolar coupling between the electron and nuclear spins, the fourth is the Fermi overlap term, and the final member is the Zeeman energy.

Quadrupole coupling has been excluded since its value is much smaller than the dipolar term, and the above is intended only as a first, preliminary approximation. The contributions of the magnetic moments appropriate to molecular rotation and nuclear spin to the Zeeman energy are also excluded, as they are extremely small compared with that of the electron spin.

It seems likely that the strong lines of Table I arise from transitions of the type $\Delta F=\Delta J=\Delta L$. The six lines are then ascribed to the six possibilities $J=L\pm\frac{1}{2}$, $F=J-1$, J, $J+1$ for given initial L. In principle, there are other multiplet components where $\Delta F\neq\Delta J$ or $\Delta J\neq\Delta L$, but theory shows that they are so weak that they would scarcely be observed. Any other interpretation appears hard to reconcile with the observed intensity behavior. However, it has not as yet been shown that the observed spacing of the components and the Zeeman behavior can be explained on the basis of the hamiltonian function (1). This problem is being investigated further.

The author is indebted to Professor E. B. Wilson, Jr., for suggesting the problem and to Professor J. H. Van Vleck for much help during the course of the research.

* Now at Bell Telephone Laboratories, Murray Hill, New Jersey.
† This work supported in part by the ONR.
[1] McAfee, Hughes, and Wilson, Rev. Sci. Instr. **20**, 281 (1949).

Remarks on the Optics of Radio Waves

Otto Halpern
University of Southern California, Los Angeles, California
(Received April 23, 1951)

IT is common practice in optics, primarily in the range of the visible spectrum, to consider an obstacle (e.g., a plane wall) as a *minor* disturbance if its thickness d times 2π is small compared to the wavelength measured inside. This is indeed a correct approximation for all practical cases as long as the index of refraction n

remains a number of the order unity. The *generally* correct theorem can be stated by the condition[1]

$$\pi d\epsilon/\lambda \ll 1, \tag{1}$$

where ϵ is the dielectric constant. For $(\epsilon)^{\frac{1}{2}} \gg 1$ the two conditions differ greatly.

A routine calculation shows that the reflection coefficient of a wall of thickness d and dielectric constant ϵ is given by

$$r = x^2/(1+x^2), \tag{2}$$

where $x = \pi d\epsilon/\lambda$. In the derivation it has been assumed that $2\pi d(\epsilon)^{\frac{1}{2}}/\lambda \ll 1$, but $(\epsilon)^{\frac{1}{2}} \gg 1$. It is clear from (2) that the wall acts like a good mirror until x becomes small compared to one.

This theorem becomes of practical importance if one deals with very thin layers of good metallic conductors. Here the complex index of refraction $\sim(\sigma/\nu)^{\frac{1}{2}}$ so that common practice would lead one to assume that for $(2\pi d/\lambda)(\sigma/\nu)^{\frac{1}{2}} \ll 1$ or $d \ll (\lambda/2\pi)(\nu/\sigma)^{\frac{1}{2}} =$ skin depth, the layer approaches transparency. The true condition[2] now reads

$$\pi d\sigma/c \ll 1. \tag{3}$$

We see that (3) is independent of the frequency. But approximate transparency of the layer now requires a thickness d which for an average good metallic conductor ($\sigma \sim 3\times 10^{17}$ sec^{-1}) becomes smaller than 10^{-8} cm. Every metallic layer in the customary sense of the word is therefore a good mirror for radiowaves down to wavelengths which still have conductivities that do not differ too much from their dc values.

[1] A potential well of thickness d and depth V remains a good reflector for a de Broglie wave of energy $E \ll V$ as long as $\pi dV/E \geqq 1$.

[2] In the case of ferromagnetic conductors the permeability μ has to enter as a factor in the denominator of (3).

Cross-Over Transition in the Decay of Tc^{99m}

J. W. Mihelich and M. Goldhaber
Department of Physics
and
Elizabeth Wilson
*Department of Chemistry, Brookhaven National Laboratory, Upton, Long Island, New York**

(Received April 19, 1951)

PREVIOUS attempts to discover cross-over transitions in a number of two-step isomers of Te and Sn have been unsuccessful.[1] These transitions were expected to be electric 2^5-pole. It seemed of interest, therefore, to search for a cross-over transition which could be expected to be magnetic 2^4-pole. Such a transition might occur in Tc^{99m} (6 hr). In this case Medicus, Maeder, and Schneider[2] have shown that the isomeric transition proceeds in two steps. The first lifetime-determining transition has the exceedingly low energy of 1.8 ± 0.3 kev. It is followed "promptly" by a second γ-ray of 141.2 ± 0.5-kev energy. For this transition Medicus *et al.*[2] find an internal conversion coefficient of 0.095 ± 0.020 and a ratio $\alpha_K:\alpha_L:\alpha_{M+N} = (7.9\pm0.5):1:(0.30\pm0.03)$ which permits its identification as a magnetic dipole transition on the basis of the K-conversion coefficients calculated by Rose *et al.*[3] Kessler and Meggers[4] have recently shown that the spin and magnetic moment of Tc^{99} in the ground state can be ascribed to a $g_{9/2}$ state, in agreement with shell theory, which suggests $p_{1/2}$ as the most plausible assignment for the metastable state. With these level assignments one might expect the cross-over transition $p_{1/2} \rightarrow g_{9/2}$ (magnetic 2^4-pole) with an intensity of the order 1 percent of the two-step transition. We have therefore searched for conversion electrons from a cross-over transition with a high resolution 180° photographic beta-spectrograph of low magnetic field. Tc^{99m} was obtained as a daughter of Mo^{99} (68 hr) which had been produced by bombarding molybdenum with slow neutrons in the Brookhaven reactor. The active molybdenum was dissolved in H_3PO_4 to which a small amount of $HClO_4$ had been added. The solution was distilled once; and the distillate, after addition of inactive molybdenum carrier, was redistilled. The H^+ concentration of the second distillate (containing the technetium) was adjusted to $4M$, and the technetium activity was coprecipitated, as the sulfide, with 0.1 mg of Pt added as H_2PtCl_6. The sulfide was centrifuged, washed, and mounted on a thin Al strip which was inserted in the beta-spectrograph. Figure 1 shows the internal

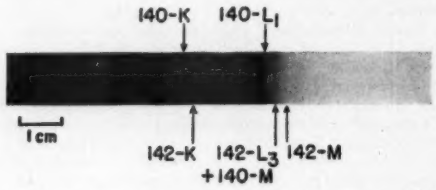

FIG. 1. Internal conversion electrons from Tc^{99m}.

conversion electron spectrum obtained, indicating clearly the presence of a cross-over transition. The approximate relative intensities were obtained by photometering the original film (no screen x-ray film). The results obtained are given in Table I.

TABLE I. Electron energies and intensities. The work functions of the various shells are given in parentheses in Col. 2.

Electron energy (kev)	Assignment	γ-energy (kev)	Intensity
119.3	$\gamma_1 - K$ (21.04)	140.3	100
121.3	$\gamma_2 - K$ (21.04)	142.3	9.7
137.5	$\gamma_1 - L_I$ (3.05)	140.2	13.1
139.5	$\gamma_2 - L_{III}$ (2.68)	142.2	5.3
	$\gamma_1 - M_I$ (0.63)	140.1	
141.7	$\gamma_2 - M_I$ (0.63)	142.3	0.93

The best values for the γ-ray energies are $\gamma_1 = 140.3\pm0.2$ kev and $\gamma_2 = 142.3\pm0.2$ kev. The difference is more accurately known: 2.0 ± 0.1 kev. Our energies differ slightly from those given by Medicus *et al.*[2] A weak electron line of 62 kev was also observed and is probably a K photoelectron line ejected from the Pt carrier by the 140-kev γ-ray.

The experimental K/L ratios are compared with the theoretical ones given by Tralli and Lowen[5] in Table II.

TABLE II. K/L ratios.

γ (kev)	K/L (exp.)	K/L (theor.)
140.3	7.7	12 (2^1 magnetic)
142.3	2.5[a]	4.7 (2^4 magnetic)

[a] The relative intensity of the L line of γ_2 was calculated on the assumption that the M line of γ_1, which coincides with it, has an intensity 10 percent of that of the L line of γ_1.

It is seen that the experimental K/L ratios are lower than expected from theory. Similar findings in the Te and Sn isomers have been previously interpreted as indications of admixtures of 2^5 electric transitions to the 2^4 magnetic transitions.[1] However, a different interpretation is given by Sunyar and Goldhaber,[6] who conclude that 2^4 magnetic transitions are pure, but that the calculated K/L ratios are too high. The 2^1 magnetic transition of Tc^{99m} is also found to be fairly pure.[6] From the table of K-conversion coefficients of Rose *et al.*[3] we find $\beta_4 = 31$. From this value and the observed $K/L+M$ ratio a partial half-life of 430 hr is obtained for the cross-over transition. The partial mean life for γ-ray emission alone, $\tau_\gamma = 1.06\times10^8$ sec, agrees well with the expected value for a 2^4 magnetic transition, 0.86×10^8 sec, calculated from the semi-empirical formula[6] $\tau_\gamma(\text{sec}) = 10^6(2I+1)/(A^2E^9)$, where I is the spin of the metastable state, A the mass number of the isomer, and E the transition energy (in Mev).

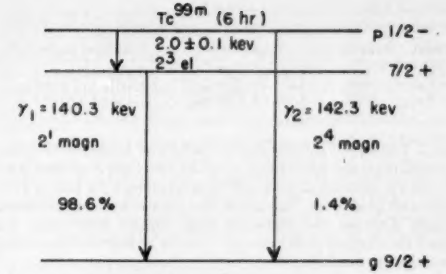

FIG. 2. Decay scheme of Tc^{99m}.

In the decay scheme shown in Fig. 2 we prefer to denote the first excited state of spin 7/2 and even parity as 7/2+ rather than $g_{7/2}$ for the following reason: a splitting of 140 kev between the $g_{9/2}$ and $g_{7/2}$ levels would seem to be too small to be compatible with the otherwise very successful assumption of strong spin-orbit coupling, from which one would expect a splitting of the order of 1–2 Mev. A still smaller splitting between a $g_{9/2}$ and a 7/2+ level (9.3 kev) has been observed in Kr^{83} by Bergström.[7] It is therefore plausible that the experimentally found small splittings are due to low-lying 7/2+ states of the configuration $(g_{9/2})^3$ (in Tc^{99}) and $(g_{9/2})^7$ (in Kr^{83}). This conjecture has been further generalized:[6] for the configurations $(g_{9/2})^{2\ \&\ or\ 7}$ the 7/2+ and the $g_{9/2}$ states reverse positions in about half the cases, thus accounting for the occurrence of electric 2^k-pole isomeric transitions in the $g_{9/2}$ shell $(7/2+ \rightarrow p_{1/2})$.

Our thanks are due Mr. E. L. Church and Dr. G. Friedlander for valuable help.

* Research carried out under contract with the AEC.
[1] Katz, Hill, and Goldhaber, Phys. Rev. **78**, 9 (1950). J. W. Mihelich and R. D. Hill, Phys. Rev. **79**, 781 (1950). R. D. Hill, Phys. Rev. **81**, 470 (1950).
[2] Medicus, Maeder, and Schneider, Helv. Phys. Acta **22**, 603 (1949); and **24**, 72 (1950).
[3] Rose, Goertzel, Spinrad, Harr, and Strong, privately distributed tables of K-conversion coefficients.
[4] K. G. Kessler and W. F. Meggers, Phys. Rev. **80**, 905 (1950), and **82**, 341 (1951).
[5] N. Tralli and J. S. Lowen, Phys. Rev. **76**, 1541 (1949).
[6] A. W. Sunyar and M. Goldhaber, Bull. Am. Phys. Soc. **26**, No. 3, 25 (1951).
[7] I. Bergström, Phys. Rev. **81**, 638 (1951).

Neutral Mesons Produced in the Capture of π^- Mesons in Hydrogen*

A. SACHS AND J. STEINBERGER
Columbia University, New York, New York
(Received April 20, 1951)

THE spectrum of the gamma-rays emitted in the interaction of π^- mesons with hydrogen has been measured by Panofsky, Aamodt, and Hadley.[1] They observe two groups of gamma-rays, one at 130 Mev and one at 70 Mev. The analysis of the experiment and the conclusions which may be derived from it rest on the assumptions (a) that the gamma-rays are due to mesons, (b) that these mesons have come to rest, and (c) that the low energy gamma-rays are the decay products of neutral mesons. We have experimentally verified these assumptions for the low energy group.

The experimental arrangement (Fig. 1) is the following: Mesons produced in the Columbia cyclotron are magnetically analyzed in the fringing field of the main magnet. They are collimated and monitored in two stilbene crystal counters, 2½ in. in diameter. They are decelerated from an initial energy of 80 Mev in absorber A, and enter the vessel B. This is filled with hydrogen at a pressure of 2500 lb/in.[2] and cooled to 80°K, corresponding to a density of 0.04 g/cm³. On each side of the container, behind 1.5 radiation lengths of lead converter, two 3½-in. diameter liquid scintillators are placed. All six counters are in coincidence, with a resolving time of 10^{-8} sec between pairs 1–2, 3–6, and 4–5. The coincidences are measured with and without lead converters, with hydrogen and helium gas fillings, and with various amounts of absorber.

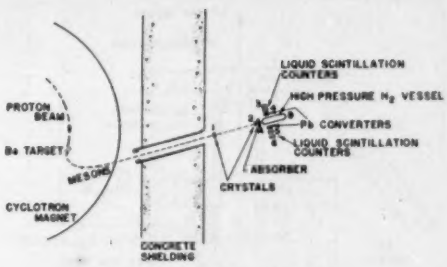

FIG. 1. Experimental arrangement.

The counting rate without converters is negligible. This shows that gamma-rays are detected. The fact that two gamma-rays are detected in coincidence shows that they are the decay products of a neutral meson. The counting rate with the helium-filled target is also negligible compared to that with hydrogen, showing that the coincidences are indeed due to a reaction in hydrogen. Finally, the variation of coincidence rate with absorber thickness shows that the gamma-rays are produced by stopping mesons (Fig. 2).

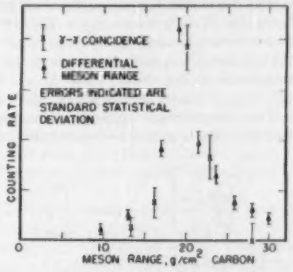

FIG. 2. Counting rate of gamma-gamma-coincidences as a function of the thickness of absorber A, showing that the coincidences are caused by stopped mesons.

It is therefore clear that some fraction of negative mesons coming to rest in the atomic orbits of hydrogen nuclei are converted into neutral mesons.

We wish to thank J. Spiro and H. F. Edwards for the operation of the cyclotron.

* Research assisted by the ONR and AEC.
[1] Panofsky, Aamodt, and Hadley, Phys. Rev. **81**, 565 (1951).

An Attempt to Detect μ-Meson Pairs from 322-Mev Bremsstrahlung*

J. W. MATHER, E. A. MARTINELLI, AND W. N. JARMIE
Radiation Laboratory, Department of Physics, University of California, Berkeley, California
(Received April 30, 1951)

IT has been suggested that high energy photons should create pairs of μ-mesons, either by an electromagnetic process (since it is thought probable that the μ-meson is a Dirac particle) or by virtue of recent considerations of Wentzel.[1] Steinberger suggested one might look for the effect using the Berkeley synchrotron.

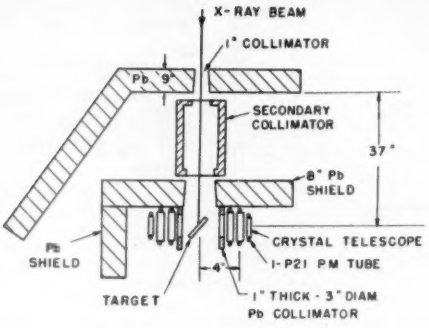

FIG. 1. Experimental arrangement.

The total yield of such pairs is given by

$$n\int_{E_0}^{E_{\max}}\sigma(E)\frac{dF(E)}{dE}dE,$$

where n is the number of nuclear centers per unit area, E_0 is the threshold, $E_{\max}$ is 322 Mev, $dF(E)/dE$ is the total photon spectrum, and $\sigma(E)$ is the cross section for pair production. In our computations we have assumed the cross section to be of the form: $\sigma(E)=\sigma_0[(E-E_0)/m_\mu c^2]^3$. For electromagnetic pair production,[3] as an example, σ_0 is $0.085\bar{\phi}$ where $\bar{\phi}$ is $(1/137)(Ze^2/m_\mu c^2)^2$ (using the μ-mass instead of the electron mass). Using this value for a 1-inch CH_2 target gives 4.6×10^{-11} pairs per equivalent quantum (e.q.) and for $\frac{1}{2}$-inch lead: 2.3×10^{-9} pairs per e.q., where the number of e.q. is the total energy in the beam divided by the maximum photon energy (322 Mev). The beam used for this experiment was on the order of 2×10^9 e.q. per minute.

The experimental apparatus, consisting of two scintillation counter telescopes and associated electronics, is shown in Figs. 1 and 2. The liquid scintillator is 0.5 percent of terphenyl in xylene enclosed in glass cylinders 4 in. diam.$\times$1.25 in. and 3 in. diam.$\times$0.5 in. (for the anticoincidence) with thin windows for a pair of 1P21 photomultipler tubes. The use of two phototubes per scintillator greatly flattened the geometric pulse height distribution and raised the electron signal rate by a factor of five without raising the noise appreciably.

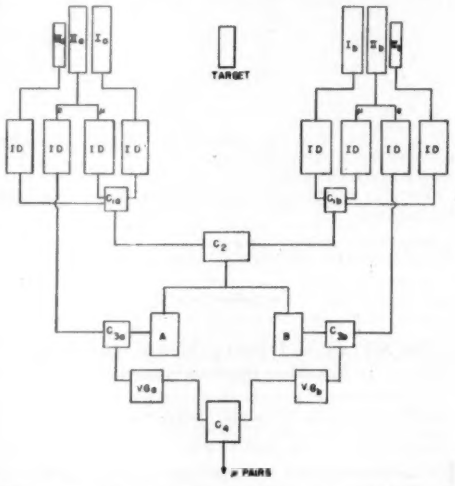

FIG. 2. Electronics arrangement: I, II, III$_{a \text{ and } b}$—3 crystal telescope; ID—inverter discriminators; μ—meson pulse; e—electron pulse; C_{1a}, C_{1b}—coincidence-anticoincidence unit; C_2—pair coinc. $\tau\sim10^{-7}$ sec; C_{3a}, C_{3b}—electron-gate coinc. $\tau\sim10^{-7}$; C_4—final coinc. $\tau=10^{-7}$; A, B—4 channel—$2\mu S$ tandem gate maker; VG_a, VG_b—pulse widener.

TABLE I.

Target	Angle (lab)	Total counts	Calculated accidentals
Cu	90°	1 per 10^9 e.q.	1.4 per 10^9 e.q.
CH_2	90°	1 per 5.6×10^{10} e.q.	0.17 per 5.6×10^{10} e.q.
CH_2	135°	1 per 2.5×10^{11} e.q.	2.2 per 2.5×10^{11} e.q.

Each meson channel was adjusted to count π^+ mesons (by means of the μ-electron decay) with maximum efficiency, and the result of this was found to be in good agreement with the work of Steinberger and Bishop.[3]

CH_2 and Cu targets were used for 90° observations and CH_2 for 135°. The number of pairs one would expect to count can be calculated as follows:

$$\text{No.}=n(\Omega)^2(D)^2C\eta\int Q(E)\sigma(E)dF(E)/dEdE,$$

where Ω, the solid angle subtended by each counter telescope at the target, is squared if we assume the angular distribution of the μ's to be random and spherically symmetric; D is the fraction of the decay electrons accepted by the delayed electron gates; C is the fraction of the μ^- mesons which give a decay electron in carbon; η is the counter efficiency for seeing the μ-electron decay; and $Q(E)$ accounts for the small part of the total energy spectrum of the μ-pairs which will be accepted by the counters. This includes two effects, since the energy acceptance of the crystals limits the total energy of the pair and also the manner in which the total energy is split. The last factor greatly reduces the number of pairs detected.

For the electromagnetic theory, for example, where the energy splitting distribution (for small μc^2) is fairly flat, reasonable values for these quantities give the following results:

1×10^{-16} pairs per e.q. in CH_2 at 90°
5×10^{-15} pairs per e.q. in Pb at 90°.

These rates are impossibly small, and the angular distribution for this process is probably somewhat forward, so it was decided to look for other modes of μ-pair production at 90° and 135° where the background conditions are decidedly better. It is assumed that these processes would have a reasonably spherically symmetric angular distribution.

The results of several bombardments are shown in Table I. To observe a real counting rate of this order of magnitude would mean that a process, similar to electromagnetic production, would have to have a cross section 2×10^8 larger than the electromagnetic cross section. Both of the CH_2 results give an upper limit on the total μ-pair yield which is 3 percent of the (experimental) π^+ yield. A previous value of 2 percent has been given by Peterson, Gilbert, and White,[4] as a by-product of their investigations of photomeson production using photographic plates. The background with a Cu target was too high to make an estimate possible.

The relatively high accidental rate is inherently due to the electron singles rate flooding the wide gates necessary to receive the decay electron. Any possible improvement should therefore include a means of drastically reducing the electron singles rate. A possible means of doing this would be to shield the electron counters from the target. A faster coincidence for the μ-mesons would only be of partial help, as it was found that approximately $\frac{1}{4}$ of the coincidences formed were real. It should be noted that the accidental rate will go theoretically as the fourth power of the beam intensity. Experimentally this variation was verified.

Another major problem is how to make a practical increase in the energy acceptance of the counters without detrimentally in-

creasing the accidental rate. Other improvements should be noted, such as a higher beam energy (although multiple π-production might hinder this); an improved β-gate; and generally refined electronics. It can be seen, using reasonable factors for these improvements, that while the μ-pair/π^+ ratio could be improved, the electromagnetic pair production yield would be far from reached.

It is a pleasure to acknowledge the guidance of Dr. E. McMillan on this project, and some helpful discussions with J. Steinberger and A. S. Bishop. We also thank George McFarland and the synchrotron crew for their assistance; John Barale, Al Stripeika, and Vern Ogren for their invaluable help with the complex electronics; and Harry Powell who did the glass work for the counters.

* This work was performed under the auspices of the AEC.

[1] G. Wentzel, Phys. Rev. **79**, 710 (1950).
[2] W. Heitler, *The Quantum Theory of Radiation* (Oxford University Press, London, England, 1944), second edition.
[3] J. Steinberger and A. S. Bishop, Phys. Rev. **78**, 493 (1950).
[4] Peterson, Gilbert, and White, Phys. Rev. **81**, 1003 (1951); and UCRL-703 Rev.

The Optical Absorption and Photoconductivity of Rutile*

D. C. Cronemeyer and M. A. Gilleo
Laboratory for Insulation Research, Massachusetts Institute of Technology, Cambridge, Massachusetts
(Received April 30, 1951)

RUTILE (TiO_2) single crystals[1] have been investigated by optical and electrical methods. The optical density of a 1-mm plate, cut perpendicular to the optic axis, is shown in Fig. 1. The absorption edge at 0.4μ is steep even at room temperature, and becomes very sharp at low temperatures ($<30°K$). The 0.4μ absorption has been identified as the fundamental lattice absorption of rutile at 3.06 ev. This absorption has been correlated with the high temperature (350°–850°C) conductivity measurements which give a value $E_G=3.05$ ev.

The 1-mm thick crystal shows photoconductivity (ac method) peaking on the rise of the fundamental absorption at 0.41μ and having a long wavelength response extending into the infrared beyond 1μ, with a corresponding tail of the optical absorption.

Upon slightly reducing the crystal in a hydrogen atmosphere at 600°C (or heating in vacuum), a blue color which accompanies the oxygen loss from the crystal is noted. The weight loss during reduction has been studied; the reduction-oxidation cycle proves reversible for small oxygen loss as far as weight changes are concerned. This reversibility shows that the formation of oxygen ion vacancies in the crystal does not lead to a loss of titanium under these conditions. The blue coloring arises from the visible tail of an optical absorption band with its maximum at approximately 1.8μ, as shown by the dotted lines in Fig. 1.

A simple atomic model[2] has been used for a calculation of the

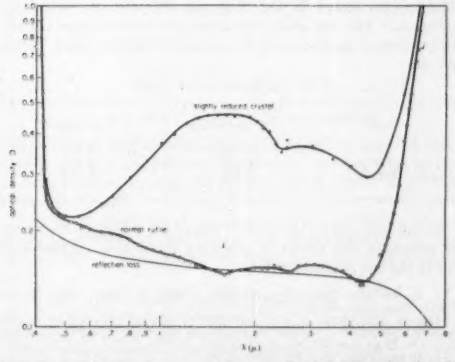

Fig. 1. Optical density *vs* wavelength for normal and slightly reduced rutile.

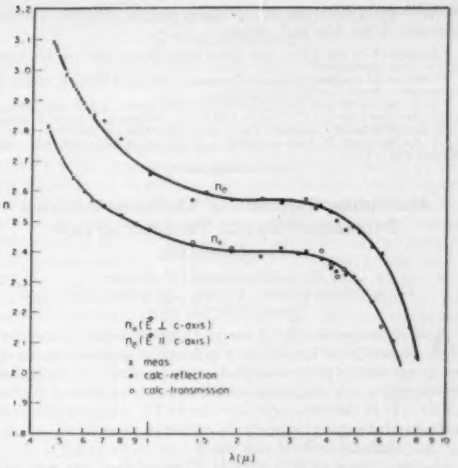

Fig. 2. Index of refraction *vs* wavelength of ordinary and extraordinary ray.

various impurity and lattice-defect levels inserted in the electronic energy structure of the material. An impurity atom of valence +3 or +5 will act as an acceptor or donor, respectively, if it enters substitutionally at a titanium site (Ti^{+4}); for such an impurity, the ionization energy would be that of a hydrogen atom immersed in a polarizable medium of dielectric constant κ_e. In this case, the ionization energy is vastly reduced and amounts to the ionization energy divided by the square of the dielectric constant, that is, $13.6/\kappa_e^2$ ev. Similarly, a vacant oxygen site may be considered as a doubly-charged center resembling a helium atom and having the ability to trap two electrons with the reduced ionization energies of helium, $24.6/\kappa_e^2$ and $54.4/\kappa_e^2$ ev. The value $\kappa_{eo}=(2.40)^2$ has been determined from the flat portion of the index of refraction curve (Fig. 2) for the ordinary ray. For rutile, the index of refraction has been calculated from the reflecting power curves of Liebisch and Rubens.[3] Transmission data support this calculation in the 1.5μ to 5μ region.

The three optical absorptions (corresponding to impurity-level ionization energies) predicted in this manner are given in Table I. Experimental values derived from maxima of optical absorption and of photoconductivity are indicated for comparison. If this same type of calculation is carried out using the static dielectric constant, ionization energies as small as 0.002 ev are found for the hydrogen-like impurity levels. The approximation of using the macroscopic index of refraction should have greater validity in the case of a material with high index of refraction, since the electronic charge cloud is spread out over a larger volume of the material. For the case of the alkali halides a similar calculation yields only qualitative agreement with experiment.

This work was done under the supervision of Professor A. von Hippel to whom we are indebted for his interest and encouragement. We are grateful to Professors L. Harris and R. C. Lord,

Table I. Impurity-level ionization energies for rutile.

Origin of added energy level	Electronic configuration	Ionization energy calculated		observed
Impurity atom, valence 3 or 5	Hydrogen	0.42 ev	2.9 $\lambda(\mu)$	2.8–3.2[b] $\lambda(\mu)$
Vacant oxygen site	Helium	0.74	1.7	1.5–1.9[b]
	He^+	1.64	0.76	0.73[c]

[a] From absorption measurements; the evidence is not conclusive.
[b] Definite evidence from absorption and from photoconductivity for wavelengths between 1 and 3μ.
[c] Some evidence from photoconductivity measurements.

Massachusetts Institute of Technology, for the absorption measurements in the 0.8μ to 7μ region.

* Sponsored by the ONR, the Army Signal Corps, and the Air Force under ONR contract.

[1] Courtesy of the National Lead Company, Titanium Division, Research Laboratory, South Amboy, New Jersey.

[2] H. A. Bethe, Report 43-12, Radiation Laboratory, M.I.T., November, 1942; discussed by H. C. Torrey and C. A. Whitmer, *Crystal Rectifiers* (McGraw-Hill Book Company, Inc., New York, 1948), p. 65.

[3] T. Liebisch and H. Rubens, Sitzber. preuss. Akad. Wiss., Physik-math. Klasse, 211 (1921).

Absorption Spectrum of Thallium-Activated Potassium Chloride Phosphor at Low Temperatures

PETER D. JOHNSON AND F. J. STUDER
General Electric Research Laboratory, Schenectady, New York

(Received April 4, 1951)

AN important feature of recent quantitative theoretical work on solid-state luminescence is the effect of zero-point energy in maintaining broad absorption and emission spectra at low temperatures.[1] A comparison of experimental optical absorption of KCl:Tl in the band near 5 ev due to Tl^+, reported here, with calculated absorption indicates the existence of zero-point energy[2] of the calculated order of magnitude.

A clear crystal of KCl:0.00021 Tl grown from the melt in a furnace of the type described by Strong[3] is clamped in the copper sample holder of the cooling apparatus shown in cross section in Fig. 1. The only openings in the holder are two 3×5-mm rectangles

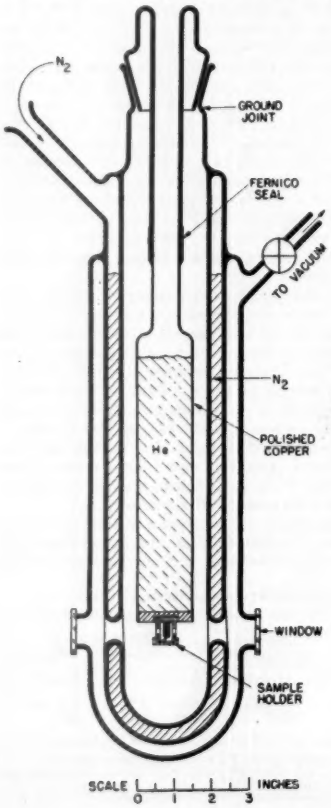

FIG. 1. Apparatus for optical absorption of crystals at liquid helium temperature.

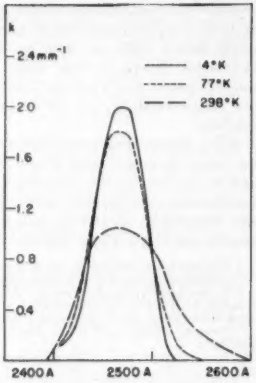

FIG. 2. Absorption spectrum of KCl:Tl as a function of temperature.

to allow passage of transmitted light. An advantage in the construction of this apparatus is that there are only two quartz windows in the optical path. These, being at room temperature, can be attached with vacuum sealing wax. Except for the inner container, the apparatus is of Pyrex, silvered on all surfaces exposed to the vacuum. The apparatus with crystal in position is placed between a low voltage hydrogen discharge lamp and the entrance slit of a recording grating spectroradiometer. Heating of the crystal by the hydrogen lamp is found to be negligible. Recordings of the light from the source transmitted by the crystal at room temperature, then with liquid N_2 in both coolant containers, and finally with liquid helium in the inner container are obtained. From these and a recording of the unattenuated output of the hydrogen lamp, the absorption as a function of wavelength at the various temperatures as given in Fig. 2 is determined. The error in estimation of half-widths of the absorption band is less than 10 percent. On continued irradiation by the hydrogen lamp at 77°K or 4°K a weak absorption band not shown in Fig. 2, possibly due to V-centers,[4] developed in the crystal with peak at 2340A. The thallous ion absorption reported here has been obtained taking care to minimize development of V-centers, since the two absorption bands overlap to some extent.

Table I compares the experimental half-widths in electron volts with the calculated values. If zero-point energy is neglected, only the 4°K half-width is affected appreciably, being reduced to 0.031 ev. There is no doubt that the experimental values can be reconciled only with the values calculated using zero-point energy; and the zero-point energy used in the calculations must be of the correct order of magnitude. It should be pointed out also that the experimental variation with temperature in peak height of absorption shown in Fig. 2 agrees well with the calculated absorption.[1] The area under the absorption curve is substantially independent of temperature, the oscillator strength being 0.06 in all cases.

TABLE I. Absorption half-width.

Temp.	Experimental	Calculated
4°K	0.108 ev	0.122
77°K	0.127	0.132
298°K	0.204	0.193

We are indebted to Dr. M. D. Fiske of the cryogenic laboratory for assistance and advice in designing the double vacuum flask and in the use of liquid helium.

[1] F. E. Williams, Phys. Rev. **80**, 306L (1950); J. Chem. Phys. **19**, 457 (1951); Phys. Rev. **82**, 281 (1951).

[2] During preparation of this manuscript, relevant information on the emission spectra of a number of phosphors has been reported. C. Klick, Bull. Am. Phys. Soc. **26**, No. 2, 18 (1951).

[3] J. Strong, Phys. Rev. **36**, 1663 (1930).

[4] Casler, Pringsheim, and Yuster, J. Chem. Phys. **18**, 1564 (1950).

The Beta-Ray Spectrum of Tl^{206}

D. E. Alburger and G. Friedlander
*Brookhaven National Laboratory, Upton, Long Island, New York**
(Received April 25, 1951)

THE beta-decay of 4.23-minute Tl^{206} has been studied because of its relationship to previously reported work[1] on Bi^{206} and Po^{210}. All three of these nuclides decay to Pb^{206}, and it therefore seemed worthwhile to determine whether any of the excited states of Pb^{206} are involved in Tl^{206} decay. Previous work[2] with absorption methods indicated that Tl^{206} emits beta-rays of about 1.7-Mev maximum energy and no gamma-rays.

Samples of pure thallium metal were irradiated in the Brookhaven nuclear reactor and a beta-activity of 4.3±0.1-min half-life was observed. A search for gamma-radiation from strong sources was made with a scintillation spectrometer by photographing the pulse height distribution presented on an oscilloscope screen. These photographs revealed no gamma-ray structure, other than a continuum of energies mostly below 500 kev which can be accounted for only as bremsstrahlung from the beta-rays.

A lens spectrometer set for 3 percent resolution was used to study in detail the electron spectrum from evaporated foils of thallium metal approximately 2 mg/cm² thick. The foils were activated in the reactor for 5 minutes and delivered in a "rabbit" through the pneumatic tube system to an outlet near the spectrometer. A monitor counter, arranged to detect beta-rays directly from the source, allowed the counting interval to be matched to the source strength, thereby removing the effect of source decay.

In a search for gamma-rays no internal conversion lines were found. The Kurie plot of the beta-spectrum is shown in Fig. 1. Relativistic Fermi functions from Feister's table[3] were used in the calculations, and calibration was taken from the conversion line of Cs^{137}. The plot is linear above about 0.6 Mev and has an end point at 1.51±0.01 Mev. The deviation from linearity is about what one would expect from the source thickness and does not contradict the conclusion that the spectrum is simple and of the allowed type.

The result is in general agreement with an analysis of the internally converted gamma-rays of Bi^{206} and Po^{210} by Goldhaber and Sunyar,[4] according to which the first excited state of Pb^{206} at 803 kev is assigned a spin of 3 and odd parity. Since the decay of Tl^{206} to the ground state of Pb^{206} is allowed and therefore involves

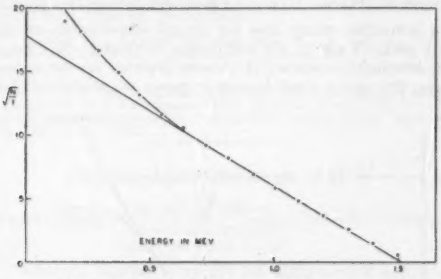

FIG. 1. Kurie plot of the Tl^{206} beta-ray spectrum.

a small nuclear spin change, one would expect that partial beta-decay to the first excited state is forbidden. Further analysis has not been possible, because the complete level scheme of Pb^{206} is not yet established.

We wish to thank Dr. H. T. Motz and E. der Mateosian for making their laboratory facilities at the reactor available for this work and Mr. A. Weinstein for preparing the evaporated thallium samples.

* Research carried out under contract with the AEC.
[1] D. E. Alburger and G. Friedlander, Phys. Rev. **81**, 523 (1951).
[2] Way, Fano, Scott, and Thew, Natl. Bur. Standards (U. S.) Circ. 499.
[3] I. Feister, Phys. Rev. **73**, 373 (1950).
[4] We are indebted to Drs. Goldhaber and Sunyar for making their unpublished results known to us.

The Combination of Resistivities in Semiconductors*

V. A. Johnson and K. Lark-Horovitz
Purdue University, Lafayette, Indiana
(Received April 25, 1951)

THE analysis[1] of resistivity *vs* reciprocal temperature curves for semiconductors, particularly germanium alloys, has shown that the experimental resistivity may be explained as due to a combination of a resistivity ρ_L due to the scattering of carriers by lattice ions and a resistivity ρ_I due to scattering by impurity ions; a complete analysis must also consider scattering processes due to neutral impurity atoms,[2] grain boundaries between crystallites, and the presence of ionized impurity centers of both signs.[3] Shockley and Schottky in discussions have first pointed out that the total resistivity is not given by the arithmetic sum of the partial resistivities;[4] more recently this fact has been discussed by Jones.[5] The following discussion of the proper combination of ρ_L and ρ_I corrects errors in Fig. 1 and Eq. (6) of reference 4 and also points out that our original argument[6] for obtaining higher mobility values from observed data is modified only slightly by this correction.

If one assumes that the two scattering processes are approximately independent of each other, the effective mean free path is given by

$$1/l = 1/l_L + 1/l_I, \tag{1}$$

where l_L and l_I are the mean free paths associated with lattice and impurity scattering separately. If one assumes the Rutherford scattering model[7] for evaluating ρ_I, the resistivity when only impurity scattering is present, then l_I is proportional to the fourth power of the velocity. Let ρ_L represent resistivity due to lattice scattering alone, with ρ_I negligible. With both lattice and impurity scattering present, the use of Eq. (1) in the usual expression for the resistivity of semiconductors leads to the following relation between the sum $\rho_L+\rho_I$ and ρ, the total resistivity:

$$F=(\rho_L+\rho_I)/\rho=(1+b^2/6)\left\{1-b^2\int_0^\infty xe^{-x}(x^2+b^2)^{-1}dx\right\}, \tag{2}$$

where $b^2=6\rho_I/\rho_L$. Figure 1 shows the dependence of the ratio F upon the fraction $\rho_I/(\rho_L+\rho_I)$. By private communication, we have learned that Shockley had previously calculated this function and obtained results identical with those of Fig. 1.

By using Eq. (1) in the calculation of the Hall coefficient R, one obtains the following relation [equivalent to Jones' Eq. (3)]:

$$r=R/(1/ne)=(\pi^{1/2}/48)(b^2+6)^2F^{-2}\int_0^\infty x^{9/2}e^{-x}(b^2+x^2)^{-2}dx. \tag{3}$$

The dependence of r upon $\rho_I/(\rho_L+\rho_I)$ is shown in Fig. 2. The abscissas in Jones' figure are values of ρ_I/ρ; if allowance for this difference is made, it is found that our curve and that of Jones are in substantial agreement. The figure is also consistent with Shockley's proof that $r \geq 1$.

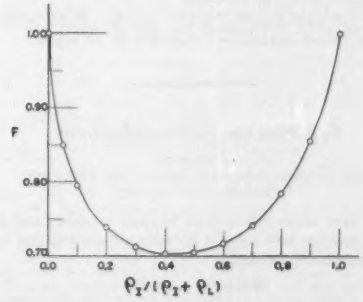

FIG. 1. The dependence of $F=(\rho_I+\rho_L)/\rho$ upon the ratio $\rho_I/(\rho_I+\rho_L)$.

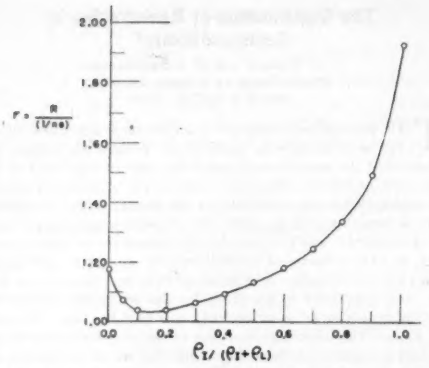

FIG. 2. The dependence of r, the ratio of the Hall coefficient R to $1/ne$, upon the ratio $\rho_I/(\rho_I+\rho_L)$.

We calculate mobility values higher than those suggested by Jones, for the following reason. Since the mobility associated with lattice scattering, b_L, is given by $b_L=(ne\rho_L)^{-1}$ and since $R=r/(ne)$, we find

$$b_L=R/(r\rho_L). \tag{4}$$

However, the experimental resistivity curve is the ρ-curve, and from its analysis one obtains ρ_L'- and ρ_I'-curves, which are determined as the curves of appropriate temperature behavior that add to give the ρ-curve. Since $\rho_L+\rho_I=F\rho_I$ and since F is constant to within four percent as the ρ_I/ρ_L ratio varies from $\frac{1}{4}$ to 3, it should be a good approximation to take $F\rho_L'$ as ρ_L, $F\rho_I'$ as ρ_I, and ρ_L'/ρ_I' as ρ_L/ρ_I. The r value can be found from Fig. 2 with ρ_L/ρ_I known, and thus b_L has been estimated for a number of N-type germanium samples, both polycrystalline and single crystal. The result is that the mobility values of about one-third of the samples is in agreement with the directly determined value,[6] and the values for the other two-thirds are too low by ten to thirty-five percent. However, the mobilities obtained in this way exceed those calculated from $(8/3\pi)(R/\rho_L)$ by factors up to a maximum of 1.65. There is a tendency for the mobility b_L to decrease with increasing impurity content, whereas one expects b_L to be determined by the properties of the germanium lattice and thus independent of impurities. Since the calculated mobilities for the impure samples tend to be too low, it is likely that the discrepancy is due to failure to consider scattering mechanisms other than lattice and impurity scattering.

* Work assisted by Signal Corps Contract.
[1] K. Lark-Horovitz, NDRC Report 14-585, p. 36; Phys. Rev. **69**, 258 (1946).
[2] G. L. Pearson and J. Bardeen, Phys. Rev. **75**, 881 (1949).
[3] C. S. Hung and V. A. Johnson, Phys. Rev. **79**, 535 (1950).
[4] V. A. Johnson and K. Lark-Horovitz, Phys. Rev. **79**, 176 (1950).
[5] H. Jones, Phys. Rev. **81**, 149 (1951).
[6] V. A. Johnson and K. Lark-Horovitz, Phys. Rev. **79**, 409 (1950).
[7] E. Conwell and V. F. Weisskopf, Phys. Rev. **77**, 388 (1950).
[8] Pearson, Haynes, and Shockley, Phys. Rev. **78**, 295 (1950).

Criterion for Superconductivity

J. BARDEEN
Bell Telephone Laboratories, Murray Hill, New Jersey
(Received April 19, 1951)

WE have taken interactions between electrons and lattice vibrations into account by using a wave function for the complete system of the form:[1]

$$\Psi=\varphi_e(x_i,q_r)Q(q_r). \tag{1}$$

The wave function for the electrons, φ_e, which involves the vibrational coordinates, q_r, parametrically, is approximated by Slater-Fock determinental wave functions in which the wave functions for the individual electrons are of the form:

$$\Psi_k=a_k(q_r)\psi_k+\Sigma_{k'}a_{kk'}(q_r)\psi_{k'}. \tag{2}$$

The interactions important for superconductivity are those for which the Bloch states have energies close to the Fermi surface:

$$\epsilon_k\simeq\epsilon_{k'}\simeq E_F. \tag{3}$$

In the paper cited, k and k' were chosen in such a way that

$$E_F<\epsilon_k<E_F+\Delta E;\quad E_F-\Delta E<\epsilon_{k'}<E_F, \tag{4}$$

where ΔE is of the order of the energy change resulting from the interaction terms. The criterion for superconductivity was obtained from the condition that the states Ψ_k have a lower energy than the Bloch states they replace. This requirement is

$$\Delta E\sim N(E)|\mathfrak{M}_{kk'}q_{kk'}|^2_{kk'}>(\hbar\omega_{kk'})_{kk'}. \tag{5}$$

The distribution of states and criterion are then similar to those of Fröhlich's theory.[2]

It has been pointed out to the author by Van Vleck[3] that one will get a still lower energy by taking the k in the lower energy range and the k' in the higher range. When Eq. (5) is satisfied, the difference in energy is not large. However, there will always be some decrease in energy by forming the linear combinations no matter how weak the interaction. How should one then distinguish between interactions which occur in the normal phase and those which give rise to superconductivity? While a satisfactory answer has not been obtained, the following indicates the considerations which are involved.

Superconductivity is believed to be associated with a high curvature of the energy surface in k-space and consequent small effective mass of electrons with energies near E_F, as illustrated in Fig. 1.[4] The interactions in the normal state must be such that the effective mass is not altered very much.

We have calculated the first-order change in wave functions for a Fermi distribution of electrons at temperature T and find[5]

$$\Psi_k=\psi_k+\Sigma_{k'}\mathfrak{M}_{kk'}q_{kk'}\psi_{k'}/\{\epsilon_k-\epsilon_{k'}+\hbar\omega_{kk'}\coth[(\epsilon_k-\epsilon_{k'})/2\kappa T]\}. \tag{6}$$

The sum over k' is over all states, occupied as well as unoccupied. The term in $\hbar\omega_{kk'}$ comes from derivatives of φ_e with respect to the q's. The energy is changed in the second order:

$$E_k=\epsilon_k+\Sigma_{k'}|\mathfrak{M}_{kk'}q_{kk'}|^2/\{\epsilon_k-\epsilon_{k'}+\hbar\omega_{kk'}\coth[(\epsilon_k-\epsilon_{k'})/2\kappa T]\}. \tag{7}$$

The interaction energy does not depend very strongly on the wave vector k nor on the distribution of electrons in k-space. The interaction terms are of the sort expected for the normal phase; they give a small decrease in energy of the electrons but

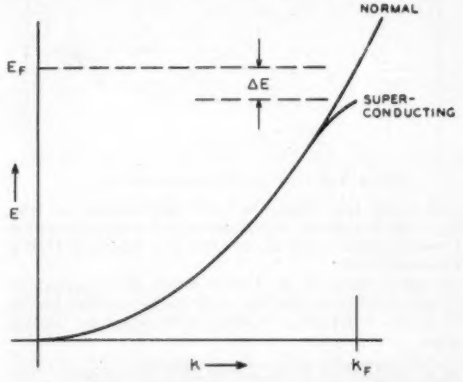

FIG. 1. Schematic diagram of energy, E, *versus* wave vector, k, for electrons in the normal and superconducting phases. The energy decrease $\Delta E\sim\kappa T_c$ is greatly exaggerated.

no appreciable change in effective mass nor in the electrical properties.

Superconductivity arises from interactions for which the energy denominators are small and for which the second-order perturbation theory breaks down. The condition

$$\Sigma_{k'}|a_{kk'}|^2 > \sim 1 \tag{8}$$

requires first that the temperature be sufficiently low, otherwise $\coth[(\epsilon_{k'}-\epsilon_k)/2\kappa T]$ is large, and second that the matrix elements be sufficiently large compared with $(\hbar\omega_{kk'})_{Av}$. The second of these conditions is *essentially the same as the criterion* (5) and the interactions involved are those for which $|\epsilon_{k'}-\epsilon_k| < \sim \Delta E$. Those for which $|\epsilon_{k'}-\epsilon_k| > \sim \Delta E$ and for which the perturbation theory is valid are expected to be the same in the normal and superconducting states and can be taken into account by redefining the Bloch functions as in Eq. (6).

The wave functions in the superconducting phase at $T=0°K$ have been taken to be of the form[1]

$$\Psi_k = N_k(q_r)(\psi_k + \Sigma_{k'} b_{kk'} q_{kk'} \psi_{k'}), \tag{9}$$

where the sum is over k' such that $|\epsilon_{k'}-\epsilon_k| < \Delta E$. Normalization is given by the factor $N_k(q_r)$, the $b_{kk'}$ are chosen to give a minimum energy, and the $\psi_{k'}$ are Bloch functions modified as indicated above. The minimum is now obtained when k' runs only over the normally unoccupied states. The wave functions are similar to those previously discussed; the energies of states near E_F are depressed to give a small effective mass as shown in Fig. 1. Electrical properties are similar to those of a metal with a small concentration of electrons (actually holes, since the configuration is similar to that of an almost filled band) with small effective mass. We have shown that such a model leads to the London equations.[4]

Nevertheless, the theory is unsatisfactory. If, as previously assumed, the interactions in Eq. (9) do not occur in any way in the normal phase, the calculated energy difference between the normal and superconducting phases is too large.[1] This suggests that these interactions do occur in the normal phase, but in such a way that the effective mass is not altered. An adequate theory for the transition, including a criterion for superconductivity, requires better wave functions for both the normal and superconducting phases.

[1] J. Bardeen, Phys. Rev. **80**, 567 (1950). This reference may be used for definitions of the symbols used above.
[2] H. Fröhlich, Phys. Rev. **79**, 845 (1950).
[3] Private communication.
[4] J. Bardeen, Phys. Rev. **79**, 167 (1950); Phys. Rev. **81**, 829 (1951). The cooperative nature of the phenomenon is believed to come from the fact that such an energy reduction will depend markedly on the distribution of electrons in k-space.
[5] The derivation will be published elsewhere. The matrix elements should be determined by a self-consistent field procedure as was done for the calculation of the conductivity of monovalent metals. See J. Bardeen, Phys. Rev. **52**, 688 (1937).

Complex Alpha-Spectrum of U^{235}

A. Ghiorso
*Radiation Laboratory and Department of Chemistry, University of California, Berkeley, California**
(Received March 26, 1951)

It has been possible to resolve the alpha-particle radiation emitted by U^{235} into at least three groups by use of our alpha-pulse analyzer. The material used for this work had been highly enriched relative to U^{234} as well as U^{238}, so that the alpha-radiation from U^{234} was only about 35 percent of the total activity.

The sample used for pulse analysis consisted of approximately 100 μg of uranium electrodeposited onto an area 15 mm in diameter on a thin platinum plate. A collimator consisting of a brass ring, 3 mm high and 27 mm in diameter, was placed around the sample so that the sample area was centered. The purpose of the collimator is to eliminate from detection those alpha-particles which emerge from the sample at a small angle relative to the plane of the sample mounting; these are the particles which contribute most to the low energy straggling observed at 2π-geometry

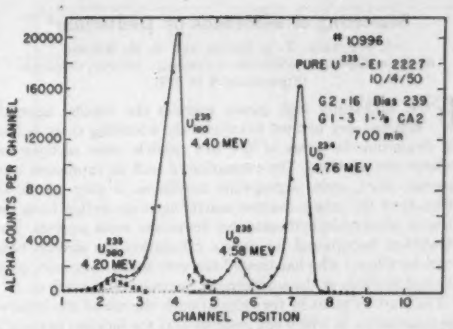

FIG. 1. Pulse analysis of U^{235} alpha-particles.

because of sample self-absorption and backscattering. This type of collimator enables one to obtain 35 percent geometry with an almost negligible low energy straggling; for a thin sample the low energy "tail" is down to *ca* 0.1 percent at a point approximately 150 kev lower than the peak.

A typical pulse analysis obtained with our 48-channel differential alpha-pulse analyzer is shown in Fig. 1. By comparison with

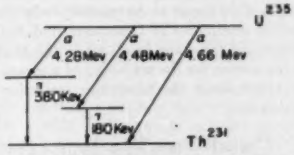

FIG. 2. Proposed decay sequence of U^{235}.

a pulse analysis of radioactively pure samples of U^{234} and U^{235}, it can be shown by a process of elimination that the isotope U^{235} is responsible for the peaks at 4.58, 4.40, and 4.20 Mev. The 4.58-Mev peak had previously been suspected because of a 180-kev gamma-ray which has been observed[1-4] in high abundance associated with U^{235}. The 4.20-Mev peak is a new group, and the low abundance 380-kev gamma-ray which would be associated with it has not been reported by any workers in this field. The possibility of a fourth alpha-particle group at 4.47 Mev is suggested by the shape of the main U^{235} peak when it is compared with the U^{234} peak.

The abundances of the various groups[5] and their consequent partial alpha-half-lives are as follows:

U_0^{235}	4.58 Mev	10.2 percent	6.99×10^9 years
U_{100}^{235}	4.40 Mev	85.6 percent	8.33×10^8 years
U_{380}^{235}	4.20 Mev	4.2 percent	1.70×10^{10} years.

These are calculated on the basis of Nier's value for the total half-life of U^{235} of 7.13×10^8 years.[6]

The decay sequence of U^{235} is presumably that given in Fig. 2.

The author is indebted to Dr. C. E. Larson and the Y-12 Plant of Carbide and Carbon Chemicals Division of the Oak Ridge National Laboratory for making available the sample of highly enriched U^{235}, and wishes to thank Mr. Robert C. Lilly for the careful preparation of the U^{235} sample.

* This work was performed under the auspices of the AEC.
[1] M. H. Studier, reported in Metallurgical Laboratory Report CC-3056 (July, 1945), unpublished.
[2] R. L. Macklin and W. S. Miller, Uranium Project Report A-3640 (April, 1946), unpublished.
[3] B. F. Scott, Argonne National Laboratory Report CC-3715 (January 1947), unpublished.
[4] R. L. Macklin, Phys. Rev. **76**, 595 (1949).
[5] In the interest of clarity, a new nomenclature is suggested for the subscript labeling of alpha-energy groups. Such subscripts would denote the energy difference in kev between the ground state and each group; thus, for U^{235} the ground-state transition is indicated as U_0^{235}, the next highest energy group which would normally be called U_1^{235} is now labeled as U_{100}^{235}, and similarly U_2^{235} is called U_{380}^{235}.
[6] A. O. Nier, Phys. Rev. **55**, 150 and 153 (1939).

Scattering of π-Mesons by Deuterium*

S. FERNBACH, T. A. GREEN, AND K. M. WATSON
Radiation Laboratory, University of California, Berkeley, California
(Received April 19, 1951)

FOR sufficiently high meson energies the impulse approximation[1] may be used to express the scattering cross section for deuterium in terms of the free particle cross sections for protons and neutrons. The evaluation of such an expression is of interest, since, under appropriate conditions, it may permit an estimate of the meson-neutron scattering cross section from the directly observable hydrogen and deuterium cross sections. The theoretical background for such a calculation has already been given by Chew,[1] who has treated the very similar but more complicated problem of the scattering of neutrons by deuterium.

The starting point in the calculation is the use of the impulse approximation, in which one assumes that the incident particle is scattered by a free nucleon wave packet whose momentum distribution is the same as that of one or the other of the bound nucleons. Then, following Chew, one argues that the contribution of each nucleon to the scattering amplitude is given, to a good approximation, by the product of the free particle scattering amplitude and an overlap integral which depends on the initial and final wave functions. One may simplify the calculation of the differential cross section by integrating it over the relative coordinates of the outgoing nucleons, thus considering only the scattering angle of the meson as the quantity to be observed. Then, according to the arguments of Gluckstern and Bethe,[2] one can use plane waves for the wave functions in the final state. The differential cross section for the scattering of a meson into the solid angle $d\Omega$, situated about the laboratory scattering angle θ, may then be written:

$$\frac{d\sigma}{d\Omega}(\theta)=\left[\frac{d\sigma_p}{d\Omega}(\theta)+\frac{d\sigma_n}{d\Omega}(\theta)\right]H_1(\theta)+2\cos\omega\left(\frac{d\sigma_p}{d\Omega}\frac{d\sigma_n}{d\Omega}\right)^{\frac{1}{2}}H_2(\theta), \quad (1)$$

where $d\sigma_p(\theta)/d\Omega$ and $d\sigma_n(\theta)/d\Omega$ are the free particle cross sections, $\cos\omega$ is an unknown phase factor, and the weighting factors $H_1(\theta)$ and $H_2(\theta)$ are defined by

$$H_1(\theta)=(1/J_0)\int d\mathbf{k}J(\mathbf{k})\phi_D^2[\mathbf{k}+\tfrac{1}{2}(\mathbf{q}(\mathbf{k})-\mathbf{q}_0)],$$

$$H_2(\theta)=(1/J_0)\int d\mathbf{k}J(\mathbf{k})\phi_D[\mathbf{k}+\tfrac{1}{2}(\mathbf{q}(\mathbf{k})-\mathbf{q}_0)]\times\phi_D[\mathbf{k}-\tfrac{1}{2}(\mathbf{q}(\mathbf{k})-\mathbf{q}_0)]. \quad (2)$$

In Eq. (2), $\mathbf{q}_0$ and $\mathbf{q}(\mathbf{k})$ are the momenta of the incident and outgoing mesons, respectively, $\mathbf{k}$ is the relative momentum of the outgoing nucleons, ϕ_D is the fourier transform of the deuteron wave function; $J(\mathbf{k})$ is the volume of momentum space available to the scattered meson, and J_0 is the corresponding quantity for scattering by free particles. The integrations are to be extended over all values of $\mathbf{k}$ compatible with energy conservation.

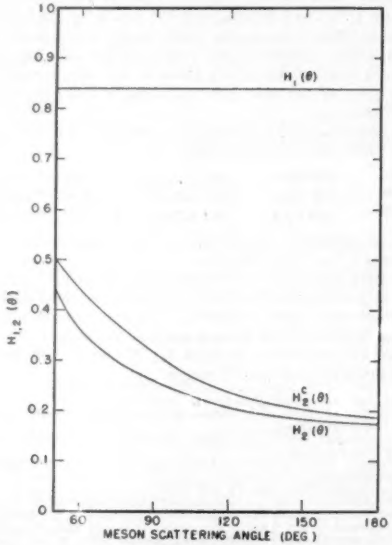

FIG. 1. Free particle and correlation term weighting factors for $\pi-D$ scattering.

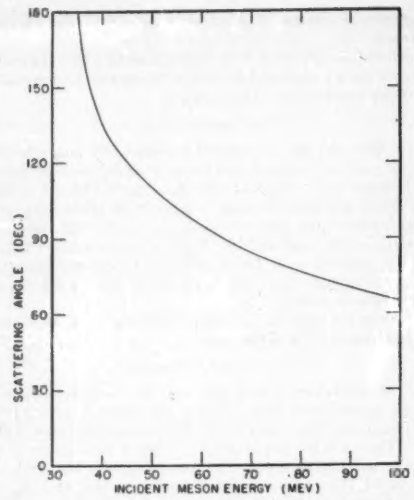

FIG. 2. Meson scattering angle beyond which correlation term is small.

Equation (1) should best approximate the differential cross section for high meson energies and large scattering angles. In Fig. 1 we have plotted $H_1(\theta)$ and $H_2(\theta)$ for 70-Mev incident mesons and for scattering angles greater than 50 degrees.

One may obtain another approximate expression for the differential cross section, this one being best for small scattering angles, by neglecting the restriction imposed on $\mathbf{q}(\mathbf{k})$ by energy conservation. If one replaces $\mathbf{q}(\mathbf{k})$ and $J(\mathbf{k})$ by appropriate average values and integrates over all $\mathbf{k}$-space, there results the closure approximation, for which

$$H_1^c(\theta)=1, \quad H_2^c(\theta)=\langle\sin|\mathbf{q}-\mathbf{q}_0|r/|\mathbf{q}-\mathbf{q}_0|r\rangle_{Av}. \quad (3)$$

In Eq. (3), $\mathbf{q}$ is defined, for a given angle θ, by the free particle energy-momentum conservation laws, while the average is taken over the square of the deuteron wave function. As θ increases, $H_2^c(\theta)$ decreases from its initial value, unity. For purposes of comparison with the plane wave approximation, we have plotted $H_2^c(\theta)$ in Fig. 1. One sees that the two approximations give values of $H_1(\theta)$ and $H_2(\theta)$ which agree to within 15 percent. This indicates that the readily applied closure approximation may be used with some justification for the discussion of the cross section at other meson energies. On this basis we have calculated, for various incident meson energies, the scattering angle beyond which the correlation effects will be small. As a criterion of smallness we have taken $H_2^c(\theta)<\frac{1}{2}H_1^c(\theta)$. The results are shown in Fig. 2. They are of interest, since they indicate under which experimental conditions one might estimate the meson-neutron cross section without a knowledge of the phase factor $\cos\omega$.

* This work was performed under the auspices of the AEC.
[1] G. F. Chew, Phys. Rev. **80**, 196 (1950).
[2] R. L. Gluckstern and H. A. Bethe, Phys. Rev. **81**, 761 (1951).

Scintillation Studies of Os^{185}

MAURICE M. MILLER AND ROGER G. WILKINSON
*Department of Physics, Indiana University, Bloomington, Indiana**
(Received April 19, 1951)

THE γ- and x-radiations following K-capture in Os^{185} have been investigated by means of a single-crystal scintillation spectrometer. NaI(Tl) crystals were employed in conjunction with either an EMI 5311 or RCA 5819 photomultiplier tube. Pulse amplification was furnished by a model 100 amplifier and cathode-follower preamp. A conventional single-channel differential discriminator was used for the pulse height analysis. The source was the one investigated by Bunker, Canada, and Mitchell[1] a year earlier in a magnetic lens spectrometer.

For the γ-ray measurements a small (1-cm cube) crystal of NaI(Tl) was used in order to minimize secondary events which contribute to abnormally large photopeaks. The photoelectron spectrum (Fig. 1) shows two peaks, 0.65 ± 0.01 and 0.88 ± 0.01 Mev, the scale having been calibrated with the 0.661-Mev radiation of Cs^{137}. The dotted line is the Compton distribution expected of the higher energy γ-ray. A comparison of true areas under the two photopeaks shows the lower energy γ-ray to be 6.1 times as intense as the higher energy one, due account being taken for the variation of the photoelectric cross section. The energy and intensity measurements are in essential agreement with those of Bunker, Canada, and Mitchell.

For the x-ray measurements a few milligrams of the source material were placed directly on a 0.1-cm wafer of NaI(Tl). Peaks were found at 60 kev, 26 kev, and then, with the gain increased by a factor of 6, at 10 kev (Fig. 2). The 60-kev line is interpreted as essentially due to K-L radiation following K capture with some admixture of the higher energy K-M radiation. The 26-kev line is the "escape" peak[2] of the 60-kev K radiation. The 10-kev line is considered to be due to L-M radiation following either K or possible L capture.

The K radiation and the 0.65-Mev photopeak were obtained on the same discriminator run and an intensity comparison was made. For this type of measurement, crystals of 0.5-cm and 0.8-cm thickness were used with a mica sheet (10 mg/cm^2) interposed between source and detector to absorb Auger electrons. The fluorescent yield of the Re($Z=75$) K radiation was taken to be 90 percent,[3] and the efficiencies of the two thicknesses of crystals for photoproduction were calculated for 0.65 Mev. The K radiation detection efficiency was assumed 100 percent, since the area of the escape peak was included in the K intensity measurement. The results for each thickness crystal show that the K radiation amounts to 100 ± 10 percent of the sum of the intensities of the 0.65-Mev and 0.88-Mev γ-rays. If one neglects the possibility of L capture feeding the excited states, the K capture to the ground state takes place in 10 percent or less of the total number of disintegrations.

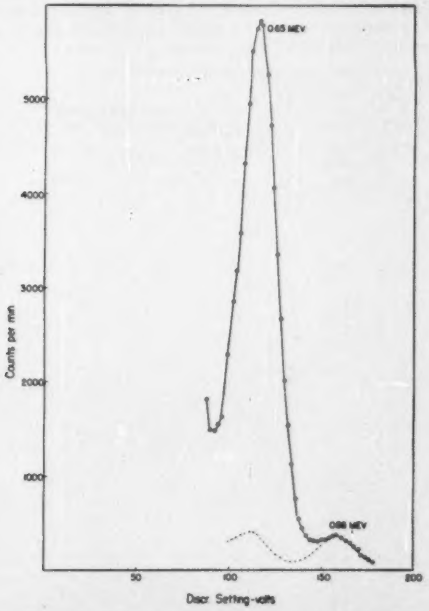

FIG. 1. Photopeaks from the gamma-rays of Os^{185}. Dotted line is pulse-height distribution expected if only the 0.88-Mev radiation is present.

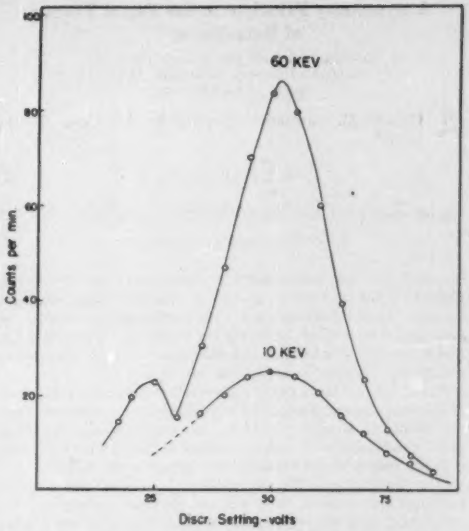

FIG. 2. The x-rays of Os^{185}. The 10-kev run was taken with 6 times the amplifier gain of the upper curve. Multiply ordinate by 128 in each case.

Recent empirical shell model evidence[4] would assign to the ground state of Re^{185} a $d_{5/2}$ characterization or possibly $g_{7/2}$ owing to the filling in of the $h_{11/2}$ shell by protons 66 to 74. Similar "hiding" in the $i_{13/2}$ level would probably place the 109th neutron of $_{76}Os^{185}$ in an $f_{7/2}$ state. This suggests that a K capture to the ground state of Re^{185} involves a parity change ($\Delta L=1$) and $\Delta I=0$ or 1, which points to a first-forbidden transition with $\log(ft)$ in the range 6.5 to 7.5.[5] The energy available for such a transition, while certainly larger than 0.88 Mev, would not be much larger than $2m_0c^2$, since no positrons were found in the course of the spectroscopic investigation. $\log(ft)$ would then be about 7.8, bearing out the experimental supposition of a forbidden character for the ground state K capture.

It would seem from this experiment that relative intensities of gamma-rays can be measured by scintillation counter methods with at least the accuracy of ordinary spectrometer measurements; and, in addition, x-rays down to 10 kev can be studied. These properties make the scintillation spectrometer a promising instrument for the quantitative study of disintegration schemes which result from K and L capture.

* This work was assisted by the joint program of the ONR and AEC.
[1] Bunker, Canada, and Mitchell, Phys. Rev. **79**, 610 (1950).
[2] The presence of such "escape" peaks has been explained by West, Meyerhof, and Hofstadter, Phys. Rev. **81**, 141 (1951).
[3] The fluorescent yield was found from a semi-empirical relation pointed out by Steffen, Huber, and Humbel, Helv. Phys. Acta **22**, 167 (1949).
[4] Maria Goeppert Mayer, Phys. Rev. **78**, 16 (1950).
[5] L. W. Nordheim, Phys. Rev. **78**, 294 (1950).

A Symmetry Principle in the Fermi Theory of Beta-Decay*

GEORGE L. TRIGG† AND EUGENE FEENBERG
Washington University, Saint Louis, Missouri
(Received April 19, 1951)

A GENERAL interaction operator for beta-decay in the form[1,2]

$$V=G\sum_{k=1}^{5}[C_kV_k+C_k^*V_k^*] \tag{1}$$

can be constructed from the five invariant operators

$$V_k=\sum_l Q_l\,{}^k\Omega_l(\psi^*(-)\,{}^k\Omega\phi(-))_l \tag{2}$$

in which Q_l is a displacement operator acting on the charge variable of the lth nucleon, $\psi(-)$ is a quantized wave amplitude for negative electrons, and $\phi(-)$ the corresponding quantity for neutrinos. The symbols ${}^k\Omega$ denote the scalar (1), polar vector (2), tensor (3), axial vector (4), and pseudoscalar (5) type operators constructed from products of Dirac matrices.

In a theory containing only one invariant operator V_k the phase of the coupling constant C_k has no physical consequences. Conventionally C_k is taken real.[1,3] In the general theory containing linear combinations the relative phases of the C_k's enter directly into the transition probabilities and influence the half-lives and energy distributions. The conventional choice of real coupling constants then appears to be without physical justification.[3] We report here on some consequences of permitting arbitrary relative phases. The recent paper by De Groot and Tolhoek should be consulted for background and details of calculation.

In the approximation which neglects the distortion of the electron wave functions by the coulomb field of the nucleus the allowed transition probability for $\beta^{\pm}$ emission per unit energy range and unit time is simply

$$P_{\pm}(E)=(1/2\pi^3)pE(E-E_0)^2G^2\Big[(|C_1|^2+|C_2|^2)\Big|\int 1\Big|^2 +(|C_2|^2+|C_1|^2)\Big|\int\sigma\Big|^2\mp(1/E)\Big\{(C_1C_2^*+C_1^*C_2)\Big|\int 1\Big|^2 +(C_3C_4^*+C_3^*C_4)\Big|\int\sigma\Big|^2\Big\}\Big]. \tag{3}$$

Existing measurements place a fairly small upper limit on the ratio of cross to diagonal terms. The cross terms vanish if

$$\begin{aligned}C_1C_2^*+C_1^*C_2&=0,\\ C_3C_4^*+C_3^*C_4&=0.\end{aligned} \tag{4}$$

In the same way, assuming real coupling constants, De Groot and Tolhoek obtain $C_1C_2=C_3C_4=0$. These drastic conditions appear as highly singular special cases in the context of complex coupling constants.

Equation (4) is also a consequence of the symmetry principle introduced by De Groot and Tolhoek. These authors postulate that transition probabilities for positron and negatron emission have the same form when effects produced by the coulomb field of the nucleus are neglected. From the postulate they obtain either $C_1=C_4=C_5=0$ or $C_2=C_3=0$.

In the usual representation of the Dirac matrices the operator for charge conjugation is $\mathcal{C}=i\beta\alpha_y$. Wave amplitudes for positively charged particles are provided by the operation of charge conjugation applied to $\psi(-)$ and $\phi(-)$: i.e.,

$$\psi(+)=\mathcal{C}\bar{\psi}(-),\quad \phi(+)=\mathcal{C}\bar{\phi}(-), \tag{5}$$

the bar denoting a Dirac function identical with the starred quantity except that it is written as a four element column vector. Similarly a bar on Ω replaces each element by its conjugate complex (transpose of $\Omega^\dagger$). It is then possible to write

$$\begin{aligned}V_k^*&=\sum_l Q_l{}^\dagger\,{}^k\Omega_l{}^\dagger(\bar{\psi}^*(-)\,{}^k\bar{\Omega}\bar{\phi}(-))_l\\ &=\sum_l Q_l{}^\dagger\,{}^k\Omega_l{}^\dagger(\psi^*(+)\mathcal{C}\,{}^k\mathcal{C}\bar{\Omega}\phi(+))_l\\ &=\epsilon_k\sum Q_l{}^\dagger\,{}^k\Omega_l(\psi^*(+)\,{}^k\Omega\phi(+))_l\end{aligned} \tag{6}$$

with $\epsilon_1=\epsilon_4=\epsilon_5=-1$, $\epsilon_2=\epsilon_3=1$.[2,4] Except for a numerical factor and the appearance of $Q^\dagger$ in place of Q, V_k^* is the same functional of $\psi^*(+)$ and $\phi(+)$ as V_k is of $\psi^*(-)$ and $\phi(-)$. Now, restating the postulate of De Groot and Tolhoek, we ask for conditions on the coupling constants required to insure the relation[5]

$$P_+(E,Z)=P_-(E,-Z) \tag{7}$$

in all orders. These conditions are

$$\epsilon_kC_k^*=e^{i\theta}C_k,\quad k=1,2,3,4,5, \tag{8}$$

with θ an arbitrary phase. Equation (4) is a consequence of Eq. (8). Choosing $\theta=\pi$ for convenience, C_1, C_4, and C_5 are real numbers while C_2 and C_3 are pure imaginary. The antisymmetric interaction of Critchfield and Wigner[6] is a special case, with C_1, C_4, and C_5 assigned particular values and $C_2=C_3=0$.

* Assisted by the joint program of the ONR and AEC.
† AEC Predoctoral Fellow.
[1] M. Fierz, Z. Physik **104**, 553 (1937).
[2] S. R. De Groot and H. A. Tolhoek, Physica **16**, 456 (1950).
[3] We are indebted to Dr. Fierz for a communication on this point.
[4] W. H. Furry, Phys. Rev. **51**, 125 (1937).
[5] Between a given pair of nuclear states.
[6] C. L. Critchfield, Phys. Rev. **63**, 417 (1943).